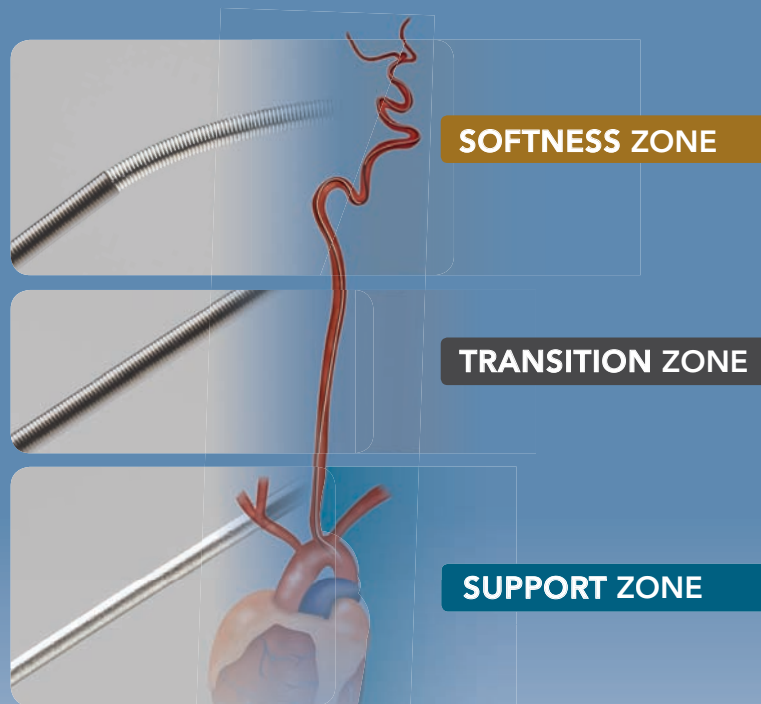


Advanced

by MicroVention



ENHANCED CONTROL TO MAXIMIZE COIL PERFORMANCE

The **V-Trak® Advanced Coil System**, the next generation to power the performance of our most technically advanced line of coils. Offering the optimal combination of support and flexibility.

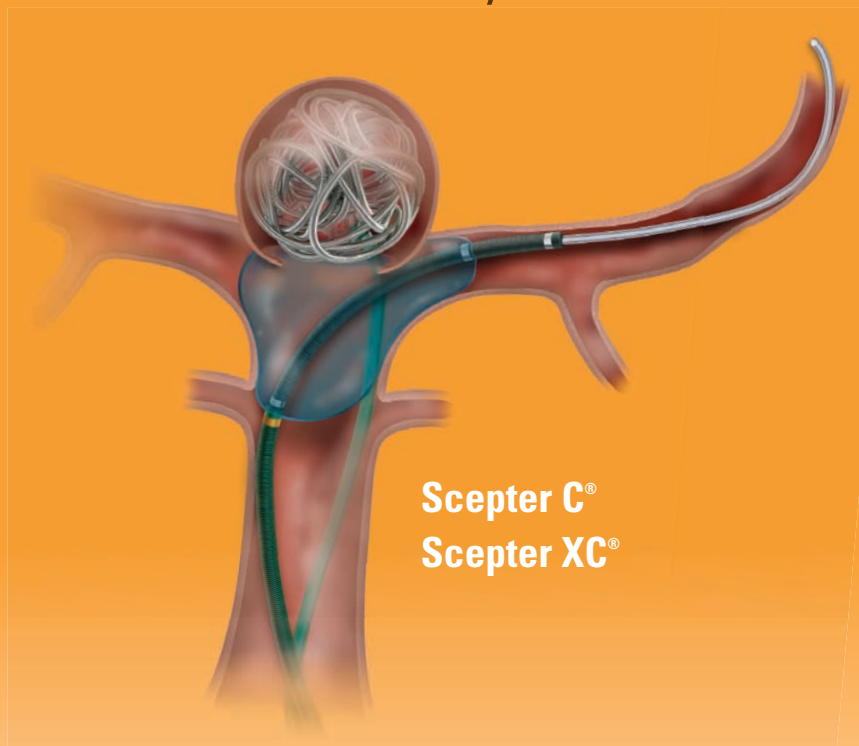
microvention.com

MICROVENTION, V-Trak, Scepter C, Scepter XC and Headway are registered trademarks of MicroVention, Inc. Scientific and clinical data related to this document are on file at MicroVention, Inc. Refer to Instructions for Use, contraindications and warnings for additional information. Federal (USA) law restricts this device for sale by or on the order of a physician. © 2015 MicroVention, Inc. 5/15

CE
0297

Versatility

by MicroVention



Scepter C®
Scepter XC®

Scepter
Occlusion Balloon
Catheter

REDEFINING DELIVERABILITY, VERSATILITY AND CONTROL

MicroVention has developed two occlusion balloon catheters. **Scepter C®** compliant balloon is designed for reliable vessel occlusion yet conforms to vessel anatomy. **Scepter XC®** x-tra compliant balloon conforms to extremely complex anatomies where neck coverage is more challenging.

• Used with



For more information or a product demonstration,
contact your local MicroVention representative:



MicroVention, Inc.

Worldwide Headquarters

1311 Valencia Avenue

Tustin, CA 92780 USA

MicroVention UK Limited

MicroVention Europe, S.A.R.L.

MicroVention Deutschland GmbH

PH +1.714.247.8000

PH +44 (0) 191 258 6777

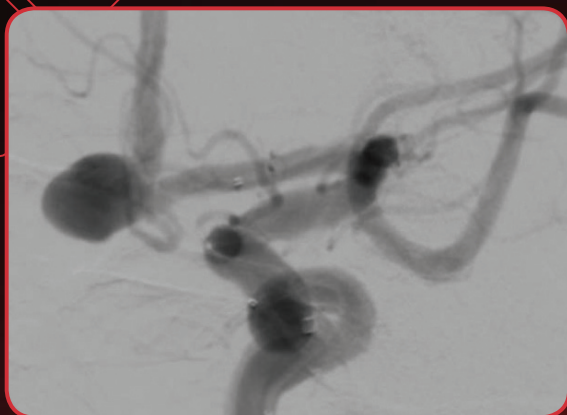
PH +33 (1) 39 21 77 46

PH +49 211 210 798-0

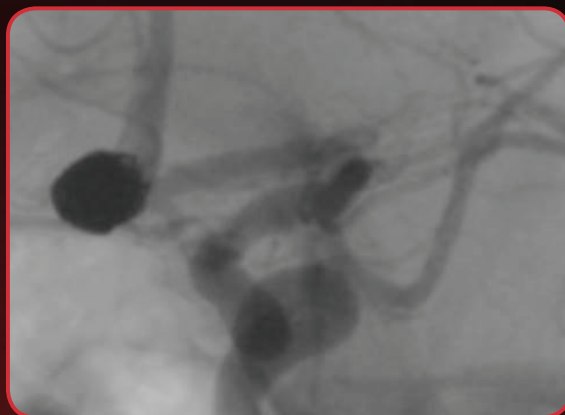
BARRICADE™ COIL SYSTEM

COILS THAT PERFORM

STENT ASSISTED COILING OF LEFT ACA ANEURYSM WITH THE BARRICADE COIL SYSTEM



PRE-TREATMENT



POST TREATMENT

“In this tortuous system, the Barricade coils were stable and conforming without issues of catheter kickback, even when working close to the neck, and they filled in the margins of neck very well.”

-Gary R. Duckwiler, M.D.

COILS THAT SAVE \$

BARRICADE
COILS
SAVED
\$17,900*

Images courtesy of Gary R. Duckwiler, M.D.

* Estimated savings in this case, data on file.

The Barricade Coil System is intended for the endovascular embolization of intracranial aneurysms and other neurovascular abnormalities such as arteriovenous malformations and arteriovenous fistulae. The System is also intended for vascular occlusion of blood vessels within the neurovascular system to permanently obstruct blood flow to an aneurysm or other vascular malformation and for arterial and venous embolizations in the peripheral vasculature. Refer to the instructions for use for complete product information.

18 TECHNOLOGY DRIVE #169, IRVINE CA 92618 | p: 949.788.1443 | f: 949.788.1444
WWW.BLOCKADEMEDICAL.COM

MKTG-045 Rev. A





The brain at your fingertips

 **Rapid Medical**

www.rapid-medical.com > [comaneci](#)



Navigate... Ablate... Palliate

The STAR™ Tumor Ablation System is the proven leader in spine RF ablation with thousands of patients treated.



Steerable and navigational
RF ablation instrument



Dual thermocouples for
active temperature monitoring
on a single instrument



Compatibility with StabiliT®
when augmentation
indicated

STAR Clinical Studies Demonstrate¹⁻⁴:

- Fast, durable pain relief
- Rapid improvement in mobility and quality of life
- Reduction or discontinuation of pain medication
- Site-specific ablation zones and real time temperature monitoring
- May be combined with radiation and/or chemotherapy

To learn more please visit our website at
www.dfineinc.com or call 866.963.3463



DFINE®

Targeted Vertebral Solutions

Indications for Use: The STAR™ Tumor Ablation System is indicated for palliative treatment in spinal procedures by ablation of metastatic malignant lesions in a vertebral body. As with most surgical procedures, there are risks associated with the STAR procedure, including serious complications. For complete information regarding risks, contraindications, warnings, precautions, and adverse events please review the System's Instructions for Use.

¹ Pain Physician 2014 Jul-Aug; 17(4):317-27 ² Radiology 2014 Oct; 273 (1): 261-7 ³ J. Vasc Interv Radiol 2015; 18: 573-581 ⁴ Pain Physician 2015; 18: 573-581



ASFNR • ASHNR • ASPNR • ASSR • SNIS

THE FOUNDATION OF THE ASNR




WASHINGTON MARRIOTT WARDMAN PARK • WASHINGTON, DC

**THE FOUNDATION OF THE
ASNR SYMPOSIUM 2016:
EMERGENCY NEURORADIOLOGY
MAY 21-22**

**ASNR 54TH ANNUAL MEETING
MAY 23-26**



THE FOUNDATION OF THE ASNR SYMPOSIUM 2016: EMERGENCY NEURORADIOLOGY Symposium 2016:

- Features world-renowned speakers providing a comprehensive review of Emergency Neuroradiology and neuroimaging issues in critical care.
- Highlighting Neuroimaging as an indispensable tool for triage and management of both adults and children in emergency settings.
- Review of efficient and appropriate use of CT and MRI that are critical to the urgent management of brain, spine, head & neck, and neurovascular emergencies, all of which will be highlighted by expert faculty.
- Review best practices for traumatic and non-traumatic emergencies, including methods to ensure optimal workflow, image post-processing, PACS integration, telemedicine, safety, and quality.
- Includes discussions of challenges and solutions for providing 24/7 coverage that will be presented and debated.
-  Closing Reception of The Foundation of The ASNR Symposium with a performance by the comedy troupe, Capitol Steps.

ASNR 54TH ANNUAL MEETING:

- Focused programming on the latest products and services to deliver the highest quality care in the realm of Neuroradiology and allied professions.
- Informative updates on general Neuroradiology showcasing specialty programming from the ASFNR, ASHNR, ASPNR, ASSR, and SNIS.
- Concurrent lectures, original presentations, scientific posters and educational exhibits throughout the week.
- Welcome Reception with Technical Exhibitors featuring ASNR physician members jazz quartet entertainment.

**Howard A. Rowley, MD,
ASNR 2016 Program Chair/President-Elect
Programming developed in cooperation with ...**

American Society of Functional Neuroradiology (ASFNR)
Christopher G. Filippi, MD

American Society of Head and Neck Radiology (ASHNR)
Lindell R. Gentry, MD

American Society of Pediatric Neuroradiology (ASPNR)
Erin Simon Schwartz, MD

American Society of Spine Radiology (ASSR)
Gregory J. Lawler, MD

Society of NeuroInterventional Surgery (SNIS)
Charles J. Prestigiacomo, MD

American Society of Neuroradiology (ASNR) Committee Programming:

Health Policy Committee
Robert M. Barr, MD, FACR

Computer Science and Informatics (CSI) Committee
John L. Go, MD, FACR

Research Scientists Committee
Dikoma C. Shungu, PhD and Timothy P.L. Roberts, PhD

ASNR 54TH ANNUAL MEETING

c/o American Society of Neuroradiology
800 Enterprise Drive, Suite 205
Oak Brook, Illinois 60523-4216
Phone: 630-574-0220
Fax: 630 574-0661
www.asnr.org/2016

**SCAN NOW
TO VISIT
OUR WEBSITE**



Smooth and stable.

Target Detachable Coils deliver consistently smooth deployment and exceptional microcatheter stability. Designed to work seamlessly together for framing, filling and finishing. Target Coils deliver the high performance you demand.

For more information, please visit www.strykerneurovascular.com/Target or contact your local Stryker Neurovascular sales representative.



Target[®]
DETACHABLE COILS

2015 LUCIEN LEVY BEST RESEARCH ARTICLE

Other nominated papers were:

“Responses of the Human Brain to Mild Dehydration and Rehydration Explored In Vivo by ¹H-MR Imaging and Spectroscopy” by A. Biller, M. Reuter, B. Patenaude, G.A. Homola, F. Breuer, M. Bendszus, and A.J. Bartsch

“Wall Mechanical Properties and Hemodynamics of Unruptured Intracranial Aneurysms” by J.R. Cebral, X. Duan, B.J. Chung, C. Putman, K. Aziz, and A.M. Robertson

“MR Elastography Demonstrates Increased Brain Stiffness in Normal Pressure Hydrocephalus” by N. Fattahi, A. Arani, A. Perry, F. Meyer, A. Manduca, K. Glaser, M.L. Senjem, R.L. Ehman, and J. Huston

“Outcomes Are Not Different between Patients with Intermediate and High DWI-ASPECTS after Stent-Retriever Embolectomy for Acute Anterior Circulation Stroke” by S.K. Kim, W. Yoon, M.S. Park, T.W. Heo, B.H. Baek, and Y.Y. Lee

“Comparison of Inner Ear Contrast Enhancement among Patients with Unilateral Inner Ear Symptoms in MR Images Obtained 10 Minutes and 4 Hours after Gadolinium Injection” by T.Y. Kim, D.W. Park, Y.J. Lee, J.Y. Lee, S.H. Lee, J.H. Chung, and S. Lee

“MR Imaging Characteristics of Wingless-Type-Subgroup Pediatric Medulloblastoma” by Z. Patay, L.A. DeSain, S.N. Hwang, A. Coan, Y. Li, and D.W. Ellison

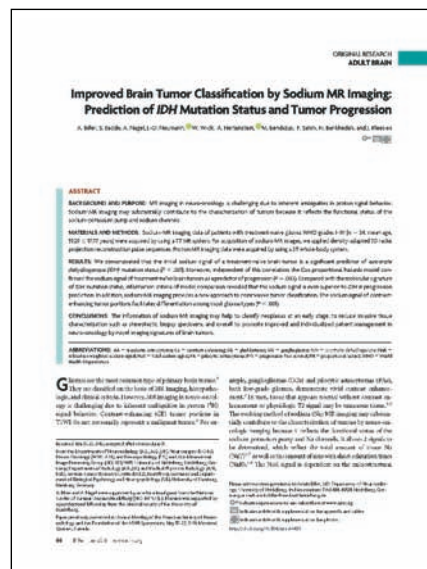
AWARD WINNER AND NOMINEES

The Editors of *AJNR* are pleased to announce the annual Lucien Levy Best Research Article Award has been presented to

“Improved Brain Tumor Classification by Sodium MR Imaging: Prediction of IDH Mutation Status and Tumor Progression”

by A. Biller, S. Badde, A. Nagel, J.-O. Neumann, W. Wick, A. Hertenstein, M. Bendszus, F. Sahm, N. Benkhedah, and J. Kleesiek

This award is named for the late *AJNR* Senior Editor who championed its establishment and recognizes the best original research paper accepted in 2015. The winning paper, submitted by authors from the University of Heidelberg, German Cancer Research Centre, and University of Hamburg, was published electronically on October 22, 2015 and appeared in the January 2016 print issue. It was selected by a vote of the Journal's Editor-in-Chief and Senior Editors.





AMA Preferred Provider Offers and Services



AMA Preferred Provider Offers and Services

Special offers that fit you and your practice's needs.

Which savings would benefit you the most? Discounts on pharmaceuticals, medical supplies and equipment? Or on travel, practice financing, and financial and insurance services? Now physicians can save in all of these professional and personal categories and more through the AMA Preferred Provider Offers and Services program.

Please activate your 2016 AMA membership by calling **(800) 262-3211** or visit **ama-assn.org/go/join**.



* Subsidiary of the American Medical Association.

Go Green!

AJNR urges American Society of Neuroradiology members to reduce their environmental footprint by voluntarily suspending their print subscription.

The savings in paper, printing, transportation, and postage not only help members cut down on clutter, but go to fund new electronic enhancements and expanded content.

The digital edition of *AJNR* presents the print version in its entirety, along with extra features including:

- Publication Preview
- Case of the Week
- Podcasts
- Special Collections
- The *AJNR* Blog
- Weekly Poll

It also **reaches subscribers much faster than print**. An **electronic table of contents** will be sent directly to your mailbox to notify you as soon as it publishes.

Readers can **search, reference, and bookmark** current and archived content 24 hours a day on www.ajnr.org, rather than thumb through stacks of accumulated paper issues for articles and images they need.



<http://www.ajnr.org/cgi/feedback>

ASNR members who wish to opt out of print can do so by using the Feedback form on the *AJNR* Website (<http://www.ajnr.org/cgi/feedback>). Just type "Go Green" in the subject line to stop print and spare our ecosystem.

MODERN IMAGING AND RADIATION THERAPY:

APPROPRIATE, COLLABORATIVE AND TARGETED

67th ANNUAL SCIENTIFIC MEETING | GOLD COAST, AUSTRALIA



RANZCR 2016
ranzcr2016.com

KEYNOTE SPEAKERS

Radiology

Dr Russell Fritz

National Orthopedic Imaging Associates
San Francisco, USA

Professor Fiona Gilbert

Cambridge University Hospitals
Cambridge, UK

Professor Meng Law

University of Southern California
Los Angeles, USA

Dr Claude Sirlin

University of California
San Diego, USA

Radiation Oncology

Dr Silvia Formenti

New York Presbyterian Hospital
New York, USA

Professor William Mendenhall

University of Florida
Florida, USA

Dr Colleen Lawton

Medical College of Wisconsin
Wisconsin, USA

KEY DATES

Submit Your Abstract Now

ranzcr2016.com/abstract-information

Call for Abstracts Close

April 2016

Registrations Open

April 2016

Details published are correct at the time of design and are subject to change without notice.
For up to date information please visit ranzcr2016.com

INTERESTED IN SPONSORING AND/OR EXHIBITING?

Contact Helen McGowan at Helen@wsm.com.au or +61 3 9645 6311



13 – 16 OCTOBER 2016

GOLD COAST CONVENTION & EXHIBITION CENTRE

ranzcr2016.com



Simplify the MOC Process



Manage your CME Credits Online

CMEgateway.org

It's Easy and Free!

Log on to CME Gateway to:

- View or print reports of your CME credits from multiple societies from a single access point.
- Print an aggregated report or certificate from each participating organization.
- Link to SAMs and other tools to help with maintenance of certification.

American Board of Radiology (ABR) participation!

By activating ABR in your organizational profile, your MOC-fulfilling CME and SAM credits can be transferred to your own personalized database on the ABR Web site.

Sign Up Today!

go to CMEgateway.org

Available to Members of Participating Societies

American Board of Radiology (ABR)	Radiological Society of North America (RSNA)
American College of Radiology (ACR)	Society of Interventional Radiology (SIR)
American Roentgen Ray Society (ARRS)	SNM
American Society of Neuroradiology (ASNR)	The Society for Pediatric Radiology (SPR)
Commission on Accreditation of Medical Physics Educational Programs, Inc. (CAMPEP)	

50th Annual Meeting

American Society of
Head & Neck Radiology
Comprehensive Head and Neck Imaging:
50 Years of Progress



September 7 - 11, 2016

Hyatt Regency Washington on Capitol Hill
Washington, DC

29.25 AMA PRA Category 1 Credit(s)[™]

Certain sessions of the meeting program
will be submitted for SAM qualification.

Hands-on US and US-Guided Biopsy Seminar
Saturday, September 10, 2016

Separate Registration Required

Registration is Limited to 20 Attendees Per Session.

Not accredited for AMA PRA Category 1 Credit(s)[™]

For More Information, visit www.ashnr.org

Target® Detachable Coil

See package insert for complete indications, contraindications, warnings and instructions for use.

INTENDED USE / INDICATIONS FOR USE

Target Detachable Coils are intended to endovascularly obstruct or occlude blood flow in vascular abnormalities of the neurovascular and peripheral vessels.

Target Detachable Coils are indicated for endovascular embolization of:

- Intracranial aneurysms
- Other neurovascular abnormalities such as arteriovenous malformations and arteriovenous fistulae
- Arterial and venous embolizations in the peripheral vasculature

CONTRAINDICATIONS

None known.

POTENTIAL ADVERSE EVENTS

Potential complications include, but are not limited to: allergic reaction, aneurysm perforation and rupture, arrhythmia, death, edema, embolus, headache, hemorrhage, infection, ischemia, neurological/intracranial sequelae, post-embolization syndrome (fever, increased white blood cell count, discomfort), TIA/stroke, vasospasm, vessel occlusion or closure, vessel perforation, dissection, trauma or damage, vessel rupture, vessel thrombosis. Other procedural complications including but not limited to: anesthetic and contrast media risks, hypotension, hypertension, access site complications.

WARNINGS

- Contents supplied STERILE using an ethylene oxide (EO) process. Do not use if sterile barrier is damaged. If damage is found, call your Stryker Neurovascular representative.
- For single use only. Do not reuse, reprocess or sterilize. Reuse, reprocessing or sterilization may compromise the structural integrity of the device and/or lead to device failure which, in turn, may result in patient injury, illness or death. Reuse, reprocessing or sterilization may also create a risk of contamination of the device and/or cause patient infection or cross-infection, including, but not limited to, the transmission of infectious disease(s) from one patient to another. Contamination of the device may lead to injury, illness or death of the patient.

- After use, dispose of product and packaging in accordance with hospital, administrative and/or local government policy.
- **This device should only be used by physicians who have received appropriate training in interventional neuroradiology or interventional radiology and preclinical training on the use of this device as established by Stryker Neurovascular.**
- Patients with hypersensitivity to 316LVM stainless steel may suffer an allergic reaction to this implant.
- MR temperature testing was not conducted in peripheral vasculature, arteriovenous malformations or fistulae models.
- The safety and performance characteristics of the Target Detachable Coil System (Target Detachable Coils, InZone Detachment Systems, delivery systems and accessories) have not been demonstrated with other manufacturer's devices (whether coils, coil delivery devices, coil detachment systems, catheters, guidewires, and/or other accessories). Due to the potential incompatibility of non Stryker Neurovascular devices with the Target Detachable Coil System, the use of other manufacturer's device(s) with the Target Detachable Coil System is not recommended.
- To reduce risk of coil migration, the diameter of the first and second coil should never be less than the width of the ostium.
- In order to achieve optimal performance of the Target Detachable Coil System and to reduce the risk of thromboembolic complications, it is critical that a continuous infusion of appropriate flush solution be maintained between a) the femoral sheath and guiding catheter, b) the 2-tip microcatheter and guiding catheters, and c) the 2-tip microcatheter and Stryker Neurovascular guidewire and delivery wire. Continuous flush also reduces the potential for thrombus formation on, and crystallization of infusate around, the detachment zone of the Target Detachable Coil.
- Do not use the product after the "Use By" date specified on the package.
- Reuse of the flush port/dispenser coil or use with any coil other than the original coil may result in contamination of, or damage to, the coil.
- Utilization of damaged coils may affect coil delivery to, and stability inside, the vessel or aneurysm, possibly resulting in coil migration and/or stretching.

- The fluoro-saver marker is designed for use with a Rotating Hemostatic Valve (RHV). If used without an RHV, the distal end of the coil may be beyond the alignment marker when the fluoro-saver marker reaches the microcatheter hub.
 - If the fluoro-saver marker is not visible, do not advance the coil without fluoroscopy.
 - Do not rotate delivery wire during or after delivery of the coil. Rotating the Target Detachable Coil delivery wire may result in a stretched coil or premature detachment of the coil from the delivery wire, which could result in coil migration.
 - Verify there is no coil loop protrusion into the parent vessel after coil placement and prior to coil detachment. Coil loop protrusion after coil placement may result in thromboembolic events if the coil is detached.
 - Verify there is no movement of the coil after coil placement and prior to coil detachment. Movement of the coil after coil placement may indicate that the coil could migrate once it is detached.
 - Failure to properly close the RHV compression fitting over the delivery wire before attaching the InZone® Detachment System could result in coil movement, aneurysm rupture or vessel perforation.
 - Verify repeatedly that the distal shaft of the catheter is not under stress before detaching the Target Detachable Coil. Axial compression or tension forces could be stored in the 2-tip microcatheter causing the tip to move during coil delivery. Microcatheter tip movement could cause the aneurysm or vessel to rupture.
 - Advancing the delivery wire beyond the microcatheter tip once the coil has been detached involves risk of aneurysm or vessel perforation.
 - The long term effect of this product on extravascular tissues has not been established so care should be taken to retain this device in the intravascular space.
- Damaged delivery wires may cause detachment failures, vessel injury or unpredictable distal tip response during coil deployment. If a delivery wire is damaged at any point during the procedure, do not attempt to straighten or otherwise repair it. Do not proceed with deployment or detachment. Remove the entire coil and replace with undamaged product.
- After use, dispose of product and packaging in accordance with hospital, administrative and/or local government policy.

CAUTIONS / PRECAUTIONS

- Federal Law (USA) restricts this device to sale by or on the order of a physician.
- Besides the number of InZone Detachment System units needed to complete the case, there must be an extra InZone Detachment System unit as back up.
- Removing the delivery wire without grasping the introducer sheath and delivery wire together may result in the detachable coil sliding out of the introducer sheath.
- Failure to remove the introducer sheath after inserting the delivery wire into the RHV of the microcatheter will interrupt normal infusion of flush solution and allow back flow of blood into the microcatheter.
- Some low level overhead light near or adjacent to the patient is required to visualize the fluoro-saver marker; monitor light alone will not allow sufficient visualization of the fluoro-saver marker.
- Advance and retract the Target Detachable Coil carefully and smoothly without excessive force. If unusual friction is noticed, slowly withdraw the Target Detachable Coil and examine for damage. If damage is present, remove and use a new Target Detachable Coil. If friction or resistance is still noted, carefully remove the Target Detachable Coil and microcatheter and examine the microcatheter for damage.
- If it is necessary to reposition the Target Detachable Coil, verify under fluoroscopy that the coil moves with a one-to-one motion. If the coil does not move with a one-to-one motion or movement is difficult, the coil may have stretched and could possibly migrate or break. Gently remove both the coil and microcatheter and replace with new devices.
- Increased detachment times may occur when:
 - Other embolic agents are present.
 - Delivery wire and microcatheter markers are not properly aligned.
 - Thrombus is present on the coil detachment zone.
- Do not use detachment systems other than the InZone Detachment System.
- Increased detachment times may occur when delivery wire and microcatheter markers are not properly aligned.
- Do not use detachment systems other than the InZone Detachment System.



Stryker Neurovascular
47900 Bayside Parkway
Fremont, CA 94538

strykerneurovascular.com

Date of Release: MAR/2016

EX_EN_US

Copyright © 2016 Stryker
NV00018669.AA

AXS Catalyst™ 6 Distal Access Catheter

See package insert for complete indications, complications, warnings, and instructions for use.

INTENDED USE/INDICATIONS FOR USE

The AXS Catalyst Distal Access Catheter is indicated for use in facilitating the insertion and guidance of appropriately sized interventional devices into a selected blood vessel in the peripheral and neurovascular systems. The AXS Catalyst Distal Access Catheter is also indicated for use as a conduit for retrieval devices.

CONTRAINDICATIONS

None known.

ADVERSE EVENTS

Potential adverse events associated with the use of catheters or with the endovascular procedures include, but are not limited to: access site complications, allergic reaction, aneurysm perforation, aneurysm rupture, death, embolism (air, foreign body, plaque, thrombus), hematoma, hemorrhage, infection, ischemia, neurological deficits, pseudoaneurysm, stroke, transient ischemic attack, vasospasm, vessel dissection, vessel occlusion, vessel perforation, vessel rupture, and vessel thrombosis.

WARNING

Contents supplied sterile using an ethylene oxide (EO) process. Do not use if sterile barrier is damaged. If damage is found, call your Stryker Neurovascular representative. For single use only. Do not reuse, reprocess or sterilize. Reuse, reprocessing or sterilization may compromise the structural integrity of the device and/or lead to device failure which, in turn, may result in patient injury, illness or death. Reuse, reprocessing or sterilization may also create a risk of contamination of the device and/or cause patient infection or cross-infection, including, but not limited to, the transmission of infectious disease(s) from one patient to another.

Contamination of the device may lead to injury, illness or death of the patient. After use, dispose of product and packaging in accordance with hospital, administrative and/or local government policy.

- Limited testing has been performed with solutions such as contrast media, and saline. The use of these catheters for delivery of solutions other than the types that have been tested for compatibility is not recommended.
- Not intended for use with power injectors.
- If flow through catheter becomes restricted, do not attempt to clear catheter lumen by infusion. Doing so may cause catheter damage or patient injury. Remove and replace catheter.

- Never advance or withdraw an intravascular device against resistance until the cause of the resistance is determined by fluoroscopy. Movement of the device against resistance could dislodge a clot, perforate a vessel wall, or damage the device.

PRECAUTIONS

- Carefully inspect all devices prior to use. Verify size, length, and condition are suitable for the specific procedure. Do not use a device that has been damaged in any way. Damaged device may cause complications.
- To control the proper introduction, movement, positioning and removal of the catheter within the vascular system, users should employ standard clinical angiographic and fluoroscopic practices and techniques throughout the interventional procedure.
- Use the product prior to the "Use By" date printed on the label.
- To prevent thrombus formation and contrast media crystal formation, maintain a constant infusion of appropriate flush solution through catheter lumen.
- Torquing the catheter may cause damage which could result in kinking or separation of the catheter shaft.



Stryker Neurovascular
47900 Bayside Parkway
Fremont, CA 94538

strykerneurovascular.com

Date of Release: MAR/2016

EX_EN_US

Copyright © 2016 Stryker
NV00018756.AA

Success accelerated.

With superior trackability, resilient design and strong aspiration force, the AXS Catalyst™ 6 Distal Access Catheter is designed for fast access and rapid revascularization with Trevo® XP Retrievers.*†

*To facilitate revascularization with Trevo XP ProVue Retrievers.
†Bench test results. n=3 trackability, aspiration. n=1 kink resistance.
Bench test results may not necessarily be indicative of clinical performance.



AXS Catalyst™ 6

DISTAL ACCESS CATHETER



ENGINEERING STROKE SOLUTIONS

ACCLINO® flex Stent



HIGH FLEXIBILITY

- For microcatheters with 0.017" ID (Ø 3.5 and 4.5 mm) and 0.021" ID (Ø 6.5 mm)
- Repositionable up to 90 %

AJNR

AMERICAN JOURNAL OF NEURORADIOLOGY

APRIL 2016
VOLUME 37
NUMBER 4
WWW.AJNR.ORG

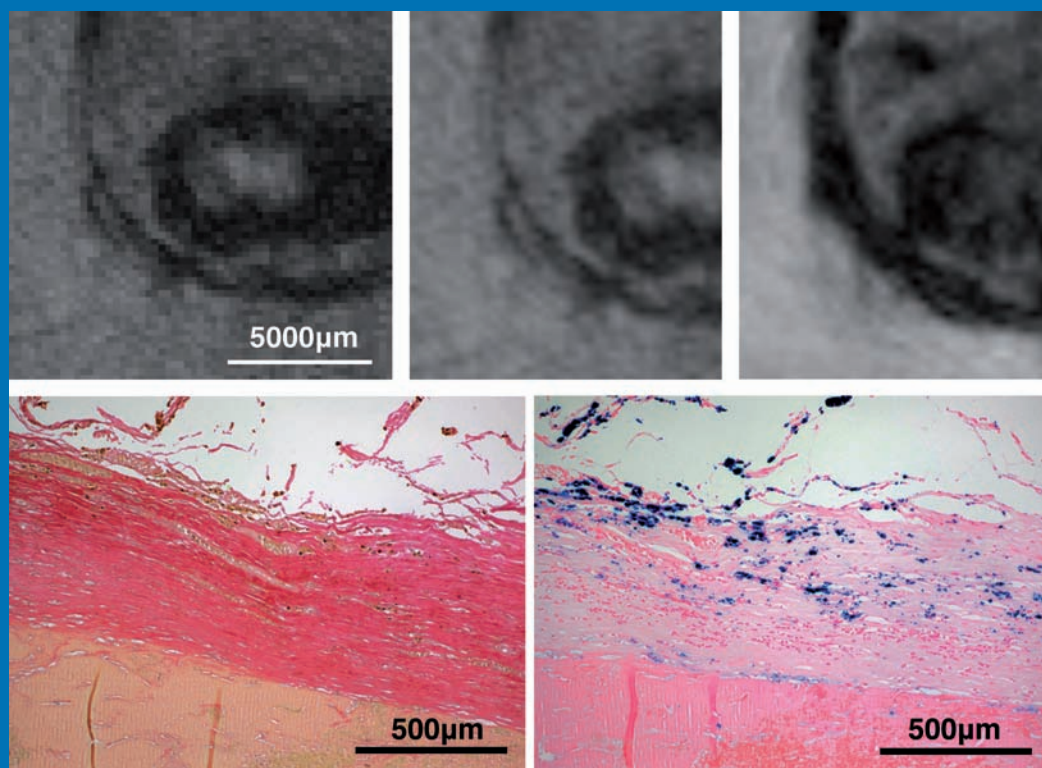
THE JOURNAL OF DIAGNOSTIC AND
INTERVENTIONAL NEURORADIOLOGY

Giant intracranial aneurysms at 7T

Dynamic contrast-enhanced MR in head and neck cancer

Volume-of-interest C-arm CT during endovascular treatment

Official Journal ASNR • ASFNR • ASHNR • ASPNR • ASSR



AJNR

AMERICAN JOURNAL OF NEURORADIOLOGY

APRIL 2016
VOLUME 37
NUMBER 4
WWW.AJNR.ORG

Publication Preview at www.ajnr.org features articles released in advance of print.
Visit www.ajnrblog.org to comment on AJNR content and chat with colleagues
and AJNR's News Digest at <http://ajnrdigest.org> to read the stories behind the
latest research in neuroimaging.

585 **PERSPECTIVES** A. Kapadia

EDITORIAL

586 **Current Evaluation of the Safety and Efficacy of Aneurysm Treatment with the WEB Device** L. Pierot, et al.

INTERVENTIONAL

REVIEW ARTICLE




 588 **Dynamic Contrast-Enhanced MR Imaging in Head and Neck Cancer: Techniques and Clinical Applications** S. Gaddikeri, et al.

HEAD & NECK

PRACTICE PERSPECTIVES

596 **ICD-10: History and Context** J.A. Hirsch, et al.

GENERAL CONTENTS

   600 **Clinical Applications of Simultaneous PET/MR Imaging Using (R)-[¹¹C]-Verapamil with Cyclosporin A: Preliminary Results on a Surrogate Marker of Drug-Resistant Epilepsy** J.-W. Shin, et al.

ADULT BRAIN

607 **Cortical Cerebral Blood Flow, Oxygen Extraction Fraction, and Metabolic Rate in Patients with Middle Cerebral Artery Stenosis or Acute Stroke** Z. Liu, et al.



ADULT BRAIN

 615 **Risk Factors for Growth of Intracranial Aneurysms: A Systematic Review and Meta-Analysis** W. Brinjikji, et al.

**ADULT BRAIN
INTERVENTIONAL**

    621 **Computational Identification of Tumor Anatomic Location Associated with Survival in 2 Large Cohorts of Human Primary Glioblastomas** T.T. Liu, et al.

ADULT BRAIN

  629 **Radiologic Features and Expression of Vascular Endothelial Growth Factor Stratify Survival Outcomes in Patients with Glioblastoma** K. Wang, et al.

ADULT BRAIN

 636 **Giant Intracranial Aneurysms at 7T MRI** T. Matsushige, et al.

ADULT BRAIN

 642 **A Spiral Spin-Echo MR Imaging Technique for Improved Flow Artifact Suppression in T1-Weighted Postcontrast Brain Imaging: A Comparison with Cartesian Turbo Spin-Echo** Z. Li, et al.

ADULT BRAIN

648 **Low-Dose Volume-of-Interest C-Arm CT Imaging of Intracranial Stents and Flow Diverters** P. Yang, et al.

**INTERVENTIONAL
PATIENT SAFETY**

AJNR (Am J Neuroradiol ISSN 0195-6108) is a journal published monthly, owned and published by the American Society of Neuroradiology (ASNR), 800 Enterprise Drive, Suite 205, Oak Brook, IL 60523. Annual dues for the ASNR include \$170.00 for journal subscription. The journal is printed by Cadmus Journal Services, 5457 Twin Knolls Road, Suite 200, Columbia, MD 21045; Periodicals postage paid at Oak Brook, IL and additional mailing offices. Printed in the U.S.A. POSTMASTER: Please send address changes to American Journal of Neuroradiology, P.O. Box 3000, Denville, NJ 07834, U.S.A. Subscription rates: nonmember \$380 (\$450 foreign) print and online, \$305 online only; institutions \$440 (\$510 foreign) print and basic online, \$875 (\$940 foreign) print and extended online, \$365 online only (basic), extended online \$790; single copies are \$35 each (\$40 foreign). Indexed by PubMed/Medline, BIOSIS Previews, Current Contents (Clinical Medicine and Life Sciences), EMBASE, Google Scholar, HighWire Press, Q-Sensei, RefSeek, Science Citation Index, and SCI Expanded. Copyright © American Society of Neuroradiology.

	655	WEB Treatment of Intracranial Aneurysms: Clinical and Anatomic Results in the French Observatory <i>L. Pierot, et al.</i>	INTERVENTIONAL ADULT BRAIN
	660	The Added Value of Volume-of-Interest C-Arm CT Imaging during Endovascular Treatment of Intracranial Aneurysms <i>G. Chintalapani, et al.</i>	INTERVENTIONAL ADULT BRAIN
	667	Mechanical Thrombectomy for Isolated M2 Occlusions: A Post Hoc Analysis of the STAR, SWIFT, and SWIFT PRIME Studies <i>J.M. Coutinho, et al.</i>	INTERVENTIONAL ADULT BRAIN
	673	Mechanical Thrombectomy of Distal Occlusions in the Anterior Cerebral Artery: Recanalization Rates, Periprocedural Complications, and Clinical Outcome <i>J. Pfaff, et al.</i>	INTERVENTIONAL
	679	Endovascular Treatment of Unruptured Paraclinoid Aneurysms: Single-Center Experience with 400 Cases and Literature Review <i>K. Shimizu, et al.</i>	INTERVENTIONAL ADULT BRAIN
	686	Associations between Cerebral Embolism and Carotid Intraplaque Hemorrhage during Protected Carotid Artery Stenting <i>G.H. Chung, et al.</i>	INTERVENTIONAL ADULT BRAIN EXTRACRANIAL VASCULAR
	692	Supersselective Intra-Arterial Ethanol Sclerotherapy of Feeding Artery and Nidal Aneurysms in Ruptured Cerebral Arteriovenous Malformations <i>F. Settecase, et al.</i>	INTERVENTIONAL ADULT BRAIN PEDIATRICS
	698	White Matter Abnormality Correlates with Developmental and Seizure Outcomes in West Syndrome of Unknown Etiology <i>J. Natsume, et al.</i>	PEDIATRICS
	706	Cerebral Blood Flow Improvement after Indirect Revascularization for Pediatric Moyamoya Disease: A Statistical Analysis of Arterial Spin-Labeling MRI <i>T. Blauwblomme, et al.</i>	PEDIATRICS FUNCTIONAL
	713	Voxel-Based Morphometry and fMRI Revealed Differences in Brain Gray Matter in Breastfed and Milk Formula-Fed Children <i>X. Ou, et al.</i>	PEDIATRICS FUNCTIONAL
	720	Evaluation of Subependymal Gray Matter Heterotopias on Fetal MRI <i>U.D. Nagaraj, et al.</i>	PEDIATRICS
	726	Asymptomatic Interhypothalamic Adhesions in Children <i>F.N. Ahmed, et al.</i>	PEDIATRICS
	730	Increased Facet Fluid Predicts Dynamic Changes in the Dural Sac Size on Axial-Loaded MRI in Patients with Lumbar Spinal Canal Stenosis <i>H. Kanno, et al.</i>	SPINE
	736	The Imaging Psoas Sign in Lumbar Spinal Infections: Evaluation of Diagnostic Accuracy and Comparison with Established Imaging Characteristics <i>L.N. Ledbetter, et al.</i>	SPINE
	742	Age- and Level-Dependence of Fatty Infiltration in Lumbar Paravertebral Muscles of Healthy Volunteers <i>R.J. Crawford, et al.</i>	SPINE
	749	Multicenter Validation of Mean Upper Cervical Cord Area Measurements from Head 3D T1-Weighted MR Imaging in Patients with Multiple Sclerosis <i>Y. Liu, et al.</i>	SPINE ADULT BRAIN
	755	The Cervical Spinal Canal Tapers Differently in Patients with Chiari I with and without Syringomyelia <i>A. Thompson, et al.</i>	SPINE
	759	Radiographic Local Control of Spinal Metastases with Percutaneous Radiofrequency Ablation and Vertebral Augmentation <i>A.N. Wallace, et al.</i>	SPINE INTERVENTIONAL
	766	CT-Fluoroscopic Cervical Transforaminal Epidural Steroid Injections: Extraforaminal Needle Tip Position Decreases Risk of Intravascular Injection <i>G.M. Lagemann, et al.</i>	SPINE INTERVENTIONAL

ONLINE FEATURES

CONSENSUS STATEMENT

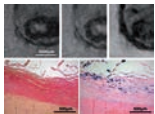
- 🔑 E31 **Training Guidelines for Endovascular Ischemic Stroke Intervention: An International Multi-Society Consensus Document**

LETTERS

- E35 **Asymptomatic Interhypothalamic Adhesions in Children** *M.T. Whitehead, et al.*
E36 **Reply** *D.M. Mirsky, et al.*
E37 **Integrative Analysis of 334 Patients with Blister-Like Aneurysms**
L. Yang, et al.
E38 **Reply** *S. Peschillo, et al.*
E39 **Regarding “Clinical and Imaging Follow-Up of Patients with Coiled Basilar Tip Aneurysms Up to 20 Years”** *A. Malhotra, et al.*
E40 **Reply** *W.J. van Rooij, et al.*

BOOK REVIEWS *R.M. Quencer, Section Editor*

Please visit www.ajnrblog.org to read and comment on Book Reviews.



MR images (*top*) and histopathologic sections (*bottom*) of a partially resected aneurysm. The low signal MRA image (*top middle*) and susceptibility-weighted image (*top right*) show a triple layered wall with hyperintense middle layer. This is reflected in the histopathologic sections (*bottom*) with a decellularized middle layer without iron deposition.



Indicates Editor's Choices selection



Indicates Fellows' Journal Club selection



Indicates open access to non-subscribers at www.ajnr.org



Indicates article with supplemental on-line table



Indicates article with supplemental on-line photo



Indicates article with supplemental on-line video



Evidence-Based Medicine Level 1



Evidence-Based Medicine Level 2



AMERICAN JOURNAL OF NEURORADIOLOGY

Publication Preview at www.ajnr.org features articles released in advance of print.
Visit www.ajnrblog.org to comment on AJNR content and chat with colleagues
and AJNR's News Digest at <http://ajnrndigest.org> to read the stories behind the
latest research in neuroimaging.

APRIL 2016 • VOLUME 37 • NUMBER 4 • WWW.AJNR.ORG

Official Journal:

American Society of Neuroradiology
American Society of Functional Neuroradiology
American Society of Head and Neck Radiology
American Society of Pediatric Neuroradiology
American Society of Spine Radiology

EDITOR-IN-CHIEF

Jeffrey S. Ross, MD

*Professor of Radiology, Department of Radiology,
Mayo Clinic College of Medicine, Phoenix, Arizona*

SENIOR EDITORS

Harry J. Cloft, MD, PhD

*Professor of Radiology and Neurosurgery,
Department of Radiology, Mayo Clinic College of
Medicine, Rochester, Minnesota*

Thierry A.G.M. Huisman, MD

*Professor of Radiology, Pediatrics, Neurology, and
Neurosurgery, Chairman, Department of Imaging
and Imaging Science, Johns Hopkins Bayview,
Director, Pediatric Radiology and Pediatric
Neuroradiology, Johns Hopkins Hospital,
Baltimore, Maryland*

C.D. Phillips, MD, FACR

*Professor of Radiology, Weill Cornell Medical
College, Director of Head and Neck Imaging,
New York-Presbyterian Hospital, New York,
New York*

Pamela W. Schaefer, MD

*Clinical Director of MRI and Associate Director of
Neuroradiology, Massachusetts General Hospital,
Boston, Massachusetts, Associate Professor,
Radiology, Harvard Medical School, Cambridge,
Massachusetts*

Charles M. Strother, MD

*Professor of Radiology, Emeritus, University of
Wisconsin, Madison, Wisconsin*

Jody Tanabe, MD

*Professor of Radiology and Psychiatry,
Chief of Neuroradiology,
University of Colorado, Denver, Colorado*

STATISTICAL SENIOR EDITOR

Bryan A. Comstock, MS

*Senior Biostatistician,
Department of Biostatistics,
University of Washington, Seattle, Washington*

EDITORIAL BOARD

Ashley H. Aiken, *Atlanta, Georgia*
A. James Barkovich, *San Francisco, California*
Walter S. Bartynski, *Charleston, South Carolina*
Barton F. Branstetter IV, *Pittsburgh, Pennsylvania*
Jonathan L. Brisman, *Lake Success, New York*
Julie Bykowski, *San Diego, California*
Donald W. Chakeres, *Columbus, Ohio*
Asim F. Choudhri, *Memphis, Tennessee*
Alessandro Cianfoni, *Lugano, Switzerland*
Colin Derdeyn, *St. Louis, Missouri*
Rahul S. Desikan, *San Francisco, California*
Richard du Mesnil de Rochemont, *Frankfurt,
Germany*
Clifford J. Eskey, *Hanover, New Hampshire*
Massimo Filippi, *Milan, Italy*
David Fiorella, *Cleveland, Ohio*
Allan J. Fox, *Toronto, Ontario, Canada*
Christine M. Glastonbury, *San Francisco,
California*
John L. Go, *Los Angeles, California*
Wan-Yuo Guo, *Taipei, Taiwan*
Rakesh K. Gupta, *Lucknow, India*
Lotfi Hachein-Bey, *Sacramento, California*
David B. Hackney, *Boston, Massachusetts*
Christopher P. Hess, *San Francisco, California*
Andrei Holodny, *New York, New York*
Benjamin Huang, *Chapel Hill, North Carolina*
George J. Hunter, *Boston, Massachusetts*
Mahesh V. Jayaraman, *Providence, Rhode Island*
Valerie Jewells, *Chapel Hill, North Carolina*
Timothy J. Kaufmann, *Rochester, Minnesota*
Kenneth F. Layton, *Dallas, Texas*
Ting-Yim Lee, *London, Ontario, Canada*
Michael M. Lell, *Erlangen, Germany*
Michael Lev, *Boston, Massachusetts*
Karl-Olof Lovblad, *Geneva, Switzerland*
Franklin A. Marden, *Chicago, Illinois*
M. Gisele Matheus, *Charleston, South Carolina*
Joseph C. McGowan, *Merion Station,
Pennsylvania*
Kevin R. Moore, *Salt Lake City, Utah*
Christopher J. Moran, *St. Louis, Missouri*
Takahisa Mori, *Kamakura City, Japan*
Suresh Mukherji, *Ann Arbor, Michigan*
Amanda Murphy, *Toronto, Ontario, Canada*
Alexander J. Nemeth, *Chicago, Illinois*
Laurent Pierot, *Reims, France*
Jay J. Pillai, *Baltimore, Maryland*
Whitney B. Pope, *Los Angeles, California*
M. Judith Donovan Post, *Miami, Florida*
Tina Young Poussaint, *Boston, Massachusetts*
Joana Ramalho, *Lisbon, Portugal*

Otto Rapalino, *Boston, Massachusetts*
Álex Rovira-Cañellas, *Barcelona, Spain*
Paul M. Ruggieri, *Cleveland, Ohio*
Zoran Rumboldt, *Rijeka, Croatia*
Amit M. Saindane, *Atlanta, Georgia*
Erin Simon Schwartz, *Philadelphia, Pennsylvania*
Aseem Sharma, *St. Louis, Missouri*
J. Keith Smith, *Chapel Hill, North Carolina*
Maria Vittoria Spampinato, *Charleston, South
Carolina*
Gordon K. Sze, *New Haven, Connecticut*
Krishnamoorthy Thamburaj, *Hershey, Pennsylvania*
Kent R. Thielen, *Rochester, Minnesota*
Cheng Hong Toh, *Taipei, Taiwan*
Thomas A. Tomsick, *Cincinnati, Ohio*
Aquila S. Turk, *Charleston, South Carolina*
Willem Jan van Rooij, *Tilburg, Netherlands*
Arastoo Vossough, *Philadelphia, Pennsylvania*
Elysa Widjaja, *Toronto, Ontario, Canada*
Max Wintermark, *Charlottesville, Virginia*
Ronald L. Wolf, *Philadelphia, Pennsylvania*
Kei Yamada, *Kyoto, Japan*

EDITORIAL FELLOW

Hillary R. Kelly, *Boston, Massachusetts*

SPECIAL CONSULTANTS TO THE EDITOR

AJNR Blog Editor

Neil Lall, *Denver, Colorado*

Case of the Month Editor

Nicholas Stence, *Aurora, Colorado*

Case of the Week Editors

Juan Pablo Cruz, *Santiago, Chile*
Sapna Rawal, *Toronto, Ontario, Canada*

Classic Case Editor

Sandy Cheng-Yu Chen, *Taipei, Taiwan*

Facebook Editor

Peter Yi Shen, *Sacramento, California*

Health Care and Socioeconomics Editor

Pina C. Sanelli, *New York, New York*

Physics Editor

Greg Zaharchuk, *Stanford, California*

Podcast Editor

Yvonne Lui, *New York, New York*

Twitter Editor

Ryan Fitzgerald, *Little Rock, Arkansas*

YOUNG PROFESSIONALS

ADVISORY COMMITTEE

Asim K. Bag, *Birmingham, Alabama*
Anna E. Nidecker, *Sacramento, California*
Peter Yi Shen, *Sacramento, California*

Founding Editor

Juan M. Taveras

Editors Emeriti

**Mauricio Castillo, Robert I. Grossman,
Michael S. Huckman, Robert M. Quencer**

Managing Editor

Karen Halm

Electronic Publications Manager

Jason Gantenberg

Executive Director, ASNR

James B. Gantenberg

Director of Communications, ASNR

Angelo Artemakis



Title: Free Will. Acrylic on canvas, 24" × 16"

Anish Kapadia, MD, University of Toronto, Toronto, Ontario, Canada

Current Evaluation of the Safety and Efficacy of Aneurysm Treatment with the WEB Device

L. Pierot, A. Arthur, L. Spelle, and D. Fiorella

We read with interest the recent review of 6 European studies of the Woven EndoBridge (WEB) aneurysm embolization system (Sequent Medical, Aliso Viejo, California) for the treatment of wide-neck bifurcation aneurysms (WNBA).¹ The WEB was introduced in 2010 in Europe and has undergone important evolution during the past 5 years. The devices involved have moved from dual-layer to single-layer construction, with a reduction in the size of the microcatheter used to deliver the device. This technique has been evaluated in several retrospective and prospective good clinical practice (GCP) studies with independent monitoring of all patient data, independent analysis of all adverse events, and independent adjudication of all anatomic results by a core laboratory. No other endovascular treatment for intracranial aneurysms has been so thoroughly evaluated immediately after its commercialization.

The results of 2 early prospective, multicenter studies (WEB Clinical Assessment of IntraSaccular Aneurysm Therapy [WEBCAST] and the French Observatory) were recently published, demonstrating that the treatment with the WEB is both feasible and safe.^{2,3} Because the study protocols were homogeneous, an analysis of the combined population of these 2 studies was conducted.⁴ In this population of 113 patients with 114 aneurysms treated with WEB, the treatment was successfully performed in 96.5% of aneurysms. Thromboembolic events and intraoperative rupture were observed in 15.0% and 0.9% of patients, respectively. However, these adverse events were not associated with permanent clinical worsening in most cases. One-month morbidity was 2.7%, and there was no mortality. At 1 year, delayed morbidity was 0.0% and mortality (unrelated to the treatment) was 3.9% (mostly related to cancer or cirrhosis). These safety numbers are comparable with those reported for aneurysm coiling.^{5,6}

In the same population, anatomic results were evaluated at 1 year, and adequate occlusion was reported in 82.0% (including complete occlusion in 56.0% and neck remnant in 26.0%). The rate of neck remnant was low compared with standard coiling as reported in the Clinical and Anatomical Results in the Treatment of Ruptured Intracranial Aneurysms (CLARITY) series: 46.0% in aneurysms treated with bare coils and 49.0% in aneurysms treated with Matrix detachable coils (Stryker, Kalamazoo, Michigan).⁷ Certainly longer follow-up is needed to evaluate the anatomic stability of this treatment, and very long-term follow-up (5 years) is foreseen in these prospective GCP studies. In a retrospective European series, anatomic results were reported stable between midterm (mean, 13 months) and long-term (mean, 26 months)

follow-up, with adequate occlusion at long-term in 84.2% of aneurysms, including complete occlusion in 68.4% and neck remnant in 15.8%.^{8,9}

The stability of occlusion after WEB treatment is probably related to appropriate device sizing. The frequency and the role of the so-called “compression” phenomenon in the long-term stability of aneurysm occlusion remain unknown. Further analysis of the combined WEBCAST and French Observatory cohorts will provide further insight into these 2 points. Moreover, as the device itself and our understanding of the procedure continue to evolve, it is likely that early and long-term occlusion rates will be even better in future studies.

It is probably not feasible and not ethical to evaluate the WEB in a randomized trial versus other aneurysm treatments. The WEB device is dedicated to a very specific subgroup of intracranial aneurysms (WNBA). Against which technique should the WEB be evaluated in a randomized trial (surgical clipping, balloon-assisted coiling, stent-assisted coiling, or flow diversion)? The safety and efficacy of these techniques for treatment of WNBA have not been evaluated in prospective, GCP studies—probably an essential first step before designing and powering a randomized controlled trial.

In summary, the WEB device is the first to be precisely and extensively evaluated for safety and efficacy since the beginning of its clinical use. Initial results have shown good safety and efficacy at midterm follow-up in comparison with the published literature for coil embolization of similar aneurysms. Further efficacy evaluation is foreseen in long-term follow-up of existing studies and new studies, which will be conducted to evaluate the latest generation of the device (WEBCAST2) and its efficacy in ruptured aneurysms (CLARITY). A prospective GCP trial is also underway in the United States with more than 100 of 150 planned patients already enrolled.

Disclosures: Laurent Pierot—*RELATED: Consulting Fee or Honorarium:* Sequent Medical; *UNRELATED: Consultancy:* Medtronic, MicroVention, Neuravi; *OTHER:* Principal Investigator for WEB studies (WEBCAST, French Observatory, WEBCAST2). Adam Arthur—*UNRELATED: Consultancy:* Codman,* Medtronic,* MicroVention,* Penumbra,* Sequent Medical,* Silk Road,* Stryker*; *Grants/Grants Pending:* Sequent Medical,* Siemens,* Penumbra*; *OTHER:* investor: Valor Medical; research support: Codman, Penumbra, Sequent Medical, Siemens; *OTHER:* Principal Investigator for the WEB Intracranial Therapy study (WEB-IT). Laurent Spelle—*RELATED: Consulting Fee or Honorarium:* Sequent Medical; *UNRELATED: Consultancy:* Medtronic, Stryker; *OTHER:* Principal Investigator for WEB study (CLARITY). David Fiorella—*RELATED:* grant: Siemens,* Sequent Medical,* MicroVention*; *Consulting Fee or Honorarium:* Medtronic, Johnson & Johnson, MicroVention, Penumbra; *Support for Travel to Meetings for the Study or Other Purposes:* MicroVention, Penumbra, Codman/Johanson & Johnson, Medtronic; *OTHER: Consultancy:* Medtronic/ev3, Sequent Medical, MicroVention, Penumbra, Johnson & Johnson/Codman; research support: Siemens, Penumbra, Sequent Medical, MicroVention; *OTHER:* Principal Investigator for WEB-IT. *Money paid to the institution.

REFERENCES

1. Armoiry X, Turjman F, Hartmann DJ, et al. **Endovascular treatment of intracranial aneurysms with the WEB device: a systematic review of clinical outcomes.** *AJNR Am J Neuroradiol* 2015 Nov 19. [Epub ahead of print] CrossRef Medline
2. Pierot L, Costalat V, Moret J, et al. **Safety and efficacy of aneurysm**

- treatment with WEB®: results of WEBCAST Study. *J Neurosurg* 2015 Sep 18. [Epub ahead of print] Medline
3. Pierot L, Moret J, Turjman F, et al. **WEB treatment of intracranial aneurysms: clinical and anatomic results in the French Observatory.** *AJNR Am J Neuroradiol* 2015 Oct 29. [Epub ahead of print] CrossRef Medline
 4. Pierot L, Spelle L, Molyneux A, et al; WEBCAST and French Observatory Investigators. **Clinical and anatomical follow-up in patients with aneurysms treated with the WEB device: 1-year follow-up report in the cumulated population of 2 prospective, multicenter series (WEBCAST and French Observatory).** *Neurosurgery* 2016;78: 133–41 CrossRef Medline
 5. Pierot L, Spelle L, Vitry F; ATENA Investigators. **Immediate clinical outcome of patients harboring unruptured intracranial aneurysms treated by endovascular approach: results of the ATENA study.** *Stroke* 2008;39:2497–504 CrossRef Medline
 6. Cognard C, Pierot L, Anxionnat R, et al; Clarity Study Group. **Results of embolization used as the first treatment choice in a consecutive nonselected population of ruptured aneurysms: clinical results of the Clarity GDC study.** *Neurosurgery* 2011;69:837–41; discussion 842 CrossRef Medline
 7. Pierot L, Cognard C, Ricolfi F, et al; CLARITY investigators. **Mid-term anatomic results after endovascular treatment of ruptured intracranial aneurysms with Guglielmi detachable coils and Matrix coils: analysis of the CLARITY series.** *AJNR Am J Neuroradiol* 2012; 33:469–73 CrossRef Medline
 8. Lubicz B, Klisch J, Gauthier JY, et al. **WEB-DL endovascular treatment of wide-neck bifurcation aneurysms: short- and midterm results in a European study.** *AJNR Am J Neuroradiol* 2014;35:432–38 CrossRef Medline
 9. Pierot L, Klisch J, Liebig T, et al. **WEB-DL endovascular treatment of wide-neck bifurcation aneurysms: long-term results in a European series.** *AJNR Am J Neuroradiol* 2015;36:2314–19 CrossRef Medline

Dynamic Contrast-Enhanced MR Imaging in Head and Neck Cancer: Techniques and Clinical Applications

S. Gaddikeri, R.S. Gaddikeri, T. Tailor, and Y. Anzai



ABSTRACT

SUMMARY: In the past decade, dynamic contrast-enhanced MR imaging has had an increasing role in assessing the microvascular characteristics of various tumors, including head and neck cancer. Dynamic contrast-enhanced MR imaging allows noninvasive assessment of permeability and blood flow, both important features of tumor hypoxia, which is a marker for treatment resistance for head and neck cancer. Dynamic contrast-enhanced MR imaging has the potential to identify early locoregional recurrence, differentiate metastatic lymph nodes from normal nodes, and predict tumor response to treatment and treatment monitoring in patients with head and neck cancer. Quantitative analysis in its early stage and standardization and refinement of technique are essential. In this article, we review the techniques of dynamic contrast-enhanced MR imaging data acquisition, analytic methods, current limitations, and clinical applications in head and neck cancer.

ABBREVIATIONS: AIF = arterial input function; DCE-MR imaging = dynamic contrast-enhanced MR imaging; EES = extracellular extravascular space; GCA = gadolinium contrast agent; HNC = head and neck cancer; K_{ep} = transfer function from EES to the plasma space; K^{trans} = volume transfer constant; V_e = extravascular extracellular volume fraction

Head and neck cancer (HNC) accounted for approximately 3% of all new cancers and 2% of all cancer-related deaths in 2010 in the United States.¹ Conventional cross-sectional imaging (CT and MR imaging) plays an important role in assessing locoregional extension of a primary tumor and gross nodal metastases. The shortcomings of conventional imaging include failure to identify early locoregional recurrence, detection of nodal metastasis in normal-sized lymph nodes, prediction of tumor response to treatment, and treatment monitoring in patients with HNC. CT perfusion has been reported to provide vascular information about HNC, though there is increasing concern for exposure to ionizing radiation.² FDG-PET is also widely used for initial staging and monitoring response to treatment. However, there is increasing restriction in the number of FDG-PET scans that any patient can undergo during the entire treatment course.³

Dynamic contrast-enhanced MR imaging (DCE-MR imaging)

is an imaging technique in which rapid sequential MR images are obtained through an area of interest before, during, and after a bolus administration of contrast material. This process allows quantification of various vascular biomarkers, such as blood volume, blood flow, permeability, and wash-in and washout properties.

Angiogenesis (formation of new vessels) is one of the hallmarks of cancer because it is necessary for tumor survival and growth. This process of neoangiogenesis results in tortuous and leaky vessels because the vessel walls in tumor may be discontinuous.⁴ Characteristics of tumor microvasculature include lack of muscularis propria, widened interendothelial junctions, and a discontinuous or absent basement membrane, all of which contribute to increased permeability.⁴ It has been reported that the degree of angiogenesis in a tumor correlates well with tumor biology.^{5,6} Well-differentiated tumors may have near-normal microvasculature, whereas poorly differentiated tumors have disorganized and leaky vessels.⁵ The leaky blood vessels are inefficient in the delivery of oxygen, thus potentially contributing to tumor hypoxia. The process of gadolinium leakage from intravascular-to-extravascular compartments depends on multiple factors such as blood flow to tissue, microvascular attenuation, vascular permeability, and fractional volume of extracellular extravascular space (EES).⁷ These biologic features can be assessed by DCE-MR imaging.

In this article, we review the technical considerations of DCE-MR imaging, qualitative and quantitative analysis, and potential clinical applications in HNC.

From the Department of Radiology (S.G., T.T., Y.A.), University of Washington Medical Center, Seattle, Washington; Department of Neuroradiology (R.S.G.), Rush University, Chicago, Illinois; and Department of Radiology (Y.A.), University of Utah Health Care, Salt Lake City, Utah.

Please address correspondence to Yoshimi Anzai, MD, MPH, Department of Radiology, University of Utah, 30 North 1900 East, 1A071, Salt Lake City, UT 84132; e-mail: yoshimi.anzai@hsc.utah.edu

Indicates open access to non-subscribers at www.ajnr.org

Indicates article with supplemental on-line table.

<http://dx.doi.org/10.3174/ajnr.A4458>

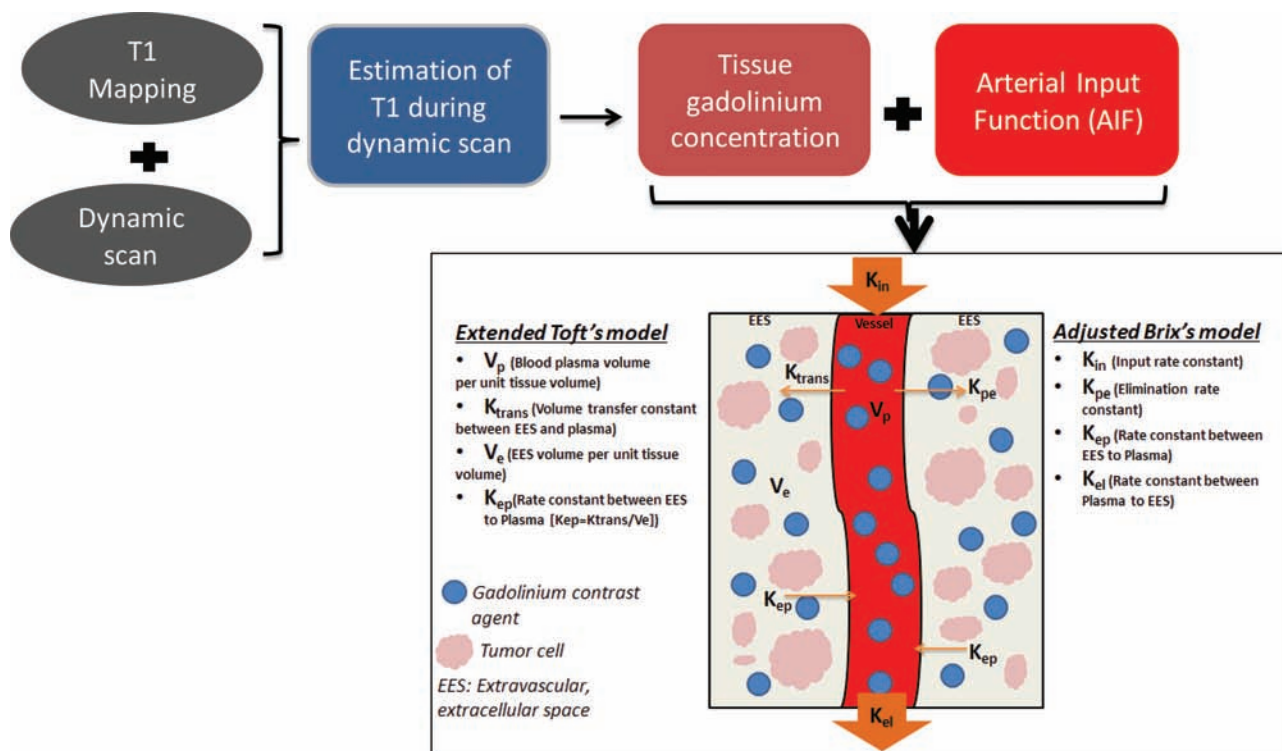


FIG 1. Flow chart demonstrating a typical quantitative method of data analysis. The information from the T1 mapping and dynamic data is used to estimate the changes in T1 relaxivity during the dynamic scan, which, in turn, provides the information of tissue gadolinium concentration. By fitting the tissue gadolinium concentration and arterial input function data in to commonly used “2-compartment” models (extended Toft or adjusted Brix model), various parameters can be assessed. The difference between the Toft and extended Toft model is the inclusion of assessment of blood plasma volume per unit tissue volume in the later version.

Technique

Basic Principles of DCE–MR Imaging. Following intravenous administration, gadolinium contrast agent (GCA) travels through the microvasculature and leaks from the intravascular compartment to the EES by passive diffusion, altering signal intensity of the tissue by changing the relaxation rates of water protons. The changes in relaxation and signal depend on how GCA distributes within the tissues. The transfer function from plasma to EES is commonly referred to as volume transfer constant (K^{trans}) (Fig 1). As the concentration of intravascular GCA decreases, GCA starts moving from the EES back into the plasma space. The transfer function from EES to the plasma space is referred to as (K_{ep}) (Fig 1).⁸ DCE–MR imaging uses rapid T1-weighted imaging to measure the relaxivity changes resulting from gadolinium leakage in and out of the EES. T1-relaxation is generally assumed to be proportional to the degree of concentration of GCA in the EES.⁹ The time-concentration curve often reveals the dynamics of GCA accumulation and washout across time. With the knowledge of concentration of GCA (signal intensity) in the EES and vascular compartment (arterial input function [AIF]) with time, DCE MR imaging allows quantitative assessment of vascular function in HNC.

Data Acquisition

The DCE–MR image acquisition consists of 3 steps: 1) a baseline T1 mapping before administration of GCA, 2) dynamic data acquisition, and 3) arterial input function assessment.

Baseline T1 Mapping. To obtain accurate kinetic fitting of DCE–MR imaging data, T1 mapping is critical.¹⁰ The basic as-

sumption for pharmacokinetic modeling of DCE–MR imaging data is that tissue T1 relaxivity (and hence the signal intensity of tissue) at each time point is directly proportional to the tissue concentration of GCA.¹¹ However, this relationship is not always linear because it is influenced by the T1 characteristics of the native tissue.¹² To compensate for this nonlinear relationship between signal intensity and tissue GCA concentration, baseline T1 mapping and equilibrium magnetization at each imaging time point are essential.^{12,13} The T1 values calculated on a voxel-by-voxel basis are termed the T_{10} map.

Various techniques of imaging data acquisition for T1 mapping are described in the literature, such as variable flip angle techniques (double flip angle versus multiple flip angle),^{14,15} the inversion recovery technique,^{16,17} and the Look-Locker technique.^{18,19} Originally, the Look-Locker technique was reported to have a high degree of accuracy and precision^{20,21} within a reasonable acquisition time,²² compared with the conventional inversion recovery technique.²³ More recently, it has been reported that the multiple flip angle technique provides more accurate and robust T1 mapping and kinetic parameter estimation than the double flip angle technique. Furthermore, T1 mapping by using multiple flip angles can be obtained with a short scan time without sacrificing signal-to-noise ratio. As such, multiple flip angle T1 mapping is the preferable method of choice for DCE–MR imaging in HNC.²⁴

Dynamic Data Acquisition. The dynamic data acquisition follows immediately after baseline T1 mapping. The images are acquired before, during, and after intravenous gadolinium administration. The critical component of high-quality DCE–MR imaging is high

Table 1: Dynamic sequence at the University of Washington is performed on a 3T scanner

Parameters	Philips ^a	Siemens ^b	GE ^c
Coil	16-Channel neurovascular coil		
Parallel imaging	SENSE	iPAT	ASSET
Sequence	3D-T1WI FFE	3D-T1WI FISP or 3D-T1WI FLASH	3D-T1WI FSPGR
TR/TE for T1 mapping	5.2/2.5 ms		
MFA for T1 mapping	30°, 20°, 15°, 10°, and 2°		
TR/TE/FA for dynamic imaging	5.2/2.5 ms/5°		
FOV	212 × 149 mm ²		
Voxel	0.95/0.95/3.00 mm ³		
Section thickness	3 mm		
Signal averaging	NSA: 1	ACQ: 1	NEX: 1
Number of sections per dynamic scan/section orientation	20/Axial		
Temporal resolution	3.6 seconds		
Total T1 mapping acquisition time	26.5 seconds		
Total dynamic acquisition time	6.10 minutes		
Fat saturation	No		
Contrast injection	Single dose of 20-mL gadoteridol (ProHance ^d) injected at a rate of 5 mL/s through a peripheral arm vein, followed by a 20-mL saline flush with a power injector		

Note:—FFE indicates fast-field echo; FSPGR, fast-spoiled gradient recalled; MFA, multiple flip angles; SENSE, sensitivity encoding; iPAT, integrated parallel acquisition technique; ASSET, array spatial sensitivity encoding technique; NSA, number of signal averages; ACQ, acquisitions; FA, flip angle.

^a Philips Healthcare, Best, the Netherlands.

^b Siemens, Erlangen, Germany.

^c GE Healthcare, Milwaukee, Wisconsin.

^d Bracco Diagnostics, Princeton, New Jersey.

Table 2: Commonly used model-free (semiquantitative) parameters for DCE-MRI analysis

Parameter	Definition	Units
Area under curve	Area under the signal intensity or gadolinium dynamic curve	a.u.min or mmol.min/L
Relative signal intensity	S_t/S_0	NA
Initial slope or enhancement slope/rate	Maximum or average slope in the initial enhancement	a.u./min
Washout slope/rate	Maximum or average slope in the washout phase	a.u./min
Peak enhancement ratio or maximum signal enhancement ratio	$(S_{\max} - S_0)/S_0$	NA
T_{\max} or time to peak	Time from contrast arrival to peak	S
Maximum intensity–time ratio	PER/ T_{\max}	S ^{−1}

Note:— S_t indicates MR signal intensity at time t ; S_0 , precontrast signal intensity; S_{\max} , maximum signal intensity; a.u, arbitrary unit; min, minute; PER, peak enhancement ratio; T_{\max} , time to maximum enhancement; NA, not applicable; S, seconds.

temporal resolution (2–4 seconds). This allows accurate assessment of the hemodynamic process as GCA passes through the microvasculature in the tissue of interest. Higher temporal resolution may compromise SNR and/or coverage (number of sections). The trade-offs among temporal resolution, SNR, and spatial resolution need to be carefully balanced because a reasonable SNR and spatial resolution (in-plane resolution, 0.5–1.7 mm) are required for adequate assessment of tumor vascular function.²⁵ The dynamic sequence can be tailored depending on the planned method for data analysis. For example, high spatial resolution with reasonable temporal resolution imaging is sufficient for a “semiquantitative” time-intensity curve analysis, whereas a very high temporal resolution with reasonable spatial resolution is critical for “quantitative” kinetic analysis.

The application of DCE–MR imaging has been reported with both 1.5T and 3T scanners.^{26–30} Various types of fast 2D and 3D T1-weighted sequences have been described, including fast spin-echo T1WI,^{31–34} FISP^{35–40} fast-spoiled gradient recalled acquisition,^{29,41–44} turbo fast-field echo,^{28,45–47} and turbo FLASH.^{48,49} Application of parallel imaging for DCE–MR imaging has increased temporal resolution by severalfold,⁵⁰ and thus fast 3D

acquisitions are gradually replacing 2D acquisitions in DCE–MR imaging. Details of the dynamic sequence practiced at the University of Washington are summarized in Table 1.

Arterial Input Function. Another crucial component of DCE–MR imaging is the assessment of an AIF. The AIF estimates the rate of change in the concentration of contrast in the plasma (vascular space) with time. An accurate AIF is essential for quantitative analysis of dynamic data by using any of the currently available analytic methods. Generally, AIF is commonly obtained from the dynamic dataset.^{51–53} The changes in signal intensity during the passage of GCA can be measured simultaneously in both the blood vessels and the tissue of interest. AIF allows conversion of the blood plasma signal intensity to intravascular contrast agent concentration on implementation of a calibration algorithm. Any visible large artery within an area of interest can be selected for AIF with the dynamic dataset. For HNC imaging with DCE–MR imaging, the carotid and vertebral arteries are well-suited for AIF selection because they run along the long axis of the neck and are of relatively large caliber.⁵⁴

Table 3: Commonly used quantitative parameters in the DCE-MRI pharmacokinetic analysis

Parameter	Definition	Units
K^{trans}	Volume transfer constant between EES and blood plasma	Min^{-1}
V_e	EES volume per unit tissue volume	NA
V_p	Blood plasma volume per unit tissue volume	NA
K_{ep} or K_{21}	Rate constant from EES to blood plasma	Min^{-1}
K_{pe} or K_{12}	Rate constant from blood plasma to EES	Min^{-1}
K_{el}	Elimination rate constant	Min^{-1}
Amp or AH	Amplitude of the normalized dynamic curve	NA

Note:—Amp or AH, amplitude of the normalized dynamic curve; NA, not applicable; Min, minute.

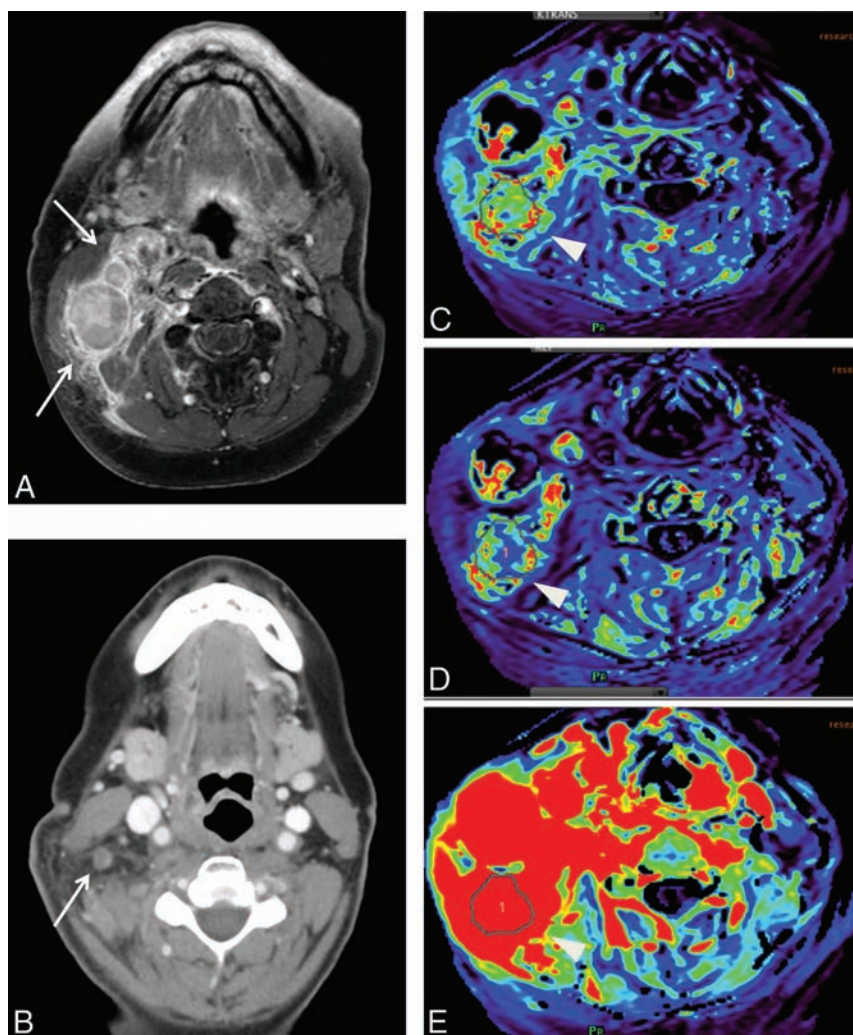


FIG 2. A 57-year-old male patient with T2N3bM0 undifferentiated nasopharyngeal cancer. Pre-treatment gadolinium-enhanced axial T1-weighted MR imaging of the neck demonstrates metastatic right level IIb lymph nodes (A). Parametric maps (C, D, and E) show higher volume transfer constant ($K^{trans} = 0.26/\text{min}$), K_{ep} , and area under curve, respectively. Axial contrast-enhanced neck CT at 6 months post-chemoradiation treatment demonstrates a favorable response to treatment (B).

Data Analysis

DCE-MR imaging is commonly analyzed with semiquantitative analysis or quantitative analysis.

Semiquantitative Method

The semiquantitative method is a model-free analysis by using the observed data points on a time-intensity curve. It is a simple and easily implementable method by using commercially available software.^{31,35-41,44,55-58} Commonly calculated pa-

rameters on the time-intensity curve are listed in Table 2. The time-intensity curve obtained following placement of an ROI on the tumor provides a rough estimate of how fast the GCA enters and exits the tumor. It has been reported that malignant tumors have a longer time to peak and lower relative maximum enhancement compared with benign lesions in the head and neck.⁵⁹ The prolonged time to peak and lower relative maximum enhancement were also noted in metastatic lymph nodes compared with benign lymph nodes among patients with HNC.⁴² The limitation of this semiquantitative analysis is that the semiquantitative parameters do not necessarily have physical correlates; rather, they may represent mixed measures. For example, the area under curve is a combination of tissue blood flow, vascular permeability, and fractional interstitial space and is, therefore, not an accurate estimate of blood volume. Therefore, the physiologic meanings of these parameters remain ambiguous as to what biologic property they represent.²⁵

Quantitative Methods

Quantitative analysis of DCE-MR imaging data is based on the generalized pharmacokinetic models. The 2 most important assumptions of these models are the following: 1) GCA is distributed in ≥ 1 compartment of the human body, and 2) distribution of the contrast agent in a particular compartment is uniform.

A typical quantitative method of data analysis is outlined in the flow chart (Fig 1). The most frequently used pharmacokinetic models in head and neck DCE-MR imaging data analysis include the Toft and Kermode model (Toft model),^{29,30,45,60,61} the Brix model,^{28,34} and their modifications (Fig 1). These are based on the assumption of a “2-compartment model,” in which the GCA is distributed into the “central” and “peripheral” compartments. The

central compartment consists of intravascular extracellular volume fraction (blood plasma), and the peripheral compartment consists of extravascular extracellular volume fraction (V_e). The Toft model generally requires the knowledge of AIF and T1 mapping for accurate assessment of quantitative parameters. Fitting the DCE-MR imaging data into 1 of these models allows estimation of various model-base parameters, which potentially aids in the understanding of tumor physiolo-

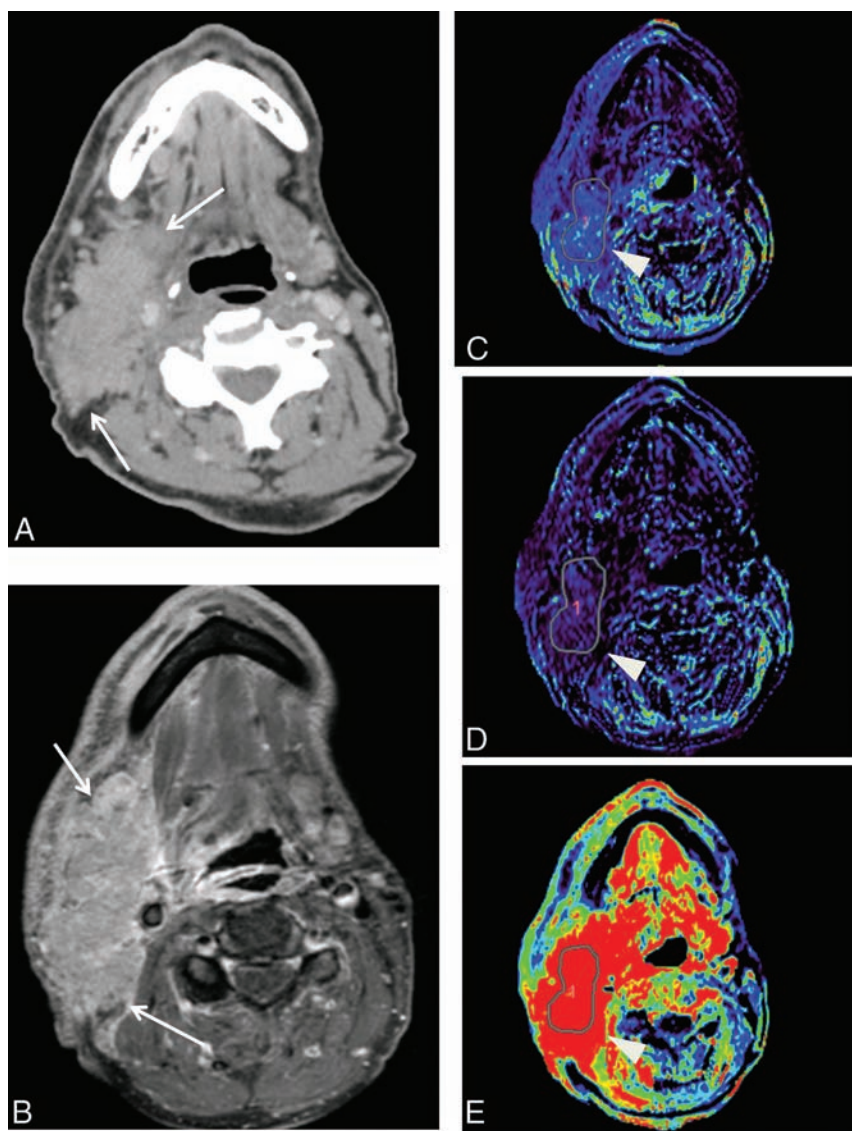


FIG 3. A 52-year-old male patient with squamous cell carcinoma of the right palatine tonsil. Pretreatment axial contrast-enhanced neck CT demonstrates metastatic right level II lymph nodes (A). Parametric maps (C, D, and E) show a lower volume transfer constant ($K^{\text{trans}} = 0.06/\text{min}$), K_{ep} , and area under curve, respectively. Gadolinium-enhanced axial T1-weighted MR imaging of the neck at 12 months post-chemoradiation treatment demonstrates an unfavorable response to treatment (B).

ogy and pathology.⁶² Frequently used parameters that can be obtained from quantitative DCE-MR imaging data are summarized in Table 3.

Quantitative methods of data analysis provide parameters quantifying microvasculature physiology and tumor biology. Additionally, the model-based parameters are more precise and reproducible and are reported to be independent of scanners and tissue type.⁶³ Hence, these parameters may be potentially useful for sequential follow-up to determine treatment response in an individual patient and also as biologic markers for predicting and monitoring the therapeutic efficacy in multicenter trials.

Clinical Applications of DCE-MR Imaging in Head and Neck Cancer

One of the most exciting aspects of DCE-MR imaging application in HNC is its potential to serve as an imaging biomarker for hypoxia. The abnormal tumor vessels are inefficient in the delivering

oxygen or chemotherapy drugs to the tissue. In addition, this inefficiency causes increased interstitial fluid pressure, which ultimately reduces tumor perfusion, further facilitating tumor hypoxia.⁶⁴ Although a study by Newbold indicated that tumors with higher K^{trans} were associated with hypoxia defined by pimonidazole and carbonic anhydrase staining, and hence poor outcome,⁴⁶ others reported that tumors with lower K^{trans} were associated with poor response.^{27,29,61,65} K^{trans} generally reflects a combination of perfusion and permeability. Lower K_{ep} is also reported to correlate with poor response to treatment.⁶¹ A tumor with higher K^{trans} , highly perfused tumor has higher oxygenation, better delivery of chemotherapeutic drugs, likely explaining improved treatment response.⁶⁶⁻⁶⁷ Skewness of K^{trans} is also reported to predict treatment response, that a tumor with larger skewed K^{trans} has a worse prognosis potentially reflecting tumor heterogeneity.²⁹

DCE-MR imaging has been reported to be useful for various applications in HNC imaging, such as differentiating squamous cell carcinoma from lymphoma and undifferentiated carcinomas,⁶⁸ detecting metastatic lymph nodes,⁴² assessing tumor cell proliferation and microvessel attenuation,^{55,69} and predicting early treatment response and treatment outcome.^{27-29,41,46,61}

We searched MEDLINE, PubMed, and Google for the literature published during the most recent 6-year interval (2008–2013) containing all of the following: DCE-MR imaging, HNC, and

quantitative (model-based) analysis of dynamic data for pretreatment assessment and/or monitoring treatment response. The Online Table summarizes various studies in the literature and their respective contributions to DCE-MR imaging of HNC by using various quantitative methods. Early assessment of treatment response is critical for advanced head and neck cancers. The question remains as to whether pretreatment measures of DCE parameters suffice to address the treatment response or it is necessary to measure changes in DCE parameters to assess treatment response. Figs 2 and 3 demonstrate 2 patients with HNC with nodal metastasis exhibiting different responses to chemoradiation.

Challenges

DCE-MR imaging of HNC is clearly in its early stage. Substantial variability exists in quantification methods, parameter choice,

and analytic methods. Many factors in the data acquisition and analysis can affect the reliability of results in DCE-MR imaging studies. For example, the accuracy and precision of the pharmacokinetic parameter estimates are largely determined by SNR, temporal resolution of the MR image, AIF, and estimation of T1 mapping.⁷⁰ Systematic errors can be introduced from various sources, such as the breakdown of linearity in the gadolinium concentration calibration curve and inaccuracy of T1 mapping.^{71,72}

Standardization of data acquisition and analysis will facilitate the translation of DCE-MR imaging to clinical settings, in particular to multicenter clinical trials.⁷³ The DCE-MR imaging subcommittee of the Radiological Society of North America Quantitative Imaging Biomarkers Alliance initiative provides guidelines for data acquisition, analysis, and quality control on 1.5T systems. The image intensity should be converted to gadolinium concentration through the use of a multiple flip angle precontrast T1 map after corrections for patient motion, B1 field inhomogeneity, and coil sensitivity.⁷⁴ The pharmacokinetic parameter K^{trans} (Toft model) and area under curve (model-free parameter) are recommended as standard quantitative end points that should be used in clinical trials and practice.

Another challenge with DCE-MR imaging parameters is validation with tumor histology and hypoxia. A potential reason includes tumor heterogeneity at the subvoxel level. Therefore, some authors suggest that DCE-MR imaging parameters may be better validated with immunohistochemical measurements averaged over several fields randomly picked from the ROI.⁷⁵

CONCLUSIONS

Although DCE-MR imaging has the potential to provide biologic information of tumor angiogenesis and vascular function in HNC, its technical development is still in an early stage. The standardization of image acquisition and data analysis is critical to moving forward with a multicenter head and neck tumor registry and in determining the clinical role of DCE-MR imaging in head and neck oncologic imaging.

Disclosures: Tina Tailor—RELATED: Grant: American Society of Head and Neck Radiology, William N. Hanafey Award.

REFERENCES

- Jemal A, Bray F, Center MM, et al. **Global cancer statistics.** *CA Cancer J Clin* 2011;61:69–90 CrossRef Medline
- Razek AA, Tawfik AM, Elsorogy LG, et al. **Perfusion CT of head and neck cancer.** *Eur J Radiol* 2014;83:537–44 CrossRef Medline
- Bussink J, van Herpen CM, Kaanders JH, et al. **PET-CT for response assessment and treatment adaptation in head and neck cancer.** *Lancet Oncol* 2010;11:661–69 CrossRef Medline
- Carmeliet P, Jain RK. **Angiogenesis in cancer and other diseases.** *Nature* 2000;407:249–57 CrossRef Medline
- Kaur B, Tan C, Brat DJ, et al. **Genetic and hypoxic regulation of angiogenesis in gliomas.** *J Neurooncol* 2004;70:229–43 CrossRef Medline
- Patankar TF, Haroon HA, Mills SJ, et al. **Is volume transfer coefficient (K(trans)) related to histologic grade in human gliomas?** *AJNR Am J Neuroradiol* 2005;26:2455–65 Medline
- Paldino MJ, Barboriak DP. **Fundamentals of quantitative dynamic contrast-enhanced MR imaging.** *Magn Reson Imaging Clin N Am* 2009;17:277–89 CrossRef Medline
- Knopp MV, Weiss E, Sinn HP, et al. **Pathophysiologic basis of contrast enhancement in breast tumors.** *J Magn Reson Imaging* 1999;10:260–66 Medline
- Cheng HL. **Investigation and optimization of parameter accuracy in dynamic contrast-enhanced MRI.** *J Magn Reson Imaging* 2008;28:736–43 CrossRef Medline
- Di Giovanni P, Azlan CA, Ahearn TS, et al. **The accuracy of pharmacokinetic parameter measurement in DCE-MRI of the breast at 3 T.** *Phys Med Biol* 2010;55:121–32 CrossRef
- Brix G, Semmler W, Port R, et al. **Pharmacokinetic parameters in CNS Gd-DTPA enhanced MR imaging.** *J Comput Assist Tomogr* 1991;15:621–28 CrossRef Medline
- Evelhoch JL. **Key factors in the acquisition of contrast kinetic data for oncology.** *J Magn Reson Imaging* 1999;10:254–59 Medline
- Leach MO, Brindle KM, Evelhoch JL, et al; Pharmacodynamic/Pharmacokinetic Technologies Advisory Committee, Drug Development Office, Cancer Research UK. **The assessment of antiangiogenic and antivascular therapies in early-stage clinical trials using magnetic resonance imaging: issues and recommendations.** *Br J Cancer* 2005;92:1599–610 CrossRef Medline
- Wang HZ, Riederer SJ, Lee JN. **Optimizing the precision in T1 relaxation estimation using limited flip angles.** *Magn Reson Med* 1987;5:399–416 CrossRef Medline
- Deoni SC, Rutt BK, Peters TM. **Rapid combined T1 and T2 mapping using gradient recalled acquisition in the steady state.** *Magn Reson Med* 2003;49:515–26 CrossRef Medline
- Jahng GH, Stables L, Ebel A, et al. **Sensitive and fast T1 mapping based on two inversion recovery images and a reference image.** *Med Phys* 2005;32:1524–28 CrossRef Medline
- Ogg RJ, Kingsley PB. **Optimized precision of inversion-recovery T1 measurements for constrained scan time.** *Magn Reson Med* 2004;51:625–30 CrossRef Medline
- Karlsson M, Nordell B. **Analysis of the Look-Locker T(1) mapping sequence in dynamic contrast uptake studies: simulation and in vivo validation.** *Magn Reson Imaging* 2000;18:947–54 CrossRef Medline
- Freeman AJ, Gowland PA, Mansfield P. **Optimization of the ultrafast Look-Locker echo-planar imaging T1 mapping sequence.** *Magn Reson Imaging* 1998;16:765–72 CrossRef Medline
- Brix G, Schad LR, Deimling M, et al. **Fast and precise T1 imaging using a TOMROP sequence.** *Magn Reson Imaging* 1990;8:351–56 CrossRef Medline
- Kay I, Henkelman RM. **Practical implementation and optimization of one-shot T1 imaging.** *Magn Reson Med* 1991;22:414–24 CrossRef Medline
- Henderson E, McKinnon G, Lee TY, et al. **A fast 3D Look-Locker method for volumetric T1 mapping.** *Magn Reson Imaging* 1999;17:1163–71 CrossRef Medline
- Crawley AP, Henkelman RM. **A comparison of one-shot and recovery methods in T1 imaging.** *Magn Reson Med* 1988;7:23–34 CrossRef Medline
- Yuan J, Chow SK, Yeung DK, et al. **Quantitative evaluation of dual-flip-angle T1 mapping on DCE-MRI kinetic parameter estimation in head and neck.** *Quant Imaging Med Surg* 2012;2:245–53 CrossRef Medline
- Yankeelov TE, Gore JC. **Dynamic contrast enhanced magnetic resonance imaging in oncology: theory, data acquisition, analysis, and examples.** *Curr Med Imaging Rev* 2009;3:91–107 Medline
- Chawla S, Kim S, Dougherty L, et al. **Pretreatment diffusion-weighted and dynamic contrast-enhanced MRI for prediction of local treatment response in squamous cell carcinomas of the head and neck.** *AJR Am J Roentgenol* 2013;200:35–43 CrossRef Medline
- Chawla S, Kim S, Loevner LA, et al. **Prediction of disease-free survival in patients with squamous cell carcinomas of the head and neck using dynamic contrast-enhanced MR imaging.** *AJNR Am J Neuroradiol* 2011;32:778–84 CrossRef Medline
- Chikui T, Kawano S, Kawazu T, et al. **Prediction and monitoring of the response to chemoradiotherapy in oral squamous cell carcinoma.**

- mas using a pharmacokinetic analysis based on the dynamic contrast-enhanced MR imaging findings. *Eur Radiol* 2011;21:1699–708 CrossRef Medline
29. Shukla-Dave A, Lee NY, Jansen JF, et al. Dynamic contrast-enhanced magnetic resonance imaging as a predictor of outcome in head-and-neck squamous cell carcinoma patients with nodal metastases. *Int J Radiat Oncol Biol Phys* 2012;82:1837–44 CrossRef
 30. Wang P, Popovtzer A, Eisbruch A, et al. An approach to identify, from DCE MRI, significant subvolumes of tumors related to outcomes in advanced head-and-neck cancer. *Med Phys* 2012;39:5277–85 CrossRef Medline
 31. Yabuuchi H, Fukuya T, Tajima T, et al. Salivary gland tumors: diagnostic value of gadolinium-enhanced dynamic MR imaging with histopathologic correlation. *Radiology* 2003;226:345–54 CrossRef Medline
 32. Yabuuchi H, Matsuo Y, Kamitani T, et al. Parotid gland tumors: can addition of diffusion-weighted MR imaging to dynamic contrast-enhanced MR imaging improve diagnostic accuracy in characterization? *Radiology* 2008;249:909–16 CrossRef Medline
 33. Tunca F, Giles Y, Salmaslioglu A, et al. The preoperative exclusion of thyroid carcinoma in multinodular goiter: dynamic contrast-enhanced magnetic resonance imaging versus ultrasonography-guided fine-needle aspiration biopsy. *Surgery* 2007;142:992–1002; discussion 1002.e1001–1002 CrossRef Medline
 34. Juan CJ, Chen CY, Jen YM, et al. Perfusion characteristics of late radiation injury of parotid glands: quantitative evaluation with dynamic contrast-enhanced MRI. *Eur Radiol* 2009;19:94–102 CrossRef Medline
 35. Asaumi J, Hisatomi M, Yanagi Y, et al. Assessment of ameloblastomas using MRI and dynamic contrast-enhanced MRI. *Eur J Radiol* 2005;56:25–30 CrossRef Medline
 36. Asaumi J, Yanagi Y, Hisatomi M, et al. The value of dynamic contrast-enhanced MRI in diagnosis of malignant lymphoma of the head and neck. *Eur J Radiol* 2003;48:183–87 CrossRef Medline
 37. Asaumi J, Yanagi Y, Konouchi H, et al. Application of dynamic contrast-enhanced MRI to differentiate malignant lymphoma from squamous cell carcinoma in the head and neck. *Oral Oncol* 2004;40:579–84 CrossRef Medline
 38. Hisatomi M, Asaumi J, Yanagi Y, et al. Assessment of pleomorphic adenomas using MRI and dynamic contrast enhanced MRI. *Oral Oncol* 2003;39:574–79 CrossRef Medline
 39. Matsuzaki H, Hara M, Yanagi Y, et al. Magnetic resonance imaging (MRI) and dynamic MRI evaluation of extranodal non-Hodgkin lymphoma in oral and maxillofacial regions. *Oral Surg Oral Med Oral Pathol Oral Radiol* 2012;113:126–33 CrossRef Medline
 40. Unetsubo T, Konouchi H, Yanagi Y, et al. Dynamic contrast-enhanced magnetic resonance imaging for estimating tumor proliferation and microvessel density of oral squamous cell carcinomas. *Oral Oncol* 2009;45:621–26 CrossRef Medline
 41. Agrawal S, Awasthi R, Singh A, et al. An exploratory study into the role of dynamic contrast-enhanced (DCE) MRI metrics as predictors of response in head and neck cancers. *Clin Radiol* 2012;67:e1–5 CrossRef Medline
 42. Fischbein NJ, Noworolski SM, Henry RG, et al. Assessment of metastatic cervical adenopathy using dynamic contrast-enhanced MR imaging. *AJNR Am J Neuroradiol* 2003;24:301–11 Medline
 43. Noworolski SM, Fischbein NJ, Kaplan MJ, et al. Challenges in dynamic contrast-enhanced MRI imaging of cervical lymph nodes to detect metastatic disease. *J Magn Reson Imaging* 2003;17:455–62 CrossRef Medline
 44. Yuan Y, Kuai XP, Chen XS, et al. Assessment of dynamic contrast-enhanced magnetic resonance imaging in the differentiation of malignant from benign orbital masses. *Eur J Radiol* 2013;82:1506–11 CrossRef Medline
 45. Chikui T, Kitamoto E, Kawano S, et al. Pharmacokinetic analysis based on dynamic contrast-enhanced MRI for evaluating tumor response to preoperative therapy for oral cancer. *J Magn Reson Imaging* 2012;36:589–97 CrossRef Medline
 46. Newbold K, Castellano I, Charles-Edwards E, et al. An exploratory study into the role of dynamic contrast-enhanced magnetic resonance imaging or perfusion computed tomography for detection of intratumoral hypoxia in head-and-neck cancer. *Int J Radiat Oncol Biol Phys* 2009;74:29–37 CrossRef Medline
 47. Yuan J, Chow SK, Yeung DK, et al. A five-colour colour-coded mapping method for DCE-MRI analysis of head and neck tumours. *Clin Radiol* 2012;67:216–23 CrossRef Medline
 48. Støre G, Smith HJ, Larheim TA. Dynamic MR imaging of mandibular osteoradionecrosis. *Acta Radiol* 2000;41:31–37 CrossRef Medline
 49. Van Cann EM, Rijpkema M, Heerschap A, et al. Quantitative dynamic contrast-enhanced MRI for the assessment of mandibular invasion by squamous cell carcinoma. *Oral Oncol* 2008;44:1147–54 CrossRef Medline
 50. Tsao J, Boesiger P, Pruessmann KP. k-t BLAST and k-t SENSE: dynamic MRI with high frame rate exploiting spatiotemporal correlations. *Magn Reson Med* 2003;50:1031–42 CrossRef Medline
 51. Port RE, Knopp MV, Hoffmann U, et al. Multicompartment analysis of gadolinium chelate kinetics: blood-tissue exchange in mammary tumors as monitored by dynamic MR imaging. *J Magn Reson Imaging* 1999;10:233–41 Medline
 52. van Osch MJ, Vonken EJ, Viergever MA, et al. Measuring the arterial input function with gradient echo sequences. *Magn Reson Med* 2003;49:1067–76 CrossRef Medline
 53. McIntyre DJ, Ludwig C, Pasan A, et al. A method for interleaved acquisition of a vascular input function for dynamic contrast-enhanced MRI in experimental rat tumours. *NMR Biomed* 2004;17:132–43 CrossRef Medline
 54. Kim YR, Rebro KJ, Schmainda KM. Water exchange and inflow affect the accuracy of T1-GRE blood volume measurements: implications for the evaluation of tumor angiogenesis. *Magn Reson Med* 2002;47:1110–20 CrossRef Medline
 55. Konouchi H, Asaumi J, Yanagi Y, et al. Evaluation of tumor proliferation using dynamic contrast enhanced-MRI of oral cavity and oropharyngeal squamous cell carcinoma. *Oral Oncol* 2003;39:290–95 CrossRef Medline
 56. Matsuzaki H, Yanagi Y, Hara M, et al. Minor salivary gland tumors in the oral cavity: diagnostic value of dynamic contrast-enhanced MRI. *Eur J Radiol* 2012;81:2684–91 CrossRef Medline
 57. Matsuzaki H, Yanagi Y, Hara M, et al. Diagnostic value of dynamic contrast-enhanced MRI for submucosal palatal tumors. *Eur J Radiol* 2012;81:3306–12 CrossRef Medline
 58. Yuan Y, Yue XH, Tao XF. The diagnostic value of dynamic contrast-enhanced MRI for thyroid tumors. *Eur J Radiol* 2012;81:3313–18 CrossRef Medline
 59. Furukawa M, Parvathaneni U, Maravilla K, et al. Dynamic contrast-enhanced MR perfusion imaging of head and neck tumors at 3 Tesla. *Head Neck*. 2013;35:923–29 CrossRef Medline
 60. Jansen JF, Schöder H, Lee NY, et al. Tumor metabolism and perfusion in head and neck squamous cell carcinoma: pretreatment multimodality imaging with 1H magnetic resonance spectroscopy, dynamic contrast-enhanced MRI, and [18F]FDG-PET. *Int J Radiat Oncol Biol Phys* 2012;82:299–307 CrossRef
 61. Jansen JF, Schöder H, Lee NY, et al. Noninvasive assessment of tumor microenvironment using dynamic contrast-enhanced magnetic resonance imaging and 18F-fluoromisonidazole positron emission tomography imaging in neck nodal metastases. *Int J Radiat Oncol Biol Phys* 2010;77:1403–10 CrossRef Medline
 62. Taylor JS, Tofts PS, Port R, et al. MR imaging of tumor microcirculation: promise for the new millennium. *J Magn Reson Imaging* 1999;10:903–07 Medline
 63. Jackson A, O'Connor JP, Parker GJ, et al. Imaging tumor vascular heterogeneity and angiogenesis using dynamic contrast-enhanced magnetic resonance imaging. *Clin Cancer Res* 2007;13:3449–59 CrossRef Medline
 64. Fukumura D, Jain RK. Tumor microenvironment abnormalities: causes, consequences, and strategies to normalize. *J Cell Biochem* 2007;101:937–49 CrossRef Medline

65. Kim S, Loevner LA, Quon H, et al. **Prediction of response to chemoradiation therapy in squamous cell carcinomas of the head and neck using dynamic contrast-enhanced MR imaging.** *AJNR Am J Neuroradiol* 2010;31:262–68 CrossRef Medline
66. Tofts PS, Brix G, Buckley DL, et al. **Estimating kinetic parameters from dynamic contrast-enhanced T(1)-weighted MRI of a diffusible tracer: standardized quantities and symbols.** *J Magn Reson Imaging* 1999;10:223–32 Medline
67. Miller JC, Pien HH, Sahani D, et al. **Imaging angiogenesis: applications and potential for drug development.** *J Natl Cancer Inst* 2005;97:172–87 CrossRef Medline
68. Lee FK, King AD, Ma BB, et al. **Dynamic contrast enhancement magnetic resonance imaging (DCE-MRI) for differential diagnosis in head and neck cancers.** *Eur J Radiol* 2012;81:784–88 CrossRef Medline
69. Tuncbilek N, Karakas HM, Altaner S. **Dynamic MRI in indirect estimation of microvessel density, histologic grade, and prognosis in colorectal adenocarcinomas.** *Abdom Imaging* 2004;29:166–72 CrossRef Medline
70. Henderson E, Rutt BK, Lee TY. **Temporal sampling requirements for the tracer kinetics modeling of breast disease.** *Magn Reson Imaging* 1998;16:1057–73 CrossRef Medline
71. Larsson HB, Stubgaard M, Søndergaard L, et al. **In vivo quantification of the unidirectional influx constant for Gd-DTPA diffusion across the myocardial capillaries with MR imaging.** *J Magn Reson Imaging* 1994;4:433–40 CrossRef Medline
72. Tofts PS. **Modeling tracer kinetics in dynamic Gd-DTPA MR imaging.** *J Magn Reson Imaging* 1997;7:91–101 CrossRef Medline
73. Yang X, Knopp MV. **Quantifying tumor vascular heterogeneity with dynamic contrast-enhanced magnetic resonance imaging: a review.** *J Biomed Biotechnol* 2011;2011:732848 CrossRef Medline
74. Singh A, Haris M, Rathore D, et al. **Quantification of physiological and hemodynamic indices using T(1) dynamic contrast-enhanced MRI in intracranial mass lesions.** *J Magn Reson Imaging* 2007;26:871–80 CrossRef Medline
75. Jansen JF, Carlson DL, Lu Y, et al. **Correlation of a priori DCE-MRI and (1)H-MRS data with molecular markers in neck nodal metastases: initial analysis.** *Oral Oncol* 2012;48:717–22 CrossRef Medline

ICD-10: History and Context

 J.A. Hirsch,  G. Nicola,  G. McGinty,  R.W. Liu,  R.M. Barr,  M.D. Chittle, and  L. Manchikanti

ABSTRACT

SUMMARY: In recent months, organized medicine has been consumed by the anticipated transition to the 10th iteration of the International Classification of Disease system. Implementation has come and gone without the disruptive effects predicted by many. Despite the fundamental role the International Classification of Disease system plays in health care delivery and payment policy, few neuroradiologists are familiar with the history of its implementation and implications beyond coding for diseases.

ABBREVIATIONS: CM = Clinical Modification; CMS = Centers for Medicare and Medicaid Services; CPT = Current Procedural Terminology; ICD = International Classification of Disease; RUC = Specialty Society Relative Value Scale Update Committee; WHO = World Health Organization

The International Classification of Disease (ICD) system was created for the accurate tracking of diseases within a population. Across the years, it has become an integral part of the payment infrastructure of the US health care system along with the Current Procedural Terminology (CPT) coding system for medical procedures. As our knowledge of disease advances and the US health care system payment policy evolves from volume to value, so must the ICD system. Now that ICD-10 is finally implemented after 2 congressionally legislated delays, the physician community remains wary of potential upheaval related to complex changes required for billing systems. We believe a review of the history of the International Classification of Disease system will be useful to the practicing neuroradiologist.

History

Pre-ICD-10. Some scholars track the origin of ICD to 1763. The French physician and botanist Dr François Bossier de Sauvages de Lacroix developed a categorization of 10 distinct classes of dis-

eases, which were further divided into 2400 unique diseases.¹ Sauvages de Lacroix was a contemporary and friend of the Swedish naturalist Carl Von Linné, considered the father of modern taxonomy. His classification system, built on earlier work by the English physician Thomas Sydenham, was similar to methods used by botanists at the time. Recognizing the importance of disease classification, the first International Statistical Congress held in Brussels in 1853 appointed Jacob Marc d'Espine and William Farr to develop a system of classifying causes of mortality that could be used across borders and languages.² This was the genesis of what became known as the "International List of Causes of Death." History will prove the sagacity of these early thought leaders. In 1893, Jacques Bertillon, a Parisian statistician, and his committee established the first "International List of Causes of Death."³ At around that time, the "International List of Causes of Death" was presented in the United States at the International Statistical Institute, and in 1898, various countries in North America, including the United States, adopted this system.⁴ Across time, this "International List of Causes of Death" was updated and published about once per decade in 1900, 1910, 1920, 1929, and 1938.⁵

The many twists and turns taken by this process during the half-century described are beyond the intended scope of this article. Suffice it to say that challenges were raised to the development of a reporting system for morbidity. In 1948, the World Health Organization (WHO) took charge of the classification system, which was expanded the following year to include coding for causes of morbidity in addition to mortality. The system was rechristened the International Classification of Disease system.^{2,4} Under the auspices of the WHO, ICD development continued in a more predictable manner. The first 5 versions of the ICD system

Received November 18, 2015; accepted November 23.

From the Department of Radiology (J.A.H., R.W.L., M.D.C.), Massachusetts General Hospital, Harvard Medical School, Boston, Massachusetts; Department of Radiology (G.N.), Hackensack Radiology Group, University Medical Center, River Edge, New Jersey; Department of Radiology (G.M.), Weill Cornell Medical College, New York, New York; Mecklenburg Radiology Associates (R.M.B.), Charlotte, North Carolina; and Department of Anesthesiology and Perioperative Medicine (L.M.), Pain Management Center of Paducah, University of Louisville, Paducah, Kentucky.

J.A.H. and L.M. developed the original draft. All other authors had an opportunity to review and provide meaningful edits towards the final manuscript.

Please address correspondence to Joshua A. Hirsch, MD, Department of Radiology, Massachusetts General Hospital, Harvard Medical School, 55 Fruit St, Gray Building 2nd floor, Boston, MA 02114; e-mail: jahirsch@mgh.harvard.edu; @JoshuaAHirsch

<http://dx.doi.org/10.3174/ajnr.A4696>

were each entirely contained within a single volume. That volume included an alphabetic index and a tabular list. By the sixth revision, the coding system included morbidity and mortality designations and required 2 volumes. Most important, ICD-6 expanded to include a section on psychiatric disorders. This sixth version was now called the *Manual of the International Statistical Classification of Diseases, Injuries, and Causes of Death* (http://apps.who.int/iris/bitstream/10665/70934/2/ICD_10_1967_v1_eng.pdf). Revisions have continued on an approximately decade-by-decade basis under the WHO, and the seventh and eight revisions were published in 1957 and 1968.³

In what could be called a parallel effort, the United States Public Health Service adapted the ICD to index hospital records and classify surgical procedures (ICDA) and published this system in 1962. The seventh edition of the ICD, therefore, expanded to include materials thought to be necessary for categorizing needs for hospitals. The Public Health Service went on to publish an eighth revision of the ICD, specifically focused on the unique needs of the United States known as ICDA-8. It had additional focus on morbidity and mortality reporting.³

The ICD-9 was published in 1977 by the Department of Knowledge Management and Sharing of the World Health Organization. ICD-9 was an important transition to increased granularity with 4-digit-level categories and a variety of optional 5-digit subdivisions. It was also pivotal in moving the system out of the WHO once ICD became a part of the public domain. ICD-9-Clinical Modification (CM) was the next expansion in the United States. The intention was to allow diagnostic coding of inpatient, outpatient, and physician office (nonfacility) use. It was developed by the National Center for Health Statistics. The CM expansion provided an opportunity to capture enhanced morbidity data and to update more frequently. This system is updated on October 1 of each year. ICD-9-CM was by now a 3-volume set with the first 2 volumes pertaining to diagnostic codes and the third containing procedural codes, though the latter never gained the popularity and widespread use in the United States of those developed through the Current Procedural Terminology process. The Centers for Medicare and Medicaid Services (CMS) and the National Center for Health Statistics both contribute to the oversight of the ICD-9-CM.³ In 1983, the Inpatient Prospective Payment System was adopted to pay for hospital care in the Medicare program, which insures the elderly and those with chronic disease. ICD-9-CM volumes 1, 2, and 3 were used for assigning cases to the Diagnoses-Related Groups used to derive payment amounts.

The Tenth Edition. Neuroradiologists might be surprised to learn that work on ICD-10 began >30 years ago. Historically, updates occurred approximately once per decade. The initial effort on ICD-10 concluded in 1992. The ICD-10-CM was then introduced for its annual process of review in 1992. ICD-10 is much more granular than ICD-9, with an expansion from 17,000 codes to approximately 155,000. US-based providers might be further surprised to find out that many other countries transitioned to some form of ICD-10 many years ago. For example, Canada introduced a modified system, ICD-10-CA, in 2000. The international version of ICD-10 is used in >100 countries for cause-of-death reporting and statistics. In 2003, the Health Insurance Portability

and Accountability Act of 1996 named ICD-9 as the code set for reporting diagnoses and procedures in electronic administrative transactions.⁶ On January 16, 2009, the US Department of Health and Human Services published a regulation requiring the replacement of ICD-9 with ICD-10 as of October 1, 2013.

ICD-10-CM uses the same basic hierarchical structure as ICD-9-CM. The first 3 digits represent common traits, with each subsequent character providing greater specificity. ICD-10-CM is alphanumeric, with a possible 7 digits of specificity as opposed to the 5 digits of the ICD-9. An oddity is that the letter *U* is the only letter not used.⁷ Other noteworthy changes include the addition of information relevant to ambulatory and managed care and greatly expanded injury codes that reflect the site of injury. Given the dramatic changes occurring within organized medicine in 2013, some authors called for a delay in the implementation of ICD-10 from the original planned date of October 1, 2013.⁸ This idea gained greater traction when the American Medical Association formally adopted a policy that favored delaying implementation.^{8,9} The original implementation date was extended by the Department of the Health and Human Services in the latter half of 2012 to October 1, 2014.¹⁰ There was continued discomfort regarding implementation of ICD-10 by the 2014 date. The Protecting Access to Medicare Act of 2014 was primarily considered in the context of providing a temporary patch for the sustainable growth rate.^{11,12} Embedded within that legislation was a further delay in the implementation of ICD-10 until October 1, 2015.¹² Finally October 1, 2015, was the date that ICD-10-CM went live in the United States.

Relationship to Current Procedural Terminology

Procedural reimbursement in the United States involves a complex interplay between the American Medical Association and the Centers for Medicare and Medicaid Services. In the mid-1960s, the American Medical Association, working with multiple major medical specialty societies, developed an iterative coding system for describing medical procedures and services. This system was termed the Current Procedural Terminology coding system.¹³ The first edition of CPT (1966) primarily described surgical procedures. CPT when first established did not have a relationship with reimbursement. With time, CPT became critical not only to procedural reimbursement but also, assuming additional roles in administrative management, tracking new procedures and evolving aspects of pay for performance as we describe below.

The Health Insurance Portability and Accountability Act required the Department of Health and Human Services to name national standards, including specifying code sets, for electronic transactions of health care information. This resulted in an expansion of CPT beyond procedure and service reporting into the tracking of new services and procedures, as well as facilitating the reporting of measures useful for pay for performance. The revised CPT codes are accepted by Medicare for use in claims processing and have been incorporated wholesale into the coding system of Medicare, designated the Health Care Common Procedure Coding System.¹³

CPT is a work product that is owned by the American Medical Association. A concurrent activity is known as the American Medical Association Specialty Society Relative Value Scale Update

Committee. This committee is colloquially known as the RUC, and it attempts to provide a scale of relativity across the range of medical procedures in making recommendations for reimbursement values to CMS.^{14,15} CMS representatives attend the RUC meetings, and CMS considers the recommendations of the RUC before ultimately deciding the reimbursement for medical services. The American Society of Neuroradiology is represented at both the Current Procedural Terminology and the Specialty Society Relative Value Scale Update Committees.

DISCUSSION

After several legislatively mandated delays, ICD-10-CM went live on October 1, 2015. Implementation is costly but, nonetheless, required.¹⁶ Our belief is that ultimately the enhanced granularity will be useful not only for disease tracking but also for serving as necessary infrastructure for reimbursement of value over volume in the evolving US health care delivery system. The evolving payment paradigm requires sophisticated tracking tools such as ICD-10 to accurately gauge the effectiveness of the treating provider or treating institution, as well as tracking costs of these therapies. Without an increase in the granularity of disease classification, bending the US health care system cost curve by rewarding value over volume would not be possible. With that scenario in mind, coding mistakes are a real and a potentially costly possibility. While CMS has reluctantly agreed to allow a 1-year grace period for coding mistakes, there is no guarantee that commercial carriers will follow suit.

As ICD-10-CM granularity has increased, a seldom-discussed but realistic question is the ongoing relevance of CPT. With >150,000 distinct codes, including those that describe procedures, one could imagine a circumstance in which sufficient granularity would be available to raise questions about the need for CPT codes. As outlined above, Current Procedural Terminology arose to meet a specific need in the mid-1960s. The CPT system is embedded in calculations of the CMS of relativity in the reimbursement system we currently use.

Additionally, providers need to be very aware of “high-risk” codes. These are ICD-9 codes that map to multiple different ICD-10 variations. In fact, there are >3600 instances in which ICD-10-CM codes can map to multiple different ICD-9-CM codes. Conversely, and more unusual, there are >500 codes that are more specific in the ICD-9-CM than in ICD-10-CM.¹⁷

Organized medicine often faces unfunded mandates. This one is noteworthy because of its cost. A 2008 study¹⁸ predicted that implementation of ICD-10 would cost typical practices between \$83,292 and \$2.7 million, depending on the size of the practice, though a more recent study nearly tripled those estimates.¹⁶ In addition, cash flow disruptions have been predicted to range from \$50,000 to \$15 million for large practices.^{18,19} Large hospital systems can spend vast sums of money implementing a new electronic medical record.²⁰ Moreover, while information technology has the power to deliver powerful improvement in the delivery of medical care, it could also be accused of depersonalizing that care. We make these points to contextualize the challenges of unfunded mandates such as ICD-10 in this era of remarkable expenditures.²¹

While ICD-10-CM implementation is only occurring in the

United States in 2015, readers of this vignette will recall that work on it started >30 years ago and that previously, updates to the system occurred on a reasonably semi-predictable 10-year basis. Work on ICD-11 has already been ongoing for quite a few years. A beta draft was published on-line in 2012 for initial consultation and commenting and a completed product is expected by 2018.²²

CONCLUSIONS

ICD-10-CM has been noteworthy for the controversy that has surrounded its implementation. It is a far more granular system than its predecessor, allowing better disease tracking, but this granularity also leads to physician anxiety in the context of payment policy. The transition to ICD-10-CM is inconsistently supported by payers and has been hampered by other regulatory requirements related to the Affordable Care Act to which providers are subject.

Neuroradiologists have enjoyed continuous, multiyear representation at the 2 committees that are integrally involved in determining physician reimbursement in the United States. CPT is 1 of the 2 committees. With the increasing granularity associated with ICD-10-CM, in the setting of a new payment paradigm, one might begin to wonder about how that system might impact current procedural coding. Internationally, as US doctors embrace ICD-10-CM, it is worth remembering that work has begun on ICD-11. We can only presume that transitioning to this system is a number of years off in the United States. One can only wonder what Sauvages de Lacroix would think about the seismic transitions that have occurred since he proposed classifying diseases in 1763.

Disclosures: Joshua A. Hirsch—UNRELATED: Consultancy: Medtronic/CareFusion, Comments: Both are related to the spine. Medtronic is ongoing. CareFusion was in the last 36 months (single course). Neither is related to the topic of the article. Raymond W. Liu—UNRELATED: Expert Testimony: legal work. Robert M. Barr—UNRELATED: Board Membership: Novant Health. Laxmaiah Manchikanti—UNRELATED: Consultancy: Semnur Pharmaceuticals, Comments: I provided limited consulting services to Semnur Pharmaceuticals, which is developing nonparticulate steroids (US \$1400).

REFERENCES

1. Jetté N, Quan H, Hemmelgarn B, et al; IMECCHI Investigators. **The development, evolution, and modifications of ICD10: challenges to the international comparability of morbidity data.** *Med Care* 2010; 48:1105–10 CrossRef Medline
2. World Health Organization: History of the Development of the ICD. <http://www.who.int/classifications/icd/en/HistoryOfICD.pdf>. Accessed November 4, 2015
3. Manchikanti L, Falco FJ, Hirsch JA. **Necessity and implications of ICD-10: facts and fallacies.** *Pain Physician* 2011;14:E405–25 Medline
4. Gershenov M. **The ICD family of classifications.** *Methods Inf Med* 1995;34:172–75 Medline
5. Jakob R, Ustun B, Madden R, et al. **The WHO Family of International Classifications.** *Bundesgesundheitsblatt Gesundheitsforschung Gesundheitsschutz* 2007;50:924–31 CrossRef Medline
6. Health Insurance Portability and Accountability Act (HIPAA) of 1996. Pub L No. 104–191, Stat 1968
7. Grider DJ. **Format and structure of ICD-10-CM.** In: Grider DJ. *Preparing for ICD-10-CM: Making the Transition Manageable.* Chicago: American Medical Association; 2010:77–114
8. Manchikanti L, Falco FJ, Hirsch JA. **Ready or not! Here comes ICD-10.** *J Neurointerv Surg* 2013; 5:86–91 CrossRef Medline
9. AMA Adopts New Policies During Final Day of Semi-Annual Meeting. November 15, 2011. <http://news.cision.com/american->

- medical-association/r/ama-adopts-new-policies-during-final-day-of-semi-annual-meeting,c9187364. Accessed January 13, 2016
10. Office of the Secretary, HHS. **HIPAA administrative simplification: modifications to medical data code set standards to adopt ICD-10-CM and ICD-10-PCS—final rule.** *Fed Regist* 2009;74:3328–62 Medline
 11. Hirsch JA, Manchikanti L. **The sustainable growth rate: a 2014 update.** *J Neurointerv Surg* 2014;6:411–12 CrossRef Medline
 12. Hirsch JA, Leslie-Mazwi TM, Nicola GN, et al. **The ICD-10 system: a gift that keeps on taking.** *J Neurointerv Surg* 2015;7:619–22 CrossRef Medline
 13. Hirsch JA, Leslie-Mazwi TM, Nicola GN, et al. **Current procedural terminology: a primer.** *J Neurointerv Surg* 2015;7:309–12 CrossRef Medline
 14. Hirsch JA, Silva E 3rd, Nicola GN, et al. **The RUC: a primer for neurointerventionalists.** *J Neurointerv Surg* 2014;6:61–64 CrossRef Medline
 15. Hirsch JA, Donovan WD, Leslie-Mazwi TM, et al. **Component coding and the neurointerventionalist: a tale with an end.** *J Neurointerv Surg* 2013;5:615–19 CrossRef Medline
 16. AMA News Room. American Medical Association: ICD-10 cost estimates increased for most physicians. February 12, 2014. <http://www.ama-assn.org/ama/pub/news/news/2014/2014-02-12-icd10-cost-estimates-increased-for-most-physicians.page>. Accessed November 4, 2015
 17. Manchikanti L, Hammer M, Boswell MV, et al. **Survival strategies for tsunami of ICD-10-CM for interventionalists: pursue or perish!** *Pain Physician* 2015;18:E685–712 Medline
 18. Nachimson Advisors. **The impact of implementing ICD-10 on physician practices and clinical laboratories.** Reisterstown, Maryland: Nachimson Advisors, October 8, 2008. <http://www.nachimsonadvisors.com/Documents/ICD-10%20Impacts%20on%20Providers.pdf>. Accessed January 13, 2016
 19. Meyer H. **Coding complexity: US health care gets ready for the coming of ICD-10.** *Health Aff* 2011;30:968–74 CrossRef Medline
 20. Murphy K. **Epic EHR implementation costs Brigham and Women's Hospital.** December 10, 2015. <https://ehrintelligence.com/news/epic-ehr-implementation-costs-brigham-and-womens-hospital>. Accessed January 13, 2016
 21. Manchikanti L, Hirsch JA. **A case for restraint of explosive growth of health information technology: first, do no harm.** *Pain Physician* 2015;18:E293–98 Medline
 22. World Health Organization: The international classifications of diseases 11th revision is due by 2018. <http://www.who.int/classifications/icd/revision/en/>. Accessed October 3, 2015

Clinical Applications of Simultaneous PET/MR Imaging Using (R)-[¹¹C]-Verapamil with Cyclosporin A: Preliminary Results on a Surrogate Marker of Drug-Resistant Epilepsy

J.-W. Shin, K. Chu, S.A. Shin, K.-H. Jung, S.-T. Lee, Y.-S. Lee, J. Moon, D.Y. Lee, J.S. Lee, D.S. Lee, and S.K. Lee



ABSTRACT

BACKGROUND AND PURPOSE: The development of resistance to antiepileptic drugs is explained well by the transporter hypothesis, which suggests that drug resistance is caused by inadequate penetration of drugs into the brain barrier as a result of increased levels of efflux transporter such as p-glycoprotein. To evaluate the brain expression of p-glycoprotein in patients with drug-resistant epilepsy, including neocortical epilepsy, we developed a noninvasive quantitative analysis including asymmetry indices based on (R)-[¹¹C]-verapamil PET/MR imaging with cyclosporin A, a p-glycoprotein inhibitor.

MATERIALS AND METHODS: Six patients with drug-resistant epilepsy, 5 patients with drug-sensitive epilepsy, and 8 healthy controls underwent dynamic (R)-[¹¹C]-verapamil PET/MR imaging with an intravenous infusion of cyclosporin A. Asymmetry indices [(Right Region – Left Region)/(Right Region + Left Region) × 200%] of the standard uptake values in each of the paired lobes were calculated.

RESULTS: All patients with drug-resistant epilepsy had significantly different asymmetry from the healthy controls, whereas all patients with drug-sensitive epilepsy had asymmetry similar to that in healthy controls. In the temporal lobe, the asymmetry indices of patients with left temporal lobe drug-resistant epilepsy were more positive than those of healthy controls (healthy controls: 4.0413 ± 1.7452 ; patients: 7.2184 ± 1.8237 ; $P = .048$), and those of patients with right temporal drug-resistant epilepsy were more negative (patients: -1.6496 ± 3.4136 ; $P = .044$). In addition, specific regions that had significant asymmetry were different between the lateral and medial temporal lobe epilepsy groups. In the frontal lobe, the asymmetry index of patients with right frontal lobe drug-resistant epilepsy was more negative than that in healthy controls.

CONCLUSIONS: We confirmed that statistical parametric mapping analysis by using asymmetry indices of (R)-[¹¹C]-verapamil PET/MR imaging with cyclosporin A could be used as a surrogate marker for drug-resistant epilepsy, and this approach might be helpful for localizing or lateralizing the epileptic zone.

ABBREVIATIONS: AI = asymmetry index; CS = cyclosporin A; DRE = drug-resistant epilepsy; DSE = seizure-free drug-sensitive epilepsy; Pgp = p-glycoprotein; SPAM = statistical probabilistic anatomic mapping; SUV = standard uptake value; TLE = temporal lobe epilepsy; VPM-PET/MR-CS = (R)-[¹¹C]-verapamil PET and MR imaging with intravenous infusion of cyclosporin A without serial arterial sampling

Epilepsy, which is characterized by recurrent spontaneous seizures, is one of the most common neurologic disorders.¹ Despite the development of third-generation antiepileptic drugs during the past 3 decades, 20%–30% of patients with epilepsy

remain resistant to drug treatment.^{2,3} The mechanisms of drug resistance in epilepsy remain unclear. Among the mechanisms of drug resistance in epilepsy, increasing experimental and clinical evidence supports the transporter hypothesis.⁴ Several studies have suggested that the increased expression of efflux transporters, such as p-glycoprotein (Pgp), at the blood-brain barrier in the focal tissue limits the penetration of antiepileptic drugs into the focus.^{5,6} In the human brain, Pgp exhibited a highly localized

Received May 24, 2015; accepted after revision August 17.

From the Department of Neurology (J.-W.S., K.C., K.-H.J., S.-T.L., J.M., D.Y.L., S.K.L.), Comprehensive Epilepsy Center, Laboratory for Neurotherapeutics, Biomedical Research Institute; and Department of Nuclear Medicine (S.A.S., Y.-S.L., J.S.L., D.S.L.); and Department of Biomedical Sciences (S.A.S., J.S.L.), Seoul National University Hospital, Seoul National University College of Medicine, Seoul, South Korea; Department of Neurology (J.-W.S.), CHA Bundang Medical Center, CHA University, Seongnam, Korea; and Department of Molecular Medicine and Biopharmaceutical Sciences (Y.-S.L., D.S.L.), Graduate School of Convergence Science and Technology, Kyunggi, South Korea.

J.-W.S. and K.C. contributed equally to this work.

This study was supported by the Ministry of Health and Welfare (A0700001-1232-1280100), Republic of Korea.

Please address correspondence to Sang Kun Lee, MD, PhD, Department of Neurology, Seoul National University Hospital, 101, Daehangro, Jongro-Gu, Seoul 110-744, South Korea; e-mail: sangkun2923@gmail.com

Indicates open access to non-subscribers at www.ajnr.org

Indicates article with supplemental on-line tables.

Indicates article with supplemental on-line photo.

<http://dx.doi.org/10.3174/ajnr.A4566>

overexpression on the vascular endothelium and the end-feet of the vascular glia in cases of drug-resistant epilepsy (DRE).⁷

Consequently, the problem of drug resistance in epilepsy might be resolved by the development of a new treatment strategy targeting the transporter mechanism. In developing such a strategy, surrogate markers should objectively pinpoint the expression of transporters such as Pgp. More important, surrogate markers should be used noninvasively to render the technique readily applicable in clinical practice. Several recent clinical trials have evaluated Pgp expression in humans via positron-emission tomography by using the Pgp substrate (R)-[¹¹C]-verapamil and Pgp inhibitors, such as tariquidar or cyclosporin A (CS).^{8,9} Several investigators have performed (R)-[¹¹C]-verapamil PET in patients with epilepsy to compare the expression of Pgp between patients with DRE and healthy controls, by using the percentage changes in verapamil influx or the efflux rate before and after Pgp inhibitor injection. However, to our knowledge, there has been no study for MRI-negative neocortical epilepsies, and previous methods were applied only to medial temporal lobe epilepsy (TLE). Furthermore, they confirmed that the change in the verapamil influx rate was smaller in patients with DRE compared with healthy controls; this difference necessitated the use of complex analytic methods, including invasive serial arterial sampling, which has limited applicability in clinical practice.

Another problem is that in (R)-[¹¹C]-verapamil PET, it is impossible to find focal hypo- or hyper-radio uptake regions because when one uses the Pgp inhibitor, individually distinct Pgp functions of the whole brain and regional differences in Pgp expression may result in interindividual variability of radiotracer uptake in the whole brain and specific brain regions.^{10,11}

Therefore, to develop a more feasible surrogate marker that can be used in clinical practice, we performed (R)-[¹¹C]-verapamil PET and MR imaging with intravenous infusion of cyclosporin A without serial arterial sampling (VPM-PET/MR-CS). The subject population comprised patients who were drug-resistant and seizure-free with various types of epilepsy, MRI-negative neocortical epilepsy. We analyzed the data by using statistical probabilistic anatomical mapping (SPAM) with the asymmetry index (AI) of the standard uptake value (SUV). We hypothesized that Pgp activity is higher in the epileptic foci compared with the contralateral normal area in patients with drug-resistance, and the asymmetry will be larger than that in healthy individuals or patients who are seizure-free.

MATERIALS AND METHODS

Subjects

Patients with epilepsy (age range, 18–53 years) who were either drug-resistant or drug-sensitive were recruited between January 2013 and March 2014 from epilepsy clinics led by an epileptologist (S.K.L.) at Seoul National University Hospital. All patients had been examined for 24 hours by using video electroencephalography monitoring, and patients with DRE had previously undergone presurgical evaluation. “DRE” was defined as the failure of adequate trials of 2 tolerated and appropriately chosen and used antiepileptic drugs schedules (whether as monotherapies or in combination) to achieve sustained freedom from seizures.¹² “Seizure-free drug-sensitive

epilepsy” (DSE) was defined as a well-controlled state, free of all seizures, in a patient receiving antiepileptic drugs for at least 1 year before PET scanning. We investigated the baseline characteristics and the results of the previous video electroencephalography monitoring, brain MR imaging, single-photon emission CT, and [¹⁸F]-fluorodeoxyglucose-PET examinations in each patient (On-line Table 1).

Healthy control subjects (age range, 20–40 years) without other disorders, including neurologic or psychiatric disorders, who were not taking any drugs were recruited through a notice on the bulletin board of the Biomedical Research Institute of the Seoul National University Hospital. Before inclusion, all subjects underwent a screening interview, neurologic and general medical examinations, complete blood count, and routine biochemical (liver and kidney function) testing. This study was approved by the institutional review board at Seoul National University Hospital and was performed in accordance with the Investigational New Drug application of the Korea Food and Drug Administration and was registered at www.ClinicalTrials.gov (NCT02144792).

PET/MR Imaging and Experimental Procedures

The PET imaging procedures in our study were performed as described previously.⁸ Participants underwent a 60-minute PET scan after an intravenous injection of 370 MBq of (R)-[¹¹C]-verapamil radiotracer (range, 333–407 MBq). Simultaneous acquisitions of 3D dynamic PET images and T1-weighted MR images were performed by using a Biograph mMR (Siemens, Erlangen, Germany). During the scans, subjects were instructed to lie in a supine position with their heads affixed to a device designed to minimize movement. After routine corrections such as normalization, ultrashort echo time MR imaging–based attenuation, scatter, and decay corrections, the PET imaging data acquired in list mode were reconstructed by using a filtered back-projection. The dynamic volumetric images were sequenced by using the following framing: 8 × 2.5, 16 × 5, 10 × 60, and 10 × 240 seconds. To evaluate Pgp expression, we initiated intravenous CS infusion (2.5 mg/kg/h and 50 mg/mL; Sandimmune; Novartis Pharmaceuticals, Basel, Switzerland) 1 hour before the acquisition of the PET/MR imaging scans. CS infusion was continued during the PET scan to a maximum of 2 hours from the start of the infusion. Blood samples were taken before and after the PET scan to determine CS concentrations by high-performance liquid chromatography.

PET Data Analysis and Acquisition of Asymmetry Indices

PET images were coregistered to the subject’s T1 MR images and spatially normalized to a T1 template provided by statistical parametric mapping by using SPM8 software (<http://www.fil.ion.ucl.ac.uk/spm/software/spm8>) (Fig 1). Voxelwise calculations of SUV, [Voxel Intensity (Bq/mL)/Injected Dose (Bq)/Body Weight (g)], was performed in each dynamic PET frame. Dynamic SUVs in 98 brain ROIs were obtained by using the population-based SPAM, which was constructed by incorporating anatomic and functional variabilities among 152 healthy volunteers and automatically labeling brain structures in functional data in the Montreal Neurological Institute space.^{13,14} Because the uptake of (R)-[¹¹C]-verapamil in the choroid

plexus results in a spillover of radioactivity into the neighboring medial temporal structures, including the hippocampus, parahippocampal gyrus, and amygdala, our investigator (S.A.S.), who was unaware of the participants' clinical statuses, masked out the choroid plexus in the individual normalized PET image; volumes for the hippocampus of the individually modified SPAM maps were calculated (On-line Table 2). Static SUVs were then obtained as the weighted mean of the dynamic SUVs during the 2.5- to 40-minute scans with the frame duration as weight. On the basis of the static SUVs in each cortex, AIs were calculated by using the equation $[(\text{Right Region} - \text{Left Region}) / (\text{Right Region} + \text{Left Region}) \times 200\%]$ for all the respective participants.

If Pgp is overexpressed in the right region, the SUV of (R)-[^{11}C]-verapamil in the right region is smaller than that in the left region, resulting in a negative AI. If Pgp is overexpressed in the left region, the SUV in the left region is smaller than that in the right region, resulting in a positive AI. We compared asymmetry in healthy controls and patients with epilepsy by using the AIs. To compare the AIs between patients with lateral TLE and the medial TLE group, AIs were assessed in 6 ROI pairs of the temporal lobe. The medial temporal structures included the hippocampus, amygdala, and parahippocampal gyrus. The lateral temporal structures included the superior, middle, and inferior temporal lobes (Fig 2).

Genotyping Methods

We used the genotyping method described by Kim et al.¹⁵ Genotyping of the *ABCB1* 2677G>T, 1236C>T, and 3435C>T single-nucleotide polymorphisms was performed by using validated TaqMan SNP Genotyping Assays (Applied Biosystems, Foster City, California).

Statistical Analyses

Statistical analyses were performed by using SPSS for Windows (Version 21.0; IBM, Armonk, New York). A Mann-Whitney *U* test and Fisher exact test were used to compare the basal characteristics between the DRE and DSE groups, including age, sex, duration of epilepsy, and the number of antiepileptic drugs taken. In addition, AIs of healthy controls, patients with DRE, and those with DSE were compared by using a Mann-Whitney *U* test. Associations between *ABCB1* polymorphisms and whole-brain SUVs and associations between serum concentration of CS and whole-brain SUVs were determined by using Spearman correlations. A *P* value < .05 was considered significant.

RESULTS

Ten healthy men (median age, 27 years; range, 22–36 years), 6 patients with DRE (median age, 37 years; range, 26–52 years), and 5 patients with DSE (median age, 25 years; range, 18–53 years) underwent VPM-PET/MR-CS. Data from 2 healthy controls and 1 patient with DSE were excluded due to technical errors. In 2 healthy controls, the PET/MR imaging stopped working during the scan. One patient with DSE did not receive the full dose of cyclosporin A due to the infusion pump stopping during the PET/MR imaging. No difference in basal characteristics was found between the patients with DRE and those with DSE, except for the duration of epilepsy (DRE: median, 20.5 years; range, 5–42

years; DSE: median, 2.6 years; range, 1–4 years; *P* < .001), number of antiepileptic drugs (DRE: median 3.5; range, 2–4; DSE: median, 1.1; range 1–3; *P* = .009), and seizure frequency (DRE: median, 10.3 per month; range, 0.2–30 per month; DSE, no seizure event per month; *P* < .001).

There was interindividual variability in the radioactivity of the whole brain in healthy participants, and regional distributions of radioactivity were different in each individual (On-line Fig 1A). Moreover, radioactivity of the whole brain was independent of the serum concentration of CS (*r* = .100, *P* = .701) and *ABCB1* up-regulation (On-line Fig 1B and On-line Table 3).

Five healthy controls reported hot flushes in the body during the infusion of CS, and 1 healthy control had mild nausea. However, no other side effects were observed during the experimental period.

Different Values of AIs in Patients with DRE and Healthy Subjects

All patients with DRE had more asymmetry between ipsilateral ROIs and contralateral ROIs than healthy subjects, while there were no significant differences in AIs between patients with DSE and healthy controls (Figs 3 and 4). In TLE, PET data from 3 patients with left temporal lobe DRE showed significantly more positive AIs than those from healthy controls (healthy controls: 4.0413 ± 1.7452 ; patients: 7.2184 ± 1.8237 ; *P* = .048), suggesting that Pgp overexpression was in the left temporal area. PET data from 2 patients who had right temporal lobe DRE showed significantly more negative AIs than those from healthy controls (patients, -1.6496 ± 3.4136 ; *P* = .044), suggesting Pgp overexpression in the right temporal area (Fig 3B).

PET data from a patient who had a right frontal lobe DRE showed the largest negative AI. This means that the SUV of the right frontal lobe in this patient was much lower than that of the left frontal lobe and that the AI of this patient was different from AIs of healthy controls (healthy controls: -1.9963 ± 1.6329 ; patient, -9.0502) (Fig 3A).

In addition, we compared AIs in the temporal lobe between patients with drug-resistant and drug-sensitive left TLE. AIs in patients with DRE were larger than those in patients with DSE, though this result was not statistically significant (DRE: 7.2183 ± 1.8237 ; DSE: 3.9473 ± 0.5101 , *P* = .100).

Possibility of Localization by Using VPM-PET/MR-CS

We investigated whether localization of the epileptic focus is possible by using our method. We compared the characteristics of AIs between the medial TLE and lateral TLE groups. The lateral TLE group had significantly different AIs from those of healthy subjects in the superior (healthy subjects: 3.7592 ± 2.7825 ; patients: 15.0673 ± 10.2462 ; *P* = .024) and middle temporal gyri (healthy subjects: 0.4077 ± 3.0872 ; patients: 7.3093 ± 1.9225 ; *P* = .012), but not in the medial temporal structures. Moreover, significant differences in AIs were observed between patients with medial TLE and healthy subjects in the hippocampus but not in the lateral structures (healthy subjects: 10.4622 ± 4.9800 ; patients: -4.2948 ± 2.7194 ; *P* = .044) (On-line Table 4).

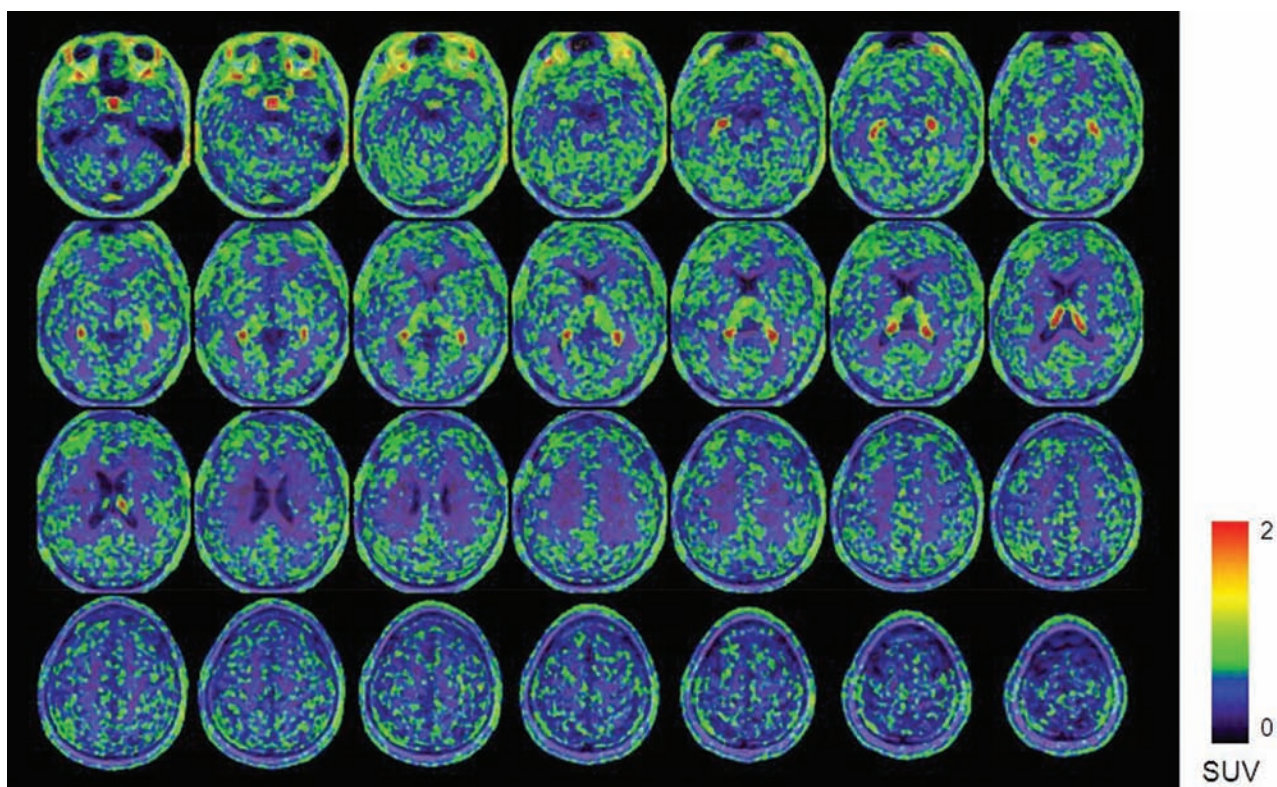


FIG 1. (R)-[^{11}C]-verapamil PET/MR uptake images after 1 hour of CS infusion in a patient who had drug-resistant left neocortical temporal lobe epilepsy. The color scale reflects the SUV as shown by the heat map.

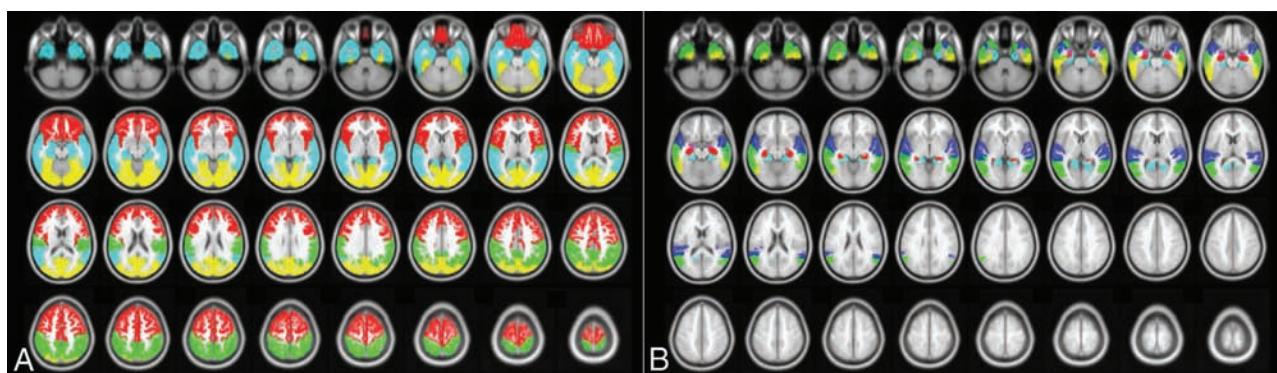


FIG 2. T1-weighted MR images (axial view, A) marking volumes of interest including the frontal, parietal, temporal, occipital cortices, and temporal ROIs (B), including the hippocampus, amygdala, parahippocampus, superior temporal gyrus, middle temporal gyrus, and inferior temporal gyrus by the population-based SPAM. A, Red indicates the frontal cortex; cyan, the temporal cortex; green, the parietal cortex; yellow, the occipital cortex. B, Red indicates the hippocampus; violet, the amygdala; cyan, the parahippocampus; blue, the superior temporal gyrus; green, the middle temporal gyrus; yellow, the inferior temporal gyrus.

DISCUSSION

The primary objective of this study was to confirm the usefulness of noninvasive quantitative PET methods including SPAM, with AIs of the SUVs as a surrogate marker in DRE. We also wanted to determine whether this method could help us localize the epileptic zone. In our study, significant asymmetry of Pgp expression was confirmed in all patients with DRE compared with healthy controls, and the absolute values of AIs in patients with drug-resistant left TLE also were larger than those in healthy subjects and patients with drug-sensitive left TLE. There was no difference between the DSE group and healthy controls. In addition, we were

able to find different asymmetry patterns between patients with lateral TLE and those with medial TLE.

Two previous studies examined patients with DRE by using (R)-[^{11}C]-verapamil PET. In a pilot study, (R)-[^{11}C]-verapamil PET was performed in 7 patients with drug-resistant TLE who had hippocampal atrophy.¹⁶ In this study, the increased efflux of (R)-[^{11}C]-verapamil in the ipsilateral region was more pronounced than in the contralateral region, though this difference was not statistically significant. In a recent case-control study, 14 patients with drug-resistant TLE caused by unilateral hippocampal sclerosis underwent (R)-[^{11}C]-verapamil PET with tariquidar; when

compared with patients with DSE, the influx of (R)-[¹¹C]-verapamil was less significantly increased in the patients with drug-resistant TLE.¹⁷ In our study, AIs of the left TLE group were more positive than those in healthy controls, suggesting an overexpression of Pgp in the left temporal lobe and a low uptake of (R)-[¹¹C]-verapamil. The AIs of the right TLE were also more negative than those in healthy controls. In addition, asymmetries in patients with drug-resistant left TLE were larger than those in patients with drug-sensitive left TLE. Considering the coherence of

the results of several studies, including our results, (R)-[¹¹C]-verapamil PET might serve as an important and useful noninvasive surrogate marker for DRE.

To our knowledge, this is the first report to confirm that (R)-[¹¹C]-verapamil PET could facilitate evaluation of a surrogate marker in patients with DRE including neocortical epilepsy. In addition to lateral temporal lobe epilepsy, a patient who had drug-resistant MRI-negative right frontal lobe epilepsy had different asymmetry in the frontal lobe than healthy subjects. This patient

had a much larger negative AI than the healthy controls, suggesting an overexpression of Pgp in the right frontal lobe. In addition, there also was no difference in drug-sensitive frontal lobe epilepsy.

For localization, we tried to compare the asymmetry patterns between patients with DRE with medial TLE and lateral TLE. All patients with lateral TLE had a significant asymmetry in the superior and middle temporal gyrus, but not in the medial temporal structures. Moreover, 2 patients with medial TLE had significantly different asymmetry in the hippocampus, but not in the lateral temporal structures. Given the different patterns between the medial and lateral

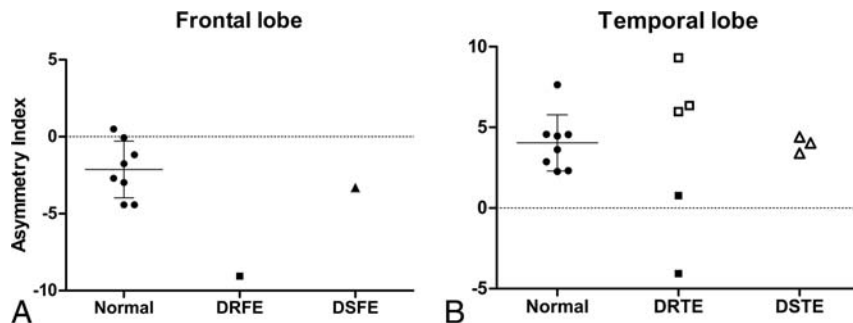


FIG 3. A, Asymmetry indices of the frontal lobes in healthy controls and in patients with drug-resistant or drug-sensitive right frontal lobe epilepsy. B, AIs of temporal lobes in healthy controls and patients with DRE or DSE temporal lobe epilepsy. Filled squares are diagnosed right temporal lobe epilepsy, and blank squares and triangles are diagnosed left temporal lobe epilepsy. When the AI was positive, the standard uptake value of (R)-[¹¹C]-verapamil in the left region was lower than that in the right region in each paired lobe. The bars represent mean \pm SD. DRFE indicates drug-resistant frontal lobe epilepsy; DSFE, drug-sensitive frontal lobe epilepsy; DRTE, drug-resistant temporal lobe epilepsy; DSTE, drug-sensitive temporal lobe epilepsy.

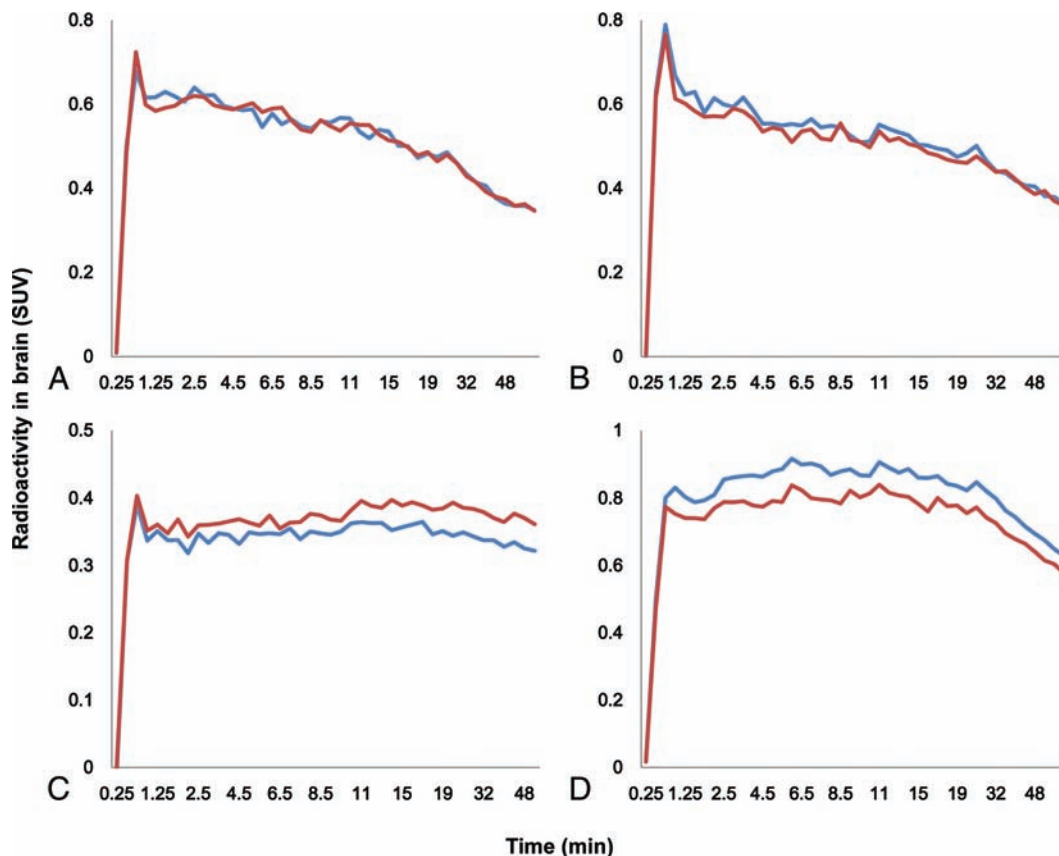


FIG 4. The time-activity curves of (R)-[¹¹C]-verapamil in the frontal lobe of a healthy subject (A); the temporal lobe of a healthy subject (B); the frontal lobe of patient 6, who had drug-resistant right frontal lobe epilepsy (C); and the temporal lobe of patient 2, who had drug-resistant left temporal lobe epilepsy (D). The blue line indicates right lobe; the red line, left lobe.

TLE groups, this method could be helpful in localizing the epileptic zone.

Among the cases, a second patient (patient 2) had the longest standing drug-resistant left TLE, and decreased SUV in all of the left lobes indicated broad Pgp overexpression in the left hemisphere (data not shown). Considering that the DRE group, including this patient, had a longer duration of disease than the DSE group, seizure duration might be an important factor in the overexpression of Pgp. We also analyzed the relationship between the duration of epilepsy and the absolute value of the AIs in patients with left DRE and DSE TLE ($n = 6$) by using the Spearman non-parametric correlation coefficient and found a significant correlation ($r = 0.928$, $P = .008$). Indeed, a recent study investigated the correlation between Pgp overexpression and clinical features (age, age at the onset of habitual seizures, duration of seizure history, seizure frequency per year, and number of Pgp inducers or substrates taken). There was a positive correlation among seizure frequency, number of medications that induce Pgp, and overexpression of Pgp, with no other significant relationships observed.⁷ Given the various results from many studies, there is ongoing debate regarding which clinical features affect the overexpression of Pgp, and additional studies are required to address this issue.

The use of (R)-[¹¹C]-verapamil PET with a Pgp inhibitor in humans presents several difficulties. First, high dosages of Pgp that cannot be used in (R)-[¹¹C]-verapamil PET could be used with a medium dosage of a Pgp inhibitor to increase the baseline signal and thus create larger differences in the brain concentrations of the tracer between the healthy and diseased brain.⁹ At an acceptable dose, 17%–58% of Pgp inhibition with tariquidar (2–8 mg/kg) and 38%–50% of Pgp inhibition with CS (2.5 mg/kg/h) were observed by evaluating Pgp inhibition on (R)-[¹¹C]-verapamil PET imaging.¹⁸ However, interindividual variability regarding affinity and response to the substrate or inhibitor may also complicate the outcome when using a moderate dose of a Pgp inhibitor.¹⁹ Our data also showed individual variability among all the participants, similar to that observed in previous studies.¹⁰ In addition, the interindividual variability was unrelated to polymorphisms of the *ABCB1* gene, including 3435T/T carriers, which had influenced the influx rate of the Pgp substrate drug in a previous study.²⁰

Given the small sample size in our study, we could not determine the influence of these polymorphisms on regional Pgp activity statistically. Also, several studies have shown that the effect of Pgp inhibitors is rapid, and the Pgp function is promptly restored on the elimination of the inhibitors.^{21,22} Our study showed a rapid decrease in the radioactivity of the whole brain soon after the infusion of Pgp inhibitor was terminated, despite the maintenance of the serum concentration of CS (data not shown). Therefore, a novel Pgp inhibitor with enhanced affinity and a longer half-life for binding Pgp will be required. This study has several limitations. First, due to the small sample size in each group, we were unable to detect statistically significant differences in patients with frontal lobe epilepsy. However, despite the small sample size, we showed robust differences in the asymmetry patterns of patients with DRE and healthy controls and patients with DSE. Second, our study did not consider cerebral blood flow measure-

ments. The regional uptake of (R)-[¹¹C]-verapamil can become dependent on regional cerebral blood flow when Pgp is partially inhibited.²³ However, because (R)-[¹¹C]-verapamil is a low-extraction radiotracer, its uptake is considered insensitive to changes in cerebral blood flow.¹⁰ In addition, Muzi et al⁸ reported that the CS modulation of Pgp increased the blood-brain transfer of (R)-[¹¹C]-verapamil into the brain by 73%, and this increase was significantly greater than changes in blood flow by 13%.

Despite some problems with the use of VPM-PET/MR-CS, considering the different asymmetry in the DRE group, but not in the DSE group, from that of healthy subjects, the AI could be a useful surrogate marker of DRE in clinical practice. If one used SPAM with the AI of VPM-PET/MR-CS, it might be possible to predict the drug response in each patient and consider the appropriate surgical treatment more proactively. In addition, patients with DRE exhibiting Pgp overexpression could be treated with a Pgp inhibitor. A recent pilot study reported that the adjunctive use of verapamil (120 mg/day), which was used as a Pgp inhibitor in patients with DRE, improved the response rate.²⁴ In the future, our method should be applied to more variable neocortical epilepsy cases.

CONCLUSIONS

On the basis of the results obtained to date, we confirmed the importance of Pgp expression in DRE by using a noninvasive method including SPAM analysis with AIs. Therefore, an AI obtained by using VPM-PET/MR-CS might be used as a surrogate marker of Pgp expression in patients with epilepsy and might serve as an important prognostic factor for individualized drug therapy. Moreover, the results showing that ipsilateral lesions had low SUVs and the difference in asymmetry patterns between medial and lateral temporal epilepsy groups showed that our method may be a useful tool for localization of the epileptic zone. In the future, prospective studies by using VPM-PET/MR-CS in patients with recent-onset epilepsy are necessary for assessing predictive value.

REFERENCES

1. Browne TR, Holmes GL. **Epilepsy.** *N Engl J Med* 2001;344:1145–51 CrossRef Medline
2. Löscher W, Schmidt D. **Modern antiepileptic drug development has failed to deliver: ways out of the current dilemma.** *Epilepsia* 2011;52:657–78 CrossRef Medline
3. Sillanpää M, Schmidt D. **Natural history of treated childhood-onset epilepsy: prospective, long-term population-based study.** *Brain* 2006;129:617–24 CrossRef Medline
4. Löscher W, Klitgaard H, Twyman RE, et al. **New avenues for anti-epileptic drug discovery and development.** *Nat Rev Drug Discov* 2013;12:757–76 CrossRef Medline
5. Löscher W, Potschka H. **Drug resistance in brain diseases and the role of drug efflux transporters.** *Nat Rev Neurosci* 2005;6:591–602 CrossRef Medline
6. Potschka H. **Role of CNS efflux drug transporters in antiepileptic drug delivery: overcoming CNS efflux drug transport.** *Adv Drug Deliv Rev* 2012;64:943–52 CrossRef Medline
7. Liu JY, Thom M, Catarino CB, et al. **Neuropathology of the blood-brain barrier and pharmacoresistance in human epilepsy.** *Brain* 2012;135:3115–33 CrossRef Medline
8. Muzi M, Mankoff DA, Link JM, et al. **Imaging of cyclosporine inhibition of P-glycoprotein activity using ¹¹C-verapamil in the brain:**

- studies of healthy humans. *J Nucl Med* 2009;50:1267–75 CrossRef Medline
9. Wagner CC, Bauer M, Karch R, et al. **A pilot study to assess the efficacy of tariquidar to inhibit P-glycoprotein at the human blood-brain barrier with (R)-11C-verapamil and PET.** *J Nucl Med* 2009;50:1954–61 CrossRef Medline
 10. Bauer M, Karch R, Neumann F, et al. **Assessment of regional differences in tariquidar-induced P-glycoprotein modulation at the human blood-brain barrier.** *Cereb Blood Flow Metab* 2010;30:510–15 CrossRef Medline
 11. Dukart J, Mueller K, Horstmann A, et al. **Differential effects of global and cerebellar normalization on detection and differentiation of dementia in FDG-PET studies.** *Neuroimage* 2010;49:1490–95 CrossRef Medline
 12. Kwan P, Arzimanoglou A, Berg AT, et al. **Definition of drug resistant epilepsy: consensus proposal by the ad hoc Task Force of the ILAE Commission on Therapeutic Strategies.** *Epilepsia* 2010;51:1069–77 CrossRef Medline
 13. Kang KW, Lee DS, Cho JH, et al. **Quantification of F-18 FDG PET images in temporal lobe epilepsy patients using probabilistic brain atlas.** *Neuroimage* 2001;14:1–6 CrossRef Medline
 14. Lee JS, Lee DS. **Analysis of functional brain images using population-based probabilistic atlas.** *Current Medical Imaging Reviews* 2005;1:81–87 CrossRef
 15. Kim DW, Lee SK, Chu K, et al. **Lack of association between ABCB1, ABCG2, and ABCC2 genetic polymorphisms and multidrug resistance in partial epilepsy.** *Epilepsy Res* 2009;84:86–90 CrossRef Medline
 16. Langer O, Bauer M, Hammers A, et al. **Pharmacoresistance in epilepsy: a pilot PET study with the P-glycoprotein substrate R-[(11)C]verapamil.** *Epilepsia* 2007;48:1774–84 CrossRef Medline
 17. Feldmann M, Asselin MC, Liu J, et al. **P-glycoprotein expression and function in patients with temporal lobe epilepsy: a case-control study.** *Lancet Neurol* 2013;12:777–85 CrossRef Medline
 18. Kalvass JC, Polli JW, Bourdet DL, et al; International Transporter Consortium. **Why clinical modulation of efflux transport at the human blood-brain barrier is unlikely: the ITC evidence-based position.** *Clin Pharmacol Ther* 2013;94:80–94 CrossRef Medline
 19. Syvänen S, Eriksson J. **Advances in PET imaging of P-glycoprotein function at the blood-brain barrier.** *ACS Chem Neurosci* 2013;4:225–37 CrossRef Medline
 20. Taubert D, von Beckerath N, Grimberg G, et al. **Impact of P-glycoprotein on clopidogrel absorption.** *Clin Pharmacol Ther* 2006;80:486–501 CrossRef Medline
 21. Syvänen S, Blomquist G, Sprycha M, et al. **Duration and degree of cyclosporin induced P-glycoprotein inhibition in the rat blood-brain barrier can be studied with PET.** *Neuroimage* 2006;32:1134–41 CrossRef Medline
 22. Syvänen S, Hooker A, Rahman O, et al. **Pharmacokinetics of P-glycoprotein inhibition in the rat blood-brain barrier.** *J Pharm Sci* 2008;97:5386–400 CrossRef Medline
 23. Deo AK, Borson S, Link JM, et al. **Activity of P-glycoprotein, a β -amyloid transporter at the blood-brain barrier, is compromised in patients with mild Alzheimer disease.** *J Nucl Med* 2014;55:1106–11 CrossRef Medline
 24. Asadi-Pooya AA, Razavizadegan SM, Abdi-Ardekani A, et al. **Adjunctive use of verapamil in patients with refractory temporal lobe epilepsy: a pilot study.** *Epilepsy Behav* 2013;29:150–54 CrossRef Medline

Cortical Cerebral Blood Flow, Oxygen Extraction Fraction, and Metabolic Rate in Patients with Middle Cerebral Artery Stenosis or Acute Stroke

Z. Liu and Y. Li

ABSTRACT

BACKGROUND AND PURPOSE: With the advances of magnetic resonance technology, the CBF, oxygen extraction fraction, and cerebral metabolic rate of oxygen can be measured in MRI. Our aim was to measure the CBF, oxygen extraction fraction, and cerebral metabolic rate of oxygen use in patients with different severities of middle cerebral artery stenosis or acute stroke by using the arterial spin-labeling and susceptibility-weighted imaging techniques.

MATERIALS AND METHODS: Fifty-seven patients with MCA stenosis or acute stroke were recruited and classified into 4 groups: mild MCA stenosis (group 1), severe MCA stenosis (group 2), occluded MCA (group 3), and acute stroke (group 4). Arterial spin-labeling and SWI sequences were used to acquire CBF, oxygen extraction fraction, and cerebral metabolic rate of oxygen.

RESULTS: The oxygen extraction fraction in hemispheres with mild MCA stenosis (group 1) was remarkably higher than that in the contralateral hemisphere. In addition, hemispheres with severe MCA stenosis (group 2) had significantly lower CBF and a significantly higher oxygen extraction fraction than the contralateral hemisphere. Hemispheres with occluded MCA (group 3) or acute stroke (group 4) had a significantly lower CBF and cerebral metabolic rate of oxygen and a significantly higher oxygen extraction fraction than the contralateral hemisphere.

CONCLUSIONS: The oxygen extraction fraction gradually increased in groups 1–3. When this offset a decrease in CBF, the cerebral metabolic rate of oxygen remained at a normal level. An occluded MCA led to reduction in both the CBF and cerebral metabolic rate of oxygen. Moreover, the oxygen extraction fraction and cerebral metabolic rate of oxygen significantly increased and decreased, respectively, in the occluded MCA region during acute stroke.

ABBREVIATIONS: ASL = arterial spin-labeling; Hct = hematocrit; CMRO₂ = cerebral metabolic rate of oxygen; HR = high-resolution; OEF = oxygen extraction fraction; rCBF = relative cerebral blood flow; rCMRO₂ = relative cerebral metabolic rate of oxygen; rOEF = relative oxygen extraction fraction; Y_v = venous oxygen saturation

A reduction in cerebral blood flow in brain tissue is typically accompanied by a compensatory increase in the oxygen extraction fraction (OEF) to maintain normal neuronal function.¹ However, the risk of stroke is greatly increased once the maximum OEF is achieved.² The presence of increased OEF in stroke is an independent predictor of subsequent stroke in patients.^{3,4} Consequently, both CBF and OEF are important indicators for stroke; however, neither parameter sufficiently predicts the risk of this condition. It is possible to use both parameters and the arterial oxygen content to derive cerebral metabolic rate of oxygen

(CMRO₂) use, which is of critical importance in the occurrence of stroke.¹

Positron-emission tomography provides the most accurate in vivo OEF and CMRO₂ measurements; however, it is expensive and requires administration of radioactive isotopes. Both OEF and CBF can be determined using MR susceptometry and arterial spin-labeling (ASL).^{5,6} MR susceptometry uses gradient-echo phase maps to estimate oxygen saturation in segments of the jugular and gray matter veins.^{7,8} This technique requires blood vessels to have a substantially greater length than the diameter.^{7,8} Susceptibility-weighted imaging is a type of MR susceptometry that can obtain measurements of venous oxygen saturation by using the phase difference between the venous blood and surrounding tissue.^{9,10} ASL is a noninvasive technique that can measure CBF.^{11,12} The gray matter CMRO₂ can be obtained from local CBF and OEF measurements.

Most previous PET studies have focused on OEF and CMRO₂ in patients with an occluded carotid artery; few studies have in-

Received April 20, 2015; accepted after revision August 9.

From the Department of Medical Imaging (Z.L.), First Hospital of Nanchang City, The Third Affiliated Hospital of Nanchang University, Nanchang City, China; and Department of Preventive Medicine (Y.L.), Heze Medical College, HeZe, Shandong, China.

Please address correspondence to Zhenghua Liu, MD, Department of Medical Imaging, First Hospital of Nanchang City, The Third Affiliated Hospital of Nanchang University, Nanchang City 330006, China; e-mail: wuxiaoshui@126.com

<http://dx.doi.org/10.3174/ajnr.A4624>

Table 1: Number, age, clinical characteristics, Hct, and Hb of the healthy subjects and patients

Groups	No.	Age Range (yr)	Mean Age (yr)	Males (No.)	Females (No.)	Hct ($\times 10^{-2}$)	Hb
Healthy subjects	10	40–67	55.9	5	5	34.9 \pm 12.6	13.1 \pm 1.2
Mild stenotic MCA Group 1	13	37–65	50.4	6	7	40.2 \pm 4.9	14.2 \pm 1.4
Severe stenotic MCA Group 2	11	45–75	58.0	6	5	39.2 \pm 5.1	13.1 \pm 2.1
Occluded MCA Group 3	16	36–72	58.5	8	8	39.8 \pm 4.4	13.8 \pm 2.3
Patients with acute stroke Group 4	17	38–73	57.6	9	8	40.3 \pm 6.6	13.6 \pm 2.1

Note:—Hb indicates hemoglobin.

investigated the stenotic or occluded middle cerebral artery.^{13,14} To the best of our knowledge, no studies have assessed CBF, OEF, and CMRO₂ relative to the degree of MCA stenosis. To address this question, we measured CBF, OEF, and CMRO₂ in patients with different degrees of MCA stenosis or stroke via ASL and susceptibility-weighted phase imaging.

MATERIALS AND METHODS

Subjects

This prospective study was approved by the institutional review board, and written informed consent was obtained from all subjects or their guardians. Ten healthy volunteers (5 men, 5 women) with a mean age of 55.9 years (age range, 40–67 years) were enrolled in the study. All volunteers had normal findings on neurologic examination and brain MR imaging, no stenotic middle cerebral or carotid artery, and no history of neurologic disease.

Eighty-four patients with MCA stenosis or acute stroke were recruited in the study and underwent clinical evaluation, laboratory testing, MR imaging examination, and color Doppler sonography to assess the cervical vasculature. Inclusion criteria were as follows: 1) unilateral stenosis of the M1 segment of the MCA or unilateral acute MCA stroke, 2) no stenosis in the internal carotid and/or common carotid artery, 3) no extracranial-intracranial vessel bypass operation, and 4) no motion artifacts in the susceptibility-weighted or ASL images. Periodic stripe-like artifacts in the phase-code direction of the images were identified as motion artifacts. One and 5 patients were excluded due to motion artifacts and bilateral MCA stenosis, respectively. Six patients were excluded because no sonographic examination of the cervical vasculature had been performed, and 10 patients were excluded because arteriosclerosis was found in the internal carotid and/or common carotid artery by color Doppler ultrasonography. Five patients were excluded because 5 veins were not detected in the SWIs in a unilateral hemisphere. Subsequently, 57 patients (29 men, 28 women) with a mean age of 55.9 years (age range, 37–75 years) were included in the study. Nine patients had a history of hypertension, 6 had diabetes mellitus, and 4 had both comorbidities. Fourteen patients had an acute unilateral MCA stroke. The time between symptom onset and MR imaging examination in patients with acute stroke was between 12 and 65 hours, with a median of 32 hours. All subjects and patients underwent measurements for hemoglobin (grams per deciliter) and hematocrit (Hct) levels within 3 days of MR imaging examinations.

Patient Categorization

Classification of the degree of MCA stenosis was based on the diameter of the vessel at the point of maximal narrowing relative to the normal distal lumen diameter, which was obtained from high-resolution (HR) T2-weighted images. For data analysis, MCA stenosis was graded as mild (<50% diameter reduction) or severe (>50% diameter reduction) stenosis or occlusion.

Patients were divided into 4 groups: 3 without and 1 with stroke (Table 1). Patients without stroke were classified according to the degree of MCA narrow-

ing: mild MCA stenosis (group 1), severe MCA stenosis (group 2), and occluded MCA (group 3). All patients had normal findings on brain MR imaging, except on the MR angiography, with an acceptable level of white matter abnormalities (ie, pencil-thin lining of periventricular hyperintensity and foci of high signal intensity in the deep white matter) for subjects older than 60 years of age. The white matter abnormalities were not high signals in the diffusion-weighted images. The lesions in these patients with acute stroke were located in the region of the MCA. The number, age, and clinical characteristics of the various subgroups are listed in Table 1.

MR Imaging Measurements

All MR imaging examinations were performed on a 3T whole-body scanner (Signa HDxt; GE Healthcare, Milwaukee, Wisconsin) with an 8-channel head coil. The MR imaging acquisition protocols included axial T2-weighted imaging, diffusion-weighted imaging, 3D time-of-flight MRA, HR-T2WI, SWI, and pulsed-continuous ASL. The total scan time for each patient was approximately 18 minutes.

T2WI parameters were as follows: TR, 9600 ms; TE, 117 ms; TI, 2400 ms; section thickness, 6 and 1.0 mm gap between sections; FOV, 24 \times 24 cm²; matrix size, 288 \times 256; and NEX, 2. Axial single-shot spin-echo echo-planar sequences were used to acquire DWI with the following parameters: TR/TE, 4000/70 ms; b factors, 0 and 1000 s/mm²; matrix size, 128 \times 128; FOV, 24 \times 24 cm²; NEX, 4; section thickness, 6 mm; and section gap, 1 mm.

3D TOF MRA was performed with the following parameters: TR/TE, 20/3.4 ms; flip angle, 20°; FOV, 22 \times 22 cm²; matrix size, 384 \times 192; and section thickness, 1.6 mm. The HR-T2WI sequence was perpendicular to the stenotic M1 segment of the MCA shown on 3D TOF MRA. HR-T2WI sequence parameters were as follows: TR/TE, 2800/60 ms; FOV, 12 \times 12 cm²; matrix size, 512 \times 256; section thickness, 2 mm; section gap, 0.5 mm; and NEX, 4. Figure 1 shows representative MRA and HR-T2WI findings.

A 3D single-shot fast spin-echo with an in-plane spiral readout acquisition was performed to generate the quantitative CBF maps for ASL. The ASL pulse parameters were the following: point, 512; arm, 8; postlabeling delay, 2025 ms; NEX, 3; FOV, 22 \times 22 cm²; spatial resolution, 3.4 \times 3.4 \times 2 mm³; section thickness, 2.0 mm; scan locations, 44; and bandwidth, 62.5. The acquisition time was 4 minutes 26 seconds.

For axial 3D SWI, a fully flow-compensated 3D fast low-angle shot sequence was used with the following parameters to obtain

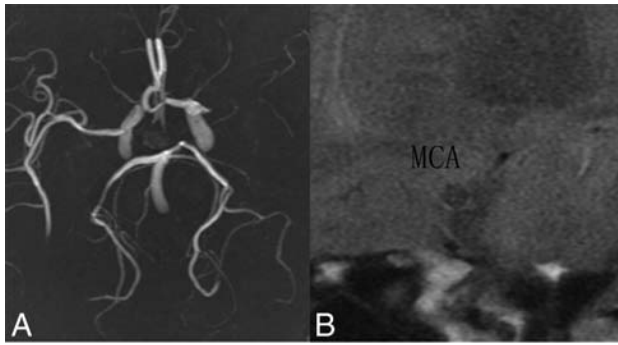


FIG 1. Representative MR angiography and high-resolution T2-weighted imaging findings. *A*, 3D time-of-flight MRA reveals an occlusive left middle cerebral artery. *B*, Plaque with heterogeneous signal intensity was present in the MCA lumen on HR-T2WI.

the OEF: TR/TE, 55.9/12.1 ms; NEX, 1; matrix, 448×384 ; flip angle, 15° ; and FOV, $22 \times 22 \text{ cm}^2$. The acquisition time was 6 minutes 50 seconds.

After acquisition, the magnitude and phase images were reconstructed. The phase images were processed with high-pass filtering to remove unwanted phase shifts (field variations) from the main magnet.⁹

Theory

The principle of MR susceptometry is based on the measurement of differences in susceptibility between a candidate cerebral vein and its surroundings as obtained from axial phase images.¹⁵ The cerebral veins can be approximated as infinitely long cylinders parallel to a static magnetic field. The differences in susceptibility between the vein and tissue manifest as⁹:

$$1) \quad \Delta\varphi_{\text{vein-tissue}} = 2\pi \times \gamma \times \Delta\chi_{\text{vein-tissue}} \times (\cos^2\theta - 1/3) \times B_0 \times \text{TE},$$

where γ is the gyromagnetic ratio, TE is the echo time, B_0 is the main magnetic strength, and θ is the angle between the vein and B_0 . Meanwhile, $\Delta\chi_{\text{vein-tissue}}$ is the susceptibility shift between the vein and tissue, as follows^{9,16}:

$$2) \quad \Delta\chi_{\text{vein-tissue}} = \Delta\chi_{\text{do}} \times \text{Hct} \times (1 - Y_v),$$

where $\Delta\chi_{\text{do}}$ (deoxygenated blood) is 0.27 ppm,¹⁵ Hct is the blood hematocrit, and Y_v is the venous oxygen saturation. Under normal conditions, arterial oxygen saturation is nearly 100%. Consequently, OEF can be approximated as $\text{OEF} = 1 - Y_v$.⁹

CBF was calculated by using the following equation¹⁷:

$$3) \quad \text{CBF} = \lambda[1 - \exp(-T_{\text{sat}}/T_{1\text{gm}})] \times \frac{\exp\left(\frac{W}{T_{1\text{B}}}\right)}{2\alpha T_{1\text{B}} \left[1 - \exp\left(-\frac{\tau}{T_{1\text{B}}}\right)\right]} \times \frac{\Delta S}{\text{SO}},$$

where the partition coefficient, λ , is 0.9; the time of saturation performed before imaging, T_{sat} , is 2.0 seconds; the longitudinal relaxation time (T1) of gray matter for 3T, $T_{1\text{gm}}$,¹⁸ is 1.2 seconds; the postlabel delay, W, is 2.0 seconds; the longitudinal relaxation time (T1) of blood for 3T, $T_{1\text{B}}$,¹⁸ is 1.4 seconds; the labeling

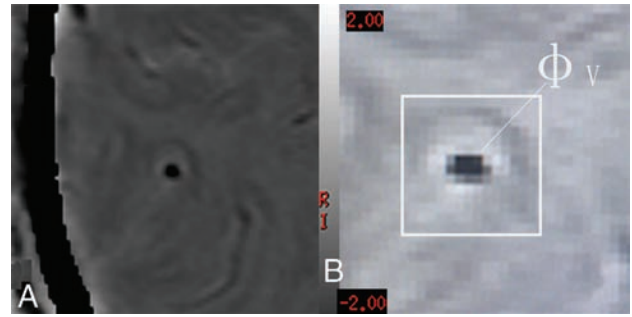


FIG 2. Illustration of MR susceptometry for determining Y_v . *A*, A phase image obtained from susceptibility-weighted imaging. *B*, Zoomed view of the phase image for the gray matter, with the vein as the representative phase value within the vessel. The rectangle shows the ROI of the gray matter, including the vein.

efficiency, which is a combination of both label pseudocontinuous ASL (0.8) and background suppression (0.75), α , is 0.6 (0.8×0.75); the labeling time, τ , is 1.5 seconds; ΔS is the difference between the reference and labeled image signal intensities; and SO, the signal intensity of the proton density-weighted reference image.

Oxygen consumption manifests as¹⁶:

$$4) \quad \text{CMRO}_2 = (Y_a - Y_v) \times \text{CBF} \times C_a,$$

where Y_a is the arterial oxygen saturation approximated as 1, CBF is brain-blood perfusion, and C_a is the oxygen concentration of blood per 100 mL. C_a is determined by using the hemoglobin level and O_2 carrying capacity per gram of hemoglobin. For a healthy person, this is $55.6 \mu\text{mol O}_2$.¹⁶ In this study, we obtained the CMRO_2 by measuring Y_v in the gray matter candidate veins by using SWI and determining the local CBF in the region supplied by the MCA by using ASL.

Image Processing

Susceptibility-weighted and ASL images were transferred to the workstation (AW4.4, GE Healthcare) for postprocessing. SWI was reconstructed as axis magnitude and phase images. High-pass filtering (32×32 Hanning) was performed on the phase images to remove variance in the background field.

The phase value measurements of the candidate vein (φ_v) and surrounding tissue (φ_t) were based on methods proposed by Fan et al¹⁶ and Fujima et al.¹⁹ φ_v and φ_t were measured in ROIs by using a square ROI (20×20 pixels) containing the gray matter candidate vein placed on the phase image (Fig 2). When the length of the vessel exceeds $6 \times$ its diameter, it can be fitted to the long-cylinder model in MR susceptometry.⁸ Consequently, we selected veins that had a length of at least $6 \times$ their diameter. The orientation of the vein in the gray matter was verified as parallel to B_0 by tracing the vessel through several adjacent axial, sagittal, and coronal sections. The sagittal and coronal sections were reconstructed from the phase axis section. When there was a tilt angle of the vein, it was calculated as follows⁸:

$$5) \quad \theta = \tan^{-1} \left\{ \sqrt{[(x_1 - x_2)^2 + (y_1 - y_2)^2] / \Delta z^2} \right\},$$

where x_1 and y_1 are the coordinates of the vein measured for phase in the axis section, x_2 and y_2 are the coordinates of the vein

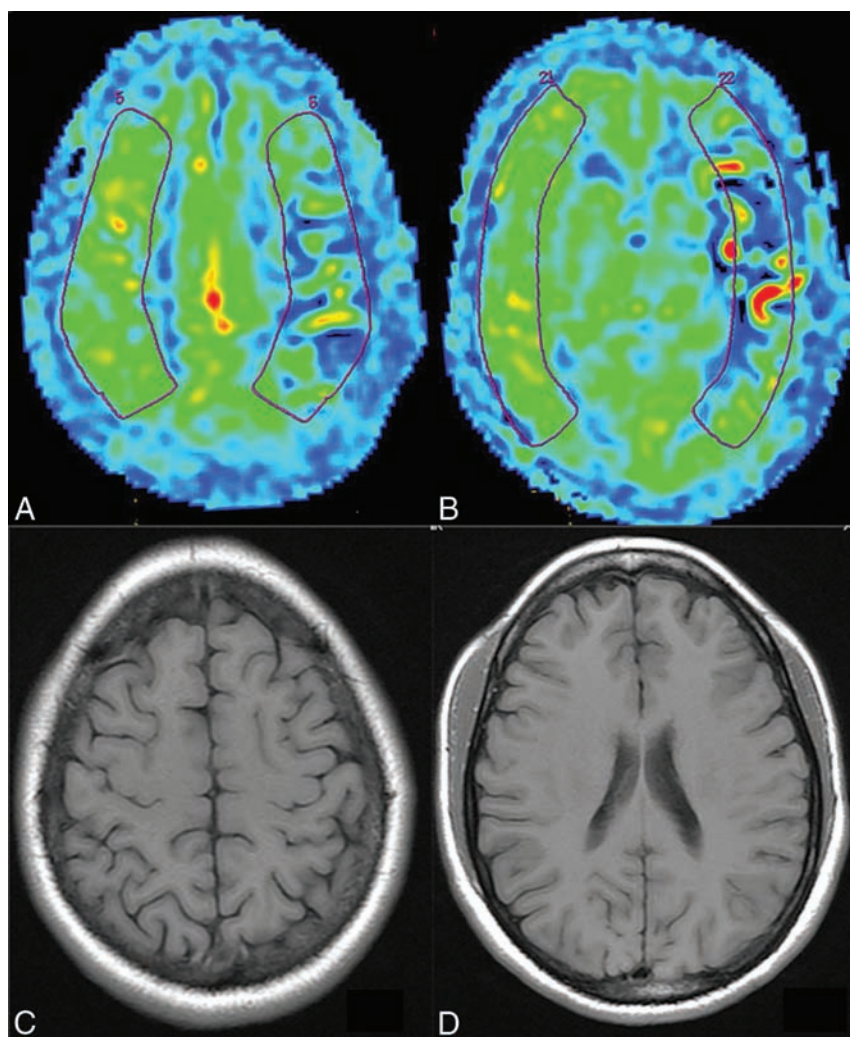


FIG 3. Placement of the ROI for cerebral blood flow measurements on an arterial spin-labeling CBF map. The ROI was positioned from the top (A) to the level of the thalami (B) in a 50-year-old patient with an occlusive MCA. C and D, Anatomic images corresponding to A and B.

Table 2: Statistical results for the CBF, OEF, and CMRO₂ in healthy subjects

	CBF (mL/100 g/min)		OEF (%)		CMRO ₂ (μmol/100 g/min)	
	Left	Right	Left	Right	Left	Right
<i>T</i>	53.4 ± 8.6	54.4 ± 9.6	36.8 ± 3.1	37.4 ± 3.3	146.8 ± 29.7	151.6 ± 32.6
<i>P</i>		1.028		1.269		1.366
		.331		.236		.205

in the fifth axis section above or below the phase axis section, and Δz is the section thickness $\times 5$. Subsequently, the mean and SD phase values were calculated in the ROI.

The definition of φ_v was the darkest pixel or the average of at least 4 dark pixels of similar phase value in the largest vessels (Fig 2).^{16,19} Estimation of φ_T was by using the average phase value up to the threshold value (mean ± 2 SDs) in the ROI.^{16,19} For 1 candidate vein, φ_v and φ_T were measured 3 times by an experimenter who was blinded to the vascular results and the values were averaged. The $\Delta\varphi_{\text{vein-tissue}}$ value was calculated as $\varphi_v - \varphi_T$. We randomly chose 5 candidate veins on each side of the region in the cerebral cortex supplied by the MCA for each subject, to obtain 5 average $\Delta\varphi_{\text{vein-tissue}}$ values. The veins in the stroke regions were not included in the measurement. Data were excluded if 5

candidate veins were not available. Data from 5 patients were excluded due to this.

The ASL data were postprocessed by using an automated reconstruction script to generate CBF maps. This included motion correction, pair-wise subtraction between control and labeled images, and the generation of mean-difference images and quantitative CBF maps.

Regional perfusion in both MCAs was measured by ROIs based on a published template for healthy subjects and patients (Fig 3).²⁰ The ROIs of the regional CBF in each hemisphere were 2100–4000 mm². The regional CBF of tissue supplied by the MCA was quantified in both hemispheres from the top to bottom sections (15–20 sections), and the data were averaged. The regional CMRO₂ was calculated for the tissue supplied by the MCA by using Y_v and the local CBF values.

All patients with acute stroke had lesions located in the region around the MCA. The stroke regions were not included in the ROIs of CBF measurement.

Statistical Analysis

All data were analyzed by using SPSS 19.0 (IBM, Armonk, New York). Paired *t* tests were used to compare CBF, OEF, and CMRO₂ between hemispheres in each subject. The ratios of the mean contralateral/lesion hemispheric CBF, OEF, and CMRO₂ values were calculated and defined as the relative CBF (rCBF), OEF (rOEF), and CMRO₂ (rCMRO₂) in the patient groups. Analysis of variance and Student-Newman-Keuls tests were conducted to compare rCBF, rOEF, and rCMRO₂ among the groups. A *P* value

of $< .05$ was statistically significant.

RESULTS

The largest diameter that an ischemic lesion demonstrated on DWI was 1.8–5.4 cm (median value, 2.6 cm).

The diameter of the vessel at the point of maximal narrowing relative to the normal distal lumen diameter was 0.675 ± 0.105 cm, 0.371 ± 0.078 cm, 0 cm, and 0.298 ± 0.254 cm in groups 1, 2, 3, and 4, respectively. The tilt angle of all veins lay in the 10°–34° range (mean values, $25.8^\circ \pm 5.1^\circ$).

For the control subjects, the mean gray matter Y_v , CBF, OEF, and CMRO₂ of the hemispheres supplied by the MCA was 0.629 ± 0.032 (0.579–0.674), 55.7 ± 9.4 (31.9–67.4) mL \times 100

Table 3: Statistical results of the paired t test for the CBF, OEF, and CMRO₂ in the 4 patient subgroups

	Contralateral Stenosis					
	CBF (mL/100 g/min)		OEF (%)		CMRO ₂ (μmol/100 g/min)	
Group 1	51.9 ± 9.5	50.7 ± 11.2	38.5 ± 3.9	40.6 ± 4.2	153.2 ± 24.0	155.5 ± 22.9
T						
P	0.796		4.027		0.377	
	.442		.002		.713	
Group 2	54.6 ± 5.9	47.9 ± 9.8	38.4 ± 1.9	42.6 ± 3.8	150.3 ± 28.5	149.4 ± 46.1
T						
P	4.146		4.690		0.132	
	.002		.001		.898	
Group 3	54.0 ± 10.3	37.2 ± 9.7	37.1 ± 2.9	44.5 ± 3.9	154.0 ± 43.4	125.3 ± 35.3
T						
P	6.295		6.128		2.926	
	<.001		<.001		.010	
Group 4	55.3 ± 9.5	40.8 ± 11.8	38.3 ± 4.1	43.9 ± 3.5	161.2 ± 47.4	135.0 ± 41.3
T						
P	5.898		4.626		2.647	
	<.001		<.001		.018	

Table 4: Results of the analysis of variance test for the normal-to-lesion ratio of CBF, OEF, and CMRO₂ in the 4 patient subgroups

	Group 1	Group 2	Group 3	Group 4	F	P
rCBF	0.98 ± 0.11	0.87 ± 0.11	0.70 ± 0.17	0.74 ± 0.17	10.617	<.001
rOEF	1.06 ± 0.05	1.11 ± 0.08	1.21 ± 0.14	1.16 ± 0.14	4.316	.009
rCMRO ₂	1.03 ± 0.15	0.98 ± 0.15	0.84 ± 0.21	0.86 ± 0.23	3.041	.037

Table 5: Results of the Student-Newman-Keuls test for the normal-to-lesion ratio of CBF, OEF, and CMRO₂ in the 4 patient subgroups with increasing MCA stenotic severity

	rCBF	rOEF	rCMRO ₂
Group 1			
Group 2	>0.05	>0.05	>0.05
Group 3	<0.05	<0.05	>0.05
Group 4	<0.05	>0.05	>0.05
Group 2			
Group 3	<0.05	>0.05	>0.05
Group 4	<0.05	>0.05	>0.05
Group 3			
Group 4	>0.05	>0.05	>0.05

$\text{g}^{-1} \times \text{min}^{-1}$, $37.1\% \pm 3.2\%$ (32.6%–42.1%), and 145.8 ± 25.1 (100.6–193.4) $\mu\text{mol} \times 100 \text{ g}^{-1} \times \text{min}^{-1}$, respectively. There were no significant differences in CBF, OEF, and CMRO₂ between the hemispheres (Table 2).

In group 1, significant differences between hemispheres were observed in OEF, but not in CBF or CMRO₂. The OEF in hemispheres with mild MCA stenosis was significantly higher than that in the contralateral hemispheres. Additionally, in group 2, there were significant differences in CBF and OEF, but not in CMRO₂ (Table 3). Hemispheres with severe MCA stenosis had a significantly lower CBF and significantly higher OEF than the contralateral hemispheres. Significant differences between hemispheres were observed for CBF, OEF, and CMRO₂ in groups 3 and 4 (Table 3). In addition, hemispheres with occluded MCAs had a significantly lower CBF and CMRO₂ and significantly higher OEF than the contralateral hemispheres.

There were significant differences in rCBF, rCMRO₂ and rOEF in the 4 patient groups (Table 4). rCBF and rCMRO₂ values gradually decreased among groups, but rOEF values

gradually increased from group 1 to 3, coincident with an increase in the degree of angiostenosis. Table 5 lists the Student-Newman-Keuls results comparing the lesion-to-normal ratios in the 4 patient groups.

DISCUSSION

In the present study, the mean venous oxygen saturation, Y_v , (0.629 ± 0.032) of healthy subjects was similar to those in earlier reports (0.64 ± 0.04 ,⁶ 0.638 ± 0.03 ,⁷ 0.628 ± 0.053)²¹) that were measured in the sagittal sinus by using quantitative susceptibility mapping.

Table 6 shows that the range of mean OEF measured by PET has been reported as 35%–43%.^{22–27} The OEF ($37.1\% \pm 3.2\%$) calculated in this study was within this range. With a catheter-derived arteriovenous approach, OEF at the right jugular bulb has been calculated as $36\% \pm 5\%$,²³ which is very close to the OEF calculated in this study.

CMRO₂ measured by PET has been reported as ranging from 127 ± 17.4 to $156 \pm 22.3 \mu\text{mol} \times 100 \text{ g}^{-1} \times \text{min}^{-1}$ (Table 6).^{22–27} The measurement location was typically global brain regions in these studies.^{22–25} The CMRO₂ in gray matter was measured in 2 studies, and values of 156 ± 22.3 or $184.9 \pm 20.1 \mu\text{mol} \times 100 \text{ g}^{-1} \times \text{min}^{-1}$ were reported.^{25,27} The ROI in this study incorporated both gray matter and white matter supplied by the MCA. Gray matter CBF is 2.8 times that of white matter,²⁵ that is, CBF in white matter is significantly lower than in gray matter. Therefore, CBF in the ROI is lower than in the gray matter. The CBF decreased, leading to a decrease in CMRO₂ in the ROI. This means that CMRO₂ found in this study ($145.8 \pm 25.1 \mu\text{mol} \times 100 \text{ g}^{-1} \times \text{min}^{-1}$) is lower than gray matter CMRO₂.^{25,27} Furthermore, quantitative susceptibility mapping–based CMRO₂ measurements within left and right cortical gray matter regions associated with MCA territories have been reported as 149.3 ± 27.1 and $154.8 \pm 37.7 \mu\text{mol} \times 100 \text{ g}^{-1} \times \text{min}^{-1}$.²⁸ This finding indicates that the measurement method and CMRO₂ values in this study are consistent with quantitative susceptibility mapping–based

Table 6: Comparison of OEF and CMRO₂ with published literature values determined by using PET for healthy subjects

Study (Reference)	OEF (Mean) (Range)	CMRO ₂ (μmol/min/100 g)	No.	Mean Age (yr) (range)
Ito et al ^{22,a}	0.44 ± 0.06 (0.36 ± 0.06–0.51 ± 0.04)	147.0 ± 22.3	70	53.1 (18–77)
Hattori et al ^{23,a}	0.39 ± 0.06 (0.30–0.51)	127.0 ± 17.4	16	35 (21–46)
Coles et al ^{24,a}	0.42 ± 0.04	124.8 ± 22.3	7	30 (18–60)
Ibaraki et al ^{25,b}	0.35 ± 0.06	156.0 ± 22.3	8	NA (21–24)
Bremmer et al ^{26,a}	0.43 ± 0.06	135.9 ± 8.9	7	69 (57–80)
Kudomi et al ^{27,b}	0.39 ± 0.05	184.9 ± 20.1	7	25.3 (NA)

Note:—NA indicates not available.

^a Across subjects/brain regions.

^b Gray matter values.

CMRO₂ measurements,²⁸ suggesting the robustness of these methods for the measurement of OEF and CMRO₂.

The original phase-based regional oxygen metabolism method used a multiecho sequence.¹⁶ Multiecho phase values fit a straight line that is a phase against TE, and a new phase for a TE is extrapolated from the straight line. The difference between the new phase and the measured phase is due to noise. Multiecho sequences remove the effect of noise on phase measurements. The SD in Y_v estimates due to noise is <5% of oxygen saturation, with a signal-to-noise ratio is as low as 10,¹⁶ whereas an ordinary phase image has an average SNR in the range of 40–70. This means that thermal noise within this SNR range leads to proportionately small error values. In addition, multiecho sequences require triple the calculations of single-echo sequences, which makes it difficult to apply the former in clinical practice.

We reconstructed the magnitude and phase images by using a single-echo sequence. The mean Y_v (0.629 ± 0.032) in this study is similar to the value (0.638 ± 0.03) measured in the sagittal sinus by using a dual-echo sequence in healthy subjects.⁷ Furthermore, the OEF and CMRO₂ values of the healthy subjects in this study are in agreement with the values determined by using PET or MR imaging.^{22–28} These results demonstrate that the present method of OEF measurement is accurate; therefore, OEF measured by a single-echo sequence is simple and useful.

An earlier study used standard approximate values for Hct and hemoglobin^{16,28,29}; however, Hct and hemoglobin were calculated directly from blood measurements in this study.

At present, there is controversy over the value of $\Delta\chi_{\text{do}}$.¹⁶ The 2 reported values (0.27 and 0.18 ppm) lead to a difference of approximately 13% in SvO₂ estimates.⁷ We adopted 0.27 ppm in this study on the basis of recently published research.¹⁵

The susceptibility reproduced by the long-cylinder approximation has excellent accuracy and precision when the length of a vein exceeds 6× its diameter⁸; therefore, a vein with a length of at least 6× its diameter can be used in the long-cylinder model in MR susceptometry. On the basis of our observations, this standard is easy to meet in the veins of the brain.

All vessels were not parallel to the B₀ field, and the tilt angle was not equal to zero. Veins thread tortuously through the brain sulcus. Therefore, significant lengths that are parallel to the B₀ field are unlikely.

A 32 × 32 Hanning filter was used to enhance the phase image in this study. This resulted in <1% Y_v bias.¹⁶ Therefore, the effects on the quantification of the vein-tissue phase caused by the 32 × 32 Hanning filter can be safely ignored.

To the best of our knowledge, no previous studies have investigated changes in CBF, OEF, and CMRO₂ based on the severity of MCA stenosis. With the help of HR-T2WI, we measured and classified the degree of MCA stenosis, which has not been published previously. Moreover, ASL and SWI are noninvasive examinations compared with PET, making these

techniques attractive for a clinical setting.

As shown in Table 3, CBF significantly decreased in groups 2 and 3. In addition, OEF increased from groups 2 through 4, coincident with the severity of the MCA stenosis. This increase is a compensatory mechanism to counteract the decrease in CBF and stabilize cerebral oxygen metabolism, indicating a self-regulatory mechanism in the brain.

Tables 4 and 5 show that a small increase in rOEF was present in patients with severe MCA stenosis (group 2) compared with patients with mild MCA stenosis (group 1). Most interesting, rOEF was significantly higher in patients with occlusive MCA (group 3) compared with patients with mild MCA stenosis. This result demonstrates that collateral circulation can compensate for the shortage in CBF in patients with mild MCA stenosis, but not in those with severe MCA stenosis. Moreover, in mild or severe MCA stenosis, the CMRO₂ of the hemisphere with MCA stenosis was similar to or slightly lower than the contralateral CMRO₂. This difference indicates that an increase in the OEF can balance a decrease in CBF in the presence of mild or severe MCA stenosis, ultimately maintaining brain oxygen availability. Conversely, when an occlusion was present in the MCA, the CMRO₂ of the affected hemisphere was significantly lower than that of the contralateral hemisphere. These findings indicate that the presence of an occlusion prevents an increase in OEF to offset the decrease in CBF, leading to a decrease in CMRO₂. This decrease in CMRO₂ can disrupt normal cellular function or metabolism and ultimately lead to cell death. Furthermore, a decrease in CMRO₂ indicates that the OEF has reached a maximal or nearly maximal level. Consequently, the risk of stroke is higher in patients with severe stenosis or an occluded MCA than in the presence of mild stenosis.

The CBF in stroke regions was significantly lower than that in the normal brain. There can be significant measurement errors if the stroke area is incorporated in the ROI; therefore, we avoided the stroke region when measuring CBF in patients with acute stroke. We observed that the OEF and CMRO₂ significantly increased and decreased, respectively, in the territory of the occluded MCA during acute stroke. This observation is consistent with the findings of previous studies by using PET.^{30–33} Tables 3–5 show that the CBF, OEF, and CMRO₂ values of patients with acute stroke were similar to those of patients in group 3, but not group 2. Conversely, the degree of the angiostenosis in group 4 was similar to that of group 2, but

not group 3. Table 5 shows that there was a significant difference in rCBF between groups 2 and 4. The OEF may have reached its maximum value because of the markedly decreased CBF in group 4, which consequently led to the acute stroke. Most patients in group 3 had neurologic symptoms, such as headache. Research has revealed that there is a high incidence of stroke in patients with an increased OEF due to an occluded carotid artery.^{3,4} As a result, patients with an increased OEF in group 3 may have been close to having a stroke.

This study has several limitations. First, although we simplified the method as much as possible, it remains complex and difficult to master for clinician doctors. Second, the controversy regarding the value of $\Delta\chi_{do}$ remains. Third, this method can only obtain measurements for the entire MCA territory, not the regional OEF in the infarction area or penumbra.

CONCLUSIONS

The study obtained 2 primary results: 1) The OEF gradually increased from group 1 through 3. When the increased OEF compensated for a decreased CBF, CMRO₂ remained at a normal level; however, an occluded MCA led to a reduction in both CBF and CMRO₂. 2) The OEF and CMRO₂ were significantly increased and decreased, respectively, in the territory around the occluded MCA in acute stroke.

REFERENCES

- Derdeyn CP, Videen TO, Yundt KD, et al. **Variability of cerebral blood volume and oxygen extraction: stages of cerebral haemodynamic impairment revisited.** *Brain* 2002;125:595–607 CrossRef Medline
- Derdeyn CP, Videen TO, Simmons NR, et al. **Count-based PET method for predicting ischemic stroke in patients with symptomatic carotid arterial occlusion.** *Radiology* 1999;212:499–506 CrossRef Medline
- Derdeyn CP, Videen TO, Grubb RL Jr, et al. **Comparison of PET oxygen extraction fraction methods for the prediction of stroke risk.** *J Nucl Med* 2001;42:1195–97 Medline
- Yamauchi H, Higashi T, Kagawa S, et al. **Is misery perfusion still a predictor of stroke in symptomatic major cerebral artery disease?** *Brain* 2012;135:2515–26 CrossRef Medline
- Jain V, Langham MC, Floyd TF, et al. **Rapid magnetic resonance measurement of global cerebral metabolic rate of oxygen consumption in humans during rest and hypercapnia.** *J Cereb Blood Flow Metab* 2011;31:1504–12 CrossRef Medline
- Jain V, Langham MC, Wehrli FW. **MRI estimation of global brain oxygen consumption rate.** *J Cereb Blood Flow Metab* 2010;30:1598–607 CrossRef Medline
- Fan AP, Bilgic B, Gagnon L, et al. **Quantitative oxygenation venography from MRI phase.** *Magn Reson Med* 2014;72:149–59 CrossRef Medline
- Langham MC, Magland JF, Epstein CL, et al. **Accuracy and precision of MR blood oximetry based on the long paramagnetic cylinder approximation of large vessels.** *Magn Reson Med* 2009;62:333–40 CrossRef Medline
- Fujima N, Kudo K, Terae S, et al. **Non-invasive measurement of oxygen saturation in the spinal vein using SWI: quantitative evaluation under conditions of physiological and caffeine load.** *Neuroimage* 2011;54:344–49 CrossRef Medline
- Zaitzu Y, Kudo K, Terae S, et al. **Mapping of cerebral oxygen extraction fraction changes with susceptibility-weighted phase imaging.** *Radiology* 2011;261:930–36 CrossRef Medline
- Günther M, Oshio K, Feinberg DA. **Single-shot 3D imaging techniques improve arterial spin labeling perfusion measurements.** *Magn Reson Med* 2005;54:491–98 CrossRef Medline
- Vidorreta M, Wang Z, Rodríguez I, et al. **Comparison of 2D and 3D single-shot ASL perfusion fMRI sequences.** *Neuroimage* 2013;66:662–71 CrossRef Medline
- Derdeyn CP, Powers WJ, Grubb RL Jr, et al. **Hemodynamic effects of middle cerebral artery stenosis and occlusion.** *AJNR Am J Neuroradiol* 1998;19:1463–69 Medline
- Tanaka M, Shimosegawa E, Kajimoto K, et al. **Chronic middle cerebral artery occlusion: a hemodynamic and metabolic study with positron-emission tomography.** *AJNR Am J Neuroradiol* 2008;29:1841–46 CrossRef Medline
- Jain V, Abdulmalik O, Probert KJ, et al. **Investigating the magnetic susceptibility properties of fresh human blood for noninvasive oxygen saturation quantification.** *Magn Reson Med* 2012;68:863–67 CrossRef Medline
- Fan AP, Benner T, Bolar DS, et al. **Phase-based regional oxygen metabolism (PROM) using MRI.** *Magn Reson Med* 2012;67:669–78 CrossRef Medline
- Mildner T, Trampel R, Möller HE, et al. **Functional perfusion imaging using continuous arterial spin labeling with separate labeling and imaging coils at 3 T.** *Magn Reson Med* 2003;49:791–95 CrossRef Medline
- Binnewijzend MA, Kuijter JP, Benedictus MR, et al. **Cerebral blood flow measured with 3D pseudocontinuous arterial spin-labeling MR imaging in Alzheimer disease and mild cognitive impairment: a marker for disease severity.** *Radiology* 2013;267:221–30 CrossRef Medline
- Fujima N, Kudo K, Terae S, et al. **Spinal arteriovenous malformation: evaluation of change in venous oxygenation with susceptibility-weighted MR imaging after treatment.** *Radiology* 2010;254:891–99 CrossRef Medline
- Chalela JA, Alsop DC, Gonzalez-Atavales JB, et al. **Magnetic resonance perfusion imaging in acute ischemic stroke using continuous arterial spin labeling.** *Stroke* 2000;31:680–87 CrossRef Medline
- Xu F, Ge Y, Lu H. **Noninvasive quantification of whole-brain cerebral metabolic rate of oxygen (CMRO₂) by MRI.** *Magn Reson Med* 2009;62:141–48 CrossRef Medline
- Ito H, Kanno I, Kato C, et al. **Database of normal human cerebral blood flow, cerebral blood volume, cerebral oxygen extraction fraction and cerebral metabolic rate of oxygen measured by positron emission tomography with 15O-labelled carbon dioxide or water, carbon monoxide and oxygen: a multicentre study in Japan.** *Eur J Nucl Med Mol Imaging* 2004;31:635–43 CrossRef Medline
- Hattori N, Bergsneider M, Wu HM, et al. **Accuracy of a method using short inhalation of (15)O-O(2) for measuring cerebral oxygen extraction fraction with PET in healthy humans.** *J Nucl Med* 2004;45:765–70 Medline
- Coles JP, Fryer TD, Bradley PG, et al. **Intersubject variability and reproducibility of 15O PET studies.** *J Cereb Blood Flow Metab* 2006;26:48–57 CrossRef Medline
- Ibaraki M, Miura S, Shimosegawa E, et al. **Quantification of cerebral blood flow and oxygen metabolism with 3-dimensional PET and ¹⁵O: validation by comparison with 2-dimensional PET.** *J Nucl Med* 2008;49:50–59 Medline
- Bremner JP, van Berckel BN, Persoon S, et al. **Day-to-day test-retest variability of CBF, CMRO₂, and OEF measurements using dynamic 15O PET studies.** *Mol Imaging Biol* 2011;13:759–68 CrossRef Medline
- Kudomi N, Hirano Y, Koshino K, et al. **Rapid quantitative CBF and CMRO(2) measurements from a single PET scan with sequential administration of dual (15)O-labeled tracers.** *J Cereb Blood Flow Metab* 2013;33:440–48 CrossRef Medline
- Zhang J, Liu T, Gupta A, et al. **Quantitative mapping of cerebral metabolic rate of oxygen (CMRO₂) using quantitative susceptibility mapping (QSM).** *Magn Reson Med* 2015;74:945–52. CrossRef Medline
- Qin Q, Grgac K, van Zijl PC. **Determination of whole-brain oxygen extraction fractions by fast measurement of blood T(2) in**

- the jugular vein.** *Magn Reson Med* 2011;65:471–79 CrossRef Medline
30. Donswijk ML, Jones PS, Guadagno JV, et al. **T2*-weighted MRI versus oxygen extraction fraction PET in acute stroke.** *Cerebrovasc Dis* 2009;28:306–13 CrossRef Medline
 31. Guadagno JV, Jones PS, Fryer TD, et al. **Local relationships between restricted water diffusion and oxygen consumption in the ischemic human brain.** *Stroke* 2006;37:1741–48 CrossRef Medline
 32. Sobesky J, Zaro Weber O, Lehnhardt FG, et al. **Does the mismatch match the penumbra? Magnetic resonance imaging and positron emission tomography in early ischemic stroke.** *Stroke* 2005;36:980–85 CrossRef Medline
 33. Heiss WD, Sobesky J, Hesselmann V. **Identifying thresholds for penumbra and irreversible tissue damage.** *Stroke* 2004;35:2671–74 CrossRef Medline
 34. Derdeyn CP, Yundt KD, Videen TO, et al. **Increased oxygen extraction fraction is associated with prior ischemic events in patients with carotid occlusion.** *Stroke* 1998;29:754–58 CrossRef Medline

Risk Factors for Growth of Intracranial Aneurysms: A Systematic Review and Meta-Analysis

W. Brinjikji, Y.-Q. Zhu, G. Lanzino, H.J. Cloft, M.H. Murad, Z. Wang, and D.F. Kallmes



ABSTRACT

BACKGROUND AND PURPOSE: Understanding risk factors for intracranial aneurysm growth is important for patient management. We performed a meta-analysis examining risk factors for intracranial aneurysm growth in longitudinal studies and examined the association between aneurysm growth and rupture.

MATERIALS AND METHODS: We searched the literature for longitudinal studies of patients with unruptured aneurysms. We examined the associations of demographics, multiple aneurysms, prior subarachnoid hemorrhage, family history of aneurysm or subarachnoid hemorrhage, smoking, and hypertension; and aneurysm shape, size, and location with aneurysm growth. We studied the association between aneurysm growth and rupture. A meta-analysis was performed by using a random-effects model by using summary statistics from included studies.

RESULTS: Twenty-one studies including 3954 patients with 4990 aneurysms with 13,294 aneurysm-years of follow-up were included. The overall proportion of growing aneurysms was 3.0% per aneurysm-year (95% CI, 2.0%–4.0%). Patient risk factors for growth included age older than 50 years (3.8% per year versus 0.9% per year, $P < .01$), female sex (3.2% per year versus 1.3% per year, $P < .01$), and smoking history (5.5% per year versus 3.5% per year, $P < .01$). Characteristics associated with higher growth rates included cavernous carotid artery location (14.4% per year), nonsaccular shape (14.7% per year versus 5.2% per year for saccular, $P < .01$), and aneurysm size ($P < .01$). Aneurysm growth was associated with a rupture rate of 3.1% per year compared with 0.1% per year for stable aneurysms ($P < .01$).

CONCLUSIONS: Observational evidence provided multiple clinical and anatomic risk factors for aneurysm growth, including age older than 50 years, female sex, smoking history, and nonsaccular shape. These findings should be considered when counseling patients regarding the natural history of unruptured intracranial aneurysms.

Unruptured intracranial aneurysms have a fairly high prevalence in the general population, with estimates of aneurysm prevalence ranging from 2% to 8%.^{1,2} However, the incidence of subarachnoid hemorrhage is substantially lower, estimated to be 10–30 per 100,000 per year.³ In addition to rupture, aneurysms can result in substantial morbidity secondary to cranial nerve palsies, headache, and even anxiety.⁴ Overall, there has been a trend toward increased treatment of unruptured intracranial aneurysms with surgical clipping and endovascular coiling.⁵ With im-

provement in operative and endovascular techniques as well as postoperative care, the morbidity and mortality related to these procedures has decreased with time.⁶ When counseling patients with unruptured aneurysms, many practitioners discuss the risks of surgical or endovascular treatment in the context of the natural history of their aneurysms.⁴ Results from long-term follow-up studies, such as the International Study of Unruptured Intracranial Aneurysms, the Small Unruptured Intracranial Aneurysm Verification study (UCAS), are often used in discussing the natural history of unruptured aneurysms with patients.^{7–11}

Risk factors for aneurysm growth are relatively understudied compared with those of aneurysm rupture. However, many longitudinal observational studies may not follow patients long enough to witness aneurysm rupture but will see aneurysm growth during their short follow-up time. In addition, aneurysms that grow on surveillance imaging are generally treated; this factor potentially decreases the rupture rate in many longitudinal studies. Because growth itself may be a risk factor for rupture, an

Received May 14, 2015; accepted after revision July 21.

From the Departments of Radiology (W.B., Y.-Q.Z., G.L., H.J.C., D.F.K.) and Neurosurgery (G.L., H.J.C., D.F.K.) and Center for Science of Healthcare Delivery (M.H.M., Z.W.), Mayo Clinic, Rochester, Minnesota.

Please address correspondence to Waleed Brinjikji, MD, Mayo Clinic, 200 First St SW, OLI-112 SMH, Rochester, MN 55905, e-mail: Brinjikji.waleed@mayo.edu; @WBrinjikji

Indicates article with supplemental on-line table.

<http://dx.doi.org/10.3174/ajnr.A4575>

understanding of the clinical and anatomic risk factors for aneurysm growth is important.¹² Therefore, we performed a systematic review and meta-analysis of all published studies examining the clinical and anatomic risk factors for aneurysm growth. In addition, we performed a separate analysis to determine the rupture rate of growing aneurysms. We hypothesized that factors known to be associated with aneurysm rupture (ie, Japanese or Finnish population, hypertension, older age, increasing aneurysm size, previous SAH, and location) would also be associated with growth.

MATERIALS AND METHODS

A comprehensive literature search of the data bases PubMed, Ovid MEDLINE, and Ovid EMBASE was designed and conducted by an experienced librarian with input from the authors. The key words, “intracranial aneurysm,” “unruptured aneurysm,” “aneurysm,” “cerebral aneurysm,” “growth,” “natural history,” “rupture,” “longitudinal,” “morbidity,” “mortality,” “CT,” “MR imaging,” and “angiography,” were used in “and/or” combinations. The search included all articles published on this topic from January 1960 to November 2014. All studies with longitudinal follow-up of unruptured intracranial aneurysms reporting growth were included. Inclusion criteria were the following: 1) a series of >10 patients, with available data on clinical and anatomic risk factors for aneurysm growth; 2) a series with a mean or median follow-up of at least 12 months; 3) studies published in English; and 4) studies of a consecutive series of patients with unruptured aneurysms undergoing clinical and/or angiographic follow-up. Studies with <10 patients, published, in a language other than English, or with a mean or median follow-up of <12 months were excluded. Studies comparing the characteristics of ruptured and unruptured intracranial aneurysms on presentation were excluded as well. Two reviewers selected the included studies. Inconsistencies were handled by a third reviewer with final say regarding inclusion or exclusion of a given study.

For each study, we extracted the following information for risk factors for aneurysm growth: overall proportion of growing aneurysms, age (by using both 50 and 70 years as age cutoffs), ethnicity, sex, aneurysm location (ICA, MCA, anterior cerebral artery/anterior communicating artery, vertebrobasilar, and common carotid artery), posterior or anterior aneurysm location, aneurysm multiplicity, prior SAH, family history of aneurysm or SAH, hypertension, smoking, aneurysm shape (saccular, lobular, daughter sac, fusiform), saccular or nonsaccular morphology, and aneurysm size (by using 3, 5, 7, 10, 13, and 25 mm as cutoffs). In addition, we studied the association between aneurysm growth and rupture. Aneurysm size and age could not be analyzed as continuous variables because these data were obtained from summary data rather than individual patient data. We chose the most commonly used age and size categories to include the largest number of patients/aneurysms possible for this study. The definition of aneurysm growth varied by study; however, in general, “growth” was defined as an increase of at least 1–2 mm in maximum aneurysm dimension.

We also collected the following information from each study: patient-years of follow-up, aneurysm-years of follow-up, mean overall follow-up, study population, study design, outcomes reported, imaging used in follow-up, and study risk of bias. Because

the included studies were uncontrolled, we modified the Newcastle-Ottawa Quality Assessment Scale to assess the risk of bias. Therefore, we assessed study risk of bias on the basis of the following questions: Did the study include all patients or consecutive patients with clinical or angiographic follow-up versus a selected sample? Were angiographic and clinical follow-up satisfactory, thus allowing ascertainment of all outcomes? Was the case definition adequate (ie, the clinical and angiographic risk factors were clearly stated)? Were outcomes well ascertained? Was the length of longitudinal follow-up sufficient to estimate aneurysm growth rates? Studies judged to be at low risk of bias were defined as those with a predefined study protocol, high rates of imaging and clinical follow-up (at least 70% of angiographic and/or clinical follow-up during the study period), and adequate ascertainment of clinical and anatomic risk factors for growth. Studies judged to be at a high risk of bias were those that evaluated only a specific subset of patients with unruptured aneurysms (ie, specific size, location), had a lack of adequate ascertainment of clinical and anatomic risk factors for growth and/or rupture, and had low rates of angiographic or clinical follow-up.

Statistical Analysis

We estimated from each cohort the cumulative incidence (event rate) and 95% confidence interval of the proportion of aneurysms growing per year of follow-up for individual aneurysm characteristics and per patient-year for patient/clinical characteristics. All data are reported on a per-year basis rather than a per-patient or per-aneurysm basis. Event rates for each intervention were pooled in a meta-analysis across studies by using the DerSimonian and Laird random-effects models.¹³ Anticipating heterogeneity between studies, we chose this model a priori because it incorporates within-study variance and between-study variance. We also extracted a 2 × 2 table for each studied outcome for interaction testing and calculated *P* values for the comparisons between the previously mentioned clinical and anatomic characteristics. Meta-regression was not used in this study. Heterogeneity of treatment effect across studies was evaluated by using the *I*² statistic, in which *I*² >50% suggested substantial heterogeneity.¹⁴

RESULTS

Literature Review

Our initial literature search yielded 1029 articles. Twenty-one studies reported risk factors for aneurysm growth, including 3954 patients with 4990 aneurysms with 11,000 patient-years and 13,294 aneurysm-years of follow-up.^{9,12,15–33} Eleven of these studies reported the rupture rate of growing aneurysms. Mean patient follow-up was 4.9 years, and median was 3.2 years. The characteristics of the included studies are provided in the On-line Table. Details of our search are provided in Fig 1.

Risk Factors for Aneurysm Growth

Overall growth rate per aneurysm was 3.0% of aneurysms per aneurysm-year (95% CI, 2.0%–4.0%) (Fig 2). Patient risk factors for aneurysm growth included age older than 50 years (3.8% per year compared with 0.9% per year, *P* < .01), female sex (3.2% per

year versus 1.3% per year, $P < .01$), and prior smoking history (5.5% per year versus 3.5% per year, $P < .01$).

By location, aneurysms with the highest growth rates included cavernous carotid artery (14.4% per year), vertebrobasilar (3.6% per year), and MCA aneurysms (3.3% per year). Overall, the

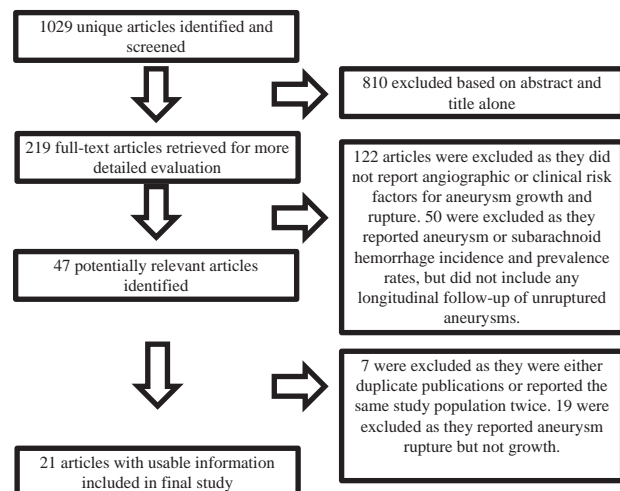


FIG 1. Flow diagram summarizing the search strategy for meta-analysis.

growth rate was higher for posterior circulation aneurysms (3.8% per year) compared with anterior circulation aneurysms (2.7% per year, $P < .01$). Aneurysms with nonsaccular shape had higher growth rates than saccular aneurysms (14.7% per year versus 5.2% per year, $P < .01$). Aneurysms of <10 mm were associated with growth rates of 2.9% per year, while aneurysms of >10 mm were associated with growth rates of 9.7% per year ($P < .01$).

Aneurysm multiplicity, family history, hypertension, and prior history of SAH were not statistically associated with higher rates of aneurysm growth ($P > .05$). These data are summarized in the Table.

Aneurysm Growth and Rupture

Ten studies examined the association between aneurysm growth and rupture. Aneurysm growth was associated with a rupture rate of 3.1% per year compared with 0.1% per year for nongrowing aneurysms ($P < .01$).

Risk of Bias

Of the 21 studies included in our meta-analysis, 15 had a high risk of bias, 4 had a moderate risk of bias, and 2 had a low risk of bias. Studies at a high risk of bias reported higher rates of aneurysm

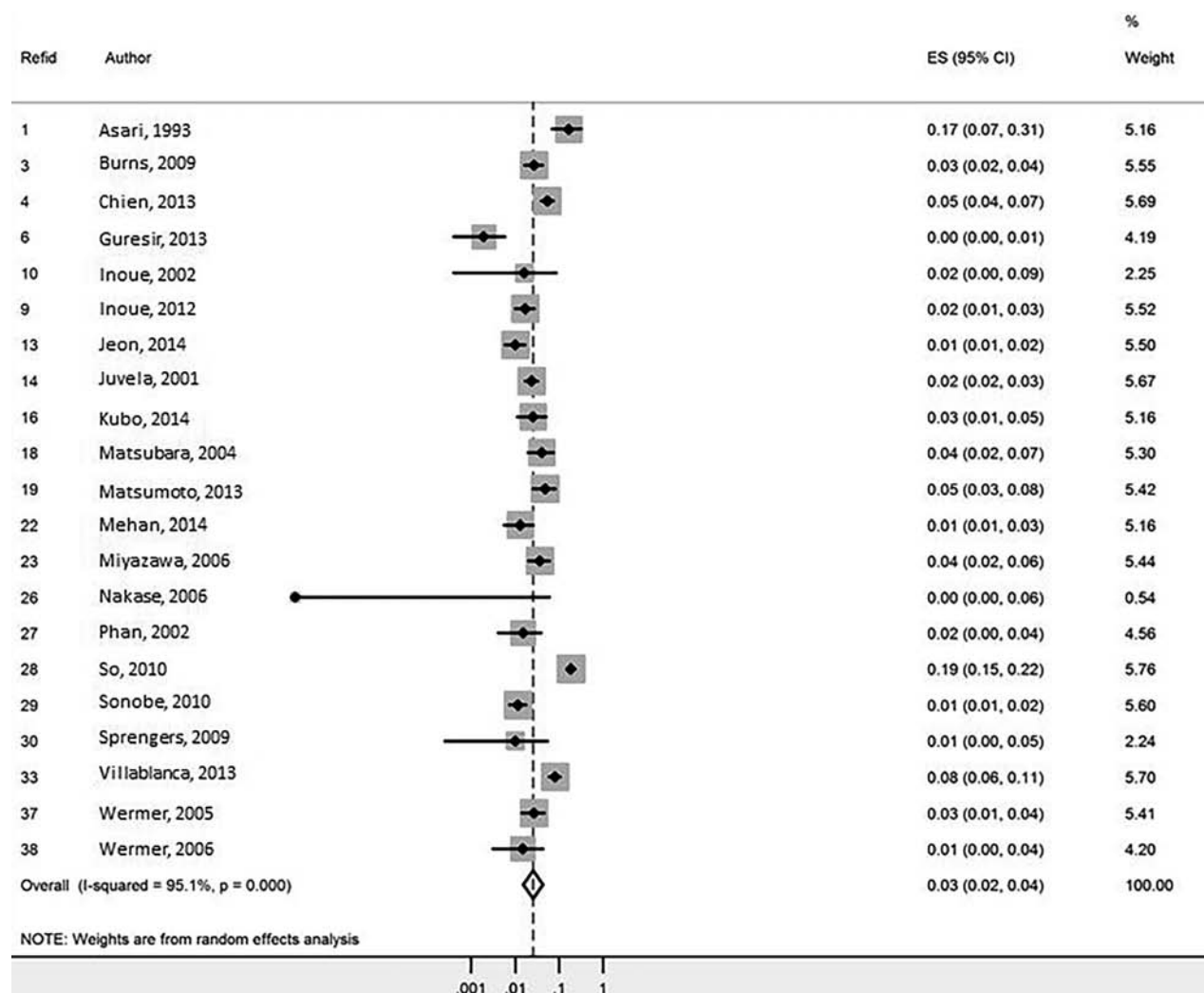


FIG 2. Forest plot for aneurysm growth meta-analysis.

Risk factors for aneurysm growth

	No. of Studies	Proportion of Growing Aneurysms per Patient-Year (95% CI)	I ²	P Value
Overall growth rate	21	3.0 (2.0–4.0)	95	–
Age (yr)				
50 or younger	6	0.9 (0.0–24.7)	93	<.0001
50 or older	3	3.8 (1.3–11.5)	96	
70 or younger	5	2.4 (0.4–16.3)	96	.04
70 or older	1	2.5 (1.2–5.4)	NA	
Population				
Japanese	9	2.7 (1.5–4.7)	82	–
Finnish	1	2.4 (1.7–3.3)	NA	–
Sex				
Male	12	1.3 (0.5–3.6)	90	<.01
Female	12	3.2 (1.6–6.3)	95	
Aneurysm location				
ICA	13	2.5 (1.1–5.5)	92	<.01
MCA	13	3.3 (1.4–7.9)	87	
ACA/AcomA	13	1.8 (0.8–4.2)	89	
VBA	12	3.6 (1.3–9.9)	85	
Cavernous carotid artery	2	14.4 (5.1–40.2)	75	
Anterior vs posterior				
Anterior	14	2.7 (1.4–5.0)	95	<.01
Posterior	13	3.8 (1.5–9.9)	84	
Multiple aneurysms				
Yes	13	2.3 (1.1–4.8)	85	.80
No	11	3.0 (1.7–5.4)	86	
Prior SAH				
Yes	9	2.2 (0.7–6.8)	92	.06
No	8	4.7 (1.9–11.6)	95	
Family history				
Yes	7	5.0 (1.6–15.1)	79	.58
No	7	3.8 (1.5–9.3)	97	
HTN				
Yes	11	3.9 (1.9–8.0)	92	.88
No	11	4.0 (1.9–8.0)	93	
Smoking				
Yes	12	5.5 (3.0–9.9)	81	<.01
No	11	3.5 (1.7–7.1)	94	
Shape				
Saccular	4	5.2 (2.3–11.8)	75	<.01
Lobular	2	15.2 (5.8–40.2)	0	
Daughter sac	1	16.7 (4.9–56.7)	NA	
Fusiform	1	13.7 (6.4–29.5)	NA	
Shape				
Saccular	4	5.2 (2.3–11.8)	75	<.01
Nonsaccular	4	14.7 (8.6–25.2)	0	
Size (mm)				
<3	4	4.1 (1.3–12.9)	88	<.01
>3	15	5.2 (2.9–9.3)	87	
<5	9	2.3 (1.2–4.2)	89	<.01
>5	13	6.5 (3.6–12.0)	84	
<7	11	2.5 (1.5–4.1)	90	<.01
>7	10	9.2 (4.1–20.6)	84	
<10	15	2.9 (1.6–5.2)	96	<.01
>10	10	9.7 (4.0–23.8)	81	
<13	15	3.0 (1.6–5.3)	96	<.01
>13	5	8.1 (1.8–36.1)	83	
Study risk of bias				
High	15	2.9 (1.6–5.6)	95	<.01
Medium	4	1.7 (0.4–7.2)	92	
Low	2	1.7 (0.8–3.4)	86	

Note:—AcomA indicates anterior communicating artery; VBA, vertebrobasilar artery; HTN, hypertension; ACA, anterior cerebral artery; NA, not applicable.

growth (2.9% per year) compared with those with a low risk of bias (1.7% per year).

DISCUSSION

This meta-analysis of 21 longitudinal studies examining the natural history of unruptured aneurysms highlights a number of im-

portant risk factors for aneurysm growth. Overall growth rates of 2.5% of aneurysms per year are not negligible. Risk factors found to be statistically associated with aneurysm growth included larger aneurysm size, posterior circulation location, irregular aneurysm shape, smoking, and female sex. Aneurysm growth was in itself a risk factor for rupture with growing aneurysms being >30 times as likely to rupture compared with stable aneurysms. These findings are noteworthy because they highlight important clinical and anatomic risk factors for progression of intracranial aneurysms that can be used in counseling patients with unruptured aneurysms. Risk factors for aneurysm growth have not been as extensively studied as those for aneurysm rupture. This meta-analysis highlights the fact that aneurysm growth is not uncommon; and in the case of larger and irregularly shaped aneurysms and aneurysms located in the cavernous carotid artery, growth rates are rather high.

Overall, large previous studies have demonstrated that annual aneurysm growth rates hover around 1.5%–2.5% of aneurysms/year, similar to our findings.^{12,20,31,34} A number of factors have been reported associated with aneurysm growth, including aneurysm size, location at a bifurcation or posterior circulation, young age, hypertension, smoking, aneurysm multiplicity, and aneurysm lobulation.^{12,16,18,21,31} Our meta-analysis of nearly 4000 patients found that growth was associated with increasing age, female sex, smoking, irregular aneurysm shape, location in the posterior circulation, cavernous carotid artery or MCA bifurcation, and larger aneurysm size.

The rupture rate of growing aneurysms varies substantially across studies. In a study of 1002 patients with 1325 unruptured aneurysms, Inoue et al²⁰ found that the annual rupture risk after aneurysm growth was 18.5%/person-year. Mehan et al¹² found that aneurysm growth was associated with an odds ratio of 55.9 for rupture on a multivariate analysis. Villablanca et al³¹ found that annual rupture rates were >10 times higher in growing compared with nongrowing aneurysms. Juvela et al²² also demonstrated a strong association between aneurysm growth and rupture. The series of Juvela et al, which has the longest follow-up of any population-based study on the natural history of unruptured aneurysms, demonstrated that 45% of aneurysms undergoing follow-up had some growth of >1 mm during the lifetime of the patient. Of these, 66% ruptured.²² In our meta-analysis, growing aneurysms were >30 times more likely to rupture than stable ones, and the overall rupture rate of these aneurysms was 3.1% per year.

Understanding factors associated with aneurysm growth is also important because imaging surveillance of intracranial aneurysms is based on the principle that aneurysms that grow or change morphology are less stable and thus more prone to rupture.⁴ Progression of the aneurysm is generally considered an indication to treat because growing aneurysms are known to be associated with aneurysm rupture.³⁵ Understanding factors associated with aneurysm growth could help in determining which subset of aneurysms deserve the closest follow-up. For example, in our study, aneurysms with daughter sacs or lobulations had a 14.7% growth rate per year, while the overall aneurysm growth rate was 2.5% per year. These findings would suggest that such aneurysms may require more regular imaging follow-up to detect

growth to allow intervention before future rupture. Ultimately, further studies are needed to determine the best screening decisions for high-risk aneurysms.

Risk factors for aneurysm rupture have been more extensively studied than aneurysm growth due to the substantial morbidity and mortality rates associated with aneurysmal subarachnoid hemorrhage.⁴ A number of large longitudinal studies on the risk factors of aneurysmal rupture have been performed, which have enhanced our understanding of the natural history of unruptured aneurysms.^{7,9,10,22,33,36–39} Overall rupture rates in these studies range from 1% to 1.4% per year.^{9,10,36,37} Clinical risk factors for aneurysm rupture in these studies included hypertension, smoking, aneurysm multiplicity, prior history of SAH, family history, and female sex.²² Anatomic risk factors included increased aneurysm size, the presence of a daughter sac, and posterior circulation location.^{9,36} These factors are similar to those seen in our meta-analysis of aneurysm growth.

A number of models have been proposed to study the risks of aneurysm rupture. The recently published PHASES score is based on data from several large population studies comprising 8382 patients with 10,272 aneurysms.⁸ Risk factors for aneurysm rupture in this risk score include Japanese or Finnish descent, hypertension, age older than 70 years, larger aneurysm size, prior SAH, and MCA/anterior cerebral artery/posterior communicating artery/posterior circulation aneurysm location. A higher PHASES score is strongly associated with a higher risk of rupture. Our study highlights a number of variables that were strongly associated with aneurysm growth that were not included in the original PHASES score, including irregular aneurysm shape (ie, lobulation, daughter sac, fusiform), female sex, and smoking. Furthermore, aneurysm growth was found to be a strong predictor of rupture. One recently published consensus study by Etminan et al³⁵ proposed a model for assessing treatment decisions for unruptured aneurysms that combined variables, including clinical characteristics, family history, and aneurysm characteristics. This study highlighted factors such as aneurysm growth, lobulation, and smoking history into their model as factors that would sway the decision toward treatment rather than observation.³⁵ Our study lends further evidence to support the conclusions of this consensus group.

Strengths and Limitations

The strengths of our study include following an a priori established protocol, the comprehensive literature search that involved multiple data bases, and the process of study selection performed by independent reviewers. The main limitation of this analysis is the lack of individual patient data, which makes prognostic analysis subject to confounding and ecologic bias. In addition, 15/21 studies having a high risk of bias further limits our results. Furthermore, many studies differed in their methods of classifications of aneurysm size, location, shape, definition of family history, and smoking history. Aneurysm growth was assessed with various imaging modalities, including CTA, DSA, and MRA, which could introduce some error or bias. In addition, studies had variable thresholds for determining growth of the aneurysm. Aneurysm measurements could vary substantially on the basis of software packages and imaging modalities used. In addition, there

is the possibility of inter- and intraobserver variability in assessing aneurysm growth. There are no validated tools to evaluate the methodologic quality of noncomparative series. Publication bias is very likely in the setting of observational studies. The results of this study are further biased because larger aneurysms are more likely to be treated than smaller aneurysms; this treatment choice clouds our understanding of the natural history of these lesions. The results of our study may be biased because they are based on only studies that reported risk factors for aneurysm growth. Last, uniform assessment and reporting of complications in a standardized fashion were lacking. Nevertheless, this meta-analysis provides useful prognostic data to share with patients and families when assessing the natural history of intracranial aneurysms.

CONCLUSIONS

Overall growth rates of intracranial aneurysms are not negligible. Risk factors for the growth of intracranial aneurysms included nonsaccular aneurysm shape, larger aneurysm size, hypertension, and female sex. Aneurysm growth is significantly associated with rupture as well. These findings should be considered when counseling patients regarding the natural history of intracranial aneurysms.

Disclosures: Giuseppe Lanzino—UNRELATED: Consultancy: Covidien.* David F. Kallmes—UNRELATED: Board Membership: GE Healthcare.* Comments: Cost-Effectiveness Board; Consultancy: ev3/Covidien/Medtronic.* Comments: clinical trial planning and implementation; Grants/Grants Pending: ev3/Covidien/Medtronic.* Codman.* Sequent Medical.* NeuroSigma.* Surmodics.* MicroVention.* Comments: research support for preclinical and clinical studies; Royalties: University of Virginia patent foundation (Spinal Fusion); Travel/Accommodations/Meeting Expenses Unrelated to Activities Listed: ev3/Covidien/Medtronic.* Comments: travel to present at an FDA panel meeting. *Money paid to the institution.

REFERENCES

1. Li MH, Chen SW, Li YD, et al. **Prevalence of unruptured cerebral aneurysms in Chinese adults aged 35 to 75 years: a cross-sectional study.** *Ann Intern Med* 2013;159:514–21 CrossRef Medline
2. Vlak MH, Algra A, Brandenburg R, et al. **Prevalence of unruptured intracranial aneurysms, with emphasis on sex, age, comorbidity, country, and time period: a systematic review and meta-analysis.** *Lancet Neurol* 2011;10:626–36 CrossRef Medline
3. Ziemba-Davis M, Bohnstedt BN, Payner TD, et al. **Incidence, epidemiology, and treatment of aneurysmal subarachnoid hemorrhage in 12 Midwest communities.** *J Stroke Cerebrovasc Dis* 2014;23:1073–82 CrossRef Medline
4. Brown RD Jr, Broderick JP. **Unruptured intracranial aneurysms: epidemiology, natural history, management options, and familial screening.** *Lancet Neurol* 2014;13:393–404 CrossRef Medline
5. Brinjikji W, Rabinstein AA, Lanzino G, et al. **Effect of age on outcomes of treatment of unruptured cerebral aneurysms: a study of the National Inpatient Sample 2001–2008.** *Stroke* 2011;42:1320–24 CrossRef Medline
6. Brinjikji W, Rabinstein AA, Lanzino G, et al. **Patient outcomes are better for unruptured cerebral aneurysms treated at centers that preferentially treat with endovascular coiling: a study of the National Inpatient Sample 2001–2007.** *AJNR Am J Neuroradiol* 2011;32:1065–70 CrossRef Medline
7. Wiebers DO, Whisnant JP, Huston J 3rd, et al; International Study of Unruptured Intracranial Aneurysms Investigators. **Unruptured intracranial aneurysms: natural history, clinical outcome, and risks of surgical and endovascular treatment.** *Lancet* 2003;362:103–10 CrossRef Medline
8. Greving JP, Wermer MJ, Brown RD Jr, et al. **Development of the PHASES score for prediction of risk of rupture of intracranial**

- aneurysms: a pooled analysis of six prospective cohort studies. *Lancet Neurol* 2014;13:59–66 CrossRef Medline
9. Sonobe M, Yamazaki T, Yonekura M, et al. **Small unruptured intracranial aneurysm verification study: SUAVE study, Japan.** *Stroke* 2010;41:1969–77 CrossRef Medline
 10. Ishibashi T, Murayama Y, Urashima M, et al. **Unruptured intracranial aneurysms: incidence of rupture and risk factors.** *Stroke* 2009;40:313–16 CrossRef Medline
 11. Bonares MJ, de Oliveira Manoel AL, Macdonald RL, et al. **Behavioral profile of unruptured intracranial aneurysms: a systematic review.** *Ann Clin Transl Neurol* 2014;3:220–32 Medline
 12. Mehan WA Jr, Romero JM, Hirsch JA, et al. **Unruptured intracranial aneurysms conservatively followed with serial CT angiography: could morphology and growth predict rupture?** *J Neurointerv Surg* 2014;6:761–66 CrossRef Medline
 13. DerSimonian R, Laird N. **Meta-analysis in clinical trials.** *Control Clin Trials* 1986;7:177–88 CrossRef Medline
 14. Higgins JP, Thompson SG, Deeks JJ, et al. **Measuring inconsistency in meta-analyses.** *BMJ* 2003;327:557–60 CrossRef Medline
 15. Asari S, Ohmoto T. **Natural history and risk factors of unruptured cerebral aneurysms.** *Clin Neurol Neurosurg* 1993;95:205–14 CrossRef Medline
 16. Burns JD, Huston J 3rd, Layton KF, et al. **Intracranial aneurysm enlargement on serial magnetic resonance angiography: frequency and risk factors.** *Stroke* 2009;40:406–11 CrossRef Medline
 17. Chien A, Liang F, Sayre J, et al. **Enlargement of small, asymptomatic, unruptured intracranial aneurysms in patients with no history of subarachnoid hemorrhage: the different factors related to the growth of single and multiple aneurysms.** *J Neurosurg* 2013;119:190–97 CrossRef Medline
 18. Güresir E, Vatter H, Schuss P, et al. **Natural history of small unruptured anterior circulation aneurysms: a prospective cohort study.** *Stroke* 2013;44:3027–31 CrossRef Medline
 19. Inoue T. **Treatment of incidental unruptured aneurysms.** *Acta Neurochir Suppl* 2002;82:11–15 Medline
 20. Inoue T, Shimizu H, Fujimura M, et al. **Annual rupture risk of growing unruptured cerebral aneurysms detected by magnetic resonance angiography.** *J Neurosurg* 2012;117:20–25 CrossRef Medline
 21. Jeon JS, Ahn JH, Huh W, et al. **A retrospective analysis on the natural history of incidental small paraclinoid unruptured aneurysms.** *J Neurol Neurosurg Psychiatry* 2014;85:289–94 CrossRef Medline
 22. Juvela S, Poussa K, Porras M. **Factors affecting formation and growth of intracranial aneurysms: a long-term follow-up study.** *Stroke* 2001;32:485–91 CrossRef Medline
 23. Kubo Y, Koji T, Kashimura H, et al. **Female sex as a risk factor for the growth of asymptomatic unruptured cerebral saccular aneurysms in elderly patients.** *J Neurosurg* 2014;121:599–604 CrossRef Medline
 24. Matsubara S, Hadeishi H, Suzuki A, et al. **Incidence and risk factors for the growth of unruptured cerebral aneurysms: observation using serial computerized tomography angiography.** *J Neurosurg* 2004;101:908–14 CrossRef Medline
 25. Matsumoto K, Oshino S, Sasaki M, et al. **Incidence of growth and rupture of unruptured intracranial aneurysms followed by serial MRA.** *Acta Neurochir (Wien)* 2013;155:211–16 CrossRef Medline
 26. Miyazawa N, Akiyama I, Yamagata Z. **Risk factors for growth of unruptured intracranial aneurysms: follow-up study by serial 0.5-T magnetic resonance angiography.** *Neurosurgery* 2006;58:1047–53; discussion 1047–53 CrossRef Medline
 27. Nakase H, Shin Y, Kanemoto Y, et al. **Long-term outcome of unruptured giant cerebral aneurysms.** *Neurol Med Chir (Tokyo)* 2006;46:379–84; discussion 384–86 CrossRef Medline
 28. Phan TG, Huston J 3rd, Brown RD Jr, et al. **Intracranial saccular aneurysm enlargement determined using serial magnetic resonance angiography.** *J Neurosurg* 2002;97:1023–28 CrossRef Medline
 29. So TY, Dowling R, Mitchell PJ, et al. **Risk of growth in unruptured intracranial aneurysms: a retrospective analysis.** *J Clin Neurosci* 2010;17:29–33 CrossRef Medline
 30. Sprengers ME, van Rooij WJ, Sluzewski M, et al. **MR angiography follow-up 5 years after coiling: frequency of new aneurysms and enlargement of untreated aneurysms.** *AJNR Am J Neuroradiol* 2009;30:303–07 Medline
 31. Villablanca JP, Duckwiler GR, Jahan R, et al. **Natural history of asymptomatic unruptured cerebral aneurysms evaluated at CT angiography: growth and rupture incidence and correlation with epidemiologic risk factors.** *Radiology* 2013;269:258–65 CrossRef Medline
 32. Wermer MJ, van der Schaaf IC, Velthuis BK, et al; ASTRA Study Group. **Follow-up screening after subarachnoid haemorrhage: frequency and determinants of new aneurysms and enlargement of existing aneurysms.** *Brain* 2005;128:2421–29 CrossRef Medline
 33. Wermer MJ, van der Schaaf IC, Velthuis BK, et al. **Yield of short-term follow-up CT/MR angiography for small aneurysms detected at screening.** *Stroke* 2006;37:414–18 CrossRef Medline
 34. Juvela S, Poussa K, Lehto H, et al. **Natural history of unruptured intracranial aneurysms: a long-term follow-up study.** *Stroke* 2013;44:2414–21 CrossRef Medline
 35. Etminan N, Beseoglu K, Barrow DL, et al. **Multidisciplinary consensus on assessment of unruptured intracranial aneurysms: proposal of an international research group.** *Stroke* 2014;45:1523–30 CrossRef Medline
 36. Morita A, Kirino T, Hashi K, et al; UCAS Japan Investigators. **The natural course of unruptured cerebral aneurysms in a Japanese cohort.** *N Engl J Med* 2012;366:2474–82 CrossRef Medline
 37. International Study of Unruptured Intracranial Aneurysms Investigators. **Unruptured intracranial aneurysms: risk of rupture and risks of surgical intervention.** *N Engl J Med* 1998;339:1725–33 CrossRef Medline
 38. Wiebers DO, Whisnant JP, Sundt TM Jr, et al. **The significance of unruptured intracranial saccular aneurysms.** *J Neurosurg* 1987;66:23–29 CrossRef Medline
 39. Wiebers DO, Whisnant JP, O'Fallon WM. **The natural history of unruptured intracranial aneurysms.** *N Engl J Med* 1981;304:696–98 CrossRef Medline

Computational Identification of Tumor Anatomic Location Associated with Survival in 2 Large Cohorts of Human Primary Glioblastomas

T.T. Liu, A.S. Achrol, L.A. Mitchell, W.A. Du, J.J. Loya, S.A. Rodriguez, A. Feroze, E.M. Westbroek, K.W. Yeom, J.M. Stuart, S.D. Chang, G.R. Harsh IV, and D.L. Rubin



ABSTRACT

BACKGROUND AND PURPOSE: Tumor location has been shown to be a significant prognostic factor in patients with glioblastoma. The purpose of this study was to characterize glioblastoma lesions by identifying MR imaging voxel-based tumor location features that are associated with tumor molecular profiles, patient characteristics, and clinical outcomes.

MATERIALS AND METHODS: Preoperative T1 anatomic MR images of 384 patients with glioblastomas were obtained from 2 independent cohorts ($n = 253$ from the Stanford University Medical Center for training and $n = 131$ from The Cancer Genome Atlas for validation). An automated computational image-analysis pipeline was developed to determine the anatomic locations of tumor in each patient. Voxel-based differences in tumor location between good (overall survival of >17 months) and poor (overall survival of <11 months) survival groups identified in the training cohort were used to classify patients in The Cancer Genome Atlas cohort into 2 brain-location groups, for which clinical features, messenger RNA expression, and copy number changes were compared to elucidate the biologic basis of tumors located in different brain regions.

RESULTS: Tumors in the right occipitotemporal periventricular white matter were significantly associated with poor survival in both training and test cohorts (both, log-rank $P < .05$) and had larger tumor volume compared with tumors in other locations. Tumors in the right peritrial location were associated with hypoxia pathway enrichment and *PDGFRA* amplification, making them potential targets for subgroup-specific therapies.

CONCLUSIONS: Voxel-based location in glioblastoma is associated with patient outcome and may have a potential role for guiding personalized treatment.

ABBREVIATIONS: CEL = contrast-enhancing lesion; GBM = glioblastoma; GSEA = Gene Set Enrichment Analysis; KEGG = Kyoto Encyclopedia of Genes and Genomes; OS = overall survival; SVZ = subventricular zone; TCGA = The Cancer Genome Atlas; TFCE = threshold-free cluster enhancement

Glioblastoma (GBM, World Health Organization grade IV) is the most common primary brain cancer in adults. Despite decades of refinement, however, multimodal therapy of microsurgical resection, radiation, and chemotherapy results in median

survival after diagnosis of only 12–15 months.¹ GBMs are heterogeneous with respect to genetic, molecular, and MR imaging characteristics.^{2–4} Multiscale genomics and imaging analyses have revealed that GBMs with *IDH1* mutations, which have a favorable prognosis,^{5,6} tend to occur in brain regions different from those in which GBMs with wildtype *IDH1* predominate, suggesting a potential prognostic role of tumor location in GBM. Prior imaging studies have also supported a relationship between GBM tumor location and clinical prognosis.^{7,8} Integrated multiscale analysis of MR imaging–based tumor location, patient characteristics, and genomic data may permit classification of patients with GBM

Received May 27, 2015; accepted after revision August 2.

From the Stanford Center for Biomedical Informatics Research and Biomedical Informatics Training Program (T.T.L., D.L.R.), Department of Radiology (T.T.L., L.A.M., W.A.D., K.W.Y., D.L.R.), Stanford Institute for Neuro-Innovation and Translational Neurosciences (A.S.A.), Institute for Stem Cell Biology and Regenerative Medicine (A.S.A.), and Department of Neurosurgery (A.S.A., J.J.L., S.A.R., E.M.W., S.D.C., G.R.H.), Stanford University School of Medicine, Stanford, California; Department of Neurological Surgery (A.F.), University of Washington School of Medicine, Seattle, Washington; and Biomolecular Engineering (J.M.S.), University of California Santa Cruz, Santa Cruz, California.

T.T.L. and D.L.R. conceived and designed the study; G.R.H. and S.D.C. developed and maintained the Stanford GBM imaging database used as the training cohort; T.T.L., A.S.A., L.A.M., W.A.D., J.J.L., S.A.R., A.F., E.M.W., K.W.Y., and S.D.C. acquired imaging data and performed annotations and preprocessing; T.T.L., J.M.S., and D.L.R. analyzed and interpreted the data; T.T.L. and D.L.R. wrote the manuscript; J.M.S., G.R.H., D.L.R., L.A.M., A.S.A., T.T.L., K.W.Y., and A.F. edited the manuscript; and all authors read and approved the manuscript.

Please address correspondence to Daniel L. Rubin, MD, MS, Department of Radiology, 1201 Welch Rd, Stanford, CA 94305; e-mail: dlrubin@stanford.edu

Indicates open access to non-subscribers at www.ajnr.org

Indicates article with supplemental on-line appendix and tables.

Indicates article with supplemental on-line photo.

<http://dx.doi.org/10.3174/ajnr.A4631>

into subgroups with distinct genomic, tumor location, and clinical outcome characteristics.

The complexity and limited scalability of image-feature analysis has deterred inclusion of imaging data in multiscale integrated analysis. Radiogenomic studies that associate molecular features with quantitatively assessed image features describing tumor shape and texture often lack information regarding tumor location, likely due to the challenging and different image-preprocessing techniques required to obtain this information. To date, information about tumor location has predominantly been qualitatively determined by radiologists, who annotate the locations of the tumors in high-level anatomic terms (eg, temporal lobe and so forth). Such qualitative assessment of tumor location can be onerous and may be affected by interobserver variability, lack of reproducibility, and scalability. In addition, qualitative assessment of tumor location has limited spatial granularity and fails to use the full resolution of MR imaging data available at the voxel level. A large-scale analysis of brain tumor image data at the voxel level could provide more anatomic detail compared with conventional qualitative approaches. Voxel-based image analysis linking the MR imaging appearance of GBM to patient survival has previously been undertaken in 1 study,⁹ but the results were not evaluated in an independent validation dataset and the study lacked analysis of imaging correlates with survival and tumor genomics.

The purpose of this study was to use computational imaging informatics methods to identify MR imaging voxel-based tumor location features and to seek associations of these with tumor molecular profiles, patient characteristics, and clinical outcomes. Our goal was to identify subtypes of GBMs on the basis of computationally derived tumor location that provide insight into prognosis and potentially guide more personalized therapy.

MATERIALS AND METHODS

Patient Samples

Gadolinium-based contrast-enhanced T1-weighted preoperative axial MR images of patients diagnosed with GBM and whose overall survival (OS) was known were acquired from 2 independent sources: the Stanford University Medical Center ($n = 253$) and The Cancer Genome Atlas (TCGA, $n = 131$).^{5,10} Institutional review board approval was obtained with informed consent for all patients. We selected the larger cohort for training and the small cohort for testing. The GBM cases in the training cohort were acquired by using 1.5T Signa Excite or Genesis Signa or Signa HDx MRI scanners (GE Healthcare, Milwaukee, Wisconsin) (TE, 8–20 mm; TR, 360–1800 mm) with a section thickness of 2 or 5 mm. The images for the TCGA cohort were collected from 4 institutions by using 1.5T or 3.5T Signa Excite (GE Healthcare), 1.5T Genesis Signa (GE Healthcare), 1.5T Intera (Philips Healthcare, Best, the Netherlands), and 1.5T or 3T Achieva (Philips Healthcare) or 1.5T Magnetom Vision (Siemens, Erlangen, Germany) MRI scanners, respectively (TE, 3–20 mm; TR, 15–3280 mm) with section thicknesses in the range of 1–5 mm, as previously described,¹⁰ and were downloaded from the Cancer Imaging Archive (www.cancerimagingarchive.net).¹¹ Patients were included if preoperative imaging scans and OS information were available. Patient-matched level 3 gene expression and copy number data were downloaded

from the TCGA data portal (<https://tcga-data.nci.nih.gov/tcga/dataAccessMatrix.htm>).

Image-Processing Pipeline to Extract Tumor Locations

We derived voxelwise tumor localization on the basis of a common brain coordinate space for the 2 patient cohorts as described below (Fig 1A). First, an ROI was drawn to delineate the whole tumor, which includes the contrast-enhancing portion of the lesion (CEL) and the central necrosis on each axial section of the T1-weighted images in OsiriX imaging software (<http://www.osirix-viewer.com>), and it was confirmed by a board-certified neuroradiologist (L.A.M.). Similarly, a necrosis ROI in the center of a tumor was defined as the nonenhancing, low-signal-intensity region surrounded by a rim of enhancing tumor region on T1-weighted MR imaging. Tumor volume was computed in OsiriX.¹² An automated image-processing pipeline was then developed to align all T1-weighted imaging volume to a common coordinate space in 3D Slicer (<http://www.slicer.org>) as follows: Briefly, a skull-stripping algorithm was applied to each T1-weighted imaging volume to extract cerebral tissue, followed by affine registration to a 1.0-mm isotropic brain atlas (Montreal Neurological Institute 152) by using a mutual information algorithm with a 12-*df* transformation.^{13,14} The same transform was used to align the ROI volume to the same Montreal Neurological Institute atlas coordinate space. The resulting registered T1-weighted imaging and registered tumor binary ROI volumes were confirmed by consensus of 3 readers (T.T.L., A.S.A., L.A.M.).

Training and Validation Data Cohorts

To identify regions significantly associated with poor survival, we used the Stanford University Medical Center cohort ($n = 253$) for learning and the TCGA cohort ($n = 131$) as an independent validation set (Fig 1B). The training cohort was stratified into poor, medium, and good overall survival groups defined by 2 cutoffs: <11 months and >17 months, which were 3 months below and above the median overall survival of 14 months, respectively (Fig 1B). The middle group was not assessed in the analyses to ensure a clear distinction between good and poor survival. We plotted the tumor locations across each group of patients in the training cohort as frequency heat maps, in which common events of tumor occurrence are shown as “hot” and less frequent events as “cooler” areas (Fig 1B).

Voxels significantly associated with poor survival in classifying the Stanford University Medical Center training cohort were then used to dichotomize patients in the validation TCGA cohort (Fig 1B). Lesions in the validation TCGA cohort having a nonzero number of voxels falling within the poor survival regions were classified as group I lesions. All other lesions were classified as group II lesions. The analysis was implemented in a Matlab script R2012a (MathWorks, Natick, Massachusetts). The survival difference between the 2 groups was evaluated by using the Kaplan-Meier survival analysis implemented in the survival package in R programming language (www.r-project.org).

Statistical Analysis of Voxels Associated with Outcome

To identify voxels significantly associated with poor survival, we applied the threshold-free cluster enhancement (TFCE) method

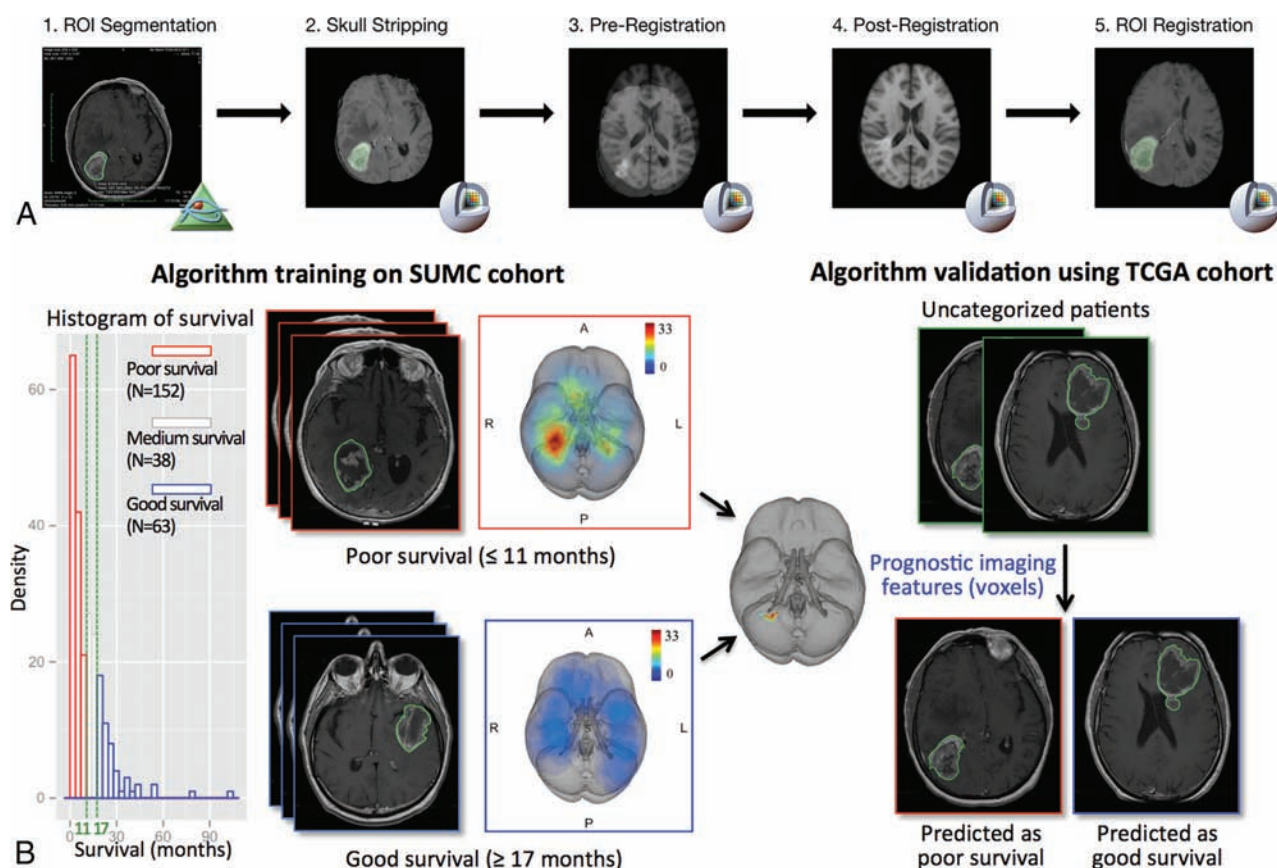


FIG 1. An overview of the image-processing pipeline and model training and validation procedure to identify locations associated with survival. **A**, The image-processing pipeline is applied to both training (Stanford University Medical Center) and validation (TCGA) cohorts. **B**, Algorithm training identifies anatomic regions associated with survival, which is validated in the TCGA cohort. The training algorithm using the threshold-free cluster enhancement method takes as the input group labels dichotomized by survival outcome and the superimposed tumor heat map of the Stanford University Medical Center patient cohort analyzed in the image-processing pipeline; the pipeline outputs anatomic regions significantly associated with the 2 survival groups, which are used to classify the TCGA validation set into a poor survival group and a good survival group on the basis of tumor regions present or absent in the prognostic region.

with parameters optimized for 3D imaging volume implemented in FSL, Version 5.05 (<http://www.fmrib.ox.ac.uk/fsl/>), on a Linux system comparing the 2 clinical phenotypes (poor-versus-good survival).¹⁵ TFCE takes as input a cohort of patients' tumor ROI volumes and their binary survival group labels stratified by survival and computes a *P* value for each voxel associated with each group. A total of 100 permutations were performed to correct for multiple comparisons and control for a family-wise error with a false discovery rate < .05. To evaluate the robustness of the results, we explored 286 pairs of lower and upper cutoffs in the overall survival at 3–15 months and 15–36 months to determine good and poor survival groups, respectively. The 286 pairs of cutoffs included the survival cutoffs defined in Ellingson et al.⁹ Each combination of survival cutoffs was used to define a poor survival group and a good survival group and was run for the prognostic region sensitivity analysis (On-line Appendix).

Molecular and Genetic Analysis

The Significance Analysis of Microarrays method¹⁶ was run on the microarray expression of the 2 identified patient groups (group I: tumors in the right peritrial location versus group II: tumors not in the right peritrial location) to compute a test sta-

tistic for each gene, measuring the strength of association with the location groups to create a ranked list of all genes. The preranked gene list and previously curated gene set data base¹⁷ were used as the input of the Gene Set Enrichment Analysis (GSEA; <http://www.broad.mit.edu/gsea>) to compute molecular enrichment between the 2 GBM location groups. Top enriched gene sets with a family-wise error rate *P* value < .05 were reported and further confirmed by conducting the single-sample GSEA on the related pathway from the Kyoto Encyclopedia of Genes and Genomes (KEGG) data base,¹⁸ as previously described.⁴ The Significance Analysis of Microarrays was also run on log2 copy number data between the 2 location groups to identify amplified genes in each image location group by using the samr package in R (<http://statweb.stanford.edu/~tibs/SAM/>).¹⁶

Known Clinical Variables

Log-rank tests were used for categoric GBM clinical variables, including age younger than 64 years, sex, extent of surgical resection (biopsy, subtotal resection, or gross total resection) (available for 24 patients), and categoric tumor volume groups (large: top 30%; intermediate: middle 40%; and small: bottom 30%). The survival analysis was performed by using the sur-

Table 1: Summary of clinical variables in the training cohort

	Survival Groups		
	Poor (OS ≤ 11 mo)	Medium (11 < OS < 17 mo)	Good (OS ≥ 17 mo)
Total No.	152	38	63
Median age (yr)	69.0	57.2	59.5
% Male	61.2	60.5	57.1
Median survival (mo)	4.1	14.1	21.2
Mean survival (mo)	4.8	14.0	26.3
Mean CEL volume (cm ³)	34.1	34.0	28.9
STR/GTR/biopsy only (No.)	53/13/86	17/8/13	17/36/10

Note:—STR indicates subtotal resection; GTR, gross total resection.

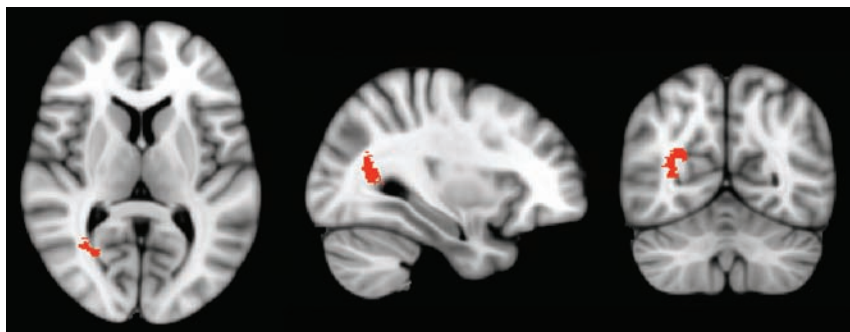


FIG 2. Axial, sagittal, and coronal section views of the region associated with poor survival in the training cohort (false discovery rate, $P < .05$). The cluster of voxels associated with poor survival was localized in the occipitotemporal periventricular white matter in the right hemisphere (right peritrial).

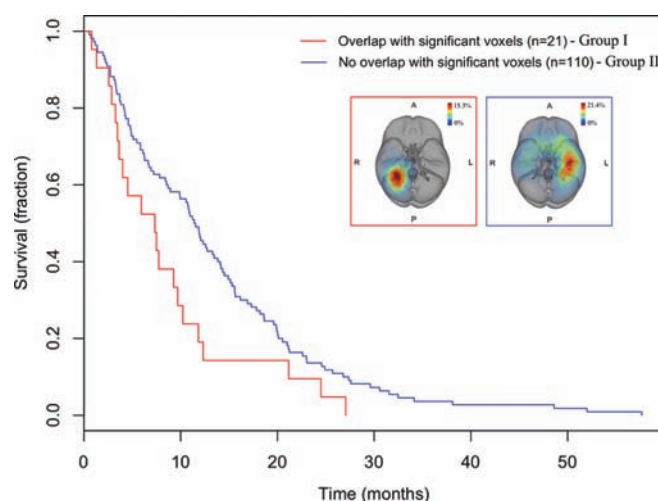


FIG 3. Kaplan-Meier survival curves of patients with GBMs depict decreased overall survival in TCGA patients with an overlap (group I) versus nonoverlap (group II) with the voxels significantly associated with survival identified from the training cohort (log-rank test, $P = .034$).

vival package in R programming language. Significant variables in the univariate models ($P < .05$) were included in the multivariate Cox proportional hazards regression model. The percentage of necrosis volume in the whole-tumor volume was available for 91 patients in the TCGA cohort.

RESULTS

Clinical Characteristics of the Training Cohort

An overview of image analysis and prognostic model construction is summarized in Fig 1. Clinical characteristics of the 3 survival groups in the training cohort are summarized in Table

1, and known clinical prognostic markers were confirmed by univariate analysis. Younger age was associated with better survival (age younger than 64 years, OS = 13.7 versus age older than or equal to 64 years, 9.5 months, log-rank $P < .002$). More extensive surgical resection was associated with better overall survival (log-rank $P = 0$), with gross total resection associated with longest average overall survival (22.5 months) compared with those patients with a subtotal resection (11.1 months) or those undergoing biopsy only (6.5 months). In contrast, tumor volume was not significantly associated with survival (hazard ratio = 1, $P = .58$).

Right Deep White Matter Tumors Are Associated with Poor Prognosis

The heat maps showing the frequency of tumor occurrence revealed that the poor and good survival groups had distinct imaging location phenotypic trends: The poor survival group had tumors in the right deep periventricular white matter region; in contrast, tumors associated with good survival occurred throughout the brains of patients without any particular anatomic region with high tumor frequency (Fig 1B). TFCE analysis further confirmed that the voxels associated with poor prognosis (false discovery rate-adjusted $P < .05$) were in the occipitotemporal periventricular white matter in the right hemisphere (“right peritrial”) (Fig 2 and On-line Table 1), but no voxels were found to be significantly associated with tumors in the good survival group. Robustness analysis of 286 different pairs of lower and upper survival cutoffs at 3–15 months and 15–36 months showed that the results were largely invariant to the choice of survival cutoffs; the voxels

associated with poor prognosis consistently occurred in the same region of the brain (On-line Figs 1 and 2). Among these 286 pairs included the survival cutoffs defined by Ellingson et al,⁹ no voxels were found to be significantly associated with survival, possibly a result of the small number of patients in the good survival group ($n = 8$).

Prognostic Region Validated in the TCGA Dataset

In the training cohort, tumors in the right peritrial location were significantly associated with poor survival (log-rank $P = .012$). We then assessed whether this association generalized to

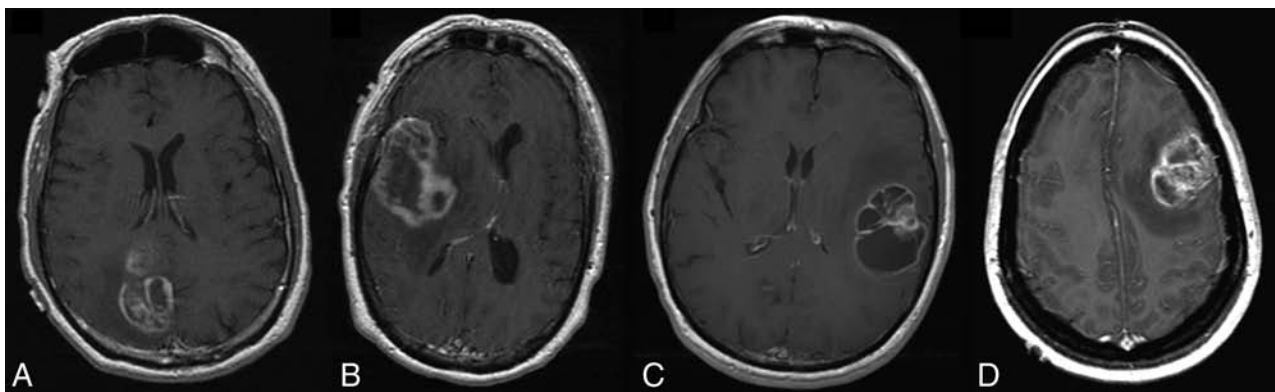


FIG 4. Axial postcontrast T1-weighted images of 4 patients from group II. A, A 69-year-old man with a right parietal GBM and an overall survival of 27 months. B, A 49-year-old man with a right temporal GBM and an overall survival of 25 months. C, A 63-year-old man with a left temporal GBM and an overall survival of 21 months. D, A 36-year-old woman with a left frontal GBM, an overall survival of 6 months, and the smallest tumor volume in the group of intermediate tumors.

Table 2: Univariate and multivariate Cox survival analysis of clinical variables

	Univariate Cox		Multivariate Cox	
	HR (95% CI)	P Value	HR (95% CI)	P Value
TCGA test cohort ^a				
Age younger than 64 yr	0.19 (0.26–0.55)	4.1e–7 ^b	0.36 (0.24–0.53)	3.7e–7 ^b
Male sex	1.05 (0.73–1.50)	.79	–	–
CEL tumor volume (cm ³)				
Large	1.68 (1.10–2.54)	.015 ^b	1.80 (1.18–2.75)	.0064 ^b
Intermediate	–	–	–	–
Small	0.90 (0.58–1.37)	.62	1.11 (0.71–1.71)	.65
Right laterality	0.927 (0.65–1.32)	.67	–	–
STR	2.52 (0.73–8.68)	.14	–	–
Tumor location = right peritrial location	1.66 (1.03–2.67)	.036 ^b	2.0 (1.01–2.64)	.045 ^b
Restricted set of intermediate and large tumors ^c				
Age younger than 64 yr	0.19 (0.26–0.55)	4.1e–7	0.46 (0.30–0.72)	.00062
Tumor location = right peritrial location	1.84 (1.10–3.08)	.019	1.87 (1.11–3.15)	.018

Note:—HR indicates hazard ratio; STR, subtotal resection.

^a Age, CEL tumor volume, and tumor location were independently significant in multivariate analysis (overall $P < 3.52e-8$). Surgical resection is subtotal resection or gross total resection, available for 24 cases in the TCGA test cohort.

^b P value $< .05$, indicating the variable is significant.

^c Tumor location remained significant in Cox analysis performed on the restricted set of intermediate and large tumors.

an independent validation set from TCGA samples. Patients with GBM of the TCGA cohort were dichotomized into 2 groups on the basis of whether their tumors overlapped the prognostic right peritrial region. The group with tumors overlapping the right peritrial location (group I) had significantly shorter overall survival than did those with tumors occurring in other locations (group II) (log-rank $P = .034$) (Fig 3). Examples of GBMs in group II are shown in Fig 4.

As in the training dataset, univariate survival analysis showed that age younger than 64 years (log-rank $P < 5e-7$) was a significant prognostic factor in the test set, whereas sex (log-rank $P = .79$) and tumor laterality (left or right hemisphere) (log-rank $P = .67$) were not significant in TCGA. We found that the surgical resection level, available for a small number of patients ($n = 24/131$), was not significantly associated with survival. The result may be due to the small number of patients available; thus, it was excluded in the multivariate analysis. Cox analysis on tumor volume categorized into 3 groups showed that large tumor volume was associated with poor survival (hazard ratio = 1.68, $P = .015$).

The right peritrial tumor location was significantly associated with poor survival, independent of age and tumor volume in the TCGA cohort ($P = .045$) (Table 2).

The mean tumor volume in group I was 1.8 times the size of that in group II in the training cohort (Wilcoxon test, $P < 1.5e-6$) and 1.4 times that in the test cohort (Wilcoxon $P < .01$) (On-line Fig 3). However, the percentage of necrosis in the whole tumor was not significantly different between the 2 groups in the test cohort (Wilcoxon $P = .41$). The number of patients with GBMs in each hemisphere was about the same in both cohorts (124 left versus 118 right in the training cohort, and 70 left versus 61 right in the TCGA cohort), indicating the hotspot (highest frequency) of tumor occurrence found in the right peritrial location was associated with a larger

volume of the tumors in this region. Moreover, tumors in the right hemisphere were 1.5 and 1.1 times larger than those in the left hemisphere in the training (Wilcoxon $P < .0002$) and the test ($P = .42$) cohorts, respectively, but tumor incidence in the right hemisphere did not confer a worse survival outcome in either cohort (both, log-rank $P > .05$), suggesting the specificity of the tumor localization being associated with prognosis.

To separate the effects of tumor volume and the right peritrial tumor location in predicting prognosis, we examined whether the right peritrial location still predicted worse prognosis when restricting the analysis to comparable tumor sizes. Because the right peritrial location is more relevant to larger tumors and to increase the statistical power of the analysis, we excluded small tumors ($n = 38$), combining the intermediate and large tumors ($n = 93$). When restricted to the combined subset of intermediate and large tumors, the right peritrial location was significantly associated with prognosis (hazard ratio = 1.84, log-rank $P = .019$; Table 2). Intermediate-sized tumors may actually be more comparable in size with large tumors than with small tumors (Fig 4D).

These results support tumor location contributing to clinical outcome, even after accounting for tumor size.

Hypoxia Pathway Enrichment and Stem Cell Marker Amplification in Group I

To identify significant transcriptomic alterations at the pathway level, the GSEA gene expression analysis revealed that 11 of the 37 significantly enriched pathways (family-wise error rate $P < .05$) in group I were hypoxia and *HIF1A* pathways (On-line Table 2). Single-sample GSEA, which generates a gene set enrichment score for each sample, further validated the hypoxia pathway being enriched in group I (Wilcoxon P value = 0.0072), compared with group II (On-line Fig 4). We did not find a significant association between the gene expression-based subtypes previously identified and the location subgroups (On-line Table 3).

Significance Analysis of Microarrays of log2 copy number data showed that several genes involved in stem cell (*CHIC2*, *KIT*, *PDGFRA*) and neural cell development (*GSX2*) (all false discovery rate $q < 0.05$) were significantly amplified in group I GBMs, compared with group II GBMs (On-line Table 4).^{19–22} The Fisher exact test by using discrete copy number alteration confirmed that *PDGFRA* ($P = .023$), *CHIC2* ($P = .016$), *GSX2* ($P = .025$), and *KIT* ($P = .025$) genes were significantly amplified in group I tumors (On-line Tables 5–9). Most interesting, all 4 genes (*KIT* and *PDGFRA* encoding receptor tyrosine kinases, *GSX2*, and *CHIC2*) are colocalized on human chromosome band 4q12.²³ Other genes on the chromosome 4q12 (*KDR*, *LNX1*, *REST*) were also tested but were not significantly amplified in group I tumors.

To further tease out the confounding effect of tumor size from tumor location contributing to molecular alterations, we found that tumor volume was not significantly associated with *PDGFRA* amplification (Wilcoxon test, $P = .12$) or *HIF* overexpression (Spearman correlation coefficient = -0.048 , $P = .62$). Single-sample GSEA confirmed significant upregulation of the hypoxia pathway in right peritrial tumors in intermediate-sized tumors only (Wilcoxon $P = .015$) and in the combined subset of intermediate and large tumors (Wilcoxon $P = .015$), respectively. The Fisher exact test by using discrete copy number data showed that the correlation between *PDGFRA* amplification and the right peritrial tumor location is significant in intermediate-sized tumors (Fisher exact test, $P = .018$, $n = 53$) and in the combined set of intermediate and large-sized tumors (Fisher exact test, 2-tailed $P = .035$; $n = 93$) (On-line Tables 5–9). These results provide further evidence that the genomic events are more associated with location than tumor size.

DISCUSSION

We have developed and applied an automated computational image-analysis pipeline that extracted quantitative tumor location information from MR images by aligning images from 384 cases of GBM to a common stereotactic space at a voxel level of resolution (Fig 1A). This allowed a more granular and quantitative characterization of tumor location than the predominant approach in prior work using qualitative assessment of anatomic location in general terms such as lobes and white matter. Using our voxel-based computational approach to studying tumor location in GBM, we have shown that a subgroup of GBMs localized

in the occipitotemporal periventricular white matter of the right hemisphere (right peritrial) is associated with poor survival. We also showed that GBM tumors located in this region are characterized by large volume and a distinct molecular-alteration profile comprising hypoxia pathway enrichment and amplification of stem cell markers.

In related work, Ellingson et al⁹ computed the stereospecific frequency of tumor occurrence. Our work differs from that of Ellingson et al in a number of ways. First, the survival cutoffs for defining good and poor survival in Ellingson et al were 12 and 36 months, whereas ours were 11 and 17 months. Most patients with GBM have a poor prognosis, with a 3-year survival rate of 3%–5%.²⁴ We performed survival analysis by using the patient groups produced by the cutoffs of Ellingson et al and found that no location voxels were significantly associated with survival (On-line Fig 2); this result is possibly due to the small proportion of patients in the good survival group ($n = 8$). Although it is interesting to study long-term survivors ($OS > 36$ months), the good survival group we defined may be more relevant for GBM clinical treatment stratification.

A second difference between our work and that of Ellingson et al⁹ is that in contrast to an older voxelwise-based method they used for identifying tumor locations, our computational method applied a threshold-free cluster enhancement technique.¹⁵ The TFCE method provides better sensitivity and more interpretable output through enhancing voxel connectivity in a neighborhood than traditional voxel-based methods. A third difference between our work and that of Ellingson et al is that they reported results from a single cohort, whereas in our analysis, we trained on data from 1 institution and validated our results by using an independent public dataset consisting of data from multiple institutions (TCGA). A fourth difference is that unlike the prior work of Ellingson et al, we performed downstream molecular analysis, which allowed us to gain biologic insight into the GBM location associated with poor prognosis. Finally, Ellingson et al showed that tumor location in the right temporal lobe was generally more likely to be associated with shorter than with longer survival. Our analysis provides higher anatomic specificity by pinpointing a small region in the right peritrial deep white matter that appears to be associated with poor prognosis (On-line Table 1), consistent with previous qualitative analyses showing the relationship between poor survival and invasion of tumor cells into adjacent deep white matter tracts and the ependymal region.^{7,8}

The association of invasive clinical phenotypes, location, and poor survival in the right peritrial location may relate to underlying neuroanatomy and tumor neurobiology. The relationship of tumor localization in the right hemisphere—rather than bilaterally—to survival may reflect differences in functional neuroanatomy. The eloquent brain regions, critical for language, motor, or sensory functions, are commonly found in the left hemisphere for most right-handed individuals.²⁵ The fact that the right peritrial location is associated with poor prognosis may reflect a more delayed clinical presentation due to lack of eloquent functions in this region. This hypothesis is further supported by our observation that GBMs in the right hemisphere have larger CEL volume compared with those in the left hemisphere. Once tumors have grown larger, they are likely to have more extensive infiltration

and tend to be more difficult to resect, which may confer worse prognosis.²⁶ The poorer prognosis for tumors occurring in the right peritrial white matter rather than the entire right cerebral hemisphere may reflect differences in tumor neurobiology. This finding concurs with prior reports of worse prognosis for tumors of the subventricular zone (SVZ) deep white matter (adjacent to the right peritrial location) that were based on qualitative assessment of tumor location.^{7,8} These studies have suggested that the SVZ region along the wall of the lateral ventricle, which contains neural stem cells, may be a niche environment conducive to the origin and/or development of primitive, aggressive glial tumors.^{7,9}

Furthermore, our molecular profiling comparing the 2 location groups of the TCGA cohort demonstrated that *PDGFRA* is more likely to be amplified in group I. This finding is corroborated by previous reports that correlated glioma formation with increased expression of *PDGFRA* in neural stem cells of the SVZ.^{3,20} Other amplified genes (*KIT* and *CHIC2*) on the same chromosome 4q12 locus were also enriched in stem cell functions (On-line Tables 4–9). Thus, our results support the possibility that tumor neural stem cells may arise from the lateral ventricle of the SVZ region. Future work is needed to test this hypothesis.

Enrichment of the hypoxia pathway in group I is consistent with results of other studies that have shown that neural stem cells are maintained in a hypoxic niche.^{27,28} We also found significantly larger contrast-enhancing volume ($P = .004$) of the right peritrial tumors relative to those without right peritrial involvement, potentially reflecting increased vascularity associated with elevated proangiogenic factors that are known to be inducible by hypoxia.²⁹ Prior radiogenomic analysis has also shown that high contrast enhancement is associated with high expression of hypoxia-related genes.³⁰ Notably, the percentage of central necrosis of the whole tumor volume in group I was not greater than that in group II ($P = .41$); thus, the enrichment in the hypoxia pathway was not a result of greater central necrosis.

The outcome and differential molecular analyses performed on a subgroup of tumors with comparable sizes showed that the right peritrial tumors maintained significant associations with poor prognosis (log-rank $P = .019$), with *HIF1A* and hypoxia pathway enrichment (Wilcoxon $P = .015$), and with *PDGFRA* amplification (Wilcoxon $P = .035$), independent of tumor volume. These results further imply that the poor prognosis of tumors may result from the stem cell niche in the right peritrial region enriched for *HIF1A*/hypoxia overexpression and *PDGFRA* amplification,³¹ rather than from the proliferative potential associated with larger tumor volume.

GBM is known to have extensive genetic heterogeneity.^{32,33} However, intratumoral heterogeneity was not directly addressed in this study because the genetic material was obtained from a single region of the tumor. Another limitation of our current study is that it lacked information on the precise biopsy locations from which the gene expression samples were taken (this information was not available to us). Validation by using such data, if available in the future, would strengthen our finding that the right peritrial location is correlated with stem cell marker amplification and hypoxia enrichment.

Our work advances knowledge in that by using a computa-

tional pipeline with imaging informatics and radiogenomic analysis, we demonstrate that the anatomic location of GBM is a key prognostic variable,³⁴ specifically for GBMs located in the right peritrial white matter. We also show that certain molecular alterations may be linked to specific tumor locations. The results from our work could help improve characterization of GBM subtypes and potentially guide more personalized treatment decisions. Our strategy for quantitative assessment of tumor locations, if applied to other anatomic location-specific diseases, may similarly identify connections among disease location, molecular signature, and patient outcome.

CONCLUSIONS

We conclude that voxel-based location in GBM is associated with patient outcome. Tumor location in the right occipitotemporal peritrial white matter is predictive of survival, independent of other known prognostic clinical variables, such as patient age and tumor volume. This result was further validated in an independent patient cohort. Using GBM anatomic location as the response variable, we were able to identify genomic enrichment associated with the imaging phenotype.

ACKNOWLEDGMENTS

We thank Drs Sanjiv Sam Gambhir, Jarrett Rosenberg, and Sofie Salama for helpful comments and discussion. We also gratefully acknowledge support for this study from Craig and Kimberly Darian and Carol Bade to Dr Steven Chang. We also appreciate Drs Rajan Jain and Laila Poisson for providing us the surgical resection information for the 24 TCGA patients from the Henry Ford Hospital.

Disclosures: Tiffany T. Liu—RELATED: Grant: National Institutes of Health (U01CA142555).* Joshua M. Stuart—RELATED: Grant: Agilent Fellowship for graduate student research in brain image-genomics.* Daniel L. Rubin—RELATED: Grant: National Institutes of Health.* *Money paid to the institution.

REFERENCES

- Wen PY, Kesari S. **Malignant gliomas in adults.** *N Engl J Med* 2008; 359:492–507 CrossRef Medline
- Larjavaara S, Mäntylä R, Salminen T, et al. **Incidence of gliomas by anatomic location.** *Neuro Oncol* 2007;9:319–25 CrossRef Medline
- Dunn GP, Rinne ML, Wykosky J, et al. **Emerging insights into the molecular and cellular basis of glioblastoma.** *Genes Dev* 2012;26: 756–84 CrossRef Medline
- Verhaak RG, Hoadley KA, Purdom E, et al; Cancer Genome Atlas Research Network. **Integrated genomic analysis identifies clinically relevant subtypes of glioblastoma characterized by abnormalities in *PDGFRA*, *IDH1*, *EGFR*, and *NF1*.** *Cancer Cell* 2010;17:98–110 CrossRef Medline
- Brennan CW, Verhaak RG, McKenna A, et al. **The somatic genomic landscape of glioblastoma.** *Cell* 2013;155:462–77 CrossRef Medline
- Yan H, Parsons DW, Jin G, et al. ***IDH1* and *IDH2* mutations in gliomas.** *N Engl J Med* 2009;360:765–73 CrossRef Medline
- Lim DA, Cha S, Mayo MC, et al. **Relationship of glioblastoma multiforme to neural stem cell regions predicts invasive and multifocal tumor phenotype.** *Neuro Oncol* 2007;9:424–29 CrossRef Medline
- Colen RR, Vangel M, Wang J, et al; TCGA Glioma Phenotype Research Group. **Imaging genomic mapping of an invasive MRI phenotype predicts patient outcome and metabolic dysfunction: a TCGA glioma phenotype research group project.** *BMC Med Genomics* 2014;7:30 CrossRef Medline
- Ellingson BM, Lai A, Harris RJ, et al. **Probabilistic radiographic atlas**

- of glioblastoma phenotypes. *AJNR Am J Neuroradiol* 2013;34:533–40 CrossRef Medline
10. Gutman DA, Cooper LA, Hwang SN, et al. **MR imaging predictors of molecular profile and survival: multi-institutional study of the TCGA glioblastoma data set.** *Radiology* 2013;267:560–69 CrossRef Medline
 11. Clark K, Vendt B, Smith K, et al. **The Cancer Imaging Archive (TCIA): maintaining and operating a public information repository.** *J Digit Imaging* 2013;26:1045–57 CrossRef Medline
 12. Rosset A, Spadola L, Ratib O. **OsiriX: an open-source software for navigating in multidimensional DICOM images.** *J Digit Imaging* 2004;17:205–16 CrossRef Medline
 13. Johnson H, Harris G, Williams K. **BRAINSFit: mutual information registrations of whole-brain 3D images, using the Insight Toolkit.** *Insight Journal* 2007. <http://hdl.handle.net/1926/1291>. Accessed December 15, 2015
 14. Fedorov A, Beichel R, Kalpathy-Cramer J, et al. **3D Slicer as an image computing platform for the Quantitative Imaging Network.** *Magn Reson Imaging* 2012;30:1323–41 CrossRef Medline
 15. Smith SM, Nichols TE. **Threshold-free cluster enhancement: addressing problems of smoothing, threshold dependence and localisation in cluster inference.** *Neuroimage* 2009;44:83–98 CrossRef Medline
 16. Tusher VG, Tibshirani R, Chu G. **Significance analysis of microarrays applied to the ionizing radiation response.** *Proc Natl Acad Sci U S A* 2001;98:5116–21 CrossRef Medline
 17. Subramanian A, Tamayo P, Mootha VK, et al. **Gene set enrichment analysis: a knowledge-based approach for interpreting genome-wide expression profiles.** *Proc Natl Acad Sci U S A* 2005;102:15545–50 CrossRef Medline
 18. Kanehisa M, Goto S. **KEGG: Kyoto encyclopedia of genes and genomes.** *Nucleic Acids Res* 2000;28:27–30 CrossRef Medline
 19. Jörnsten R, Abenius T, Kling T, et al. **Network modeling of the transcriptional effects of copy number aberrations in glioblastoma.** *Mol Syst Biol* 2011;7:486 CrossRef Medline
 20. Jackson EL, Garcia-Verdugo JM, Gil-Perotin S, et al. **PDGFR alpha-positive B cells are neural stem cells in the adult SVZ that form glioma-like growths in response to increased PDGF signaling.** *Neuron* 2006;51:187–99 CrossRef Medline
 21. Puputti M, Tynninen O, Sihto H, et al. **Amplification of KIT, PDGFRA, VEGFR2, and EGFR in gliomas.** *Mol Cancer Res* 2006;4:927–34 CrossRef Medline
 22. Méndez-Gómez HR, Vicario-Abejón C. **The homeobox gene *Gsx2* regulates the self-renewal and differentiation of neural stem cells and the cell fate of postnatal progenitors.** *PLoS One* 2012;7:e29799 CrossRef Medline
 23. Blom T, Roselli A, Tanner M, et al. **Mutation and copy number analysis of *LNK1* and *Numbl* in nervous system tumors.** *Cancer Genet Cytogenet* 2008;186:103–09 CrossRef Medline
 24. Krex D, Klink B, Hartmann C, et al; German Glioma Network. **Long-term survival with glioblastoma multiforme.** *Brain* 2007;130(pt 10):2596–606 CrossRef Medline
 25. Kim SS, McCutcheon IE, Suki D, et al. **Awake craniotomy for brain tumors near eloquent cortex: correlation of intraoperative cortical mapping with neurological outcomes in 309 consecutive patients.** *Neurosurgery* 2009;64:836–45; discussion 345–46 CrossRef Medline
 26. Sanai N, Berger MS. **Glioma extent of resection and its impact on patient outcome.** *Neurosurgery* 2008;62:753–64; discussion 264–66 CrossRef Medline
 27. Heddeston JM, Li Z, McLendon RE, et al. **The hypoxic microenvironment maintains glioblastoma stem cells and promotes reprogramming towards a cancer stem cell phenotype.** *Cell Cycle* 2009;8:3274–84 CrossRef Medline
 28. Li Z, Bao S, Wu Q, et al. **Hypoxia-inducible factors regulate tumorigenic capacity of glioma stem cells.** *Cancer Cell* 2009;15:501–13 CrossRef Medline
 29. Kaur B, Khwaja FW, Severson EA, et al. **Hypoxia and the hypoxia-inducible-factor pathway in glioma growth and angiogenesis.** *Neuro Oncol* 2005;7:134–53 CrossRef Medline
 30. Diehn M, Nardini C, Wang DS, et al. **Identification of noninvasive imaging surrogates for brain tumor gene-expression modules.** *Proc Natl Acad Sci U S A* 2008;105:5213–18 CrossRef Medline
 31. Li L, Candelario KM, Thomas K, et al. **Hypoxia inducible factor-1 α (HIF-1 α) is required for neural stem cell maintenance and vascular stability in the adult mouse SVZ.** *J Neurosci* 2014;34:16713–19 CrossRef Medline
 32. Snuderl M, Fazlollahi L, Le LP, et al. **Mosaic amplification of multiple receptor tyrosine kinase genes in glioblastoma.** *Cancer Cell* 2011;20:810–17 CrossRef Medline
 33. Sottoriva A, Spiteri I, Piccirillo SG, et al. **Intratumor heterogeneity in human glioblastoma reflects cancer evolutionary dynamics.** *Proc Natl Acad Sci U S A* 2013;110:4009–14 CrossRef Medline
 34. Sturm D, Witt H, Hovestadt V, et al. **Hotspot mutations in *H3F3A* and *IDH1* define distinct epigenetic and biological subgroups of glioblastoma.** *Cancer Cell* 2012;22:425–37 CrossRef Medline

Radiologic Features and Expression of Vascular Endothelial Growth Factor Stratify Survival Outcomes in Patients with Glioblastoma

K. Wang, Y.Y. Wang, J.F. Wang, J. Ma, T. Jiang, and J.P. Dai



ABSTRACT

BACKGROUND AND PURPOSE: Vascular endothelial growth factor is a well-known tumor-specific biomarker that mediates angiogenesis in glioblastoma via hypoxia-dependent mechanisms. Our aim was to investigate the correlation of clinical characteristics, radiologic features, and vascular endothelial growth factor expression with survival outcomes in patients with glioblastoma.

MATERIALS AND METHODS: Clinical and radiologic data of 185 patients with glioblastoma were retrospectively reviewed. Vascular endothelial growth factor expression was examined in all cases via immunohistochemical analysis. Univariate and multivariate analyses were performed to identify the prognostic factors of progression-free survival and overall survival.

RESULTS: Vascular endothelial growth factor expression levels were associated with the presence of ringlike tumor contrast enhancement. Age, preoperative Karnofsky Performance Scale score, gross total resection, and adjuvant therapy were identified as prognostic factors. Among patients undergoing gross total resection, high vascular endothelial growth factor expression was associated with longer progression-free survival ($P = .011$) and overall survival ($P = .039$). For tumors with high vascular endothelial growth factor expression, both the non-contrast-enhancing tumor component and peritumoral edema could stratify overall survival ($P = .039$ and $.018$, respectively), while only the presence of the non-contrast-enhancing tumor component predicted a longer progression-free survival ($P = .024$).

CONCLUSIONS: Vascular endothelial growth factor expression level was not an independent prognostic factor in glioblastoma. However, high vascular endothelial growth factor expression might predict longer survival in patients in whom gross total resection was achieved. Furthermore, peritumoral edema and the non-contrast-enhancing tumor component could stratify survival outcomes in patients with high vascular endothelial growth factor tumors.

ABBREVIATIONS: GTR = gross total resection; <GTR = tumor residual; HR = hazard ratio; KPS = Karnofsky performance status scale; nCET = non-contrast-enhancing tumor component; PFS = progression-free survival; OS = overall survival; VEGF = vascular endothelial growth factor

Glioblastoma is a rapidly progressive and highly angiogenic tumor. The outcome of patients with glioblastoma is poor, owing to ineffective therapies. Even when surgical resection followed by adjuvant therapy is provided, the median progression-

free survival (PFS) of these patients is only 6.9 months, and the median overall survival (OS) is 14.7 months.¹ Clinical characteristics, including patient age, Karnofsky Performance Scale (KPS), and the extent of resection, have been investigated previously as prognostic factors for glioblastoma, while the prognostic role of radiologic features and potentially associated tumor-specific biomarkers remains unclear.

Vascular endothelial growth factor (VEGF) is a well-known tumor-specific biomarker that mediates angiogenesis in glioblastoma via hypoxia-dependent mechanisms, contributes to the generation of blood vessels with distinctive features, and promotes vascular permeability, resulting in the observation of the radiologic contrast enhancement in tumors, which should

Received May 30, 2015; accepted after revision August 19.

From the Departments of Neuroradiology (K.W., J.M., J.P.D.) and Neurosurgery (Y.Y.W., J.F.W., T.J.), Beijing Tiantan Hospital, and Beijing Neurosurgical Institute (Y.Y.W., T.J., J.P.D.), Capital Medical University, Beijing, China; and Beijing Institute for Brain Disorders (T.J.), Brain Tumor Center, Beijing, China.

This work was supported by the National High Technology Research and Development Program (No.2011CB707804 and No.2015CB755500) and the National Natural Science Foundation of China (No. 81271541).

Kai Wang and Yinyan Wang contributed equally to this study.

The authors declare that they have no conflict of interest.

Please address correspondence to Jianping Dai, MD, PhD, Beijing Tiantan Hospital, Capital Medical University, 6, Tiantanxili, Beijing, 100050, China; e-mail: djpbj@hotmail.com; and Tao Jiang, MD, PhD, Beijing Neurosurgical Institute, Capital Medical University, 6, Tiantanxili, Beijing, 100050, China; e-mail: taojiang1964@163.com; @taojiang1964

Indicates open access to non-subscribers at www.ajnr.org

Indicates article with supplemental on-line table.

<http://dx.doi.org/10.3174/ajnr.A4567>

otherwise be prevented by an intact blood-brain barrier.² The prognostic role of VEGF expression has been investigated in different types of malignancies, such as breast cancer,³ gastric track cancer,⁴⁻⁶ and lung cancer.^{7,8} The levels of VEGF expression were found to be correlated with microvessel attenuation in human glioma.⁹ Moreover, the association of VEGF expression with survival outcome in patients with malignant tumor has been suggested.^{10,11} In a subsequent study, radiologic features (eg, edema) were introduced as a factor in the correlation between VEGF expression and prognostic outcome. This suggests that VEGF expression is predictive of survival in tumors with little or no edema.¹²

Further understanding of the role played by VEGF expression in predicting the survival of patients with glioblastoma is of clinical significance and is currently needed. Therefore, the present study aimed to identify the potential association of clinical and radiologic features and VEGF expression with survival outcome in patients with glioblastoma.

MATERIALS AND METHODS

Patients

The medical records of 185 adult patients with glioblastoma who underwent surgical treatment at our institution between January 2007 and November 2008 were retrospectively reviewed. Inclusion criteria were as follows: 1) 18 years of age or older; 2) availability of presurgical MR imaging scans, including T1-weighted, T2-weighted, and postcontrast T1-weighted images; 3) pathologically confirmed glioblastoma; 4) no previous craniotomy or stereotactic biopsy; and 5) no previous diagnosis of any brain tumor. The histopathologic diagnosis of tumors was confirmed by 2 independent neuropathologists. This study was approved by our institutional review board, and written consent was obtained from all enrolled patients.

Treatment

In our study, "gross total resection" (GTR) was defined as no visible contrast-enhancing tumor on postoperative MR images obtained within 72 hours after surgery, according to an assessment comparing pre- and postoperative MR images.¹³ All cases in which GTR was not achieved were considered as having tumor residual (<GTR). Patients with severe edema who required corticosteroid treatment to alleviate intracranial hypertension were excluded to avoid a possible influence on radiologic evaluation results. The adjuvant treatment included radiation therapy or chemotherapy alone or concomitant temozolomide and fractionated radiation therapy followed by up to 6 cycles of adjuvant temozolomide.¹

Image Acquisition

MR imaging was performed on a Trio 3T scanner (Siemens, Erlangen, Germany). It included axial T1-weighted (TR, 450 ms; TE, 15 ms; section thickness, 5 mm), T2-weighted fast spin-echo (TR, 6000 ms; TE, 140 ms; section thickness, 5 mm), and contrast-enhanced (gadopentetate dimeglumine, DTPA-Gd injection; Beilu Pharmaceutical Co., Beijing, China; 0.1 mmol/kg) axial T1-weighted images (TR, 450 ms; TE, 15 ms; section thickness, 5 mm). Postcontrast images were acquired immediately following

injection of contrast agent. Postoperative MR images for determining the extent of resection were obtained within 72 hours after surgery.¹⁴

Identification of Imaging Features

Radiologic features of the tumor were assessed by 2 experienced neuroradiologists (Q. Chen and X. Chen, who have 14 and 12 years of experience, respectively, in brain disease diagnosis by using MR imaging) blinded to the patient clinical information. In cases in which imaging features identified by the 2 neuroradiologists were inconsistent, a third senior neuroradiologist (J.M., with 25 years of experience in brain disease diagnosis) examined the images for a final assessment. The patterns of tumor contrast enhancement were identified on the basis of the size and morphologic features of the largest enhanced area on contrast-enhanced MR images regardless of whether it was single- or multifocal and were categorized as ringlike or non-ringlike-enhanced patterns. Tumors displaying cystic necrosis with peripheral enhancement were defined by an enhanced ringlike pattern; tumors not displaying this pattern were classified as having non-ringlike-enhanced patterns. Limited (or no) edema (−) was defined as edema extending ≤1 cm from the margin of the tumor based on T2-weighted images; otherwise, edema was scored as moderate to severe (+).¹⁵ The non-contrast-enhancing tumor component (nCET) was defined as a region of hyperintensity on T2-weighted images (with corresponding hypointensity on contrast-enhanced T1-weighted images) that was associated with a mass effect and architectural distortion, including blurring of the gray-white interface (Fig 1).¹⁶

Immunohistochemistry

Immunohistochemical analysis of VEGF expression was performed for all patients. VEGF expression was scored by using 4-level grading criteria: (−) indicated <5% positive cells, (+) indicated mild expression with 6%–25% positive cells, (++) indicated moderate expression with 26%–50% positive cells, and (+++) indicated strong expression with >50% positive cells. Glioblastoma tumors were classified into 2 groups based on the level of VEGF expression as follows: low (−~++) and high (+++ expression groups.

Statistical Analysis

The χ^2 test was performed to detect the differences in clinical and radiologic features between patients with high and low VEGF expression. Consistency in the assessment of radiologic features by the 2 radiologists was evaluated by using the κ consistency test. Survival curves were generated by using the Kaplan-Meier method, and log-rank analysis was performed to compare PFS and OS. Significant prognostic factors (those with a *P* value < .05) identified by univariate analysis were entered into multivariate survival analysis by using the Cox proportional hazard ratio (HR) model.

RESULTS

Patient Characteristics

A total of 185 patients with glioblastoma with post-T1 contrast enhancement were included in this study. Of these, tumors of

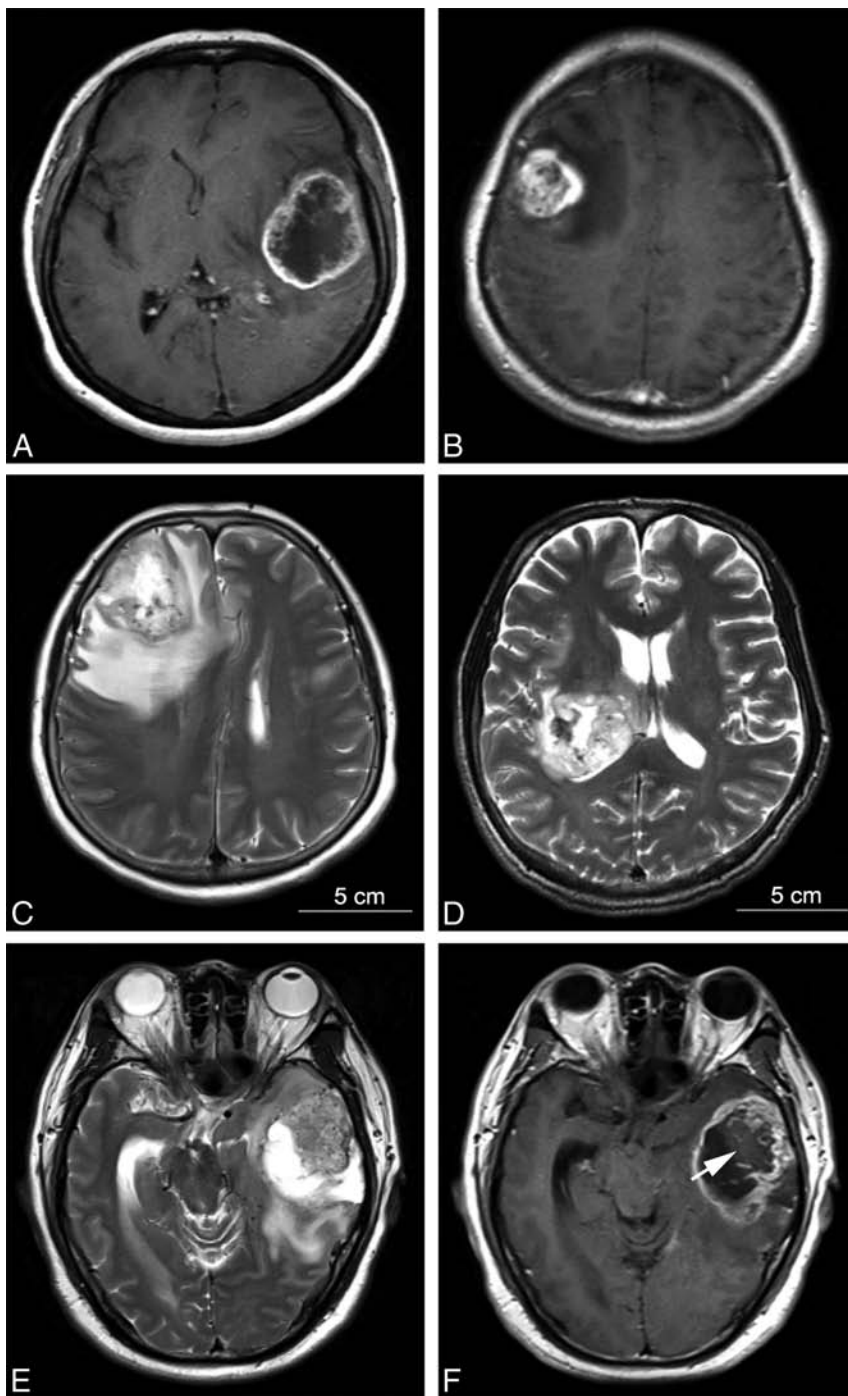


FIG 1. MR imaging features of patients with glioblastoma. The contrast-enhanced T1-weighted images showed ringlike contrast enhancement (A) and non-ringlike contrast enhancement (B). T2-weighted images show obvious peritumoral edema (+) (C) and little (or absent) peritumoral edema (–) (D). The non-contrast-enhancing tumor component refers to the tumor region of T2 hyperintensity (less than the intensity of CSF) (E) that was not enhanced on the contrast-enhanced T1-weighted image (white arrow) (F).

124 patients exhibited ringlike enhancement. Patient sex, preoperative KPS, enhancement pattern, and extent of resection were significantly different between the high and low VEGF expression groups ($P < .001$, χ^2 test, On-line Table). On the basis of the postoperative contrast-enhanced T1-weighted images obtained <72 hours after the operation, 112 (60.5%, 112/185) had GTR, and 156 received adjuvant therapy following tumor resection. In addition, there was no significant dif-

ference in the expression of isocitrate dehydrogenase 1, *O6-methylguanine DNA methyltransferase*, and epidermal growth factor receptor between patients with high-versus-low VEGF expression.

Association of the Radiologic Features and Extent of Resection with VEGF Expression

All data regarding tumor volume and location are summarized in the On-line Table. The mean tumor volume of patients with high VEGF expression (+++) was significantly larger than that of patients with low VEGF expression (– ~++) ($P = .033$). However, we observed no significant differences in the involvement of brain lobes between tumors with low and high VEGF expression.

The κ values for the consistency between the 2 evaluators for enhancement patterns, peritumoral edema, and nCET were 0.85 ($P = .014$), 0.81 ($P = .008$), and 0.76 ($P = .021$), respectively. Ringlike enhancement was more likely to be observed in glioblastomas with high VEGF expression than in those with low VEGF expression (75.6% versus 60.2%, $P = .027$, χ^2 test). The prevalence of peritumoral edema and nCET in the low-versus-high VEGF expression groups was not significantly different (peritumoral edema: 66.0% versus 74.4%, $P = .218$; nCET: 35.0% versus 46.3%, $P = .116$; χ^2 test). Moreover, GTR was significantly more likely to be achieved in glioblastomas with high VEGF expression than in those with low VEGF expression (72.0% versus 51.5%, $P = .005$).

Progression-Free Survival

Tumor recurrences were identified by MR images in 143 (77.3%) patients during the follow-up period. The median follow-up period for PFS analysis was 9.8 months (range, 1.0–53.1 months), and the median PFS was 7.6 months (range, 2.1–32.6 months). Univariate analysis revealed that age ($P = .018$), preoperative KPS ($P = .015$), extent of resection ($P = .013$), and adjuvant therapy ($P = .021$) were valuable prognostic factors for PFS (Table 1). These 4 factors remained significant in the multivariate Cox proportional hazards analysis. Age at diagnosis of 50 years or older ($P = .032$, HR = 1.642) and preoperative KPS of <80 ($P = .024$, HR = 2.215) were associated with shorter PFS, whereas GTR ($P = .022$, HR = 1.849) and adjuvant therapy ($P = .038$, HR = 0.652) indicated longer PFS (Table 2).

Table 1: Univariate analysis of survival outcomes for patients with glioblastoma

Characteristic	PFS			OS		
	P Value	HR	95% CI	P Value	HR	95% CI
Age 50 years or older	.018	1.591	1.375–2.894	.029	1.701	1.222–3.139
Sex (men)	.315	0.764	0.452–1.291	.092	0.631	0.370–1.078
Preoperative KPS <80	.015	2.045	1.165–2.445	.038	2.290	1.267–3.835
Epilepsy	.339	0.676	0.303–1.508	.421	1.408	0.611–3.243
Ringlike enhancement	.367	0.760	0.419–1.379	.456	0.790	0.424–1.470
Peritumoral edema	.304	1.359	0.757–2.439	.232	1.450	0.788–2.667
nCET	.176	0.696	0.411–1.180	.544	0.847	0.494–1.451
<GTR	.013	1.751	1.382–2.543	.022	1.782	1.349–3.739
Adjuvant therapy	.021	0.628	0.395–0.928	.032	0.603	0.514–0.980
VEGF expression + + +	.194	0.578	0.253–1.321	.183	0.577	0.256–1.297

Table 2: Multivariate analysis of survival outcomes

Predictors	P Value ^a	HR	95% CI
PFS			
Age (50 years or older)	.032	1.642	1.054–2.152
KPS <80	.024	2.215	1.179–2.728
<GTR	.022	1.849	1.392–2.548
Adjuvant therapy	.038	0.652	0.556–0.984
OS			
Age (50 years or older)	.043	1.348	1.008–2.181
KPS <80	.028	1.782	1.162–3.361
<GTR	.031	1.615	1.118–2.425

^a Cox proportional hazard regression analyses.

Overall Survival

At the time of analysis, 23 patients with available follow-up data were alive. The median follow-up period for OS analysis was 13.8 months (range, 2.0–86.8 months), and the median OS was 15.1 months (range, 3.8–67.6 months). Univariate analysis identified age ($P = .029$), preoperative KPS ($P = .038$), extent of resection ($P = .022$), and adjuvant therapy ($P = .032$) as prognostic factors of OS (Table 1). In the multivariate Cox proportional hazards analysis, age at diagnosis of 50 years or older ($P = .043$, HR = 1.348) and preoperative KPS of <80 ($P = .028$, HR = 1.782) were identified as poor prognostic factors for OS, whereas GTR ($P = .031$, HR = 1.615) indicated longer OS. However, adjuvant therapy failed to show a predictive value for survival outcomes (Table 2).

Prognostic Value of VEGF Expression Levels in Patients with GTR

To examine the prognostic value of VEGF expression when the extent of resection was taken into account, we classified patients into 4 groups according to their VEGF expression levels and the extent of resection as follows: GTR and high VEGF expression, <GTR and high VEGF expression, GTR and low VEGF expression, and <GTR and low VEGF expression. Survival outcomes were compared among these groups by using the log-rank test. We found that patients with glioblastoma with high VEGF expression and GTR had significantly longer survival than others ($P = .011$ for PFS and $P = .039$ for OS) (Fig 2). However, there was no significant difference in survival outcomes among the other 3 groups.

Prognostic Value of Peritumoral Edema in Patients Stratified by VEGF Expression Levels

The potential interactive and synergistic roles of peritumoral edema and VEGF expression in predicting the survival of pa-

tients with glioblastoma were also investigated. Patients were subdivided into 4 groups according to the presence of peritumoral edema and VEGF expression levels. Survival outcomes were compared among these groups by using the log-rank test. For OS, tumors with VEGF expression (+++) and peritumoral edema (–) indicated a longer survival compared with the other 3 groups ($P = .013$, log-rank). Specifically, peritumoral edema could stratify OS for tumors with high VEGF

expression ($P = .018$, log-rank), but not for those with low VEGF expression ($P = .074$, log-rank). For PFS, however, there was no significant difference among the 4 groups ($P = .226$, log-rank), and peritumoral edema could not stratify survival for different VEGF expression levels (Fig 3).

Prognostic Value of the Non-Contrast-Enhancing Tumor Component in Patients Stratified by VEGF Expression Levels

Kaplan-Meier curves according to the presence of nCET and VEGF expression levels showed that patients with high VEGF expression and nCET had a better survival ($P = .027$ for PFS and $P = .036$ for OS, log-rank). In the high VEGF expression group specifically, the presence of nCET predicted longer PFS ($P = .024$, log-rank) and OS ($P = .039$, log-rank). However, the prognostic value of nCET for PFS and OS was not observed in patients with low VEGF expression ($P = .716$ for PFS and $P = .645$ for OS, log-rank) (Fig 4).

DISCUSSION

In this study, we combined clinical, radiologic, and genetic characteristics in an investigation of prognostic factors for glioblastoma in a large cohort of patients. We found that peritumoral edema and nCET were of predictive value for survival in patients with a high expression level of VEGF. Notably, VEGF expression was a prognostic factor for patients achieving GTR, but not for those who did not.

Tumor-specific molecular markers have long been studied for their potential prognostic role in cancers. VEGF expression has been described as a valuable indicator of tumor recurrence in many types of malignancy.¹⁷ It was found that high expression levels of VEGF correlated with poor prognosis, while anti-VEGF therapy was shown to suppress tumor development and improve prognosis in glioblastoma.^{18,19} Glioblastoma is thought to exhibit abnormally high levels of VEGF.^{20,21} In this study, we found that VEGF expression alone was not a prognostic factor for patients with glioblastoma. However, VEGF might interact with other potential factors to determine survival outcomes.

VEGF regulates pathologic angiogenesis, resulting in the formation of new blood vessels to facilitate tumor growth.²² A previous study suggested that rapid tumor cell proliferation leads to oxygen shortage and necrosis in the center of a tumor, which is prone to present as a ringlike pattern of contrast enhancement. Consistent with these findings, we also observed that glioblas-

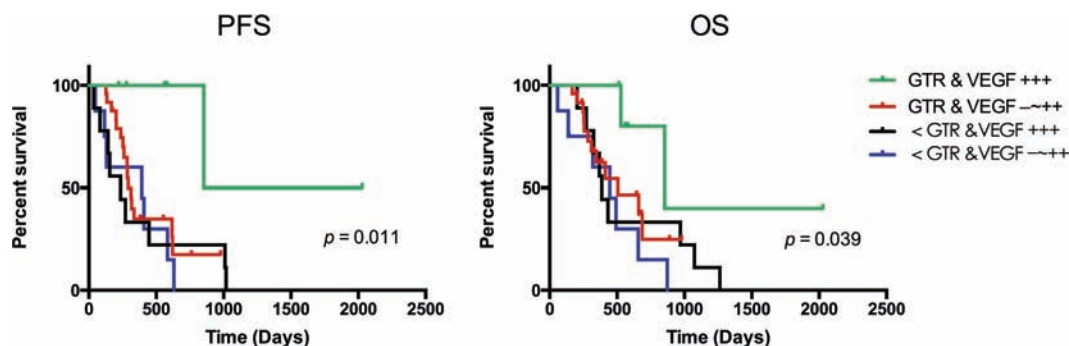


FIG 2. Survival outcomes of patients with glioblastoma. Kaplan-Meier survival curves of patients classified by the extent of resection and vascular endothelial growth factor expression are shown. Patients who had high tumor VEGF expression (+++) and achieved gross total resection had significantly longer progression-free survival and overall survival than those with low tumor VEGF expression and residual tumor after surgery ($P = .011$ and $.039$, respectively).

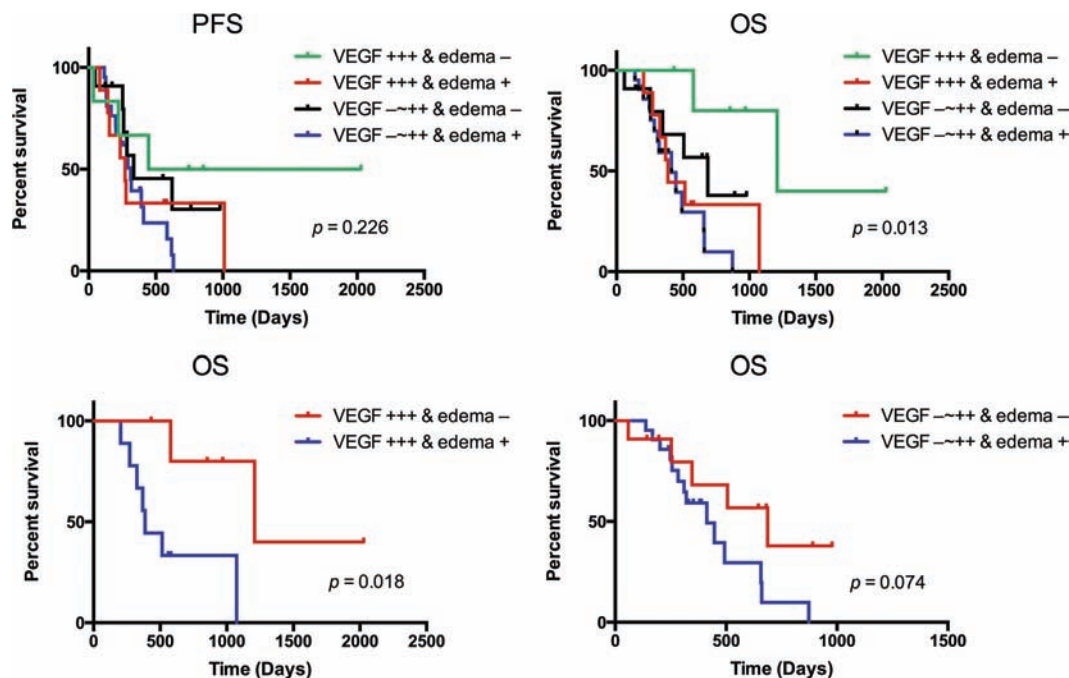


FIG 3. Kaplan-Meier plots of patients with glioblastoma showing the association between the progression-free survival and overall survival according to combined vascular endothelial growth factor expression levels and peritumoral edema. Tumors with high VEGF expression (+++) and without peritumoral edema correlated with better OS ($P = .013$, log-rank), but not PFS ($P = .226$, log-rank). Furthermore, peritumoral edema could stratify the OS for tumors with high VEGF expression ($P = .018$, log-rank), but not those with low VEGF expression ($P = .074$, log-rank).

tomas with high VEGF expression were more likely to present with a ringlike enhancement pattern than those with low VEGF expression. In addition, tumors with ringlike enhancement often exhibit a relatively clear radiologic border on postcontrast T1-weighted images and thus might more easily be localized during an operation for total resection. This might explain why GTR was more likely achieved in glioblastomas with high VEGF expression than in those with low VEGF expression.

Furthermore, we evaluated the interactive effects between the extent of resection and VEGF expression in predicting survival of patients with glioblastoma. Our results suggested that the prognostic value of VEGF expression was only valuable in patients who achieved GTR, thus implying a codependent effect of the 2 factors in predicting survival. Because lesions with high VEGF expression are prone to necrosis and, accordingly, exhibit ringlike enhancement patterns, tumors with ringlike enhancement patterns have

relatively distinguishable margins that may facilitate resection. It was also reported that patients with cystic glioblastoma with thin-wall ringlike enhancement might also benefit from GTR,²³ suggesting that cystic tumors might be circumscribed lesions with a distinct pattern of invasiveness or limited infiltration of the surrounding neutrophils. Therefore, patients with glioblastoma with high VEGF expression (+++) were more likely to benefit from GTR in terms of prolonging survival. Nevertheless, the inherent reason that VEGF expression might play a predictive role in the survival of patients with glioblastoma with GTR but not in those without GTR remains to be further investigated.

VEGF is known to be a potent permeability factor that causes edema,^{24,25} and the inhibition of VEGF reduces edema and tumor burden in patients with glioblastoma.^{26,27} It has been shown that VEGF expression is predictive of longer survival in cases of tumors with little or no edema, but not in those with extensive

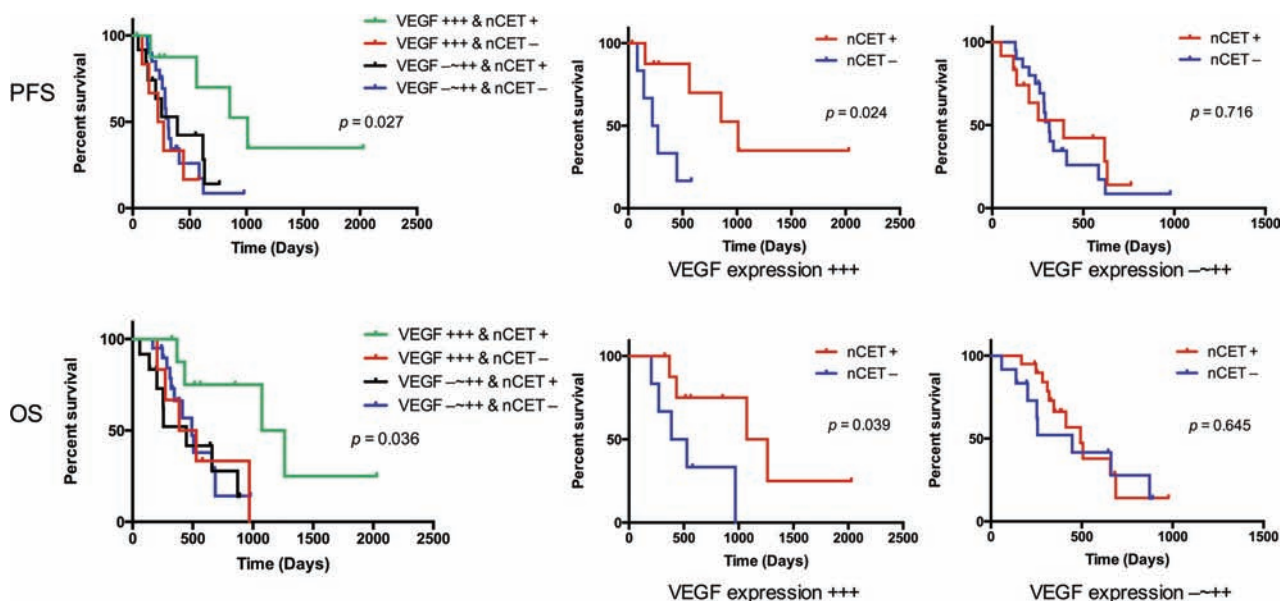


FIG 4. Kaplan-Meier survival curves show the progression-free survival and overall survival of patients with glioblastoma tumors with different vascular endothelial growth factor expression levels and non-contrast-enhancing tumor components. Tumors with high VEGF expression and the presence of nCET predict better survival (PFS, $P = .027$; OS, $P = .036$, log-rank). Moreover, nCET enables stratification of the PFS and OS of patients with high VEGF expression (PFS, $P = .024$; OS, $P = .039$, log-rank), but not of patients with low VEGF expression (PFS, $P = .716$; OS, $P = .645$, log-rank).

edema, indicating that edema could be regulated by both VEGF-dependent and VEGF-independent pathways.¹² Most interesting, the current study demonstrated that peritumoral edema could stratify the survival of patients with high VEGF expression (+++), but not of those with low VEGF expression (-~++). Although VEGF expression was correlated with edema and could promote peritumoral edema development, some tumors with high VEGF expression might not develop significant peritumoral edema.¹² In addition, VEGF and neuronal pentraxin-2 may affect MR imaging features of edema and enhancement, suggesting that edema development might not be directly regulated by VEGF.²⁸ For tumors with high VEGF expression (+++), the survival difference between patients with and without peritumoral edema might be partly attributed to the underlying mechanism of tumorigenesis, in which the angiogenic effect of VEGF may act differently in a manner that remains to be determined. Furthermore, as mentioned above, tumors with high VEGF expression are prone to necrosis and, accordingly, exhibit ringlike enhancement patterns, which may present relatively distinguishable margins and facilitate better resection. In tumors with no peritumoral edema, GTR would suggest less residual tumor cells and would thus predict longer PFS.

Previous studies have demonstrated that nCET is a valuable prognostic indicator in patients with glioblastoma; this finding was regarded as novel.¹⁶ In the current study, we showed that nCET was a prognostic factor for tumors with high VEGF expression (+++), but not for those with low (-~++) VEGF expression. In general, hypoxia induces the increased expression of VEGF and leads to tumor necrosis, suggesting a rapid growth and more aggressive behavior.¹² However, it was found that the nCET regions might lack necrosis and likely correspond to tumor areas with a lower pathologic grade and less aggressive behavior. A previous study showed that nCET was a valuable prognostic indica-

tor.¹⁶ Although nCET did not show a prognostic value in the current study, it was more likely to be present in glioblastomas with high VEGF expression. Thus, we speculate that nCET and VEGF might play synergistic roles in affecting survival outcomes. In addition, the prognostic value of nCETs might be partly owing to their association with oligodendroglioma components. Genetic analysis may provide additional clues to explain why the prognostic value of nCET depends on VEGF expression levels.

The current study has some limitations. First, we retrospectively enrolled patients from a single institution. Second, the combined prognostic role of VEGF expression and clinical and radiologic features requires further confirmation by a prospective multicenter investigation. Finally, due to the relatively suboptimal timing of the postoperative scans, the potential presence of granulation tissue may confound MR imaging results. Future studies should also focus on the association between clinical and radiologic characteristics and the survival of patients with tumors exhibiting other molecular markers.

CONCLUSIONS

In summary, we showed that VEGF expression was a valuable prognostic factor in patients who achieved GTR, whereas peritumoral edema and nCET could stratify survival outcomes for tumors with high VEGF expression. Thus, our findings suggest synergistic roles for tumor-specific biomarkers, surgical resection, and preoperative MR imaging features in predicting survival outcomes.

ACKNOWLEDGMENTS

We thank Drs Q. Chen and X. Chen for their efforts in tumor imaging evaluation.

Disclosures: Tao Jiang—RELATED: Grant: This work was supported by the National Basic Research Program of China (No. 2011CB707804 and No. 2015CB755500). * Jianping Dai—RELATED: Grant: This work was supported by the National Natural Science Foundation of China (No. 81271541). * *Money paid to the institution.

REFERENCES

- Stupp R, Mason WP, van den Bent MJ, et al; European Organisation for Research and Treatment of Cancer Brain Tumor and Radiotherapy Groups; National Cancer Institute of Canada Clinical Trials Group. **Radiotherapy plus concomitant and adjuvant temozolomide for glioblastoma.** *N Engl J Med* 2005;352:987–96 CrossRef Medline
- Inoue H, Aihara M, Tomioka M, et al. **Specific enhancement of vascular endothelial growth factor (VEGF) production in ischemic region by alprostadil—potential therapeutic application in pharmaceutical regenerative medicine.** *J Pharmacol Sci* 2013;122:158–61 CrossRef Medline
- Zhang SJ, Hu Y, Qian HL, et al. **Expression and significance of ER, PR, VEGF, CA15-3, CA125 and CEA in judging the prognosis of breast cancer.** *Asian Pac J Cancer Prev* 2013;14:3937–40 CrossRef Medline
- Chen J, Tang D, Wang S, et al. **High expressions of galectin-1 and VEGF are associated with poor prognosis in gastric cancer patients.** *Tumour Biol* 2014;35:2513–19 CrossRef Medline
- Vidal O, Soriano-Izquierdo A, Pera M, et al. **Positive VEGF immunostaining independently predicts poor prognosis in curatively resected gastric cancer patients: results of a study assessing a panel of angiogenic markers.** *J Gastrointest Surg* 2008;12:1005–14 CrossRef Medline
- Yang PW, Hsieh MS, Huang YC, et al. **Genetic variants of EGF and VEGF predict prognosis of patients with advanced esophageal squamous cell carcinoma.** *PLoS One* 2014;9:e100326 CrossRef Medline
- Chen P, Zhu J, Liu DY, et al. **Over-expression of survivin and VEGF in small-cell lung cancer may predict the poorer prognosis.** *Med Oncol* 2014;31:775 CrossRef Medline
- Fleitas T, Martinez-Sales V, Vila V, et al. **VEGF and TSP1 levels correlate with prognosis in advanced non-small cell lung cancer.** *Clin Transl Oncol* 2013;15:897–902 CrossRef Medline
- Schmidt NO, Westphal M, Hagel C, et al. **Levels of vascular endothelial growth factor, hepatocyte growth factor/scatter factor and basic fibroblast growth factor in human gliomas and their relation to angiogenesis.** *Int J Cancer* 1999;84:10–18 Medline
- Leon SP, Folkert RD, Black PM. **Microvessel density is a prognostic indicator for patients with astroglial brain tumors.** *Cancer* 1996;77:362–72 Medline
- Zhou YH, Tan F, Hess KR, et al. **The expression of PAX6, PTEN, vascular endothelial growth factor, and epidermal growth factor receptor in gliomas: relationship to tumor grade and survival.** *Clin Cancer Res* 2003;9:3369–75 Medline
- Carlson MR, Pope WB, Horvath S, et al. **Relationship between survival and edema in malignant gliomas: role of vascular endothelial growth factor and neuronal pentraxin 2.** *Clin Cancer Res* 2007;13:2592–98 CrossRef Medline
- Wen PY, Macdonald DR, Reardon DA, et al. **Updated response assessment criteria for high-grade gliomas: response assessment in neuro-oncology working group.** *J Clin Oncol* 2010;28:1963–72 CrossRef Medline
- Vogelbaum MA, Jost S, Aghi MK, et al. **Application of novel response/progression measures for surgically delivered therapies for gliomas: Response Assessment in Neuro-Oncology (RANO) Working Group.** *Neurosurgery* 2012;70:234–43; discussion 243–44 CrossRef Medline
- Carrillo JA, Lai A, Nghiemphu PL, et al. **Relationship between tumor enhancement, edema, IDH1 mutational status, MGMT promoter methylation, and survival in glioblastoma.** *AJNR Am J Neuroradiol* 2012;33:1349–55 CrossRef Medline
- Pope WB, Sayre J, Perlina A, et al. **MR imaging correlates of survival in patients with high-grade gliomas.** *AJNR Am J Neuroradiol* 2005;26:2466–74 Medline
- Poon RT, Fan ST, Wong J. **Clinical implications of circulating angiogenic factors in cancer patients.** *J Clinical Oncol* 2001;19:1207–25 Medline
- Lu KV, Bergers G. **Mechanisms of evasive resistance to anti-VEGF therapy in glioblastoma.** *CNS Oncol* 2013;2:49–65 CrossRef Medline
- Reardon DA, Wen PY, Desjardins A, et al. **Glioblastoma multiforme: an emerging paradigm of anti-VEGF therapy.** *Expert Opin Biol Ther* 2008;8:541–53 CrossRef Medline
- Desjardins A, Friedman HS. **Bevacizumab therapy for glioblastoma: a passionate discussion.** *CNS Oncol* 2014;3:1–3 CrossRef Medline
- Poulsen HS, Urup T, Michaelsen SR, et al. **The impact of bevacizumab treatment on survival and quality of life in newly diagnosed glioblastoma patients.** *Cancer Manag Res* 2014;6:373–87 CrossRef Medline
- Flamme I, Frölich T, Risau W. **Molecular mechanisms of vasculogenesis and embryonic angiogenesis.** *J Cell Physiol* 1997;173:206–10 Medline
- Maldaun MV, Suki D, Lang FF, et al. **Cystic glioblastoma multiforme: survival outcomes in 22 cases.** *J Neurosurg* 2004;100:61–67 CrossRef Medline
- Fischer I, Gagner JP, Law M, et al. **Angiogenesis in gliomas: biology and molecular pathophysiology.** *Brain Pathol* 2005;15:297–310 Medline
- Jain RK, di Tomaso E, Duda DG, et al. **Angiogenesis in brain tumours.** *Nat Rev Neurosci* 2007;8:610–22 CrossRef Medline
- Pope WB, Lai A, Nghiemphu P, et al. **MRI in patients with high-grade gliomas treated with bevacizumab and chemotherapy.** *Neurology* 2006;66:1258–60 CrossRef Medline
- Vredenburgh JJ, Desjardins A, Herndon JE, 2nd, et al. **Phase II trial of bevacizumab and irinotecan in recurrent malignant glioma.** *Clin Cancer Res* 2007;13:1253–59 CrossRef Medline
- Pope WB, Chen JH, Dong J, et al. **Relationship between gene expression and enhancement in glioblastoma multiforme: exploratory DNA microarray analysis.** *Radiology* 2008;249:268–77 CrossRef Medline

Giant Intracranial Aneurysms at 7T MRI

T. Matsushige, B. Chen, A. Ringelstein, L. Umutlu, M. Forsting, H.H. Quick, U. Sure, and K.H. Wrede



ABSTRACT

SUMMARY: Giant intracranial aneurysms are rare vascular pathologies associated with high morbidity and mortality. The purpose of this in vivo study was to assess giant intracranial aneurysms and their wall microstructure by 7T MR imaging, previously only visualized in histopathologic examinations. Seven giant intracranial aneurysms were evaluated, and 2 aneurysms were available for histopathologic examination. Six of 7 (85.7%) showed intraluminal thrombus of various sizes. Aneurysm walls were depicted as hypointense in TOF-MRA and SWI sequences with excellent contrast ratios to adjacent brain parenchyma (range, 0.01–0.60 and 0.58–0.96, respectively). The triple-layered microstructure of the aneurysm walls was visualized in all aneurysms in TOF-MRA and SWI. This could be related to iron deposition in the wall, similar to the findings in 2 available histopathologic specimens. In vivo 7T TOF-MRA and SWI can delineate the aneurysm wall and the triple-layered wall microstructure in giant intracranial aneurysms.

ABBREVIATIONS: GA = giant intracranial aneurysm; SEM = standard error of the mean

Intracranial saccular aneurysms are defined as saccular dilations of cerebral arterial vessels. The overall prevalence of unruptured intracranial aneurysms is estimated between 0.5% and 7% of the general population with a 0.5%–1.1% rupture risk per year on average.¹ Considering the natural history, giant intracranial aneurysms (GAs, defined as >25 mm in maximum diameter) belong to a rare subgroup (approximately 0.5% of all unruptured cerebral aneurysms), which are highly prone to rupture.^{2,3}

The pathophysiology of the growth in GAs is considered to differ from that of non-GAs. The presence of intraluminal thrombus formation associated with repeated intramural hemorrhage and neovascularization in the wall seems to play an important role in GA

growth.^{4,5} Prior histopathologic studies of intracranial aneurysms have shown inflammation and associated iron deposits in the wall that correlated with growth and rupture of the aneurysm.^{6,7} Previous MR imaging studies have revealed important morphologic features in these aneurysms, which are only partially assessable by DSA.^{8,9} Better delineation and characterization of GAs may help to improve our comprehension of the distinct pathophysiology of this rare aneurysm subgroup. The purpose of this study was to assess GAs and their wall microstructure by 7T MR imaging, previously only visualized in histopathologic examinations.

MATERIALS AND METHODS

The study was approved by the authorized ethics committee of the local university, and all patients provided written consent before the examination. Inclusion criteria were the following: 1) patients with a GA previously diagnosed via DSA and conventional 1.5T or 3T MR imaging, 2) 18 years of age or older, and 3) able to give informed consent. Exclusion criteria were the following: 1) the presence of a cardiac pacemaker or any other electronic implants, 2) pregnancy or breastfeeding, or 3) claustrophobia. Patients were recruited from January 2011 to December 2014 and included 4 men and 3 women with an average age of 66 years (range, 50–80 years).

High-Resolution 7T MR Imaging

Seven patients with GAs were evaluated by using a 7T whole-body MR imaging system (Magnetom 7T; Siemens, Erlangen, Germany) equipped with a 32-channel Tx/Rx head coil (Nova Med-

Received June 23, 2015; accepted after revision August 20.

From the Department of Neurosurgery (T.M., B.C., U.S., K.H.W.), University Hospital Essen, University Duisburg-Essen, Essen, Germany; Department of Neurosurgery (T.M.), Graduate School of Biomedical and Health Sciences, Hiroshima University, Hiroshima, Japan; Erwin L. Hahn Institute for Magnetic Resonance Imaging (T.M., B.C., L.U., H.H.Q., K.H.W.), University Duisburg-Essen, Essen, Germany; and Department of Diagnostic and Interventional Radiology and Neuroradiology (A.R., L.U., M.F.) and High Field and Hybrid MR Imaging (H.H.Q.), University Hospital Essen, Essen, Germany.

This work was supported by the University Duisburg Essen Interne Forschungsförderung Essen grant to Karsten H. Wrede.

Paper previously presented at: Annual Meeting of the International Society for Magnetic Resonance in Medicine, May 30–June 5, 2015; Toronto, Ontario, Canada; and as a poster at: Annual Meeting of the German Society of Neurosurgery, June 7–10 2015; Karlsruhe, Germany.

Please address correspondence to Toshinori Matsushige, MD, University Hospital Essen, Department of Neurosurgery, Hufelandstr 55, 45147 Essen, Germany; e-mail address: Toshinori.Matsushige@uk-essen.de

<http://dx.doi.org/10.3174/ajnr.A4569>

ical, Wilmington, Massachusetts). The system is equipped with a gradient system providing 45-mT/m maximum amplitude and a slew rate of 200 mT/m/ms. Applied sequences included TOF-MRA^{10,11} and MPAGE¹² from the standard 7T vascular protocol and SWI for detecting iron deposition. Detailed parameters for all sequences are summarized in Table 1.

Image Analysis

Before the evaluation, image data for all individual cases were coregistered between sequences by using the FMRIB Linear Image Registration Tool (FLIRT; <http://www.fmrib.ox.ac.uk>). Image evaluation was performed by using the FSLView tool (FMRIB Software Library, Version 5.0; <http://fsl.fmrib.ox.ac.uk/fsl/fslview/>) by 2 raters in a consensus reading. Assessed features were the following: aneurysm and parent artery diameter, wall thickness, signal intensity of the aneurysm wall, intraluminal thrombus, intraluminal flow, and surrounding brain tissue. The ROIs were placed in the wall of the dome farthest away from the aneurysm base, including 4 representative voxels (0.44×0.44 mm) of each structure. The ROIs in the tissues surrounding the wall amounted to 16 voxels (0.88×0.88 mm). Absolute values for contrast ratios of aneurysm wall layers and adjacent tissues were calculated as follows:

$$\left| \frac{(Intensity_a - Intensity_b)}{(Intensity_a + Intensity_b)} \right|$$

For every mean value, the standard error of mean (SEM, σ / \sqrt{n}) was calculated as an estimate of the population mean.

Histopathologic Examination

To surgically expose the aneurysm neck, partial resection of the wall and thrombus was mandatory in 2 thrombosed MCA aneurysms preoperatively scanned with 7T MR imaging. Aneurysm

domes were successfully resected parallel to the parent artery. Histopathologic sections were prepared from areas corresponding to MR imaging ROIs with 5- μ m thickness and were stained by using H&E, Van Gieson elastic, and Prussian blue.

RESULTS

All patients were examined without any adverse events, and all MR imaging sequences were successfully acquired. Table 2 summarizes basic demographic data for all patients and major anatomic features of the aneurysms. The mean diameters of aneurysms and parent arteries were 29.8 mm (SEM, 1.9; range, 25.1–37.9 mm) and 3.3 mm (SE, 0.4; range, 1.7–5.3 mm), respectively. All aneurysms except 1 were surrounded by brain parenchyma, and 4 aneurysms were accompanied by brain edema. The aneurysm arising from the cavernous portion of the ICA (subject 2) extended into the intracranial space with the cranial part of the dome. Figure 1 illustrates specific features of aneurysm delineation for all 7 cases in TOF-MRA, MPAGE, magnitude imaging, and SWI.

Thickness of the Aneurysm Wall

The mean aneurysm wall thickness was 0.96 mm (SEM, 0.1; range, 0.73–1.39 mm) in the TOF-MRA sequence, 1.08 mm (SEM, 0.11; range, 0.79–1.55 mm) in MPAGE, 1.34 mm (SEM, 0.08; range, 1.11–1.67 mm) in magnitude images, and 1.45 mm (SEM, 0.09; range, 1.22–1.86 mm) in SWI. The thicknesses in histopathologic sections of aneurysm walls near the fundus were 0.83–0.95 mm (subject 3) and 0.50–0.57 mm (subject 5). The thickness measured in histopathologic sections corresponded best with thickness measured in the TOF-MRA sequence for both patients who underwent surgery. Measured thicknesses of aneurysm walls are summarized in Fig 2.

Signal Intensity of the Aneurysm Wall

Aneurysm walls were depicted as hypointense on TOF-MRA and strongly hypointense on magnitude images and SWI compared with adjacent structures. In MPAGE, walls were delineated with a heterogeneous mostly hypointense signal. All aneurysms demonstrated a characteristic feature, showing a high contrast ratio of the wall to adjacent brain parenchyma. Signal intensities of intraluminal thrombus were heterogeneous between and within aneurysms. How-

Table 1: Major scan parameters for sequences at 7T MRI

Sequence	TOF-MRA	MPAGE	SWI
FOV (mm ²)	168 × 199	270 × 236	168 × 224
Matrix	896 × 756	384 × 336	896 × 672
Resolution (mm ²)	0.22 × 0.22	0.7 × 0.7	0.25 × 0.25
Section thickness (mm)	0.41	0.7	1.5
TR (ms)	20	2500	27
TE (ms)	4.34	1.54	15
Flip angle (degree)	18	7	14
Bandwidth (Hz/pixel)	95	570	140
Scan time	6 minutes 22 seconds	6 minutes 13 seconds	13 minutes 34 seconds

Table 2: Patient demographics and anatomic characteristics for all examined aneurysms

Nr.	Age (yr)	Sex	Location	Thrombosis	Maximum Diameter (mm)	Aneurysm Neck Diameter (mm)	Parent Vessel Diameter (mm)	Treatment
1	50	F	ICA	Partially	25.06	4.38	3.85	Endovascular ^a
2	56	F	ICA (cavernous)	Partially	37.87	7.95	3.43	Endovascular ^b
3	75	M	MCA	Partially	35.78	6.79	3.04	Clipping ^c
4	80	M	MCA	Completely	28.99	7.31	1.70	Observation
5	61	F	MCA	Partially	25.95	5.60	2.46	Clipping ^c
6	69	M	Basilar artery	Completely	27.21	22.10	3.57	Observation
7	71	M	Basilar artery	None	27.75	25.86	5.31	Observation

Note:—Nr. indicates patients in chronological order.

^a Coiling with a stent.

^b Parent vessel occlusion.

^c Subject with histopathologic assessment.

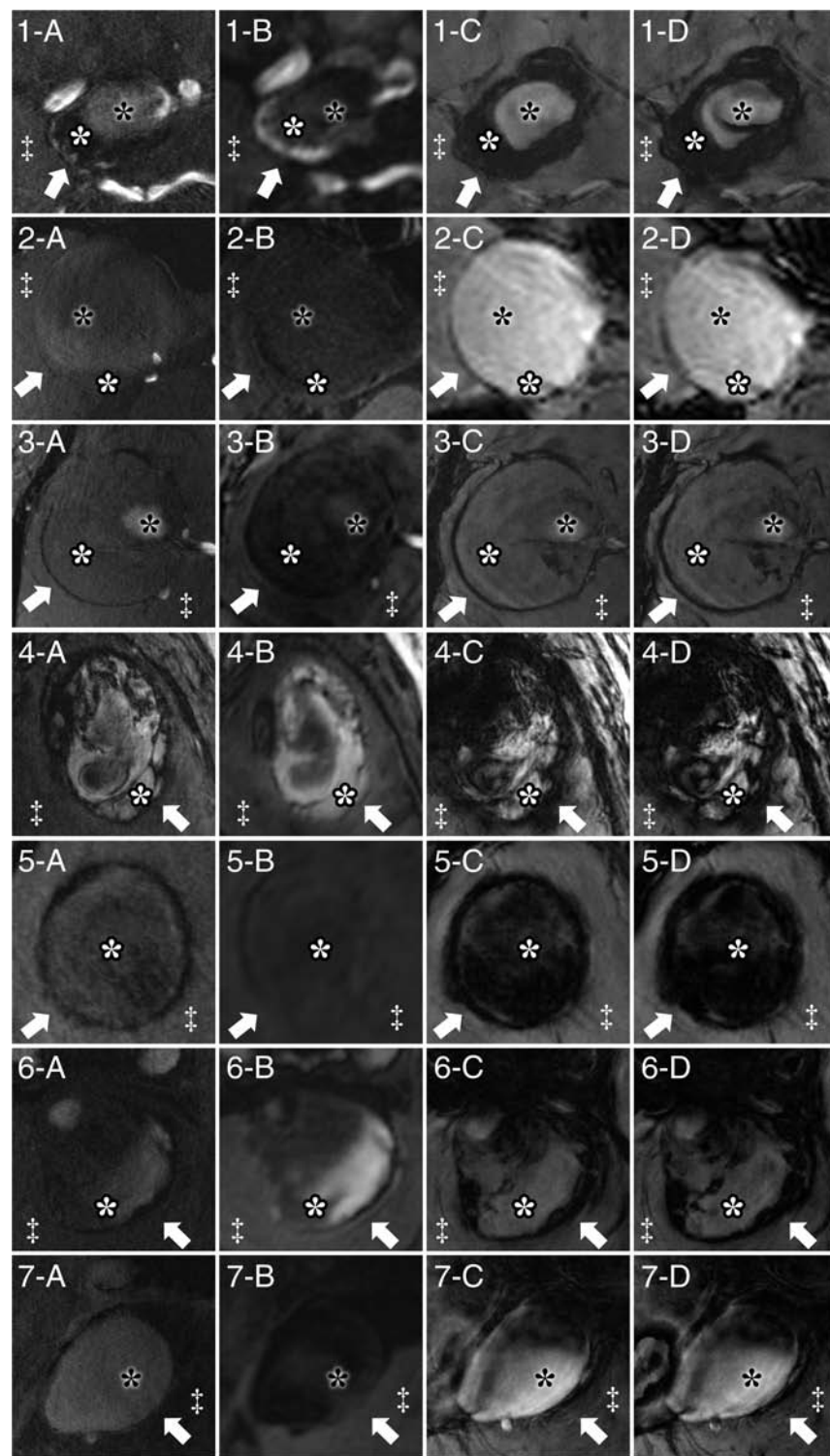


FIG 1. Delineation of giant intracranial aneurysms by 7T MR imaging for all 7 patients by TOF-MRA (A), MPRAGE (B), magnitude imaging (C), and SWI (D). Specific structures are marked identically in all subfigures. Arrows indicate the aneurysm wall; *white asterisks*, intraluminal thrombus; *black asterisks*, flow lumen; and *double daggers*, brain parenchyma. Aneurysm walls show hypointense signal in TOF-MRA, magnitude imaging, and SWI and heterogeneous signal intensity in MPRAGE.

ever, thrombus areas adjacent to the aneurysm wall were generally hyperintense in comparison with the wall. Contrast between intraluminal thrombus and brain parenchyma was low for all MR imaging sequences. Partially thrombosed aneurysms (subjects 1, 3, and 5) showed heterogeneous contrast

between thrombus and intraluminal flow. Details of contrast ratios are summarized in Table 3.

In TOF-MRA and SWI, aneurysm walls adjacent to brain parenchyma were depicted partially with a distinct triple-layered microstructure showing a hyperintense signal in the middle layer

surrounded by hypointense outer and inner layers. Mean contrast ratios between the middle layer and outer/inner layers were high (0.27–0.84) with better contrast in SWI than in TOF (Table 4). In 2 available histopathologic specimens, the hyperintense layer corresponded to the tunica media. There was no iron deposition within this part of the wall in the Prussian blue stain, while adventitia and smooth muscle layer adjacent to intraluminal thrombus showed strong iron uptake (Fig 3).

DISCUSSION

To our knowledge, this is the first in vivo study investigating GAs using ultra-high-field 7T MR imaging. Because most patients with GAs present with urgent clinical symptoms,⁵ for most of these cases, 7T MR imaging examinations remain inaccessible. Considering the scarce opportunity to recruit patients with this extremely rare vascular disease, this study of GAs can help to further understand the complex pathophysiology of aneurysm formation, growth, and rupture.

In previously published in vivo aneurysm wall imaging studies, depiction of microstructures within aneurysm walls was limited by spatial resolution,^{13–15} because wall thicknesses ranged from 20 to 500 μm.^{16,17} To date, there is only 1 report on intracranial vessel wall microstructures delineated with 7T MR imaging using an ultra-high ex vivo 0.11 × 0.11 mm² resolution.¹⁸ The study showed excellent correlation with the histopathologic findings. However, the presented ex vivo protocol took 40.5 hours per specimen and is therefore unsuitable for clinical in vivo application. In view of the previously published data, spatial resolution has to be well below aneurysm wall thickness to be capable of demonstrating microstructures within the wall. The spatial resolution used in our study was 5.7–13.2 times higher compared with previous in vivo aneurysm wall studies,^{10,11,13–15} which was sufficient to visualize the microstructures in vivo for the first time.

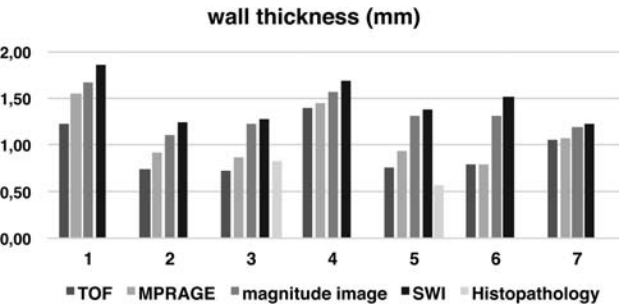


FIG 2. Thickness of aneurysm walls is presented for all MR imaging sequences and histopathology (only available for cases 3 and 5). In every subject, aneurysm wall thickness was larger on magnitude images and SWI compared with TOF-MRA and MPRAGE. Histopathologic measurements correlated best with TOF-MRA measurements in all subjects.

Table 3: Contrast ratios of aneurysm wall and intraluminal thrombus to adjacent structures

	WBCR (mean) (SEM, range)	WTCR (mean) (SEM, range)	TBCR (mean) (SEM, range)	TLCR (mean) (SEM, range)
TOF	0.41 (0.08, 0.01–0.60)	0.33 (0.10, 0.03–0.58)	0.15 (0.10, 0.23–0.57)	0.31 (0.11, 0.16–0.62)
MPRAGE	0.20 (0.06, 0.06–0.49)	0.36 (0.09, 0.07–0.57)	0.17 (0.13, 0.25–0.56)	0.23 (0.07, 0.03–0.38)
Magnitude image	0.67 (0.05, 0.44–0.83)	0.54 (0.15, 0.08–0.82)	0.26 (0.10, 0.06–0.75)	0.30 (0.16, 0.02–0.84)
SWI	0.84 (0.05, 0.58–0.96)	0.70 (0.15, 0.13–0.93)	0.12 (0.16, 0.19–0.95)	0.34 (0.18, 0.07–0.97)

Note:—WBCR indicates aneurysm wall to brain parenchyma; WTCR, aneurysm wall to intraluminal thrombus; TBCR, intraluminal thrombus to brain parenchyma; TLCR, intraluminal thrombus to intraluminal flow.

Histopathology revealed a distinct pattern of iron deposition within the aneurysm wall, showing a homogeneous distribution in the adventitia and smooth muscle layer adjacent to intraluminal thrombus, sparing the tunica media. Honkanen et al¹⁹ characterized the aneurysm wall in an ex vivo study setup comparing 4.7T MR imaging and histopathology, showing the capability of a T2* sequence to detect iron-loaded macrophages depicting the degenerated aneurysm walls as hypointense structures. In the present study, the ultra-high spatial resolution in TOF-MRA and SWI could depict iron-related signal decay in voxels within the aneurysm wall as a typical triple-layered microstructure, which correlates with the histopathologic findings. Due to the lower spatial resolution of MPRAGE, partial volume effects of surrounding inner and outer aneurysm wall layers blurred the tunica media signal. Thus, MPRAGE was not able to depict the distinct triple-layered wall structure, showing only a diffuse hypointense signal.

The surrounding brain parenchyma and intraluminal thrombus, often seen in GAs, provide additional image contrast and therefore help to differentiate the aneurysm wall from its surrounding structures. In some cases, heterogeneous signal in parts of the intraluminal thrombus led to local low-contrast areas around the aneurysm wall, making differentiation slightly more difficult. The inhomogeneous iron deposition caused by different ages of thrombus layers²⁰ is presumably associated with the heterogeneous signal intensity in some thrombus. As expected, the local B0 field inhomogeneity due to the deposited iron caused stronger signal alterations in SWI compared with TOF-MRA and MPRAGE. These susceptibility effects are amplified at 7T compared with lower magnetic field strengths. Because of strong blooming effects in SWI at ultra-high magnetic field strengths, aneurysm wall thickness was overestimated approximately 1.5-fold compared with TOF-MRA, which showed excellent correlation with histopathologic measurements.

It is debatable whether the triple-layered microstructures are fragile or represent a stable region of the aneurysm wall and to what extent iron accumulation derives from infiltrating macrophages. Considering previously published data from histopathologic and clinical studies and the present high-resolution MR imaging findings, the triple-layered microstructures are likely to reflect the fragility of the aneurysm wall. The grade of iron depo-

Table 4: Contrast ratios of aneurysm wall layers

	WLCR (Outer) (mean) (SEM, range)	WLCR (Inner) (mean) (SEM, range)
TOF	0.39 (0.04, 0.24–0.59)	0.27 (0.04, 0.15–0.49)
MPRAGE	NA	NA
Magnitude image	0.49 (0.10, 0.25–1.00)	0.33 (0.11, 0.14–1.00)
SWI	0.84 (0.06, 0.52–1.00)	0.71 (0.08, 0.31–1.00)

Note:—WLCR (outer) indicates wall middle layer to outer layer; WLCR (inner), wall middle layer to inner layer; NA, not applicable.

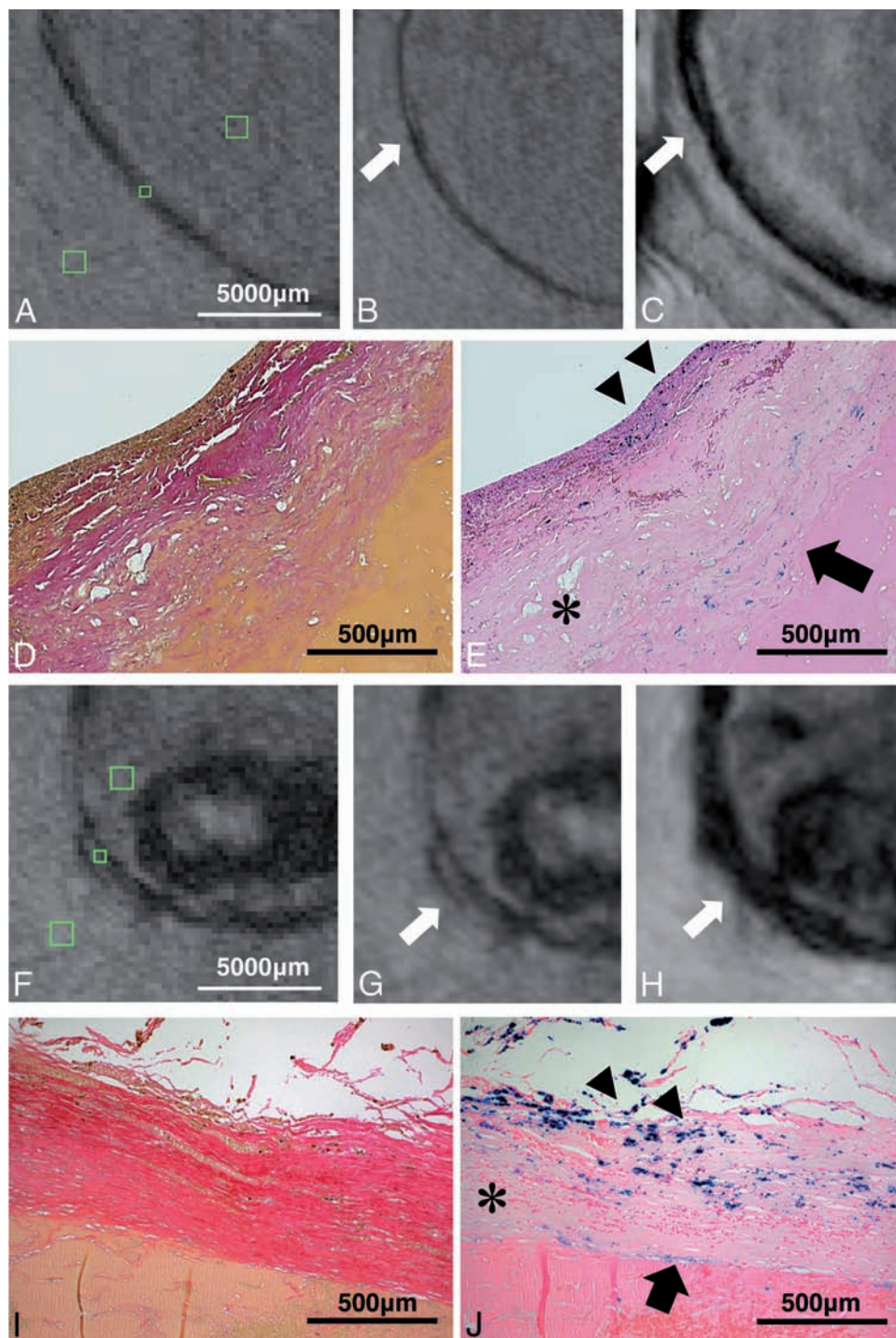


FIG 3. Histopathologic images and MR imaging of both partially resected aneurysms are illustrated. There is an excellent correspondence between hypointense signal in TOF-MRA and SWI and iron deposition in the aneurysm wall in histopathologic sections (subject 3: A–E; subject 5: F–J). *Green squares* on TOF-MRA (without zoom interpolation) indicate ROIs in the aneurysm wall and surrounding structures (brain parenchyma and intraluminal thrombus) (A and F). Magnified images depict the hypointense aneurysm wall in TOF-MRA (B and G) and the strongly hypointense aneurysm wall in SWI (C and H). Aneurysm walls partially show the triple-layered microstructure (hyperintense layer in the middle) in both sequences (*arrows*). Histopathology shows aneurysm walls with Van Gieson elastic staining (original magnification $\times 50$) (D and I) and iron deposition in inner smooth muscle (*arrowheads*) and adventitial layer (*arrow*) in Prussian blue staining (original magnification $\times 50$) (E and J). Note the decellularized layer in the middle layer without iron deposition (*asterisks*).

sition, likely linked to inflammation, is detectable and can be quantified by using high-field MR imaging. This information might therefore serve as a future follow-up marker and help in deciding the treatment timing and technique.

Limitations

The present series consisted of a relatively small number of 7 patients with GAs. However, considering the extremely low incidence of this rare pathology, the possibility of recruiting a consid-

erably larger number of patients within a reasonable time is limited. More than half of our patients presenting with giant aneurysms during these 3 years were unsuitable for scanning at 7T MR imaging because of numerous contraindications. On the one hand, heterogeneous sizes and locations of scanned aneurysms seem to be a limitation of the study; on the other hand, identical signal characteristics of aneurysm walls could be shown in various locations and therefore indicate these signal characteristics as a general feature of GAs. Wall imaging in this study was focused on the fundus of the aneurysm. Walls of intracranial aneurysms are highly heterogeneous,^{15,21} making it difficult to characterize the complete aneurysm wall by using MR imaging and histopathology, when only parts of the aneurysm wall are investigated by both methods. A future ex vivo or in vivo study might overcome this limitation by 3D aligning of MR imaging and histopathologic images, allowing exact quantification of the complete aneurysm wall. Finally, susceptibility artifacts from adjacent air-filled sinuses can strongly impair aneurysm delineation close to the skull base, especially in SWI, making it difficult to visualize large parts of the aneurysm wall and therefore reducing applicability of 7T MRA as a follow-up marker.

CONCLUSIONS

High-resolution in vivo 7T SWI and TOF-MRA imaging can delineate the triple-layered wall microstructure in giant intracranial aneurysms previously only depicted by using ex vivo MR imaging or histopathologic examinations. Quantification of iron deposition in the aneurysm wall might serve as a future follow-up marker and help in deciding the treatment timing and technique.

ACKNOWLEDGMENTS

The authors thank Lena C. Schäfer (RT) for performing all the 7T examinations.

Disclosures: Bixia Chen—RELATED: Grant: Interne Forschungsförderung Essen, Comments: The Interne Forschungsförderung Essen grant is a scientific grant given by the University Duisburg-Essen; UNRELATED: Travel/Accommodations/Meeting Expenses Unrelated to Activities Listed: German Academic Exchange Service travel grant to the International Society for Magnetic Resonance in Medicine Annual Meeting and Exhibition. Karsten H. Wrede—RELATED: Grant: Interne Forschungsförderung Essen, Comments: The grant is a scientific one given by the University Duisburg-Essen.

REFERENCES

1. Brown RD Jr, Broderick JP. **Unruptured intracranial aneurysms: epidemiology, natural history, management options, and familial screening.** *Lancet Neurol* 2014;13:393–404 CrossRef Medline
2. Wiebers DO, Whisnant JP, Huston J 3rd, et al; International Study of Unruptured Intracranial Aneurysms Investigators. **Intracranial aneurysms: natural history, clinical outcome, and risks of surgical and endovascular treatment.** *Lancet* 2003;362:103–10 CrossRef Medline
3. Morita A, Kirino T, Hashi K, et al; UCAS Japan Investigators. **The natural course of unruptured cerebral aneurysms in a Japanese cohort.** *N Engl J Med* 2012;366:2474–82 CrossRef Medline
4. Barth A, de Tribolet N. **Growth of small saccular aneurysms to giant aneurysms: presentation of three cases.** *Surg Neurol* 1994;41:277–80 CrossRef Medline
5. dos Santos ML, Spotti AR, dos Santos RM, et al. **Giant intracranial aneurysms: morphology and clinical presentation.** *Neurosurg Rev* 2013;36:117–22; discussion 122 CrossRef Medline
6. Kataoka K, Taneda M, Asai T, et al. **Structural fragility and inflammatory response of ruptured cerebral aneurysms: a comparative study between ruptured and unruptured cerebral aneurysms.** *Stroke* 1999;30:1396–401 CrossRef Medline
7. Frösen J, Piippo A, Paetau A, et al. **Remodeling of saccular cerebral artery aneurysm wall is associated with rupture: histological analysis of 24 unruptured and 42 ruptured cases.** *Stroke* 2004;35:2287–93 CrossRef Medline
8. Roccatagliata L, Guédin P, Condette-Auliac S, et al. **Partially thrombosed intracranial aneurysms: symptoms, evolution, and therapeutic management.** *Acta Neurochir* 2010;152:2133–42 CrossRef Medline
9. Martin AJ, Hetts SW, Dillon WP, et al. **MR imaging of partially thrombosed cerebral aneurysms: characteristics and evolution.** *AJNR Am J Neuroradiol* 2011;32:346–51 CrossRef Medline
10. Johst S, Wrede KH, Ladd ME, et al. **Time-of-flight magnetic resonance angiography at 7 T using venous saturation pulses with reduced flip angles.** *Invest Radiol* 2012;47:445–50 CrossRef Medline
11. Wrede KH, Johst S, Dammann P, et al. **Improved cerebral time-of-flight magnetic resonance angiography at 7 Tesla: feasibility study and preliminary results using optimized venous saturation pulses.** *PLoS One* 2014;9:e106697 CrossRef Medline
12. Wrede KH, Johst S, Dammann P, et al. **Caudal image contrast inversion in MPRAGE at 7 Tesla: problem and solution.** *Acad Radiol* 2012;19:172–78 CrossRef Medline
13. Park JK, Lee CS, Sim KB, et al. **Imaging of the walls of saccular cerebral aneurysms with double inversion recovery black-blood sequence.** *J Magn Reson Imaging* 2009;30:1179–83 CrossRef Medline
14. Kim TW, Choi HS, Koo J, et al. **Intramural hematoma detection by susceptibility-weighted imaging in intracranial vertebral artery dissection.** *Cerebrovasc Dis* 2013;36:292–98 CrossRef Medline
15. Kleinloog R, Korkmaz E, Zwanenburg JJ, et al. **Visualization of the aneurysm wall: a 7.0-Tesla magnetic resonance imaging study.** *Neurosurgery* 2014;75:614–22; discussion 622 CrossRef Medline
16. Steiger HJ, Aaslid R, Keller S, et al. **Strength, elasticity and viscoelastic properties of cerebral aneurysms.** *Heart Vessels* 1989;5:41–46 CrossRef Medline
17. Boussel L, Wintermark M, Martin A, et al. **Monitoring serial change in the lumen and outer wall of vertebrobasilar aneurysms.** *AJNR Am J Neuroradiol* 2008;29:259–64 CrossRef Medline
18. Dieleman N, van der Kolk AG, Zwanenburg JJ, et al. **Imaging intracranial vessel wall pathology with magnetic resonance imaging: current prospects and future directions.** *Circulation* 2014;130:192–201 CrossRef Medline
19. Honkanen P, Frösen JK, Abo-Ramadan U, et al. **Visualization of luminal thrombosis and mural iron accumulation in giant aneurysms with ex vivo 4.7T magnetic resonance imaging.** *Surg Neurol Int* 2014;5:74 CrossRef Medline
20. Corti R, Osende JI, Fayad ZA, et al. **In vivo noninvasive detection and age definition of arterial thrombus by MRI.** *J Am Coll Cardiol* 2002;39:1366–73 CrossRef Medline
21. Kadasi LM, Dent WC, Malek AM. **Cerebral aneurysm wall thickness analysis using intraoperative microscopy: effect of size and gender on thin translucent regions.** *J Neurointerv Surg* 2013;5:201–06 CrossRef Medline

A Spiral Spin-Echo MR Imaging Technique for Improved Flow Artifact Suppression in T1-Weighted Postcontrast Brain Imaging: A Comparison with Cartesian Turbo Spin-Echo

Z. Li, H.H. Hu, J.H. Miller, J.P. Karis, P. Cornejo, D. Wang, and J.G. Pipe



ABSTRACT

BACKGROUND AND PURPOSE: A challenge with the T1-weighted postcontrast Cartesian spin-echo and turbo spin-echo brain MR imaging is the presence of flow artifacts. Our aim was to develop a rapid 2D spiral spin-echo sequence for T1-weighted MR imaging with minimal flow artifacts and to compare it with a conventional Cartesian 2D turbo spin-echo sequence.

MATERIALS AND METHODS: T1-weighted brain imaging was performed in 24 pediatric patients. After the administration of intravenous gadolinium contrast agent, a reference Cartesian TSE sequence with a scanning time of 2 minutes 30 seconds was performed, followed by the proposed spiral spin-echo sequence with a scanning time of 1 minutes 18 seconds, with similar spatial resolution and volumetric coverage. The results were reviewed independently and blindly by 3 neuroradiologists. Scores from a 3-point scale were assigned in 3 categories: flow artifact reduction, subjective preference, and lesion conspicuity, if any. The Wilcoxon signed rank test was performed to evaluate the reviewer scores. The *t* test was used to evaluate the SNR. The Fleiss κ coefficient was calculated to examine interreader agreement.

RESULTS: In 23 cases, spiral spin-echo was scored over Cartesian TSE in flow artifact reduction ($P < .001$). In 21 cases, spiral spin-echo was rated superior in subjective preference ($P < .001$). Ten patients were identified with lesions, and no statistically significant difference in lesion conspicuity was observed between the 2 sequences. There was no statistically significant difference in SNR between the 2 techniques. The Fleiss κ coefficient was 0.79 (95% confidence interval, 0.65–0.93).

CONCLUSIONS: The proposed spiral spin-echo pulse sequence provides postcontrast images with minimal flow artifacts at a faster scanning time than its Cartesian TSE counterpart.

ABBREVIATION: SE = spin-echo

T1-weighted MR imaging after the injection of gadolinium-based contrast agent is widely used in the diagnosis of many neurologic diseases, such as tumors, infections, and inflammatory conditions. 2D multisection Cartesian spin-echo (SE) and turbo spin-echo–based pulse sequences are the clinically preferred methods for postcontrast T1WI. A challenge with these Cartesian

images is the presence of ghosting artifacts due to flowing blood from the venous sinuses. These artifacts can obscure the visualization of lesions and reduce image quality. With contrast-agent enhancement, these flow artifacts are further exacerbated by bright-blood signals. Gradient flow compensation and spatial saturation bands are helpful in alleviating, but not eliminating, these flow-induced artifacts in Cartesian acquisitions.

Spiral MR imaging, a non-Cartesian acquisition technique, has several advantages over its Cartesian counterpart.^{1,2} A primary benefit is the ability of the spiral to traverse *k*-space more efficiently per unit of time than Cartesian trajectories, thus providing a higher scan speed. With spiral acquisitions, motion- and flow-induced errors are manifest as incoherent artifacts in the image domain. As a result, spiral acquisition reduces the sensitivity of the pulse sequence to structured artifacts.³ The spiral trajectory also inherently provides zero gradient moments at the origin of *k*-space, which substantially decreases the sensitivity of the sequence to in-plane flow-related artifacts.⁴ Spiral SE MR imaging

Received May 28, 2015; accepted after revision August 19.

From the Departments of Imaging Research (Z.L., D.W., J.G.P.) and Radiology (J.P.K.), Barrow Neurological Institute, Phoenix, Arizona; and Department of Radiology (H.H.H., J.H.M., P.C.), Phoenix Children's Hospital, Phoenix, Arizona.

Z. Li and H.H. Hu are co-first authors.

Z.L., H.H.H., J.H.M., D.W., and J.G.P. receive research funding support from Philips Healthcare.

Paper previously presented as electronic poster No. 135 at: American Society of Neuroradiology Annual Meeting and the Foundation of the ASNR Symposium, April 25–30, 2015; Chicago, Illinois.

Please address correspondence to Zhiqiang Li, PhD, Barrow Neurological Institute, Keller Center for Imaging Innovation, 350 W Thomas Rd, Phoenix AZ 85013; e-mail: lizhiqiang@gmail.com

<http://dx.doi.org/10.3174/ajnr.A4600>

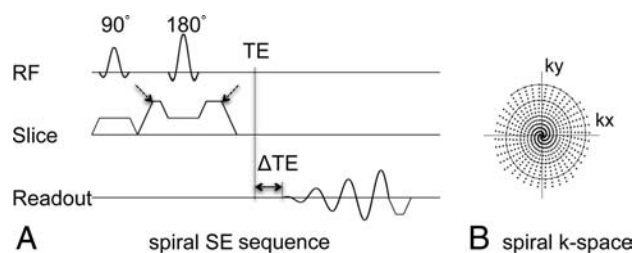


FIG 1. Pulse sequence diagram of the proposed 2D spiral SE sequence (A). Δ TE indicates the temporal shift of the spiral readout relative to the traditional TE (ie, the Hahn echo). Spiral data at multiple Δ TE shifts (-0.2 , 0.57 , and 1.34 ms used at 3T) were collected in this work to facilitate chemical shift–encoded water-fat imaging. The *dashed arrows* point to the crusher gradients in the section direction used to spoil through-plane flow signal. B, The *solid circular tracing* shows 1 spiral interleaf, and the *dots* indicate sampled data points in k -space from all interleaves, as summarized in Table 1. RF indicates radiofrequency.

Table 1: 3T imaging parameters of conventional 2D multisecton Cartesian TSE and the proposed 2D spiral SE^a

Parameter	Cartesian TSE	Spiral SE
Orientation	Axial	Axial
Phase-encoding direction	Anterior/posterior	NA
FOV (mm)	220×220	220×220
In-plane resolution (mm)	0.8×1.0	0.85×0.85
Section thickness (mm)	3	3
Section gap (mm)	0.3	0.3
No. of sections	15	15
Excitation flip angle	70°	90°
TE (ms)	9	10
Δ TE (ms)	0, 1.0	-0.2 , 0.57 , 1.34
Echo-train length	3	NA
TR (ms)	674	674
No. of spiral interleaves	NA	38
Gradient flow compensation	On	Off
Spatial saturation band	On	Off
No. of section packages	2	1
Scanning time	2 min 30 sec	1 min 18 sec

Note:—NA indicates not applicable; Δ TE, TE shifts.

^a Note the use of gradient flow compensation and a spatial saturation band with the Cartesian TSE technique, whereas they are absent in the spiral SE sequence. Note also differences in scanning times despite comparable spatial resolution and section coverage.

has been reported in pelvic imaging,⁵ black-blood imaging of peripheral vasculature,⁶ and functional MR imaging.⁷

The purpose of this work was to develop a 2D spiral SE technique for T1-weighted brain imaging with minimal flow artifacts and faster scanning speed and compare it with a conventional 2D Cartesian TSE pulse sequence, with comparable spatial resolution and volumetric coverage. We prospectively evaluated the performance of the 2D spiral SE technique and its subsequent image quality in a cohort of pediatric patients.

MATERIALS AND METHODS

This prospective, Health Insurance Portability and Accountability Act–compliant study was approved by the Phoenix Children’s Hospital and the Barrow Neurological Institute review boards under expedited review as a minimum-risk study, and informed consent was waived from patients at the Phoenix Children’s Hospital for adding the proposed spiral sequence to a standard brain MR imaging examination.

2D Spiral SE MR Imaging

To overcome slower scan speeds and pronounced flow artifacts in conventional Cartesian TSE and SE techniques in postcontrast T1WI, we proposed, in this work, a SE pulse sequence by using a spiral-out readout, as shown in Fig 1. In Cartesian imaging, motion- and flow-induced errors express themselves as coherent ghosting artifacts along the phase-encoding direction. In spiral imaging, there is no defined phase-encoding direction (Fig 1B). Therefore, motion- and flow-induced errors are manifest in all directions as incoherent artifacts. The reduced sensitivity to in-plane flow-induced artifacts is also because the gradient moments at the beginning of the spiral readout are nulled for all orders (ie, static, velocity, acceleration, jerk, and so forth), which leads to reduced phase errors at the center of k -space. Thus, the proposed spiral SE sequence obviates additional gradient flow compensation, typically used in Cartesian TSE to suppress in-plane flow signals. An additional measure used in this work was large crusher gradients along the section direction around the 180° refocusing radiofrequency pulse of the SE. These further reduce through-plane flow-induced artifacts.⁶ The overall reduced sensitivity of spiral SE to flow-induced errors eliminates the need for additional spatial saturation bands that are typically used in Cartesian TSE acquisitions to null signals from through-plane inflowing blood. Removal of these saturation bands in spiral SE also reduces magnetization transfer effects and improves the gray-white matter tissue contrast.

Water-Fat Imaging Capability

In this work, multiecho chemical shift–encoded Dixon water-fat imaging capability^{8,9} was added to the proposed spiral SE technique; thus, it is similar to the conventional Cartesian TSE sequence of our institution, the comparison reference, which has built-in Dixon capability from the manufacturer. Three echoes were used in the spiral SE pulse sequence to achieve reliable water-fat separation and deblurring.¹⁰

Data Acquisition

All data were acquired on two 3T scanners (Ingenia; Philips Healthcare, Best, the Netherlands) by using either a 13- or a 32-channel head array. In each patient, the axial 2D Cartesian TSE scan was obtained first after intravenous contrast (gadopentetate dimeglumine, Magnevist; Bayer HealthCare Pharmaceuticals, Wayne, New Jersey) administration, followed by the proposed spiral SE scan. The imaging parameters are summarized in Table 1.

SNR Evaluation

To compare the SNR of the spiral SE and Cartesian TSE sequences, we initially scanned 2 healthy adult volunteers, without the use of intravenous contrast. SNR can typically be measured by estimating the noise SD from either the background region or the difference of 2 consecutive image sets acquired under identical conditions.^{11,12} Because the background air regions in spiral reconstructed images do not contain pure Gaussian noise, the latter method of acquiring 2 identical image sets was adopted in this work, and the difference of the 2 images was used to estimate noise and ultimately SNR. In each volunteer, areas with relatively uni-

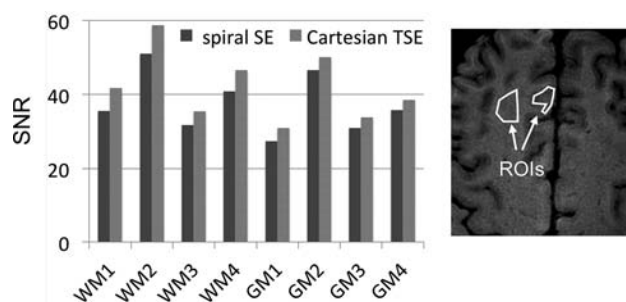


FIG 2. Measured SNR in 8 ROIs (4 white matter and 4 gray matter). The ROI size range was 269–1080 voxels with a mean of 530 voxels (range, 56.5–226.9 mm², with mean of 111.3 mm²), with 1 example shown on the right. The relative SNR of spiral SE to Cartesian TSE was 89.3% \pm 3.0%.

form gray or white matter signals were selected from the spiral SE image, and ROIs were manually drawn. Selected areas included cortical gray matter, subcortical white matter, deep white matter (centrum semiovale), and so forth, and 1 example was illustrated in Fig 2. The ROIs and signal and noise measurements were made by using ImageJ software (National Institutes of Health, Bethesda, Maryland).

Patient Studies

Twenty-four pediatric patients (18 boys, 6 girls) were prospectively enrolled in this study from October to December 2014. There were no specific inclusion/exclusion criteria. The age ranged from 7 months to 13 years 8 months, with a distribution of 6.1 ± 3.9 years. Twenty-two of the 24 patients were scanned with sedation. The cohort is briefly summarized in Table 2.

Data Analysis

The water-reconstructed images from Cartesian TSE and spiral SE were independently assessed by 3 radiologists, with 2 (P.C.), 9 (J.H.M.), and 23 (J.P.K.) years of experience in neuroradiology, respectively. The images were rated in 3 categories, including flow artifact reduction, subjective preference (meaning the radiologists would rather interpret one image than the other), and lesion conspicuity, if present. For each patient, the readers were given the combined dataset (Cartesian TSE and spiral SE) in a 2-column format with the left-right order randomized as either Cartesian TSE/spiral SE or spiral SE/Cartesian TSE. The readers reviewed all images (ie, all sections), and an overall score was given for each patient in each category by using a 3-point score system, with -1 representing the left superior to the right, zero representing the left equivalent to the right, and 1 representing the left inferior to the right. The scores were then converted by the remaining investigators in a separate session so that -1 denoted Cartesian TSE superior to spiral SE, zero denoted Cartesian TSE equivalent to spiral SE, and 1 denoted Cartesian TSE inferior to spiral SE.

Statistical Analysis

The SPSS software package (Version 15.0; IBM, Armonk, New York) was used for statistical analysis. The *t* test was used to assess any statistically significant difference in SNR between Cartesian TSE and spiral SE. We used the nonparametric 1-sample Wilcoxon signed rank test to determine whether the scores from each of the 3 radiologists for each of the 3 categories differed from zero,

Table 2: Summary of study cohort

Patient	Sex	Age	Clinical Indication for Brain MRI Exam
1	M	2 yr 6 mo	Optic nerve hypoplasia
2 ^a	M	1 yr 7 mo	Edema, craniosynostosis repair, head swelling, fever
3 ^b	M	12 yr 7 mo	Hydrocephalus
4	M	10 yr 0 mo	Suspicion of brain tumor
5	M	3 yr 2 mo	Hemiparesis dominant left side
6 ^{a,b}	F	9 yr 4 mo	Spell convulsion
7	M	13 yr 8 mo	Suspicion of brain tumor
8 ^a	F	5 yr 5 mo	Hearing loss
9	M	0 yr 10 mo	Adrenogenital disorders
10 ^a	M	3 yr 2 mo	Bilateral retinoblastoma
11	M	4 yr 0 mo	Cerebellar ataxia
12	M	0 yr 7 mo	Adduction deficit
13	F	8 yr	Hearing loss
14	M	8 yr 7 mo	Papilledema
15 ^a	M	7 yr 8 mo	Low-grade glioma
16	M	5 yr 2 mo	Central nervous system tumor mass
17	F	2 yr 6 mo	Fever, meningitis
18 ^a	F	2 yr 1 mo	Epilepsy
19	F	4 yr 3 mo	Headache
20 ^a	M	11 yr 2 mo	Ablepharon-macrostomia syndrome, encephalopathy
21 ^a	M	9 yr 1 mo	Malignant neoplasm of brain
22	M	11 yr 3 mo	Headache
23 ^a	M	3 yr 1 mo	Brain tumor, infection
24 ^a	M	6 yr 7 mo	Intracranial abscess, mastoiditis

^a Patients with space-occupying lesions or signal abnormalities seen on MRI.

^b Patients who were not sedated.

where zero implied similarity between the spiral SE and Cartesian TSE images. A *P* value $< .05$ was chosen to reflect statistical significance. Interradiologist agreement was evaluated with the Fleiss κ coefficient.

RESULTS

Tables 1 and 2 summarize pertinent imaging parameters and descriptors of the study cohort, respectively. Figure 2 illustrates SNR measurements in the gray and white matter of healthy volunteers between spiral SE and Cartesian TSE sequences. The *t* test did not yield a statistically significant difference in SNR between spiral SE and Cartesian TSE (*P* = 0.32) when considering all gray and white matter ROIs. However, the SNR of the spiral SE approach was slightly lower, and the SNR of the spiral SE to Cartesian TSE was 89.3% \pm 3.0%. The main reason for the lower SNR with the spiral SE acquisition is its shorter scanning time (Table 1).

Scores from radiologists' evaluations are outlined in Fig 3. While the categories of flow artifact reduction and subjective preference included all 24 patient datasets, the category of lesion conspicuity was limited to 10 cases because only these cases were identified as having either contrast-enhancing (6 cases) or non-contrast-enhancing (4 cases) pathology, none of which was in the posterior fossa. All 3 observers rated spiral SE better than Cartesian TSE in terms of flow artifacts in 23 of the 24 cases (Fig 3A). In the remaining case, 2 readers rated both techniques as equivalent in flow artifact reduction, while the third reader preferred the proposed spiral SE. The improvement in flow artifact reduction with spiral SE over Cartesian TSE was statistically significant (*P* $< .001$).

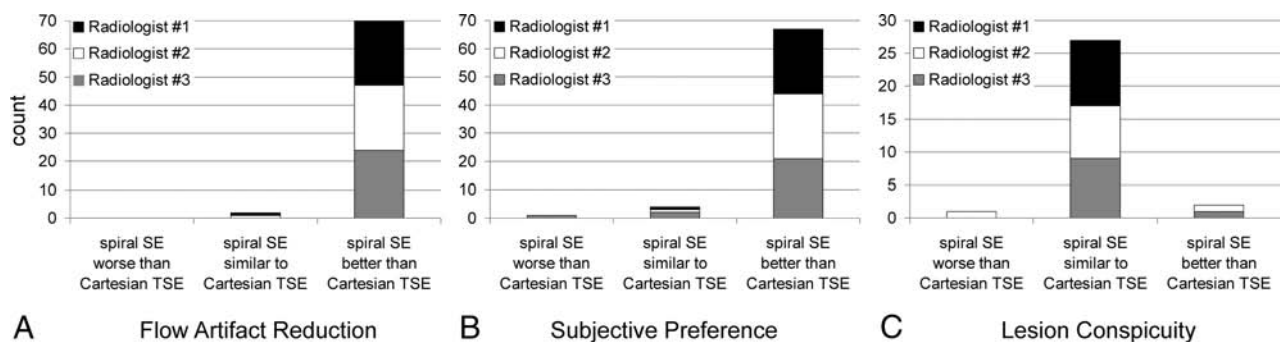


FIG 3. Barplots summarizing the score assessment of patient data by 3 radiologists, in terms of flow artifact reduction (A), subjective preference (B), and lesion conspicuity (C). In the categories of flow artifact reduction (A) and subjective preference (B), the maximum count per radiologist is 24, 1 for each patient. Thus, the cumulative count is 72. In the category of lesion conspicuity (C), which was evaluated in a subgroup of 10 patients, the maximum count of each radiologist is 10, with a cumulative total of 30. Note the preference of the spiral SE images in A and B.

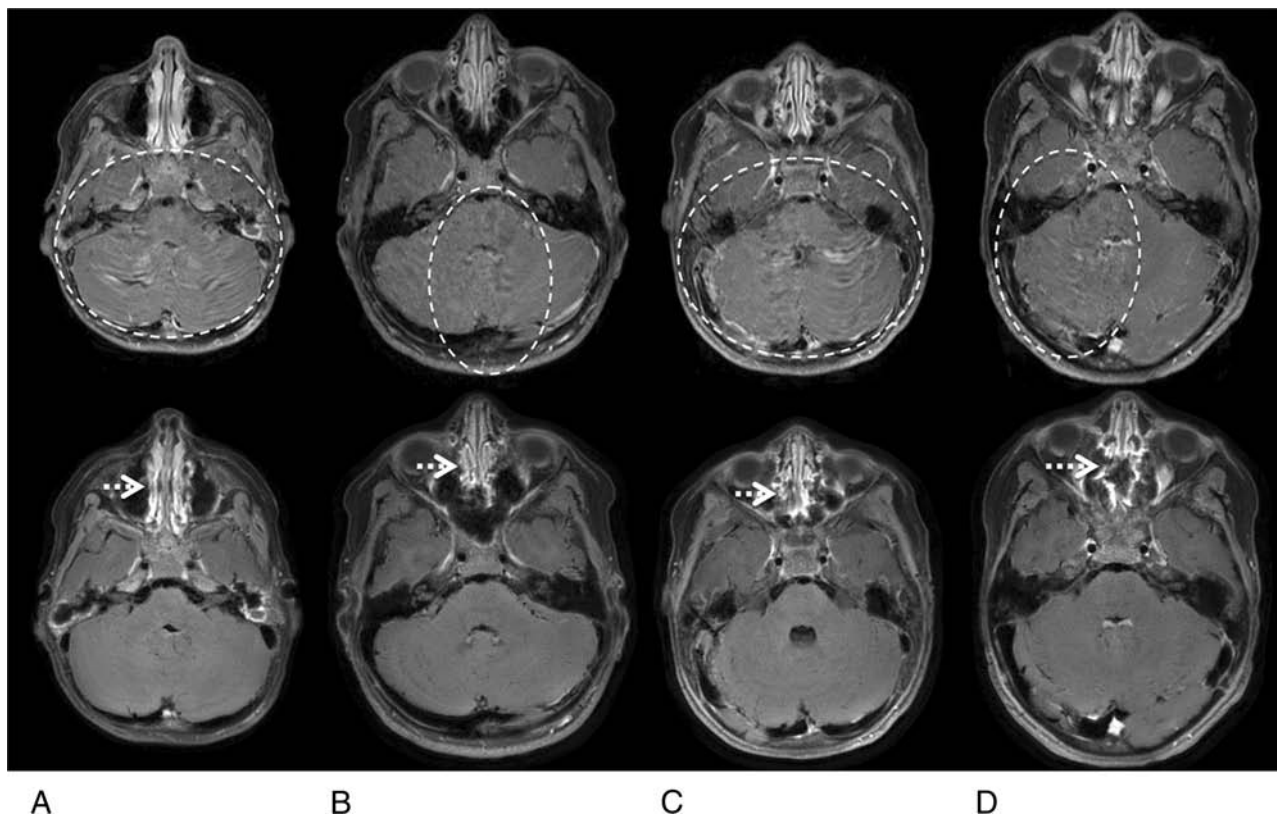


FIG 4. Representative water-reconstructed images from patients 1 (A), 4 (B), 18 (C), and 22 (D), comparing flow artifacts between Cartesian TSE (top) and spiral SE sections (bottom). In the Cartesian TSE images, the *dashed circles* denote areas with noticeable flow artifacts, seen predominantly as signal ghosting. It is evident that the flow artifacts are substantially reduced in the corresponding spiral SE images, especially in the cerebellum where strong flow artifacts are typically observed in Cartesian TSE. The *dotted arrows* in the spiral SE images point to residual blurring in the nasal cavity, in comparison with the sharper appearance seen in the Cartesian TSE data.

In 21 of the 24 cases, the 3 radiologists preferred spiral SE over Cartesian TSE in terms of subjective preference (Fig 3B). In 2 cases, 2 reviewers preferred spiral SE, while the third reviewer rated both techniques equivalent. In another case, one reviewer preferred Cartesian TSE, while the other 2 reviewers rated both techniques equivalent. A statistically significant improvement with spiral SE over Cartesian TSE in subjective preference was observed ($P < .001$).

In 8 of the 10 cases with lesions, spiral SE was rated by all 3 observers as equivalent to Cartesian TSE in providing lesion conspicuity (Fig 3C). In 1 case, 2 observers preferred spiral SE, while

the third observer scored the 2 techniques as equivalent. In another case, 2 observers rated the 2 techniques equivalent while the third observer considered Cartesian TSE better. With this limited number of data points, the scores for lesion conspicuity between spiral SE and Cartesian TSE were not statistically different. The interreader Fleiss κ coefficient was 0.79 (95% confidence interval, 0.65–0.93) for all 3 categories of flow artifact reduction, subjective preference, and lesion conspicuity.

Figure 4 illustrates representative examples, highlighting the suppression of flow artifacts with the proposed 2D spiral SE sequence. The Cartesian TSE images showed substantial flow arti-

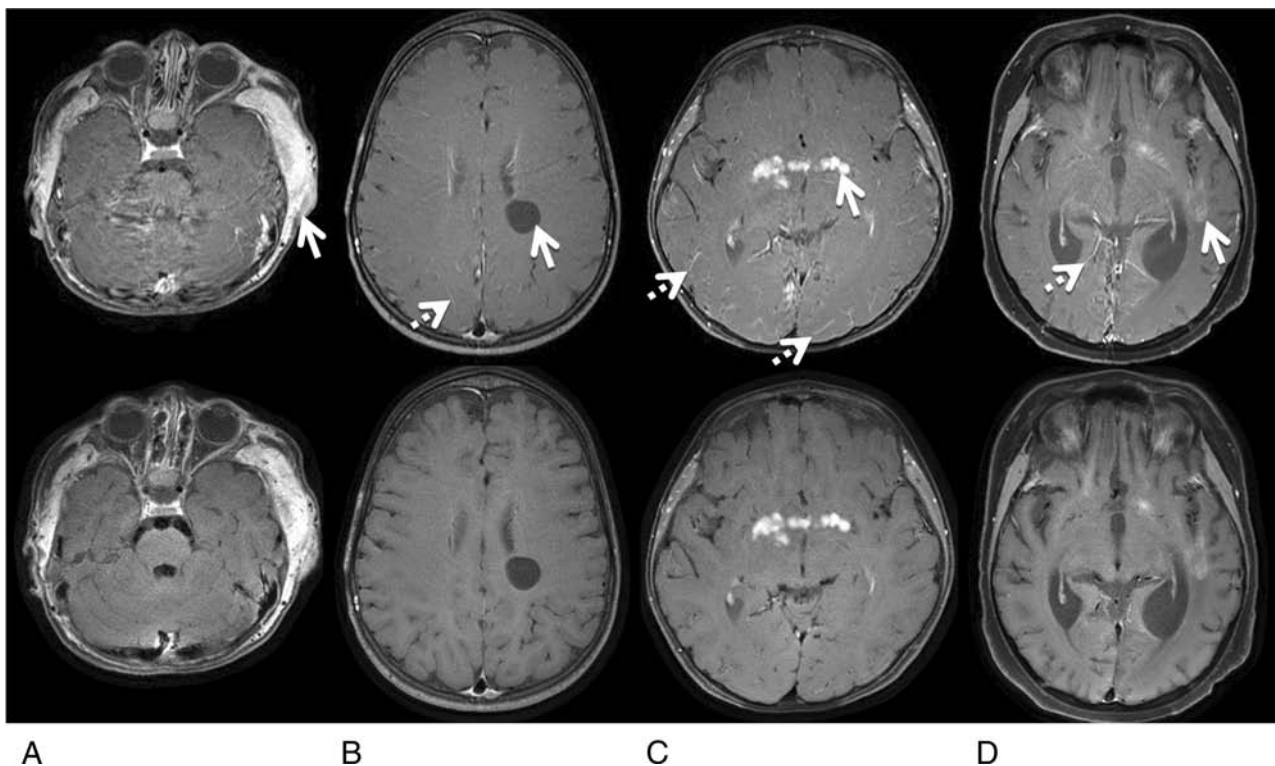


FIG 5. Representative images with lesions from patients 2 (A), 8 (B), 15 (C), and 20 (D), comparing lesion conspicuity between Cartesian TSE (*top*) and spiral SE sections (*bottom*). A, The MR image shows extracranial soft-tissue enhancement related to postsurgical infection. B, The patient has a nonenhancing neural cyst. C, The patient has an enhancing hypothalamic glioma. D, The patient has scattered enhancing intracranial leukemia tumors. The *solid arrows* in the Cartesian images point to these lesions, and the *dotted arrows* point to noticeable bright-blood signals in the small vessels that are absent in spiral SE images.

facts from the venous sinuses with resultant poor posterior fossa image quality. These artifacts were not present on the corresponding spiral SE images. Figure 5 shows 4 cases with intra- and extracranial contrast-enhancing and intracranial nonenhancing lesions. Lesion delineation is comparable between the spiral SE and Cartesian TSE data. Other observations include slightly higher gray-white matter tissue contrast and dark blood vessels in spiral SE images, in contrast to Cartesian TSE data.

DISCUSSION

Artifacts from pulsatile blood flow are a potential major concern in postcontrast T1WI Cartesian SE and TSE brain imaging. In this study, we have shown that a 2D spiral SE acquisition is capable of substantially reducing these flow artifacts, without compromising spatial resolution and volumetric coverage. The reduction in flow artifacts is achieved by exploiting the advantages of a spiral k -space readout. The spiral approach provides inherent gradient flow compensation and incoherent manifestation of residual artifacts. Through-plane flow signals were further reduced by the use of crusher gradients along the section-encoding axis. Parallel imaging was not used in this study but can be additionally applied to accelerate both techniques. In this work, spiral data were acquired with 3 TE shifts, which were necessary to achieve a robust water-fat separation.¹⁰ The algorithm¹⁰ with only 2 TE shifts can be used to further reduce scanning time. With this approach, however, an external B0 field map is required.

The SNR of the spiral SE technique was slightly lower than that of Cartesian TSE, albeit with a 2-fold reduction in scanning time.

If SNR is more desirable than the scanning speed, it can be achieved by adjusting the image protocol. For instance, a gain of $\sqrt{2}$ in SNR can be obtained by acquiring data with a signal average of 2, which results in an SNR higher than the Cartesian TE, even though the total scanning time is comparable. Magnetization transfer effects are more pronounced in Cartesian TSE¹³ due to the use of multiple refocusing radiofrequency pulses and a spatial saturation band to spoil the inflow blood signal, which likely explains the gray-white matter contrast being slightly higher in the spiral SE data shown in Fig 5. The clinical utility of this magnetization transfer effect should be evaluated in the future.

The radiologists thought that the primary reason for the spiral images being preferred was due to the reduction in flow-related artifacts. Another factor was the black-blood vascular signal in the spiral data. Given the substantial reduction of flow artifacts and consistent black-blood signals with spiral SE data, it is plausible that any lesion obscured by flow artifacts or bright-blood signals in the Cartesian TSE acquisition can be more confidently detected with the spiral SE technique. Additional factors impacted the subjective preference, for instance, other forms of artifacts related to physiologic or bulk motion. These factors collectively contributed to the spiral SE acquisition being preferred over the Cartesian TSE approach by the evaluating radiologists. In current study, we did not adopt a more objective metric to compare the 2 techniques. Larger studies in the future should assess more objective and quantitative comparisons (eg, tissue contrast).

In this study, the 3 reviewing radiologists, though blinded and

randomly presented with the data, may have been able to identify the spiral images on the basis of the significant reduction in flow artifacts. This potential source of bias in the evaluation might be difficult to avoid.

A limitation of this study was that no patients were found with lesions in the posterior fossa that was affected by strong flow artifacts in the Cartesian TSE datasets, and enhancing lesions were only found in a small number of cases. Although the study was limited to a cohort of pediatric patients, the present work is applicable to the general adult population. Future studies include the expansion to a large cohort of adult patients and include patients with brain parenchymal and high-flow vascular lesions. With a large patient population, seeing pathologies in the posterior fossa to prove the value of the improved flow artifact suppression with spiral SE is likely. Seeing more enhancing lesions is expected, making it feasible to statistically investigate the enhancement with spiral SE.

Another limitation was the fixed acquisition order (ie, Cartesian TSE followed by spiral SE after contrast administration). A randomized order would have permitted a more thorough analysis of the performance of the spiral SE sequence. In addition, the reference scan for comparison was a 2D Cartesian TSE acquisition, not a longer Cartesian SE pulse sequence. In the clinical setting of our institution, time did not permit performing the latter. In this study, spiral SE was not compared with gradient-echo-based sequences, such as Cartesian MPRAGE. Performing such a comparison would be beneficial in future studies.

CONCLUSIONS

We have demonstrated a relatively simple 2D spiral SE approach in T1-weighted postcontrast brain MR imaging that has minimal flow artifacts in comparison with its 2D Cartesian TSE counterpart. 2D spiral SE can be performed more efficiently and provides faster scanning speed than 2D Cartesian TSE, without sacrificing spatial resolution or volumetric coverage.

ACKNOWLEDGMENTS

We thank Amber Pokorney at Phoenix Children's Hospital for assistance with patient data collection.

Disclosures: Zhiqiang Li—RELATED: Grant: As part of the group at the Barrow Neurological Institute, Z.L. received grant support from Philips Healthcare.* Houchun H. Hu—RELATED: Grant: Philips Healthcare (research support).* Jeffrey H. Miller—RELATED: Consulting Fee or Honorarium: Philips Healthcare; Support for Travel to Meetings for the Study or Other Purposes: Philips Healthcare. Dinghui Wang—RELATED: Grant: research support from Philips Healthcare.* James G. Pipe—RELATED: Grant: Philips Healthcare. *Money paid to the institution.

REFERENCES

1. Ahn CB, Kim JH, Cho ZH. **High-speed spiral-scan echo planar NMR imaging-I.** *IEEE Trans Med Imaging* 1986;5:2–7 CrossRef Medline
2. Meyer CH, Hu BS, Nishimura DG, et al. **Fast spiral coronary artery imaging.** *Magn Reson Med* 1992;28:202–13 CrossRef Medline
3. Bernstein MA, King KF, Zhou XJ. *Handbook of MRI Pulse Sequence.* San Diego: Elsevier Academic Press; 2004
4. Nishimura DG, Irarrazabal P, Meyer CH. **A velocity k-space analysis of flow effects in echo-planar and spiral imaging.** *Magn Reson Med* 1995;33:549–56 CrossRef Medline
5. Yacoe ME, Li KC, Cheung L, et al. **Spiral spin-echo magnetic resonance imaging of the pelvis with spectrally and spatially selective radiofrequency excitation: comparison with fat-saturated fast spin-echo imaging.** *Can Assoc Radiol J* 1997;48:247–51 Medline
6. Wang WT, Hu P, Meyer CH. **Black-blood imaging using a spin-echo spiral sequence with flow-spoiling gradients.** In: *Proceedings of the Annual Meeting of International Society for Magnetic Resonance in Medicine*, Seattle, Washington. May 6–12, 2006
7. Brewer KD, Rioux Ja, D'Arcy CN, et al. **Asymmetric spin-echo (ASE) spiral improves BOLD fMRI in inhomogeneous regions.** *NMR Biomed* 2009;22:654–62 CrossRef Medline
8. Dixon WT. **Simple proton spectroscopic imaging.** *Radiology* 1984; 153:189–94 CrossRef Medline
9. Glover GH, Schneider E. **Three-point Dixon technique for true water/fat decomposition with B0 inhomogeneity correction.** *Magn Reson Med* 1991;18:371–83 CrossRef Medline
10. Wang D, Zwart NR, Li Z, et al. **Analytical three-point Dixon method: with applications for spiral water-fat imaging.** *Magn Reson Med* 2015 Mar 11. [Epub ahead of print] CrossRef Medline
11. Kaufman L, Kramer DM, Crooks LE, et al. **Measuring signal-to-noise ratios in MR imaging.** *Radiology* 1989;173:265–67 CrossRef Medline
12. Price RR, Axel L, Morgan T, et al. **Quality assurance methods and phantoms for magnetic resonance imaging: report of AAPM nuclear magnetic resonance Task Group No. 1.** *Med Phys* 1990;17: 287–95 CrossRef Medline
13. Constable RT, Anderson AW, Zhong J, et al. **Factors influencing contrast in fast spin-echo MR imaging.** *Magn Reson Imaging* 1992; 10:497–511 CrossRef Medline

Low-Dose Volume-of-Interest C-Arm CT Imaging of Intracranial Stents and Flow Diverters

P. Yang, A. Ahmed, S. Schafer, D. Niemann, B. Aagaard-Kienitz, K. Royalty, and C. Strother

ABSTRACT

BACKGROUND AND PURPOSE: Volume-of-interest C-arm CT is a novel technique for imaging of intracranial high-contrast objects. We performed this study to evaluate the potential diagnostic value and radiation dose reduction of this technique for imaging of intracranial stents and flow diverters.

MATERIALS AND METHODS: Twenty-seven patients were imaged with a VOI C-arm CT scan following treatment with a flow diverter or stent-assisted coiling. The radiation dose-area product was recorded for VOI scans. For comparison, the dose-area product from 30 previously acquired consecutive full-view DynaCTs was used. Thermoluminescence dosimetry by using 35 evenly distributed thermoluminescence dosimeters in an anthropomorphic head phantom was also performed by using both conventional full field and VOI acquisitions. Three observers were presented with VOI images for assessment of the potential diagnostic value.

RESULTS: The dose-area product measurements showed an exposure reduction of 85% compared with the full field acquisitions used for comparison. The thermoluminescence dosimetry evaluations also showed a considerable dose reduction of 79.8% throughout the volume. For most of the evaluated cases, the observers thought that diagnostically useful information was provided by the VOI images ($\alpha = .810$). Visualization of device details, such as the extent of opening, positioning, wall apposition, and aneurysm coverage, was judged of good diagnostic quality for most cases (88.9%–92.6%).

CONCLUSIONS: In this study, VOI C-arm CT provided high-quality diagnostic images of intracranial stents and flow diverters at a dramatic reduction of radiation exposure. Image content was thought to add useful information. It is a promising method to assess device status during procedures and at follow-up.

ABBREVIATIONS: CACT = C-arm CT; FD = flow diverter; FFOV = full FOV; TLD = thermoluminescence dosimetry

For safe and effective use, careful assessment during and after deployment of intracranial stents and flow diverters is required to ensure full deployment, proper positioning, and full apposition to the vascular wall. These features are important because they may influence further treatment decisions (eg, balloon dilation and anticoagulation during and/or after a procedure). They are also important in predicting postprocedural aneurysm occlusion. Currently, however, clear visualization is

often impossible with standard-projection x-ray imaging and fluoroscopy.

Currently available C-arm CT (CACT) provides high-spatial-resolution images of implantable devices. It has been widely used and is accepted as providing such information.^{1–4} The radiation dose required, however, is approximately twice that of a conventional multidetector row CT of the brain and thus is a limitation of the technique.⁵ This limitation increases in a workflow in which multiple CACT scans are used during a procedure. Several methods are available to reduce the CACT radiation dose. These include x-ray tube current modulation, peak kilovoltage optimization, and x-ray beam collimation.⁶

A different strategy for dose reduction is to reduce the patient exposure in areas of low interest (eg, those away from an implanted device and the related vasculature). Suggested approaches for this strategy range from reducing the dose outside the area of interest by using x-ray beam attenuating techniques or by box collimating to the area of interest. The beam-attenuating

Received May 26, 2015; accepted after revision August 18.

From the Department of Neurosurgery (P.Y.), Changhai Hospital, Second Military Medical University, Shanghai, China; Departments of Radiology (P.Y., C.S.) and Neurological Surgery (A.A., D.N., B.A.-K.), University of Wisconsin School of Medicine and Public Health, Madison, Wisconsin; and Siemens Medical Solutions USA (S.S., K.R.), Hoffman Estates, Illinois.

Please address correspondence to Pengfei Yang, MD, Department of Neurosurgery, Changhai Hospital, Second Military Medical University, Shanghai, China; Department of Radiology, University of Wisconsin-Madison, Madison, Wisconsin; e-mail: 15921196312@163.com, pyang75@wisc.edu

<http://dx.doi.org/10.3174/ajnr.A4590>

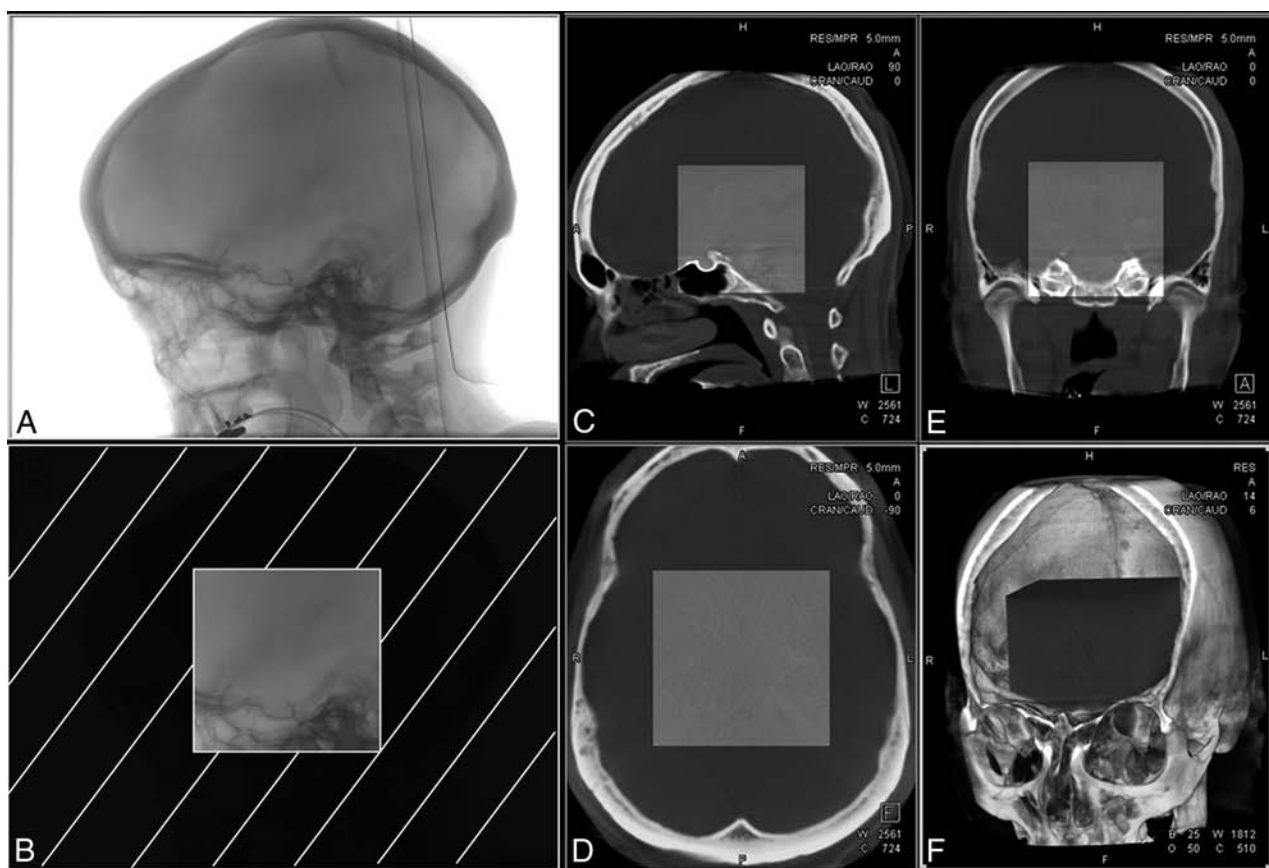


FIG 1. Difference between full FOV CACT and VOI CACT acquisitions. Projection image for FFOV captures of the full head of the patient (A), while the box-collimated VOI scan (B) only exposes and acquires data from a small area of the patient (12% of the FFOV). Triplanar section cuts (C–E) and volumetric illustration (F) demonstrate the fused FFOV CACT and the VOI CACT (central area).

approach yields high-quality 3D images in the volume of interest, while the areas outside the VOI have, because of an increase in noise, reduced image quality.^{6–8} Conventional box-collimated methods have problems stemming from object truncation, usually resulting in compromised image quality of the reconstructions. Attempts to limit truncation artifacts by using mathematic techniques to account for the missing data have had limited success, with the postprocessed image quality still being inferior to reconstructions in which truncation was not present.^{9–13}

Recently, however, a newly introduced method has yielded results in which image quality of a device inside a tightly collimated VOI differs little, if at all, from reconstructions made by using nontruncated VOI acquisitions.^{14,15} In this study, we investigated the radiation dose reduction achieved by using the technique and the potential benefits that such images might provide during endovascular treatment of intracranial aneurysms with flow diverters or stent-assisted coiling.

MATERIALS AND METHODS

Patient Selection

Twenty-seven consecutive patients having VOI CACT scans were identified from an institutional review board–approved data base. VOI CACT was routinely performed after flow-diverter placement and often after stent placement for stent-assisted coiling of aneurysms. Our sample includes a heterogeneous population of patients with variations in aneurysm

locations, vessel sizes, pathologies, and device types. These reflect the distribution of pathologies seen during this interval. Most pathologies were aneurysms (25/27, 92.6%) followed by stenosis (2/27, 7.4%). Included are 21 saccular aneurysms (77.8%) and 4 fusiform aneurysms (14.8%). Of the 25 aneurysms, 10 (40%) were treated with conventional stent-assisted coiling and 15 (60%) were treated with flow diversion. All aneurysms in this series were unruptured. The devices used were either the Neuroform EZ Stent System (Stryker Neurovascular, Kalamazoo, Michigan), the Enterprise self-expanding stent (Codman & Shurtleff, Raynham, Massachusetts), or the Pipeline Embolization Device (Covidien, Irvine, California).

Data Acquisition

A VOI acquisition was performed as desired by the treating physician during an intervention (eg, post-flow-diverter placement or end point of treatment). In all acquired datasets, the patient was positioned in a head-first, supine position and the injection catheter was placed at the origin of the artery supplying the vascular structure that had been treated. The volume-of-interest scan is a variation of a high-quality CACT (DynaCT; Siemens, Erlangen, Germany), modified by introducing lateral and vertical collimation, effectively reducing the image FOV by either 28% or 12% (Fig 1).

For our study, the 12% collimation mode was used exclusively, with collimators placed automatically by the system on selection

of the VOI examination protocol by the operator. The contrast-injection protocol was 40 mL of iohexol (Omnipaque, 300 mg/L iodine; GE Healthcare, Piscataway, New Jersey) diluted to between 20% and 50% and injected at the rate of 2 mL/s with an x-ray delay of 2 seconds. From experience, this protocol is known to provide good visualization of the vascular structures without obscuring visualization of an implanted device. The acquisition parameters for the VOI acquisitions were 70 kV(peak) and 1.2 $\mu\text{Gy}/\text{Frame}$. The acquisition parameters for the 30 previously acquired full FOV (FFOV) DynaCTs were identical to these factors.

Image Postprocessing

Reconstructing truncated projection data by using conventional projection image preprocessing and a Feldkamp back-projection algorithm results in an incorrect Hounsfield unit and a bright ring with a broad halo at the boundary of the reconstructed image. To avoid these artifacts, the VOI technique uses the approximate, truncation-robust algorithm for CT, which replaces the projection image-preprocessing step used in the conventional reconstruction (the main contributor to the aforementioned image artifacts) with a Laplacian derivative filter followed by a nonlocal 2D residual filter.^{14,15} The Laplacian derivative filter minimizes the signal drop at the edges of the recorded images, which is the main contributor to image artifacts. Volumetric images reconstructed from truncated data by using this method yield highly similar characteristics and image content (ie, image quality) compared with nontruncated acquisitions.¹⁴ All acquired datasets were retrospectively processed by using a prototype software implementation of this algorithm.

Dose Measurement

Common x-ray radiation measures reported from examinations performed in the angiography suite are dose-area product (milligray \times square centimeter), a product of the radiation dose measured at the x-ray tube exit window and the exposed area, and skin exposure (milligray), an estimate based on standard calibration measurements and system position. These static measurements do not yield a good understanding of how the radiation dose to the patient is distributed during a rotational scan acquisition. To supplement this information and to gain a better understanding of the dose distribution during a VOI CACT acquisition, for our study, we used an anthropomorphic head phantom and thermoluminescence dosimetries (TLDs).

The head phantom consisted of a human skull embedded in tissue-mimicking material (Rando Head Phantom; The Phantom Laboratory, Salem, New York) with evenly distributed bore holes allowing the placement of radiation detectors. TLDs are radiation-sensitive chips (1 cm in diameter, 0.5 mm high) that emit stored ionizing radiation as light when heated. Thirty-five TLDs were placed symmetrically throughout the phantom. The phantom was then placed on the table of a clinical biplane C-arm system (DynaCT; Siemens), and independent measurements were made for the conventional full FOV DynaCT rotational acquisitions and a 12% square collimated VOI mode that was identical to the VOI acquisition mode used for the clinical subjects. Acquisition parameters were set to the following: 200° scan range, 496 projection images, 70 kVp, and 1.2 $\mu\text{Gy}/\text{Frame}$. For

the phantom studies, 3 rotational acquisitions were performed in an effort to minimize errors resulting from possible x-ray tube output fluctuations. The exposed TLDs were evaluated by an accredited laboratory (Calibration Lab, Madison, Wisconsin). These TLD results were read in custom-designed software and interpolated across the phantom by using a second-order polynomial function. While this first-order approximation cannot fully account for the attenuation and scatter characteristics of different tissues, it gives the observer a good representation of the distribution of the radiation exposure.¹⁶ Finally, the dose-area products of 30 consecutive full field of view DynaCTs were recorded and used for comparison with the dose-area products of the VOI acquisitions.

Image Evaluation

Three experienced neuroendovascular surgeons independently performed a subjective evaluation of the VOI images. For each case, the reviewers were given images from both volume-rendered and multiplanar-rendered reconstructions and a video showing manipulation of the 3D volumes in a way that best demonstrated the device and its relationship with the relevant vasculature. All the reviewers were asked to complete an evaluation form assessing the following details by using a 2-point rating scale (ie, yes or no): Did the VOI CACT images determine whether the device was completely open, the apposition of the device to the arterial wall, the position of the device related to the aneurysm ostium, visualization of the entire device configuration after deployment, and clear visualization of the arteries of interest? No other clinical data were provided to the reviewers.

Statistics

The statistical analysis was performed by using SPSS 20.0 (IBM, Armonk, New York). The qualitative evaluation data were presented as percentages. Intraclass correlation was performed, and Cronbach α coefficients were calculated to evaluate the interobserver consistency for each qualitative variable. The interobserver consistencies were described as unacceptable ($\alpha < .5$), poor ($.5 \leq \alpha < .6$), acceptable ($.6 \leq \alpha < .7$), good ($.7 \leq \alpha < .9$), and excellent ($\alpha \geq .9$).

RESULTS

Dose Measurement

TLD radiation dose measurements yielded an average dose of 74.5 mGy (median, 68.8 mGy; range, 32.5–179.9 mGy) for full FOV DynaCT and 15.4 mGy (median, 7.9 mGy; range, 2.1–54.5 mGy) for VOI CACT. An evaluation of dose distribution across identical locations showed a dose reduction of $\sim 40\%$ at the back of the head (x-ray tube rotating under the table) and up to 90% at the front of the head (Fig 2). The average reduction in radiation dose was 79.8% (median, 88.9%; range, 36.5%–97.5%). A comparison of dose-area product measurements as reported for the 30 previously acquired full FOV DynaCT studies with dose-area product measured in the VOI acquisitions showed a similar reduction of $\sim 85\%$ for the VOI studies. From our results, the average radiation dose-area product of a VOI acquisition recorded at the tube exit window was 1140 $\mu\text{Gy} \times \text{m}^2$; this is equivalent to that of a single 10-second biplane 2D DSA angiogram.⁵

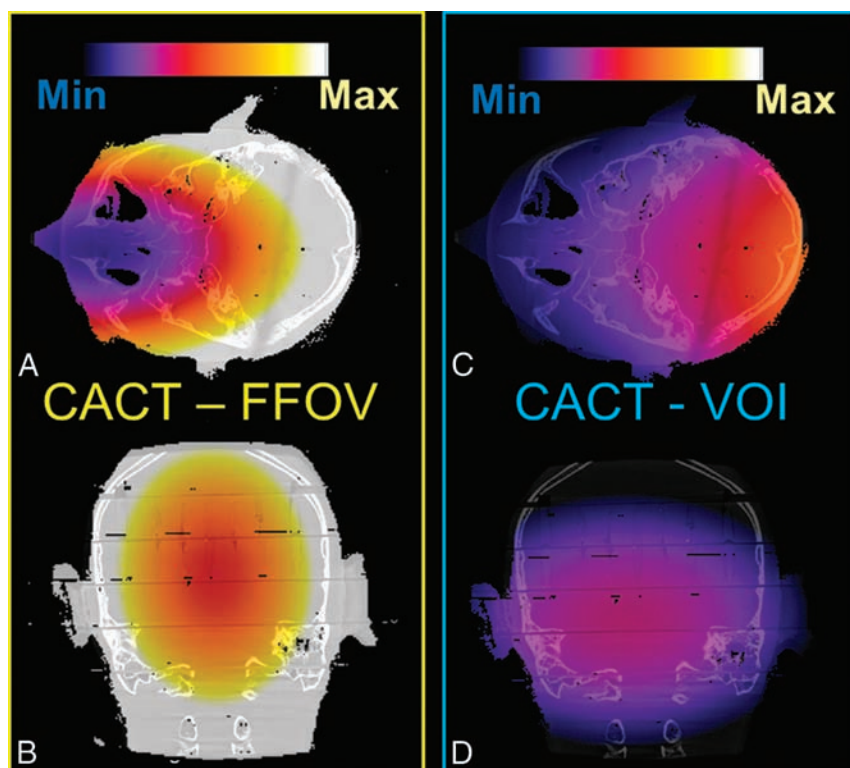


FIG 2. Comparison of dose distribution between FFOV CACT (A and B) and VOI CACT with an exposure area of 12% of the FFOV acquisition (C and D). All images are displayed on the same scale, normalized to the maximum radiation dose measured in the FFOV CACT image. The shape of the dose distribution is similar between both modes, with substantial reduction in the dose for the VOI CACT, especially at the front of the head. Min indicates minimum; Max, maximum.

Results of qualitative evaluation of VOI CACT images from 3 independent observers

Evaluating Details	Observer 1	Observer 2	Observer 3	Cronbach α
Clinically useful information gained	24/27, 88.9%	24/27, 88.9%	25/27, 92.6%	.810
Determination of stent opening	25/27, 92.6%	19/27, 70.4%	23/27, 85.2%	.628
Determination of stent apposition	23/27, 85.2%	19/27, 70.4%	21/27, 77.8%	.766
Determination of stent position	18/27, 66.7%	18/27, 66.7%	26/27, 96.3%	.601
Good visualization of entire stent	25/27, 92.6%	21/27, 77.8%	22/27, 81.5%	.734
Good visualization of arteries of interest	25/27, 92.6%	17/27, 63.0%	21/27, 77.8%	.761

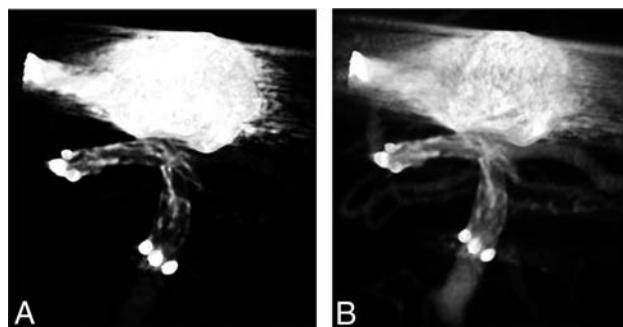


FIG 3. A volume-rendering image (A) shows the open cell design of a Neuroform EZ stent for the treatment of a basilar tip aneurysm. Another image with a different window level (B) shows the stent struts protruding into the left superior cerebellar artery.

Qualitative Image Evaluation

The qualitative evaluation results of all 3 independent observers and statistical results of intraclass correlations are presented in

the Table. For all 6 evaluated variables, acceptable-to-excellent interobserver agreements were observed. For most cases (88.9%–92.6%), 3 observers were in good agreement ($\alpha = .810$) that VOI CACT was clinically useful.

DISCUSSION

In this small series, we have shown that the VOI can provide information that is not available from conventional 2D DSA and fluoroscopy, such as full stent deployment, good wall apposition, optimal stent position, and full ostium coverage. Such information may impact the safety and efficacy of stent-assisted coiling. It thus seems likely that the content of VOI images may influence treatment decisions both during and after an intervention (eg, posttreatment anticoagulation regimen, balloon dilation of a stent, placement of a second stent, and so forth). We have also demonstrated that this information may be achieved by using a dramatically reduced radiation dose compared with conventional full FOV CACT imaging.

Clinical Use of VOI

In our study, independent observer evaluations showed good agreement among 3 observers on the ability of VOI to visualize the fine details of a device and its relationships to a lesion and the adjacent vasculature. These details include the following: First, device configurations such as pore distribution; cell type (which makes the identification of different stents possible); and degree of stent opening, kinking, and fracture (Fig

3). Before the advent of CACT, information on how stent struts are configured within a stent could only be inferred indirectly (eg, from the deflections of a microguidewire as it was advanced through the device). Soon after the introduction of CACT, reports appeared showing the ability of this technology to create high-spatial-resolution images of these high-contrast objects.¹⁷ With VOI CACT, microstructural changes of devices can be visualized, allowing a more complete understanding of these variations in stent configurations. The use of contrast in conjunction with a VOI acquisition allows visualization of these features and their relationship to the lesion being treated and the adjacent vasculature. However, it is still unclear how this information would affect posttreatment antiplatelet and anticoagulation regimens. Second, these details also include the relationships between a device and a vessel, such as the apposition of the stent to the vessel wall, and its positioning relative to an aneurysm ostium. These features were also clearly seen with this technique. Although 2D angiography

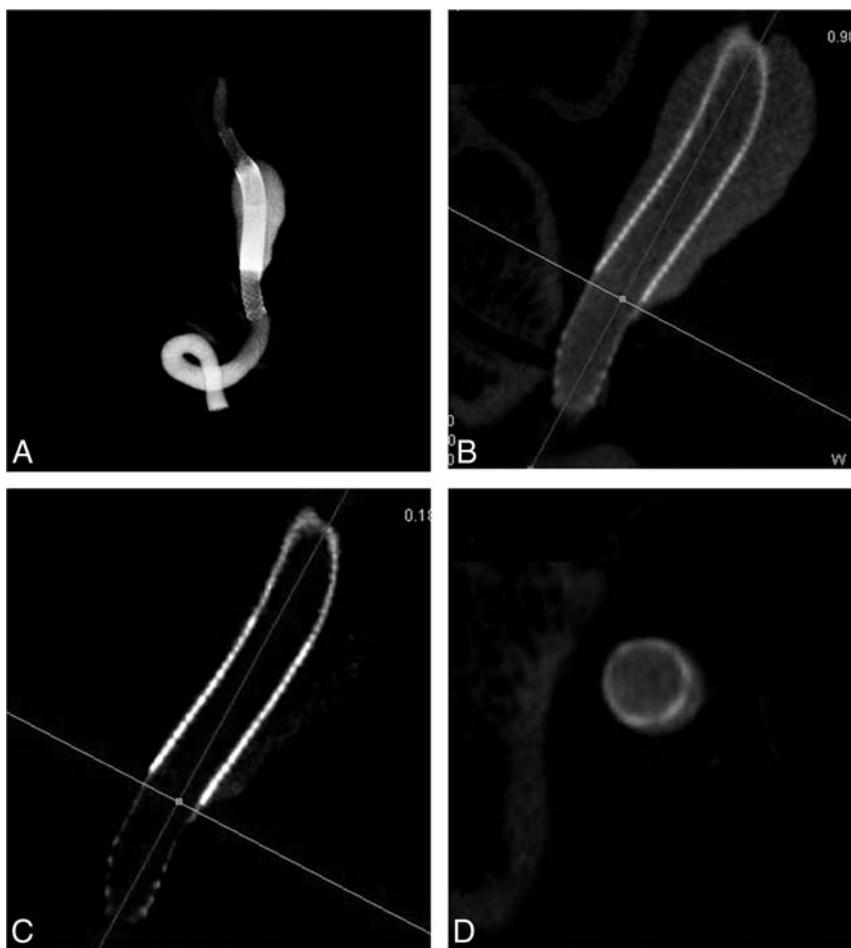


FIG 4. A volume-rendering image (A) shows double flow diverters (Pipeline Embolization Device) for the treatment of a fusiform aneurysm located at the V4 segment of the vertebral artery. Horizontal brighter lines in images of different window levels (B and C) indicate the most proximal part of aneurysm, which is not covered by double Pipeline Embolization Devices. The corresponding axial view (D) clearly shows that the aneurysm is not fully covered by double layers, which may indicate the malposition of the second FD and require further adjustment or implanting another FD.

and fluoroscopy provide some information about these features, in our experience, the accuracy and ease of stent visualization is not nearly as good as that achieved with VOI CACT (Figs 4 and 5).

VOI CACT performed in conjunction with diluted contrast also provides fine details about both a Pipeline Embolization Device mesh (ie, telescoped or stretched) and a Pipeline Embolization Device or stent relationship with an aneurysm ostium (Fig 4). According to previous reports,^{18,19} the actual porosity of the flow diverter (FD) may be calculated or closely approximated on the basis of the number of the intersections, the angle between the filaments, and the known filament width. This information may potentially be very useful for predicting the angiographic outcome of the treated aneurysms and by providing real parameters for computational fluid dynamics simulations. However, this application will be limited in instances in which there is either the use of multiple FDs or FDs and coils.

Previous studies have shown that image quality of VOI CACT may be further improved, compared with conventional CACT,^{6,7} due to the inherent reduction of scatter radiation achieved by collimation. However, the image quality of VOI CACT can also be degraded because of other factors. For example, beam-hardening

artifacts may arise because of such factors as insufficiently diluted contrast medium or the presence of platinum coils and platinum marker tips on a microcatheter or stent. Theoretically, the contrast concentration used should be as low as possible while still providing adequate opacification of the vessel. Because the elements of different devices have different radio-opacities, the optimal contrast concentration will vary somewhat from case to case; in our study, the contrast concentration ranged from 20% to 50%. Pipeline Embolization Devices and stents used for stent-assisted coiling cause few artifacts, whereas platinum coils, depending on the packing density, may cause severe degradation of the image quality. Nonetheless, depending on the aneurysm morphology, the packing density and, most important, the orientation of the aneurysm to the stent, clinically useful information may still often be obtained, even in the presence of these artifacts. To minimize artifacts of this nature, metal artifact-reduction techniques can be used.²⁰ In our study, one of our limitations was that we did not evaluate the use of these algorithms. Another limitation for understanding the full clinical utility of this technique is that with currently available stents, full deployment can only be obtained after detachment from the delivery system. This drawback only allowed us to perform a retrospective (eg, postdeployment) analysis

rather than use VOI to assess positioning and deployment before a decision had been reached to implant a device. As more devices become available that may be fully deployed before detachment, we expect the VOI to assume an even more important role in monitoring of interventions.

Radiation Dose Reduction

Earlier studies have shown the potential of using VOI CACT as an effective radiation-saving technique in clinical applications—for example, imaging high-contrast osseous structures such as the inner ear^{21,22} and implants such as intracranial stents. Although these previous studies have shown dramatic reduction of the radiation dose by using VOI CACT, the diagnostic utility and dose reduction have not, to our knowledge, been evaluated in an endovascular clinical practice. Because the radiation dose is directly related to the size of collimated FOV, the dose may be chosen according to the requirements of the scan (ie, it can potentially be further reduced compared with the reduction achieved in this study). The low radiation burden associated with a VOI acquisition, in our opinion, largely removes the limitation of performing multiple acquisitions, as needed, during a procedure.

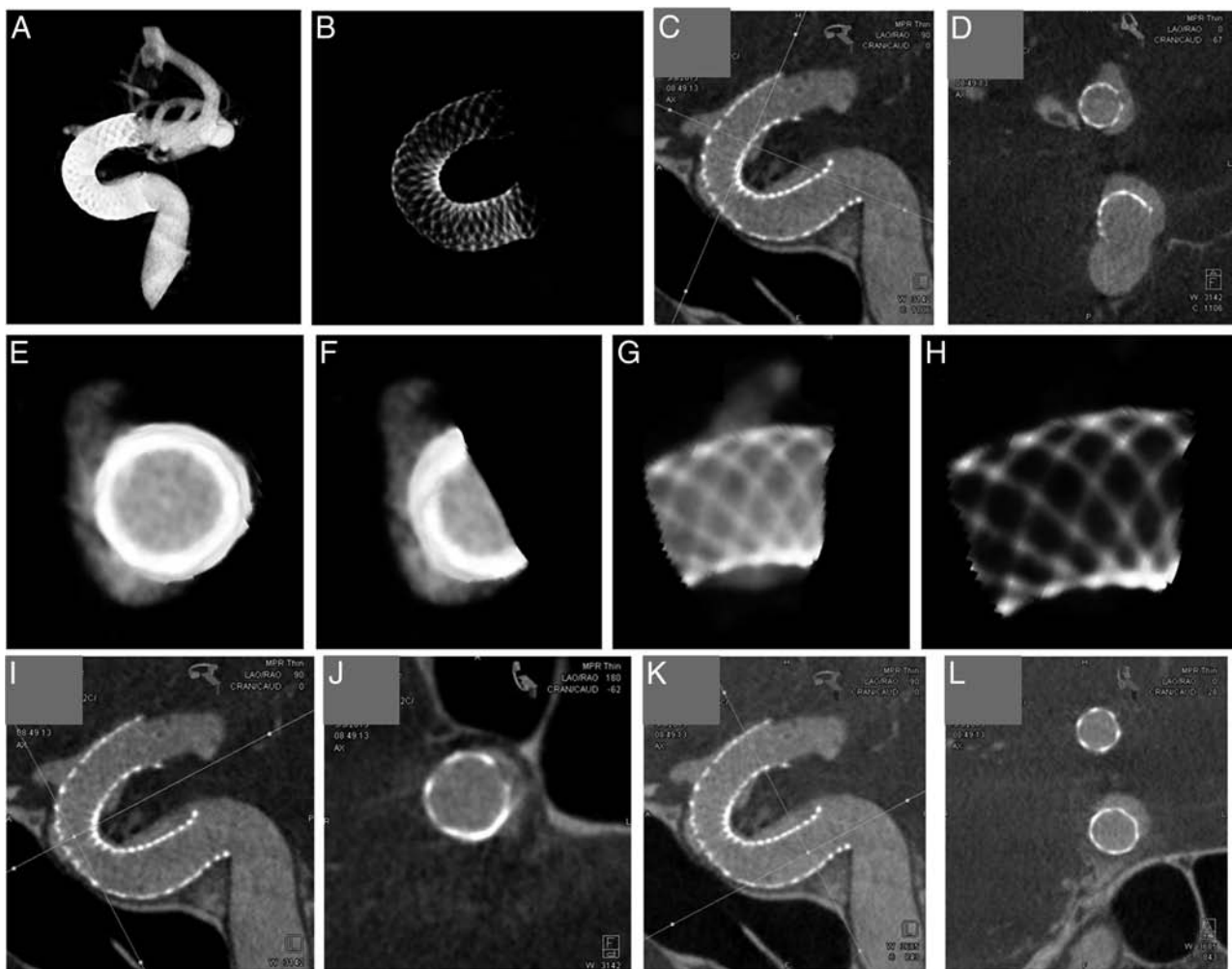


FIG 5. Images (A and B) show a Pipeline Embolization Device for the treatment of an anterior wall aneurysm of the ICA. Horizontal line (C) indicates the position of the image (D), which shows the opening status of the FD and its real coverage of the aneurysm. Another volume-rendering image (E) shows the ROI with the aneurysm and FD. After we cut out the contralateral part of the ROI (F), turned approximately 90° (G), and adjusted the window level (H), the image shows fine details about the mesh, which may facilitate the calculation of the actual porosity of the FD covering the aneurysm. The horizontal line in I and the vertical line in K indicate the position of images J and L, respectively, which show the poor apposition of the FD, which may be neglected on traditional 2D angiography or fluoroscopy.

CONCLUSIONS

The VOI CACT imaging technique offers a dramatic reduction in radiation to the patient while still providing high-quality images of implanted devices. The information provided by these images has clinical significance that may influence treatment during and following an intervention. The dramatic reduction of the radiation dose may allow multiple image acquisitions (if needed) of focused anatomic regions during both critical stages of device deployment and subsequent angiographic follow-up.

Disclosures: Sebastian Schafer—RELATED: Other: employee of Siemens USA. Beverly Aagaard-Kienitz—RELATED: Other: Siemens.* Comments: This was a prototype, so research support regarding this software was provided by Siemens; UNRELATED: Consultancy: Occasionally, I am an unpaid advisor to Siemens. Kevin Royalty—RELATED: Employment: I am a full-time employee of Siemens USA. Charles Strother—RELATED: Other: Under a master research agreement between Siemens and the University of Wisconsin School of Medicine and Public Health, I receive research support*; UNRELATED: Under a master research agreement between Siemens and the University of Wisconsin School of Medicine and Public Health, I receive research support.* *Money paid to the institution.

REFERENCES

1. Benndorf G, Strother CM, Claus B, et al. Angiographic CT in cerebrovascular stenting. *AJNR Am J Neuroradiol* 2005;26:1813–18 Medline
2. Kalender WA, Kyriakou Y. Flat-detector computed tomography (FD-CT). *Eur Radiol* 2007;17:2767–79 CrossRef Medline
3. Richter G, Engelhorn T, Struffert T, et al. Flat panel detector angiographic CT for stent-assisted coil embolization of broad-based cerebral aneurysms. *AJNR Am J Neuroradiol* 2007;28:1902–08 CrossRef Medline
4. Kizilkilic O, Kocer N, Metaxas GE, et al. Utility of VasoCT in the treatment of intracranial aneurysm with flow-diverter stents. *J Neurosurg* 2012;117:45–49 CrossRef Medline
5. Struffert T, Hauer M, Banckwitz R, et al. Effective dose to patient measurements in flat-detector and multislice computed tomography: a comparison of applications in neuroradiology. *Eur Radiol* 2014;24:1257–65 CrossRef Medline
6. Schafer S, Noël PB, Walczak AM, et al. Filtered region of interest cone-beam rotational angiography. *Med Phys* 2010;37:694–703 CrossRef Medline
7. Kolditz D, Kyriakou Y, Kalender WA. Volume-of-interest (VOI) imaging in C-arm flat-detector CT for high image quality at reduced dose. *Med Phys* 2010;37:2719–30 CrossRef Medline

8. Chityala R, Hoffmann KR, Rudin S, et al. **Region of interest (ROI) computed tomography (CT): comparison with full field of view (FFOV) and truncated CT for a human head phantom.** *Proc SPIE Int Soc Opt Eng* 2005;5745:583–90 Medline
9. Cho S, Bian J, Pelizzari CA, et al. **Region-of-interest image reconstruction in circular cone-beam microCT.** *Med Phys* 2007;34:4923–33 CrossRef Medline
10. Ohnesorge B, Flohr T, Schwarz K, et al. **Efficient correction for CT image artifacts caused by objects extending outside the scan field of view.** *Med Phys* 2000;27:39–46 Medline
11. Van Gompel G, Tisson G, Van Dyck D, et al. **A new algorithm for 2D region of interest tomography.** *Proc SPIE* 2004;5370:2105–13 CrossRef
12. Faridani A, Finch DV, Ritman EL, et al. **Local tomography II.** *SIAM J Appl Math* 1997;57:1095–127 CrossRef
13. Katsevich A. **Cone beam local tomography.** *SIAM J Appl Math* 1999;59:2224–46 CrossRef
14. Xia Y, Dennerlein F, Bauer S, et al. **Scaling calibration in region of interest reconstruction with the 1D and 2D ATRACT algorithm.** *Int J Comput Assist Radiol Surg* 2014;9:345–56 CrossRef Medline
15. Dennerlein F, Maier A. **Approximate Truncation Robust Computed Tomography: ATRACT.** *Phys Med Biol* 2013;58:6133–48 CrossRef Medline
16. Schafer S, Nithiananthan S, Mirota DJ, et al. **Mobile C-arm cone-beam CT for guidance of spine surgery: image quality, radiation dose, and integration with interventional guidance.** *Med Phys* 2011;38:4563–74 CrossRef Medline
17. Benndorf G, Klucznik RP, Strother CM. **Images in cardiovascular medicine: angiographic computed tomography for imaging of underdeployed intracranial stent.** *Circulation* 2006;114:e499–500 CrossRef Medline
18. Wang K, Yuan S. **Actual metal coverage at the neck is critical for flow-diverting stents in treating intracranial aneurysms.** *AJNR Am J Neuroradiol* 2013;34:E31–32 CrossRef Medline
19. Hong B, Wang K, Huang Q, et al. **Effects of metal coverage rate of flow diversion device on neointimal growth at side branch ostium and stented artery: an animal experiment in rabbit abdominal aorta.** *Neuroradiology* 2012;54:849–55 CrossRef Medline
20. van der Bom IM, Hou SY, Puri AS, et al. **Reduction of coil mass artifacts in high-resolution flat detector conebeam CT of cerebral stent-assisted coiling.** *AJNR Am J Neuroradiol* 2013;34:2163–70 CrossRef Medline
21. Kolditz D, Struffert T, Kyriakou Y, et al. **Volume-of-interest imaging of the inner ear in a human temporal bone specimen using a robot-driven C-arm flat panel detector CT system.** *AJNR Am J Neuroradiol* 2012;33:E124–28 CrossRef Medline
22. Shen Y, Yi Y, Zhong Y, et al. **High resolution dual detector volume-of-interest cone beam breast CT: demonstration with a bench top system.** *Med Phys* 2011;38:6429–42 CrossRef Medline

WEB Treatment of Intracranial Aneurysms: Clinical and Anatomic Results in the French Observatory

 L. Pierot,  J. Moret,  F. Turjman,  D. Herbreteau,  H. Raoult,  X. Barreau,  S. Velasco,  H. Desal,  A.-C. Januel,  P. Courtheoux,  J.-Y. Gauthier,  C. Cognard,  A. Molyneux,  J. Byrne, and  L. Spelle

ABSTRACT

BACKGROUND AND PURPOSE: Flow disruption with the WEB device is a new technique for the endovascular treatment of wide-neck bifurcation aneurysms. To obtain precise data regarding the safety and efficacy of this treatment with high-quality methodology, the prospective French Observatory study was conducted. Analysis of these data is presented, including 1-year follow-up.

MATERIALS AND METHODS: Patients with bifurcation aneurysms for which WEB treatment was indicated were included in this prospective, multicenter Good Clinical Practice study. Clinical data, including adverse events and clinical status at 1 month and 1 year, were collected and independently analyzed by a medical monitor. An independent core laboratory evaluated the anatomic results at 1 year following the procedure.

RESULTS: Ten French neurointerventional centers included 62 patients (39 women), 33–74 years of age (mean, 56.6 ± 9.80 years) with 63 aneurysms. Aneurysm locations were the middle cerebral artery in 32 aneurysms (50.8%), anterior communicating artery in 16 (25.4%), basilar artery in 9 (14.3%), and internal carotid artery terminus in 6 (9.5%). Morbidity and mortality at 1 month were, respectively, 3.2% (2/62 patients) and 0.0% (0/62). Morbidity and mortality (unrelated to the treatment) at 1 year were, respectively, 0.0% (0/59) and 3.4% (2/59 patients). At 1 year, complete occlusion was observed in 30/58 aneurysms (51.7%); neck remnant, in 16/58 aneurysms (27.6%); and aneurysm remnant, in 12/58 aneurysms (20.7%).

CONCLUSIONS: This prospective French Observatory study showed very good safety of aneurysm treatment with the WEB, with a high rate of adequate aneurysm occlusion at 1 year (79.3%).

ABBREVIATIONS: DL = Dual-Layer; SL = Single-Layer; SLS = Single-Layer Spherical; WEBCAST = WEB Clinical Assessment of IntraSaccular Aneurysm Therapy

Endovascular treatment is now the first-line therapy for both ruptured and unruptured aneurysms, but aneurysms with a complex anatomy (especially wide-neck aneurysms) are, in some cases, untreatable or difficult to treat with standard coiling.^{1,2}

Received June 15, 2015; accepted after revision July 30.

From the Department of Neuroradiology (L.P.), Hôpital Maison-Blanche, Université Reims-Champagne-Ardenne, Reims, France; Hôpital Beaujon, (J.M., L.S.), Assistance Publique-Hôpitaux de Paris, Clichy, France; Centre Hospitalier Universitaire de Lyon (F.T.), Lyon, France; Centre Hospitalier Universitaire de Tours (D.H.), Tours, France; Centre Hospitalier Universitaire de Rennes (H.R., J.-Y.G.), Rennes, France; Centre Hospitalier Universitaire de Bordeaux (X.B.), Bordeaux, France; Centre Hospitalier Universitaire de Poitiers (S.V.), Poitiers, France; Centre Hospitalier Universitaire de Nantes (H.D.), Nantes, France; Centre Hospitalier Universitaire de Toulouse (A.-C.J., C.C.), Toulouse, France; Centre Hospitalier Universitaire de Caen (P.C.), Caen, France; and Oxford Neurovascular and Neuroradiology Research Unit (A.M., J.B.), Oxford Radcliffe Hospital, Oxford, UK.

The French Observatory was financially supported by Sequent Medical.

Conflict of interest: L.P., D.H., C.C., A.M., and L.S. have proctoring/consulting contracts with Sequent Medical.

Please address correspondence to Laurent Pierot, MD, PhD, Department of Neuroradiology, Hôpital Maison-Blanche, 45, Rue Cognacq-Jay 51092 Reims Cedex; e-mail: lpierot@gmail.com

<http://dx.doi.org/10.3174/ajnr.A4578>

Thus, more complex endovascular techniques have been developed, such as balloon-assisted coiling, stent-assisted coiling, and flow diversion.^{3–9}

Flow disruption is a new endovascular approach, which involves placement of an intrasaccular device (Woven EndoBridge [WEB] aneurysm embolization system; Sequent Medical, Aliso Viejo, California), which modifies the blood flow at the level of the neck and induces aneurysmal thrombosis. The WEB was designed to treat wide-neck and bifurcation aneurysms. The device has been progressively developed from a Dual-Layer version (WEB DL) to Single-Layer (WEB SL) and Single-Layer Spherical (WEB SLS) versions. Treatment with the WEB has been evaluated in several retrospective series showing good safety results.^{10–13} In addition, midterm and long-term anatomic results have been evaluated in retrospective series showing good stability of the treatment.^{14,15}

To have a more rigorous evaluation of the safety and efficacy, 2 prospective, Good Clinical Practice series were initiated simultaneously in Europe (WEB Clinical Assessment of IntraSaccular

Aneurysm Therapy [WEBCAST]) and in France (French Observatory). The short-term (6-month) results of the WEBCAST trial and a comparison of safety between the WEB DL and WEB SL/SLS in the French Observatory were published previously.^{16,17} These initial analyses confirmed the good safety and efficacy of the device in the short-term. This article reports the clinical and anatomic results of the French Observatory study with midterm (1-year) follow-up.

MATERIALS AND METHODS

The French Observatory is a single-arm, prospective, consecutive, multicenter, French study dedicated to the evaluation of WEB treatment for bifurcation aneurysms.

The study received national regulatory authorization (Comité Consultatif sur le Traitement de l'Information en matière de Recherche dans le domaine de la Santé), Reims institutional review board approval, and Commission Nationale Informatique et Libertés approval. Written informed consent was obtained for all patients.

Trial Design and Procedural Modalities

Trial design and procedural modalities have already been described in a previous publication.¹⁶ Briefly, inclusion criteria were ruptured (Hunt and Hess 1, 2, or 3), unruptured, and recanalized bifurcation aneurysms located in the basilar artery, middle cerebral artery, anterior communicating artery, and internal carotid artery terminus. In each center, the indication for endovascular treatment was decided by a local multidisciplinary team, which included neurosurgeons and neuroradiologists. The selection of aneurysms treated with the WEB device was performed autonomously in each center by the interventional neuroradiologists according to aneurysm characteristics (aneurysm status, aneurysm location and size, neck size) and when other therapeutic options like stent placement or flow diversion were deemed technically difficult or impossible.

The treatment of aneurysms with the WEB was performed with techniques similar to those used in the treatment of aneurysms with coils. Pre-, intra-, and postoperative antiplatelet therapy was managed in each center as indicated for typical endovascular treatment with coils or stents and coils. The study protocol did not specify the antiplatelet regimen to be followed. Triaxial access was recommended. Appropriate device sizing was selected on the basis of 2D and 3D digital subtraction angiography. According to the size of the WEB device, different microcatheters were used to catheterize the aneurysm, including Rebar-27 (Covidien, Irvine, California), DAC 038 (Stryker Neurovascular, Kalamazoo, Michigan), and, from late 2012 to the end of the trial, microcatheters dedicated to WEB treatment, including VIA-27 and VIA-33 (Sequent Medical). Treatment with ancillary devices (balloon, coils, and stents) could be performed if deemed necessary by the treating physician.

Data Collection

Each center completed a patient file with the following data: patient age and sex; aneurysm rupture status; aneurysm characteristics, including location, size, and neck size; date of the

procedure; type of device used (DL or SL/SLS); perioperative antiplatelet medications; occurrence of complications during or after the procedure; and use of additional devices during the procedure (coils, remodeling balloons, stents, or flow diverters). The preoperative Hunt and Hess grade was collected in case of ruptured aneurysms. The modified Rankin Scale score was collected before treatment (unruptured/recanalized aneurysms) and at 30 ± 7 days and 12 ± 3 months for all patients. Vascular imaging at 1 year was collected.

Data Analysis

Clinical data were independently monitored and analyzed, including all adverse events (A.M.). Morbidity was defined as an mRS of 2 when the preoperative mRS was ≤ 2 (or in case of a ruptured aneurysm). When the preoperative mRS was > 2 , morbidity was defined as an increase of 1 point.

An expert interventional neuroradiologist (J.B.) independently evaluated aneurysm occlusion by using the previously validated 3-grade scale: complete occlusion, neck remnant, and aneurysm remnant. According to previous publications, opacification of the proximal recess of the WEB device was considered complete occlusion.^{14,18}

Statistical Analysis

Continuous variables were described as mean \pm SD. Categorical data were described numerically as a categorical total and as a percentage of the population analyzed. Binomial data were described as a ratio of the true value and the population analyzed (x/n). Confidence intervals for binomial data were calculated by the Clopper-Pearson method, and *P* values were calculated by the Fisher exact test. Analyses were conducted by using SPSS statistical software (IBM, Armonk, New York) and StatXact-8 (Cytel, Cambridge, Massachusetts) for confidence intervals and *P* values.

RESULTS

Patient and Aneurysm Population

Between November 2012 and January 2014, 10 French centers included 62 patients (39 women, 62.9%), 33–74 years of age (mean, 56.6 ± 9.80 years) with 63 aneurysms.

Seven (11.1%) aneurysms were ruptured, 51 (81.0%) were unruptured, and 5 (7.9%) were previously treated but recanalized. Aneurysm locations were the MCA in 32 aneurysms (50.8%), anterior communicating artery in 16 (25.4%), basilar artery in 9 (14.3%), and ICA terminus in 6 (9.5%). The aneurysm neck was ≥ 4 mm in 57/63 aneurysms (90.5%). Fifty-two aneurysms (82.5%) were < 10 mm in size.

Thirty patients with 31 aneurysms were treated with the WEB DL; and 32 patients with 32 aneurysms, with the WEB SL/SLS.

Before the procedure, 10 patients had no antiplatelet treatment, 26 patients had 1 antiplatelet medication (clopidogrel or aspirin), and 25 patients had 2 antiplatelet medications. For 1 patient, the antiplatelet therapy regimen could not be confirmed. He was excluded from further analysis regarding this point because he had no thromboembolic event.

Treatment Feasibility, Adjunctive Treatments, and Adverse Events

Treatment was successfully performed in all except 1 patient treated with the WEB DL (98.4%). In this patient, it was impossible to deploy the WEB, which was stuck in the microcatheter. The aneurysm was treated with coils. Clinical follow-up was uneventful.

Adjunctive devices were used in 7/62 aneurysms treated with the WEB (11.3%): coils in 4 aneurysms and a stent in 3 aneurysms.

Nine thromboembolic events were reported in 8/62 patients (12.9%), and 1/62 was associated with a permanent deficit (1.6%). Five patients had no antiplatelet agent before the procedure, 1 patient had 1 antiplatelet agent, and 2 had 2 antiplatelet agents. All thromboembolic events were treated by antiplatelet medication, including tirofiban or abciximab. In 3 patients, a remodeling balloon was used in combination with antiplatelet treatment to reopen the vessel. No stent retriever or stent was used.

Intraoperative rupture was reported in 1/62 patients (1.6%) and was not symptomatic. Intracranial hemorrhage was detected in 1/62 patients (1.6%) on a control CT performed 24 hours after the procedure and was asymptomatic. Anatomically, it was not connected with the aneurysm. Because there was no other cause, it was interpreted by the medical monitor as being related to the antiplatelet treatment used in this patient. The clinical evolution was uneventful.

Mortality/Morbidity at 1 Month

At 30 days, all patients enrolled in the study had a clinical evaluation with mRS scoring.

There was no mortality at 1 month. Morbidity was observed in 2/62 patients (3.2%) related to a thromboembolic event in 1 patient (mRS 3) and to worsening of pre-existing aneurysm mass effect in 1 patient (this patient had a partially thrombosed large aneurysm of the basilar artery with progressive brain stem compression, mRS 3). When we looked at the conventional mRS score cohorts of mRS 0–2 and mRS 3–6, the confidence intervals essentially overlapped; this finding implied no difference in the rates of mRS 0–2 and mRS 3–6 from the procedure to 12 months.

Mortality/Morbidity at 1 Year

At 12 months, 59 of the 62 patients enrolled in the study were clinically evaluated with mRS scoring. Three patients included in the 30-day mortality/morbidity analysis were not included in the 1-year mortality/morbidity (1 patient not treated with WEB, 1 patient retreated before 1 year, and 1 patient lost to follow-up were not evaluated).

Two patients died between 1-month and 1-year follow-up: 1 unrelated to aneurysm disease or treatment and 1 from worsening of pre-existing mass effect described previously. All-cause mortality was 2/59 (3.4%), and neuro-related mortality was 1/59 (1.7%). The 2 patients who had an mRS of ≥ 2 at 1 month were improved at 1 year (mRS 1 and 2); this outcome led to no morbidity at 1 year.

Retreatment

One patient with aneurysm recanalization was retreated at 6 months by using a flow diverter. One patient had an attempted

retreatment at 10 months with a flow diverter, which was unsuccessful.

Anatomic Results at 1 Year

Of the 63 aneurysms in the intention-to-treat population, aneurysm occlusion was evaluated in 58 aneurysms at 1 year. The vascular imaging technique was digital subtraction angiography in 50/58 (86.2%) cases, CTA in 3 cases (5.2%), and MRA in 5 cases (8.6%). Aneurysm occlusion was not evaluated in 1 patient who was not treated with a WEB, 1 patient who had retreatment before 1 year (see above), 1 patient lost to follow-up, and 2 patients who died before 1 year (see above).

Complete occlusion was observed in 30/58 aneurysms (51.7%) in the global population, in 14/28 (50.0%) patients treated with WEB DL, and in 16/30 (53.3%) patients treated with WEB SL/SLS.

Neck remnant was observed in 16/58 aneurysms (27.6%) in the global population, in 8/28 (28.6%) patients treated with WEB DL, and in 8/30 (26.7%) patients treated with WEB SL/SLS.

Aneurysm remnant was observed in 12/58 aneurysms (20.7%) in the global population, in 6/28 (21.4%) patients treated with WEB DL, and in 6/30 (20.0%) patients treated with WEB SL/SLS.

DISCUSSION

The WEB French Observatory is, to date, the largest multicenter, prospective, Good Clinical Practice series dealing with WEB aneurysm treatment. Short and midterm follow-ups confirm the safety and efficacy of this treatment. At 1 month and 1 year, there was no mortality related to the treatment. Low morbidity was reported at 1 month (3.2%), with clinical improvement at 1 year leading to no morbidity at that time point. At 1 year, complete aneurysm occlusion was observed in 51.7% of aneurysms, with adequate occlusion (complete occlusion and neck remnant) in 79.3%.

New technologies for the endovascular treatment of intracranial aneurysms must be carefully evaluated for safety and efficacy; this evaluation has not always been performed in the past. For aneurysm treatment with the WEB device, careful evaluation of safety and efficacy has been built through a series of prospective, Good Clinical Practice clinical studies (French Observatory, WEBCAST, and WEBCAST 2 and the ongoing WEB Intracranial Therapy study under an FDA investigational device exemption). The French Observatory study was conducted during the early phase of clinical use of the WEB and included the learning curve with the WEB in terms of procedural technique, WEB sizing, and the approach to antiplatelet therapy. It shows that WEB treatment permits the management of ruptured, unruptured, recanalized, and complex wide-neck bifurcation aneurysms located at the MCA, anterior communicating artery, ICA terminus, and basilar artery with a very high success rate (98.4%). Despite the use of a relatively large microcatheter, the treatment appears to be feasible in the most cases.

The current results confirm the great safety of WEB treatment as has been reported in retrospective series and WEBCAST.^{10–17} The rate of thromboembolic events with the WEB (14.5%) was quite similar to that reported in the Analysis of Treatment by Endovascular Approach of Nonruptured Aneurysms (ATENA)

and Clinical and Anatomical Results In the Treatment of Ruptured Intracranial Aneurysms (CLARITY) series (respectively, 7.3% and 13.3%).^{1,2} Only 1 patient (1.6%) had a permanent deficit. Most patients treated in this study had wide-neck aneurysms (90.5% compared with 30.9% in ATENA), and the rate of TE events was higher in wide-neck aneurysms.¹⁹ The rate of intraoperative rupture was low (1 patient, 1.6%) and comparable with the 2.0% observed in ATENA and 3.7% in CLARITY.^{1,2} Moreover, the intraoperative rupture was not symptomatic.

Safety is also confirmed at 12 months with 2 deaths unrelated to the treatment, no new morbidity, and clinical improvement of patients who had morbidity at 1 month. No significant delayed adverse events were observed, as is the case with flow diverters. Remarkably, no delayed aneurysm rupture or intracranial parenchymal hemorrhage was reported.^{20,21}

The present results also highlight the high quality of aneurysm occlusion obtained with this technique, confirming the data from 6-month follow-up in the WEBCAST and from an already published retrospective European series.^{14,15,17} Complete occlusion, neck remnant, and aneurysm remnant were observed at 1 year in, respectively, 51.7%, 27.6%, and 20.7%. The clinical impact of neck remnant after WEB treatment is unknown and probably not different from that observed after coiling. However, long-term follow-up is clearly needed to evaluate this point and is foreseen for 2 years in the French Observatory and 5 years in other Good Clinical Practice studies (WEBCAST, WEBCAST 2).

In the European series, similar to these French Observatory results, complete and adequate occlusion was reported at midterm follow-up (median, 13 months) in, respectively, 69.0% and 89.7%.^{14,15} This series also confirmed the long-term (median, 27 months) stability of WEB aneurysm treatment, showing complete and adequate occlusion in, respectively, 68.4% and 84.2%. There was no worsening of aneurysm occlusion between the mid- and long term. Comparison with other techniques is difficult because no series really focused on wide-neck bifurcation aneurysms. In the Matrix and Platinum Science trial, a subgroup analysis was conducted showing that in unruptured aneurysms with wide necks (not necessarily bifurcation), the rate of complete and adequate occlusion (at 12 months) was, respectively, 20.3% and 49.1% with coils and 45.7% and 78.6% with stent placement and coiling.²² If anatomic results with stent placement and coiling are relatively similar to those observed with the WEB, safety is worse with stent placement and coiling.

In a recent article, Cognard and Januel²³ reported on their initial experience with WEB aneurysm treatment. At short-term follow-up, among 14 aneurysms, 1 was completely occluded (7.2%) and neck and aneurysm remnants were observed in, respectively, 9 (64.3%) and 4 (28.6%) aneurysms. Long-term follow-up (mean, 18.6 months) was obtained in a very limited number of 7 patients and showed worse results. Indeed, this series was a very small, monocenter, self-analyzed report, dealing with complex aneurysms treated at the very beginning of the WEB experience. However, it introduces the concept of WEB shape modification with time, a parameter that was not analyzed in the French Observatory series.

Patients included in the French Observatory study were treated with Dual- or Single-Layer devices. Previous analyses

showed a similar safety of treatment with the devices, with a trend toward less thromboembolic events in patients treated with Single-Layer devices.¹⁶ Anatomically, results were similar in both groups of patients, with complete occlusion in 50.0% of patients treated with WEB DL, 53.3% of patients treated with WEB SL/SLS, and adequate occlusion in, respectively, 78.6% and 80.0%.

This study has several limitations. First, the population was relatively small (62 patients). However, it is the first prospective, multicenter study evaluation with high-quality methodology evaluating the midterm safety and efficacy of this treatment. Second, it was not a randomized study, and comparison with other techniques was not easy. However, safety data are excellent and quite comparable with those observed in large coiling series. Efficacy data are more difficult to compare with those in historical series because most were mixed sidewall and bifurcation and narrow- and wide-neck aneurysms. Third, the potential WEB “compression” phenomenon has not been evaluated, to our knowledge. Further work will be conducted on this topic.

CONCLUSIONS

This study, with independent analysis of clinical events and anatomic results, confirms the very good safety profile of WEB treatment for bifurcation aneurysms, with rates of thromboembolic events and intraoperative rupture comparable with those observed with standard coiling and very low morbidity and mortality rates. A high rate of complete (51.7%) and adequate occlusion (79.3%) was obtained at 1-year follow-up.

Disclosures: Laurent Pierot—RELATED: Consulting Fee or Honorarium: Sequent Medical; UNRELATED: Consultancy: Covidien/ev3, MicroVention, Neuravi. Jacques Moret—UNRELATED: Consultancy: MicroVention, Covidien. Francis Turjman—RELATED: Other: Sequent Medical, Comments: fees by cases included in the registry; UNRELATED: Consultancy: Medtronic,* Codman,* Stryker Neurovascular*; Grants/Grants Pending: Medtronic*; Payment for Development of Educational Presentations: Codman,* Balt.* Denis Herbreteau—RELATED: Consulting Fee or Honorarium: Sequent Medical (proctoring); Support for Travel to Meetings for the Study or Other Purposes: Sequent Medical (proctoring, congress). Xavier Barreau—RELATED: Fees for Participation in Review Activities such as Data Monitoring Boards, Statistical Analysis, Endpoint Committees, and the Like: Sequent Medical lab; UNRELATED: Consultancy: Stryker, Codman, MicroVention. Christophe Cognard—RELATED: Consulting Fee or Honorarium: Sequent Medical; UNRELATED: Consultancy: MicroVention, Stryker, Codman, Medtronic, Sequent Medical. Andrew Molyneux—RELATED: Consulting Fee or Honorarium: Sequent Medical, Comments: for regulatory advice and independent clinical event adjudication; Support for Travel to Meetings for the Study or Other Purposes: Sequent Medical; Fees for Participation in Review Activities such as Data Monitoring Boards, Statistical Analysis, Endpoint Committees, and the Like: Sequent Medical; UNRELATED: Expert Testimony: clinical negligence cases in the UK and Ireland. James Byrne—RELATED: Grant: Sequent Medical,* Comments: I provided a core laboratories reading service for this study paid for by the manufacturer of the WEB device; Support for Travel to Meetings for the Study or Other Purposes: Sequent Medical; UNRELATED: Board Membership: Stryker UK Ltd, Comments: clinical event adjudication for an unrelated registry. Laurent Spelle—UNRELATED: Consultancy: Stryker, Medtronic; Payment for Lectures (including service on Speakers Bureaus): Stryker, Medtronic. *Money paid to the institution.

REFERENCES

1. Cognard C, Pierot L, Anxionnat R, et al, Clarity Study Group. **Results of embolization used as the first treatment choice in a consecutive nonselected population of ruptured aneurysms: clinical results of the Clarity GDC study.** *Neurosurgery* 2011;69:837–41; discussion 842 CrossRef Medline
2. Pierot L, Spelle L, Vitry F; ATENA Investigators. **Immediate clinical outcome of patients harboring unruptured intracranial aneurysms**

treated by endovascular approach: results of the ATENA study. *Stroke* 2008;39:2497–504 CrossRef Medline

3. Pierot L, Cognard C, Spelle L, et al. **Safety and efficacy of balloon remodeling technique during endovascular treatment of intracranial aneurysms: critical review of the literature.** *AJNR Am J Neuroradiol* 2012;33:12–15 CrossRef Medline
4. Pierot L, Spelle L, Leclerc C, et al. **Endovascular treatment of unruptured intracranial aneurysms: comparison of safety of remodeling technique and standard treatment with coils.** *Radiology* 2009;251:846–55 CrossRef Medline
5. Pierot L, Cognard C, Anxionnat R, et al; CLARITY Investigators. **Remodeling technique for endovascular treatment of ruptured intracranial aneurysms had a higher rate of adequate postoperative occlusion than did conventional coil embolization with comparable safety.** *Radiology* 2011;258:546–53 CrossRef Medline
6. Shapiro M, Becske T, Sahlein, et al. **Stent-supported aneurysm coiling: a literature survey of treatment and follow-up.** *AJNR Am J Neuroradiol* 2012;33:159–63 CrossRef Medline
7. Pierot L. **Flow diverter stents in the treatment of intracranial aneurysms: where are we?** *J Neuroradiol* 2011;38:40–46 CrossRef Medline
8. Berge J, Biondi A, Machi P, et al. **Flow-diverter Silk stent for the treatment of intracranial aneurysms: 1-year follow-up in a multicenter study.** *AJNR Am J Neuroradiol* 2012;33:1150–55 CrossRef Medline
9. Pierot L, Wakhloo AK. **Endovascular treatment of intracranial aneurysms: current status.** *Stroke* 2013;44:2046–54 CrossRef Medline
10. Pierot L, Liebig T, Sychra V, et al. **Intrasaccular flow-disruption treatment of intracranial aneurysms: preliminary results of a multicenter clinical study.** *AJNR Am J Neuroradiol* 2012;33:1232–38 CrossRef Medline
11. Pierot L, Klisch J, Cognard C, et al. **Endovascular WEB flow disruption in middle cerebral artery aneurysms: preliminary feasibility, clinical, and anatomical results in a multicenter study.** *Neurosurgery* 2013;73:27–34; discussion 34–35 CrossRef Medline
12. Papagiannaki C, Spelle L, Januel AC, et al. **WEB intrasaccular flow disruptor—prospective, multicenter experience in 83 patients with 85 aneurysms.** *AJNR Am J Neuroradiol* 2014;35:2006–11 CrossRef Medline
13. Mine B, Pierot L, Lubicz B. **Intrasaccular flow-diversion for treatment of intracranial aneurysms: the Woven EndoBridge.** *Expert Rev Med Devices* 2014;11:315–25 CrossRef Medline
14. Lubicz B, Klisch J, Gauvrit JY, et al. **WEB-DL endovascular treatment of wide-neck bifurcation aneurysms: short- and midterm results in a European study.** *AJNR Am J Neuroradiol* 2014;35:432–38 CrossRef Medline
15. Pierot L, Klisch J, Liebig T, et al. **WEB-DL endovascular treatment of wide-neck bifurcation aneurysms: long-term results in a European series.** *AJNR Am J Neuroradiol* 2015 Jul 30. [Epub ahead of print] CrossRef Medline
16. Pierot L, Moret J, Turjman F, et al. **WEB treatment of intracranial aneurysms: indications, feasibility, complications, and 1-month safety results with WEB DL and WEB SL/SLS in the French Observatory.** *AJNR Am J Neuroradiol* 2015;36:922–27 CrossRef Medline
17. Pierot L, Costalat V, Moret J, et al. **Safety and efficacy of aneurysm treatment with WEB: results of WEBCAST study.** *J Neurosurg* 2015 Sep 18. [Epub ahead of print] CrossRef Medline
18. Fiorella D, Arthur A, Byrne J, et al. **Interobserver variability in the assessment of aneurysm occlusion with the WEB aneurysm embolization system.** *J NeuroIntervent Surg* 2015;7:591–95 CrossRef Medline
19. Pierot L, Cognard C, Anxionnat R, et al; CLARITY Investigators. **Ruptured intracranial aneurysms: factors affecting the rate and outcome of endovascular treatment complications in a series of 782 patients (CLARITY study).** *Radiology* 2010;256:916–23 CrossRef Medline
20. Mustafa W, Kadziolka K, Noudel R, et al. **Direct carotid-cavernous fistula following intracavernous carotid aneurysm treatment with a flow-diverter stent: a case report.** *Interv Neuroradiol* 2010;16:447–50 Medline
21. Tomas C, Benaissa A, Herbreteau D, et al. **Delayed ipsilateral parenchymal hemorrhage following treatment of intracranial aneurysms with flow-diverter.** *Neuroradiology* 2014;56:155–61 CrossRef Medline
22. Hets SW, Turk A, English JD, et al; Matrix and Platinum Science Trial Investigators. **Stent-assisted coiling versus coiling alone in unruptured intracranial aneurysms in the Matrix and Platinum Science trial: safety, efficacy, and mid-term outcomes.** *AJNR Am J Neuroradiol* 2014;35:698–705 CrossRef Medline
23. Cognard C, Januel AC. **Remnants and recurrences after the use of the WEB intrasaccular device in large-neck bifurcation aneurysms.** *Neurosurgery* 2015;76:522–30; discussion 530 CrossRef Medline

The Added Value of Volume-of-Interest C-Arm CT Imaging during Endovascular Treatment of Intracranial Aneurysms

G. Chintalapani, P. Chinnadurai, A. Maier, Y. Xia, S. Bauer, H. Shaltoni, H. Morsi, and M.E. Mawad



ABSTRACT

BACKGROUND AND PURPOSE: Successful endovascular treatment of intracranial aneurysms requires understanding the exact relationship of implanted devices to the aneurysm, parent artery, and other branch vessels during the treatment. Intraprocedural C-arm CT imaging has been shown to provide such information. However, its repeated use is limited due to increasing radiation exposure to the patient. The goal of this study was to evaluate a new volume-of-interest C-arm CT imaging technique, which would provide device-specific information through multiple 3D acquisitions of only the region of interest, thus reducing cumulative radiation exposure to the patient.

MATERIALS AND METHODS: VOI C-arm CT images were obtained in 28 patients undergoing endovascular treatment of intracranial aneurysms. VOI images were acquired with the x-ray source collimated around the deployed device, both horizontally and vertically. The images were reconstructed by using a novel prototype robust reconstruction algorithm to minimize truncation artifacts from double collimation. The reconstruction accuracy of VOI C-arm CT images was assessed quantitatively by comparing them with the full-head noncollimated images.

RESULTS: Quantitative analysis showed that the quality of VOI C-arm CT images is comparable with that of the standard Feldkamp, Davis, and Kress reconstruction of noncollimated C-arm CT images (correlation coefficient = 0.96 and structural similarity index = 0.92). Furthermore, 91.5% reduction in dose-area product was achieved with VOI imaging compared with the full-head acquisition.

CONCLUSIONS: VOI imaging allows multiple 3D C-arm CT acquisitions and provides information related to device expansion, parent wall apposition, and neck coverage during the procedure, with very low additional radiation exposure to the patient.

ABBREVIATIONS: ATRACT = Approximated Truncation Robust Algorithm for CT; DAP = dose-area product; FDK = Feldkamp, Davis, and Kress; SSIM = Structural Similarity Index Metric

Endovascular treatment of intracranial aneurysms primarily involves deployment of devices either in the parent artery and/or the aneurysm itself, allowing the aneurysm to thrombose with time. Self-expanding metallic stents, both open-cell and closed-cell designs, are routinely used during stent-assisted coiling. It has been shown that asymmetric, malapposed, misaligned, or pro-

lapsed stent elements can result in changes in hemodynamics, leading to subacute or in-stent stenosis.¹ Thus, obtaining relevant device-specific information such as stent expansion, wall apposition, and aneurysm neck coverage during the treatment is very critical for successful embolization. Similarly, with new-generation flow-diverter devices, inadequate wall apposition, device positioning across the aneurysm neck, and deployment techniques have been shown to influence the amount of metal coverage across the neck, the extent of flow diversion, and the time to form thrombus.^{2,3} Thus, it is very critical to obtain this information during the procedure to evaluate the accuracy of deployment and treatment efficacy, but also to allow additional corrective measures in case of inaccurate deployment.

C-arm CT imaging technology has been shown to provide high-quality CT-like 3D images during interventional procedures that facilitate proper assessment of the deployed device and intraprocedural guidance.⁴⁻¹⁰ Although much of this information can be obtained on 2D fluoroscopic images, desirable material properties of these devices, such as low profile and high flexibility,

Received October 1, 2014; accepted after revision August 20, 2015.

From the Angiography Division (G.C., P.C.), Siemens Medical Solutions USA, Hoffman Estates, Illinois; Pattern Recognition Lab (A.M., Y.X.), Friedrich-Alexander-University, Erlangen-Nuremberg, Germany; Angiography Division (S.B.), Siemens AG, Healthcare Sector, Forchheim, Germany; Neurovascular Center (H.S.), CHI St. Luke's Health System, Houston, Texas; and Department of Radiology (H.M., M.E.M.), Baylor College of Medicine, Houston, Texas.

This study was conducted as part of an investigator-sponsored research study with Siemens Medical Solutions USA.

Abstracts previously presented at: American Society of Neuroradiology Annual Meeting and the Foundation of the ASNR Symposium, April 21–16, 2012; New York, New York; and May 18–23, 2013; San Diego, California.

Please address correspondence to Gouthami Chintalapani, PhD, 2501 North Barrington Rd, Hoffman Estates, IL 60192; e-mail: gouthami.chintalapani@siemens.com

<http://dx.doi.org/10.3174/ajnr.A4605>

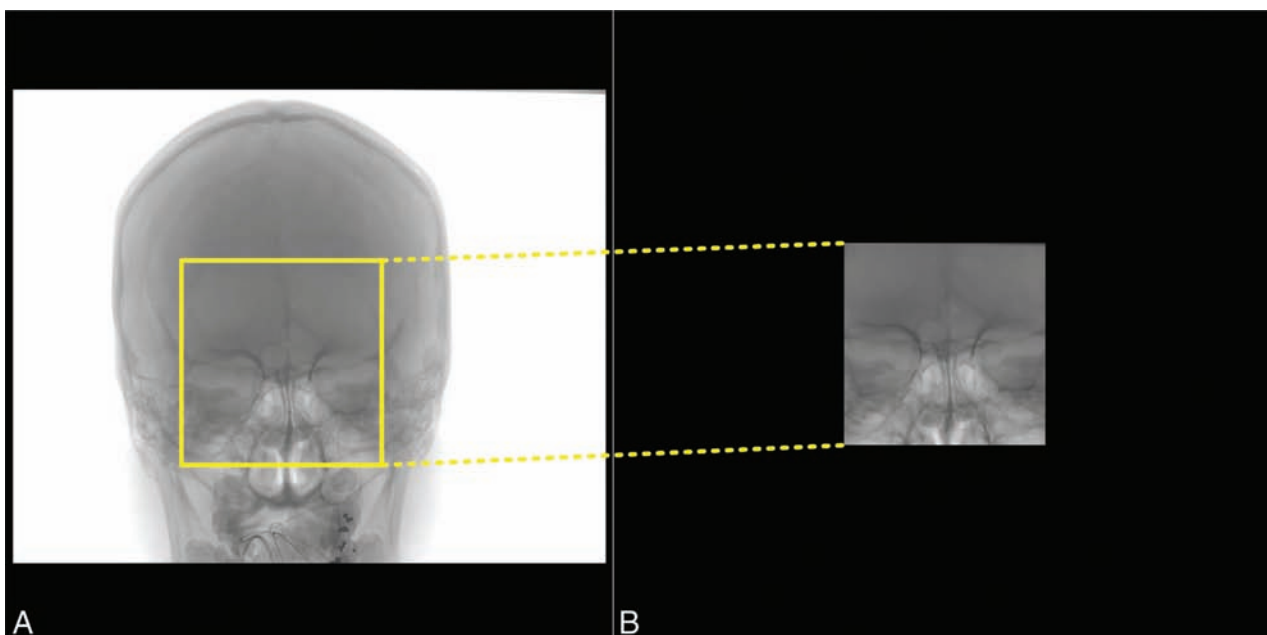


FIG 1. Sample projection image from noncollimated full-head C-arm CT acquisition (A) and VOI C-arm CT acquisition (B) with the x-ray source collimated in both horizontal and vertical directions.

often make it difficult to visualize them under conventional 2D angiographic imaging and present a great need for C-arm CT imaging during the intervention. However, acquisition of multiple C-arm CT images is limited because of the added radiation exposure to the patient. The reported effective dose of a typical full-head C-arm CT scan is 2.9 mSv.¹¹ Thus, multiple C-arm CT acquisitions in a single treatment session can easily increase the cumulative dose delivered to the patient.

Alternatively, the radiation dose due to the C-arm CT acquisition can be reduced with collimation. Because the physician's focus is on the device and its relationship to the parent artery, the x-ray source can be collimated in both horizontal and vertical directions to image only the ROI and block the radiation exposure outside the ROI (Fig 1). With double collimation, the conventional Feldkamp, Davis, and Kress (FDK) reconstruction algorithm results in severe truncation artifacts because patient anatomy is not fully exposed in all projections, thus violating the assumptions of conventional conebeam reconstruction algorithms. Often, these artifacts result in incorrect image information and narrow window values inside the VOI and greatly limit the utility of VOI C-arm CT acquisitions. Thus, they need to be corrected.

Recently, a novel truncation-robust reconstruction algorithm, called Approximated Truncation Robust Algorithm for Computed Tomography (ATRACT), has been proposed in the literature. It is obtained by reformulating the conventional FDK reconstruction method into a scheme that is, by construction, less sensitive to data truncation.^{12,13} The standard FDK reconstruction algorithm consists of 3 steps: 1) preweighting of the projection images, 2) 1D ramp filtering, and 3) a back-projection step. The ATRACT algorithm is based on a decomposition of the conventional ramp filtering (step 2) into a local Laplace filtering and a nonlocal residual filtering. The particular ATRACT variant we applied (2D ATRACT) is based on a 2D Laplace filtering and a 2D convolution-based residual fil-

tering,¹³ which can be computed very efficiently, as opposed to the originally proposed 2D radon-based filtering.¹²

In this article, we propose to evaluate the utility of the VOI acquisition and the accuracy of the ATRACT reconstruction algorithm. Our primary research objective was to determine whether the VOI C-arm CT image acquisition can be incorporated into routine clinical workflow and whether the information discerned from such images can be useful during treatment.

MATERIALS AND METHODS

VOI C-arm CT images were acquired in 28 patients under an institution-approved protocol. Twenty-five of 28 aneurysms were internal carotid artery aneurysms and were treated by using a flow-diverter device (Pipeline Embolization Device; Covidien, Irvine, California). The remaining 3 aneurysms (2 basilar tip bifurcation aneurysms and 1 anterior communicating artery bifurcation aneurysm) were treated with stents and coils. All the treatments were performed in an interventional suite equipped with a biplane flat panel detector angiographic system (Axiom Artis zee biplane; Siemens AG, Forchheim, Germany). Routine 2D DSA and 3D angiographic images were acquired during the treatment. A noncontrast full-head C-arm CT acquisition (syngo DynaCT Head 20-second protocol; Siemens AG) is routinely acquired as part of our clinical workflow immediately after stent or flow-diverter placement, to examine parenchymal enhancement for ruling out possible hemorrhages.

Additionally, VOI C-arm CT images were acquired in these patients after device deployment. The x-ray source was collimated in both vertical and lateral directions, and the C-arm was isocentered around the deployed stent or flow diverter (Fig 1). The FOV of the VOI C-arm CT acquisitions was set to 11.7×11.7 cm, approximately 12% of the full FOV (30×40 cm). VOI C-arm CT images were acquired by using the following parameters: 20-second rotation, 200° angular coverage; 0.4° angular increment; 1240×960 projection matrix; 496 projections; 30 frames per second; $1.2\text{-}\mu\text{Gy/frame}$ sys-

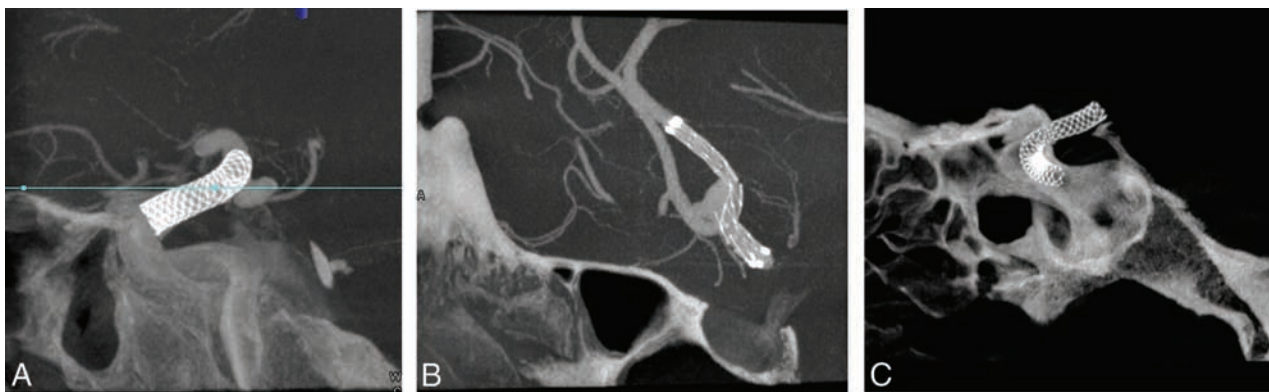


FIG 2. Sample cross-sections from the ATRACT reconstruction of VOI C-arm CT images from the patient cohort. VOI images show clear visibility of stent and flow-diverter devices and their relationship with the parent artery.

tem dose; 48-cm zoom. VOI C-arm CT images were reconstructed with the ATRACT reconstruction algorithm on an off-line workstation, equipped with a Xeon Quad Core processor with a NVIDIA Quadro FX 5800 graphics card (Intel, Santa Clara, California).

Thirty-one VOI images were obtained in 28 patients. Eighteen of 31 VOI C-arm CT images were acquired without contrast injection to assess the reconstruction accuracy of ATRACT. The remaining 13 of 31 VOI C-arm CT images were acquired with contrast medium injected into the internal carotid artery to assess device visibility in VOI images. Iodinated contrast (iohexol, Omnipaque 300; GE Healthcare, Piscataway, New Jersey) was diluted to 20% concentration with normal saline and injected for 22.5 seconds (20-second rotation time, 2.5-second x-ray delay, 1-mL/s injection rate, 22.5-mL total volume [5-mL of iodinated contrast diluted with 20-mL of saline]).

One of the main goals of the study was to quantitatively assess the ATRACT reconstruction of VOI images. Historically, medical image quality has been assessed qualitatively by expert raters. However, such comparison is often subject to user error and viewing conditions and requires multiple raters. These shortcomings can be overcome by mathematic formulations that can be computed easily and applied universally. These quantitative measures can be classified into 2 categories consisting of purely mathematically defined measures such as correlation coefficient, mean squared error, and so forth; and the second class incorporating human visual perception of image quality into the formulation.

Because the noncollimated full-head acquisition was also performed on the same patient as part of the routine care, conventional FDK reconstruction of the full-head acquisition serves as a ground truth reference image, facilitating quantitative assessment. We selected 2 numeric metrics, correlation coefficient¹⁴ and the Structural Similarity Index Metric (SSIM),¹⁵ to capture the image differences due to the VOI acquisition. The Pearson Correlation Coefficient measures the degree to which both images are similar and is computed by using a simple mathematic formula. Correlation coefficient values range from -1 to $+1$. A value of $+1$ indicates that both images are identical, a value of zero means that images are completely uncorrelated, and a value of -1 means that the images are negatively correlated; for example, the image being compared is an inverse of the reference image.

SSIM also assumes a value between -1 to $+1$ and was proposed as a method to measure image quality based on an initial

uncompressed image as a reference. Compared with other traditional metrics, SSIM also tries to capture perceived visual changes through image degradation. The concept of structural information is derived from the idea that neighboring pixels belonging to a structure have strong interdependencies when they are spatially close and thus define the structure of the objects in the image. In the context of this article, a higher SSIM value (close to 1) indicates that image degradation due to truncation artifacts from the VOI acquisition is eliminated with ATRACT robust reconstruction and that ATRACT also preserves anatomic and device-related information similar to that in the noncollimated acquisition. On the other hand, a low SSIM value indicates poor image quality of VOI C-arm CT images, indicating that the truncation artifacts are still prevalent. Furthermore, a value of 1 is only achievable if both images are identical.

RESULTS

Excellent visibility of stents and flow-diverter devices was noted in the VOI C-arm CT images in all 28 patients, acquired both with and without contrast medium injection (Fig 2). Stent expansion, wall apposition, and neck coverage were depicted clearly in the VOI C-arm CT images reconstructed with the ATRACT robust reconstruction algorithm. VOI C-arm CT images from conventional FDK reconstructions have severe truncation artifacts, resulting in capping/cupping artifacts and a substantial offset in Hounsfield unit values as seen in Fig 3B. These truncation artifacts were greatly reduced with the ATRACT reconstruction (Fig 3C).

Figure 3D shows a plot of gray-scale intensity values along the colored lines shown on the sample cross-sections in Fig 3A–C. The profile of the gray-scale value plot from the ATRACT 2D VOI C-arm CT reconstruction aligns closely with the conventional FDK reconstruction of the noncollimated full-head C-arm CT acquisition compared with the conventional FDK reconstruction of the VOI C-arm CT images, in which only the high-contrast objects are visualized. A slight misalignment of the gray-scale values is caused by the residual differences because the images were aligned and resampled by using 3D-3D fusion. A slight disparity in the Hounsfield unit values was observed in the line profile graph at the beginning and the end of the line (also seen in Fig 3C outside the VOI). Indeed, this divergence of Hounsfield unit values was observed in the region outside the VOI being defined by the collimation size used during data acquisition and indicates incorrect reconstruction due to insufficient projection

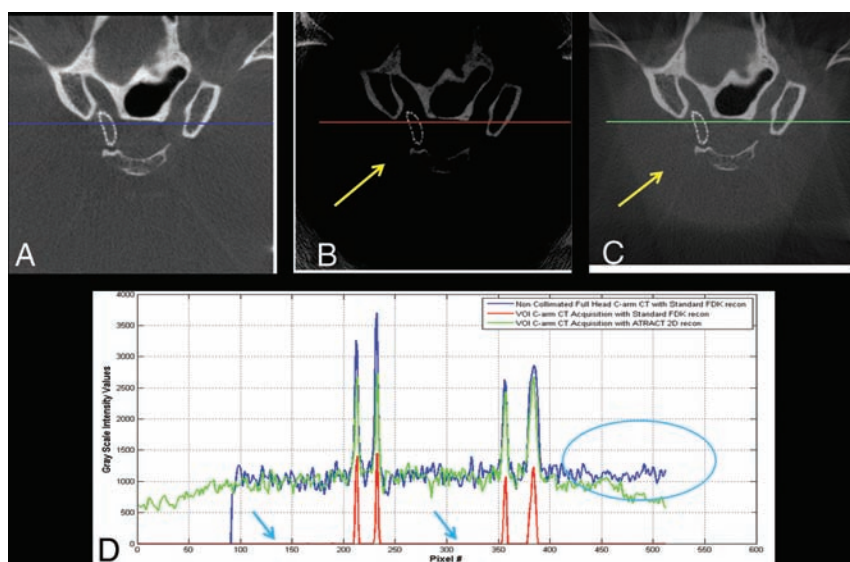


FIG 3. Sample cross-section of a C-arm CT acquisition after Pipeline (flow-diverter) embolization of a right ICA aneurysm. A, Cross-section from a secondary reconstruction of a full-head C-arm CT acquisition (also used as a reference image for comparison). B, Cross-section from a standard FDK reconstruction of a VOI C-arm CT acquisition. C, Cross-section from the ATRACT robust reconstruction of the same VOI C-arm CT acquisition. D, Plot of normalized gray-scale values as shown by the colored lines above. Note the information loss from truncation artifacts (see arrows in B and D) recovered with the ATRACT robust reconstruction algorithm in C.

data in the region outside the defined VOI, which is not of diagnostic interest.

Similar conclusions were drawn from quantitative analysis (Fig 4). Similarity metrics showed an improvement in image quality with ATRACT 2D truncation-correction reconstruction (Fig 4). The average correlation coefficient was 0.96 ($\sigma = 0.02$), and the average SSIM was 0.92 ($\sigma = 0.01$). Moreover, the SSIM value is close to 1 for flow-diverter and other bony landmarks, indicating a very strong image similarity for high-contrast radio-attenuated objects. The average reconstruction time for ATRACT 2D truncation-correction reconstruction is 77.2 seconds compared with 43.5 seconds for the conventional FDK reconstruction of the full-head acquisition. The reconstruction time was measured from the time of initiating the reconstruction to loading the volume into the 3D workstation and includes the time to write the reconstructed volume to the data base.

Figure 5 shows the dose-area product (DAP) of VOI C-arm CT images and the corresponding noncollimated C-arm CT image from the same patient. An average reduction of 91.5% in the DAP is observed with the VOI C-arm CT acquisition (mean percentage reduction in DAP = 91.5%, SD percentage reduction in DAP (σ) = 0.39%, maximum percentage reduction in DAP = 92.45%). Note that these dose reductions were measured in the DAP and may not result in a similar reduction rate in effective dose measurements.

Illustrative Case 1. A 58-year-old woman who presented with a basilar tip bifurcation aneurysm was treated with stents and coils (Fig 6). A noncollimated full-head C-arm CT acquisition (20-second DynaCT protocol) was performed to examine the brain parenchyma immediately after the stent was deployed. Additionally, a 20-second VOI C-arm CT was acquired with dilute contrast injection (injection protocol given above) to study the relationship of the device with the

parent artery. Figure 6B shows the ATRACT reconstruction of the VOI acquisition. The stent deployed into the right posterior cerebral artery was well-apposed and provided good neck coverage, thus avoiding a need to deploy a second stent into the left posterior cerebral artery. Furthermore, the stent was manually delineated from the 3D images and overlaid on the live fluoroscopic images for assistance during coiling (Fig 6C). A 91.7% reduction in DAP values was achieved in this example with the VOI C-arm CT acquisition.

Illustrative Case 2. A 62-year-old woman referred for endovascular treatment of a right internal carotid artery aneurysm was treated with a Pipeline flow-diverter device. Routine clinical images were obtained before and after flow-diverter deployment. A noncollimated full-head C-arm CT acquisition (20-second DynaCT protocol) was performed to examine the parenchyma immediately after the flow diverter was deployed. Malapposition of the flow-diverter device was observed

on 2D DSA images and confirmed on the posttreatment C-arm CT imaging (Fig 7). Balloon angioplasty was performed, and 20-second DynaCT Head VOI C-arm CT images were acquired with dilute contrast injection (injection protocol given above) to confirm the device apposition after angioplasty. The reconstructed VOI images shown in Fig 7C indicate good apposition of the flow-diverter device to the wall of the internal carotid artery after balloon angioplasty, good coverage of the neck of the aneurysm, and some stasis of contrast medium in the aneurysm. The additional C-arm CT image after angioplasty was acquired with 91% reduction in the DAP compared with the original full-head acquisition.

DISCUSSION

C-arm CT imaging has become ubiquitous in the endovascular treatment of intracranial aneurysms. The information gained from C-arm CT imaging enables the operator to assess the treatment, make informative choices, and take corrective measures accordingly during the procedure. However, multiple C-arm CT acquisitions can contribute substantially toward cumulative radiation exposure to the patient. A new imaging technique, VOI C-arm CT imaging, is presented, which acquires C-arm CT images of only the ROI at a reduced dose.

VOI C-arm CT imaging uses extensive collimation in both horizontal and vertical directions, thus achieving dose savings by avoiding radiation exposure to anatomic regions that are outside the ROI. However, collimation results in severe truncation artifacts. Thus, we evaluated a novel truncation-robust reconstruction algorithm, 2D ATRACT, which reduces truncation artifacts from the VOI acquisition. Before ATRACT, various techniques to reconstruct meaningful VOI C-arm CT images with minimal truncation artifacts have been proposed in the literature. The common theme of these

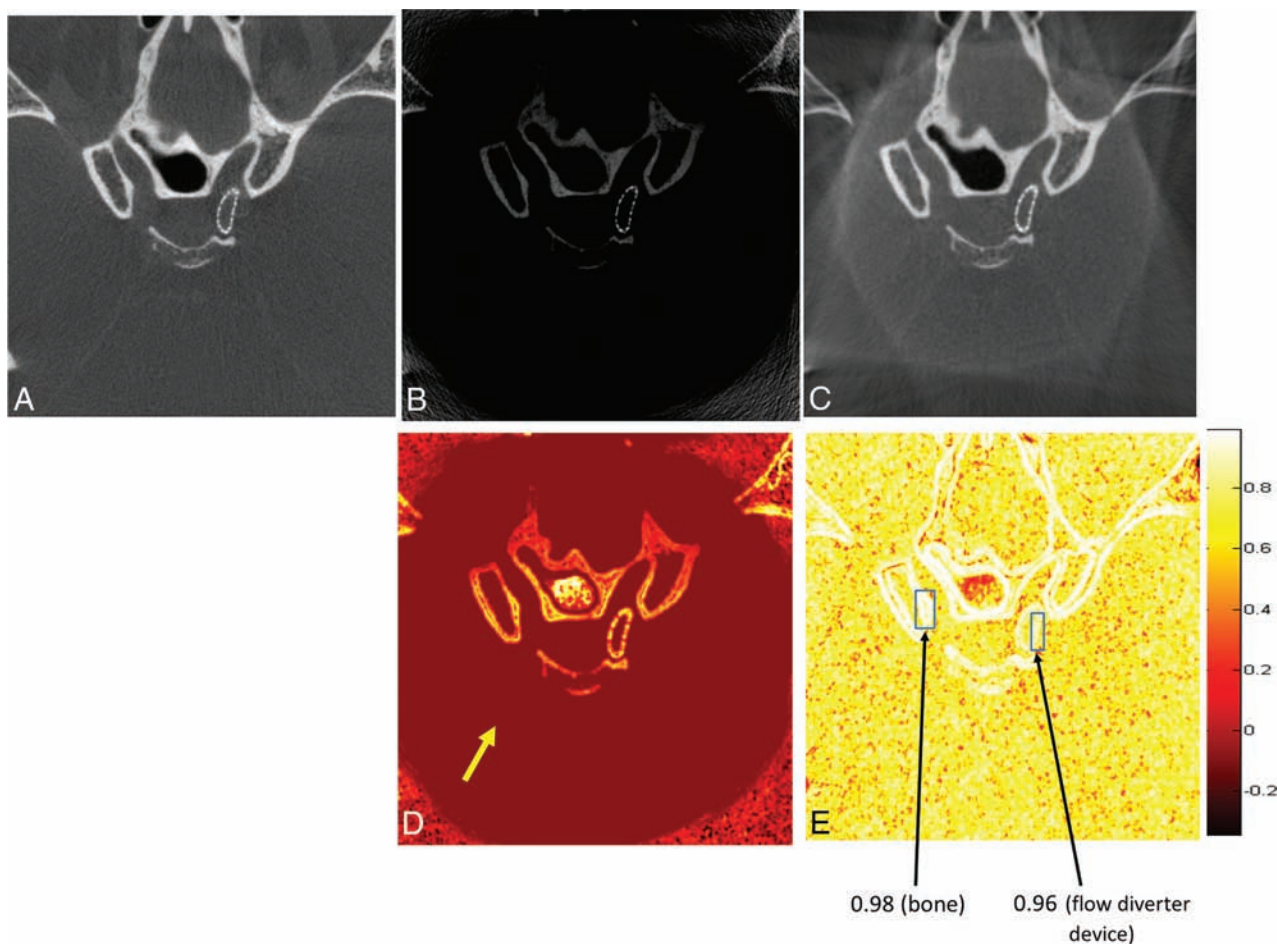


FIG 4. Quantitative comparison of image quality of the VOI C-arm CT acquisition by using the Structural Similarity Index Metric. *A*, Cross-section of a secondary reconstruction from a full-head C-arm CT acquisition. *B*, Cross-section from a standard FDK reconstruction of a VOI C-arm CT acquisition. *C*, Corresponding cross-section from an ATRACT reconstruction of the VOI C-arm CT acquisition. *D*, SSIM map of *B* and *A*. *E*, SSIM map of *C* and *A*. Each pixel in *D* and *E* represents SSIM values ranging from -1 to $+1$. *A*, This image is used as the ground truth reference image; the VOI acquisition is aligned with the full-head acquisition to establish voxel-to-voxel correspondence. Note the improvement in SSIM values corresponding to soft tissue before and after truncation correction as shown by the yellow arrow in *D*. Bony landmarks and devices have SSIM values close to 1, indicating a strong similarity between the ATRACT 2D VOI reconstruction and the standard FDK full-head reconstruction as shown by arrows in *E*.

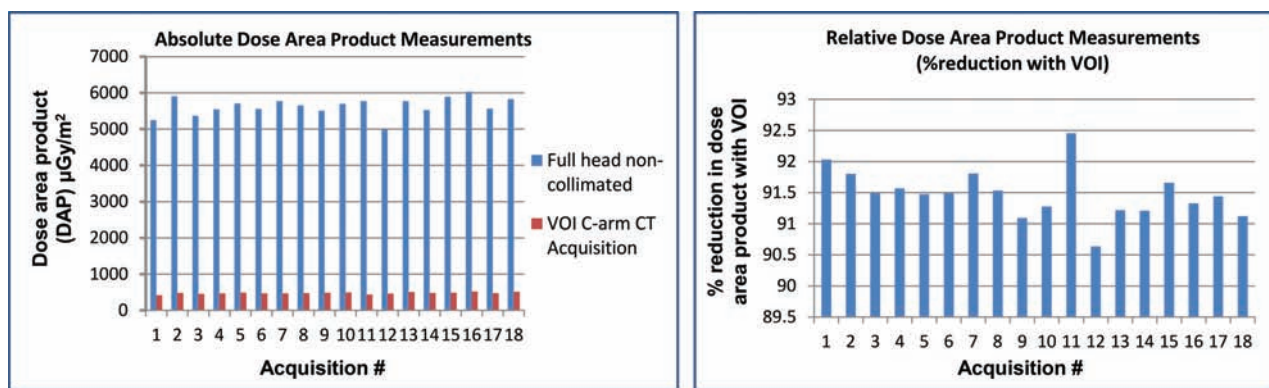


FIG 5. Comparison of an absolute and relative dose-area product between the noncollimated full-head C-arm CT acquisition and the collimated VOI C-arm CT acquisition. Note that these measurements are from the same patient for each study. An average reduction of 91.45% in the DAP is observed with the VOI acquisition.

techniques is to fill in the missing information either by using preinterventional CT,¹⁶ extrapolating missing data on the basis of some heuristic approach,¹⁷ acquiring a low-resolution full-head scan and combining it with truncated VOI projection data with full-field data to create a full projection matrix suit-

able for a FDK reconstruction algorithm,¹⁸ or using advanced filtering algorithms to eliminate truncated data.^{19,20}

Because most of these methods were designed for a stationary C-arm gantry and a rotating object and less robust extrapolation techniques, their utility for neurointerventional applications is

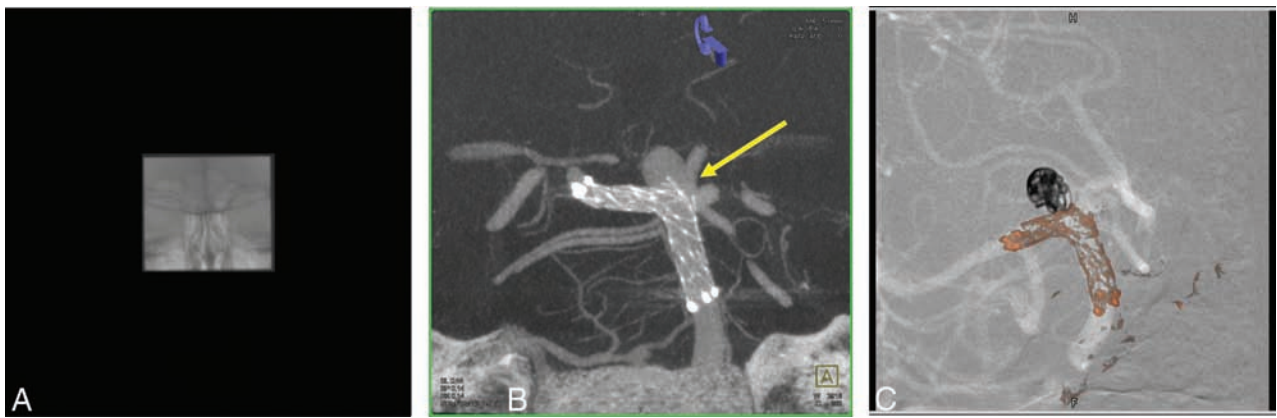


FIG 6. VOI C-arm CT images of a basilar tip aneurysm in a 58-year-old woman treated with stent and coils. Contrast-enhanced VOI C-arm CT images were acquired immediately after the stent was deployed. *A*, Frontal projection of a VOI C-arm CT acquisition. *B*, ATRACT reconstruction of the same VOI C-arm CT. *C*, Fluoroscopic overlay of the stent for assistance during coiling. Note that the high-contrast objects like stents are well-visualized with the VOI C-arm CT images. In this particular example, based on the C-arm CT imaging neck coverage was good after the deployment for first stent from the right side, thus avoiding the need for a second stent.

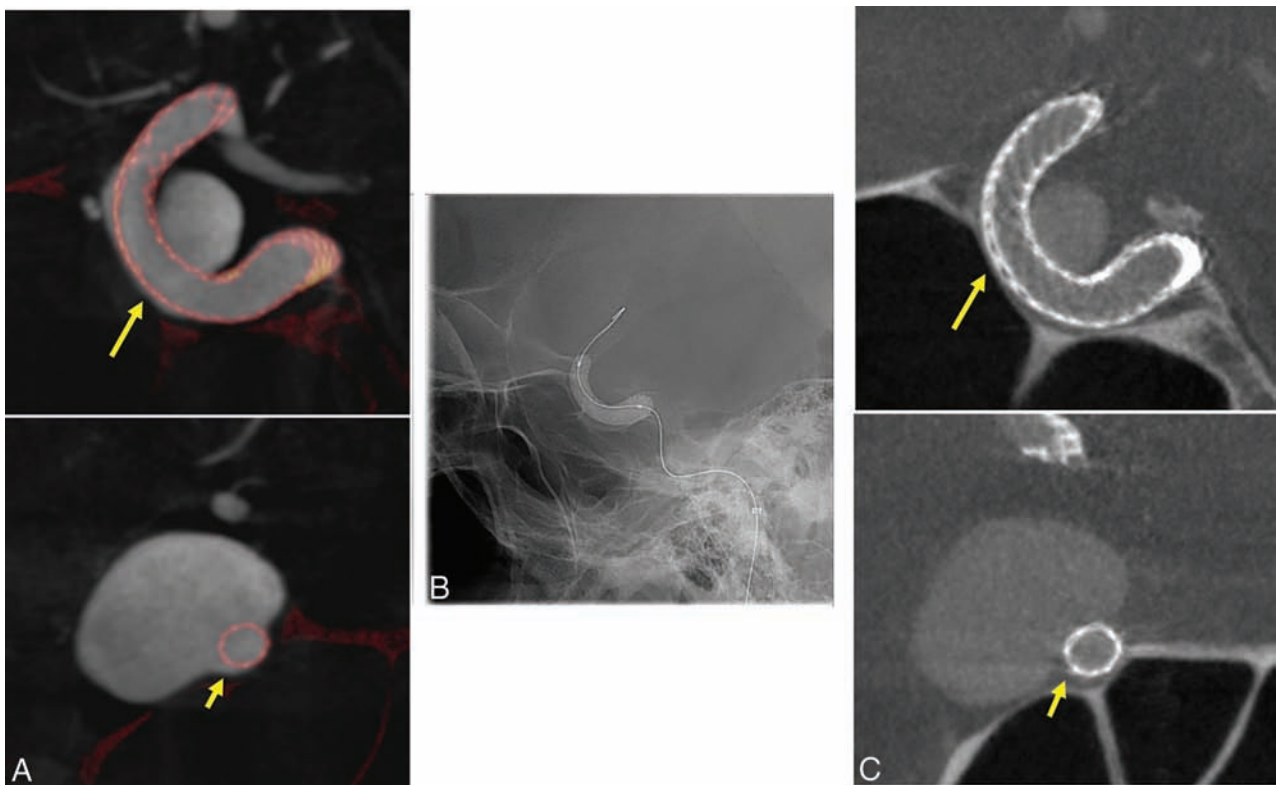


FIG 7. Sample C-arm CT cross-sectional images of an ICA aneurysm in a 62-year-old woman treated with the Pipeline (flow-diverter) Embolization Device. *A* and *B*, C-arm CT images postdeployment show the malapposition of the flow-diverter device to the parent artery. *B*, 2D fluoroscopic image shows the balloon angioplasty fully expanding the flow-diverter device. *C*, Cross-sections from the ATRACT VOI C-arm CT images show improved wall apposition of the flow-diverter device to the parent artery.

very limited. Kolditz et al²¹ developed a technique to obtain a sparse overview scan and a high-resolution VOI scan. However, the sparse overview scans add dose and time and impose registration constraints between the overview and the VOI scan. Patel et al²² explored a similar technique by mounting a microangiographic fluoroscope onto the regular angiography equipment to preserve the small details required for neuroradiologic applications. Similar techniques that use dual detectors have been proposed for breast imaging applications that can be extended to neuroradiology applications.²³

In contrast, ATRACT is based on an analytic reformulation of the standard FDK algorithm into a reconstruction scheme that is, by construction, less sensitive to lateral data truncation. Even in the presence of severe lateral data truncation, the algorithm effectively reduces truncation artifacts and provides high-quality reconstructions without explicit extrapolation or prior knowledge, thus making it clinically feasible.^{12,13}

The clinical examples presented in this article illustrate the added value of VOI C-arm CT imaging. The VOI imaging technique provides clear visualization of stents and flow-diverter de-

vices and their relationship with the parent artery. Quantitative analysis showed a strong correlation between truncation-corrected VOI images and noncollimated C-arm CT images. High contrast objects, such as metallic implants, showed relatively higher correlation compared with the soft-tissue information. For quantitative comparison, images were aligned by using 3D-3D fusion because VOI C-arm CT images were acquired with the device at the isocenter and the C-arm position was different for full-head and VOI C-arm CT acquisitions. The resulting resampling from 3D-3D fusion could have potentially contributed to the discrepancies in image similarity metrics.

During the acquisition of VOI C-arm CT images, it is very crucial to isocenter the C-arm around the deployed device. Depending on the type of device (stent markers and coils are easily visible on fluoroscopic imaging compared with the flow-diverter device in the cavernous segment surrounded by bony anatomy), it is often difficult to isocenter the C-arm and multiple fluoroscopic x-ray images were required to visualize the device, especially with a small VOI, because there are not many landmarks to be seen in the ROI. Automatic isocentering based on a sparse low-dose overview scan or pretreatment 3D images or 2D biplane angiographic images during treatment is desirable. Given that the dose savings are proportional to the size of the VOI, advanced algorithms to automatically detect the ROI and to automatically identify the size of the VOI are needed to further seamlessly integrate VOI imaging into clinical workflow.

CONCLUSIONS

VOI C-arm CT imaging with a new truncation-robust reconstruction algorithm allows acquisition of multiple intraprocedural C-arm CT images with a relatively lower additional dose delivered to the patient. VOI C-arm CT images provide device-specific information about its relationship with the parent artery during the procedure, thus resulting in a valuable tool to assess treatment efficacy and allow additional corrective measures in case of inaccurate deployment.

Disclosures: Gouthami Chintalapani—UNRELATED: Employment: full-time employee at Siemens Medical Solutions USA. Ponraj Chinnadurai—UNRELATED: Employment: Siemens Medical Solutions USA Inc, Comments: employed as a full-time senior staff scientist, Angiography Division, Siemens Medical Solutions USA, Hoffman Estates, Illinois. Andreas Maier—RELATED: Grant: Siemens is supporting the research project of Yan Xia at the University of Erlangen. Yan Xia is now working under my supervision towards his PhD on VOI reconstruction algorithms, which are used in this article*; Consulting Fee or Honorarium: I have been a researcher at Siemens AG, and I developed parts of the algorithms that are used in this work as a Siemens employee; UNRELATED: Employment: I have been a researcher at Siemens AG; Grants/Grants Pending: Siemens is supporting several of my research projects*; Patents (planned, pending or issued): I have several patents with Siemens AG. Sebastian Bauer—UNRELATED: Employment: Siemens AG, Forchheim, Germany. *Money paid to the institution.

REFERENCES

- Benndorf G1, Ionescu M, Y Alvarado MV, et al. **Wall shear stress in intracranial self-expanding stents studied using ultra-high-resolution 3D reconstructions.** *AJNR Am J Neuroradiol* 2009;30:479–86 CrossRef Medline
- Ionita C, Natarajan S, Wang W, et al. **Evaluation of a second-generation self-expanding variable-porosity flow diverter in a rabbit elastase aneurysm model.** *AJNR Am J Neuroradiol* 2011;32:1399–407 CrossRef Medline
- Makoyeva A, Bing F, Darsaut T, et al. **The varying porosity of braided self-expanding stents and flow diverters: an experimental study.** *AJNR Am J Neuroradiol* 2013;34:596–602 CrossRef Medline
- Akpek S, Brunner T, Benndorf G, et al. **Three-dimensional imaging and cone beam volume CT in C-arm angiography with flat panel detector.** *Diagn Interv Radiol* 2005;11:10–13 Medline
- Benndorf G, Strother CM, Claus B, et al. **Angiographic CT in cerebrovascular stenting.** *AJNR Am J Neuroradiol* 2005;26:1813–18 Medline
- Doelken M, Struffert T, Richter G, et al. **Flat-panel detector volumetric CT for visualization of subarachnoid hemorrhage and ventricles: preliminary results compared to conventional CT.** *Neuroradiology* 2008;50:517–23 CrossRef Medline
- Heran NS, Song JK, Namba K, et al. **The utility of DynaCT in neuroendovascular procedures.** *AJNR Am J Neuroradiol* 2006;27:330–32 Medline
- Kizilkilic O, Kocer N, Metaxas GE, et al. **Utility of VasoCT in the treatment of intracranial aneurysm with flow-diverter stents.** *J Neurosurg* 2012;117:45–49 CrossRef Medline
- Kamran M, Nagaraja S, Byrne JV. **C-arm flat detector computed tomography: the technique and its applications in interventional neuro-radiology.** *Neuroradiology* 2012;52:319–27 CrossRef Medline
- Fiorella D, Hsu D, Woo HH, et al. **Very late thrombosis of a Pipeline embolization device construct: case report.** *Neurosurgery* 2010;67(3 suppl operative):E313–14 CrossRef Medline
- Struffert T, Hauer M, Banckwitz R, et al. **Effective dose to patient measurements in flat-detector and multislice computed tomography: a comparison of applications in neuroradiology.** *Eur Radiol* 2014;24:1257–65 CrossRef Medline
- Dennerlein F, Maier A. **Approximate truncation robust computed tomography: ATRACT.** *Phys Med Biol* 2013;58:6133–48 CrossRef Medline
- Xia X, Hofmann H, Dennerlein F, et al. **Towards clinical application of a Laplace operator-based region of interest reconstruction algorithm in C-arm CT.** *IEEE Trans Med Imaging* 2014;33:593–606 CrossRef Medline
- Rodgers J, Nicewander W. **Thirteen ways to look at the correlation coefficient.** *Am Stat* 1988;41:59–66
- Wang Z, Bovik AC, Sheikh HR, et al. **Image quality assessment: from error visibility to structural similarity.** *IEEE Trans Image Process* 2004;13:600–12 CrossRef Medline
- Wiegert J, Bertram M, Netsch T, et al. **Projection extension for region of interest imaging in cone-beam CT.** *Acad Radiol* 2005;12:1010–23 CrossRef Medline
- Hsieh J, Chao E, Thibault J, et al. **A novel reconstruction algorithm to extend the CT scan field-of-view.** *Med Phys* 2004;31:2385–91 CrossRef Medline
- Chityala R, Hoffmann KR, Rudin S, et al. **Region of interest (ROI) computed tomography (CT): comparison with full field of view (FFOV) and truncated CT for a human head phantom.** *Proc SPIE Int Soc Opt Eng* 2005;5745:583–90 Medline
- Cho S, Bian J, Pelizzari CA, et al. **Region-of-interest image reconstruction in circular cone-beam microCT.** *Med Phys* 2007;34:4923–33 CrossRef Medline
- Yu L, Zou Y, Sidky EY, et al. **Region of interest reconstruction from truncated data in circular cone-beam CT.** *IEEE Trans Med Imaging* 2006;25:869–81 CrossRef Medline
- Kolditz D, Struffert T, Kyriakou Y, et al. **Volume-of-interest imaging of the inner ear in a human temporal bone specimen using a robot-driven C-arm flat panel detector CT system.** *AJNR Am J Neuroradiol* 2012;33:E124–28 CrossRef Medline
- Patel V, Hoffmann KR, Ionita CN, et al. **Rotational micro-CT using a clinical C-arm angiography gantry.** *Med Phys* 2008;35:4757–64 CrossRef Medline
- Shen Y, Yi Y, Zhong Y, et al. **High resolution dual detector volume-of-interest cone beam breast CT: demonstration with a bench top system.** *Med Phys* 2011;38:6429–42 CrossRef Medline

Mechanical Thrombectomy for Isolated M2 Occlusions: A Post Hoc Analysis of the STAR, SWIFT, and SWIFT PRIME Studies

J.M. Coutinho, D.S. Liebeskind, L.-A. Slater, R.G. Nogueira, B.W. Baxter, E.I. Levy, A.H. Siddiqui, M. Goyal, O.O. Zaidat, A. Davalos, A. Bonafé, R. Jahan, J. Gralla, J.L. Saver, and V.M. Pereira

ABSTRACT

BACKGROUND AND PURPOSE: Mechanical thrombectomy is beneficial for patients with acute ischemic stroke and a proximal anterior occlusion, but it is unclear if these results can be extrapolated to patients with an M2 occlusion. The purpose of this study was to examine the technical aspects, safety, and outcomes of mechanical thrombectomy with a stent retriever in patients with an isolated M2 occlusion who were included in 3 large multicenter prospective studies.

MATERIALS AND METHODS: We included patients from the Solitaire Flow Restoration Thrombectomy for Acute Revascularization (STAR), Solitaire With the Intention For Thrombectomy (SWIFT), and Solitaire With the Intention for Thrombectomy as Primary Endovascular Treatment (SWIFT PRIME) studies, 3 large multicenter prospective studies on thrombectomy for ischemic stroke. We compared outcomes and technical details of patients with an M2 with those with an M1 occlusion. All patients were treated with a stent retriever. Imaging data and outcomes were scored by an independent core laboratory. Successful reperfusion was defined as modified Thrombolysis in Cerebral Infarction score of 2b/3.

RESULTS: We included 50 patients with an M2 and 249 patients with an M1 occlusion. Patients with an M2 occlusion were older (mean age, 71 versus 67 years; $P = .04$) and had a lower NIHSS score (median, 13 versus 17; $P < .001$) compared with those with an M1 occlusion. Procedural time was nonsignificantly shorter in patients with an M2 occlusion (median, 29 versus 35 minutes; $P = .41$). The average number of passes with a stent retriever was also nonsignificantly lower in patients with an M2 occlusion (mean, 1.4 versus 1.7; $P = .07$). There were no significant differences in successful reperfusion (85% versus 82%, $P = .82$), symptomatic intracerebral hemorrhages (2% versus 2%, $P = 1.0$), device-related serious adverse events (6% versus 4%, $P = .46$), or modified Rankin Scale score 0–2 at follow-up (60% versus 56%, $P = .64$).

CONCLUSIONS: Endovascular reperfusion therapy appears to be feasible in selected patients with ischemic stroke and an M2 occlusion.

ABBREVIATIONS: ESCAPE = Endovascular Treatment for Small Core and Proximal Occlusion Ischemic Stroke; IMS = Interventional Management of Stroke; MERCI = Mechanical Embolus Removal in Cerebral Ischemia; MT = mechanical thrombectomy; REVASCAT = Endovascular Revascularization With Solitaire Device Versus Best Medical Therapy in Anterior Circulation Stroke Within 8 Hours; STAR = Solitaire FR Thrombectomy for Acute Revascularization; SWIFT = Solitaire FR With the Intention For Thrombectomy; SWIFT PRIME = Solitaire With the Intention for Thrombectomy as Primary Endovascular Treatment

Recent data have shown that mechanical thrombectomy (MT) with a stent retriever is safe and improves functional outcome in patients with acute ischemic stroke and an occlusion of the anterior circulation.^{1–5} It is unclear, however, if these results can

be extrapolated to patients with an occlusion of the second segment of the middle cerebral artery (M2 occlusion). Because of its distal location, smaller diameter, and thinner walls, MT of the M2 segment is technically more challenging and may be associated with a higher risk of periprocedural complications. The potential benefit of reperfusion may also be different, in part because M2 occlusions generally respond better to IV thrombolysis.⁶

Received July 1, 2015; accepted August 11.

From the Divisions of Neuroradiology (J.M.C., L.-A.S., V.M.P.) and Neurosurgery (V.M.P.), Department of Medical Imaging and Department of Surgery, Toronto Western Hospital, University Health Network, University of Toronto, Ontario, Canada; Neurovascular Imaging Research Core and the University of California, Los Angeles Stroke Center (D.S.L.), Los Angeles, California; Marcus Stroke and Neuroscience Center (R.G.N.), Department of Neurology, Grady Memorial Hospital, Emory University School of Medicine, Atlanta, Georgia; Department of Radiology (B.W.B.), Erlanger Hospital at University of Tennessee, Chattanooga, Tennessee; Department of Neurosurgery (E.I.L., A.H.S.) and Toshiba Stroke and Vascular Research Center (A.H.S.), State University of New York at Buffalo, Buffalo, New York; Departments of Radiology and Clinical Neurosciences (M.G.), University of Calgary, Calgary, Alberta, Canada; Department of Neurology (O.O.Z.), Medical College of Wisconsin, Milwaukee, Wisconsin; Department of Neurosciences (A.D.), Hospital Germans Trias i Pujol, Universitat Autònoma de Barcelona, Badalona, Barcelona, Spain; Department of Neuroradiology (A.B.), Hôpital Gui-de-Chauliac, Montpellier, France; Division of Interventional Neuroradiology (R.J.) and Department of Neurology and Comprehensive Stroke Center (J.L.S.), David Geffen School of Medicine, University of California, Los Angeles, Los Angeles, California; and Departments of Diagnostic and Interventional Neuroradiology (J.G.), Inselspital, Bern University Hospital and University of Bern, Bern, Switzerland.

This work was supported by the STAR and SWIFT studies, funded by Covidien. Paper previously presented at: European Stroke Organization Congress, April 17–19, 2015; Glasgow, UK.

Please address correspondence to V.M. Pereira, MD, Room 3MCL-436, Toronto Western Hospital, 399 Bathurst St, Toronto, ON, M5T 2S8, Canada; e-mail: vitormpb@hotmial.com

<http://dx.doi.org/10.3174/ajnr.A4591>

Table 1: Anatomic definition of MCA segments

MCA Segment	Anatomic Definition
M1	Horizontal segment of the proximal MCA from the bifurcation of the ICA into the anterior and middle cerebral arteries to the genu of the MCA branch or branches at the entrance to the insula
M2	Vertical MCA branches in the Sylvian fissure originating at the genu and extending to the next genu at the level of the operculum; if the anterior temporal artery arises from the horizontal M1 segment, it will not be considered an M2 branch
M3	Branches that continue when the M2 branches change course again to a more lateral/horizontal course in the Sylvian fissure away from the insula and below the operculum
M4	Branch vessels primarily extend vertically over the frontal and parietal lobes and inferiorly over the temporal lobe

The number of patients with an M2 occlusion in the thrombectomy trials was small. The Multicenter Randomized Clinical trial of Endovascular Treatment for Acute Ischemic Stroke in the Netherlands (MR CLEAN) protocol did allow recruitment of these patients, but <8% of included patients had an isolated M2 occlusion.¹ In the Endovascular Revascularization With Solitaire Device Versus Best Medical Therapy in Anterior Circulation Stroke Within 8 Hours (REVASCAT), Endovascular Treatment for Small Core Proximal Occlusion Ischemic Stroke (ESCAPE), and Extending the Time for Thrombolysis in Emergency Neurological Deficits–Intra-Arterial (EXTEND-IA), only 10, 6, and 4 patients with an isolated M2 occlusion were treated with MT, respectively.^{2,4,5} The Solitaire With the Intention for Thrombectomy as Primary Endovascular Treatment (SWIFT PRIME) protocol excluded M2 occlusions, but there were some protocol violations.³ Thus far, none of these studies has specifically examined the subgroup of M2 occlusions. The aim of our study was to examine the technical aspects, safety, and outcomes of MT with a stent retriever in patients with an isolated M2 occlusion who were included in 3 large multicenter prospective studies.

MATERIALS AND METHODS

Description of Studies and Patient Selection

We included patients from the Solitaire FR With the Intention for Thrombectomy (SWIFT) trial, Solitaire FR Thrombectomy for Acute Revascularization (STAR) study, and the SWIFT PRIME trial. The design of these studies has been reported previously.^{3,7–9} Briefly, the SWIFT trial was a randomized clinical trial that ran from 2010 to 2011, in which patients with acute ischemic stroke and an angiographically confirmed occlusion of a the proximal cerebral artery were allocated to treatment with a stent retriever (Solitaire; Covidien, Irvine, California) or the Merci device (Concentric Medical, Mountain View, California). SWIFT had a roll-in phase during which all patients were treated with a stent retriever, and these patients were included in the current study. STAR was a prospective, multicenter, single-arm study from 2010 to 2012 in which patients with an occlusion of the anterior circulation (intracranial and terminus internal carotid artery and M1 and M2 segments of the middle cerebral artery) were included. All patients in STAR were treated with a stent retriever (Solitaire). In both SWIFT and STAR, patients were eligible only if MT was possible within 8 hours of symptom onset. In SWIFT PRIME, patients with an acute ischemic stroke and confirmed occlusion of the anterior intracranial circulation were randomized between intravenous tPA followed by MT with a stent retriever or intravenous tPA alone. The trial ran from December 2012 until Novem-

ber 2014. In all 3 studies, clinical outcome was determined at 90-day follow-up by using the modified Rankin Scale.

We compared outcomes and technical details of patients with an M2 occlusion with those with an M1 occlusion. We excluded patients from SWIFT treated with the Merci device and patients from the control arm of SWIFT PRIME. Patients with a combined M1 and M2 occlusion were categorized as having M1 occlusion. Those with an occlusion at another location (eg, carotid terminus) were excluded from the analysis. The local ethics committee at every site approved the study protocol, and all patients or their legal representatives gave written informed consent.

Outcome data were adjudicated by an independent CT and MR imaging core laboratory, an angiography core laboratory, and a clinical events committee. The angiography core laboratory assessed the location of the occlusion. Table 1 describes the definition for each segment of the middle cerebral artery used by the core laboratory of the 3 studies. Other variables scored by the core laboratory or Clinical Events Committee were final revascularization grades, hemorrhagic complications, and other adverse events. In SWIFT and SWIFT PRIME, the assessors were blinded to study group assignments.

MT Procedure

The MT procedure used in STAR, SWIFT, and SWIFT PRIME has been described previously.^{7–9} The aim was to achieve successful recanalization of the territory of the occluded vessel. The use of a balloon-guide catheter was mandatory in STAR and SWIFT and optional in SWIFT PRIME. Up to 3 passes with the stent retriever were allowed according to the protocols. The decision to perform any additional passes was at the discretion of the interventionalist and was scored as a protocol violation. The procedure could be performed with the patient under local or general anesthesia. Follow-up brain imaging was performed after 24 hours in all patients.

Data Analysis

We compared the technical details of the procedure, complication rate, and clinical outcome at follow-up between patients with an M1 versus M2 occlusion. Successful reperfusion was defined as a modified Thrombolysis in Cerebral Infarction score of $\geq 2b$ of the target territory. Both the proportions of symptomatic and any intracranial hemorrhage are provided. Symptomatic intracranial hemorrhage was defined as hemorrhage within 24 hours associated with an increase on the NIHSS of ≥ 4 points or that resulted in death. Clinical outcome at 90 days is provided as mRS 0–1, mRS 0–2, and all-cause mortality.

All analyses were by intention-to-treat. Categorical variables

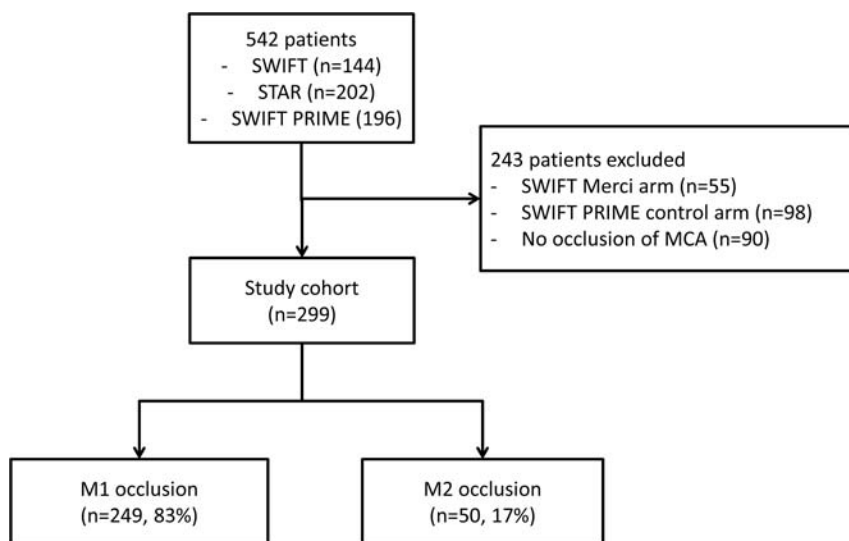


FIG 1. Flowchart of patient selection.

Table 2: Baseline characteristics^a

	M2 Occlusion (n = 50)	M1 Occlusion (n = 249)	P Value
Age (yr) (mean)	71 ± 11	67 ± 13	.04
Female	48% (24/50)	57% (143/249)	.28
NIHSS score (median) (IQR)	13 (10–17)	17 (14–20)	<.001
Medical history			
Atrial fibrillation	38% (19/50)	37% (93/249)	1.000
Hypertension	70% (35/50)	61% (152/249)	.27
Diabetes	18% (9/50)	15% (38/249)	.67
Hyperlipidemia	30% (15/50)	37% (93/249)	.42
Peripheral artery disease	0% (0/50)	4% (9/249)	.37
Current smoker	14% (7/49)	21% (53/249)	.33
Prior stroke/TIA	12% (6/50)	17% (42/249)	.53
Systolic BP (mean) (mm Hg)	150 ± 28	147 ± 23	.45
Diastolic BP (mean) (mm Hg)	84 ± 17	80 ± 15	.11
Left-sided occlusion	54% (27/50)	47% (117/249)	.44
Baseline ASPECTS (mean)	9.0 ± 1.3	8.2 ± 1.7	.003
Receipt of IV tPA	77% (36/47)	69% (161/234)	.38
Laboratory data			
Baseline serum glucose level (mean)	127 ± 51	128 ± 55	.89
INR (mean)	1.1 ± 0.5	1.1 ± 0.3	.95
Platelets (mean)	235 ± 75	234 ± 79	.95
aPTT (mean) (sec)	31 ± 20	29 ± 22	.44

Note:—IQR indicates interquartile range; BP, blood pressure; INR, international normalized ratio; aPTT, activated partial thromboplastin time.

^a Categorical variables are given as percentages with *n/N* in parentheses, where *n* is the number of patients in whom the variable was present and *N* the total number of patients for whom that particular variable was reported.

were compared between groups by using a Fisher exact test. Continuous variables were compared by using a *t* test, except in the cases in which medians and interquartile ranges are reported; then, a Wilcoxon rank sum test was used. Statistical analyses were conducted in SAS, Version 9.3 (SAS, Cary, North Carolina).

Role of the Funding Source

In all 3 studies, an academic steering committee supervised the trial design and operations. The sponsor of the study (Covidien) was responsible for site management, data management, and safety reporting. The study data were independently monitored. The statistical analyses were prepared by independent external statisticians (J. Schafer; Namsa, Minneapolis, Minnesota; S Brown, Altair Biostatistics, St. Louis Park, Minnesota).

The sponsor had no role in the preparation of the article. The corresponding author had full access to all the data in the study and had final responsibility for the decision to submit for publication. The studies were registered at ClinicalTrials.gov, numbers NCT01054560 (SWIFT), NCT01327989 (STAR), and NCT01657461 (SWIFT-PRIME).

RESULTS

Of the 542 patients enrolled in SWIFT, STAR, and SWIFT PRIME, 243 patients were excluded because they were allocated to the Merci arm of SWIFT (*n* = 55) or the control arm of SWIFT PRIME (*n* = 98) or because they did not have an occlusion of the middle cerebral artery (*n* = 90, Fig 1). Of the 299 included patients, 50 had an M2 occlusion; and 249, an M1 occlusion. Patients with an M2 occlusion were older (71 versus 67 years, *P* = .04) and had a lower median NIHSS score (13 versus 17, *P* < .001) compared with patients with an M1 occlusion (Table 2). There were no important differences in medical histories between the groups. Baseline ASPECTS was higher in those with an M2 occlusion (9.0 versus 8.2, *P* = .003). The proportion of patients who received intravenous tPA before MT did not differ significantly (77% versus 69%, *P* = .38).

Time from groin puncture to recanalization was nonsignificantly shorter in patients with an M2 occlusion (median, 29 versus 35 minutes; *P* = .41, Table 3). The average number of passes with the stent retriever was also nonsignificantly lower in patients with an M2 occlusion (mean, 1.4 versus 1.7; *P* = .07). There was no difference in the proportion of patients in whom modified TICI ≥2b was achieved (85% versus 82%,

P = .82) or in the incidence of symptomatic intracranial hemorrhages (both 2%). An mRS of 0–1 at 90 days was achieved in 50% of patients with an M2 occlusion, compared with 41% in those with an M1 occlusion (*P* = .27).

DISCUSSION

We examined the feasibility and safety of MT with a stent retriever in patients with an isolated M2 occlusion. We found no significant differences in the reperfusion rate or risk of complications between patients with an M1 or M2 occlusion. If anything, there was a trend toward a lower number of passes required with stent retrievers in patients with an M2 occlusion. Clinical outcomes were nonsignificantly better in patients with an M2 occlusion,

Table 3: Details of thrombectomy procedure and clinical and safety outcomes^a

	M2 Occlusion (N = 50)	M1 Occlusion (N = 249)	P Value
Time from groin puncture to recanalization (min) (median) (IQR)	29 (22–45)	35 (25–52)	.41
No. of passes with stent retriever (mean)	1.4 ± 0.8	1.7 ± 1.0	.07
≥3 Passes with stent retriever	13% (5/38)	23% (52/227)	.21
mTICI 2b or 3 reperfusion	85% (34/40)	82% (193/235)	.82
Rescue therapy	6% (3/50)	8% (19/249)	1.000
Complications			
Device-related serious adverse events	6% (3/50)	4% (10/249)	.46
Symptomatic ICH	2% (1/50)	2% (5/249)	1.000
Outcome at 90-day follow-up			
mRS 0–1	50% (25/50)	41% (100/243)	.27
mRS 0–2	60% (30/50)	56% (136/243)	.64
Mortality	12% (6/50)	10% (25/249)	.62

Note:—mTICI indicates modified Thrombolysis in Cerebral Infarction; ICH, intracerebral hemorrhage; IQR, interquartile range.

^a Categorical variables are given as percentages with *n*/*N* in parentheses, where *n* is the number of patients in whom the variable was present, and *N* is the total number of patients for whom that particular variable was reported.

though this result most likely is because these patients had milder strokes, as shown by the lower baseline NIHSS scores.

Few studies have previously examined endovascular treatment of patients with an M2 occlusion, and in most of these, intra-arterial thrombolysis or earlier generation thrombectomy devices were used. A post hoc analysis of the Prolyse in Acute Cerebral Thromboembolism (PROACT) II, Interventional Management of Stroke (IMS), and IMS II studies found successful reperfusion in approximately half of all patients with an M2 occlusion.¹⁰ Shi et al¹¹ studied 28 patients with an M2 occlusion who were enrolled in the Mechanical Embolus Removal in Cerebral Ischemia (MERCI) and multi-MERCI trials. They found that compared with patients with an M1 occlusion, the number of required passes with the thrombectomy device was lower in those with an M2 occlusion, similar to our data. They also found higher recanalization rates in patients with an M2 occlusion. Sheth et al¹² collected data on M2 occlusions from their single-center cohort on MT. They found no difference in recanalization rates between patients with an M2 or M1 occlusion, but the risk of intracranial hemorrhagic complications was lower in patients with an M2 occlusion. However, this observation could be related to different endovascular techniques that were used in each group. Most patients with an M2 occlusion were treated with intra-arterial tPA, while the Merci device was predominantly used in patients with an M1 occlusion. Various randomized trials have shown that the methods of endovascular reperfusion that were used in the above-mentioned studies do not improve clinical outcome in patients.^{13–15} With the introduction of stent retrievers, these older techniques are now rarely applied; thus, the external validity of these studies is now limited.

Only 2 recent retrospective studies have examined the use of stent retrievers for patients with an M2 occlusion. Dorn et al¹⁶ reported outcomes of 15 patients with an M2 occlusion from a single-center retrospective registry. Similar to our results, their data do not suggest that patients with an M2 occlusion have a higher risk of procedural complications. The other study used data from a regional stroke registry.¹⁷ Most of the patients in this series were treated with a stent retriever, though other techniques were used in 14% of patients. Their rate of symptomatic intracerebral

hemorrhage was 9%, which is somewhat higher than that in our study. However, they did not assess patients with an M1 occlusion for comparison; this feature makes interpretation more difficult. Their patients were also in a more severe clinical condition, with a median NIHSS score of 16, which is comparable with the NIHSS scores of the patients with an M1 occlusion in our study. A drawback of both studies is that they did not use an independent core laboratory to adjudicate the angiographic data and no information is provided on the definition that was used for an M2 occlusion.

Our study had no control group of medically treated patients available for comparison. As a result, we cannot determine whether MT with a stent retriever is superior to best medical management in patients with an M2 occlusion.

Individually, neither of the recent thrombectomy trials has a sufficient number of patients with an M2 occlusion to answer this question. One issue that is important in any study that examines MT for M2 occlusion is a clear description of the definition of an M2 branch. The original classification by Fischer in 1938¹⁸ designated the M1 segment as terminating at the genu where the MCA takes a 90° upward turn around the limen insulae; this definition was used in the STAR, SWIFT, and SWIFT PRIME studies. The M1 segment is then further divided into prebifurcation and postbifurcation segments with up to 82% of MCAs reported to bifurcate proximal to the genu.^{19,20} This terminology creates some degree of confusion because postbifurcation branches proximal to the genu are commonly designated as M2 segments.

There are also differences in the number and dominance of the divisions of the MCA, meaning that not all M2 divisions are the same with regard to the volume or importance of the territory that they supply. The variation in size of the divisions also means that technically not all M2 branches are accessible for mechanical thrombectomy. M2 divisions are smaller; therefore, navigating a microcatheter and deploying a stent retriever can be more challenging and associated with greater risk. Thus, when reviewing the patients included in this study, one must consider that the M2 occlusions were likely selected because they had features that made them favorable for mechanical thrombectomy, either because of their size or because they were critical to recanalize due to their supply to and area of eloquence. Patients also were required to have an NIHSS score of least an 8, which decreases the probability of smaller M2 branches being included. This selection of M2 occlusions is an important limitation of this study, and one that probably applies to all studies that examined MT for M2 occlusions.

Only high-volume stroke centers with extensive experience with MT participated in the SWIFT, STAR and SWIFT PRIME studies. In SWIFT, only centers that had participated in the MERCI or multi-MERCI trials or who had an annual MT volume of at least 30 patients were eligible. In STAR, the steering committee selected centers with 24-hour availability of MT that were

experienced with the use of stent retrievers. As a result, caution is required when generalizing these results to stroke centers in general. On the other hand, given the positive results of the recent trials, MT volumes and thus experience of neurointerventionalists are likely to increase substantially in stroke centers within the next few years.

CONCLUSIONS

In this study, we examined the technical aspects, safety, and outcomes of mechanical thrombectomy in patients with an isolated M2 occlusion who were included in 3 large multicenter prospective studies. Our data suggest mechanical thrombectomy with a stent retriever can be considered in selected patients with acute ischemic stroke and an isolated M2 occlusion.

ACKNOWLEDGMENTS

The authors would like to thank Jill Schafer and Scott Brown for their help with the data analysis.

Disclosures: Jonathan M. Coutinho—UNRELATED: Grants/Grants Pending: Remmert Adriaan Laan Fonds, Comments: nonprofit organization for neurological research. David S. Liebeskind—RELATED: Grant: National Institutes of Health—National Institute of Neurological Disorders and Stroke,* Comments: research grant; UNRELATED: Consultancy: Stryker,* Covidien,* Comments: core lab. Raul G. Nogueira—RELATED: Other: Covidien; SWIFT and SWIFT PRIME Trials Steering Committee (modest), STAR Trial core lab (significant); UNRELATED: Other: Stryker Neurovascular: Thrombectomy Revascularisation of Large Vessel Occlusions in Acute Ischaemic Stroke Trial (TREVO 2) Principal Investigator (modest) and Trevo and Medical Management Versus Medical Management Alone in Wake Up and Late Presenting Strokes (DAWN) Trial Principal Investigator (not compensated); Penumbra: 3D Separator Trial Executive Committee. ADDITIONAL: Dr Nogueira serves as a scientific consultant regarding trial design and conduct to Covidien, has served as the Principal Investigator for the TREVO 2 and DAWN trials, is part of the Penumbra 3D Separator Trial Executive Committee, has served as a data safety and monitoring board member for Stroke Trial with Rapid Medical, and is the editor-in-chief of the *Interventional Neurology* journal. Blaise W. Baxter—UNRELATED: Consultancy: Covidien, Penumbra, Stryker, Silk Road; Payment for Lectures (including service on Speakers Bureaus): Covidien, Penumbra, Stryker, Silk Road; Patents (planned, pending or issued): United States: 8,622,992 Devices and Methods for Perfusion Therapy; Travel/Accommodations/Meeting Expenses Unrelated to Activities Listed: Covidien, Penumbra, Stryker, Silk Road. Antoni Davalos—UNRELATED: Grants/Grants Pending: Covidien (unrestricted grant for REVASCAT trial)*; OTHER: Dr Davalos has served as a scientific consultant regarding trial design and conduct to Covidien. Alain Bonafé—UNRELATED: Consultancy: Covidien,* Comments: scientific consultant regarding trial design and conduct; Payment for Lectures (including service on Speakers Bureaus): Covidien. Reza Jahan—RELATED: Consulting Fee or Honorarium: Covidien Neurovascular; Support for Travel to Meetings for the Study or Other Purposes: Covidien Neurovascular; UNRELATED: Consultancy: Covidien; Payment for Lectures (including service on Speakers Bureaus): Covidien; OTHER: University of California Regents receive funding for Dr Jahan's services as a scientific consultant regarding the trial design and conduct to Covidien, and he is an employee of the University of California, which holds a patent on retriever devices for stroke. Jan Gralla—RELATED: Consulting Fee or Honorarium: Covidien,* Comments: former Global Principal Investigator of the STAR study, consultant for Covidien. Jeffrey L. Saver—RELATED: Grant: Covidien*; Consulting Fee or Honorarium: Covidien*; Support for Travel to Meetings for the Study or Other Purposes: Covidien*; UNRELATED: Consultancy: Stryker,* Neuravia*; Patents (planned, pending or issued): University of California*; OTHER: University of California Regents receive funding for Dr Saver's services as a scientific consultant regarding the trial design and conduct to Covidien and Stryker, and he is an employee of the University of California, which holds a patent on retriever devices for stroke. Vitor Mendes Pereira—UNRELATED: Consultancy: Covidien,* Comments: as a Principal Investigator of the STAR trial; OTHER: Dr Pereira serves as a scientific consultant regarding trial design and conduct to Covidien and has served as the Global Principal Investigator for the STAR trial. Elad I. Levy—RELATED: Consulting Fee or Honorarium: Covidien, Comments: SWIFT Steering Committee member, SWIFT PRIME Executive Committee member as the US Interventional Principal Investigator; UNRELATED: Consultancy: Abbott (carotid training sessions); Expert Testimony: renders medical/legal opinion; Stock/Stock Options: Intratech Medical, Blockade Medical. Osama O. Zaidat—

UNRELATED: Consultancy: Covidien; Expert Testimony: Tanoury, Nauts, McKinney & Garbarino, PLLC*; Grants/Grants Pending: Stryker, Hackney, Grover, Hoover & Bean, PLC.* Covidien,* Genentech,* MicroVention,* Comments: research grants; OTHER: Dr Zaidat serves as a consultant to Covidien. Adnan H. Siddiqui—RELATED: Consulting Fee or Honorarium: Covidien,* Comments: SWIFT PRIME Steering Committee member, Advisory Board; UNRELATED: Consultancy: Codman & Shurtleff, Guidepoint Global Consulting, Penumbra (Penumbra 3D Separator Trial Steering Committee member; received honoraria), Stryker, Pulsar Vascular, MicroVention Flow-Redirection Endoluminal Device trial Steering Committee member, Lazarus Effect, Blockade Medical, Reverse Medical, W.L. Gore & Associates; Payment for Lectures (including service on Speakers Bureaus): Codman & Shurtleff; Other: Financial Interests: Lazarus Effect, Blockade Medical, Hotspur, Intratech Medical, StimSox, Valor Medical, Medina Medical; Advisory Board: Intersocietal Commission for the Accreditation of Vascular Laboratories, Medina Medical; Honoraria: Abbott Vascular, Toshiba American Medical Systems; OTHER: Dr Siddiqui serves as a consultant to Covidien. Mayank Goyal—RELATED: Consulting Fee or Honorarium: Covidien, Comments: SWIFT PRIME Executive Committee member as the Global Imaging and Workflow Principal Investigator; also received honoraria for speaking and teaching engagements; UNRELATED: Grants/Grants Pending: Covidien,* Comments: Dr Goyal is one of the Principal Investigators for the ESCAPE Trial, which was partially funded by Covidien through an unrestricted grant to the University of Calgary; Patents (planned, pending or issued): GE Healthcare, Comments: systems and methods for diagnosing strokes, multiphase CTA technology; licensed for further development and marketing of technology; OTHER: Dr Goyal serves as a consultant to Covidien. *Money paid to the institution.

REFERENCES

1. Berkhemer OA, Fransen PS, Beumer D, et al. **A randomized trial of intraarterial treatment for acute ischemic stroke.** *N Engl J Med* 2015; 372:11–20 CrossRef Medline
2. Goyal M, Demchuk AM, Menon BK, et al; ESCAPE Trial Investigators. **Randomized assessment of rapid endovascular treatment of ischemic stroke.** *N Engl J Med* 2015;372:1019–30 CrossRef Medline
3. Saver JL, Goyal M, Bonafe A, et al; SWIFT PRIME Investigators. **Stent-retriever thrombectomy after intravenous t-PA vs. t-PA alone in stroke.** *N Engl J Med* 2015;372:2285–95 CrossRef Medline
4. Jovin TG, Chamorro A, Cobo E, et al; REVASCAT Trial Investigators. **Thrombectomy within 8 hours after symptom onset in ischemic stroke.** *N Engl J Med* 2015;372:2296–306 CrossRef Medline
5. Campbell BC, Mitchell PJ, Kleinig TJ, et al; EXTEND-IA Investigators. **Endovascular therapy for ischemic stroke with perfusion-imaging selection.** *N Engl J Med* 2015;372:1009–18 CrossRef Medline
6. del Zoppo GJ, Poeck K, Pessin MS, et al. **Recombinant tissue plasminogen activator in acute thrombotic and embolic stroke.** *Ann Neurol* 1992;32:78–86 CrossRef Medline
7. Saver JL, Jahan R, Levy EI, et al. **Solitaire flow restoration device versus the Merci retriever in patients with acute ischaemic stroke (SWIFT): a randomised, parallel-group, non-inferiority trial.** *Lancet* 2012;380:1241–49 CrossRef Medline
8. Pereira VM, Gralla J, Davalos A, et al. **Prospective, multicenter, single-arm study of mechanical thrombectomy using Solitaire flow restoration in acute ischemic stroke.** *Stroke* 2013;44:2802–07 CrossRef Medline
9. Saver JL, Goyal M, Bonafe A, et al; SWIFT PRIME Investigators. **Solitaire™ with the Intention for Thrombectomy as Primary Endovascular Treatment for Acute Ischemic Stroke (SWIFT PRIME) trial: protocol for a randomized, controlled, multicenter study comparing the Solitaire revascularization device with IV tPA with IV tPA alone in acute ischemic stroke.** *Int J Stroke* 2015;10:439–48 CrossRef Medline
10. Rahme Y, Yeatts SD, Abruzzo TA, et al. **Early reperfusion and clinical outcomes in patients with M2 occlusion: pooled analysis of the PROACT II, IMS, and IMS II studies.** *J Neurosurg* 2014;121:1354–58 CrossRef Medline
11. Shi ZS, Loh Y, Walker G, et al; MERCI and Multi-MERCI Investigators. **Clinical outcomes in middle cerebral artery trunk occlusions versus secondary division occlusions after mechanical thrombectomy: pooled analysis of the Mechanical Embolus Removal in Cerebral Ischemia (MERCI) and Multi MERCI trials.** *Stroke* 2010;41:953–60 CrossRef Medline

12. Sheth SA, Yoo B, Saver JL, et al; UCLA Comprehensive Stroke Center. **M2 occlusions as targets for endovascular therapy: comprehensive analysis of diffusion/perfusion MRI, angiography, and clinical outcomes.** *J Neurointerv Surg* 2015;7:478–83 CrossRef Medline
13. Broderick JP, Palesch YY, Demchuk AM, et al; Interventional Management of Stroke (IMS) III Investigators. **Endovascular therapy after intravenous t-PA versus t-PA alone for stroke.** *N Engl J Med* 2013;368:893–903 CrossRef Medline
14. Kidwell CS, Jahan R, Gornbein J, et al; MR RESCUE Investigators. **A trial of imaging selection and endovascular treatment for ischemic stroke.** *N Engl J Med* 2013;368:914–23 CrossRef Medline
15. Ciccone A, Valvassori L, Nichelatti M, et al; SYNTHESIS Expansion Investigators. **Endovascular treatment for acute ischemic stroke.** *N Engl J Med* 2013;368:904–13 CrossRef Medline
16. Dorn F, Lockau H, Stetefeld H, et al. **Mechanical thrombectomy of M2-occlusion.** *J Stroke Cerebrovasc Dis* 2015;24:1465–70 CrossRef Medline
17. Flores A, Tomasello A, Cardona P, et al; Catalan Stroke Code and Reperfusion Consortium Cat-SCR. **Endovascular treatment for M2 occlusions in the era of stentriever: a descriptive multicenter experience.** *J Neurointerv Surg* 2015;7:234–37 CrossRef Medline
18. Fischer E. **Die lageabweichungen der vorderen hirnarterie im gefäßbild.** *Zentralbl Neurochir* 1938;3:300–13
19. Tanriover N, Kawashima M, Rhoton AL Jr, et al. **Microsurgical anatomy of the early branches of the middle cerebral artery: morphometric analysis and classification with angiographic correlation.** *J Neurointerv Surg* 2003;98:1277–90 Medline
20. Gibo H, Carver CC, Rhoton AL Jr, et al. **Microsurgical anatomy of the middle cerebral artery.** *J Neurointerv Surg* 1981;54:151–69 Medline

Mechanical Thrombectomy of Distal Occlusions in the Anterior Cerebral Artery: Recanalization Rates, Periprocedural Complications, and Clinical Outcome

J. Pfaff, C. Herweh, M. Pham, S. Schieber, P.A. Ringleb, M. Bendszus, and M. Möhlenbruch

ABSTRACT

BACKGROUND AND PURPOSE: Patients with acute ischemic stroke in the anterior circulation are at risk for either primary or, following mechanical thrombectomy, secondary occlusion of the anterior cerebral artery. Because previous studies had only a limited informative value, we report our data concerning the frequency and location of distal anterior cerebral artery occlusions, recanalization rates, periprocedural complications, and clinical outcome.

MATERIALS AND METHODS: We performed a retrospective analysis of prospectively collected data of patients with acute ischemic stroke undergoing mechanical thrombectomy in the anterior circulation between June 2010 and April 2015.

RESULTS: Of 368 patients included in this analysis, we identified 30 (8.1%) with either primary ($n = 17$, 4.6%) or secondary ($n = 13$, 3.5%) embolic occlusion of the distal anterior cerebral artery. The recanalization rate after placement of a stent retriever was 88%. Periprocedural complications were rare and included vasospasms ($n = 3$, 10%) and dissection ($n = 1$, 3.3%). However, 16 (53.5%) patients sustained an (at least partial) infarction of the anterior cerebral artery territory. Ninety days after the ictus, clinical outcome according to the modified Rankin Scale score was the following: 0–2, $n = 11$ (36.6%); 3–4, $n = 9$ (30%); 5–6, $n = 10$ (33.3%).

CONCLUSIONS: Occlusions of the distal anterior cerebral artery affect approximately 8% of patients with acute ischemic stroke in the anterior circulation receiving mechanical thrombectomy. Despite a high recanalization rate and a low complication rate, subsequent (partial) infarction in the anterior cerebral artery territory occurs in approximately half of patients. Fortunately, clinical outcome appears not to be predominately unfavorable.

ABBREVIATIONS: ACA = anterior cerebral artery; MT = mechanical thrombectomy

Mechanical thrombectomy (MT) is an effective treatment in acute ischemic stroke secondary to a large-vessel occlusion.^{1–4} Patients with acute ischemic stroke secondary to an occlusion of the internal carotid artery–T, middle cerebral artery trunk (M1), or MCA secondary division (M2) have relatively high rates of revascularization and favorable clinical outcomes after MT.^{5,6} Unfortunately, for patients with ICA–T occlusions and MCA occlusions, there is a risk of approximately 8.6%–11.4% for secondary emboli

into the anterior cerebral artery (ACA), especially the distal branches such as the pericallosal artery, during MT.^{2,7,8} Although various technical possibilities, such as proximal flow control or combined aspiration, have been recommended to reduce the risk of secondary emboli^{9–13}, occlusions of the distal ACA occur.

Regardless of the cause of the occlusion (primary occlusion or secondary emboli during MT), cerebral infarctions in the ACA territory may cause relevant clinical deficits by affecting the primary or supplementary motor areas.¹⁴ In a previous, relatively small patient cohort ($n = 6$), treatment of secondary ACA occlusions was technically successful in 80% of the cases and uneventful in all instances.⁷

We present data on the frequency and location of distal ACA occlusions, recanalization rates, periprocedural complications, and clinical outcome.

MATERIALS AND METHODS

Patient Selection

On the basis of a prospectively collected patient cohort with acute ischemic stroke undergoing MT in the anterior circulation at our institution between June 2010 and April 2015, we

Received July 27, 2015; accepted after revision August 29.

From the Departments of Neuroradiology (J.P., C.H., M.P., M.B., M.M.) and Neurology (S.S., P.A.R.), University of Heidelberg, Heidelberg, Germany.

Mirko Pham, Christian Herweh, Simon Schieber, and Peter Arthur Ringleb contributed in data collection and reporting of this study. Johannes Pfaff, Martin Bendszus, and Markus Möhlenbruch had access to all data and supervised data collection and analysis, writing, and editing of article.

This work received no specific grant from any funding agency in the public, commercial, or not-for-profit sectors.

Please address correspondence to Johannes Pfaff, MD, University of Heidelberg, Department of Neuroradiology, Im Neuenheimer Feld 400, 69120 Heidelberg, Germany; e-mail: johannes.pfaff@med.uni-heidelberg.de

<http://dx.doi.org/10.3174/ajnr.A4594>

selected patients with a primary or secondary embolic occlusion of the distal ACA for this retrospective analysis. We excluded patients with an absent or severely hypoplastic ipsilateral A1 segment and those with proximal occlusions of the A1 segment from this analysis.

Stroke Therapy

Our institution provides neurologic, neuroradiologic, and neurointerventional services within a maximum-care university hospital center serving more than 500,000 individuals within its county limits and nearly 2.3 million within a greater metropolitan area. For each patient, a stroke neurologist performed physical neurologic examinations and detailed assessment of the NIHSS score in the emergency department on admission. Patients with suspected acute ischemic stroke received a standardized stroke imaging protocol: either MR imaging (including axial DWI, axial FLAIR, axial SWI, TOF-MRA, contrast-enhanced MRA of the aortic arch and cervical arteries, and axial PWI) or CT (including a non-contrast-enhanced CT, CT angiography, and perfusion CT) for assessment of their eligibility for intravenous rtPA and MT. The decision between MR imaging and CT was made individually on the basis of the patient's condition, known or unknown time of symptom onset, MR imaging eligibility, and immediate availability of the MR imaging and CT scanners.

Administration and dosing of intravenous rtPA followed national and international guidelines and an institutional standard operating procedure. Patients were considered eligible for MT by the treating neurointerventionalist if an occlusion of a major intracranial artery was detected by CTA or MRA, therapy could be accomplished within 8 hours of onset, the NIHSS score was ≥ 8 on evaluation, and the initial imaging excluded hemorrhage or a large infarct core of more than one-third of the middle cerebral artery territory or an ASPECTS of < 6 . In case of unknown onset of symptoms, patients were considered eligible for MT if stroke imaging ruled out a large infarct core and revealed a relevant, salvageable penumbra. No age limit was used as an inclusion or exclusion criterion for eligibility for MT, and the decision to perform MT was made individually on the basis of the patient's comorbidities, prestroke mRS, and the assumed choice of the patient. In case of fluctuating or progressive neurologic deficits, patients with minor symptoms (NIHSS score of < 8) were treated as well.

Intraprocedural use of mechanical and/or pharmacologic treatments remained at the discretion of the treating neurointerventionalist. Microcatheters and stent retrievers used for MT in this patient cohort were subject to change due to technical development during the observation period. Between June 2010 and July 2013, general anesthesia, performed by experienced neurointensivists, was routinely administered during MT. Starting in August 2013, procedures were performed with the patient under conscious sedation as well. Independent of the performed management of sedation, patients received standardized peri-interventional management and monitoring of physiologic target values according to our in-house standard operating procedure at the discretion of the neurointensivist adapted to the patient and situation.

Postinterventional Management

All patients were observed in a neurologic intensive care unit after MT. The aim was transfer to the stroke unit as soon as possible, depending on the condition of the patient. Follow-up imaging (either CT or MR imaging) was routinely performed at 20–36 hours after treatment, or earlier if neurologic deterioration occurred. Postinterventional NIHSS and mRS were assessed by detailed physical examinations performed by an independent stroke neurologist at discharge. Follow-up data after 3 months were obtained by an in-patient visit or a telephone call by a neurologist not blinded to the type of treatment. The modified Rankin Scale was used to measure the severity of the disability.

Data Collection

Data collection included baseline demographics (age and sex) and medical history (eg, hypertension, coronary artery disease, congestive heart failure, atrial fibrillation, diabetes mellitus, hypercholesterolemia, history of smoking, and previous stroke) and symptom onset time and stroke severity as measured by the NIHSS. The time of initiation of stroke imaging and the time of start of angiography were captured automatically by the CT scanner and angiography system. The onset and duration of occlusion (secondary emboli) and time of recanalization were evaluated according to the timestamp of the referring angiographic image. Vessel diameter and location of the occlusion were assessed on angiographic images as well. The location of the occlusion was categorized following the segmentation of the ACA with regard to its anatomic position relative to the corpus callosum and the origin of the frontopolar artery, orbitofrontal artery, callosomarginal artery, and distal branches as characterized by Lehecka et al.¹⁵ Devices and medication used during the interventional procedures, number of thrombectomy maneuvers, and intraprocedural complications were evaluated according to the treatment protocols. Angiographic outcome by TICI and complications (eg, vessel perforation, dissection of the anterior cerebral artery) were assessed by a senior neurointerventionalist. The incidences of cerebral infarction, parenchymal hemorrhage (by criteria of the second European-Australasian Acute Stroke Study [ECASS II])¹⁶, or subarachnoid hemorrhage were assessed by using routinely performed follow-up imaging. Clinical outcome was evaluated according to the modified Rankin Scale.

Statistical Analysis

We compared data by using the χ^2 test for categorical variables. $P < .05$ was considered significant in the final model. All statistical analyses were performed by using SPSS 21.0.0.0 (IBM, Armonk, New York).

Ethics Approval

The study was approved by our local ethics committee.

RESULTS

Between June 2010 and April 2015, 388 patients underwent MT due to an acute ischemic stroke in the anterior circulation at our institution. Twenty of 388 (5.2%) patients were excluded because of an absent or severely hypoplastic ipsilateral A1 segment. Among the remaining 368 patients, we identified 30 (8.1%) with

a distal ACA occlusion (for patient baseline characteristics, see Table 1). The distal ACA occlusion was, according to initial angiographic imaging, preexisting in 17/368 (4.6%) cases and occurred in 13/368 (3.5%) patients secondary to a recanalization maneuver (for distal ACA occlusion sites, see Table 2).

Mechanical thrombectomy with a stent retriever was intended for all patients, but a stent retriever could not be deployed in 5/30 (16.6%) because placement of a guidewire ($n = 1$, 3.3%; occlusion in the middle pericallosal artery [superior

segment]), or placement of a microcatheter behind the thrombus was not possible ($n = 4$, 13.3%; occlusion in the middle pericallosal artery [inferior segment, $n = 1$], distal pericallosal artery [$n = 2$], and callosomarginal artery [$n = 1$]). In 2 of these cases (6.6%), intra-arterial rtPA (5 mg and 2 mg, respectively) was administered immediately at the occlusion via a microcatheter. In consideration of the time window and possible risks, there was no further treatment in the other 3 (10%) cases. Deployment of a stent retriever was achieved and MT was performed in 25/30 (83.3%) patients (for type and manufacturer of the devices used as well as the number of MT maneuvers performed, see Table 3).

Table 1: Baseline characteristics of patients with a distal anterior cerebral artery occlusion

Characteristics	Patients (N = 30)
Age (yr), mean (SD)	64 (13)
Male	14 (46.6%)
Hypertension	20 (66.6%)
Diabetes mellitus	5 (16.6%)
Atrial fibrillation	13 (43.3%)
Coronary artery disease	3 (10%)
Congestive heart failure	2 (6.6%)
Hypercholesterolemia	8 (26.6%)
Previous stroke	0 (0%)
History of smoking	3 (10%)
Prestroke mRS	
0	22 (73.3%)
1	5 (16.6%)
2	3 (10%)
Initial NIHSS score, median (IQR)	18 (13–23)
Time from stroke onset to initial imaging (min), median (IQR)	90 (61–155)
CT	16
MR	14
Time from stroke onset to imaging ^a (min), median (IQR)	
CT	76 (55–150)
MR	154 (87–230)
ASPECTS ^a , median (IQR)	
CT	9 (9)
MR	7 (7–9) ^b
Initial occlusion site	
ICA (excluding Carotid-T)	1 (3.3%)
Carotid-T	18 (60%)
M1	9 (30%)
M2	2 (6.6%)
Intravenous tPA	25 (83.3%)
Time from stroke onset to groin puncture (min), median (IQR)	211 (139–289)

Note:—IQR indicates interquartile range.

^a According to the imaging modality.

^b MR-ASPECTS was assessed on axial diffusion-weighted images.

Angiographic Outcome

Recanalization of the distal ACA occlusion (TICI 2b/3) was achieved in 22/30 (73.3%) patients. However, in each of these 22 patients, at least 1 stent-retrieval maneuver was performed. With regard to all patients in whom placement of a stent retriever was possible ($n = 25$), the accumulated recanalization rate (TICI 2b/3) was 88% (Fig 1). Recanalization after a single retrieval maneuver occurred in 17/30 (56.6%) cases with a distal ACA occlusion, and in 68% (17/25) of all patients in whom placement of a stent retriever was possible. None of the patients in whom a stent retriever could not be properly placed achieved TICI 2b/3 (5/30, 16.6%). In 3 cases in which stent retrievers were used (Aperio; Acandis, Pforzheim, Germany; Revive; Codman Neurovascular, Raynham, Massachusetts; and Solitaire FR; Covidien, Irvine, California, respectively), recanalization could not be achieved. With

Table 3: List of types, manufacturers, and number of passes of devices used for mechanical thrombectomy

Device	Manufacturer	Size (mm)	No. of Patients Treated	Total No. of Passes
Aperio ^a	Acandis	4.5 × 30	1	3
Capture ^a	MindFrame ^b	4.0 × 20	1	2
Catch Mini ^a	Balt ^c	3 × 15	3	4
ERIC ^a	MicroVention	4 × 24	1	1
Revive ^d	Codman	4.5 × 22	6	9
Solitaire FR ^d	Covidien	4 × 20	12	17
Trevo ProVue ^d	Stryker ^e	4 × 20	1	2

^a Devices fitting through .017-inch microcatheters (eg, Headway 17; MicroVention).

^b Irvine, California.

^c Montmorency, France.

^d Devices fitting through .021-inch microcatheters (eg, Rebar 18; Covidien), and .027-inch microcatheters (Revive; Codman Neurovascular; Rebar 27; Covidien).

^e Kalamazoo, Michigan.

Table 2: Occlusion site and vessel diameter of the anterior cerebral artery

Occlusion Site	Total (N = 30)	Vessel Diameter (mm), mean (SD)	No. of Device Passes ^a , mean (SD)
Proximal pericallosal artery = A2 segment (between AcomA and genu of corpus callosum)	7 (23.3%)	1.9 (0.4)	1.28 (0.69)
Middle pericallosal artery = A3 segment (curving around genu of corpus callosum)			
Inferior segment	6 (20%)	1.8 (0.2)	2 (1.26)
Anterior segment	2 (6.6%)	2.1 (0.3)	1.5 (0.5)
Superior segment	8 (26.6%)	1.7 (0.4)	1.57 (0.72)
Distal pericallosal artery			
A4 and A5 segments and distal branches other than CMA	5 (16.6%)	1.7 (0.4)	1 (0)
CMA	2 (6.6%)	1.5 (0.1)	1 (0)

Note:—AcomA indicates anterior communicating artery; CMA, callosomarginal artery.

^a In patients in whom placement of a stent retriever was possible.

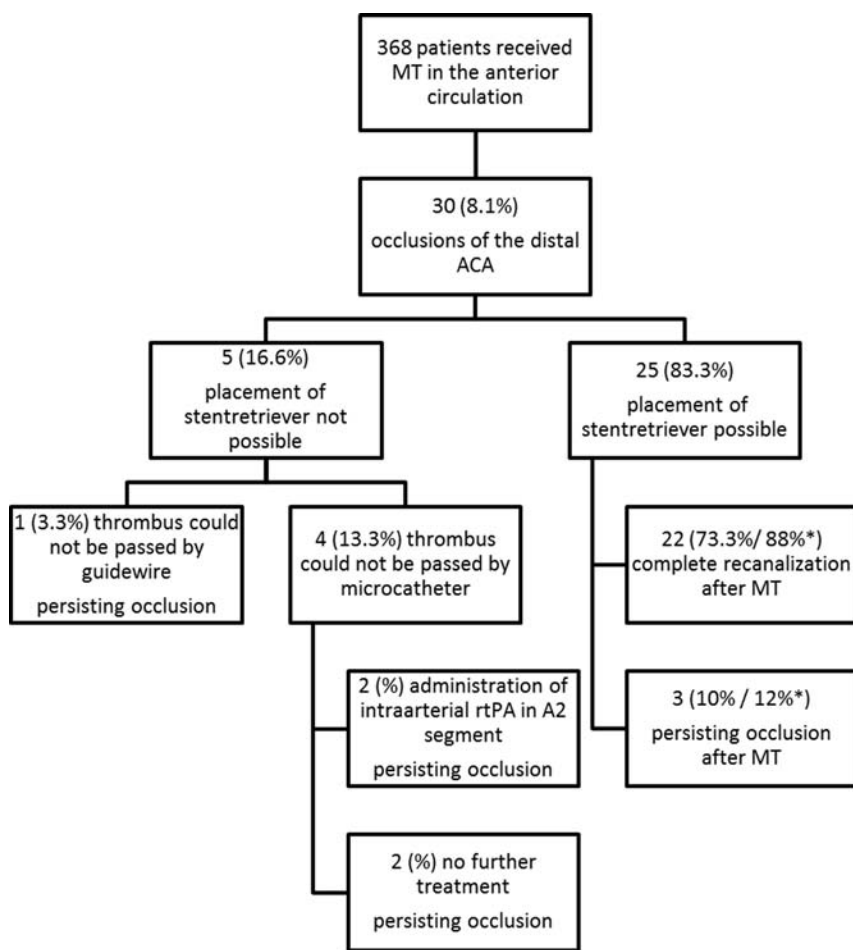


FIGURE Flowchart of treatments of distal ACA occlusions. The asterisk indicates the percentage of the overall successful stent-retriever placements.

regard to the possible risk of vessel injury and/or rupture, no other devices were used, and no further recanalization maneuvers were performed in these patients.

Intraprocedural Complications and Frequency of Infarction and Hemorrhage in the ACA Territory

There were 3 cases of vasospasms in the distal ACA following a retrieval maneuver in the superior A3 segment ($n = 2$) and the callosomarginal artery ($n = 1$). In 2 cases, the vasospasms resolved completely after intra-arterial administration of nimodipine into the affected segment via a microcatheter. The third case of vasospasm was self-limiting within 5 minutes without further treatment.

A dissection of the distal ACA (A4/A5 segment) with minimal distal flow impairment occurred in 1 patient after thrombectomy. Considering the risk of further manipulation and the location of the dissected vessel, no further treatment was considered. According to the imaging data and treatment protocols, there was no vessel perforation with secondary hemorrhage. We did not observe secondary emboli from the ACA into a new vascular territory. Furthermore, no air emboli or device detachment was observed.

Follow-up imaging revealed partial or complete ACA infarction in 16/30 (53.3%) patients, 11 of whom had a primary and 5 of

whom had a secondary occlusion. The frequency of infarction between both groups was, however, not significantly different in this small patient cohort ($P = .153$). There was only 1 case (3.3%) with hemorrhagic transformation in the ACA territory (superior frontal gyrus) with confluent petechiae within the infarcted area, but without space-occupying effect (HI2, according to ECASS II criteria). Four of 30 (13.3%) patients exhibited angiographically occult, self-limiting, minimal SAH in the ipsilateral Sylvian fissure detected on follow-up CT imaging. SAHs were estimated to be caused by recanalization maneuvers in the distal MCA (M2 segment) in these patients. None of the patients experienced SAH in the anterior cerebral artery territory.

Clinical Outcome

Ninety days after the ictus, clinical outcome according to the modified Rankin Scale score was the following: 0–2, $n = 11$ (36.6%); 3–4, $n = 9$ (30%); 5–6, $n = 10$ (33.3%).

DISCUSSION

ACA emboli may occur before or during intra-arterial treatment of an ICA or MCA occlusion. The frequency of new emboli during IV, intra-arterial, or combined IV–intra-arterial treatment of a large-vessel occlusion in the anterior circulation has been reported to be between 1.7% and 15%.^{7,8,17} In our patient cohort, the rate of new distal ACA emboli secondary to a recanalization maneuver was lower (3.5%). Similar to secondary emboli, a relatively low frequency of primary distal ACA occlusions (4.6%) occurred. However, in combination, about 8% of all patients with a large-vessel occlusion of the anterior circulation receiving MT had a distal ACA occlusion, which is consistent with the results from the Multicenter Randomized Clinical Trial of Endovascular Treatment for Acute Ischemic Stroke in the Netherlands (MR CLEAN) trial.² If one assumes that following the publication of recent study data on thrombectomy^{1–3,18} the frequency of patients receiving MT will increase, distal ACA occlusions and the corresponding prevention and treatment options will become an even more relevant topic than they are today.

Because recanalization is a predictor of good clinical outcome,¹⁹ high recanalization rates should be achieved. Considering the risk of an infarction and possible neurologic deficits following an ACA occlusion¹⁴ and against the background of positive experience in the treatment of distal M2 occlusions,²⁰ interventional neuroradiologists are urged to consider treatment of distal ACA occlusions to achieve high recanalization rates. In

our patient cohort, the recanalization rate was 73.3% of all distal ACA occlusions, respectively, 88% after successful placement of a stent retriever. This is comparable with recanalization rates of M1 or M2 occlusions after MT.^{20–22} In 4 (13.3%) patients, placement of a microcatheter behind the thrombus was not possible. However, these cases were in 2010 and early 2012 when only “large” microcatheters (Rebar-18 and Rebar-27; Covidien) were available at our site. With the introduction of smaller microcatheters and stent retrievers, successful retrieval maneuvers in small and/or tortuous distal intracranial vessels will probably be easier.²³ For example, the outside diameter of the device-delivering microcatheter could be reduced by 29% by using a Headway 17 microcatheter (1.7F; MicroVention, Tustin, California) instead of a Rebar-18 microcatheter (2.4F). Thus, our department started using microcatheters with a 0.017-inch inner diameter in selected cases in the second quarter of 2012, when placement of our standard microcatheter (0.021-inch inner diameter) was not possible. So far, virtually every distal occlusion could be reached successfully.

The risk of periprocedural complications with MT in distal ACA occlusions does not seem to be higher than that in the MCA. We experienced 1 case of dissection (3.3%) and 3 cases of vasospasm (10%) but no case of symptomatic intracranial hemorrhage into the ACA territory. In comparison, the frequency of dissection (1.8%–4.5%), vasospasm (3%–22.5%, including asymptomatic vasospasm), and symptomatic intracranial hemorrhage (5%–10.9%) was reported within the same range or even higher during endovascular treatment of MCA occlusions.^{21,24,25}

Independent of the underlying cause of the occlusion, primary occlusion or thrombus fragmentation and secondary emboli as a by-product of recanalization maneuvers, occlusions of the ACA may cause infarction and significant neurologic deficits.¹⁴ Despite a high recanalization rate, ipsilateral infarction (at least partial) in the ACA territory occurred in 53.5% of our cases. This relatively high rate of ACA territory infarction might be secondary to insufficiency or absences of collaterals in the setting of concurrent or preceding ICA or MCA occlusion.^{26,27} With a frequency of 38.5% of ACA infarction in patients with secondary emboli, our data are comparable with those in previous studies, in which the frequency was reported to be 32% and 40%, respectively.^{7,8} Because primary occlusions are present longer than secondary occlusions before recanalization, the frequency of ACA infarction in patients with primary occlusions was higher (64.7%). However, our analysis did not reach statistical significance for this matter ($P = .153$). This finding should be viewed cautiously. A larger patient population might demonstrate a significant difference and, following the law of stroke (time is brain²⁸), probably with a disadvantage for primary occlusions.

Compared with outcomes in recent clinical trials, clinical outcomes after 90 days were not predominately^{1–3} unfavorable in this patient cohort. This outcome might be because of the following: a possible MCA and ACA territory infarction, due to a larger infarct volume and/or the involvement of the supplementary motor cortex.^{14,29}

Limitations

This analysis has several limitations. First, because this article focuses on occlusions of the distal ACA, the overall occurrence of occlusions of the ACA (including the A1 segment) is likely to be higher. Under this premise, our data might underestimate the frequency of occlusions and infarctions in the ACA territory.

Second, allocation of clinical deficits to the ACA territory is, especially in patients with concurrent MCA infarction, not always possible. Therefore, comparison of clinical outcome of these patients with those of patients with isolated MCA territory infarction needs to be viewed cautiously.

Third, because occlusions were treated with different revascularization devices, a recommendation of a specific device for treatment of distal ACA occlusions is not possible and was not the aim of the study. In this patient cohort and in the large interventional stroke trials, the standard approach for treatment of an intracranial vessel occlusion was MT by using a stent retriever. However, MT in distal cerebrovascular occlusions appears to be feasible even with a direct-aspiration first-pass technique.³⁰ The smaller diameter and pronounced kinking of a vessel should be taken into account when choosing catheters and devices to minimize alteration of the vessel wall.

CONCLUSIONS

Occlusions of the distal ACA affect approximately 8% of patients with acute ischemic stroke in the anterior circulation undergoing MT. Despite a high recanalization rate and a low complication rate, subsequent (partial) infarction in the ACA territory occurred in approximately half of patients. Fortunately, clinical outcome appears not to be predominately unfavorable.

Disclosures: Christian Herweh—UNRELATED: Travel/Accommodations/Meeting Expenses Unrelated to Activities Listed: Travel accommodations and registration for the Live Interventional Neuroradiology & Neurosurgery Course, 2015, paid by Covidien. Mirko Pham—UNRELATED: Grants/Grants Pending: M.P. is supported by a Memorial Stipend from Else Kröner-Fresenius-Stiftung*; Payment for Lectures (including service on Speakers Bureaus): M.P. received speaker honorarium from Penumbra Europe GmbH; Travel/Accommodations/Meeting Expenses Unrelated to Activities Listed: Travel expenses from Covidien. Peter A. Ringleb—UNRELATED: Consultancy: Advisory Boards for Boehringer Ingelheim, Daiichi Sankyo, and Covidien; Payment for Lectures (including service on Speakers Bureaus): Bayer, Daiichi Sankyo, Boehringer Ingelheim, Comments: Lectures; Travel/Accommodations/Meeting Expenses Unrelated to Activities Listed: Boehringer Ingelheim, Bayer, Comments: travel support. Martin Bendszus—UNRELATED: Board Membership: Data Safety Monitoring Board Vascular Dynamics; Consultancy: Roche, Guerbet; Grants/Grants Pending: Deutsche Forschungsgemeinschaft; * Hopp Foundation; * Novartis; * Codman; * Guerbet; * Siemens; Payment for Lectures (including service on Speakers Bureaus): Guerbet, Novartis, Codman, Roche. Markus Möhlenbruch—UNRELATED: Board Membership: Codman Neurovascular; Consultancy: Acandis, MicroVention; Payment for Lectures (including service on Speakers Bureaus): Codman Neurovascular. *Money paid to the institution.

REFERENCES

- Campbell BC, Mitchell PJ, Kleinig TJ, et al; EXTEND-IA Investigators. Endovascular therapy for ischemic stroke with perfusion-imaging selection. *N Engl J Med* 2015;372:1009–18 CrossRef Medline
- Berkhemer OA, Fransen PS, Beumer D, et al; MR CLEAN Investigators. A randomized trial of intraarterial treatment for acute ischemic stroke. *N Engl J Med* 2015;372:11–20 CrossRef Medline
- Goyal M, Demchuk AM, Menon BK, et al; ESCAPE Trial Investigators. Randomized assessment of rapid endovascular treatment of ischemic stroke. *N Engl J Med* 2015;372:1019–30 CrossRef Medline
- Möhlenbruch M, Seifert M, Okulla T, et al. Mechanical thrombectomy compared to local-intraarterial thrombolysis in carotid T and

middle cerebral artery occlusions: a single center experience. *Clin Neuroradiol* 2012;22:141–47 CrossRef Medline

5. Shi ZS, Loh Y, Walker G, et al. **Clinical outcomes in middle cerebral artery trunk occlusions versus secondary division occlusions after mechanical thrombectomy: pooled analysis of the Mechanical Embolus Removal in Cerebral Ischemia (MERCi) and Multi MERCi trials.** *Stroke* 2010;41:953–60 CrossRef Medline
6. Frahm D, Wunderlich S, Schubert MI, et al. **Mechanical thrombectomy in acute occlusion of the carotid-T: a retrospective single center study in 51 patients.** *Clin Neuroradiol* 2014 Jul 25. [Epub ahead of print] CrossRef Medline
7. Kurre W, Vorlaender K, Aguilar-Pérez M, et al. **Frequency and relevance of anterior cerebral artery embolism caused by mechanical thrombectomy of middle cerebral artery occlusion.** *AJNR Am J Neuroradiol* 2013;34:1606–11 CrossRef Medline
8. King S, Khatri P, Carrozella J, et al; IMS & IMS II Investigators. **Anterior cerebral artery emboli in combined intravenous and intra-arterial rtPA treatment of acute ischemic stroke in the IMS I and II trials.** *AJNR Am J Neuroradiol* 2007;28:1890–94 CrossRef Medline
9. Stampfl S, Kabbasch C, Muller M, et al. **Initial experience with a new distal intermediate and aspiration catheter in the treatment of acute ischemic stroke: clinical safety and efficacy.** *J Neurointervent Surg* 2015 May 29. [Epub ahead of print] CrossRef Medline
10. Chueh JY, Kühn AL, Puri AS, et al. **Reduction in distal emboli with proximal flow control during mechanical thrombectomy: a quantitative in vitro study.** *Stroke* 2013;44:1396–401 CrossRef Medline
11. Chueh JY, Puri AS, Wakhloo AK, et al. **Risk of distal embolization with stent retriever thrombectomy and ADAPT.** *J Neurointervent Surg* 2014 Dec 24. [Epub ahead of print] CrossRef Medline
12. Nguyen TN, Malisch T, Castonguay AC, et al. **Balloon guide catheter improves revascularization and clinical outcomes with the Solitaire device: analysis of the North American Solitaire Acute Stroke Registry.** *Stroke* 2014;45:141–45 CrossRef Medline
13. Turk AS, Frei D, Fiorella D, et al. **ADAPT FAST study: a direct aspiration first pass technique for acute stroke thrombectomy.** *J Neurointervent Surg* 2014;6:260–64 CrossRef Medline
14. Alonso A, Gass A, Rossmanith C, et al. **Clinical and MRI patterns of pericallosal artery infarctions: the significance of supplementary motor area lesions.** *J Neurol* 2012;259:944–51 CrossRef Medline
15. Lehecka M, Dashti R, Hernesniemi J, et al. **Microneurosurgical management of aneurysms at the A2 segment of anterior cerebral artery (proximal pericallosal artery) and its frontobasal branches.** *Surg Neurol* 2008;70:232–46; discussion 246 CrossRef Medline
16. Hacke W, Kaste M, Fieschi C, et al. **Randomised double-blind placebo-controlled trial of thrombolytic therapy with intravenous alteplase in acute ischaemic stroke (ECASS II): Second European-Australasian Acute Stroke Study Investigators.** *Lancet* 1998;352:1245–51 CrossRef Medline
17. Smith WS, Sung G, Starkman S, et al; MERCi Trial Investigators. **Safety and efficacy of mechanical embolectomy in acute ischemic stroke: results of the MERCi trial.** *Stroke* 2005;36:1432–38 CrossRef Medline
18. Möhlenbruch M, Stampfl S, Behrens L, et al. **Mechanical thrombectomy with stent retrievers in acute basilar artery occlusion.** *AJNR Am J Neuroradiol* 2014;35:959–64 CrossRef Medline
19. Rha JH, Saver JL. **The impact of recanalization on ischemic stroke outcome: a meta-analysis.** *Stroke* 2007;38:967–73 CrossRef Medline
20. Dorn F, Lockau H, Stetefeld H, et al. **Mechanical thrombectomy of M2-occlusion.** *J Stroke Cerebrovasc Dis* 2015;24:1465–70 CrossRef Medline
21. Dorn F, Stehle S, Lockau H, et al. **Endovascular treatment of acute intracerebral artery occlusions with the Solitaire stent: single-center experience with 108 recanalization procedures.** *Cerebrovasc Dis* 2012;34:70–77 CrossRef Medline
22. Pereira VM, Gralla J, Davalos A, et al. **Prospective, multicenter, single-arm study of mechanical thrombectomy using Solitaire flow restoration in acute ischemic stroke.** *Stroke* 2013;44:2802–07 CrossRef Medline
23. Haussen DC, Lima A, Nogueira RG. **The Trevo XP 3x20 mm retriever ('Baby Trevo') for the treatment of distal intracranial occlusions.** *J Neurointervent Surg* 2015 May 6. [Epub ahead of print] CrossRef Medline
24. Behme D, Gondecki L, Fiethen S, et al. **Complications of mechanical thrombectomy for acute ischemic stroke—a retrospective single-center study of 176 consecutive cases.** *Neuroradiology* 2014;56:467–76 CrossRef Medline
25. Akins PT, Amar AP, Pakbaz RS, et al; SWIFT Investigators. **Complications of endovascular treatment for acute stroke in the SWIFT trial with Solitaire and Merci devices.** *AJNR Am J Neuroradiol* 2014; 35:524–28 CrossRef Medline
26. Singer OC, Berkefeld J, Nolte CH, et al. **Collateral vessels in proximal middle cerebral artery occlusion: the ENDOSTROKE study.** *Radiology* 2015;274:851–58 CrossRef Medline
27. Souza LC, Yoo AJ, Chaudhry ZA, et al. **Malignant CTA collateral profile is highly specific for large admission DWI infarct core and poor outcome in acute stroke.** *AJNR Am J Neuroradiol* 2012;33:1331–36 CrossRef Medline
28. Saver JL. **Time is brain: quantified.** *Stroke* 2006;37:263–66 CrossRef Medline
29. Ribo M, Flores A, Mansilla E, et al. **Age-adjusted infarct volume threshold for good outcome after endovascular treatment.** *J Neurointervent Surg* 2014;6:418–22 CrossRef Medline
30. Navia P, Larrea JA, Pardo E, et al. **Initial experience using the 3MAX cerebral reperfusion catheter in the endovascular treatment of acute ischemic stroke of distal arteries.** *J Neurointervent Surg* 2015 Jul 15. [Epub ahead of print] CrossRef Medline

Endovascular Treatment of Unruptured Paraclinoid Aneurysms: Single-Center Experience with 400 Cases and Literature Review

K. Shimizu, H. Imamura, Y. Mineharu, H. Adachi, C. Sakai, and N. Sakai



ABSTRACT

BACKGROUND AND PURPOSE: Paraclinoid aneurysms have been increasingly treated endovascularly. The natural history of these aneurysms has gradually been elucidated. The purpose of this study was to assess the safety and efficacy of endovascular treatment for these aneurysms.

MATERIALS AND METHODS: We performed a retrospective review of 377 patients with 400 paraclinoid aneurysms treated between January 2006 and December 2012. Their clinical records, endovascular reports, and radiologic and clinical outcomes were analyzed. Because aneurysms ≥ 7 mm are at higher risk of rupture, we classified aneurysms as small (< 7 mm) or large (≥ 7 mm).

RESULTS: Overall, 115 of the 400 aneurysms (28.8%) were large (≥ 7 mm). Thromboembolic complications were found significantly more often with large aneurysms than with small ones (7.4% vs 1.0%, $P = .001$). Hemorrhagic complications were found only with small aneurysms (0.7%). The 6-month morbidity rates were similar for small (1.0%) and large (0.8%) aneurysms. Immediate angiographic outcomes were similar ($P = .37$), whereas recurrences and retreatment occurred more frequently with large aneurysms ($P = .001$ and $P = .007$, respectively). Multivariate analysis showed that aneurysm size was the only independent predictor for recurrence ($P = .005$). Most recurrences (81%) were detected by scheduled angiography at 6 months.

CONCLUSIONS: Aneurysm size influenced the type of complication (thromboembolic or hemorrhagic) and the recurrence rate. Given the approximately 1% annual rupture rate for aneurysms ≥ 7 mm, analysis of our data supports the rationale of using prophylactic endovascular treatment for unruptured paraclinoid aneurysms ≥ 7 mm.

ABBREVIATION: UCAS = Unruptured Cerebral Aneurysm Study

Paraclinoid aneurysms are located in the clinoid and ophthalmic segments of the ICA.¹ Because of the anatomic structures adjacent to the segments of the ICA (eg, anterior clinoid process, cavernous sinus, optic apparatus), microsurgical treatment of a paraclinoid aneurysm can be challenging.² With the development of novel devices and the need for less-invasive treatment, an increasing number of paraclinoid aneurysms have been treated by endovascular treatment. The natural history of unruptured intracranial aneurysms has been

reported as represented by the International Study of Unruptured Intracranial Aneurysms and the Unruptured Cerebral Aneurysm Study (UCAS) by Japanese investigators.³⁻⁸ According to these studies, the size and location of the aneurysms were regarded as leading predictors of rupture. The UCAS Japan investigators reported that the annual rupture rate of paraclinoid aneurysms was 1% overall when they were 7–24 mm in largest dimension.⁷ Therefore, aneurysms ≥ 7 mm would be good candidates for prophylactic endovascular treatment. There have been no studies reported, however, that analyzed the complication and recurrence rates relative to the annual rupture rate.⁹⁻¹⁵

The purpose of the present study was to assess the safety and efficacy of endovascular treatment for paraclinoid aneurysms in a cohort of 400 cases. The advantage of this study was that we could estimate the clinical outcome of endovascular treatment for these aneurysms in comparison with the natural history of an aneurysm of the same size in the same ethnic population by using the UCAS Japan data.

Received June 4, 2015; accepted after revision August 21.

From the Department of Neurosurgery (K.S., H.I., H.A., N.S.), Kobe City Medical Center General Hospital, Kobe, Japan; Division of Neuroendovascular Therapy (C.S., N.S.), Institute of Biomedical Research and Innovation, Kobe, Japan; and Department of Neurosurgery (Y.M.), Kyoto University Graduate School of Medicine, Kyoto, Japan.

Please address correspondence to Kampei Shimizu, MD, Department of Neurosurgery, Kobe City Medical Center General Hospital, 2-1-1 Minatojima-Minamimachi, Chuo-ku, Kobe 650-0047, Japan; e-mail: k.shimizu.830923@gmail.com

Indicates open access to non-subscribers at www.ajnr.org

<http://dx.doi.org/10.3174/ajnr.A4577>

MATERIALS AND METHODS

Study Population

Between January 2006 and December 2012, a total of 889 endovascular coil embolizations were conducted for unruptured intracranial aneurysms at Kobe City Medical Center General Hospital. Among these procedures, 415 were applied to 403 paraclinoid aneurysms in 380 patients. Surgical clipping was chosen for only 6 paraclinoid aneurysms during this period. Three aneurysms in 3 patients were excluded because they were treated by parent artery occlusion. Thus, a total of 400 paraclinoid aneurysms in 377 patients were included in the study.

Paraclinoid aneurysms at our institution are categorized as anterior wall, ventral paraclinoid, true ophthalmic, or carotid cave aneurysms according to the al-Rodhan et al¹⁶ classification modified by Iihara et al.¹⁷ Aneurysm size was categorized as small (<7 mm) or large (≥ 7 mm). We retrospectively reviewed the medical records and radiologic data for these patients. Informed consent for the treatment was obtained from all the patients, and our institutional review board approved the protocol.

The patient characteristics used in this analysis included age, sex, medical history (hypertension, diabetes mellitus, dyslipidemia, polycystic kidney, number of aneurysms, smoking habit, family history of SAH), and neurologic symptoms. Radiologic characteristics included dome and neck size, dome:neck ratio, and location of aneurysms.

Endovascular Procedures

Procedures were performed with the patient under local anesthesia. All the patients were pretreated with daily doses of 100 mg of aspirin and 75 mg of clopidogrel for >5 days in preparation for a stent-assisted technique. After femoral puncture, a bolus of 4000–5000 U of heparin was administered intravenously, followed by intermittent intravenous infusion of 1000–2000 U of heparin to maintain the activated clotting time at 2 times the patient's baseline throughout the procedure. After the procedure, the patients were administered continuous intravenous argatroban 60 mg/day for 48 hours. Patients who underwent a stent-assisted procedure continued treatment with the dual antiplatelet therapy described above for 6 months, followed by 100 mg of aspirin or 75 mg of clopidogrel per day indefinitely. Otherwise, patients were treated with 100 mg of aspirin or 75 mg of clopidogrel per day for 6 months, followed by no antiplatelet therapy.

The decision about whether a stent-assisted technique should be used was based on the risk of coil protrusion into the parent artery. We started measuring aspirin-reaction units and P2Y₁₂ reaction units in 2010 and used these values for the decision-making process in 2013. Therefore, the antiplatelet function test was not taken into account for the selection of antiplatelet drugs during the study period.

Angiographic Outcomes and Follow-Up

Angiographic outcomes were divided into 3 categories: complete occlusion, neck remnant, body filling.¹⁸ Immediate angiographic outcomes were assessed by using DSA on the date of treatment. Follow-up angiographic outcomes were assessed by DSA and/or MRA. Recurrence was defined as any decrease in the occluded area demonstrated by DSA or MRA. Recurrences were subdivided

into those that required intervention and those that were treated conservatively. For each aneurysm, angiographic follow-up by DSA was scheduled for 6 months after treatment. Radiographic follow-up by MRA was performed at various intervals. When recanalization was suspected, DSA was performed to identify indications for additional treatment.

Complications related to the procedures were recorded based on symptoms and radiologic examination. Ischemic and hemorrhagic complications were diagnosed by using CT and MRI. When patients displayed neurologic symptoms, including headache, radiologic examinations were conducted just after treatment. Otherwise, those examinations were routinely conducted on the day after treatment. Other complications, such as visual impairment and oculomotor nerve palsy, were considered to be procedure-related based on the time of onset and radiographic analysis. Good clinical outcome was defined as an mRS of 0–2 at 6 months. Complications that left a neurologic deficit at 6 months were described as permanent morbidity.

In this study, aneurysm size was classified as small (<7 mm) or large (≥ 7 mm). We compared the results according to the aspects of the aneurysm location, therapeutic strategy (adjunctive technique), angiographic outcome, recurrence rate, frequency of complications, and subsequent clinical outcomes.

Statistical Analysis

The χ^2 test, Fisher exact test, and Student *t* test were used as appropriate. Factors found to be predictive for recurrence in the univariate analysis ($P < .15$) were entered into a multivariate logistic regression analysis. A value of $P < .05$ was considered to indicate statistical significance. All statistical analyses were performed with JMP software, version 10.0 (SAS Institute, Cary, North Carolina).

RESULTS

Demographics

A total of 400 unruptured paraclinoid aneurysms in 377 patients were treated endovascularly. Characteristics of the patients and aneurysms are summarized in Table 1. Two hundred eighty-five aneurysms (71.3%) were small, and 350 (87.5%) occurred in female patients. The mean age of the patients was 56.2 ± 11.2 years (range, 27–80 years), and 23 patients (6.1%) were ≥ 70 years. The numbers of patients who had a medical history of hypertension, diabetes mellitus, dyslipidemia, or polycystic kidney disease were 151 (40.1%), 19 (5.0%), 83 (22.0%), and 0, respectively. Seventy-eight patients (20.7%) were former or current smokers, 45 (11.9%) had a family history of SAH, and 86 (22.6%) had multiple aneurysms. Three hundred eighty-three aneurysms (95.8%) were asymptomatic. Variables that were seen significantly more often or were more frequently observed in patients with large aneurysms included older age ($P = .003$), former or current smoking habit ($P = .042$), and symptoms caused by the aneurysm ($P = .002$).

Radiologic characteristics of the aneurysms are summarized in Table 2. The mean dome:neck ratio was significantly lower with small aneurysms (1.6 ± 0.4) than with large aneurysms (2.2 ± 0.7) ($P < .001$). The location of aneurysms was also significantly different between the groups ($P = .003$). The most prevalent lo-

Table 1: Characteristics of patients and aneurysms^a

Characteristic	Patients	Aneurysms			P
		Total	<7 mm	≥7 mm	
Total no.	377	400	285	115	
Age					
Mean, y	56.2 ± 11.2	56.8 ± 11.1	55.7 ± 11.1	59.3 ± 10.6	.003
≥70 y	23 (6.1%)	23 (5.8%)	17 (6.0%)	6 (5.2%)	.209
Female sex	330 (87.5%)	350 (87.5%)	250 (87.7%)	100 (87.0%)	.835
Medical history					
Hypertension	151 (40.1%)	162 (40.5%)	108 (37.9%)	54 (47.0%)	.095
Diabetes mellitus	19 (5.0%)	20 (5.0%)	14 (4.9%)	6 (5.2%)	.899
Dyslipidemia	83 (22.0%)	86 (21.5%)	63 (22.1%)	23 (20.0%)	.643
Polycystic kidney	0 (0%)	0 (0%)	0 (0%)	0 (0%)	1
Multiple aneurysms	86 (22.6%)	108 (27.0%)	81 (28.4%)	27 (23.5%)	.314
≥3 Aneurysms	11 (2.9%)	18 (4.5%)	12 (4.2%)	6 (5.2%)	.660
Former or current smoking	78 (20.7%)	82 (20.5%)	51 (17.9%)	31 (27.0%)	.042
Familial history of SAH	45 (11.9%)	45 (11.3%)	35 (12.3%)	10 (8.7%)	.304
Reason for detection					
Screening or headache or dizziness	362 (96.0%)	383 (95.8%)	277 (97.2%)	106 (92.2%)	.002
Symptoms	5 (1.3%)	5 (1.3%)	0 (0%)	5 (4.4%)	
SAH due to another aneurysm	10 (2.7%)	12 (3.0%)	8 (2.8%)	4 (3.5%)	

^a Results are expressed as mean or no. (%).

Table 2: Radiologic characteristics of aneurysms

Characteristic	Total	Small (<7 mm)	Large (≥7 mm)	P
Total no.	400	285	115	
Largest dimension of aneurysm				
Mean, mm	6.5 ± 2.8	5.1 ± 1.0	10.0 ± 2.8	
Distribution				
<5 mm	136 (34.0%)	136 (47.7%)		
5–6 mm	149 (37.3%)	149 (52.3%)		
7–9 mm	63 (15.8%)		63 (54.8%)	
10–24 mm	52 (13.0%)		52 (45.2%)	
≥25 mm	0 (0.0%)			
Neck size ≥4 mm	135 (33.8%)	59 (20.7%)	76 (66.1%)	<.001
Dome:neck ratio				
Mean, mm	1.7 ± 0.6	1.6 ± 0.4	2.2 ± 0.7	<.001
≤2	299 (74.8%)	243 (85.3%)	56 (48.7%)	<.001
Wide neck 1 ^a	326 (81.5%)	243 (85.3%)	83 (72.2%)	.002
Location of aneurysm				
Anterior wall	97 (24.3%)	59 (20.7%)	38 (33.0%)	
Ventral paraclinoid	101 (25.3%)	70 (24.6%)	31 (27.0%)	
True ophthalmic	52 (13.0%)	34 (11.9%)	18 (15.7%)	
Carotid cave	150 (37.5%)	122 (42.8%)	28 (24.3%)	.003

^a One neck of ≥4 mm or dome:neck ≤2.

cation for small aneurysms was the carotid cave (42.8%), whereas that for large aneurysms was the anterior wall (33.0%).

Treatment Specifics

Treatment strategies are summarized in Table 3. All aneurysms were treated by endovascular coil embolization. A stent-assisted technique was more frequently used for large aneurysms (43.5%) than for small aneurysms (17.2%) ($P < .001$). The procedures failed for 3 small aneurysms (1.1%) and 1 large aneurysm (0.87%). Among these 4 failures, 2 small aneurysms were re-treated on another day by using different strategies. In the other 2 cases, the patients refused retreatment.

Angiographic Outcomes

Details about the angiographic outcomes are shown in Table 3. Follow-up angiography (DSA or MRA) at 6 months was available

for 386 aneurysms (96.5%). Among them, 273 (68.3%) were examined by DSA. MRA at 2 years (18 ± 6 months) was available for 291 aneurysms (72.8%). A total of 37 aneurysms (9.6%) recurred during the follow-up period, with 81% of them (30/37) detected by a scheduled angiography at 6 months.

Among the small aneurysms, immediate complete occlusion was achieved for 29 (10.2%), a neck remnant for 80 (28.1%), and body filling for 176 (61.8%). Radiologic follow-up was available for 96.5% (275/285), with a mean interval of 30 ± 19 months (range, 6–96 months). During the follow-up period, the complete occlusion rate increased to 72.4%. Eighteen aneurysms (6.5%) recurred, and retreatment was needed for 3 of them (1.1%).

For the large aneurysms, immediate complete occlusion was achieved in 9 (7.8%), a neck remnant in 40 (34.8%), and body filling in 66 (57.4%). Radiologic follow-up was available for 96.5% (111/115), with a mean interval of 36 ± 21 months (range, 6–83 months). During the follow-up period, complete occlusion was achieved in 55.0%. There were 19 recurrences (17.1%), and 7 (6.3%) underwent retreatment. The distributions of the immediate angiographic outcomes were almost the same in the small and large aneurysm groups ($P = .37$). During the follow-up period, however, the rate of body filling was significantly higher for large aneurysms than for small aneurysms ($P < .001$). As a result, the numbers of recurrences and retreatments were significantly higher for large aneurysms ($P = .001$ and $P = .007$, respectively).

The following factors were evaluated as predictors of recurrence: age, sex, location of the aneurysm, side, large (≥ 7 mm), wide neck (≥ 4 mm or aspect [dome:neck] ratio of ≤ 2), medical history (hypertension, diabetes mellitus, smoking habit), body filling at initial treatment, use of stent-assisted technique, ischemic complication (Table 4). The univariate analysis indicated that only the large size of an aneurysm was a significant predictor of recurrence ($P = .001$). In the multivariate analysis, large size was also a significant ($P = .005$) predictor after correction by side and ischemic complication ($P = .101$ and 0.097 in the univariate analysis, respectively). To show the trend for what we assessed to be major recanalization, the predictors of retreatment were also subjected to univariate analysis (Table 5). Among the factors listed above, large size ($P = .008$) and former or current smoking habit ($P = .031$) were associated with retreatment.

Procedure-Related Complications

There were 16 procedural complications (3.9%) (Table 6). Thromboembolic complications were most frequent, which occurred in 12 patients (2.9%). Among them, permanent morbidity was observed in 3 patients (0.7%). Permanent morbidity included in-stent thrombosis that resulted in ICA occlusion in 1 patient and visual impairment due to an embolism in the ophthalmic

Table 3: Treatment strategies and results

	Total	<7 mm	≥7 mm	P
No. treated aneurysms	400	285	115	
Strategy				
Stent-assisted	99 (24.8%)	49 (17.2%)	50 (43.5%)	<.001
Not stent-assisted	301 (75.3%)	236 (82.8%)	65 (56.5%)	
Simple technique	20 (5.0%)	14 (4.9%)	6 (5.2%)	
Balloon-assisted	277 (69.3%)	219 (76.8%)	58 (50.4%)	
Failed	4 (1.0%)	3 (1.1%)	1 (0.87%)	
Immediate angiographic outcome				
Complete occlusion	38 (9.5%)	29 (10.2%)	9 (7.8%)	.374
Neck remnant	120 (30.0%)	80 (28.1%)	40 (34.8%)	
Body filling	242 (60.5%)	176 (61.8%)	66 (57.4%)	
Follow-up angiographic outcome ^a				
Complete occlusion	260 (67.4%)	199 (72.4%)	61 (55.0%)	<.001
Neck remnant	81 (21.0%)	60 (21.8%)	21 (18.9%)	
Body filling	45 (11.7%)	16 (5.8%)	29 (26.1%)	
Recurrence ^a	37 (9.6%)	18 (6.5%)	19 (17.1%)	.001
Conservative treatment	27 (7.0%)	15 (5.4%)	12 (10.8%)	.059
Retreatment	10 (2.6%)	3 (1.1%)	7 (6.3%)	.007
Rupture during follow-up ^a	1 (0.3%)	0	1 (0.9%)	.286

^a Follow-up data of 386 patients.

Table 4: Predictors of recurrence^a

Predictor	Recurrent	Not Recurrent	Univariate Analysis	Multivariate Analysis	
			P	P	OR (95% CI)
No. treated aneurysms	37	349			
Mean age, y	56.4 ± 11.6	56.9 ± 11.2	.784		
Men	6 (16.2%)	39 (11.2%)	.415		
Location			.733		
Anterior wall	8 (21.6%)	87 (24.9%)			
Ventral paraclinoid	12 (32.4%)	84 (24.1%)			
True ophthalmic	4 (10.8%)	45 (12.9%)			
Carotid cave	13 (35.1%)	133 (38.1%)			
Right side	21 (56.8%)	149 (42.7%)	.101	.114	1.75 (0.88–3.6)
Size ≥7 mm	19 (51.4%)	92 (26.4%)	.001	.005	2.75 (1.36–5.58)
Wide neck ^b	30 (81.1%)	284 (81.4%)	.965		
Medical history					
Hypertension	19 (51.4%)	137 (39.3%)	.154		
Diabetes mellitus	3 (8.1%)	15 (4.3%)	.399		
Former or current smoker	10 (27.0%)	67 (19.2%)	.257		
Body filling at initial treatment	21 (58.3%)	213 (61.2%)	.737		
Not stent-assisted	29 (78.4%)	261 (74.8%)	.631		
Ischemic complication	3 (8.1%)	9 (2.6%)	.097	.264	2.35 (0.48–8.83)

^a Results are given as the mean or no. (%).

^b Neck of ≥4 mm or aspect (dome:neck) ratio ≤ 2.

artery in 2 patients. In the other 9 patients (2.2%), the symptoms were mild and resolved spontaneously within a few days. Thromboembolic complications were found significantly more often in patients with large aneurysms (9/122) than in those with small ones (3/290) ($P = .001$).

Hemorrhagic complications (intraprocedural aneurysm rupture) occurred in 2 patients (0.5%), both with small aneurysms. One of them (0.2%) resulted in permanent morbidity. Other complications were observed in 2 patients (0.5%). Visual disturbance and oculomotor nerve palsy due to compression by coil mass occurred in 1 patient each (0.2%). Neither resulted in permanent morbidity. Complications associated with the coil mass were seen only in large aneurysms. Overall, permanent morbidity rates were 1.0% for small aneurysms and 0.8% for large ones ($P = 1.0$).

Long-Term Clinical Outcome

In the small-aneurysm group, among 273 patients with 285 aneurysms, clinical follow-up was available for 268 patients. The mean clinical follow-up duration was 32 ± 19 months (range, 6–97 months). Poor clinical outcomes were observed in 2 patients (0.7%), both of which were procedure-related (mRS = 3 in both cases).

Among 113 patients with 115 large aneurysms, clinical follow-up was available for 112 patients. The mean clinical follow-up duration was 39 ± 21 months (range, 6–88 months). Poor clinical outcomes were observed in 3 patients (2.7%). All were unrelated to the procedure and included cerebral infarction (mRS = 4), cerebral hemorrhage (mRS = 4), and pontine hemorrhage (mRS = 6). One patient with a large aneurysm (9.0 mm) had aneurysmal rupture owing to recanalization 2 months after treatment, but the patient had a good clinical outcome after additional endovascular treatment (mRS = 0).

DISCUSSION

Unruptured intracranial aneurysms are common and occurred in approximately 1%–2% of the population, as reviewed by Vlak et al.¹⁹ Because most unruptured intracranial aneurysms are asymptomatic and are found incidentally, treatment should be considered after balancing the natural history of the aneurysm with the risk posed by the treatment. Prospective data for the natural history of unruptured intracranial aneurysms by the International Study of Unruptured Intracranial Aneurysms and UCAS Japan investigators showed

that the annual rupture rate increased for aneurysms that were ≥7 mm. The presence of a daughter sac and a history of SAH increased the rupture rate.^{5,7} In the Japanese cohort, the annual rupture rates for paraclinoid aneurysms were approximately 0.1%, 1%, and 10% when they were <7 mm, 7–24 mm, and >25 mm, respectively, in size.⁷ Analysis of our data showed that the 6-month morbidity and mortality rates for aneurysms ≥7 mm were acceptably low (0.8% and 0%, respectively). The retreatment rate with a mean follow-up interval of 39 months was also acceptable (6.3%). Prophylactic treatment of these unruptured aneurysms could be rationalized. The indications for endovascular treatment of small paraclinoid aneurysms, however, should be carefully assessed on an individual basis after considering the patient and aneurysmal factors, such as medical comorbidities, patient age, a history of SAH, the presence of a daughter sac,

Table 5: Predictors of the need for retreatment^a

Parameter	Retreatment	No Retreatment	Univariate Analysis <i>P</i>
No. re-treated aneurysms	10	376	
Mean age, y	57.6 ± 9.5	56.8 ± 11.2	.826
Men	3 (30.0%)	42 (11.2%)	.099
Location			.156
Anterior wall	2 (20.0%)	93 (24.7%)	
Ventral paraclinoid	5 (50.0%)	91 (24.2%)	
True ophthalmic	2 (20.0%)	47 (12.5%)	
Carotid cave	1 (10.0%)	145 (38.6%)	
Right side	5 (50.0%)	165 (43.9%)	.755
Size ≥ 7 mm	7 (70.0%)	104 (27.7%)	.008
Wide neck ^b	2 (20.0%)	70 (18.6%)	1
Medical history			
Hypertension	6 (60.0%)	150 (39.9%)	.212
Diabetes mellitus	2 (20.0%)	16 (4.3%)	.074
Former or current smoker	5 (50.0%)	72 (19.2%)	.031
Body filling at initial treatment	5 (50.0%)	229 (61.2%)	.521
Not stent-assisted	2 (20.0%)	94 (25.0%)	1
Ischemic complication	1 (10.0%)	11 (2.9%)	.274

^a Results are expressed as the mean or no. (%).

^b Neck of ≥4 mm or aspect (dome:neck) ratio ≤ 2.

Table 6: Complications

	Total	<7 mm	≥7 mm	<i>P</i>
No. procedures	412	290	122	
Total complications	16 (3.9%)	5 (1.7%)	11 (9.0%)	.001
Transient	12 (2.9%)	2 (0.7%)	10 (8.2%)	<.001
Permanent	4 (1.0%)	3 (1.0%)	1 (0.8%)	1
Details				
Ischemic complications				
Total	12 (2.9%)	3 (1.0%)	9 (7.4%)	.001
Transient	9 (2.2%)	1 (0.3%)	8 (6.6%)	<.001
Permanent	3 (0.7%)	2 (0.7%)	1 (0.8%)	1
Hemorrhagic complications				
Total	2 (0.5%)	2 (0.7%)	0	1
Transient	1 (0.2%)	1 (0.3%)	0	1
Permanent	1 (0.2%)	1 (0.3%)	0	1
Others				
Total	2 (0.5%)	0	2 (1.6%)	.087
Transient	2 (0.5%)	0	2 (1.6%)	.087
Permanent	0	0	0	1

aneurysmal size, and aneurysmal enlargement. Treatment may be considered when patients are predicted to be at relatively high risk of rupture because the 6-month morbidity and retreatment rates for small aneurysms are low (1.0% and 1.1%, respectively).

Unruptured paraclinoid aneurysms have been increasingly treated endovascularly for anatomic reasons.^{9-15,20} Colli et al² reviewed microsurgical outcomes of paraclinoid aneurysms, which showed that total complication rates were 21.3%–41.7%. The complications included intraoperative aneurysm rupture in 0.8%–14.3%, occlusion of the ICA in 1.2%–13.6%, and visual impairment in 1.8%–33.3%.² Mortality rates associated with microsurgical treatment in unruptured cases were 0%–10.0%.² Total neurologic complications associated with endovascular coil embolization of unruptured paraclinoid aneurysms reported after 2010, including this study, were 1.4%–6.7% and mortality was 0%,^{10-12,14,15,21} which demonstrated that endovascular treatment was more appropriate for prophylactic treatment of these aneurysms. Paraclinoid aneurysms are increasingly being treated with flow-diversion stents, which may further reduce the procedural risks associated with endovascular treatment.²²⁻²⁵

Angiographic and clinical outcomes from previous studies are summarized in Table 7. The immediate complete occlusion rate in our series was low (9.5%) compared with those in earlier studies (28.2%–86.6%).^{9-15,21} The complete occlusion rate in the late stage, however, reached approximately 70%, which was similar to those reported in previous studies (54.0%–87.8%).^{9-15,21} The results indicated that aggressive coil packing was not essential for good angiographic outcomes during the late stage because of the possibility of subsequent thrombus formation around the coil mass.

The recurrence rate in this region differed among studies, which ranged from 5.0% to 23.1%.^{9-15,21} D'Urso et al¹⁵ reported that stent-assisted coil embolization was associated with a lower recurrence rate than that seen with a simple technique (6% vs 19%, *P* = .171). Their results were replicated by Yadla et al²¹ (9.4% vs 24.6%, *P* = .03). In our series, however, stent use did not affect the recurrence rate (8.3% vs 10.0%, *P* = .63). This could be due to different indications for using the stent-assisted technique among studies. The proportion of stent-assisted embolization was higher in our series, which indicated that the total recurrence rate could be reduced if the stent-assisted technique were properly applied for likely-to-recur aneurysms in this region.

We showed that the mean interval from the initial treatment to recurrence was 7.8 ± 5.0 months, and recurrence was rarely detected after the first posttreatment year (Figure). Consistent with our results, Wang et al¹⁰ reported that recurrence was detected in 12.5% of cases at a mean interval of 9.89 ± 5.21 months. Although Yadla et al²¹ showed that recurrence was detected in 17.8% of cases, at a mean interval of 28.3 months, the difference might be caused by the scheduled timing of follow-up angiography. Follow-up angiography at 6–12 months would be reasonable for detecting late recanalization. Aneurysm rupture after recanalization has been rare, with only 3 cases reported to date, including 1 case in this study (Table 7). Still, it is of note that the rupture occurred as early as 2 months after coil embolization in these cases. Thus, additional follow-up MRA at 1 month may be needed to detect acute recanalization that could cause aneurysmal rupture.

Previous studies showed that the size of the aneurysms was associated with the recurrence rate,^{10,12,15} and analysis of our data indicated that aneurysms of ≥7 mm were at a higher risk of recurrence. Previous reports, however, did not analyze the relationship between aneurysm size and the type of complications. Analysis of our data indicated that large aneurysms were likely to be associated with ischemic complications and that small aneurysms were associated with hemorrhagic complications. This finding was consistent with previously published data by Shigematsu et al.²⁶

There were several limitations to our study. First, the study was designed as a retrospective review based on a single-center experience. Therefore, it might not be suitable to compare the data with those of a prospective cohort study (UCAS Japan). However, because of the relatively high risk of rupture for large aneurysms in this region, it is not reasonable to conduct a prospective controlled trial. Cost-effective analysis may provide further support for the rationale of prophylactic treatment for unruptured aneurysms.

Table 7: Angiographic and clinical outcomes in recent series

Study, y	No. Aneurysms	Immediate CO, %	Follow-Up CO, %	Early Follow-Up Angiography	Angiographic Follow-Up, mo	Recurrence Rate, %	Time to Recurrence, mo	No. Rupture (mo after EVT)	Morbidity Rate, %
Present series	400	9.5	67.4	DSA at 6 mo	32 ± 20	9.5	7.8 ± 5.0	1 (2)	1
Wang et al, 2013 ¹⁰	142	43.7	63.4	DSA < 12 mo	13.41 ± 2.64	12.5	9.89 ± 5.21	1 (2)	0
D'Urso et al, 2012 ¹⁵	126	38	62	MRA or DSA	31.9 ± 28.4	17	—	0	0.8
Sorimachi et al, 2012 ¹²	140	33.6	55	DSA at 6 mo	65.6 ± 37.2	11.1	—	0	0.7
Yadla et al, 2011 ²¹	147	68.6	64.1	MRA at 6–12 mo	—	17.8	28.3	0	1.4
Sun et al, 2011 ¹¹	30	86.6	81.5	DSA at 3–18 mo	7.8	7.4	—	0	3.3
Kwon et al, 2010 ¹⁴	132	58	—	MRA at 6 mo	6	5	—	0	0
Park et al, 2003 ¹³	73	72.6	87.8	Angiography at 6 mo	13.9	23.1	—	0	8.3
Thornton et al, 2000 ⁹	71	28.2	54	Angiography at 6 mo	16	16.4	—	1 (2)	5.6

Note:—CO indicates complete occlusion; EVT, endovascular treatment; —, not available.

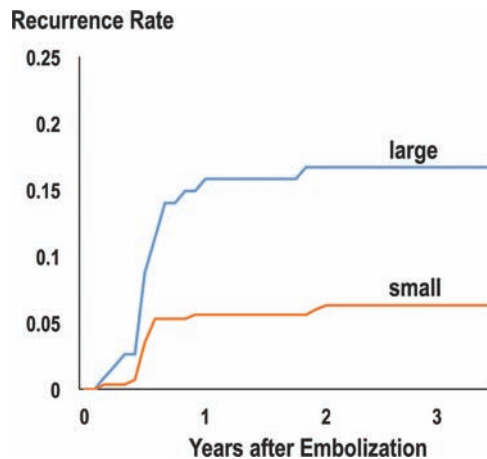


FIGURE. Recurrence rates after the initial treatment according to the size of the aneurysms. Most recurrences were detected within 1 year after treatment.

Second, indications for endovascular treatment of small aneurysms were addressed in an individualized fashion according to the patient age, history of SAH, family history of SAH, size, shape (ie, the presence of a daughter sac) and multiplicity of the aneurysm, aneurysmal enlargement, patient anxiety and mental status, and comorbidities (eg, hypertension). Many of these parameters can be associated with an increased risk of rupture for small aneurysms.²⁷ However, such parameters were not precisely provided, and we could not determine whether the decision-making process was consistent. Indications might have been altered after publication of data from large cohorts, such as in the Small Unruptured Intracranial Aneurysm Verification Study or UCAS Japan.^{7,27} This was also a limitation that stems from the retrospective nature of our study.

Third, platelet function testing was not performed in this study population, though there is evidence that the hyporesponse to clopidogrel is associated with increased risk of thromboembolic complications.^{28–31} Selection of the antiplatelet drugs might have influenced the increased incidence of thromboembolic events in large aneurysms that were treated by using the stent-assisted technique.

CONCLUSIONS

Endovascular treatment of unruptured paraclinoid aneurysms ≥ 7 mm can be achieved with high technical success, low complication rates, and excellent long-term outcomes. Treatment of unruptured paraclinoid aneurysms < 7 mm may be considered in

patients, based on an individualized assessment of risk factors, including medical comorbidities, patient age, ethnicities, aneurysm characteristics, and history of SAH.

Disclosures: Nobuyuki Sakai—UNRELATED: Grants/Grants Pending: Terumo (modest)*; Payment for Lectures (including service on speakers bureaus): Codman, Covidien, Stryker, Terumo, Comments: Modest. *Money paid to the institution.

REFERENCES

- Kim JM, Romano A, Sanan A, et al. Microsurgical anatomic features and nomenclature of the paraclinoid region. *Neurosurgery* 2000;46: 670–80; discussion 680–82 Medline
- Colli BO, Carlotti CG, Assirati JA, et al. Results of microsurgical treatment of paraclinoid carotid aneurysms. *Neurosurg Rev* 2013; 36:199–114; discussion 114–15 CrossRef Medline
- Lee EJ, Lee HJ, Hyun MK, et al. Rupture rate for patients with untreated unruptured intracranial aneurysms in South Korea during 2006–2009. *J Neurosurg* 2012;117:53–59 CrossRef Medline
- Juvela S, Porras M, Poussa K. Natural history of unruptured intracranial aneurysms: probability of and risk factors for aneurysm rupture. *J Neurosurg* 2000;93:379–87 Medline
- Unruptured intracranial aneurysms—risk of rupture and risks of surgical intervention. International Study of Unruptured Intracranial Aneurysms Investigators. *N Engl J Med* 1998;339:1725–33 CrossRef Medline
- Juvela S, Poussa K, Lehto H, et al. Natural history of unruptured intracranial aneurysms: a long-term follow-up study. *Stroke* 2013; 44:2414–21 CrossRef Medline
- UCAS Japan Investigators, Morita A, Kirino T, et al. The natural course of unruptured cerebral aneurysms in a Japanese cohort. *N Engl J Med* 2012;366:2474–82 CrossRef Medline
- Wiebers DO, Whisnant JP, Huston J, et al. Unruptured intracranial aneurysms: natural history, clinical outcome, and risks of surgical and endovascular treatment. *Lancet* 2003;362:103–10 CrossRef Medline
- Thornton J, Aletich VA, Debrun GM, et al. Endovascular treatment of paraclinoid aneurysms. *Surg Neurol* 2000;54:288–99 CrossRef Medline
- Wang Y, Li Y, Jiang C, et al. Endovascular treatment of paraclinoid aneurysms: 142 aneurysms in one centre. *J Neurointerv Surg* 2013;5: 552–56 CrossRef Medline
- Sun Y, Li Y, Li A. Endovascular treatment of paraclinoid aneurysms. *Interv Neuroradiol* 2011;17:425–30 Medline
- Sorimachi T, Ito Y, Morita K, et al. Long-term follow-up of intra-aneurysmal coil embolization for unruptured paraclinoid aneurysms. *Neurol Res* 2012;34:864–70 CrossRef Medline
- Park HK, Horowitz M, Jungreis C, et al. Endovascular treatment of paraclinoid aneurysms: experience with 73 patients. *Neurosurgery* 2003;53:14–23; discussion 24 CrossRef Medline
- Kwon BJ, Im S-H, Park JC, et al. Shaping and navigating methods of microcatheters for endovascular treatment of paraclinoid aneurysms. *Neurosurgery* 2010;67:34–40 CrossRef Medline

15. D'Urso PI, Karadeli HH, Kallmes DF, et al. **Coiling for paraclinoid aneurysms: time to make way for flow diverters?** *AJNR Am J Neuroradiol* 2012;33:1470–74 CrossRef Medline
16. al-Rodhan NR, Piepgras DG, Sundt TM. **Transitional cavernous aneurysms of the internal carotid artery.** *Neurosurgery* 1993;33:993–96; discussion 997–98 CrossRef Medline
17. Iihara K, Murao K, Sakai N, et al. **Unruptured paraclinoid aneurysms: a management strategy.** *J Neurosurg* 2003;99:241–47 CrossRef Medline
18. Ng P, Khangure MS, Phatouros CC, et al. **Endovascular treatment of intracranial aneurysms with Guglielmi detachable coils: analysis of midterm angiographic and clinical outcomes.** *Stroke* 2002;33:210–17 CrossRef Medline
19. Vlak MH, Algra A, Brandenburg R, et al. **Prevalence of unruptured intracranial aneurysms, with emphasis on sex, age, comorbidity, country, and time period: a systematic review and meta-analysis.** *Lancet Neurol* 2011;10:626–36 CrossRef Medline
20. Ferrell AS, Lessne ML, Alexander MJ, et al. **Visual complications after stent-assisted endovascular embolization of paraophthalmic and suprasellar variant superior hypophyseal aneurysms: the Duke Cerebrovascular Center experience in 57 patients.** *World Neurosurg* 2012;78:289–94 CrossRef Medline
21. Yadla S, Campbell PG, Grobelny B, et al. **Open and endovascular treatment of unruptured carotid-ophthalmic aneurysms: clinical and radiographic outcomes.** *Neurosurgery* 2011;68:1434–43; discussion 1443 CrossRef Medline
22. Fang S, Lanzino G. **Paraclinoid aneurysms: is there a new endovascular standard?** *Neurol Res* 2014;36:314–22 CrossRef Medline
23. Kim LJ, Tariq F, Levitt M, et al. **Multimodality treatment of complex unruptured cavernous and paraclinoid aneurysms.** *Neurosurgery* 2014;74:51–61; discussion 61; quiz 61 CrossRef Medline
24. Lanzino G, Crobeddu E, Cloft HJ, et al. **Efficacy and safety of flow diversion for paraclinoid aneurysms: a matched-pair analysis compared with standard endovascular approaches.** *AJNR Am J Neuroradiol* 2012;33:2158–61 CrossRef Medline
25. Loumiosis I, D'Urso PI, Tawk R, et al. **Endovascular treatment of ruptured paraclinoid aneurysms: results, complications, and follow-up.** *AJNR Am J Neuroradiol* 2012;33:632–37 CrossRef Medline
26. Shigematsu T, Fujinaka T, Yoshimine T, et al. **Endovascular therapy for asymptomatic unruptured intracranial aneurysms: JR-NET and JR-NET2 findings.** *Stroke* 2013;44:2735–42 CrossRef Medline
27. Sonobe M, Yamazaki T, Yonekura M, et al. **Small unruptured intracranial aneurysm verification study: SUAVE study, Japan.** *Stroke* 2010;41:1969–77 CrossRef Medline
28. Delgado Almandoz JE, Crandall BM, Scholz JM, et al. **Pre-procedure P2Y12 reaction units value predicts perioperative thromboembolic and hemorrhagic complications in patients with cerebral aneurysms treated with the Pipeline embolization device.** *J Neurointerv Surg* 2013;5(suppl 3):iii3–10 CrossRef Medline
29. Delgado Almandoz JE, Kadkhodayan Y, Crandall BM, et al. **Variability in initial response to standard clopidogrel therapy, delayed conversion to clopidogrel hyper-response, and associated thromboembolic and hemorrhagic complications in patients undergoing endovascular treatment of unruptured cerebral aneurysms.** *J Neurointerv Surg* 2014;6:767–73 CrossRef Medline
30. Lee DH, Kim HS, Kim SM, et al. **Change of platelet reactivity to antiplatelet therapy after stenting procedure for cerebral artery stenosis: VerifyNow antiplatelet assay before and after stenting.** *Neurointervention* 2012;7:23–6 CrossRef Medline
31. Kang H-S, Kwon BJ, Kim JE, et al. **Preinterventional clopidogrel response variability for coil embolization of intracranial aneurysms: clinical implications.** *AJNR Am J Neuroradiol* 2010;31:1206–10 CrossRef Medline

Associations between Cerebral Embolism and Carotid Intraplaque Hemorrhage during Protected Carotid Artery Stenting

G.H. Chung, J.Y. Jeong, H.S. Kwak, and S.B. Hwang

ABSTRACT

BACKGROUND AND PURPOSE: Carotid artery stent placement in patients with intraplaque hemorrhage remains controversial because of the incidence of cerebral embolism after the procedure. The purpose of this study is to determine if intraplaque hemorrhage is a significant risk factor for cerebral embolism during carotid artery stent placement.

MATERIALS AND METHODS: This prospective study assessed 94 consecutive patients with severe carotid stenosis. These patients underwent preprocedural carotid MR imaging and postprocedural DWI after carotid artery stent placement. Intraplaque hemorrhage was defined as the presence of high signal intensity within the carotid plaque that was >200% of the signal from the adjacent muscle on MPRAGE. We then analyzed the incidence of postprocedural ipsilateral ischemic events on DWI and primary outcomes within 30 days of carotid artery stent placement.

RESULTS: Forty-three patients (45.7%) had intraplaque hemorrhage on an MPRAGE image. There was no significant difference in the incidence of postprocedural ipsilateral ischemic events and primary outcomes between the intraplaque hemorrhage and non-intraplaque hemorrhage group. However, postprocedural ipsilateral ischemic events were more frequently observed in the symptomatic group (17/41 [41.5%]) than in the asymptomatic group (8/53 [15.1%]; $P = .005$).

CONCLUSIONS: Intraplaque hemorrhage was not a significant risk factor for cerebral embolism during carotid artery stent placement in patients with severe carotid stenosis. Symptomatic patients should receive more careful treatment during carotid artery stent placement because of the higher risk of postprocedural ipsilateral ischemic events.

ABBREVIATIONS: CAS = carotid artery stent placement; IPH = intraplaque hemorrhage

Extracranial carotid artery stenosis is considered a causative factor in 20%–30% of all strokes.^{1–3} Large randomized clinical trials showed that carotid endarterectomy is superior to carotid artery stent placement (CAS) for the management of carotid artery stenosis.^{4–6} Other randomized clinical trials showed that CAS and carotid endarterectomy offer similar efficacy.⁷ Although indications for CAS remain controversial, CAS has emerged as a less-invasive treatment that requires shorter hospital times than carotid endarterectomy.

Some studies found a relationship between the baseline pres-

ence of carotid intraplaque hemorrhage (IPH) and the development of ischemic stroke in previously asymptomatic and symptomatic patients.^{8–10} IPH is associated with plaque progression and, consequently, induces luminal narrowing. Thus, IPH may serve as a measure of risk for the development of future ischemic stroke. The risk of cerebral embolism after CAS in patients with IPH is controversial. Yoshimura et al¹¹ reported that a high-intensity signal on TOF MRA indicates that carotid plaques are at high risk for cerebral embolism during stent placement. However, Yoon et al¹² reported that protected CAS seems to be safe in patients with severe carotid stenosis and IPH. This study did not perform DWI to evaluate ipsilateral ischemic lesions. In addition, these studies used TOF imaging to detect IPH. Alternative techniques proposed for more accurate detection of IPH include heavily T1-weighted techniques, such as the MPRAGE sequence. Ota et al¹³ reported that the MPRAGE sequence demonstrated higher diagnostic capability in detecting IPH when compared with conventional T1-weighted sequences or TOF sequences.

We prospectively designed the study with the following in-

Received May 11, 2015; accepted after revision July 29.

From the Radiology and Research Institute, Clinical Medicine of Chonbuk National University-Biomedical Research Institute of Chonbuk National University Hospital, Jeollabuk-do, Republic of Korea.

Please address correspondence to Hyo Sung Kwak, MD, Radiology and Research Institute of Clinical Medicine of Chonbuk National University-Biomedical Research Institute of Chonbuk National University Hospital, 567 Baekje-daero, deokjin-gu, Jeonju-si, Jeollabuk-do, 561-756, Republic of Korea; e-mail: kwak8140@jbnuc.ac.kr; @kwakhs8140

<http://dx.doi.org/10.3174/ajnr.A4576>

clusion criteria: 1) preoperative multicontrast carotid plaque MR; 2) protected CAS; 3) postprocedural imaging, including DWI and noncontrast CT within 24 hours; and 4) clinical outcomes after 30 days. The aim of this study was to determine whether IPH is a significant risk factor for cerebral embolism during CAS.

MATERIALS AND METHODS

Study Population

This prospective study was conducted with institutional review board approval. We included 94 consecutive patients with carotid artery stenosis between April 2013 and January 2015. All the patients had symptomatic carotid artery stenosis of >50% (NASCET criteria) or asymptomatic carotid artery stenosis of >70% (NASCET criteria). Stenosis was initially detected in symptomatic patients by a stroke MR protocol that included contrast-enhanced MR angiography. Stenosis was diagnosed in asymptomatic patients by carotid sonography or/and a routine brain MR imaging that included contrast-enhanced MR angiography to evaluate neurologic symptoms. Multicontrast carotid plaque MR imaging was performed within 3 days before CAS, and new postoperative ischemic lesions were assessed by DWI within 2 days after CAS.

Stroke MR and Multicontrast Carotid Plaque Imaging

All MR imaging was acquired on a 3T scanner (Achieva; Philips Medical Systems, Best, the Netherlands) with a 16-channel head coil. Stroke MR imaging was performed immediately after CT scanning with the following techniques: DWI, 3D TOF MRA of the intracranial arteries, susceptibility-weighted imaging, perfusion-weighted imaging, and contrast-enhanced MRA for evaluation of carotid arteries. The total scan time was approximately 20–30 minutes. Our protocol for multicontrast carotid plaque imaging included 5 different axial scans: TOF, T1-weighted, T2-weighted, postcontrast T1-weighted, and MPAGE sequences. All the sequences were centered at the bifurcation of the index artery with the carotid plaque. T1-weighted, T2-weighted, and postcontrast T1-weighted sequences were obtained with a 2.0-mm section thickness and no intersection spacing. TOF and MPAGE sequences had a 1.0-mm section thickness and no intersection spacing. Images were obtained with an FOV of 14 × 14 cm and a matrix size of 216 × 192. Total acquisition time was approximately 40 minutes.

MR Imaging after CAS

All the patients underwent DWI within 2 days after CAS. DWI was conducted using a spin-echo-type echo-planar imaging sequence with 3 b-values, of 0, 500, and 1000 s/mm² along all 3 orthogonal axes and with the following parameters: TR/TE, 3000/80 milliseconds; flip angle, 90°; sensitivity encoding, 3; FOV, 220 × 220 mm; matrix, 128 × 128; section thickness/gap, 5 mm/30%; scanning time, 35–38 seconds.

CAS Procedure

The CAS procedures were performed by one interventional neuroradiologist (H.S.K.) with 10 years of experience. Written informed consent for the CAS procedure was obtained from all the

patients. Aspirin (100 mg/d) and clopidogrel (75 mg/d) were given for a minimum of 3 days before the procedure. All the CAS procedures were performed with the patient under local anesthesia via the percutaneous transfemoral route. Systemic anticoagulation was initiated with a 3000-U bolus of intravenous heparin followed by a 1000-U/h infusion. Routine 3- or 4-vessel cerebral angiography was performed before treatment to evaluate collateral flow. Then, the double coaxial system, which was assembled combining an outer 80-cm-long 8F introducer sheath (Super Arrow-Flex; Teleflex, Limerick, Pennsylvania) and an inner 100-cm-long 8F guiding catheter (Guider Softip; Boston Scientific, Natick, Massachusetts), was placed in the common carotid artery to enable stent placement. CAS was performed with the Emboshield distal embolic protection system (Abbott Vascular, Abbott Park, Illinois). Predilation was performed with a 4-mm balloon catheter. Deployment of a self-expandable stent (RX Acculink; Abbott Vascular), the size of which was chosen according to the presumed parent size, was performed. Poststenting angioplasty was performed with a 5- to 6-mm-diameter balloon to achieve a residual diameter stenosis of <20%. After the procedure, all the patients were monitored for 24 hours in the intensive care unit.

Definition and Outcomes

Carotid plaque imaging was interpreted using plaque analysis software (MRI-PlaqueView; VPDiagnostics, Seattle, Washington) for detection of IPH and maximal wall thickness, and was analyzed by researchers (G.H.C. and S.B.H.) trained in carotid plaque MR imaging and blinded to the study goal (Rev no. 1–1; Rev no. 2–1).¹⁴ MR-positive IPH was defined as the presence of hyperintense intraplaque of >200% of the signal intensity of the adjacent muscle for at least 2 consecutive sections on MPAGE images.^{13,15} For MPAGE-positive IPH analysis, signal intensities were measured in a 6- to 8-mm² circular region of interest over the carotid plaque. Positive DWI for analysis of ipsilateral ischemic lesions was defined as the detection of a hyperintense signal on a DWI trace with an associated signal decrease on the apparent diffusion coefficient map by 2 experienced neuroradiologists through consensus interpretation. Symptomatic carotid artery stenosis was defined as focal neurologic symptoms and DWI-positive imaging that occurred within 1 week of CAS and was attributable to an ipsilateral carotid artery vascular distribution.

Neurologic evaluation was performed before the procedure, immediately afterward, daily after CAS until discharge, and 1 month afterward using the NIHSS and modified Rankin Scale by independent neurologists who were blinded to the CAS procedure.

The primary outcome was the incidence of any stroke, myocardial infarction, or death within 30 days after CAS. A minor stroke was defined as evidence of neurologic deterioration based on an increase of the NIHSS of <4 points without the presence of aphasia or hemianopsia, or complete recovery within 1 month. A major stroke was defined as an increase of the NIHSS of ≥4 points, the presence of aphasia or hemianopsia, or any residual deficit beyond 1 month. Hyperperfusion syndrome without intracranial hemorrhage was defined as the occurrence, either alone or in combination, of an ipsilateral throbbing headache with or

Table 1: Baseline data for patients with MR-positive IPH or without IPH after carotid stenosis

	MR-Positive IPH (n = 43)	No IPH (n = 51)	P
Mean age, y	74.3 ± 6.5	72.9 ± 6.8	.324
Men, no. (%)	34 (79.1)	31 (60.8)	.074
Right side, no. (%)	15 (34.9)	23 (45.1)	.400
Symptomatic event, no. (%)	22 (51.2)	19 (37.3)	.213
Mean degree of stenosis, %	78.9 ± 12.4	75.9 ± 12.3	.247
Cerebrovascular history, no. (%)			
Previous stroke	8 (18.6)	17 (33.3)	.159
Previous cardiac disease	10 (23.3)	8 (9.8)	.433
Cerebrovascular risk factors, no. (%)			
Hypertension	26 (60.5)	32 (62.7)	.835
Diabetes mellitus	22 (51.2)	22 (41.5)	.535
Hyperlipidemia	9 (20.9)	8 (15.7)	.595
Current smoking	16 (37.2)	20 (39.2)	1.000

without nausea, vomiting, ipsilateral focal seizure, or focal neurologic deficit without radiographic evidence of infarction.

Statistical Analysis

Continuous values are expressed as means and standard deviations, whereas categorical data are expressed as counts and percentages. Patients were divided by MR positive or negative status and by symptomatic or asymptomatic status. Continuous and categorical variables were compared between groups by using the Mann-Whitney test and the Fisher exact test, respectively. Multivariate analyses for IPH or no IPH, or symptomatic or asymptomatic groups were conducted with logistic regression. Variables with $P < .20$ from univariate analysis were taken as candidate predictors and were entered into a backward-selection algorithm to identify a set of independent predictors. Statistical significance was defined as $P < .05$. All statistical analyses were performed using R 2.14.1 (<http://www.r-project.org/>).

RESULTS

Patients

The mean age of the 94 consecutive patients was 73.6 years (range, 52–87 years), and most patients were men ($n = 68$ [72.3%]). MR-positive IPH on MPRAGE images was detected in 43 patients (45.7%). The baseline data for patients with carotid stenosis with MR-positive IPH or no IPH are shown in Table 1. Symptomatic events with DWI-positive findings were present in 22 patients (51.2%) in the IPH group and in 19 patients (37.3%) in the no-IPH group. The other baseline data were similar between the IPH and no-IPH groups.

Outcomes between IPH and no-IPH Groups after CAS

Technical success of the CAS procedure was achieved in all the patients. No procedure-related complications were observed. Data on postprocedural outcomes in the MR-positive IPH and no-IPH groups are shown in Table 2. New postprocedural ischemic lesions on DWI were observed in the hemisphere in 25 patients (26.6%). The incidence of ipsilateral new ischemic lesions on DWI was similar between both groups. Hyperperfusion syndromes without intracranial hemorrhage were observed in 11 patients (11.7%). Two patients with MR-positive IPH underwent a

Table 2: Postprocedural complications in patients with or without MR-positive IPH

	MR-Positive IPH, no. (%) (n = 43)	No IPH, no. (%) (n = 51)	P
Hyperperfusion syndrome	3 (7.0)	8 (15.7)	.218
Ipsilateral ischemic lesions	9 (20.9)	16 (31.4)	.349
Minor stroke	0	0	
Major stroke	2 (4.7)	0	.207
MI or death	0	0	

Note:—MI indicates myocardial infarction.

Table 3: Characteristics of symptomatic and asymptomatic groups in patients with carotid stenosis

	Symptomatic (n = 41)	Asymptomatic (n = 53)	P
Mean age, y	74.5 ± 5.5	72.8 ± 7.5	.214
Mean degree of stenosis, %	79.0 ± 13.9	76.0 ± 10.9	.258
MR-positive IPH, no. (%)	22 (53.7)	19 (35.8)	.213
Ipsilateral ischemic lesions, no. (%)	17 (41.5)	8 (15.1)	.005 ^a
Hyperperfusion syndrome, no. (%)	5 (12.2)	6 (11.3)	1.000
Major stroke, no. (%)	1 (2.4)	1 (1.9)	.685

^a Fisher exact test.

major stroke within 30 days after CAS. No death or myocardial infarction after CAS was observed. Overall, 30-day stroke, myocardial infarction, and death rates were 2.1%. There was no significant difference in primary outcomes between the MR-positive IPH and no-IPH groups. There were no other independent variables associated with clinical outcomes after CAS between MR-positive IPH and no-IPH groups by univariate and multivariate logistic regression analysis.

Outcome between Symptomatic and Asymptomatic Groups after CAS

Forty-one patients (43.6%) were symptomatic. Data on postprocedural outcomes in symptomatic and asymptomatic groups are shown in Table 3. The symptomatic group had a significantly higher incidence of new postprocedural ischemic lesions on DWI than the asymptomatic group (41.5% vs 15.1%; $P = .005$). There was no significant difference in other primary outcomes between the 2 groups. Multivariate logistic regression analysis revealed that postprocedural new ischemic lesions on DWI were found to be independently associated with symptomatic lesions (odds ratio 3.6 [95% CI, 1.2–2.5]; $P = .010$) (Figure).

DISCUSSION

This study demonstrated that MR-positive IPH on MPRAGE images was not associated with postprocedural outcomes after CAS. Although new postprocedural ischemic lesions on DWI were more frequently found in symptomatic lesions, these were not associated with clinical outcomes after CAS. Therefore, CAS with protection can be performed safely in patients with MR-positive IPH, and the CAS procedure may be carefully performed in symptomatic patients to decrease new postprocedural ischemic lesions on DWI.

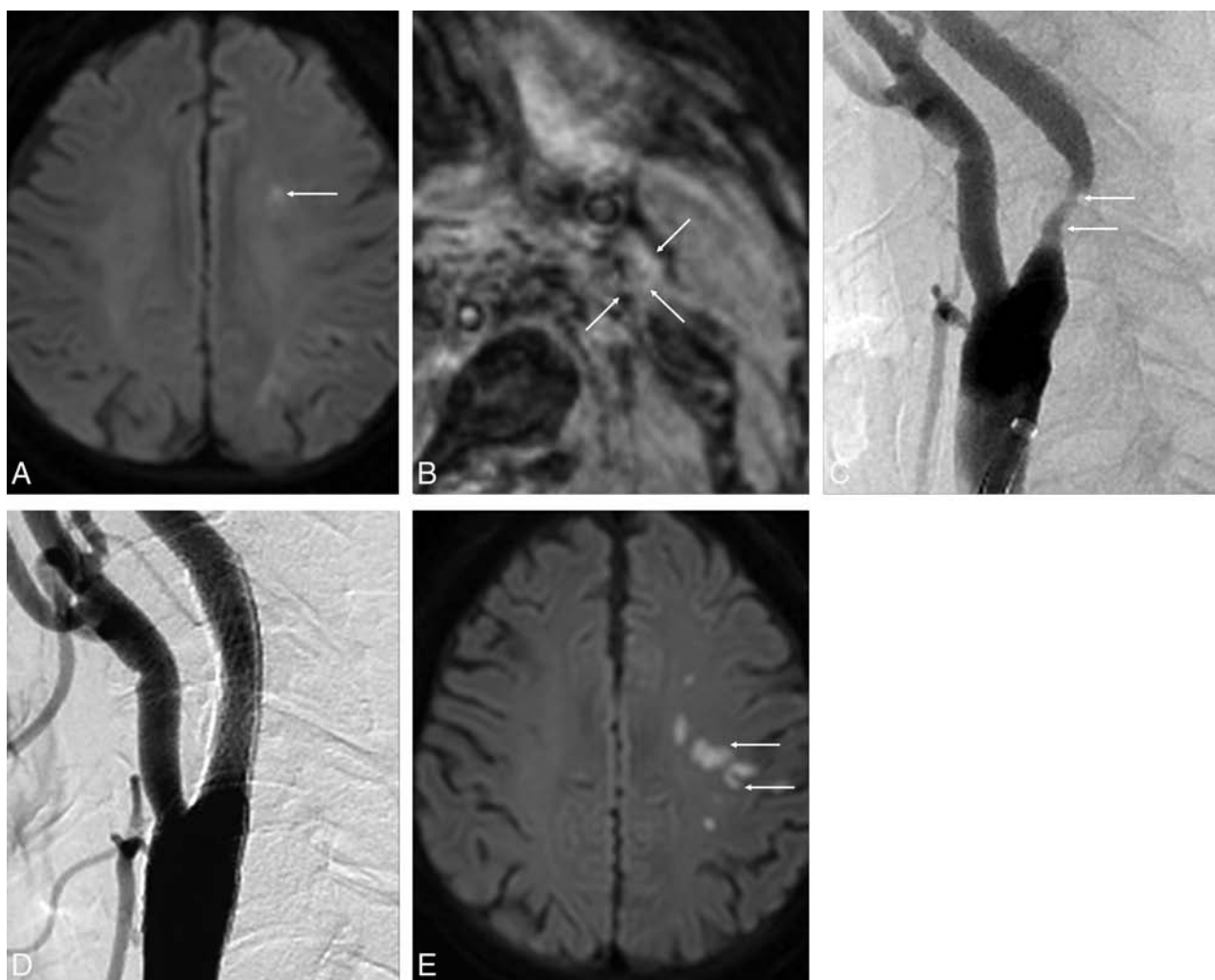


FIGURE. A 77-year-old man with a left acute embolic infarction due to severe stenosis of the left proximal internal carotid artery. *A*, Axial DWI at admission shows multiple areas of diffusion restriction in the left centrum semiovale (arrow). *B*, MPRAGE image shows isointensity of the left carotid plaque (arrows). This finding indicates a necrotic core without IPH. *C*, Lateral projection of left carotid angiography shows moderate stenosis in the proximal cervical portion of the left internal carotid artery (arrows). *D*, Carotid artery angiogram after protected CAS shows complete recanalization without residual stenosis. *E*, Axial DWI after CAS shows the new embolic lesions in the left frontal lobe (arrows).

Clinical outcomes of cerebral embolism on TOF images after the CAS procedure in patients with carotid IPH are controversial. A study by Yoshimura et al¹¹ indicated that ischemic events after CAS may be more frequent in plaques that are MR-positive for IPH and that the only independent predictor of postoperative ischemic symptoms was the presence of IPH. Another study from this group performed treatment selection such as CAS or carotid endarterectomy based on MR imaging.¹⁴ The patients with carotid IPH on TOF images underwent carotid endarterectomy, and the patients without carotid IPH underwent CAS. This study reported that treatment selection based on preoperative MR imaging of the carotid plaque seems useful to reduce postprocedural adverse events after carotid revascularization procedures. This study also indicated that carotid endarterectomy should be selected for MR-positive plaques, whereas CAS should be selected for plaques without IPH to reduce postoperative ischemic symptoms.¹⁴ However, Yoon et al,¹² who performed a similar study, reported no significant difference in primary outcomes after CAS between the IPH and no-IPH groups and found no independent

variables associated with the primary outcome. However, previous studies from both groups had some limitations. First, these studies used TOF images to evaluate carotid IPH. Sensitivity, specificity, and κ values for detection of IPH based on histologic analysis were 80%, 97%, and 0.80 for MPRAGE images; 70%, 92%, and 0.63 for fast spin-echo images; and 56%, 96%, and 0.57 for TOF images.¹³ Second, Yoon et al¹² did not perform DWI to evaluate new postprocedural ischemic lesions and instead evaluated clinical outcomes after CAS by neurologic examinations. Third, Yoshimura et al¹¹ used variable devices for distal or proximal protection for embolic capture during CAS. Our study was prospectively designed to minimize some bias. All the patients underwent multicontrast MR imaging, including MPRAGE, before CAS. We only used 1 distal embolic protection device and self-expandable stent. All the patients underwent DWI within 2 days after CAS to detect new postoperative ischemic lesions.

Recently, the Carotid Revascularization Endarterectomy Versus Stenting Trial (CREST) reported that CAS and carotid endarterectomy were associated with similar rates of the primary com-

posite outcomes, periprocedural stroke, myocardial infarction, death, or subsequent ipsilateral stroke among men and women with either symptomatic or asymptomatic carotid stenosis.⁷ However, the incidence of periprocedural stroke was lower in the carotid endarterectomy group, whereas the incidence of periprocedural myocardial infarction was lower in the CAS group. To reduce the risk of stroke after CAS, improvements in training and technique, embolic protection and stent design, and patient selection hold promise.¹⁵ In our study, 2 patients (4.7%) with MR-positive IPH experienced a major stroke within 30 days after CAS, but no myocardial infarctions or deaths were observed. Therefore, the overall 30-day stroke rate was 2.1%. Also, we found no significant difference in primary outcomes after CAS between the MR-positive IPH and no-IPH groups. The similarity of our study and Yoon's study¹² performed the CAS procedure by 1 interventional neuroradiologist with 10 years of experience and a single product for distal embolic protection.

DWI is a sensitive tool used to identify ischemic lesions after CAS. A previous meta-analysis for detection of ischemic lesions after CAS on DWI revealed a significantly lower incidence (33%) in protected patients compared with unprotected patients (45%).¹⁶ Bijuklic et al¹⁷ performed pre- and postprocedural DWI for evaluation of new cerebral ischemic lesions in 728 patients undergoing CAS with cerebral embolic protection. New ischemic lesions were found in 32.8% of the patients. Age, hypertension, lesion length, lesion eccentricity, and aortic arch type III were significantly associated with new ischemic lesions; calcified lesions were negatively associated, which is well in accordance with our findings (25/94 [26.6%]). In our study, new postprocedural ischemic lesions on DWI were not associated with carotid IPH and were significantly associated with symptomatic lesions, unlike a previous study.¹¹ Some studies reported that proximal balloon occlusion reduces embolic events after CAS compared with filter protection^{18,19}; however, a high level of technical skill and an experienced interventionalist are very important to prevent new postprocedural ischemic lesions and postprocedural clinical outcomes after CAS. In addition, carotid plaques in patients with symptomatic lesions may have variable vulnerable findings, such as IPH, fibrous cap ruptures, ulcers, thrombus, or inflammation.

Our study had several limitations. First, we lacked a criterion standard histologic reference. Ota et al¹³ evaluated the diagnostic performance of 3 T1-weighted 3T MR images by using carotid IPH imaging with histologic analysis. The MPRAGE sequence demonstrated a greater ability to detect and quantify IPH than T1-weighted fast spin-echo and TOF sequences. Therefore, we concluded that carotid MPRAGE-positive images strongly indicated the presence of IPH. Second, our study focused on atherosclerotic lesions in the proximal carotid artery. Common causes of acute ischemic stroke are major arterial atheroma, cardioembolic sources, microvascular disease, and cryptogenic factors. Therefore, in our study, symptomatic lesions were defined as focal neurologic symptoms and DWI positive scans that occur within 1 week of CAS because this minimized acute ischemic stroke by other causes. Third, these may have included many causes of vulnerable carotid plaques, such as IPH, fibrous cap rupture, ulcers, throm-

bus, large necrotic core, or inflammation. The previous cited studies reported negative clinical outcomes after CAS in patients with carotid IPH.^{11,12} Therefore, our study only focused on carotid IPH for validation. Also, the sample size was relatively small, and long-term follow-up data were not available.

CONCLUSIONS

The results of this study indicated that IPH in patients with severe carotid stenosis was not a significant risk factor for cerebral embolism after CAS. Symptomatic patients should receive more careful treatment during CAS due to the higher risk of ipsilateral postprocedural ischemic events.

Disclosures: Hyo Sung Kwak—RELATED: Grant: Supported by the Fund of Biomedical Research Institute, Chonbuk National University Hospital.* *Money paid to the institution.

REFERENCES

1. Timsit SG, Sacco RL, Mohr JP, et al. **Early clinical differentiation of cerebral infarction from severe atherosclerotic stenosis and cardioembolism.** *Stroke* 1992;23:486–91 CrossRef Medline
2. Petty GW, Brown RD Jr, Whisnant JP, et al. **Ischemic stroke subtypes: a population-based study of incidence and risk factors.** *Stroke* 1999;30:2513–16 CrossRef Medline
3. Palm F, Dos Santos M, Urbanek C, et al. **Stroke seasonality associations with subtype, etiology and laboratory results in the Ludwigshafen Stroke Study (LuSSt).** *Eur J Epidemiol* 2013;28:373–81 CrossRef Medline
4. Mas JL, Trinquart L, Leys D, et al. **Endarterectomy Versus Angioplasty in Patients with Symptomatic Severe Carotid Stenosis (EVA-3S) trial: results up to 4 years from a randomised, multicentre trial.** *Lancet Neurol* 2008;7:885–92 CrossRef Medline
5. International Carotid Stenting Study Investigators, Ederle J, Dobson J, et al. **Carotid artery stenting compared with endarterectomy in patients with symptomatic carotid stenosis (International Carotid Stenting Study): an interim analysis of a randomised controlled trial.** *Lancet* 2010;375:985–97 CrossRef Medline
6. Eckstein HH, Ringleb P, Allenberg JR, et al. **Results of the Stent-Protected Angioplasty versus Carotid Endarterectomy (SPACE) study to treat symptomatic stenoses at 2 years: a multinational, prospective, randomised trial.** *Lancet Neurol* 2008;7:893–902 CrossRef Medline
7. Brott TG, Hobson RW II, Howard G, et al. **Stenting versus endarterectomy for treatment of carotid-artery stenosis.** *N Engl J Med* 2010;363:11–23 CrossRef Medline
8. Yamada K, Song Y, Hippe DS, et al. **Quantitative evaluation of high intensity signal on MIP images of carotid atherosclerotic plaques from routine TOF-MRA reveals elevated volumes of intraplaque hemorrhage and lipid rich necrotic core.** *J Cardiovasc Magn Reson* 2012;14:81 CrossRef Medline
9. Singh N, Moody AR, Gladstone DJ, et al. **Moderate carotid artery stenosis: MR imaging-depicted intraplaque hemorrhage predicts risk of cerebrovascular ischemic events in asymptomatic men.** *Radiology* 2009;252:502–08 CrossRef Medline
10. Altaf N, Daniels L, Morgan PS, et al. **Detection of intraplaque hemorrhage by magnetic resonance imaging in symptomatic patients with mild to moderate carotid stenosis predicts recurrent neurological events.** *J Vasc Surg* 2008;47:337–42 CrossRef Medline
11. Yoshimura S, Yamada K, Kawasaki M, et al. **High-intensity signal on time-of-flight magnetic resonance angiography indicates carotid plaques at high risk for cerebral embolism during stenting.** *Stroke* 2011;42:3132–37 CrossRef Medline
12. Yoon W, Kim SK, Park MS, et al. **Safety of protected carotid artery stenting in patients with severe carotid artery stenosis and carotid intraplaque hemorrhage.** *AJNR Am J Neuroradiol* 2012;33:1027–31 CrossRef Medline

13. Ota H, Yarnykh VL, Ferguson MS, et al. **Carotid intraplaque hemorrhage imaging at 3.0-T MR imaging: comparison of the diagnostic performance of three T1-weighted sequences.** *Radiology* 2010;254:551–63 CrossRef Medline
14. Yoshimura S, Yamada K, Kawasaki M, et al. **Selection of carotid artery stenting or endarterectomy based on magnetic resonance plaque imaging reduced periprocedural adverse events.** *J Stroke Cerebrovasc Dis* 2013;22:1082–87 CrossRef Medline
15. Chiam PT, Roubin GS, Iyer SS, et al. **Carotid artery stenting in elderly patients: importance of case selection.** *Catheter Cardiovasc Interv* 2008;72:318–24 CrossRef Medline
16. Schnaudigel S, Groschel K, Pilgram SM, et al. **New brain lesions after carotid stenting versus carotid endarterectomy: a systematic review of the literature.** *Stroke* 2008;39:1911–19 CrossRef Medline
17. Bijuklic K, Wandler A, Varnakov Y, et al. **Risk factors for cerebral embolization after carotid artery stenting with embolic protection: a diffusion-weighted magnetic resonance imaging study in 837 consecutive patients.** *Circ Cardiovasc Interv* 2013;6:311–16 CrossRef Medline
18. Stabile E, Sannino A, Schiattarella GG, et al. **Cerebral embolic lesions detected with diffusion-weighted magnetic resonance imaging following carotid artery stenting: a meta-analysis of 8 studies comparing filter cerebral protection and proximal balloon occlusion.** *JACC Cardiovasc Interv* 2014;7:1177–83 CrossRef Medline
19. Bijuklic K, Wandler A, Hzizi F, et al. **The PROFI study (Prevention of Cerebral Embolization by Proximal Balloon Occlusion Compared to Filter Protection During Carotid Artery Stenting): a prospective randomized trial.** *J Am Coll Cardiol* 2012;59:1383–89 CrossRef Medline

Superselective Intra-Arterial Ethanol Sclerotherapy of Feeding Artery and Nidal Aneurysms in Ruptured Cerebral Arteriovenous Malformations

F. Settecase, S.W. Hetts, A.D. Nicholson, M.R. Amans, D.L. Cooke, C.F. Dowd, R.T. Higashida, and V.V. Halbach

ABSTRACT

SUMMARY: In the endovascular treatment of cerebral arteriovenous malformations, ethanol sclerotherapy is seldom used due to safety concerns. However, when limited reflux of an embolic agent is permissible or when there is a long distance to the target, ethanol may be preferable. We reviewed 10 patients with 14 cerebral AVM feeding artery aneurysms or intranidal aneurysms treated with intra-arterial ethanol sclerotherapy at our institution between 2005 and 2014. All patients presented with acute intracranial hemorrhage. Thirteen of 14 aneurysms were treated primarily with 60%–80% ethanol into the feeding artery. Complete target feeding artery and aneurysm occlusion was seen in all cases; 8/13 (62%) were occluded by using ethanol alone. No retreatments or recurrences were seen. One permanent neurologic deficit (1/13, 7.7%) and no deaths occurred. In a subset of ruptured cerebral AVMs, ethanol sclerotherapy of feeding artery aneurysms and intranidal aneurysms can be performed with a high degree of technical success and a low rate of complication.

ABBREVIATIONS: FAA = feeding artery aneurysm; EtOH = ethanol; INA = intranidal aneurysm

Aneurysms are often seen in association with cerebral arteriovenous malformations, occurring either along an artery supplying the AVM, within the AVM nidus, or arising from an unrelated artery. Flow-related feeding artery aneurysms and intranidal aneurysms are a primary source of hemorrhage in ruptured cerebral AVMs.^{1–3} Currently, treatment options for cerebral AVMs include surgery, stereotactic radiosurgery, and endovascular embolization, each of which may be performed as a stand-alone therapy or in combination. Embolization alone is rarely curative, and its primary role is to promote safer surgical resection by decreasing blood loss, shortening the length of surgery, reducing the risk of damage to surrounding structures, and increasing the likelihood of complete resection. Embolization may also render an AVM more amenable to radiosurgery by reducing the size of the AVM nidus and can be used to treat feeding artery or intranidal

aneurysms, especially if deep-seated and difficult to access or control surgically.^{4–7}

Embolization of an AVM requires superselective catheterization and distal placement of the microcatheter within a feeding artery, aiming to protect the parent artery from any reflux of embolic material and any en passage branches from nontarget embolization. The most commonly used embolic material is *n*-butyl cyanoacrylate, a quickly polymerizing liquid adhesive. Ethylene vinyl copolymer (Onyx; Covidien, Irvine, California)^{8–10} is a newer but less commonly used embolic agent in AVM treatment. Particles¹¹ and detachable coils are infrequently used.

Ethanol sclerotherapy is commonly used in the treatment of extracranial AVMs,^{12–15} yet it is seldom used in the treatment of cerebral AVMs due to safety concerns.^{16–25} In some circumstances, such as when distal microcatheter positioning beyond the proximal portion of a small feeding artery is not possible, however, the use of ethanol may be preferable. In this retrospective case series, we report our experience with patients whose brain AVMs presented with acute intracranial hemorrhage in whom ethanol sclerotherapy was preferable to other embolization techniques to treat feeding artery aneurysms (FAAs) or intranidal aneurysms (INAs).

Case Series

Under an institutional review board–approved protocol, a keyword search of the University of California, San Francisco neuro-interventional data base identified 10 patients with cerebral

Received June 25, 2015; accepted after revision August 10.

From the Division of Interventional Neuroradiology, Department of Radiology and Biomedical Imaging, University of California, San Francisco, San Francisco, California.

Paper previously presented at: Annual Meeting of the Society of Neurointerventional Surgery, July 27–30, 2015; San Francisco, California.

Please address correspondence to Fabio Settecase, MD, MSc, FRCPC, Division of Interventional Neuroradiology, Department of Radiology and Biomedical Imaging, University of California, San Francisco, 505 Parnassus Ave, L351, San Francisco, CA, 94143; e-mail: fabio.settecase@ucsf.edu

Indicates article with supplemental on-line table.

<http://dx.doi.org/10.3174/ajnr.A4584>

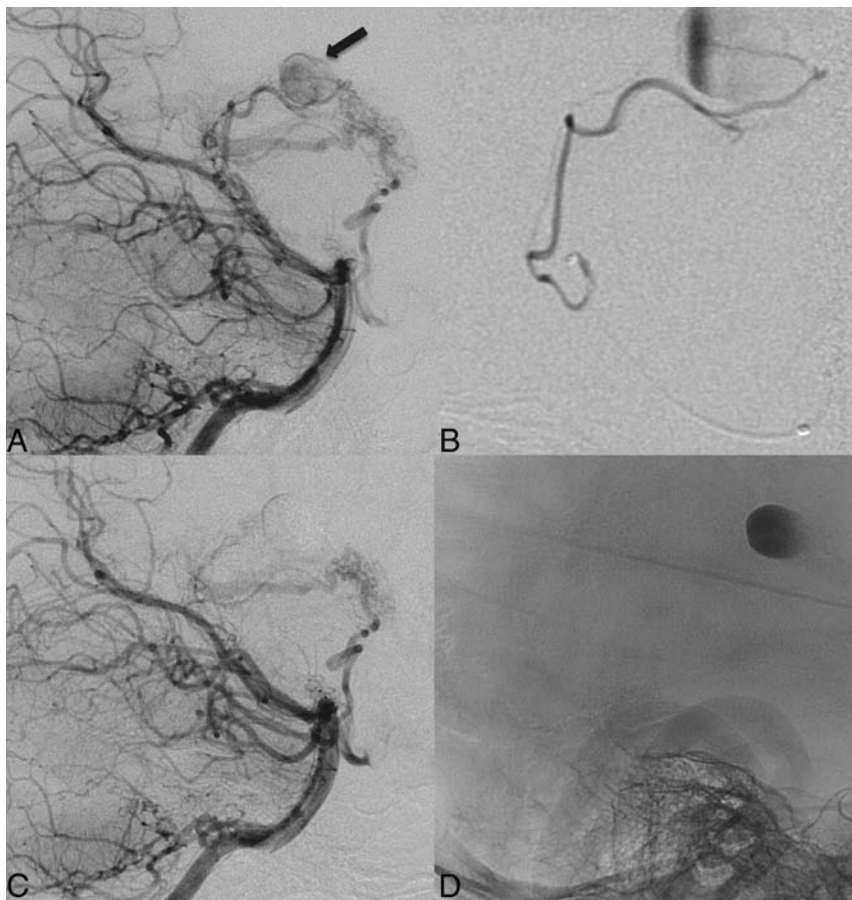


FIG 1. Ethanol sclerotherapy of a feeding artery aneurysm in a 5-year-old girl with a right thalamic AVM. *A*, Lateral view, left vertebral artery injection demonstrates an 11-mm feeding artery aneurysm (arrow) arising from the right posterolateral choroidal artery at the posterior aspect of the AVM nidus. *B*, Superselective microcatheter injection of the right posterolateral choroidal artery again demonstrates the feeding artery aneurysm. Note that the microcatheter is positioned in the proximal portion of right posterolateral choroidal artery. More distal catheterization of this artery was not possible. *C*, Lateral view left vertebral artery injection 20 minutes after intra-arterial sclerotherapy with 5 mL of 70% ethanol demonstrates lack of filling of the feeding artery and aneurysm. *D*, Unsubtracted lateral view of the skull at the end of the sclerotherapy treatment demonstrates stasis of contrast within the aneurysm.

AVMs and associated FAAs or INAs treated by using superselective intra-arterial ethanol sclerotherapy between 2005 and 2014. Neuroimaging, angiograms, operative reports, and electronic medical records were reviewed for each patient by a board-certified radiologist with a Certificate of Added Qualification in neuroradiology, 2 years' work experience in diagnostic neuroradiology, and additional training in interventional neuroradiology (F.S.).

After presentation with intracranial hemorrhage and CT and/or CT angiographic evidence of an underlying cerebral arteriovenous malformation, patients were referred to the interventional neuroradiology service for diagnostic cerebral angiography. Indications for AVM endovascular embolization were determined by clinical presentation, cross-sectional imaging, and angiographic findings. In all cases in this series, the decision to proceed with embolization was determined by the presence of intracranial hemorrhage in the setting of a cerebral AVM and the presence of either a FAA or INA suspected as the hemorrhage source and/or at risk for future hemorrhage (Figs 1 and 2). Indications for treatment and treatment strategy were agreed upon by

the attending neuroradiologist (V.V.H.) and the admitting neurosurgeon in all cases. In all cases, the primary goal of treatment was obliteration of the FAA or INA. AVM nidus-size reduction or obliteration was a secondary goal. All patients consented to the use of a number of possible embolic materials as well as ethanol. The decision to use ethanol was made during the procedure, after obtaining superselective distal catheter positioning and on the basis of several factors, including the following: distance from the microcatheter tip to the target aneurysm, position of the catheter just beyond a branch point in which 1 branch was en passage to normal brain (eg, catheter positioned in the origin of the posterolateral choroidal artery), and amount of flow present within the feeding artery before treatment. For the concentration and volume of ethanol, we also took into account the above factors. In addition, serial angiograms were obtained midsclerotherapy to determine the efficacy of ethanol sclerotherapy and whether additional volume or change in the concentration of ethanol was necessary. In cases in which residual flow within the feeding artery and incomplete aneurysm occlusion were seen, adjunctive endovascular therapies were performed, such as coil placement or *n*-butyl cyanoacrylate embolization.

Noncontrast head CTs were reviewed to determine the presence and location of intracranial hemorrhage.

Angiograms were reviewed to score the AVM grade and to determine the AVM location, the presence and number of feeding arteries or nidal aneurysms, the feeding artery from which the aneurysm arose, and the presence or absence of aneurysm filling on posttreatment runs. AVM size was estimated from MR imaging and angiography, and all AVMs were classified according to the Spetzler-Martin grading scale.²⁶ The clinical status of patients was assessed at presentation, after embolization, and throughout hospitalization by members of the interventional neuroradiology and neurosurgical teams; and at follow-up visits by a neurosurgeon. Ethanol sclerotherapy was performed in all patients. Operative reports were reviewed to determine the aneurysm size, percentage of ethanol concentration used, amount of ethanol injected, adjunctive treatments, and periprocedural complications. The electronic medical record and follow-up digital subtraction angiograms were reviewed to determine the number of treatment sessions, aneurysm recurrence, delayed complications or death, definitive AVM treatments, and duration of follow-up. No clinical or angiographic follow-up was available in 1 patient.

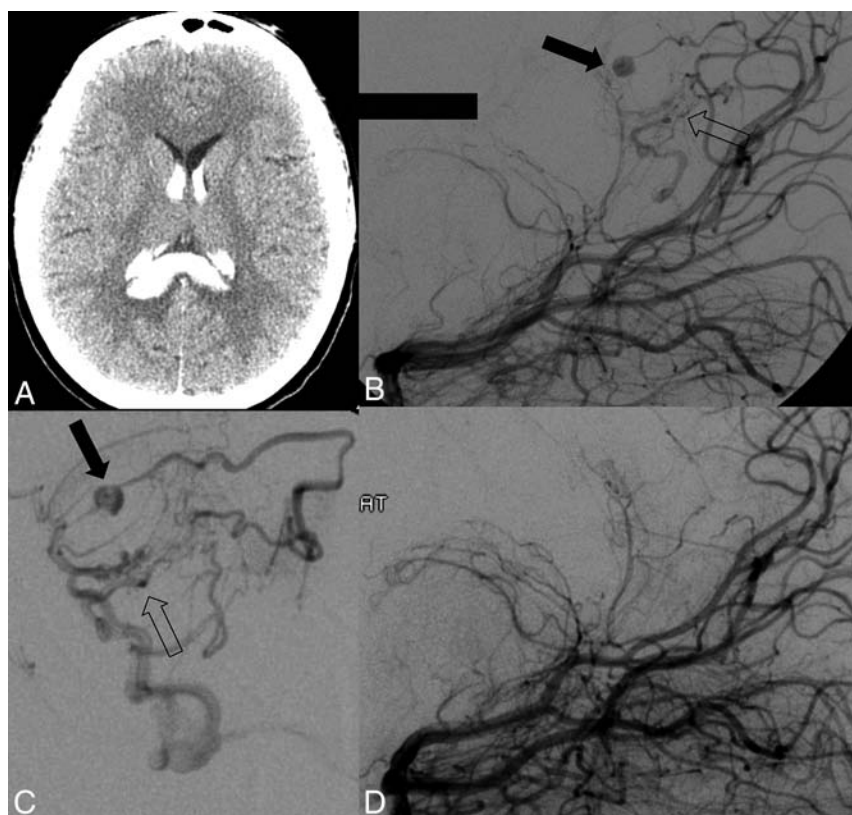


FIG 2. Ethanol sclerotherapy of a feeding artery aneurysm in a 15-year-old girl presenting with headache. **A**, Noncontrast CT head axial image demonstrates acute intraparenchymal hemorrhage centered in the splenium of the corpus callosum with intraventricular extension. **B**, Selective injection of the left vertebral artery in a reverse Schuller projection demonstrates a small AVM nidus (open arrow) and a 5-mm feeding artery aneurysm arising from the right splenic artery (black arrow). **C**, Lateral view of a superselective microcatheter injection of the right splenic artery. The AVM nidus (open arrow) and a 5-mm feeding artery aneurysm (black arrow) are again seen. **D**, Twenty minutes after ethanol sclerotherapy with 4 mL of 70% ethanol, posttherapy reverse Schuller projection of a left vertebral artery injection demonstrates the absence of the feeding artery aneurysm and AVM nidus and no evidence of arteriovenous shunting.

Endovascular Procedure

Informed consent was obtained from the patient or family before diagnostic angiography and possible endovascular therapy, including possible ethanol sclerotherapy. Potential risks discussed included those directly related to the procedure and those related to general anesthesia. All procedures were performed on a biplane angiographic unit with the patient under general anesthesia (with neuromuscular blockade administered and confirmed just before ethanol injection). Arterial lines were placed in each patient. Percutaneous vascular access was obtained through the right or left common femoral artery by using a standard coaxial technique. A complete cerebral angiogram that included both internal carotid arteries, the dominant vertebral artery, and, in some cases, the ipsilateral external carotid artery was obtained before treatment to identify the arterial feeders of the AVM. After a decision to treat was made and following any necessary upsizing of the vascular groin sheath, an intravenous bolus of 70 IU/kg body weight of heparin was administered and postheparin activated clotting time was obtained. A half dose of the initial bolus dose of IV heparin was administered at 1-hour intervals during the embolization procedure.

A guiding catheter was placed into the ipsilateral internal carotid artery or dominant vertebral artery; then, either a flow-directed microcatheter or an over-the-wire microcatheter was

advanced under fluoroscopic and roadmap guidance into the AVM feeding artery branch. No provocative testing was performed. The microcatheter was positioned as distally as possible within the feeding artery to rest as close as possible to the AVM nidus or in a position for embolizing the feeding artery aneurysm while avoiding nontarget en passage branch embolization. Once an adequate microcatheter position was obtained, the microcatheter was flushed with 0.3–0.5 mL of heparinized normal saline. Dehydrated absolute ethanol was drawn into a 1-mL Luer lock syringe and mixed with varying amounts of heparinized iohexol contrast (Omnipaque 300; GE Healthcare, Piscataway, New Jersey) to achieve the desired final concentration of ethanol for sclerotherapy. Short, gentle pulsed injections of ethanol were performed via the microcatheter under roadmap blank fluoroscopic monitoring, aiming to avoid reflux. After delivery of 1–2 mL of the ethanol-contrast mixture, 10–20 minutes were allowed to elapse before performing a midembolization angiographic run through the microcatheter to allow ethanol to take effect on the arterial endothelium. Midsclerotherapy runs were then performed to determine whether any residual filling of the aneurysm or upstream feeding artery remained.

In some cases, additional volumes of ethanol-contrast mixtures were administered and, after another 10- to 20-minute delay, angiography was repeated. If no further contrast filling of the aneurysm and upstream feeding artery was seen, no further sclerotherapy or adjunctive embolization was performed. In some cases, residual filling of the feeding artery and aneurysm was observed, and adjunctive therapies such as placement of detachable coils or injection of *n*-BCA was performed.

Patients

From 2005 to 2014, 10 patients with a ruptured cerebral AVMs and associated FAAs or INAs were treated at our hospital by using superselective intra-arterial ethanol sclerotherapy. There were 5 males and 5 females, with a mean age of 25 ± 21 years (median, 15 years; range, 1–64 years). All patients underwent CT, MR imaging, and digital subtraction angiography. Clinical presentation included intraventricular hemorrhage in all patients, intraparenchymal hemorrhage in 8/10 patients, and subarachnoid hemorrhage in 4/10 patients. The AVM Spetzler-Martin grades ranged from II to IV (Table). Aneurysm sizes ranged from 1 to 11 mm (average size, 4 ± 2.4 mm).

Patient demographics, AVM, and flow-related aneurysm characteristics

Case No.	Age (yr)	AVM Grade	AVM Location	Bleed	Aneurysm Size (mm)	Aneurysm Type	Feeding Artery to Aneurysm
1	53	IV	L frontoparietal	IVH/IPH	3	FAA	L PlCh
2	15	II	R splenium of corpus callosum	IVH/IPH	5	FAA	R splenial
3	32	III	L cerebellum	IPH/SAH	4	INA	L SCA
4	5	III	R thalamus	IPH/IVH/SAH	11	FAA	R PlCh
5	1	III	R thalamus	IPH/IVH/SAH	3 and 1	FAA	R PmCh
6	13	II	L parieto-occipital	IPH/IVH	3 and 2	INA	L PO
7	11	IV	L insula	IPH/IVH/SAH	3	INA	L PlCh
8	64	II	R thalamus	IVH	4	FAA	R PmCh
9	42	III	L thalamus	IPH/IVH	6	FAA	L ACh
10	17	III	R splenium of corpus callosum	IVH	4 and 3	INA	R pericallosal

Note:—IVH indicates intraventricular hemorrhage; IPH, intraparenchymal hemorrhage; PlCh, posterolateral choroidal artery; PO, parieto-occipital artery; PmCh, posteromedial choroidal artery; Ach, anterior choroidal artery; L, left; R, right; SCA, superior cerebellar artery.

RESULTS

Fourteen feeding artery or intranidal aneurysms were identified in 10 patients, of which, 13 were treated with superselective intra-arterial ethanol sclerotherapy (On-line Table). One of the 14 aneurysms was not treated due to its location (arising from the calcarine artery with several en passage branches). Mixtures of 60%–80% ethanol (70% ethanol was used in 7/10 patients) were delivered slowly under roadmap-mask guidance directly into the feeding artery supplying the aneurysm. Post-therapy angiography to assess aneurysm occlusion was performed 10–20 minutes after ethanol injection. The volume of ethanol injected ranged from 2 to 22 mL (median, 3.75 mL) (Table). Complete occlusion of the aneurysm and upstream feeding artery was seen in 13/13 treated aneurysms (100%) (Figs 1 and 2), with 8/13 (62%) aneurysms occluded by using ethanol sclerotherapy alone. In addition, ethanol sclerotherapy alone achieved both aneurysm occlusion and angiographic cure of the AVM in 2 cases (On-line Table, Fig 2).

Adjunctive endovascular interventions were performed after ethanol sclerotherapy to treat 5/13 (38%) aneurysms in 4 patients. After ethanol sclerotherapy of 4 aneurysms, markedly decreased but residual blood flow in the feeding artery remained on post-ethanol (EtOH) angiography. To promote complete thrombo-occlusion of the feeding artery, we placed detachable coils within the feeding artery in 4/5 aneurysms from the same microcatheter tip location as in the EtOH injection. In another patient, after an injection of 5 mL of 60% ethanol and another 5 mL of 80% ethanol into the feeding artery, slowed but persistent flow within the feeding artery and FAA was seen postsclerotherapy. During the same treatment session, 0.3 mL of 20% *n*-BCA was used to embolize the aneurysm, feeding artery, and AVM nidus with no residual AVM or aneurysm filling after *n*-BCA embolization.

Follow-up was available in 9/10 patients, with a mean follow-up of 1.3 years (range, 3 months to 5 years). None of the treated aneurysms required >1 treatment session, and there were no recurrences. One complication related to ethanol sclerotherapy was encountered (1/13, 7.7%): This patient developed transient hemiparesis and aphasia after injection of 6 mL of 70% ethanol into a posterolateral choroidal artery feeding artery with a 3-mm FAA in a Spetzler-Martin grade IV left frontoparietal AVM. At 5-year follow-up, the hemiparesis had nearly completely resolved with motor examination notable for 4+/5 strength in the

tibialis anterior. His aphasia had also improved; however, he exhibited hesitant speech with paraphasic errors. No deaths were attributed to ethanol sclerotherapy in both the periprocedural and follow-up periods.

DISCUSSION

Our experience by using ethanol sclerotherapy for feeding artery aneurysms and intranidal aneurysms in a subset of ruptured cerebral AVMs demonstrates that complete aneurysm and upstream feeding artery occlusion may be achieved in most cases (62%) with ethanol alone. Ethanol is a potent sclerosant, is relatively inexpensive, and has a widespread commercial availability. The injection of small volumes of high concentrations of ethanol results in the dehydration, precipitation, sloughing, and denudation of the vascular endothelium.^{16,19,27,28} In the presence of blood, an acute thrombosis may be initiated, leading to permanent vascular closure.^{16,27}

In 5/13 aneurysms, ethanol sclerotherapy markedly reduced blood flow within the feeding artery; however, slow contrast filling of the aneurysm persisted and adjunct endovascular therapy was necessary for complete occlusion of the aneurysm and feeding artery. Adjunctive therapies included placement of 2 detachable coils or a fibered coil into the feeding artery from the same microcatheter tip location as that used for the EtOH injection or *n*-BCA embolization of the feeding artery (On-line Table). No correlation was found between the need for adjunct endovascular therapy (ie, coils or *n*-BCA) and the size of the flow-related aneurysm or AVM or ethanol concentration or volume. Because EtOH acts directly on endothelial cells, factors that decrease the amount of time the EtOH dwells in the artery and is in contact with endothelium, such as feeding artery diameter and rate of AV shunting, are more likely to result in incomplete occlusion with EtOH alone. Nonetheless, 1 embolization session was sufficient to obtain complete obliteration for all 13 aneurysms, and no recurrences were seen after a mean follow-up of 1.3 years.

In our study, 1 complication (1/13 treated aneurysms, 7.7%) occurred after ethanol sclerotherapy of a posterolateral choroidal feeding artery to the AVM, with peritrial white matter low attenuation seen on postoperative CT, likely due to a combination of vasogenic and cytotoxic edema of nontarget brain tissue. No deaths were attributed to ethanol sclerotherapy. An initial report of ethanol sclerotherapy of cerebral

AVMs by Yakes et al¹⁶ described permanent complications developing in 8 of 17 (47%) patients, of which 3 were permanent (18%) and 5 (29%) were transient complications, and 2 deaths (2/17, 12%) occurring at 4 and 14 months after ethanol treatment due to subarachnoid hemorrhage. The very high complication rate reported in that study has limited the use of ethanol in the treatment of cerebral AVMs. Since the study of Yakes et al,¹⁶ there have been no other published reports of the use of ethanol sclerotherapy of cerebral AVMs. Ethanol sclerotherapy continues to be routinely used, however, in the treatment of peripheral AVMs.²⁹

The results of this study differ from those of the study by Yakes et al¹⁶ in several ways: First, in our study, the primary goal of therapy in each patient was obliteration of the feeding artery aneurysm or intranidal aneurysm, whereas AVM nidus obliteration or reduction in size of the AVM nidus was the primary goal in the Yakes et al¹⁶ study. The average volume of ethanol used was, therefore, much lower in our study (ie, 2–22 mL; median, 3.75 mL versus 0.8–112 mL); this difference may have contributed to a lower complication rate. Second, ethanol concentrations used in our study varied from 60% to 80%, compared with 98% ethanol used in the prior study. Yakes et al stated that nonionic contrast medium can be mixed with ethanol and precipitation does not occur; however, contrast media dilute ethanol to a level that renders it ineffective in achieving a sclerosing effect and thrombosis. In contrast, this study indicates that concentrations of 60%–80% ethanol have a potent sclerosing effect. Third, the presenting symptoms in our study were also different, with all AVMs in our study presenting with intracranial hemorrhage, whereas presentation varied in the prior study (hemorrhage in 7/17 patients, seizures, hemianopsia, headaches, trigeminal neuralgia, and thalamic syndrome).

Despite the encouraging results of intra-arterial ethanol sclerotherapy demonstrated in this study in the setting of flow-related aneurysms in ruptured AVMs, we do not recommend routine use of this agent in the endovascular treatment of AVMs. Embolic materials such as *n*-BCA or Onyx remain first-line agents in the endovascular treatment of AVMs in our practice. In each case within this series, the choice of embolic agent versus sclerosant was not made a priori, rather only after superselective microcatheterization and distal access (or attempted distal access) of the feeding artery. The cases included in this series demonstrate that there are rare circumstances in which ethanol may be preferable to embolic agents—for example, when superselective catheterization, which minimizes the risk of reflux and nontarget embolization, is not possible, such as with an inability to position a microcatheter beyond the proximal portion of a small feeding artery (Fig 1; cases 1, 2, 4, 7, and 8). While reflux of an embolic agent into the parent artery in this situation could have devastating consequences, the risk of nontarget vascular injury from reflux of ethanol from the same vessel is decreased because ethanol concentration drops in the parent artery via dilution. A second scenario in which ethanol was preferable to embolic agents occurred when a particularly long distance between the microcatheter tip and the target aneurysm existed and there was substantial risk of a standard liquid embolic agent not reaching the target (cases 1–5, 7–10). Consideration should also be given to the surgical ac-

cessibility of FAA or INA if endovascular therapy is being performed preoperatively. The AVM itself or many of the FAAs/INAs in this case series were deep-seated; this location favored endovascular over surgical treatment of the flow-related aneurysms. Careful consideration of the indications for treatment, efficacy, and risks of embolization materials (*n*-BCA and Onyx) and ethanol must be made before treatment and once the final microcatheter position in the feeding artery is attained.

Extreme caution should be used when injecting ethanol in any concentration or amount due to the high toxicity of ethanol. Nontarget necrosis of adjacent tissues may occur with overinjection, localized extravasation, or reflux.^{16,20} In addition, ethanol may exert effects distant from the target site, including the venous system causing a thrombophlebitis; or (in larger quantities) more distant effects of intoxication, hemoglobinuria, pulmonary artery hypertension, pulmonary embolus, bronchospasm, hyperthermia, cardiopulmonary collapse, and death.^{16,18–25} Ethanol sclerotherapy has also been associated with disruption in coagulation profiles as evidenced by a decrease in platelets and fibrinogen, an increase in prothrombin time, and a conversion from negative to positive D-dimers.³⁰ In 1 case report, the bispectral index, a measure of the depth of anesthesia, fell to zero during ethanol sclerotherapy of a cerebral AVM.³¹ Therefore, great care should be taken to not exceed a per-procedure administered dose of >1 mL/kg.²⁷ This study shows that volumes well below this threshold are efficacious (Table); however, close patient monitoring for the above adverse events and complications following ethanol sclerotherapy should always be performed.

In addition to the above effects, our group has also reported intraventricular contrast medium leakage mimicking intraventricular hemorrhage during intra-arterial 100% ethanol sclerotherapy into the posterolateral choroidal artery in a 5-year-old child with a ruptured AVM.³² While such a phenomenon is uncommon and not reported elsewhere, the neurointerventionalist should be aware of it, especially because many of the feeding arteries in this study involved arteries supplying the choroid plexus.

This study has several important limitations. The retrospective nature limits the generalizability of the results, and a selection bias may be present. In addition, there was no comparison group to determine whether ethanol sclerotherapy would achieve better results with similar or fewer complications in similar cases with the use of other embolic materials, such as *n*-BCA or Onyx. Selection of a comparison group of flow-related aneurysms for this series would be difficult and impractical, however, because the catheter positions in which ethanol was used in nearly all patients in this case series precluded the safe or efficacious use of embolic agents. The authors recommend against a study that compares the efficacy and safety profile of ethanol sclerotherapy with embolic agents in the setting of endovascular AVM treatment.¹⁶ In addition, because this study included only patients with ruptured AVMs, the results cannot be generalized to unruptured cerebral AVMs. Given the small number of patients in this study, results should be confirmed in a larger prospective study. Gross pathology confirmation of aneurysm obliteration was not possible in this study, and evidence of obliteration is based solely on follow-up conventional angiography in 9/10 patients.

In conclusion, this study suggests that in a subset of ruptured cerebral AVMs, ethanol sclerotherapy of FAAs and INAs can be performed with a high degree of technical success and a low rate of complications.

Disclosures: Christopher F. Dowd—UNRELATED: Other: MicroVention,* Comments: Chief Adjudicator, Flow Redirection Intraluminal Device (FRED) Trial. *Money paid to the institution.

REFERENCES

- Perata HJ, Tomsick TA, Tew JM Jr. **Feeding artery pedicle aneurysms: association with parenchymal hemorrhage and arteriovenous malformation in the brain.** *J Neurosurg* 1994;80:631–34 CrossRef Medline
- Redekop G, TerBrugge K, Montanera W, et al. **Arterial aneurysms associated with cerebral arteriovenous malformations: classification, incidence, and risk of hemorrhage.** *J Neurosurg* 1998;89:539–46 CrossRef Medline
- Pollock BE, Flickinger JC, Lunsford LD, et al. **Factors that predict the bleeding risk of cerebral arteriovenous malformations.** *Stroke* 1996;27:1–6 CrossRef Medline
- Spetzler RF, Martin NA, Carter LP, et al. **Surgical management of large AVM's by staged embolization and operative excision.** *J Neurosurg* 1987;67:17–28 CrossRef Medline
- Gobin YP, Laurent A, Merienne L, et al. **Treatment of brain arteriovenous malformations by embolization and radiosurgery.** *J Neurosurg* 1996;85:19–28 CrossRef Medline
- Henkes H, Nahser HC, Berg-Dammer E, et al. **Endovascular therapy of brain AVMs prior to radiosurgery.** *Neurol Res* 1998;20:479–92 Medline
- Richling B, Killer M. **Endovascular management of patients with cerebral arteriovenous malformations.** *Neurosurg Clin N Am* 2000;11:123–45, ix Medline
- Jahan R, Murayama Y, Gobin YP, et al. **Embolization of arteriovenous malformations with Onyx: clinicopathological experience in 23 patients.** *Neurosurgery* 2001;48:984–95; discussion 995–987 CrossRef Medline
- Pierot L, Januel AC, Herbreteau D, et al. **Endovascular treatment of brain arteriovenous malformations using Onyx: preliminary results of a prospective multicenter study.** *Interv Neuroradiol* 2005;11:159–64 Medline
- van Rooij WJ, Sluzewski M, Beute GN. **Brain AVM embolization with Onyx.** *AJNR Am J Neuroradiol* 2007;28:172–77; discussion 178 Medline
- Sorimachi T, Koike T, Takeuchi S, et al. **Embolization of cerebral arteriovenous malformations achieved with polyvinyl alcohol particles: angiographic reappearance and complications.** *AJNR Am J Neuroradiol* 1999;20:1323–28 Medline
- Yakes WF. **Endovascular management of high-flow arteriovenous malformations.** *Semin Intervent Radiol* 2004;21:49–58 CrossRef Medline
- Pekkola J, Lappalainen K, Vuola P, et al. **Head and neck arteriovenous malformations: results of ethanol sclerotherapy.** *AJNR Am J Neuroradiol* 2013;34:198–204 CrossRef Medline
- Vogelzang RL, Atassi R, Vouche M, et al. **Ethanol embolotherapy of vascular malformations: clinical outcomes at a single center.** *J Vasc Interv Radiol* 2014;25:206–13; quiz 214 CrossRef Medline
- Lee BB, Do YS, Yakes W, et al. **Management of arteriovenous malformations: a multidisciplinary approach.** *J Vasc Surg* 2004;39:590–600 CrossRef Medline
- Yakes WF, Krauth L, Ecklund J, et al. **Ethanol endovascular management of brain arteriovenous malformations: initial results.** *Neurosurgery* 1997;40:1145–52; discussion 1152–1144 CrossRef Medline
- Wong GA, Armstrong DC, Robertson JM. **Cardiovascular collapse during ethanol sclerotherapy in a pediatric patient.** *Paediatr Anaesth* 2006;16:343–46 CrossRef Medline
- Do YS, Yakes WF, Shin SW, et al. **Ethanol embolization of arteriovenous malformations: interim results.** *Radiology* 2005;235:674–82 CrossRef Medline
- Shin BS, Do YS, Lee BB, et al. **Multistage ethanol sclerotherapy of soft-tissue arteriovenous malformations: effect on pulmonary arterial pressure.** *Radiology* 2005;235:1072–77 CrossRef Medline
- Choi YH, Han MH, O-Ki K, et al. **Craniofacial cavernous venous malformations: percutaneous sclerotherapy with use of ethanol-amine oleate.** *J Vasc Interv Radiol* 2002;13:475–82 CrossRef Medline
- de Lorimier AA. **Sclerotherapy for venous malformations.** *J Pediatr Surg* 1995;30:188–93; discussion 194 CrossRef Medline
- Behnia R. **Systemic effects of absolute alcohol embolization in a patient with a congenital arteriovenous malformation of the lower extremity.** *Anesth Analg* 1995;80:415–17 CrossRef Medline
- Garel L, Mareschal JL, Gagnadoux MF, et al. **Fatal outcome after ethanol renal ablation in child with end-stage kidneys.** *AJR Am J Roentgenol* 1986;146:593–94 CrossRef Medline
- Mason KP, Michna E, Zurakowski D, et al. **Serum ethanol levels in children and adults after ethanol embolization or sclerotherapy for vascular anomalies.** *Radiology* 2000;217:127–32 CrossRef Medline
- Stefanutto TB, Halbach V. **Bronchospasm precipitated by ethanol injection in arteriovenous malformation.** *AJNR Am J Neuroradiol* 2003;24:2050–51 Medline
- Spetzler RF, Martin NA. **A proposed grading system for arteriovenous malformations.** *J Neurosurg* 1986;65:476–83 CrossRef Medline
- Yakes WF, Rossi P, Odink H. **How I do it: arteriovenous malformation management.** *Cardiovasc Intervent Radiol* 1996;19:65–71 CrossRef Medline
- Yakes WF, Haas DK, Parker SH, et al. **Symptomatic vascular malformations: ethanol embolotherapy.** *Radiology* 1989;170:1059–66 CrossRef Medline
- Legiehn GM, Heran MK. **A step-by-step practical approach to imaging diagnosis and interventional radiologic therapy in vascular malformations.** *Semin Intervent Radiol* 2010;27:209–31 CrossRef Medline
- Mason KP, Neufeld EJ, Karian VE, et al. **Coagulation abnormalities in pediatric and adult patients after sclerotherapy or embolization of vascular anomalies.** *AJR Am J Roentgenol* 2001;177:1359–63 CrossRef Medline
- Unnikrishnan KP, Sinha PK, Sriganesh K, et al. **Case report: alterations in bispectral index following absolute alcohol embolization in a patient with intracranial arteriovenous malformation.** *Can J Anaesth* 2007;54:908–11 CrossRef Medline
- Phatouros CC, Halbach VV, Malek AM, et al. **Intraventricular contrast medium leakage during ethanol embolization of an arteriovenous malformation.** *AJNR Am J Neuroradiol* 1999;20:1329–32 Medline

White Matter Abnormality Correlates with Developmental and Seizure Outcomes in West Syndrome of Unknown Etiology

J. Natsume, C. Ogawa, T. Fukasawa, H. Yamamoto, N. Ishihara, Y. Sakaguchi, Y. Ito, T. Takeuchi, Y. Azuma, N. Ando, T. Kubota, T. Tsuji, H. Kawai, S. Naganawa, and H. Kidokoro



ABSTRACT

BACKGROUND AND PURPOSE: West syndrome is an epileptic encephalopathy characterized by epileptic spasms, a specific pattern on electroencephalography of hypsarrhythmia, and developmental regression. Our aim was to assess white matter abnormalities in West syndrome of unknown etiology. We hypothesized that diffusion tensor imaging reveals white matter abnormalities, especially in patients with poor seizure and developmental outcomes.

MATERIALS AND METHODS: We enrolled 23 patients with new-onset West syndrome of unknown etiology. DTI was performed at 12 and 24 months of age. Fractional anisotropy images were compared with those of controls by using tract-based spatial statistics. We compared axial, radial, and mean diffusivity between patients and controls in the fractional anisotropy skeleton. We determined correlations of these parameters with developmental quotient, electroencephalography, and seizure outcomes. We also compared DTI with hypometabolism on fluorodeoxyglucose positron-emission tomography.

RESULTS: At 12 months of age, patients showed widespread fractional anisotropy reductions and higher radial diffusivity in the fractional anisotropy skeleton with a significant difference on tract-based spatial statistics. The developmental quotient at 12 months of age correlated positively with fractional anisotropy and negatively with radial and mean diffusivity. Patients with seizure and abnormal findings on electroencephalography after initial treatments had lower fractional anisotropy and higher radial diffusivity. At 24 months, although tract-based spatial statistics did not show significant differences between patients and controls, tract-based spatial statistics in the 10 patients with a developmental quotient of <70 had significant fractional anisotropy reduction. In patients with unilateral temporal lobe hypometabolism on PET, tract-based spatial statistics showed greater fractional anisotropy reduction in the temporal lobe ipsilateral to the side of PET hypometabolism.

CONCLUSIONS: Diffuse abnormal findings on DTI at 12 months of age suggest delayed myelination as a key factor underlying abnormal findings on DTI. Conversely, asymmetric abnormal findings on DTI at 24 months may reflect underlying focal pathologies.

ABBREVIATIONS: ACTH = adrenocorticotrophic hormone; DQ = developmental quotient; EEG = electroencephalography; FA = fractional anisotropy; TBSS = tract-based spatial statistics; WS = West syndrome

West syndrome (WS) is an epileptic encephalopathy characterized by epileptic spasms, a specific pattern on electroencephalography (EEG) of hypsarrhythmia, and developmental re-

gression. While WS has a variety of causes, the etiology remains unclear in 20% of patients.¹ Recent advances in neuroimaging have revealed underlying pathologies such as focal cortical dysplasia in these patients.² We and others have reported hypometabolism on PET and hypoperfusion on SPECT during the early stages of cryptogenic WS.³⁻⁹ Detecting these findings is useful for both predicting long-term outcomes and detecting underlying lesions.^{3-6,8,9} Further progress of modern neuroimaging techniques

Received June 16, 2015; accepted after revision August 26.

From the Departments of Pediatrics (J.N., C.O., H.Y., N.I., Y.S., Y.I., T. Takeuchi, Y.A., H. Kidokoro), Developmental Disability Medicine (J.N.), and Radiology (H. Kawai, S.N.), Nagoya University Graduate School of Medicine, Nagoya, Japan; Department of Pediatrics and Neonatology (N.A.), Nagoya City University Graduate School of Medical Sciences, Nagoya, Japan; Brain and Mind Research Center (J.N., H. Kidokoro), Nagoya University, Nagoya, Japan; Department of Pediatrics (T.F., T.K.), Anjo Kosei Hospital, Anjo, Japan; and Department of Pediatrics (T. Tsuji), Okazaki City Hospital, Okazaki, Japan.

This study was supported by a Grant-in-Aid for Scientific Research (C) 23591492 and a Grant-in-Aid for Scientific Research on Innovative Areas (Comprehensive Brain Science Network) from the Ministry of Education, Culture, Sports, Science and Technology of Japan.

The authors have no financial relationships relevant to this article to disclose or no conflicts of interest to disclose.

Please address correspondence to Jun Natsume, MD, PhD, Department of Pediatrics, Nagoya University Graduate School of Medicine, 65 Tsurumai-cho, Showa-ku, Nagoya, Aichi 466-8550, Japan; e-mail: junnatsu@med.nagoya-u.ac.jp

Indicates open access to non-subscribers at www.ajnr.org

<http://dx.doi.org/10.3174/ajnr.A4589>

is expected to clarify the underlying pathology in patients with WS of unknown etiology.

Diffusion tensor imaging is an MR imaging technique that can provide information about the orientation and integrity of white matter fibers. This method is useful for detecting underlying abnormalities in the white matter of patients with various neurologic disorders. Because it is hypothesized that widespread networks of cortical and subcortical structures are involved in the generation of epileptic spasms and hypsarrhythmia in WS,¹⁰ DTI should help reveal the pathophysiology of this syndrome.

In this prospective study, we performed serial DTI studies from the onset of epilepsy to assess underlying white matter abnormalities in patients with WS of unknown etiology. We compared the results of DTI with cognitive and motor development, EEG findings, and seizure outcomes. We also compared distributions of abnormal findings on DTI with those of hypometabolism on [¹⁸F] fluorodeoxyglucose–PET.

MATERIALS AND METHODS

This study was approved by the research ethics committee at Nagoya University Graduate School of Medicine.

Patients

Between 2007 and 2014, we performed DTI in consecutive patients with new-onset WS of unknown etiology seen in Nagoya University Hospital. We diagnosed WS from epileptic spasms in clusters that were recorded by simultaneous video-EEG recording and typical interictal EEG findings of hypsarrhythmia. Inclusion criteria for patients were as follows: 1) normal birth and absence of any etiologic factors related to WS, 2) normal development before the onset of spasms and the absence of neurologic abnormalities at onset, 3) occurrence of spasm clusters without any other types of seizures before the onset of spasms, and 4) normal findings from laboratory tests, CT, and MR imaging. Chromosomal abnormalities were investigated with G-banding or array comparative genomic hybridization.

Patients were initially treated according to the following protocol: Clonazepam was administered for 1 week. When other oral antiepileptic drugs were started in previous hospitals, they were continued for 1 week. If oral antiepileptic medications failed to control the spasms, adrenocorticotrophic hormone (ACTH) therapy was started. In the present study, 1 patient did not receive ACTH therapy. In ACTH therapy, synthetic ACTH was injected intramuscularly at 0.015 mg/kg/day for 2–4 weeks, followed by alternate-day administration for 1 week. The effectiveness of each drug was evaluated on the basis of the frequency of spasms and interictal EEG findings.

Controls

We used 2 control groups to compare the images of patients with WS. The first control group consisted of 13 children with a mean age of 12.2 ± 3.0 months (range, 8–18 months) and was used for the analysis of patients at 12 month of age. The second control group comprised 15 children with a mean age of 24.8 ± 4.5 months (range, 18–27 months) and was used for the analysis of patients at 24 months. Controls had undergone MR imaging because CNS abnormalities had been suspected on presentation but

were later ruled out. Conventional MR imaging did not show any abnormalities in controls. Final diagnoses in controls were non-pathologic sleep myoclonus, nonpathologic motion arrest, myasthenia gravis, pigmented macules without neurocutaneous disorders, peripheral facial nerve palsy, breath-holding spell, shuddering attack, nonpathologic macrocephaly, and short stature.

Image Acquisition for DTI

All patients underwent DTI 3 times. The first scans were obtained at the onset of spasms before ACTH therapy; the second, at 12 months of age; and the third, at 24 months of age. We used the second and third scans for the present study. The second and third scans were obtained >1 month after the end of ACTH therapy to avoid the effects of brain shrinkage caused by ACTH. In our previous study evaluating MR imaging by visual inspection, we did not detect cerebral shrinkage caused by ACTH therapy on MR imaging performed >1 month after the end of ACTH therapy.⁵ Scans were obtained as part of the clinical routine to search for underlying pathology. Before each scan, we explained to parents that the results would be used for research, and informed consent was obtained. All patients were sedated with oral chloral hydrate before the examination. When patients did not appear sufficiently sedated after chloral hydrate intake, intravenous midazolam or ketamine was administered.

MR imaging examination was performed on a 3T scanner (Magnetom Trio A Tim System; Siemens, Erlangen, Germany) with a 32-channel phased array head coil. DTI parameters were the following: 12 noncollinear diffusion directions (b-value = 1000 s/mm²) with a nondiffusion gradient (b-value = 0 s/mm²); TR, 7800 ms; TE, 84 ms; FOV, 269 × 269 mm; matrix, 128 × 128; and 64 axial sections (voxel size = 2.1 × 2.1 × 2.1 mm³). In addition to DTI data, the following conventional MR images were acquired to examine structural abnormalities: axial T1-weighted, T2-weighted, fluid-attenuated inversion recovery images, sagittal T1-weighted images, and coronal T2-weighted images.

Evaluation of EEG, Seizure, and Neurodevelopmental Outcomes

We used EEG findings at 12 months of age for evaluating the early response to initial treatments. EEG findings at this age were classified as normal or abnormal on the basis of the remaining epileptiform discharges during wakefulness and sleep. Evaluation of seizure outcome was performed between August and December 2014. The age at the evaluation ranged from 2 to 8 years (median, 5 years). The information was obtained from the medical charts at Nagoya University or affiliated hospitals. Seizure outcome was categorized as follows: 1) free of seizures, when the patient had no seizures during the entire follow-up after the initial treatment with clonazepam or ACTH; or 2) persistent or recurrent seizures during the entire follow-up after initial treatment.

The developmental quotient (DQ) was estimated by using the Tsumori-Image developmental questionnaire at 12 and 24 months of age.¹¹ This questionnaire was released in 1961 and is widely used in Japan.^{9,12} It consists of the 5 domains of gross motor skill, fine motor skill, sociality, activities of daily living, and language. Developmental status was considered as follows: 1) normal, when

patients had a DQ of ≥ 70 at 24 months of age; or 2) delayed cognitive and motor development, when patients had a DQ of < 70 at 24 months of age. While the DQ at 12 months tends to reflect development of motor function, the DQ at 24 months reflects language and cognitive function more than the one at 12 months.

FDG-PET

All patients underwent FDG-PET at onset and at 12 and 24 months of age. The scans were obtained to search for underlying pathologies and predict long-term outcome as in our previous studies.^{5,9} All patients were sedated by chloral hydrate suppository during the PET examination. PET images were analyzed with visual inspection by 3 pediatric neurologists (J.N., T.F., and H. Kidokoro). All 3 pediatric neurologists were regularly involved in neuroimaging studies and had experience in the interpretation of pediatric PET images. PET findings were evaluated as in our previous studies.^{5,9} Regional hypometabolism was defined as a regional decrease in FDG accumulation in ≥ 2 gyri on ≥ 2 sections.

Image Processing

DTI analyses were performed by using tract-based spatial statistics (TBSS) in the fMRI of the Brain software package (FSL; <http://www.fmrib.ox.ac.uk/fsl>).¹³ For each subject, all DTI was corrected for eddy current-induced distortion and subject motion effects. The correction was performed by affine registration to a reference volume that is included in the FMRIB Diffusion Toolbox (<http://fsl.fmrib.ox.ac.uk/fsl/fslwiki/FDT>).

A brain mask was created from the first B0 image. A diffusion tensor model at each voxel was fitted, and fractional anisotropy (FA), mean diffusivity, axial diffusivity, and radial diffusivity maps were computed. Next, the most representative FA image was first identified, and all FA data for a subject were aligned to this target image by nonlinear registration. The mean FA image was created and thinned to create a mean FA skeleton, which represents the centers of all tracts common to the group. Aligned FA data for each subject were then projected onto this skeleton, and the resulting data were fed into voxelwise cross-subject statistics. Statistical analysis was performed voxel by voxel to detect regions of significant differences in FA between the 2 groups of subjects, by using FSL Randomise (<http://fsl.fmrib.ox.ac.uk/fsl/fslwiki/Randomise>) with 5000 permutations. The Threshold-Free Cluster Enhancement option in Randomise was used to avoid an arbitrary initial cluster-forming threshold. Age was used as a nuisance covariate of no interest. Results are reported at a corrected threshold of $P < .05$. TBSS analysis was performed between FA images of all patients and controls. Analyses were also performed between subgroups of patients with a DQ of < 70 or a DQ of ≥ 70 at 12 and 24 months of age and controls.

Skeletons showing significantly reduced FA from those of controls at 12 months of age were extracted. These skeletons included whole clusters with significant reduction of FA in patients on TBSS analysis and did not include clusters of increased FA. Mean values for FA, mean diffusivity, and eigenvalues in the skeletons were calculated in each patient. Eigenvalues (λ_1 , λ_2 , λ_3) correspond to the directional apparent

diffusion coefficients as either principal axial diffusivity (λ_1) or radial diffusivity ($[\lambda_2 + \lambda_3]/2$).

Statistical Analysis

Statistical analysis was performed by using SPSS, Version 19 software (IBM, Armonk, New York). We compared mean DTI parameters in the skeleton with significant differences on TBSS between patients and controls and determined correlations of parameters with the DQ at 12 months of age in patients. We also compared DTI parameters between patients with and without abnormal findings on EEG at 12 months of age and between patients with and without persisting or relapsing seizures after initial treatment.

On the basis of FDG-PET findings at 12 and 24 months of age, TBSS analysis of DTI at 12 and 24 months of age was performed between patients with regional hypometabolism and controls and between patients without regional hypometabolism and controls. This evaluation was performed because patients with regional hypometabolism may have focal underlying pathology that causes regional abnormal findings on DTI.

Comparisons of DTI parameters between patients and controls, between patients with and without EEG abnormalities, and between patients with and without persisting or relapsing seizures were performed by the nonparametric Mann-Whitney *U* test or the Kruskal-Wallis test and post hoc analysis with Bonferroni correction for analysis among 3 groups of patients with and without seizures and controls, and those with normal or abnormal EEG findings and controls. Correlations of parameters in patients with DQ were determined by the Spearman correlation coefficient (*r*). Significance was established at $P < .05$.

RESULTS

Twenty-three patients (14 boys) with WS of unknown etiology underwent DTI during the study period. ACTH therapy was performed as an initial treatment in 22 patients, while the remaining patient did not receive ACTH therapy. The interval from the onset of spasms to initial treatment was 0–4 months (median, 1 month). After initial treatment, 15 patients were categorized as free of seizures; 6 patients experienced recurrence of spasms; and 2 patients showed partial seizures. EEG at 12 months of age showed normal findings in 11 patients, hypsarrhythmia in 3, and focal spikes in 9. In 21 of 23 patients, the presence or absence of abnormal findings on EEG was the same at 12 and 24 months of age. In 1 patient with hypsarrhythmia and 1 with focal spikes at 12 months of age, the EEG findings were normal at 24 months. In 15 patients free of seizures after initial treatment, the EEG findings at 12 months of age were normal in 10 patients and showed focal spikes in 5. The DQ ranged from 33 to 100 (median, 77) at 12 months and from 29 to 123 (median, 75) at 24 months of age.

TBSS Analysis between Patients and Controls

Two patients could not undergo DTI at 12 months of age, and DTI of another patient showed motion artifacts. TBSS analysis at 12 months was thus performed between 20 patients and 13 controls. TBSS revealed reduced FA in the corpus callosum,

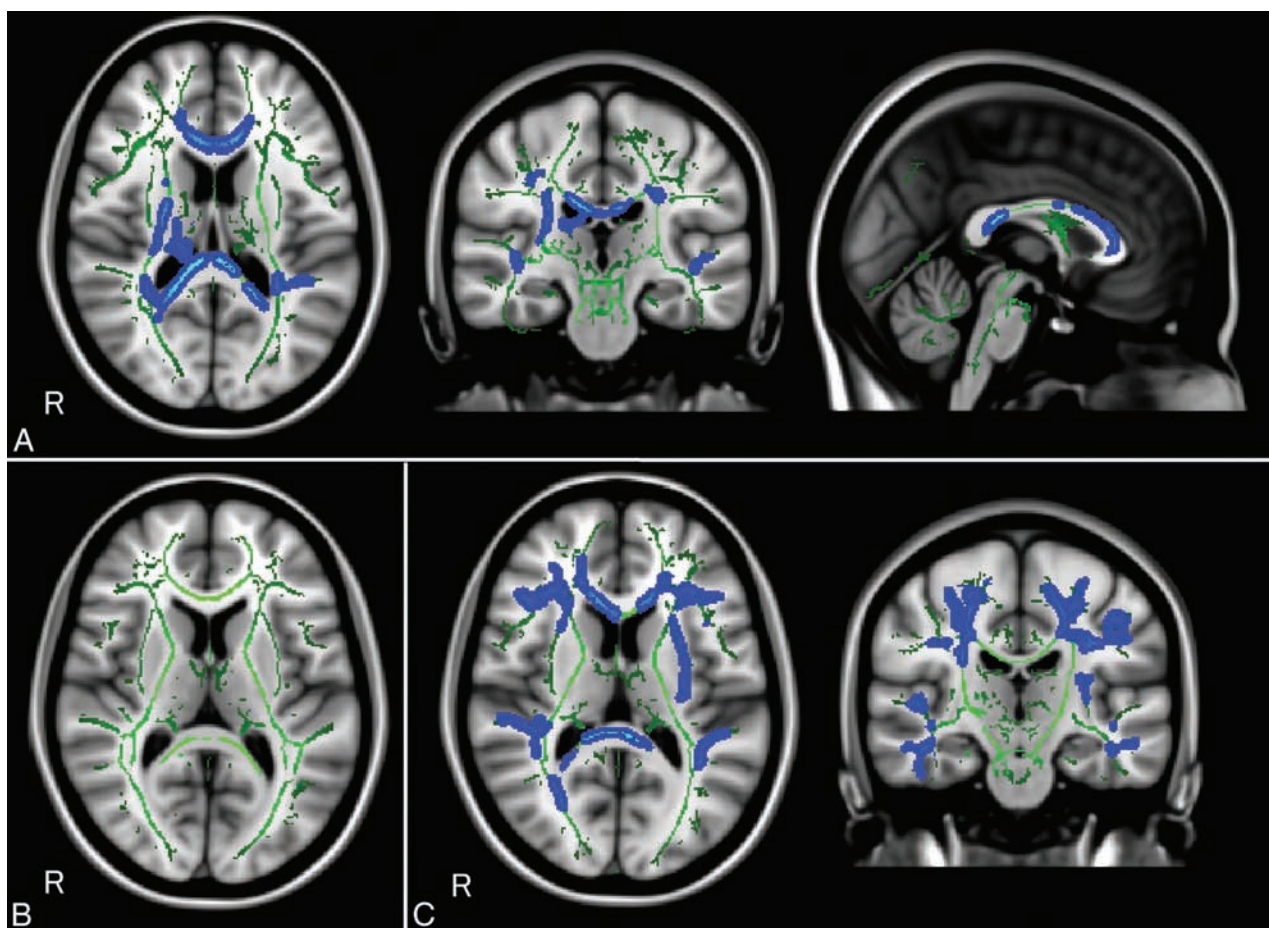


FIG 1. Tract-based spatial statistics analysis between patients and controls at 12 and 24 months of age. **A**, Tract-based spatial statistics at 12 months of age reveals reduced fractional anisotropy values (blue areas) in the corpus callosum, deep white matter, and subcortical white matter in the temporal lobes of patients. The green areas represent white matter skeletons with a threshold FA of ≥ 0.2 . **B**, Tract-based spatial statistics at 24 months of age shows no significant difference between all patients and controls. **C**, Tract-based spatial statistics reveals reduced fractional anisotropy values (blue areas) in widespread white matter areas of patients with a developmental quotient of <70 at 24 months of age.

Mean values of diffusion tensor imaging parameters in FA skeletons with a significant difference on tract-based spatial statistics at 12 months of age^a

	Patients ($n = 20$)	Controls ($n = 13$)	<i>P</i>
FA	0.46 ± 0.04	0.51 ± 0.02	$<.001$
AD, λ_1 (mm^2/s)	0.0016 ± 0.0001	0.0016 ± 0.0001	NS
RD, $(\lambda_2 + \lambda_3) / 2$ (mm^2/s)	0.00074 ± 0.00007	0.00066 ± 0.00006	.007
MD (mm^2/s)	0.0010 ± 0.0001	0.0010 ± 0.0007	NS

Note:—AD indicates axial diffusivity; MD, mean diffusivity; NS, not significant; RD, radial diffusivity.

^a Statistical analysis was performed with a nonparametric Mann-Whitney *U* test.

deep white matter, and subcortical white matter in the temporal lobes of patients (Fig 1A). No areas of increased FA were identified.

DTI of 3 patients at 24 months of age showed motion artifacts, so DTI of the remaining 20 patients was used for analysis. TBSS at 24 months of age did not show any significant difference between all patients and controls (Fig 1B). Comparisons between the 10 patients with a DQ of <70 at 24 months of age and controls revealed reduced FA values in widespread white matter in patients (Fig 1C). No areas showed significantly different FA between patients with a DQ of ≥ 70 and controls.

Parameters in the FA Skeleton with Significant Differences on TBSS and Developmental or Seizure Outcomes

Mean values of FA, mean diffusivity, and eigenvalues in the FA skeleton showing significant FA reduction in patients on TBSS at 12 months of age are shown in the Table. Axial diffusivity along the axonal direction λ_1 and mean diffusivity showed no significant difference between patients and controls. Radial diffusivity perpendicular to the axonal direction $([\lambda_2 + \lambda_3] / 2)$ was significantly higher in patients ($P = .007$).

The DQ at 12 months of age showed a significant positive correlation with FA ($r = 0.64$, $P = .003$) and negative correlations with radial and mean diffusivity ($r = -0.60$, $P = .005$ and $r = -0.53$, $P = .017$, respectively) (Fig 2). No correlation was identified between axonal diffusivity λ_1 and DQ at 12 months of age.

Patients with seizures after initial treatment showed significant decreases in FA compared with patients without seizures and with controls (mean FA: 0.42 ± 0.03 versus 0.47 ± 0.03 , $P = .019$, versus 0.51 ± 0.02 , $P < .001$, by post hoc analysis with Bonferroni correction, respectively) and increased radial diffusivity compared with patients without seizures and with controls (mean $[\lambda_2 + \lambda_3] / 2$: $0.00081 \pm 0.00005 \text{ mm}^2/\text{s}$ versus 0.00071 ± 0.00006

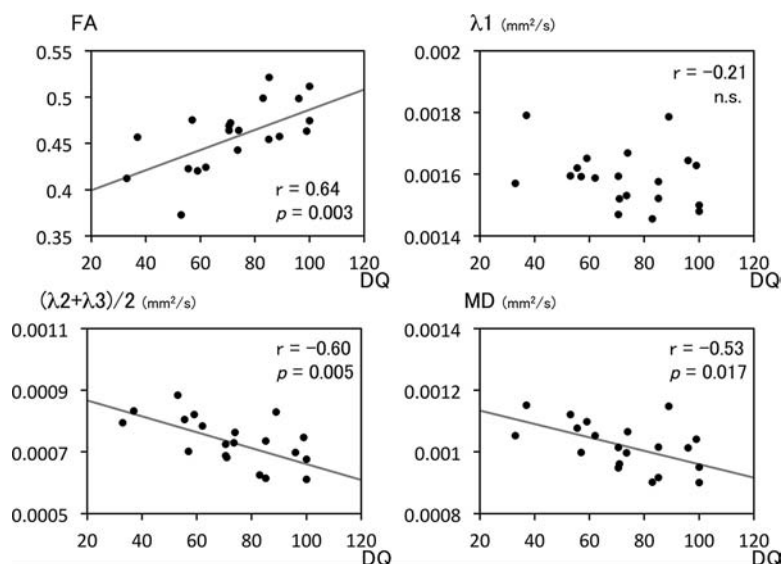


FIG 2. Correlation of the developmental quotient and diffusion tensor imaging parameters at 12 months of age. The developmental quotient at 12 months of age shows a significant positive correlation with fractional anisotropy and negative correlations with radial $[(\lambda_2 + \lambda_3)/2]$ and mean diffusivity. No correlation is evident between axonal diffusivity (λ_1) and the developmental quotient at 12 months of age.

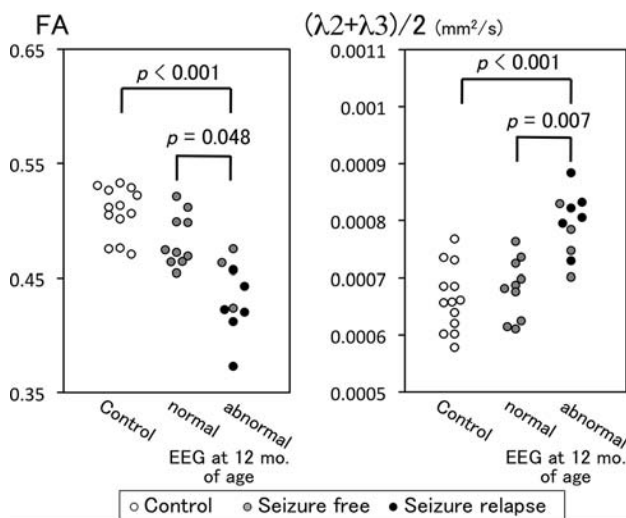


FIG 3. Abnormal findings on EEG at 12 months of age and diffusion tensor imaging parameters. Decreases in fractional anisotropy and increases in radial diffusivity are observed in patients with abnormalities findings on EEG compared with patients with normal electroencephalography findings at 12 months of age. White dots represent controls, gray dots are patients without seizures after initial treatments, and black dots are patients with relapsing or persistent seizures. Patients with relapsing or persistent seizures have low FA and high radial diffusivity.

mm^2/s , $P = .046$, versus $0.00066 \pm 0.00006 \text{ mm}^2/\text{s}$, $P = .001$, by post hoc analysis with Bonferroni correction, respectively). Decreased FA and increased radial diffusivity were observed in patients with abnormal findings on EEG at 12 months of age compared with patients with normal findings on EEG at 12 months of age and with controls (mean FA: 0.43 ± 0.03 versus 0.48 ± 0.02 , $P = .048$, versus 0.51 ± 0.02 , $P < .001$; mean $[(\lambda_2 + \lambda_3)/2]$: $0.00079 \pm 0.00005 \text{ mm}^2/\text{s}$ versus $0.00068 \pm 0.00005 \text{ mm}^2/\text{s}$, $P = .007$, versus $0.00066 \pm 0.00006 \text{ mm}^2/\text{s}$, $P < .001$, by post hoc analysis with Bonferroni correction, respectively) (Fig 3). No sig-

nificant differences in λ_1 were seen between patients with and without seizures or with and without EEG abnormality at 12 months of age.

Correlation of DTI and FDG-PET

FDG-PET at 12 months of age showed regional cortical hypometabolism in 16 patients. The regions of hypometabolism at 12 months were unilateral temporal in 3 patients, unilateral frontal in 2, unilateral parietal in 1, unilateral frontotemporal in 6, unilateral parieto-temporal in 2, unilateral temporo-occipital in 1, and unilateral fronto-parieto-temporal in 1. FDG-PET at 24 months of age revealed regional cortical hypometabolism in 8 patients and normal findings in the other 12 patients on visual inspection. Of 16 patients with PET hypometabolism at 12 months, 6 had relapse or persistent seizures and 10 had abnormal findings on EEG at 12

months. Of 8 patients with PET hypometabolism at 24 months, 5 had seizure relapse or persistent seizures and 5 had abnormal findings on EEG at 24 months. At 12 months of age, hypometabolism was on the left side in 10 patients, the right side in 5, and in the bilateral temporal lobes in 1. At 24 months of age, hypometabolism was present in the left temporo-frontal lobe in 3 patients, left temporal lobe in 1, right temporo-frontal lobe in 2, right frontal lobe in 1, and right temporal lobe and right frontal lobe in 1. FA images of patients with right-sided hypometabolism were flipped, so that all regional hypometabolism would appear on the left side. We excluded 1 patient with hypometabolism in the bilateral temporal lobes to compare the laterality of the abnormality on PET and DTI and 2 patients with right or left frontal hypometabolism on TBSS analysis to focus on temporal lobe hypometabolism. At 12 months of age, TBSS between the 15 patients with left temporal hypometabolism and controls showed reduced FA in widespread white matter symmetrically. At 24 months of age, TBSS between the 7 patients with left temporal hypometabolism and controls showed reduced FA in widespread white matter and more prominent hypometabolism in the left temporal lobe compared with the right temporal lobe (Fig 4). TBSS did not show FA reduction in 12 patients without PET hypometabolism at 24 months of age compared with controls.

DISCUSSION

DTI in patients with WS of unknown etiology showed widespread white matter abnormalities at 12 months of age. While axial diffusivity showed no significant differences compared with controls, radial diffusivity was significantly increased. The DQ correlated positively with FA and negatively with radial or mean diffusivity. Patients with persistent EEG abnormality and seizures had more prominent DTI abnormalities than patients with normal EEG and no seizures after initial treatment. Although DTI at 24 months of age did not show significant differences in the com-

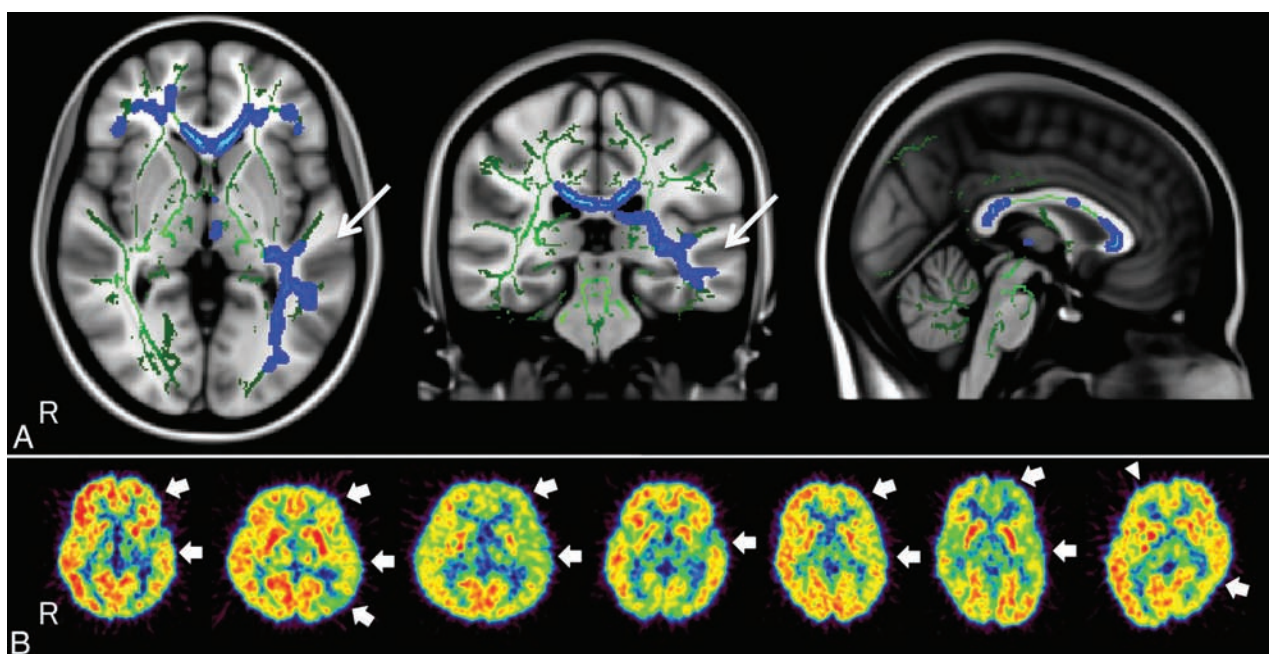


FIG 4. Comparison of tract-based spatial statistics among patients with left temporal hypometabolism on positron-emission tomography at 24 months of age. **A**, Comparison of tract-based spatial statistics among 7 patients with left temporal hypometabolism and controls shows reduced fractional anisotropy in widespread white matter (blue areas) and more prominent DTI abnormalities in the left temporal lobe (arrows) compared with the right one. The green areas represent white matter skeletons with a threshold FA of ≥ 0.2 . **B**, Fluorodeoxyglucose positron-emission tomography of 7 patients. Positron-emission tomography shows left temporal or temporofrontal hypometabolism (arrows). Note that the images from 3 patients with right temporal lobe hypometabolism are flipped, so all areas of hypometabolism are shown on the left side. The last patient shows additional hypometabolism in the contralateral frontal lobe (arrowhead).

parisons of all patients and controls, patients with poor developmental outcomes still showed decreased FA. Patients with lateralized regional hypometabolism on PET showed more prominent DTI abnormalities ipsilateral to the side of hypometabolism. This is the first report revealing abnormal findings on DTI in patients with WS of unknown etiology. A recently published study by Fosi et al¹⁴ did not show a significant difference between patients with WS and controls on TBSS analysis of DTI. The timing of MR imaging scans in their study was not clearly described and seems to be variable. The standardized timing of MR imaging in our study may be one of the reasons that MRI revealed significant abnormality.

Several factors can cause abnormal findings on DTI, such as axonal properties, fiber coherence, demyelination, and white matter maturation, especially in infants.¹⁵⁻¹⁷ Cortical malformation often affects the underlying white matter and the cortex¹⁸ and could disrupt white matter tracts and cause reductions in anisotropy.^{19,20} White matter abnormality could also be attributed to propagation of epileptic activities along white matter tracts.²¹ ACTH therapy also possibly affects white matter properties, though we performed DTI > 1 month after the end of ACTH therapy to avoid the effects of ACTH. Another major factor contributing to DTI changes in infancy is white matter maturation. In this period, age-related changes in water diffusion-based properties are observed in white matter tracts.^{17,22-26} We have reported delayed myelination on T2-weighted imaging at approximately 10 months of age in patients with cryptogenic WS.⁵

In an unpublished study of ours, a significant decrease of FA was revealed in patients with delayed myelination on T2WI at 12 months of age. The diffuse abnormal findings on DTI in the pres-

ent study were prominent at 12 months of age and had resolved by 24 months of age in patients with good developmental outcomes. Dynamic changes in abnormal findings on DTI resemble the pattern of delayed myelination in our previous study of WS, suggesting that delayed white matter maturation may contribute to the abnormal findings on DTI. Furthermore, FA reduction in our study was attributed to increased radial diffusion perpendicular to the axonal direction. Increased radial diffusion suggests abnormal myelination in experimental models, though pathologic correlates of abnormal findings on DTI in humans are still unclear.^{15,16} Given the dynamic changes in abnormal findings on DTI and the increased radial direction, delayed myelination may be the most likely pathology underlying widespread symmetric abnormal findings on DTI at 12 months of age.

A strong correlation was observed between DTI parameters and cognitive and motor development in our study. Correlations between DTI and cognitive function have been reported in healthy children and those with various pediatric disorders. Widjaja et al²⁷ studied correlations between abnormal findings on DTI and neuropsychological function in children with nonlesional focal epilepsy, revealing that widespread white matter abnormalities were associated with impaired neuropsychological function. The impairment in white matter may reflect disruption in the connectivity of cortical processing networks, which is necessary for the development of cognition.²⁷ In our study, delayed maturation of widespread white matter areas contributed to delayed cognitive and motor development. This abnormal white matter included many fiber tracts that are important for language and cognitive function, such as the uncinate fasciculus and inferior

longitudinal fasciculus. Evaluation of DTI can thus facilitate objective assessment of the developmental status in a patient with WS.

We revealed a difference in DTI parameters between patients with and without abnormal findings on EEG and those with and without seizures after treatment. Juhász et al¹⁰ hypothesized that widespread corticosubcortical circuits are involved in epileptogenic activity of patients with WS. Epileptiform activity from the primary cortical abnormality stimulates brain stem structures, and interactions of the brain stem with the striatum and cortices induce hypersarrhythmia on EEG.¹⁰ Persistent or recurrent epileptic activity may have disturbed white matter maturation and led to abnormal findings on DTI in our study. EEG findings during the follow-up period reportedly showed strong correlations with cognitive and motor development.²⁸ Our findings suggest that chronic epileptic activity may cause developmental regression by disturbing white matter maturation, though there is the other possibility that preexisting white matter abnormalities might lead to the poor outcome of seizures and EEG findings.

The persistent abnormal findings on DTI at 24 months in children with poor developmental outcome may be multifactorial. Delayed maturation of white matter, microstructural damage by epileptic activities, or the underlying cause of epilepsy may contribute to the reduction in FA values. At 24 months of age, distributions of abnormal findings on DTI corresponded to those of PET hypometabolism, though the abnormal findings on DTI were still widespread and bilateral. Regional PET hypometabolism in patients with WS reportedly suggests focal cortical dysplasia.² Focal cortical dysplasia often involves white matter changes, and a pathologic study has revealed a reduced number of myelinated axons in the white matter.¹⁸ DTI is reported to show abnormality in the subcortical and deep white matter subjacent to areas of focal cortical dysplasia.²⁰ From these observations, the asymmetric abnormal findings on DTI corresponding to areas of PET hypometabolism may represent white matter changes related to the underlying pathology, such as focal cortical dysplasia. In contrast to the reversible FA reduction due to delayed myelination at 12 months of age, abnormal findings on DTI at 24 months of age in patients with poor seizure and developmental outcomes appear to represent persistent microstructural abnormalities. This hypothesis should be proved pathologically or by other imaging techniques such as 7T MR imaging.

Our study has some limitations. First, control subjects were recruited from among patients who had undergone screening scans for CNS abnormalities. Although CNS abnormalities were ruled out clinically, the possibility of underlying CNS lesions cannot be excluded. Second, the ages of patients and controls were not the same. We recruited control subjects with the same mean age as that of patients and used age as a nuisance covariate of no interest on TBSS analysis to reduce the effects of differences in age. However, the effects of the difference in age may not be eliminated completely. Another methodologic limitation is that DTI was performed with 12 directions that were relatively small in number. DTI with more directions and information from the Human Connectome Project (<http://humanconnectome.org/>) may enable more detailed analysis of white matter fibers. Several clinical factors affect developmental outcome, such as the adverse effects of antiepileptic drugs and the delay of initial treatment. Although

we did not use phenobarbital, phenytoin, or topiramate, which were reported to have possible adverse effects on cognitive function, there was the possibility that antiepileptic drugs affect the cognitive function. It has been reported that a delay of initial treatment was a risk factor for poor developmental outcome.²⁹ In our study, only 4 patients had an interval of 2 months or longer from the onset of spasms to initial treatment, and most of the patients had a short treatment lag. Therefore, it is not likely that the delay of treatment caused the abnormal findings on DTI and poor developmental outcome.

CONCLUSIONS

DTI revealed white matter abnormalities in patients with WS of unknown etiology. These DTI abnormalities correlated with cognitive and motor development, seizure outcome, EEG abnormality, and PET hypometabolism. Serial DTI appears useful for assessing maturational status and detecting underlying pathology. The hypothesis of delayed myelination and microstructural abnormality causing the abnormal findings on DTI needs to be assessed by pathologic correlation, higher resolution neuroimaging, and correlation with therapeutic interventions.

ACKNOWLEDGMENTS

We thank Drs Shigeki Aoki and Keigo Shimoji from the Department of Radiology at Juntendo University for technical support with image analysis.

REFERENCES

1. Riikonen R. **Epidemiological data of West syndrome in Finland.** *Brain Dev* 2001;23:539–41 CrossRef Medline
2. Chugani HT, Shields WD, Shewmon DA, et al. **Infantile spasms, I: PET identifies focal cortical dysgenesis in cryptogenic cases for surgical treatment.** *Ann Neurol* 1990;27:406–13 CrossRef Medline
3. Maeda N, Watanabe K, Negoro T, et al. **Transient focal cortical hypometabolism in idiopathic West syndrome.** *Pediatr Neurol* 1993;9:430–34 CrossRef Medline
4. Maeda N, Watanabe K, Negoro T, et al. **Evolutional changes of cortical hypometabolism in West's syndrome.** *Lancet* 1994;343:1620–23 CrossRef Medline
5. Natsume J, Watanabe K, Maeda N, et al. **Cortical hypometabolism and delayed myelination in West syndrome.** *Epilepsia* 1996;37:1180–84 CrossRef Medline
6. Itomi K, Okumura A, Negoro T, et al. **Prognostic value of positron emission tomography in cryptogenic West syndrome.** *Dev Med Child Neurol* 2002;44:107–11 CrossRef Medline
7. Metsähonkala L, Gaily E, Rantala H, et al. **Focal and global cortical hypometabolism in patients with newly diagnosed infantile spasms.** *Neurology* 2002;58:1646–51 CrossRef Medline
8. Hamano S, Yoshinari S, Higurashi N, et al. **Regional cerebral blood flow and developmental outcome in cryptogenic West syndrome.** *Epilepsia* 2007;48:114–19 CrossRef
9. Natsume J, Maeda N, Itomi K, et al. **PET in infancy predicts long-term outcome during adolescence in cryptogenic West syndrome.** *AJNR Am J Neuroradiol* 2014;35:1580–85 CrossRef Medline
10. Juhász C, Chugani HT, Muzik O, et al. **Neuroradiological assessment of brain structure and function and its implication in the pathogenesis of West syndrome.** *Brain Dev* 2001;23:488–95 CrossRef Medline
11. Tsumori M, Inage K. *Determination of Psychological Growth for Infants 0–3 Years Old.* Tokyo: Dainippon Toshio; 1961
12. Hamano S, Tanaka M, Mochizuki M, et al. **Long-term follow-up study of West syndrome: differences of outcome among symptomatic etiologies.** *J Pediatr* 2003;143:231–35 CrossRef Medline

13. Smith SM, Jenkinson M, Johansen-Berg H, et al. **Tract-based spatial statistics: voxelwise analysis of multi-subject diffusion data.** *Neuroimage* 2006;31:1487–505 CrossRef Medline
14. Fosi T, Chu C, Chong WK, et al. **Quantitative magnetic resonance imaging evidence for altered structural remodeling of the temporal lobe in West syndrome.** *Epilepsia* 2015;56:608–16 CrossRef Medline
15. Budde MD, Kim JH, Liang HF, et al. **Toward accurate diagnosis of white matter pathology using diffusion tensor imaging.** *Magn Reson Med* 2007;57:688–95 CrossRef Medline
16. Song SK, Yoshino J, Le TQ, et al. **Demyelination increases radial diffusivity in corpus callosum of mouse brain.** *Neuroimage* 2005;26:132–40 CrossRef Medline
17. Mukherjee P, Miller JH, Shimony JS, et al. **Normal brain maturation during childhood: developmental trends characterized with diffusion-tensor MR imaging.** *Radiology* 2001;221:349–58 CrossRef Medline
18. Shepherd C, Liu J, Goc J, et al. **A quantitative study of white matter hypomyelination and oligodendroglial maturation in focal cortical dysplasia type II.** *Epilepsia* 2013;54:898–908 CrossRef Medline
19. Eriksson SH, Rugg-Gunn FJ, Symms MR, et al. **Diffusion tensor imaging in patients with epilepsy and malformations of cortical development.** *Brain* 2001;124:617–26 CrossRef Medline
20. Widjaja E, Zarei Mahmoodabadi S, Otsubo H, et al. **Subcortical alterations in tissue microstructure adjacent to focal cortical dysplasia: detection at diffusion-tensor MR imaging by using magnetoencephalographic dipole cluster localization.** *Radiology* 2009;251:206–15 CrossRef Medline
21. Gross DW, Concha L, Beaulieu C. **Extratemporal white matter abnormalities in mesial temporal lobe epilepsy demonstrated with diffusion tensor imaging.** *Epilepsia* 2006;47:1360–63 CrossRef Medline
22. Hüppi PS, Maier SE, Peled S, et al. **Microstructural development of human newborn cerebral white matter assessed in vivo by diffusion tensor magnetic resonance imaging.** *Pediatr Res* 1998;44:584–90 CrossRef Medline
23. Neil JJ, Shiran SI, McKinstry RC, et al. **Normal brain in human newborns: apparent diffusion coefficient and diffusion anisotropy measured by using diffusion tensor MR imaging.** *Radiology* 1998;209:57–66 CrossRef Medline
24. Hermoye L, Saint-Martin C, Cosnard G, et al. **Pediatric diffusion tensor imaging: normal database and observation of the white matter maturation in early childhood.** *Neuroimage* 2006;29:493–504 CrossRef Medline
25. Dubois J, Dehaene-Lambertz G, Perrin M, et al. **Asynchrony of the early maturation of white matter bundles in healthy infants: quantitative landmarks revealed noninvasively by diffusion tensor imaging.** *Hum Brain Mapp* 2008;29:14–27 CrossRef Medline
26. Cancelliere A, Mangano FT, Air EL, et al. **DTI values in key white matter tracts from infancy through adolescence.** *AJNR Am J Neuroradiol* 2013;34:1443–49 CrossRef Medline
27. Widjaja E, Skocic J, Go C, et al. **Abnormal white matter correlates with neuropsychological impairment in children with localization-related epilepsy.** *Epilepsia* 2013;54:1065–73 CrossRef Medline
28. Saltik S, Kocer N, Dervent A. **Informative value of magnetic resonance imaging and EEG in the prognosis of infantile spasms.** *Epilepsia* 2002;43:246–52 CrossRef Medline
29. Hamano S, Yoshinari S, Higurashi N, et al. **Developmental outcomes of cryptogenic West syndrome.** *J Pediatr* 2007;150:295–99 CrossRef Medline

Cerebral Blood Flow Improvement after Indirect Revascularization for Pediatric Moyamoya Disease: A Statistical Analysis of Arterial Spin-Labeling MRI

T. Blauwblomme, H. Lemaitre, O. Naggara, R. Calmon, M. Kossorotoff, M. Bourgeois, B. Mathon, S. Puget, M. Zerah, F. Brunelle, C. Sainte-Rose, and N. Boddaert



ABSTRACT

BACKGROUND AND PURPOSE: The severity of Moyamoya disease is generally scaled with conventional angiography and nuclear medicine. Arterial spin-labeling MR imaging is now acknowledged for the noninvasive quantification of cerebral blood flow. This study aimed to analyze CBF modifications with statistical parametric mapping of arterial spin-labeling MR imaging in children undergoing an operation for Moyamoya disease.

MATERIALS AND METHODS: We included 15 children treated by indirect cerebral revascularization with multiple burr-holes between 2011 and 2013. Arterial spin-labeling MR imaging and T1 sequences were then analyzed under SPM8, according to the general linear model, before and after the operation (3 and 12 months). Voxel-based analysis was performed at the group level, comparing all diseased hemispheres with all normal hemispheres and, at the individual level, comparing each patient with a control group.

RESULTS: Group analysis showed statistically significant preoperative hypoperfusion in the MCA territory in the Moyamoya hemispheres and a significant increase of cerebral perfusion in the same territory after revascularization ($P < .05$ family-wise error-corrected). Before the operation, individual analysis showed significant hypoperfusion for each patient co-localized with the angiographic defect on DSA. All except 1 patient had improvement of CBF after revascularization, correlated with their clinical status.

CONCLUSIONS: SPM analysis of arterial spin-labeling MR imaging offers a noninvasive evaluation of preoperative cerebral hemodynamic impairment and an objective assessment of postoperative improvement in children with Moyamoya disease.

ABBREVIATIONS: ASL = arterial spin-labeling; MM = pediatric Moyamoya disease; SPM = statistical parametric mapping

Moyamoya disease (MM) is a vascular disease defined by a progressive occlusion of the supraclinoid internal carotid arteries along with the development of leptomeningeal collaterals.¹ Its natural history includes occurrence of transient ischemic attacks, ischemic strokes, or intracerebral hemorrhage. Because there is currently no efficient medical treatment, cerebral revas-

cularization is the sole option when cerebral hemodynamics are compromised. Currently, morphologic MR imaging is sufficient for the diagnosis of MM because it shows arterial stenosis and its consequences on the brain (ischemic strokes, ivy sign).^{2,3} However, selection of surgical candidates requires a grading of MM severity with a measure of the cerebral blood flow. Several imaging techniques are available, such as xenon-enhanced CT or DSC-weighted MR imaging; however, nuclear medicine with $H_2[^{15}O]$ -PET and ^{123}I -iodoamphetamine SPECT studies is still the criterion standard to quantify alteration of CBF and cerebrovascular reserve.⁴

Recently, to avoid radiation exposure, arterial spin-labeling (ASL) MR imaging has been successfully developed to quantify CBF alterations in different stroke conditions, including MM.^{5,6} This MR imaging has the advantage of being noninvasive because it uses water protons as an endogenous tracer to measure CBF, rather than intravenous injection of a contrast agent, which may be a concern in the pediatric population. Because children under-

Received June 27, 2015; accepted after revision August 20.

From the Université René Descartes (T.B., O.N., R.C., B.M., S.P., M.Z., F.B., C.S.-R., N.B.), PRES Sorbonne Paris Cité, Paris, France; APHP, Departments of Pediatric Neurosurgery (T.B., M.B., S.P., M.Z., C.S.-R.) and Neuroradiology (O.N., R.C., F.B., N.B.), Hospital Necker, Paris, France; French Institute of Health and Medical Research U1000 (T.B., H.L., R.C., N.B.), Institut Imagine, University Paris-Sud II and University Paris Descartes, Paris, France; Department of Neuroradiology (O.N.), French Institute of Health and Medical Research U894, Hospital Sainte-Anne, Paris, France; APHP, Department of Pediatric Neurology (M.K.), French Center for Pediatric Stroke, Hospital Necker, Paris, France; and UMR 1163 (N.B.), Institut Imagine, Paris, France.

Please address correspondence to Thomas Blauwblomme, MD, Service de Neurochirurgie Pédiatrique, Hôpital Necker, 149 rue de Sèvres, 75743 Paris Cedex 15, France; e-mail: thomas.blauwblomme@nck.aphp.fr

<http://dx.doi.org/10.3174/ajnr.A4592>

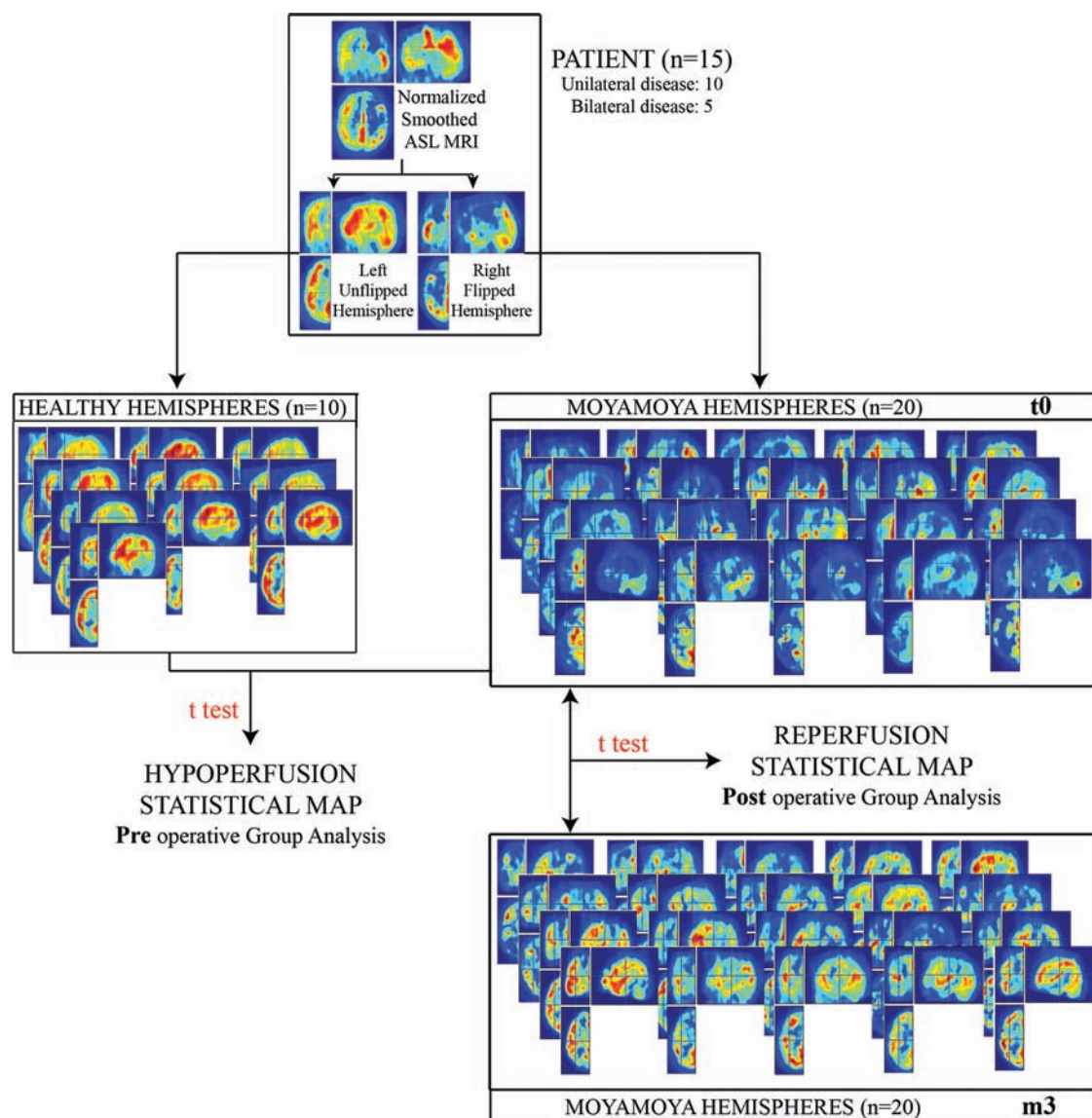


FIG 1. Methodology of the voxel-based ASL MR imaging analysis at the group level. For each of the 15 patients, smoothed normalized MRIs were split into 2 distinct hemispheres. The right hemispheres are flipped along the midsagittal plane. Five patients had bilateral Moyamoya disease, whereas 10 patients had unilateral disease; therefore there are 20 hemispheres in the Moyamoya hemisphere group and 10 hemispheres in the healthy group. Preoperative hypoperfusion maps were generated while comparing non-Moyamoya with Moyamoya hemispheres with a voxel-based analysis according to the general linear model. Postoperative reperfusion maps were obtained with intrinsic comparison of the Moyamoya hemisphere group 3 months after the operation with the preoperative ASL MR imaging, according to the general linear model.

going an operation for MM need repeated quantification of their CBF before and after surgery, ASL MR imaging may be of particular interest, and statistical approaches, as described with statistical parametric analysis (SPM) of ASL MR imaging in cognitive series, may allow intraindividual and group analysis of CBF comparisons before and after the operation.⁷ This could allow a non-invasive follow-up of patients having undergone an operation and help to prevent recurrent stroke in patients with persistent hypoperfusion.

The aim of the present study was to analyze the modifications of cerebral blood flow in a European cohort of 15 children with Moyamoya disease consecutively treated with indirect cerebral revascularization, by using SPM analysis at the individual and group levels, with pseudocontinuous ASL MR imaging.

MATERIALS AND METHODS

Study Design

We performed a monocentric retrospective analysis of all patients having undergone an operation for a MM between 2011 and 2013. A preoperative MR imaging was performed the week before the operation, and 2 MR imaging examinations were performed according to the same protocol 3 months and 1 year after the operation, respectively.

Patients

Indications for cerebral revascularization were decided in a multidisciplinary meeting according to clinical, angiographic, and MR imaging data. PET and SPECT studies were not performed because they were not available in our hospital.

All patients having undergone an operation between 2011 and

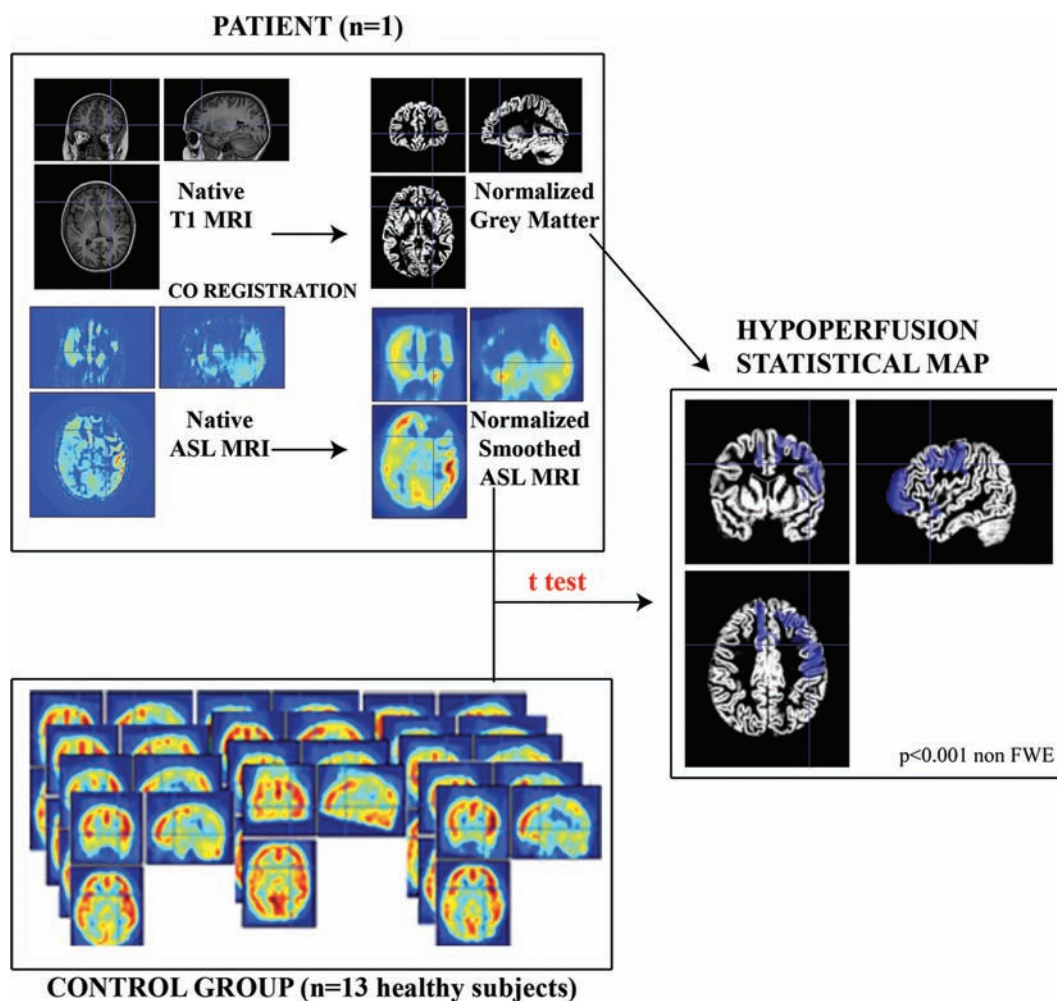


FIG 2. Methodology of the voxel-based ASL MR imaging analysis at the individual level. For each patient, ASL MR imaging was coregistered with the T1 MR imaging and then smoothed and normalized under SPM8. A voxel-based analysis was then performed between the patients with ASL MR imaging and the group of 13 healthy children, with the general linear model under SPM8. Areas with significant hypoperfusion were then displayed on the normalized gray matter (blue areas).

2013 were included in the study. Postoperative outcome was assessed by a pediatric neurologist in regard to postoperative ischemic events (TIA and strokes).

We used a control group with 13 subjects comparable for age (mean age, 6.8 ± 2.8 years; range, 3–11 years) and sex (male/female ratio = 0.75). Their anatomic brain MR imaging findings were normal, and indications for imaging were the following: systemic disease ($n = 5$), mild psychiatric disorder ($n = 3$), ophthalmologic disorder ($n = 3$), and headaches ($n = 2$). None had neurologic or neurosurgical disorders.

Surgical Technique

All patients underwent the operation with the same indirect cerebral revascularization technique: multiple burr-hole surgery.⁸ Briefly, a uni- or bilateral coronal incision with subgaleal dissection exposes the skull vault. Between 15 and 20 burr-holes are drilled according to the following technique: A triangular periosteal flap is elevated, a <1 cm burr-hole is drilled, and the dura and arachnoid layers are opened. The flap is then inserted in the subdural space; and 2 layers of watertight closure of the skin are made, with or without drainage. Progressive spontaneous anastomoses

then occur between pial vessels and external carotid branches during the weeks following the operation.

MR Imaging Sequences

MR images were obtained on a 1.5T Signa HDxt system (GE Healthcare, Milwaukee, Wisconsin) by using a 12-channel head-neck-spine coil. Brain MR imaging protocol included at least a 3D T1-weighted fast-spoiled gradient-recalled sequence (TR/TE, 16.4/7.2 ms; flip angle, 13° ; matrix size, 512×512 ; FOV, 22×22 cm, with 228 axial sections at a thickness of 0.6 mm) and 3D time-of-flight, axial FLAIR, axial T2-weighted, and diffusion and noncontrast perfusion imaging with 3D pseudocontinuous ASL MR imaging (40 axial partitions of 4 mm thickness; FOV, 240×240 mm; acquisition matrix, 8 spiral arms in each 3D partition; TE, 10.5 ms; TR, 4428 ms; postlabeling delay, 1025 ms; flip angle, 155° ; acquisition time, 4 minutes 17 seconds). No injection was required.

MR images were acquired before the operation (t0) and 3 (m3) and 12 months (m12) after the operation without general anesthesia. Sleep could be induced by premedication when needed (0.2 mg/kg of sodium pentobarbital) before 6 years of age.

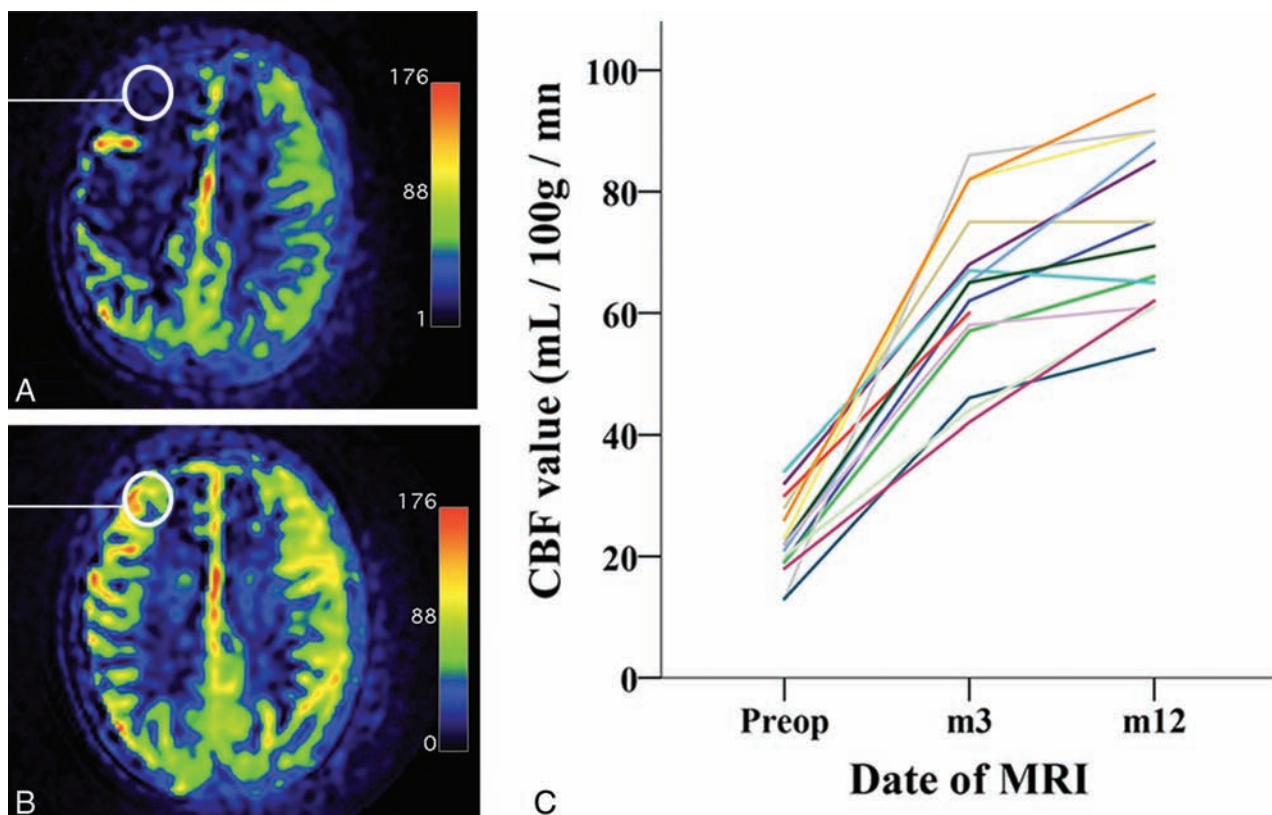


FIG 3. Quantitative analysis of ASL MR imaging. *A*, Preoperative ASL MR imaging. Note hypoperfusion on the right frontal lobe and central region. The color scale unit of the CBF map is mL/100 mg/min. *B*, Postoperative ASL MR imaging (12 months after the operation) of the same patient. Note increased CBF, with normal values of CBF in the frontal lobe and central area. *C*, Diagram shows the evolution of CBF values in an ROI in the frontal lobe (white circle on *A* and *B*) for each patient before the operation and 3 and 12 months after the operation. Preop indicates preoperative.

Statistical Methods: Voxel-Based Analysis of ASL MR Imaging

MR images were preprocessed by using statistical parametric mapping (SPM8 software; www.fil.ion.ucl.ac.uk/spm/software/spm8), implemented in Matlab (MathWorks, Natick, Massachusetts) and analyzed by using a voxel-based approach. Native T1-weighted images were segmented into gray matter, white matter, and CSF by using the VBM8 segmentation toolbox (<http://www.neuro.uni-jena.de/vbm/>).⁹ The ASL images were coregistered to the corresponding native gray images and spatially normalized to the Montreal Neurological Institute space by using the deformation matrices from the segmentation process. The resulting ASL images were smoothed by using an isotropic Gaussian filter of 10 mm. To compare Moyamoya and non-Moyamoya hemispheres, we generated mirror images by flipping each smoothed ASL image about the sagittal plane through the midline. Only the left unflipped hemisphere and the right flipped hemisphere were considered within the statistical analyses. Voxel-based group analyses (Fig 1) were performed within the framework of the general linear model by using a flexible factorial design considering 3 factors: subject, time (t0, m3, m12), and hemisphere status (healthy versus Moyamoya disease). Sex, etiology, relapse, and types of symptoms were included as confounding covariates. A proportional scaling of the ASL data was applied and set to a grand mean scaled value of 50 mL/dL/min to minimize intersubject variability.

Eventually, we performed individual analyses. We used a con-

trol group of 13 subjects matched with our patient group for sex and age. For each patient, we performed a voxel-based comparison between the control group and the patient ASL images preoperatively and at last follow-up (Fig 2).

The significance level was set to $P = .05$ corrected, family-wise error—corrected for multiple comparisons at the voxel level with a masking threshold set to 70 mL/dL/min.

Statistical Methods: Quantitative Analysis of ASL MR Imaging

A 1-cm ROI was also chosen in the frontal lobe (Fig 3), where GE software quantified CBF, before and after the operation. The ROI was chosen at the level of the corpus callosum, in the anterior third of the dorsolateral frontal lobe cortex because this region displayed important variations of CBF on the SPM analysis at the group and the individual levels. Moreover, this area in the MCA territory is particularly affected in Moyamoya vasculopathy.

Statistical analysis then compared preoperative and postoperative values, in the Moyamoya hemispheres and in the healthy hemispheres, with the Friedman nonparametric test.

RESULTS

Patients

Fifteen children were included in the study. A summary of the patient characteristics is shown in Table 1. Bilateral revascularization was performed in 5 patients, and unilateral revascularization,

Table 1: Summary of patient characteristics

Characteristic	
Median age at operation	6.8 ± 3.4 y
Range	2.7–14 y
Sex	
10 Males/5 females	M/F ratio = 2
Ethnic origin	
Caucasian	11
North African	2
Sub-Saharan African	1
Asian	1
Etiology	
Disease	8
NF-1	5
Down syndrome	1
CBL gene mutation	1
Modality of revelation	
Ischemic stroke	5
TIA	3
MRI follow-up NF-1	3
ICH	3
Headaches	1
Clinical symptoms	
Neurologic deficits	6
Partial	4
Severe	2
Headaches	6
Epilepsy	3
No symptoms	3
Preoperative stroke on MRI	
No stroke	6
Single territory	5
Multiple territory	1
ICH/IVH	3
Surgery (multiple burr-holes)	
Bilateral	5
Unilateral right	6
Unilateral left	4
Postoperative outcome	
Follow-up	28 ± 7 mo
Recurrent TIAs	1
Second surgery needed	1

Note:—NF-1 indicates neurofibromatosis type 1; ICH, intracerebral hematoma; CBL, casitas B lineage lymphomas; IVH, intraventricular hemorrhage.

in 10 patients. Recurrence of TIA in 1 patient required a second revascularization procedure.

ASL MR Imaging: Direct Quantitative Analysis

In the hemispheres affected by Moyamoya vasculopathy, the mean preoperative CBF in the frontal lobe was 22 ± 6.3 mL/100 mg/min (range, 13–34 mL/100 mg/min), whereas it was 65 ± 13.6 mL/100 mg/min (range, 42–86 mL/100 mg/min) and 73 ± 13.4 mL/100 mg/min (range, 54–96 mL/100 mg/min) 3 and 12 months after the operation, respectively (Fig 3 and Table 2). This increase was statistically significant (Friedman nonparametric test, $P < .001$).

On the other hand, in the non-Moyamoya hemispheres, mean preoperative CBF in the frontal lobe was 80.8 ± 11.3 mL/100 mg/min (range, 64–93 mL/100 mg/min), and there was no statistically significant change postoperatively (Friedman test, $P = .703$) after 3 months (mean CBF, 83 ± 10.8 mL/100 mg/min; range, 61–94 mL/100 mg/min) and 12 months (mean CBF, 83.2 ± 10.7 mL/100 mg/min; range, 62–93 mL/100 mg/min).

ASL MR Imaging: Group Analysis

Comparison of MM hemispheres ($n = 20$) with non-MM hemispheres ($n = 10$) at t0 showed a preoperative significant decrease of CBF ($P < .05$ family-wise error–corrected) located in the MCA territory (Fig 4).

Intrinsic comparison of the MM hemispheres between t0 and follow-up showed a significant increase of the CBF ($P < .05$ family-wise error–corrected) within the frontal lobe and temporoparietal junction at 3 months (m3) and 12 months (m12) after the operation. Conversely, intrinsic comparisons of the healthy hemisphere at m3 and m12 with the preoperative period did not show any significant modification of the CBF.

ASL MR Imaging: Individual Analysis

Preoperative comparisons of individual patients with MM with the control group showed, in all the cases, hypoperfusion ($P < .05$ family-wise error–corrected) in the MCA territory (Fig 5). Postoperative comparison of individual patients with MM with the control group showed dramatic improvement of cerebral perfusion in the operated territory. This was correlated with a good clinical outcome (no postoperative stroke or TIA) in all except 1 patient.

Most interesting, this latter patient had recurrent TIA, and statistical analysis showed persistent hypoperfusion, co-localized within an area where no burr-holes had been drilled, allowing a further targeted second-stage operation.

In another patient with good clinical results, contralateral asymptomatic hypoperfusion in the anterior cerebral artery territories was detected.

DISCUSSION

We report a prospective series of 15 children undergoing an operation for a Moyamoya disease with indirect cerebral revascularization followed by pre- and postoperative (3 months and 1 year after the operation) ASL MR imaging. Statistical parametric mapping analysis of ASL MR imaging showed, at the group level, preoperative statistical hypoperfusion in the MCA territory and a postoperative increase of CBF in the same territory after the operation. Individual analysis displayed, in all cases, territories of statistically significant hypoperfusion in the MCA territory and a postoperative improvement in all except 1 case.

The present study has some biases. We did not evaluate the cerebrovascular reserve, and ASL MR imaging was not compared with other reference imaging like PET, SPECT, perfusion CT, or DSC MR imaging because these techniques were not performed in our center.

In the present study, we provide more evidence to support pseudocontinuous ASL MR imaging in the initial cerebral perfusion assessment and follow-up of MM. This technique does not require contrast injection and allows quantification of the cerebral blood flow and cerebrovascular reserve (if acetazolamide studies are performed). Its first application in MM was reported in 2011, with the demonstration of good agreement between ASL MR imaging and DSA, in showing spontaneous transosseous collaterality. In this study, ASL sensitivity and specificity were 0.83 and 0.82, respectively.⁵ Further studies, mainly from Ja-

Table 2: Quantitative CBF values from the frontal lobe ROI^a

Patient	Side of the Disease	Healthy Hemisphere CBF Value (mL/100 mg/min)			Diseased Hemisphere CBF Value (mL/100 mg/min)		
		Preop	M3	M12	Preop	M3	M12
1	Bilateral	NA	NA	NA	19	62	75
2	Unilateral right	64	71	62	19	57	66
3	Unilateral left	93	94	91	28	75	75
4	Unilateral left	78	86	88	32	68	85
5	Bilateral	NA	NA	NA	23	82	90
6	Bilateral	NA	NA	NA	30	60	
7	Bilateral	NA	NA	NA	34	67	65
8	Unilateral right	78	81	81	13	86	90
9	Unilateral right	79	90	90	21	65	88
10	Unilateral right	92	90	93	22	65	71
11	Unilateral right	91	82	88	26	82	96
12	Bilateral	NA	NA	NA	22	58	61
13	Bilateral	NA	NA	NA	13	46	54
14	Unilateral left	64	61	69	20	44	61
15	Unilateral right	89	92	87	18	42	62

Note:—NA indicates no available data because there was no healthy hemisphere; Preop, preoperative.

^a In case of bilateral disease, an ROI in the right hemisphere was chosen.

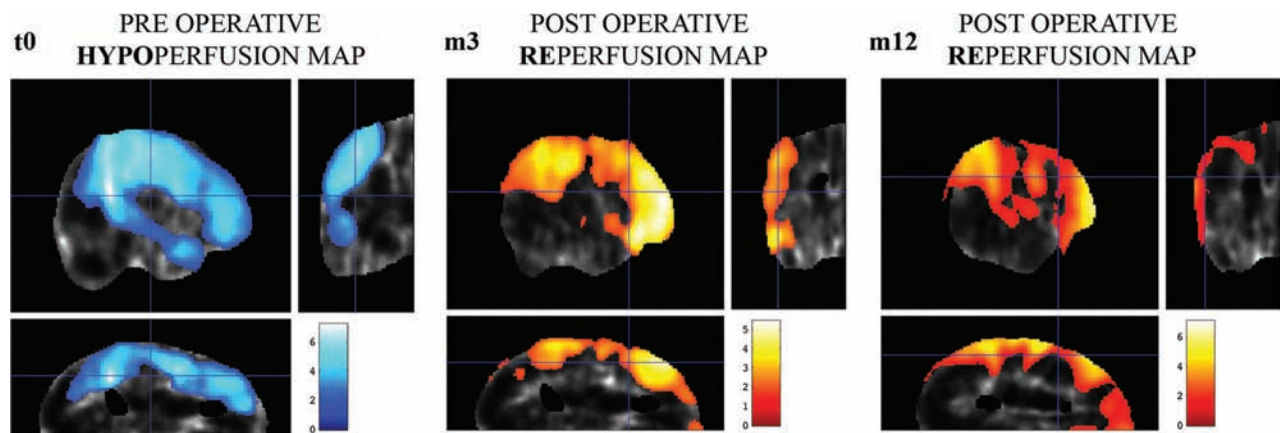


FIG 4. Results of SPM analysis of cerebral perfusion at the group level. The significance level is set at $P < .05$. Color bar displays the z score. T0: Comparison of Moyamoya hemispheres with healthy hemispheres before the operation. The blue areas represent cerebral areas with statistically significant hypoperfusion in the Moyamoya hemisphere group. M3: Comparison of Moyamoya hemispheres 3 months after the operation with Moyamoya hemispheres before the operation. The yellow and red area shows cerebral areas with a significant increase in cerebral blood flow 3 months after revascularization. M12: Comparison of Moyamoya hemispheres 12 months after the operation with Moyamoya hemispheres before the operation. The yellow and red area shows cerebral areas with a significant increase in cerebral blood flow 12 months after multiple burr-hole operations. There is an increase of the z score and the size of the revascularized area.

pan, focused on the ability of ASL-MR imaging to quantify decreased CBF. Quantitative analysis of ASL MR imaging and comparison with the values measured with ¹²³I-iodoamphetamine SPECT in patients with MM showed that ASL MR imaging could identify a decrease of CBF, which was of less amplitude than the decrease measured with SPECT studies.¹⁰ The correlation between CBF values and cerebrovascular reserve measured with SPECT studies in MM was good ($r = 0.80$)^{11,12} and comparable with studies addressing carotid stenosis from other etiologies ($r = 0.92$).¹³

Most interesting, ASL values were adversely affected by the degree of steno-occlusive changes assessed by MRA on the carotid bifurcation.¹⁴ Comparisons of CBF measured with ASL MR imaging in MM were also performed with H₂[¹⁵O]-PET studies and dynamic susceptibility contrast MR imaging, with an excellent correlation ($r = 0.79$ and 0.67 , respectively).^{6,15} Excellent correlations between arterial transit time and cerebral blood flow val-

ues were also found between perfusion CT and pseudocontinuous ASL MR imaging.¹⁶

In the present study, quantitative analysis of CBF in the frontal lobe showed postoperative improvement in the Moyamoya hemispheres and not in the healthy hemispheres. However, selection of an ROI introduces some bias because it depends on the observer's choice and limits the spatial sampling of the cerebral cortex. Therefore, we also used another methodology to analyze CBF with ASL MR imaging, by analyzing variation with the norm (healthy hemispheres or control subjects) rather than quantifying absolute CBF values. To minimize intersubject variations of CBF and to increase the sensitivity of this imaging technique, we used whole-brain normalization and voxel-based analysis of ASL MR imaging, as previously described in cognitive studies.⁷ At the group level, we were able to display preoperative hypoperfusion in the MCA territory and a postoperative increase of CBF perfusion, therefore validating the surgical technique. At the individual level,

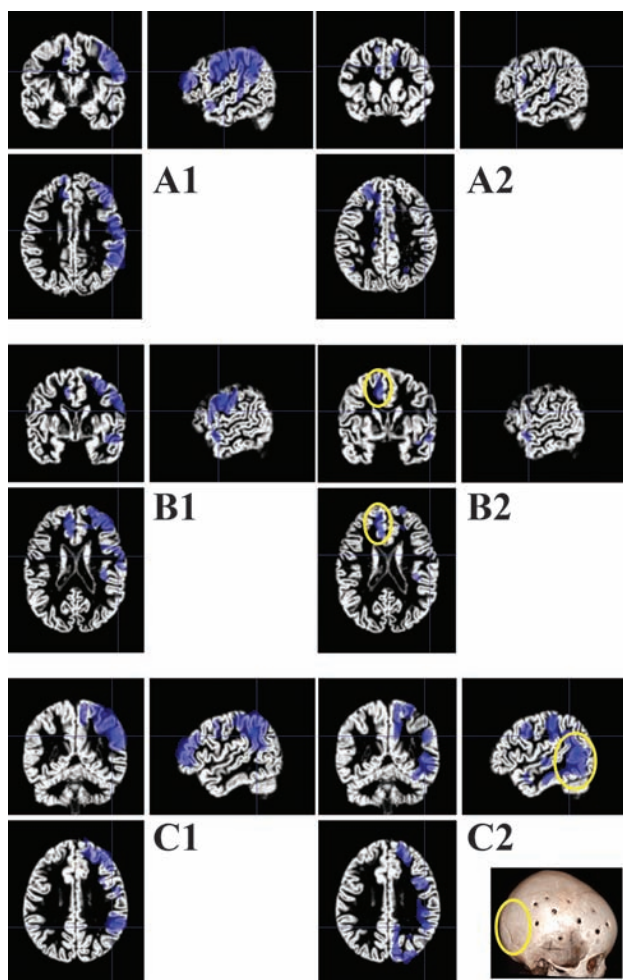


FIG 5. SPM analysis of cerebral perfusion at the individual level for 3 distinct patients. We used each patient's gray matter map obtained with the VBM toolbox as a template. The *blue areas* display voxels of significant decrease of CBF values compared with the control group ($P < .001$ non-family-wise error). A1: Right unilateral hypoperfusion in the middle cerebral artery territory. A2: Postoperative CBF map shows excellent reperfusion 12 months after the operation. B1: Right hypoperfusion in the territory of the middle cerebral artery and left hypoperfusion in the territory of the left anterior cerebral artery. B2: Postoperative control shows a good result on the right hemisphere but residual hypoperfusion on the left side (the patient had undergone a unilateral right surgical procedure 12 months before). C1: Right unilateral hypoperfusion in the middle cerebral artery territory. C2: Postoperative control shows failure of the revascularization procedure; at 6 months after the operation, the patients had recurrent TIAs and wide areas remained statistically hypoperfused in the territory of the MCA. The 3D scan shows lack of a burr-hole in the posterior temporo-parietal junction.

SPM analysis showed objective areas of hypoperfusion compared with a control group. It could, therefore, be used as a screening imaging test in asymptomatic patients, at risk for MM, as in type 1 neurofibromatosis or sickle cell disease. It allows postoperative noninvasive follow-up of the patients and an evaluation of the success or failure of revascularization, thus permitting further targeted surgeries. ASL MR imaging could, therefore, be of particular interest to initiate treatment and prevent stroke occurrence preoperatively but also postoperatively in case of residual hypoperfusion.

CONCLUSIONS

SPM analysis of ASL MR imaging in pediatric Moyamoya disease allows, at the group level, an evaluation of the surgical technique of revascularization. At the individual level, ASL MR imaging offers a noninvasive evaluation of initial hemodynamic impairment and objective assessment of postoperative improvement. In addition, ASL MR imaging may help in the decision to retreat in case of recurrent stroke or TIA.

REFERENCES

1. Scott RM, Smith ER. **Moyamoya disease and Moyamoya syndrome.** *N Engl J Med* 2009;360:1226–37 CrossRef Medline
2. Houkin K, Nakayama N, Kuroda S, et al. **Novel magnetic resonance angiography stage grading for Moyamoya disease.** *Cerebrovasc Dis* 2005;20:347–54 Medline
3. Fujiwara H, Momoshima S, Kuribayashi S. **Leptomeningeal high signal intensity (ivy sign) on fluid-attenuated inversion-recovery (FLAIR) MR images in Moyamoya disease.** *Eur J Radiol* 2005;55:224–30 CrossRef Medline
4. Lee M, Zaharchuk G, Guzman R, et al. **Quantitative hemodynamic studies in Moyamoya disease.** *Neurosurg Focus* 2009;26:E5 CrossRef Medline
5. Zaharchuk G, Do HM, Marks MP, et al. **Arterial spin-labeling MRI can identify the presence and intensity of collateral perfusion in patients with Moyamoya disease.** *Stroke* 2011;42:2485–91 CrossRef Medline
6. Goetti R, Warnock G, Kuhn FP, et al. **Quantitative cerebral perfusion imaging in children and young adults with Moyamoya disease: comparison of arterial spin-labeling-MRI and H₂(15O)-PET.** *AJNR Am J Neuroradiol* 2014;35:1022–28 CrossRef Medline
7. Aslan S, Lu H. **On the sensitivity of ASL MRI in detecting regional differences in cerebral blood flow.** *Magn Reson Imaging* 2010;28:928–35 CrossRef Medline
8. Sainte-Rose C, Oliveira R, Puget S, et al. **Multiple bur hole surgery for the treatment of Moyamoya disease in children.** *J Neurosurg* 2006;105(6 suppl):437–43 Medline
9. Luders E, Gaser C, Jancke L, et al. **A voxel-based approach to gray matter asymmetries.** *Neuroimage* 2004;22:656–64 Medline
10. Noguchi T, Kawashima M, Irie H, et al. **Arterial spin-labeling MR imaging in Moyamoya disease compared with SPECT imaging.** *Eur J Radiol* 2011;80:e557–62 CrossRef Medline
11. Sugino T, Mikami T, Miyata K, et al. **Arterial spin-labeling magnetic resonance imaging after revascularization of Moyamoya disease.** *J Stroke Cerebrovasc Dis* 2013;22:811–16 CrossRef Medline
12. Noguchi T, Kawashima M, Nishihara M, et al. **Noninvasive method for mapping CVR in Moyamoya disease using ASL-MRI.** *Eur J Radiol* 2015;84:1137–43 CrossRef Medline
13. Uchihashi Y, Hosoda K, Zimine I, et al. **Clinical application of arterial spin-labeling MR imaging in patients with carotid stenosis: quantitative comparative study with single-photon emission CT.** *AJNR Am J Neuroradiol* 2011;32:1545–51 CrossRef Medline
14. Noguchi T, Kawashima M, Nishihara M, et al. **Arterial spin-labeling MR imaging in Moyamoya disease compared with clinical assessments and other MR imaging findings.** *Eur J Radiol* 2013;82:e840–47 CrossRef Medline
15. Goetti R, O'Gorman R, Khan N, et al. **Arterial spin labelling MRI for assessment of cerebral perfusion in children with Moyamoya disease: comparison with dynamic susceptibility contrast MRI.** *Neuroradiology* 2013;55:639–47 CrossRef Medline
16. Wang R, Yu S, Alger JR, et al. **Multi-delay arterial spin labeling perfusion MRI in Moyamoya disease: comparison with CT perfusion imaging.** *Eur Radiol* 2014;24:1135–44 CrossRef Medline

Voxel-Based Morphometry and fMRI Revealed Differences in Brain Gray Matter in Breastfed and Milk Formula–Fed Children

X. Ou, A. Andres, R.T. Pivik, M.A. Cleves, J.H. Snow, Z. Ding, and T.M. Badger



ABSTRACT

BACKGROUND AND PURPOSE: Infant diets may have significant impact on brain development in children. The aim of this study was to evaluate brain gray matter structure and function in 8-year-old children who were predominantly breastfed or fed cow's milk formula as infants.

MATERIALS AND METHODS: Forty-two healthy children (breastfed: $n = 22$, 10 boys and 12 girls; cow's milk formula: $n = 20$, 10 boys and 10 girls) were studied by using structural MR imaging (3D T1-weighted imaging) and blood oxygen level–dependent fMRI (while performing tasks involving visual perception and language functions). They were also administered standardized tests evaluating intelligence (Reynolds Intellectual Assessment Scales) and language skills (Clinical Evaluation of Language Fundamentals).

RESULTS: Total brain gray matter volume did not differ between the breastfed and cow's milk formula groups. However, breastfed children had significantly higher ($P < .05$, corrected) regional gray matter volume measured by voxel-based morphometry in the left inferior temporal lobe and left superior parietal lobe compared with cow's milk formula–fed children. Breastfed children showed significantly more brain activation in the right frontal and left/right temporal lobes on fMRI when processing the perception task and in the left temporal/occipital lobe when processing the visual language task than cow's milk formula–fed children. The imaging findings were associated with significantly better performance for breastfed than cow's milk formula–fed children on both tasks.

CONCLUSIONS: Our findings indicated greater regional gray matter development and better regional gray matter function in breastfed than cow's milk formula–fed children at 8 years of age and suggested that infant diets may have long-term influences on brain development in children.

ABBREVIATIONS: BF = breastfed; CELF-4 = Clinical Evaluation of Language Fundamentals, Fourth Edition; IQ = intelligent quotient; MF = cow's milk formula-fed; RIAS = Reynolds Intellectual Assessment Scales; VBM = voxel-based morphometry

The World Health Organization recommends exclusive breastfeeding, which has been associated with better school performance and neurocognitive development in children by multiple studies.^{1–5} When breastfeeding is not possible or not chosen, cow's milk formula has been frequently the formula of choice. Milk formula is made with bovine milk protein, and while the

amino acid composition is similar to that of human breast milk, there are differences in the overall composition of milk formula and human breast milk. It is possible that these differences can impact the developing brain and therefore contribute to the observed long-term benefits on neurodevelopment associated with breastfeeding. In fact, studies are beginning to appear showing an association between breastfeeding and better development in brain structures, such as increased white matter volume, greater cortical thickness, and increased microstructural integrity and myelin water fraction in white matter.^{6–9}

Rapid advances of neuroimaging methods¹⁰ have made possible more comprehensive evaluation of brain development in children. For example, regional gray matter volume measured by MR imaging voxel-based morphometry (VBM) provides a whole-brain region-specific evaluation of the deep gray matter and brain cortex.¹¹ Gray matter consists mostly of neuronal cell bodies that generate and process nerve signals underlying brain function. Numerous VBM studies have revealed abnormal gray matter in dif-

Received July 10, 2015; accepted after revision September 10.

From the Arkansas Children's Nutrition Center (X.O., A.A., R.T.P., M.A.C., T.M.B.) and Departments of Pediatrics (X.O., A.A., R.T.P., M.A.C., J.H.S., T.M.B.) and Radiology (X.O.), University of Arkansas for Medical Sciences, Little Rock, Arkansas; and Vanderbilt University Institute of Imaging Sciences (Z.D.), Nashville, Tennessee.

This work was funded by US Department of Agriculture/Agricultural Research Service 6251-51000-005-02.

Please address correspondence to Xiawei Ou, PhD, One Children's Way, Slot 105, Little Rock, AR 72202; e-mail: ouxiawei@uams.edu

Indicates open access to non-subscribers at www.ajnr.org

EBM Evidence-Based Medicine Level 2.

<http://dx.doi.org/10.3174/ajnr.A4593>

ferent brain regions in children with a variety of neurodevelopmental or psychological disorders.¹²⁻¹⁴ VBM analysis of infant diet effects has not been previously reported, to our knowledge. However, other dietary factors, such as breakfast composition, have shown effects on regional gray matter volume in children.¹⁵

Dietary effects on brain gray matter revealed by structural MR imaging may be complemented by measures of brain functioning obtained by using fMRI. Currently, there is a lack of literature on the use of fMRI to study differences in brain functioning associated with infant diets. For example, although breastfeeding has been associated with better receptive and expressive language development in children¹⁶ and longer breastfeeding duration was associated with higher receptive language scores at 3 years of age and with higher verbal intelligence quotient (IQ) at 7 years of age,¹⁷ it is not known whether fMRI procedures would reveal diet-specific effects during brain processing on language tasks in children fed different diets as infants.

The aim of this study was to evaluate brain gray matter structure and function in 8-year-old healthy children who were fed predominantly breast milk (BF) or cow's milk formula (MF) during the first year of life. We hypothesized that breastfeeding benefits brain gray matter development and functioning in children. To test this hypothesis, we compared VBM measures of regional gray matter volume and fMRI measures of brain activation when performing visual perception and language tasks between BF and MF children. Measures of fMRI task performance and overall IQ and language skills were also compared between groups.

MATERIALS AND METHODS

Participants

Healthy 7.5–8.5-year-old children who had parental report of predominant breast milk or cow's milk-based formula feeding during infancy were recruited for this study. All procedures were approved by the University of Arkansas for Medical Sciences review board. Assents and consents were obtained from the participants and their parents. BF infants were all exclusively breastfed for at least 8 months (average, 12.6 months). MF infants were fed the same type of cow's milk-based formula after birth for at least 8 months. Infants were introduced to complementary foods on average around 5 months of age. All participants were right-handed and born full-term with birth weight between the fifth and 95th percentiles. None had a medical history of psychological/psychiatric diagnoses or neurologic impairment or injury. In addition, none of their mothers reported alcohol, tobacco, drug, or psychotropic medications use during pregnancy. All participants underwent an MR imaging examination including a structural scan and an fMRI study. After we excluded those who did not complete the MR imaging scan or had excessive motion and apparent imaging artifacts, valid structural imaging data were obtained for 42 children (BF: $n = 22$, 10 boys, 12 girls; MF: $n = 20$, 10 boys, 10 girls), and all except 1 MF girl had valid fMRI data. Participants were administered the Reynolds Intellectual Assessment Scales (RIAS) test, which measures verbal, nonverbal, and composite IQ, and the Clinical Evaluation of Language Fundamentals (CELF-4) test, which measures receptive, expressive, and overall language abilities. The RIAS and CELF-4 tests were supervised by a licensed pediatric psychological examiner. In addition,

Table 1: Demographic information, family background, and test scores of the study participants

	BF	MF	P Value
Demographics			
No. (boys/girls) for VBM	22 (10/12)	20 (10/10)	
Birth weight (kg)	3.5 ± 0.4	3.4 ± 0.5	.47
Weight (kg)	27.8 ± 6.3	27.5 ± 5.5	.98
Height (cm)	128 ± 5	129 ± 4	.25
BMI	17.0 ± 3.4	16.5 ± 2.6	.62
Age at MRI (yr)	7.98 ± 0.29	7.95 ± 0.25	.71
Family background			
Mother's education ^a (%)	35.7/42.9/21.4	8.3/50/41.7	.24
Father's education ^a (%)	35.7/50/14.3	33.3/58.3/8.3	.99
Household income ^b (%)	21.4/57.1/21.4	0/41.7/58.3	.08
Test scores			
Verbal IQ	110 ± 16	107 ± 17	.50
Nonverbal IQ	111 ± 13	114 ± 16	.73
Composite IQ	111 ± 13	110 ± 15	.68
CELF-4 (receptive)	104 ± 11	100 ± 15	.45
CELF-4 (expressive)	108 ± 10	104 ± 12	.33
CELF-4 (overall)	104 ± 12	100 ± 15	.41

Note:—BMI indicates body mass index.

^a High school or partial college/college graduate/graduate school.

^b <\$50,000/\$50,000–\$70,000/>\$70,000.

we were able to obtain family background information, including parents' education and income, for 26 subjects (12 MF and 14 BF children). The demographic information, family background, and test scores for all subjects are listed in Table 1.

MR Imaging Protocol

All MR imaging scans were performed on a 1.5T Achieva scanner (Philips Healthcare, Best, the Netherlands) with a 60-cm bore size, 33-mT/m gradient amplitude, and 100-mT/m/ms maximum slew rate at our institution. The built-in body coil was used as a transmitter, and a standard 8-channel sensitivity encoding head coil was used as a receiver. Imaging sequences included a sagittal T1-weighted 3D turbo field echo sequence for structural MR imaging with the following parameters: TR, 7.3 ms; TE, 3.4 ms; flip angle, 8°; acquisition voxel size, 1 × 1 × 1 mm; matrix size, 256 × 232 × 150; 2 averages; scan time, ~7 minutes; and an axial single-shot gradient-echo-planar imaging sequence for functional MR imaging with the following parameters: TR, 3000 ms; TE, 50 ms; flip angle, 90°; acquisition voxel size, 2.4 × 2.4 × 5 mm; matrix size, 92 × 92 × 20; 208 dynamic scans; 2 dummy scans; scan time, ~10 minutes.

Structural MR Imaging Data Processing

The raw T1-weighted 3D images were exported to a workstation with Matlab software (MathWorks, Natick, Massachusetts) for VBM analysis. The VBM8 toolbox for statistical parametric mapping (SPM8; <http://www.fil.ion.ucl.ac.uk/spm/software/spm8>) was used. A pediatric T1 template (~8 years of age) and customized tissue probability maps were created on the basis of National Institutes of Health data by the Template-O-Matic toolbox (<https://irc.cchmc.org/software/tom/agreement.php>),¹⁸ and the T1 images were then segmented into gray matter, white matter, and CSF by VBM8 by using default parameters. Nonlinear modulated normalized gray matter images were generated that enable analysis of relative differences in regional gray matter volume, corrected for individual brain size. The images were displayed and

reviewed to ensure that segmentation and normalization procedures worked properly and were then smoothed by using a Gaussian kernel of full width at half maximum, 8 mm in each direction. The smoothed gray matter images were used for the subsequent voxelwise statistical analysis between the BF and MF groups. Although there were no significant sex or age differences between groups, sex and age were included as covariates in the VBM analysis because the brain is still developing at 8 years of age and there are possible sex differences in the human brain.¹⁹

fMRI Protocol

All participants were trained before the fMRI study to perform the perception and language tasks. The tasks were adopted from the literature²⁰ with modifications regarding timing and design and incorporated into an fMRI paradigm designed on E-Prime software (Psychology Software Tools, Pittsburgh, Pennsylvania). For the perception task, the participants were requested to determine whether 2 symbols on the screen (ie, \ /) matched those presented on the previous screen (eg, \ \, / /, \ /). For the language task, participants were requested to determine whether 2 words presented on 1 screen after another rhymed. A block design consisting of 8 perception blocks and 8 language blocks alternating with each other was used for the fMRI. Each block included 9 trials, and each trial included presentation of symbols (perception block) or words (rhyming block) followed by a 2000-ms interval during which the participants were to make responses by pressing either the “yes” or “no” key on a touchpad of an Eloquence fMRI system (Invivo, Gainesville, Florida).

fMRI Data Processing

Gradient-echo EPI acquired during fMRI examinations was exported to a workstation with BrainVoyager software (Brain Innovation, Maastricht, the Netherlands) for fMRI data processing. Cubic spline interpolation was used for slice scan time correction. Images from the first dynamics were used as a reference, and translation and rotation of images in subsequent dynamics were plotted in all directions to illustrate motion. Trilinear estimation and interpolation were used for 3D-motion correction. An 8-mm full width at half maximum Gaussian filter was used for spatial smoothing. Linear trend removal and a high-pass filter with 3 cycles/points were used for temporal filtering. The T1-weighted 3D images were also exported to BrainVoyager to create an anatomic image series, and the processed fMRI was coregistered to the anatomic images automatically. The 3D dataset with anatomic images and fMRI information was then transformed to the Talairach atlas to create a 3D-aligned time course dataset. A stimulation protocol was then created in BrainVoyager to represent the block design (with hemodynamic response function refinement) used in the fMRI scans. General linear model analysis was performed to calculate activation maps for the 3D-aligned time course dataset for each subject. The average activation maps for each diet group were calculated by a multistudy multisubject general linear model. The total activation cluster size in each brain lobe that exhibited activation at a statistical threshold of $P < .001$ corrected was calculated for each subject and compared between groups. In addition, task performance parameters, such as the percentage of responses and the percentage of correct answers

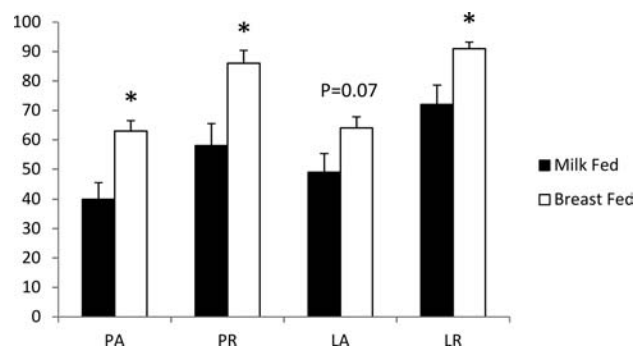


FIG 1. BF children had better performance for fMRI perception and language tasks. PA indicates percentage of correct answer for the perception task; PR, percentage of response for the perception task; LA, percentage of correct answer for the language task; LR, percentage of response for the language task. The asterisk indicates $P < .05$.

made within the allocated time interval in each trial, were also compared between groups.

Statistical Analysis

For comparisons of demographic parameters, IQ and language test scores, total gray matter volume, and fMRI task performance parameters among groups, Wilcoxon rank sum tests were used for significant differences ($P < .05$). Comparison of other non-numeric family background parameters were made by using the Fisher exact test. For the VBM comparisons of regional gray matter volume among groups, $P < .001$ uncorrected with a cluster size threshold of 30 voxels was used to illustrate overall differences, and $P < .05$ (family-wise error—corrected cluster level) was used to determine regions with significantly different regional gray matter volumes. Sex and age were included as covariates for all analyses. For the calculation and illustration of average fMRI activation maps in each group, the statistical threshold was set at $P < .001$ after Bonferroni correction for multiple comparisons and the cluster size threshold was set at 30 voxels. For the statistical comparison of fMRI activation cluster size between groups, $P < .001$ after Bonferroni correction (for the activation maps) was used to calculate total cluster size in each brain lobe in each subject, and Wilcoxon rank sum tests were used to determine significant differences ($P < .05$) between groups.

RESULTS

The weight, height, body mass index, and age at MR imaging were not different between the BF and MF children (Table 1). The family background parameters were also not different between groups. The RIAS IQ and CELF-4 scores did not differ between BF and MF. However, BF children performed better on both fMRI tasks, as indicated by the percentage of responses made within the designated time interval and the percentage of correct answers (Fig 1) in which BF and MF children differed significantly on 3 of the 4 measures.

Total gray matter volume ($763 \pm 65 \text{ cm}^3$ and $761 \pm 78 \text{ cm}^3$ for the BF and MF children, respectively) did not differ between groups. However, BF children had higher regional gray matter volume than MF children in multiple brain regions (Fig 2). Specifically, at a statistical threshold of $P < .001$ (uncorrected) with a cluster size of ≥ 30 voxels, regional gray matter volume was

greater for BF than MF children in the left and right parietal and left temporal lobes (Fig 2A), while there were no regions with lower gray matter volume (Fig 2B). At a statistical threshold of $P < .05$ (family-wise error–corrected), 1 region in the left supe-

rior parietal lobe (Fig 2C) and 1 region in the left inferior temporal lobe (Fig 2D) had significantly higher gray matter volume in BF than MF children, and no region had lower gray matter volume.

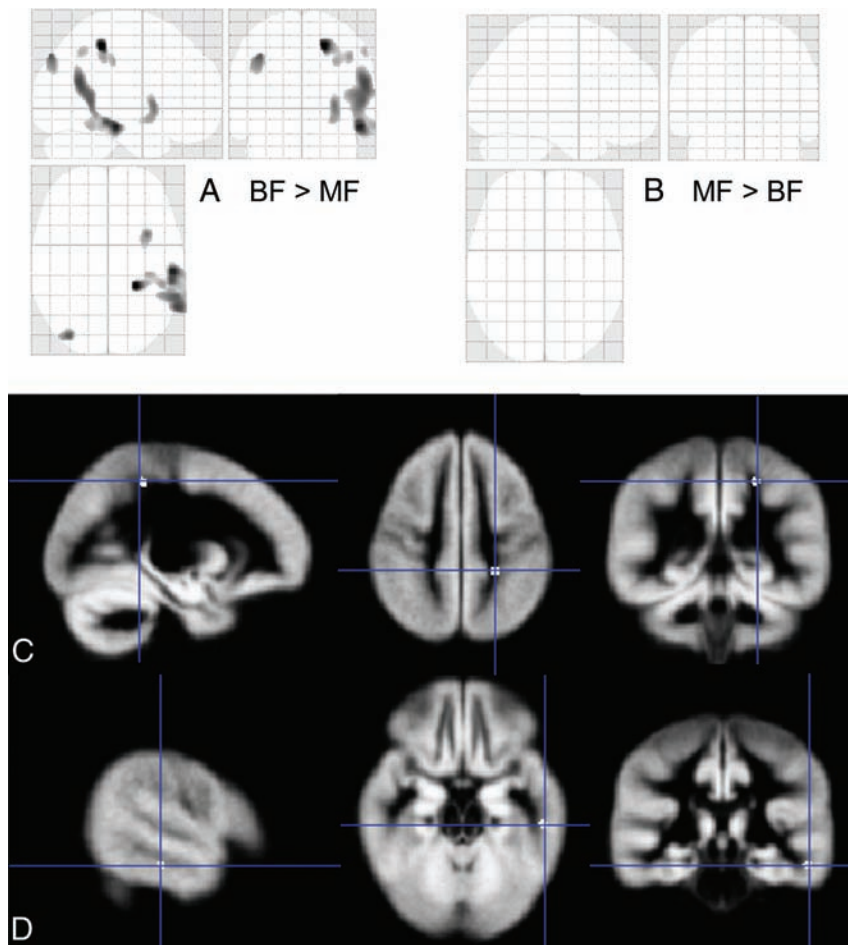


FIG 2. Comparison of regional gray matter volume measures by VBM. The results are shown in a 3-plane projection view in A and B, in which the statistical threshold was set at $P < .001$ uncorrected, with a cluster size of ≥ 30 voxels. A, Multiple regions had higher gray matter volumes in BF than MF children. B, No region had higher gray matter volume in MF than BF children. Regions with significantly higher ($P < .05$, corrected) gray matter volume in BF than MF children were overlaid on the customized gray matter template for 8-year-old children (1 region in the left superior parietal lobe, C, and 1 region in the left inferior temporal lobe, D). All images are displayed in radiologic convention (left/right flipped).

Average fMRI activation maps for the perception task (Fig 3; $P < .001$, Bonferroni-corrected cluster size of ≥ 30 voxels) showed widespread activation in the left and right middle temporal gyri, superior parietal gyrus/precuneus, and right superior/middle frontal gyri for BF children, while MF children had fewer activation regions, which mainly involved the right middle temporal gyrus and superior parietal gyrus/precuneus. Average fMRI activation maps for the language task (Fig 4, $P < .001$, Bonferroni-corrected cluster size of ≥ 30 voxels) showed that BF children had widespread activation in the left and right lingual gyri and cuneus and left fusiform and the left middle/inferior frontal gyri, while MF children had similar overall activation except for less left temporal lobe activation. The total activation cluster size ($P < .001$, Bonferroni-corrected) calculated for individual subjects in each of the involved brain areas (Table 2) showed significantly more activation for BF children in the right frontal and left and right temporal lobes for the perception task and in the left temporal/occipital lobes for the language task (all, $P < .05$).

DISCUSSION

The total brain gray matter volume did not differ between BF and MF children in our study. This is consistent with a previous report that did not observe a significant correlation between breast

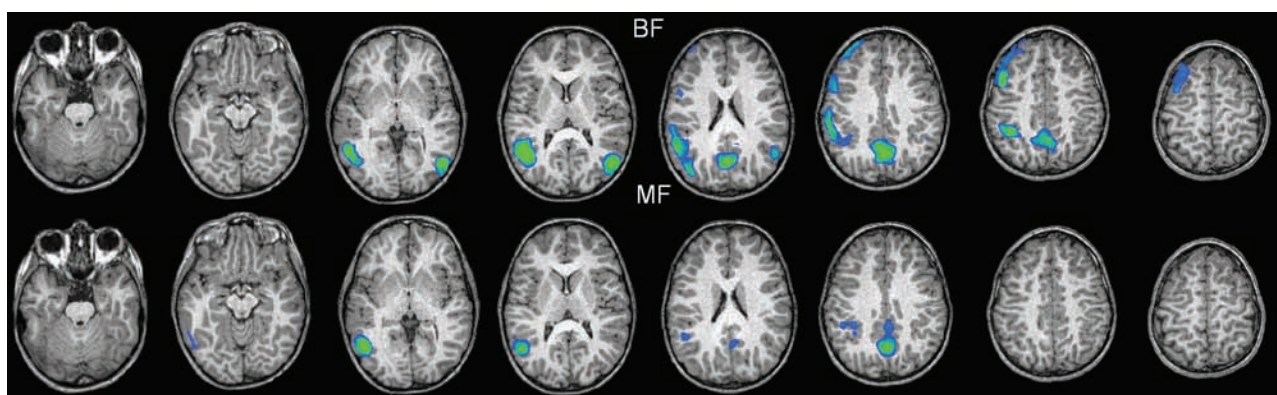


FIG 3. Average activation maps for the fMRI perception task for BF (top row) and MF (bottom row) children. Activated regions are highlighted in blue/green. The threshold was set at $P < .001$ after Bonferroni correction and a cluster size of ≥ 30 voxels. All images are displayed in radiologic convention (left/right flipped). BF children had more extensive activation in the right frontal and left/right temporal lobes.

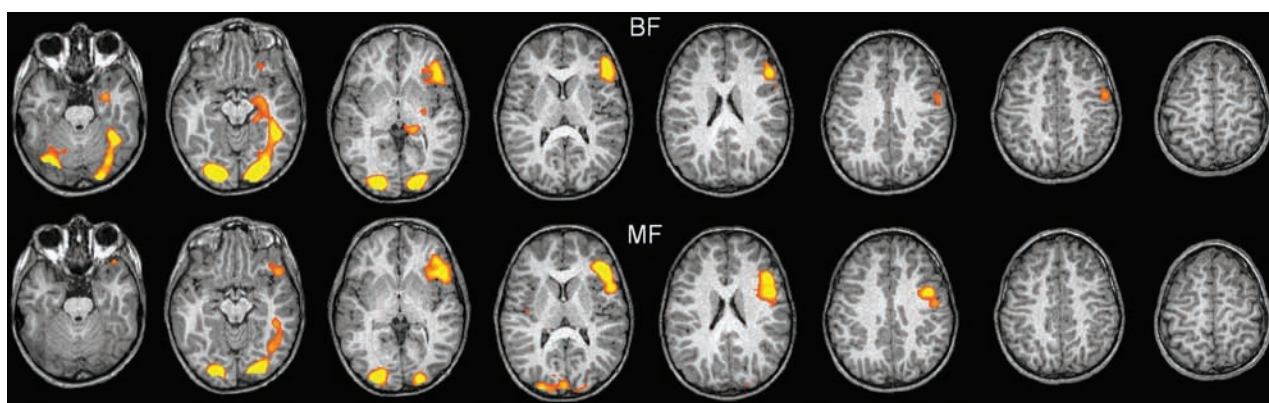


FIG 4. Average activation maps for the fMRI language task for BF (*top row*) and MF (*bottom row*) children. Activated regions are highlighted in yellow/orange. The threshold was set at $P < .001$ after Bonferroni correction and a cluster size of ≥ 30 voxels. All images are displayed in radiologic convention (left/right flipped). BF children had more extensive activation in the left temporal lobe.

Table 2: Comparison of the fMRI-activation total cluster size (No. of voxels)^a

	BF Mean (SE)	MF Mean (SE)	P Value
Perception fMRI			
Right frontal	1280 (814)	6 (6)	.002 ^b
Parietal	1263 (488)	723 (546)	.445
Left temporal	1394 (680)	112 (86)	.011 ^b
Right temporal	2263 (1364)	33 (22)	.041 ^b
Language fMRI			
Left frontal	1125 (616)	261 (113)	.513
Left temporal/occipital	2632 (650)	613 (213)	.04 ^b
Right temporal/occipital	1894 (609)	909 (369)	.251

Note:—SE indicates standard error.

^a BF children had greater activation than MF children for both fMRI tasks.

^b $P < .05$.

milk intake and total gray matter volume in ex-preterm children.⁶ However, these measures of total volume provide a gross assessment of brain structure and may not be sensitive enough to detect subtle and/or regional differences. On the other hand, regional gray matter volume analysis by VBM used in the present study can detect regional differences in the distribution of gray matter, in addition to providing whole-brain analyses. Our results revealed multiple brain regions with significantly higher gray matter volume in BF than in MF children. These findings are consistent with previous reports of better regional gray matter development associated with breastfeeding compared with formula feeding.^{7,21} Our VBM analysis observed significant regional gray matter differences in BF-versus-MF children in cortical but not deep gray matter. These results differ from those of Herba et al,²¹ who showed a larger gangliothalamic ovoid diameter in BF-versus-formula-fed infants as quantified by using sonography. These apparent discordant results may be influenced by the brain maturation pattern of deep gray matter, which develops earlier than cortical gray matter²²; thus, diet effects on gray matter may be more prominent in deep regions during infancy, but in cortical regions during later childhood. Our VBM analysis identified higher regional gray matter volume in the parietal lobe of BF-versus-MF children, in agreement with Kafouri et al,⁷ who reported a positive association between the duration of exclusive breastfeeding and cortical thickness of superior and inferior parietal lobules. In addition, our study also revealed significant regional gray matter volume

differences between BF and MF children in the left inferior temporal lobe, indicating that voxelwise whole-brain analysis may be more sensitive than the ROI cortical thickness measure. Finally, the regional gray matter volume comparison by VBM was based on modulated gray matter attenuation, while the total gray matter volume was computed from the gray matter segment obtained at an early stage of the VBM analysis (before volume modulation). The former approach is more sensitive to local gray matter volume changes, but such changes may not be sufficiently large enough to be reflected in the total gray matter volume, which is simply a sum of all voxels segmented as gray matter. The observed significant decreases of regional gray matter volume in the MF group may also be accompanied by increases in some gray matter regions that did not form statistically meaningful clusters (such as at $P < .001$ uncorrected with a cluster size of ≥ 30 in Fig 2B or at $P < .05$ corrected in Fig 2C, -D). Therefore, it is possible that in our study, the total gray matter volume was not different between groups but the regional comparison of gray matter showed only significant decreases in the MF group.

Our fMRI results also indicated that BF children may have better functional development of gray matter than MF children. Specifically, when we compared the average activation maps generated at a statistical threshold of $P < .001$ (Bonferroni-corrected) between groups, BF children had significantly more activation in the right frontal and left/right temporal lobes for the perception task and in the left temporal lobe for the language task. Greater brain activation for similar tasks has been observed in healthy adults versus children²⁰ and correlated with better task performance,²³ while reduced activation has been observed in children with dyslexia,²⁴ indicating that more activation is probably associated with better functional development of the brain. The overall greater brain activation and presumably better functional development in BF than in MF children was consistent with the fMRI task performance data in our study, which showed significantly better task performance in BF than in MF children and agreed with literature findings in larger scale studies in which better language development and higher IQ associated with breastfeeding were observed.^{1,17} Greater activation in the left temporal lobe for both tasks in BF children was also consistent with our VBM findings, in which higher regional gray matter volume was detected. The average language fMRI activation maps

for all children were consistent with activation maps reported for similar visual rhyming tasks for children,²⁰ and the BF/MF brain activation differences were significant in the left temporal lobe, which is important for phonologic processing (rhyming in our study)²⁰ and involves the fusiform gyrus, which has been regarded as an important region for visual word processing.²⁵ These results also suggest that the visual rhyming-language fMRI may be sensitive to differences in language processing associated with infant diets, despite the fact that the language measures such as verbal IQ and CELF-4 scores did not differ significantly (except for a trend toward lower scores in MF children for all language components) in our relatively small cohort of BF and MF children.

One limitation of our study is that we could not obtain family socioeconomic status data for some of the subjects and incorporate the background information into covariate analyses. However, the data we were able to collect of parents' education and income from the subjects were not different between groups (Table 1). Variables not considered in our study during infancy to 8 years of age may also impact brain development in children and may be confounders for our observed association between infant diets and brain development. Nevertheless, the diverse nature of our recruiting methods (advertisements at health fairs, pediatrician offices, summer camps, schools, social media, and community events) might be expected to lessen the confounding influence of these variables in our study. Another study limitation is our relatively small sample size, particularly because we were measuring potentially subtle effects in healthy children. However, we did find statistically significant VBM and fMRI differences between our cohorts of BF and MF children. While we did include sex as a covariate in our analyses, possible cross-sex variations in the effects of infant diets on gray matter development may need to be investigated with a larger sample size. Future studies with larger sample sizes and well-characterized cohorts may be beneficial to better delineate neuroimaging correlates of infant diet effects on children's brain development.

CONCLUSIONS

We used VBM and fMRI to evaluate the brain gray matter structure and function in healthy 8-year-old children who were predominantly BF or MF during infancy. Our imaging results showed that BF children had greater gray matter volume in specific brain regions than MF children, despite the total gray matter volume not being different between groups. Our results also showed more brain activation for the BF children when processing perception and language tasks. Our results indicate an association between infant diets and long-term brain development in healthy children.

ACKNOWLEDGMENTS

We appreciate the Human Studies Core of the Arkansas Children's Nutrition Center for all their effort in this project. We also thank all subjects and their families for participating in this study.

Disclosures: Xiawei Ou—RELATED: Grant: US Department of Agriculture.* Comments: This project is supported by US Department of Agriculture/Agricultural Research Service funding to Arkansas Children's Nutrition Center. Aline Andres—RELATED: Grant: US Department of Agriculture/Agricultural Research Service grant.* Rudolph T. Pivik—RELATED: Grant: US Department of Agriculture/Agricultural

Research Service.* Jeffrey H. Snow—RELATED: Grant: US Department of Agriculture funding of the Nutrition Center.* Thomas M. Badger—RELATED: Grant: US Department of Agriculture.* Comments: This is a center grant for the Arkansas Children's Nutrition Center to study the effects of diets and nutritional status on child development and disease prevention. *Money paid to the institution.

REFERENCES

1. Anderson JW, Johnstone BM, Remley DT. **Breast-feeding and cognitive development: a meta-analysis.** *Am J Clin Nutr* 1999;70:525–35 Medline
2. Brion MJ, Lawlor DA, Matijasevich A, et al. **What are the causal effects of breastfeeding on IQ, obesity and blood pressure? Evidence from comparing high-income with middle-income cohorts.** *Int J Epidemiol* 2011;40:670–80 CrossRef Medline
3. Kramer MS, Aboud F, Mironova E, et al; Promotion of Breastfeeding Intervention Trial (PROBIT) Study Group. **Breastfeeding and child cognitive development: new evidence from a large randomized trial.** *Arch Gen Psychiatry* 2008;65:578–84 CrossRef Medline
4. Oddy WH, Li JH, Whitehouse AJO, et al. **Breastfeeding duration and academic achievement at 10 years.** *Pediatrics* 2011;127:e137–45 CrossRef Medline
5. Quigley MA, Hockley C, Carson C, et al. **Breastfeeding is associated with improved child cognitive development: a population-based cohort study.** *J Pediatr* 2012;160:25–32 CrossRef Medline
6. Isaacs EB, Fischl BR, Quinn BT, et al. **Impact of breast milk on intelligence quotient, brain size, and white matter development.** *Pediatr Res* 2010;67:357–62 CrossRef Medline
7. Kafouri S, Kramer M, Leonard G, et al. **Breastfeeding and brain structure in adolescence.** *Int J Epidemiol* 2013;42:150–59 CrossRef Medline
8. Deoni SC, Dean DC 3rd, Piryatinsky I, et al. **Breastfeeding and early white matter development: a cross-sectional study.** *Neuroimage* 2013;82:77–86 CrossRef Medline
9. Ou X, Andres A, Cleves MA, et al. **Sex-specific association between infant diet and white matter integrity in 8-y-old children.** *Pediatr Res* 2014;76:535–43 CrossRef Medline
10. Isaacs EB. **Neuroimaging, a new tool for investigating the effects of early diet on cognitive and brain development.** *Front Hum Neurosci* 2013;7:445 CrossRef Medline
11. Ashburner J, Friston KJ. **Voxel-based morphometry: the methods.** *Neuroimage* 2000;11:805–21 CrossRef Medline
12. Adelman NE, Fromm SJ, Razdan V, et al. **Cross-sectional and longitudinal abnormalities in brain structure in children with severe mood dysregulation or bipolar disorder.** *J Child Psychol Psychiatry* 2012;53:1149–56 CrossRef Medline
13. Boddaert N, Chabane N, Gervais H, et al. **Superior temporal sulcus anatomical abnormalities in childhood autism: a voxel-based morphometry MRI study.** *Neuroimage* 2004;23:364–69 CrossRef Medline
14. Eckert MA, Leonard CM, Wilke M, et al. **Anatomical signatures of dyslexia in children: unique information from manual and voxel based morphometry brain measures.** *Cortex* 2005;41:304–15 CrossRef Medline
15. Taki Y, Hashizume H, Sassa Y, et al. **Breakfast staple types affect brain gray matter volume and cognitive function in healthy children.** *PLoS One* 2010;5:e15213 CrossRef Medline
16. Dee DL, Li RW, Lee LC, et al. **Associations between breastfeeding practices and young children's language and motor skill development.** *Pediatrics* 2007;119:S92–98 CrossRef Medline
17. Belfort MB, Rifas-Shiman SL, Kleinman KP, et al. **Infant feeding and childhood cognition at ages 3 and 7 years: effects of breastfeeding duration and exclusivity.** *JAMA Pediatr* 2013;167:836–44 CrossRef Medline
18. Wilke M, Holland SK, Altaye M, et al. **Template-O-Matic: a toolbox for creating customized pediatric templates.** *Neuroimage* 2008;41:903–13 CrossRef Medline
19. Reiss AL, Abrams MT, Singer HS, et al. **Brain development, gender and IQ in children: a volumetric imaging study.** *Brain* 1996;119:1763–74 CrossRef Medline
20. Booth JR, Burman DD, Meyer JR, et al. **Development of brain mech-**

- anisms for processing orthographic and phonologic representations. *J Cogn Neurosci* 2004;16:1234–49 CrossRef Medline
21. Herba CM, Roza S, Govaert P, et al. **Breastfeeding and early brain development: the Generation R study.** *Matern Child Nutr* 2013;9:332–49 CrossRef Medline
 22. Tzarouchi LC, Astrakas LG, Xydis V, et al. **Age-related grey matter changes in preterm infants: an MRI study.** *Neuroimage* 2009;47:1148–53 CrossRef Medline
 23. Booth JR, Burman DD, Meyer JR, et al. **Relation between brain activation and lexical performance.** *Hum Brain Mapp* 2003;19:155–69 CrossRef Medline
 24. Cao F, Bitan T, Chou TL, et al. **Deficient orthographic and phonological representations in children with dyslexia revealed by brain activation patterns.** *J Child Psychol Psychiatry* 2006;47:1041–50 CrossRef Medline
 25. McCandliss BD, Cohen L, Dehaene S. **The visual word form area: expertise for reading in the fusiform gyrus.** *Trends Cogn Sci* 2003;7:293–99 CrossRef Medline

Evaluation of Subependymal Gray Matter Heterotopias on Fetal MRI

U.D. Nagaraj, J.L. Peiro, K.S. Bierbrauer, and B.M. Kline-Fath

ABSTRACT

BACKGROUND AND PURPOSE: Subependymal grey matter heterotopias are seen in a high proportion of children with Chiari II malformation and are potentially clinically relevant. However, despite its growing use, there is little in the literature describing its detection on fetal MRI. Our aim was to evaluate the accuracy in diagnosing subependymal gray matter heterotopias in fetuses with spinal dysraphism on fetal MR imaging.

MATERIALS AND METHODS: This study is a retrospective analysis of 203 fetal MRIs performed at a single institution for spinal dysraphism during a 10-year period. Corresponding obstetric sonography, postnatal imaging, and clinical/operative reports were reviewed.

RESULTS: Of the fetal MRIs reviewed, 95 fetuses were included in our analysis; 23.2% (22/95) were suspected of having subependymal gray matter heterotopias on fetal MR imaging prospectively. However, only 50% (11/22) of these cases were confirmed on postnatal brain MR imaging. On postnatal brain MR imaging, 28.4% (27/95) demonstrated imaging findings consistent with subependymal gray matter heterotopia. Only 40.7% (11/27) of these cases were prospectively diagnosed on fetal MR imaging.

CONCLUSIONS: Fetal MR imaging is limited in its ability to identify subependymal gray matter heterotopias in fetuses with spinal dysraphism. It is believed that this limitation relates to a combination of factors, including artifacts from fetal motion, the very small size of fetal neuroanatomy, differences in imaging techniques, and, possibly, irregularity related to denudation of the ependyma/subependyma in the presence of spinal dysraphism and/or stretching of the germinal matrix in ventriculomegaly.

ABBREVIATIONS: GA = gestational age; SEH = subependymal gray matter heterotopias; VMG = ventriculomegaly

Fetal MR imaging plays an important role in the evaluation of fetuses with suspected central nervous system abnormalities; the indications for, availability of, and the use of fetal MRI are increasing.¹⁻³ The role of fetal MR imaging is important in the evaluation of spinal dysraphisms and is vital in the assessment for prenatal repair of myelomeningoceles. Because the Management of Myelomeningocele randomized controlled trial has shown that prenatal surgery for myelomeningoceles reduces the need for shunting and may improve neurologic function in some patients,

MR imaging has become imperative in evaluating these fetuses before intervention.⁴⁻⁶

Subependymal gray matter heterotopias (SEH) are seen in a relatively high proportion of children with Chiari II malformation, with a reported incidence as high as 30%.⁷ Although the exact implications in this subset of patients are still under investigation, ample reports in the literature describe the clinical relevance of SEH.⁸⁻¹² Up to 80% of patients with SEH have been reported to develop epilepsy during their lifetimes, and disorders of cognition are seen in anywhere from 20% to 60%.⁹ The presence of SEH also demonstrates a strong association with other structural anomalies in the brain in addition to Chiari malformation, including cerebral cortical malformations, callosal anomalies, and decreased white matter volume.¹⁰⁻¹² However, very little radiology literature has reported on the detection of SEH on fetal MR imaging, with only case reports and a few small case series described.¹³⁻¹⁵ Many authors believe that SEH can be identified on fetal MR imaging.^{3,16,17} In 1 small series of 15 patients, fetal MR imaging was reported to be up to 100% specific, though only 67% sensitive, in detecting SEH.¹⁷ To date, no large series have

Received July 15, 2015; accepted after revision September 8.

From the Departments of Radiology and Medical Imaging (U.D.N., B.M.K.-F), Pediatric Surgery (J.L.P.), and Pediatric Neurosurgery (K.S.B.), Cincinnati Children's Hospital Medical Center, Cincinnati, Ohio; and University of Cincinnati College of Medicine (U.D.N., J.L.P., K.S.B., B.M.K.-F), Cincinnati, Ohio.

Preliminary results were previously presented at: American Society of Neuroradiology Annual Meeting and the Foundation of the ASNR Symposium; April 25-30, 2015; Chicago, Illinois; No. O-176.

Please address correspondence to Usha D. Nagaraj, MD, Department of Radiology and Medical Imaging, Cincinnati Children's Hospital Medical Center, 3333 Burnet Ave, Cincinnati, OH 45229-3026; e-mail: usha.nagaraj@cchmc.org; @CincyRadKids

<http://dx.doi.org/10.3174/ajnr.A4585>

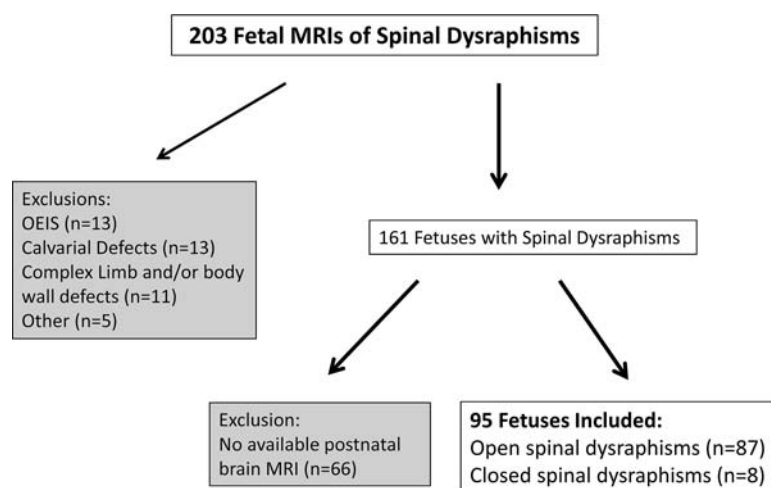


FIG 1. Breakdown of the fetuses included in our study. OEIS indicates omphalocele-exstrophy-imperforate anus-spinal defects.

examined this finding on MR imaging in fetuses with spinal dysraphism.

The purpose of this study was to examine the accuracy of diagnosing SEH in fetuses with spinal dysraphism via fetal MR imaging.

MATERIALS AND METHODS

Study Design

This study was a single-center, retrospective chart review. Illuminate InSight software (Softek Solutions, Prairie Village, Kansas), a program utilized for data aggregation and search engine functions, was used to compile a list of fetuses with open and closed spinal dysraphisms imaged via fetal MR imaging at Cincinnati Children's Hospital Medical Center in Cincinnati, Ohio, between 2004 and 2014. Additional cases of spinal dysraphism were also obtained from a radiology fetal case list. Only patients with available postnatal brain MRIs were included in this analysis. Patients with omphalocele-exstrophy-imperforate anus-spinal defects complex or complicating limb, body wall, or calvarial defects (anencephaly, encephaloceles) were excluded. The images were viewed in the PACS. A chart review was performed to obtain relevant clinical data. This study was Health Insurance Portability and Accountability Act-compliant and was approved by the institutional review board. The requirement for informed consent was waived.

Imaging Parameters

All 95 fetuses included in our analysis were scanned prenatally on a 1.5T magnet within the group of hospitals that are a part of the Fetal Care Center of Cincinnati, with 97.9% (93/95) of fetal MRIs performed at Cincinnati Children's Hospital Medical Center on either a GE Signa (Milwaukee, Wisconsin) or a Phillips Ingenia (Best, the Netherlands) system. Only diagnostic-quality MRIs for the assessment of the fetal brain were included in our study, and this was a subjective assessment made by the radiologists. T2 single-shot fast spin-echo images of the brain were the most useful in identifying SEH and were obtained in 3 planes: axial, sagittal, and coronal. Section thicknesses of 3-mm, no gap, interleaved images at ≤ 24 weeks' gestational age (GA) and 4-mm, no gap, interleaved images at > 24 weeks GA were used. Although this imaging protocol did not change during the study period, the TR and TE

varied among scanners and were changed at times of scanner upgrades to optimize image quality. At least 2 stacks in each plane were obtained to the radiologist's satisfaction. The smallest FOV possible was used. T1WI of the fetal brain and body were obtained; however, they were not useful in identifying additional SEH. Axial DWI of the fetal brain was inconsistently implemented at the radiologist's discretion and was not helpful in identifying additional SEH in any of the cases. Images were reviewed for the presence or absence of ≥ 1 subependymal gray matter heterotopia identified in at least 2 planes.

All 95 patients included in our analysis had diagnostic-quality postnatal brain MRIs available for interpretation,

as determined by the radiologists. The postnatal imaging parameters varied because 1 of 6 clinical magnets was used and the routine use of T1 3D spoiled gradient-recalled imaging was not implemented until 2009. We found that SEH were best identified on axial T2 FSE sequences postnatally, though sagittal T1WI was helpful as well in certain cases.

Image Interpretation

All images were reviewed by 2 board-certified radiologists (U.D.N., B.M.K.-F.), both with added qualifications in pediatric radiology and fellowship training in pediatric neuroradiology, 1 (B.M.K.-F) with > 10 years of postfellowship attending experience in pediatric neuroradiology in a large academic center. The readers were blinded to the pre- and postnatal imaging findings at the time of interpretation. Differences were resolved by consensus.

Statistical Analysis

Statistical analysis was performed by using Excel (Microsoft, Redmond, Washington) 2013 spreadsheet mathematic functions, including average values, SDs, value count, and Student *t* test.

RESULTS

Description of Our Cohort

Of the 203 MRIs of fetuses with spinal dysraphism reviewed, 161 fetuses were identified as having spinal dysraphism without evidence of omphalocele-exstrophy-imperforate anus-spinal defects complex or complicating limb, body wall, or calvarial defects. In this cohort, 95 fetuses had postnatal brain MRIs available for interpretation and were included in our analysis (Fig 1); 37.9% (36/95) of these fetuses were male. The average gestational age at MR imaging was 24.23 ± 3.9 weeks; 22.1% (21/95) of these patients underwent open fetal surgery for in utero repair of a myelomeningocele. The average age at postnatal brain MR imaging was 58.8 ± 159.7 days.

In total, 91.6% (87/95) had open spinal dysraphism, while the remaining were closed; 91.6% (87/95) had evidence of Chiari II malformation in the posterior cranial fossa; and of those with a normal posterior fossa, 50% (4/8) had closed spinal dysraphisms. Of the

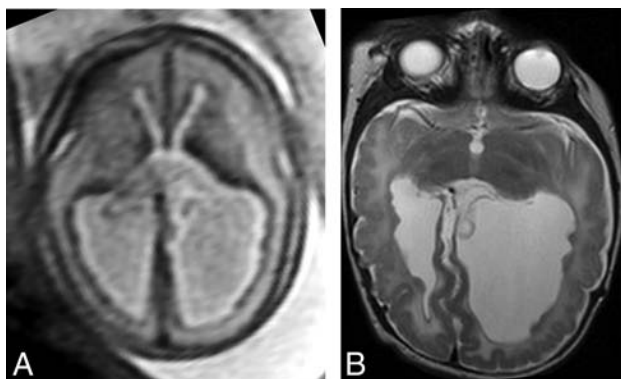


FIG 2. Example of SEH prospectively diagnosed on fetal MR imaging (true-positive finding). Axial T2 single-shot fast spin-echo imaging of the fetal brain at 25 weeks' GA (A) demonstrates multiple nodules along the ependymal surfaces of the lateral ventricles suspicious for SEH. Postnatal brain MR imaging at 5 weeks of age (B) confirms the presence of bilateral SEH on axial T2 FSE.

open spinal dysraphisms, 74.7% (65/87) had myelomeningoceles, while the remaining 25.3% (22/87) had myeloceles, defined as a neural placode flush with the skin surface.¹⁸ Eighty percent (76/95) of patients had significant ventriculomegaly (VMG) on fetal MR imaging, defined as the atria of the lateral ventricles measuring ≥ 10 mm in transverse diameter. This measurement was obtained in the axial plane at the level of the frontal horns or in the coronal plane at the level of the glomoid of the choroid plexus, analogous to previously established fetal sonography guidelines.¹⁹

Imaging Findings

In total, 23.2% (22/95) of the fetuses studied were suspected of having SEH on fetal MR imaging. The average GA of this group of patients at imaging was 25.47 ± 4.9 weeks. Of these fetuses, 50% (11/22) were confirmed as having at least 1 subependymal gray matter heterotopia on postnatal brain MR imaging (Fig 2). All 22 of these cases had VMG on fetal MR imaging. The average GA of the postnatally confirmed patients was 24.7 ± 4.7 weeks, while the average GA of the 11 patients that did not demonstrate SEH postnatally was 26.2 ± 5.3 weeks, a difference that was not statistically significant ($P = .49$).

The fetal MRIs of the examinations with false-positive findings were re-examined. Of the 11 fetuses in which SEH were initially noted on fetal MR imaging but not confirmed on postnatal brain MR imaging (false-positives), all 11 demonstrated identifiable areas of nodularity along the ependymal surfaces of the lateral ventricles on fetal MR imaging (Fig 3). The MRIs of the 11 fetuses with true-positive findings were also re-examined, and it was confirmed that SEH identified on the postnatal examination corresponded to ependymal nodularity in the same locations on fetal MR imaging in all 11 patients. However, 18.2% (2/11) of the fetuses with true-positive findings had additional areas of nodularity identified on fetal MR imaging that did not correspond to SEH on the postnatal examination.

On postnatal brain MR imaging, 28.4% (27/95) of patients demonstrated imaging findings consistent with SEH; 40.7% (11/27) of these patients were prospectively diagnosed on fetal MR imaging (true-positives). Of these, 70.4% (19/27) of neonates had ≥ 3 heterotopias identified postnatally, with 52.6%

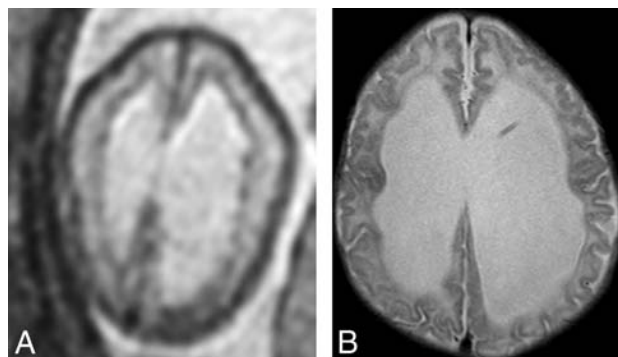


FIG 3. An example of subependymal nodularity giving the false appearance of SEH (false-positive finding). Axial T2 single-shot fast spin-echo image from fetal MR imaging at 24 weeks' GA (A) demonstrates nodularity along the ependymal surfaces of the lateral ventricles, giving the appearance of SEH. However, postnatal MR imaging at 8 weeks of age (B) does not demonstrate any SEH.

(10/19) being identified prospectively on fetal MR imaging. On the other hand, 29.6% (8/27) had 1–2 heterotopias identified on postnatal examination, with only 12.5% (1/8) identified prospectively on fetal MR imaging. Of the 16/27 fetuses having SEH confirmed postnatally but not identified prenatally (false-negative findings), 81.3% (13/16) had VMG on fetal MR imaging. On the other hand, 100% (11/11) of the fetuses with true-positive findings and 100% (11/11) of those with false-positive findings had VMG on fetal MR imaging. However, the actual mean transverse atrial diameter on fetal MR imaging of those with true-positive findings (16.6 ± 4.5 mm) was not significantly different from those with false-positive findings (15.6 ± 6.8 mm, $P = .69$) or false-negative findings (16.8 ± 7.6 mm, $P = .94$).

Average GA of the patients with SEH prospectively diagnosed (true-positive findings) was 24.7 ± 4.7 weeks, while the average GA of the fetuses with SEH not identified prenatally (false-negative findings) was 23.7 ± 3.1 weeks. The difference in GA was not found to be statistically significant ($P = .54$). To exclude the presence or absence of VMG as a confounding variable, we compared the GAs between only those with true-positive ($n = 11$, 24.7 ± 4.7 weeks) and false-negative ($n = 13$, 24.1 ± 3.3 weeks) findings with VMG and found no statistically significant difference ($P = .72$).

The fetal MRIs with SEH not identified on prenatal imaging but found on postnatal imaging (false-negatives), were also re-examined to determine whether they could be identified in retrospect. Of the 16 fetuses with false-negative findings, we were unable to identify the SEH on fetal MR imaging in 68.8% (11/16), even in retrospect. While 90.9% (10/11) of these cases were believed to have SEH too small to detect on fetal MR imaging, it was thought that fetal motion contributed to the lack of prenatal detection in 9.1% (1/11) of these patients. In the remaining 5 patients, in retrospect, mild nodularity was noted, which may have corresponded to the postnatal findings. However, in 2/5 of these patients, other areas of subependymal nodularity that did not correspond to SEH on postnatal imaging were identified (Fig 4). In addition, in 2/5 patients, the SEH were small on postnatal imaging, measuring as small as 1 mm and as large as 3 mm and were likely missed on fetal MR imaging because of their diminutive size. It is believed that in the

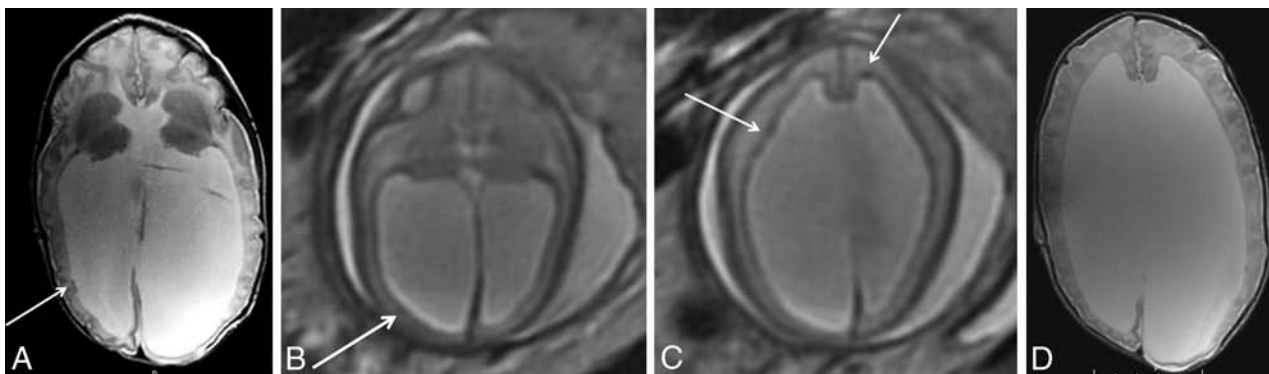


FIG 4. Example of a false-negative finding in a patient with SEH. Postnatal brain MR imaging at 15 days of age (A) demonstrates 2 small SEH along the right lateral ventricle (arrow) on axial T2 FSE imaging. In retrospect, there is some subtle asymmetric irregularity of the subependyma (arrow) on fetal MR imaging at 24 weeks' GA (B) on axial T2 single-shot fast spin-echo imaging. However, other areas of nodularity on fetal MR imaging in this patient (C, arrows) do not correspond to SEH postnatally (D).

remaining 1/5 patients with SEH identified postnatally, the lesion could not be detected prenatally because the location of the heterotopia identified in the right frontal horn was obscured prenatally due to motion artifact in this area.

DISCUSSION

We examined the accuracy of MR imaging in diagnosing SEH in fetuses with spinal dysraphism by looking at the data from our institution. We demonstrated that in our experience, fetal MR imaging is 40% sensitive and 50% specific in the diagnosis of SEH. We demonstrated a higher rate of VMG in cases with true-positive and false-positive findings than in those with false-negative findings. We also demonstrated a higher rate of false-negative findings when <3 heterotopias were identified postnatally. GA at the time of imaging did not appear to have a relationship with the sensitivity or specificity of diagnosing SEH.

A number of articles in the literature describe the appearance of SEH on fetal MR imaging.^{3,14,15,20,21} However, very few describe the diagnostic accuracy.^{17,22} The largest published series of 15 patients reported that fetal MR imaging was up to 73% sensitive and 100% specific for diagnosing SEH.¹⁷ Our study examined a much larger cohort of patients, increasing the validity of our findings. However, we focused on a specific population of patients, looking only at fetuses with prenatally diagnosed spinal dysraphisms; this type of search decreased the generalizability of our findings.

The relatively low sensitivity for detecting SEH on fetal MR imaging can be explained by multiple factors. First, although faster imaging techniques have largely eliminated the need for sedation during imaging, fetal MR images are still frequently compromised by fetal motion.²³ Second, differences in imaging techniques between pre- and postnatal imaging also contributed to low sensitivity. T2 single-shot fast spin-echo images are considered the workhorse of fetal MR imaging; however, the relative increased speed of imaging comes at the cost of decreased spatial resolution compared with the standard T2 FSE images used to image the brain postnatally.²³⁻²⁵ Although not yet well-studied, fetal MR imaging at 3T may improve spatial resolution through faster scanning times and a higher signal-to-noise ratio in future investigations.²⁶ Third, the very small size of fetal neuroanatomy also contributes to the decreased sensitivity of detecting SEH on

fetal MR imaging. Of note, GA at imaging did not appear to play a significant role in the accuracy of diagnosing SEH in our study. However, given that a large portion of the patients in our study were evaluated specifically for prenatal repair of a myelomeningocele, which is typically performed before 26 weeks' GA, this observation may not be generalizable.⁴

We also demonstrated a relatively low specificity in the diagnosis of SEH on fetal MR imaging, which is a little more difficult to explain. In our study, we looked at only patients with spinal dysraphisms, who have a much higher incidence of SEH than the general population and have other associated pathologies unique to the disease entity.^{7,27} The presence of ependymal nodularity on fetal MR imaging that does not correspond with SEH postnatally may potentially be explained by several factors. First, histologic studies in fetuses with open spinal dysraphisms have demonstrated neuroepithelial/ependymal denudation before the onset of hydrocephalus.²⁸ Thus, it is possible that the ependymal nodularity we see on fetal MR imaging is a reflection of this ependymal denudation demonstrated on histologic studies. We also suspect that hydrocephalus plays a role. The pathology literature in infants describes ventricular dilation correlating with discontinuities in the ependymal lining along with ependymal cell loss.²⁹ Histologic analysis of fetuses with hydrocephalus demonstrates loss of the germinal ependymal zone, disorganization of the subventricular zone, and abnormal migration of neuroblasts into the ventricular cavity.³⁰ Since there has been a potential link described between hydrocephalus and SEH because denudation of the neuroepithelium may cause disruption of the neuronal migrational pathways, it is possible that the nodules we see prenatally represent delayed migration of neurons that migrate later in pregnancy.³¹ On the other hand, in the presence of hydrocephalus, it is conceivable that migrational anomalies may develop later in gestation and then be apparent in the postnatal period.

The configuration of the germinal matrix on fetal MR imaging in healthy fetuses has been well-described and can potentially be used as one of the many markers in evaluating fetal brain maturation.³² It is also possible that hydrocephalus in patients with spinal dysraphisms disrupts the normal development and configuration of the germinal matrix, causing the

nodularity we see on fetal imaging. Of note, we did not appreciate any ependymal nodularity outside the SEH postnatally, which can be primarily explained by the relative absence of a germinal matrix. On the basis of our observations, we do not believe it is possible to differentiate SEH from ependymal irregularity related to other etiologies in fetuses with spinal dysraphism on MR imaging.

Our study adds to the current literature in many ways. First, it is one of the largest of its kind looking at this specific finding on fetal MR imaging, with direct comparison with the postnatal imaging findings. Second, given the increasing availability of prenatal repair of myelomeningoceles, studies examining the accuracy of MR imaging in the evaluation of the fetal brain are becoming essential.⁴⁻⁶ While there have been other studies that examined the sensitivity of fetal MR imaging in the diagnosis of SEH, this study is unique in that it reports the limited specificity and is the first to describe the appearance of ependymal nodularity on MR imaging in fetuses with spinal dysraphisms that does not correlate with SEH (or any other nodular periventricular/subependymal pathology) postnatally.^{17,22} On fetal MR imaging, the differential diagnosis for SEH includes tuberous sclerosis and subependymal hemorrhage.¹⁶ Our findings suggest that abnormal nodularity of the germinal matrix is another important differential consideration.

Our study has some limitations. First, this is a retrospective study limiting its internal validity. In addition, given that this is a single-institution study performed within a certain timeframe, the external validity may be limited as well. To acquire this number of patients for our study, we examined studies from a 10-year time span at our institution. These patients were scanned on different magnets and, because our scanners were upgraded multiple times over the years, minor differences in scanning parameters were used to optimize image quality, which may also affect our results.

CONCLUSIONS

Fetal MR imaging is limited in its ability to identify SEH in fetuses with spinal dysraphism. We believe that this limitation relates to a combination of factors: the sensitivity possibly compromised by artifacts from fetal motion, the very small size of fetal neuroanatomy, and the resolution of the fetal MR imaging technique. The specificity may be compromised by denudation of the ependyma and possibility irregularity of the germinal matrix by stretching of the developing ependyma/subependyma in the presence of VMG.

REFERENCES

1. Sonigo PC, Rypens FF, Carteret M, et al. **MR imaging of fetal cerebral anomalies.** *Pediatr Radiol* 1998;28:212–22 CrossRef Medline
2. Kline-Fath BM, Calvo-Garcia MA. **Prenatal imaging of congenital malformations of the brain.** *Semin Ultrasound CT MRI* 2011;32:167–88 CrossRef Medline
3. Glenn OA, Barkovich J. **Magnetic resonance imaging of the fetal brain and spine: an increasingly important tool in prenatal diagnosis—part 2.** *AJNR Am J Neuroradiol* 2006;27:1807–14 Medline
4. Adzick NS, Thom EA, Spong CY, et al; MOMS Investigators. **A randomized trial of prenatal versus postnatal repair of myelomeningocele.** *N Engl J Med* 2011;364:993–1004 CrossRef Medline
5. Saadai P, Farmer DL. **Clinics in perinatology: fetal surgery for myelomeningocele.** *Clin Perinatol* 2012;39:279–88
6. Sutton LN, Adzick NS, Bilaniuk LT, et al. **Improvement in hindbrain herniation demonstrated by serial fetal magnetic resonance imaging following fetal surgery for myelomeningocele.** *JAMA* 1999;282:1826–31 CrossRef Medline
7. Hino-Shishikura A, Niwa T, Aida N, et al. **Periventricular nodular heterotopia is related to severity of the hindbrain deformity in Chiari II malformation.** *Pediatr Radiol* 2012;42:1212–17 CrossRef Medline
8. Barkovich A, Kjos B. **Grey matter heterotopias: MR characteristics and correlation with developmental and neurologic manifestations.** *Radiology* 1992;182:493–99 CrossRef Medline
9. Barkovich AJ, Kuzniecky RI. **Gray matter heterotopia.** *Neurology* 2000;55:1603–08 Medline
10. Zajac-Mnich M, Kostkiewicz A, Guz W, et al. **Clinical and morphological aspects of gray matter heterotopia type developmental malformations.** *Polish J Radiol* 2014;79:502–07 CrossRef Medline
11. Mandelstam SA, Leventer RJ, Sandow A, et al. **Bilateral posterior periventricular nodular heterotopia: a recognizable cortical malformation with a spectrum of associated brain abnormalities.** *AJNR Am J Neuroradiol* 2013;34:432–38 CrossRef Medline
12. González G, Vedolin L, Barry B, et al. **Location of periventricular nodular heterotopia is related to the malformation phenotype on MRI.** *AJNR Am J Neuroradiol* 2013;34:877–83 CrossRef Medline
13. Manganaro L, Saldari M, Bernardo S, et al. **Bilateral subependymal heterotopia, ventriculomegaly and cerebellar asymmetry: fetal MRI findings of a rare association of brain anomalies.** *J Radiol Case Rep* 2013;7:38–45 CrossRef Medline
14. Meoded A, Turan S, Harman C, et al. **Pre- and postnatal ultrasound and magnetic resonance imaging of intracranial extra-axial glioneuronal heterotopia.** *Fetal Diagn Ther* 2011;30:314–16 CrossRef Medline
15. Righini A, Zirpoli S, Mrakic F, et al. **Early prenatal MR imaging diagnosis of polymicrogyria.** *AJNR Am J Neuroradiol* 2004;25:343–46 Medline
16. Mitchell LA, Simon EM, Filly RA, et al. **Antenatal diagnosis of subependymal heterotopia.** *AJNR Am J Neuroradiol* 2000;21:296–300 Medline
17. Glenn OA, Cuneo AA, Barkovich AJ, et al. **Malformations of cortical development: diagnostic accuracy of fetal MR imaging.** *Radiology* 2012;263:843–55 CrossRef Medline
18. Rufener SL, Ibrahim M, Raybaud CA, et al. **Congenital spine and spinal cord malformations: pictorial review.** *Am J Roentgenol* 2010;194(3 suppl):S26–37 CrossRef Medline
19. Melchiorre K, Bhide A, Gika AD, et al. **Counseling in isolated mild fetal ventriculomegaly.** *Ultrasound Obstet Gynecol* 2009;34:212–24 CrossRef Medline
20. Simon EM, Goldstein RB, Coakley FV, et al. **Fast MR imaging of fetal CNS anomalies in utero.** *AJNR Am J Neuroradiol* 2000;21:1688–98 Medline
21. Tang PH, Bartha AI, Norton ME, et al. **Agenesis of the corpus callosum: an MR imaging analysis of associated abnormalities in the fetus.** *AJNR Am J Neuroradiol* 2009;30:257–63 CrossRef Medline
22. Blondiaux E, Sileo C, Nahama-Allouche C, et al. **Periventricular nodular heterotopia on prenatal ultrasound and magnetic resonance imaging.** *Ultrasound Obstet Gynecol* 2013;42:149–55 CrossRef Medline
23. Prayer D, Brugger PC, Prayer L. **Fetal MRI: techniques and protocols.** *Pediatr Radiol* 2004;34:685–93 Medline
24. Dhoub A, Blondiaux E, Moutard ML, et al. **Correlation between pre- and postnatal cerebral magnetic resonance imaging.** *Ultrasound Obstet Gynecol* 2011;38:170–78 CrossRef Medline
25. Li T, Mirowitz SA. **Fast multi-planar gradient echo MR imaging: impact of variation in pulse sequence parameters on image quality and artifacts.** *Magn Reson Imaging* 2004;22:807–14 CrossRef Medline
26. Welsh RC, Nemec U, Thomason ME. **Fetal magnetic resonance imaging at 3.0 T.** *Top Magn Reson Imaging* 2011;22:119–31 CrossRef Medline

27. Miller E, Widjaja E, Blaser S, et al. **The old and the new: supratentorial MR findings in Chiari II malformation.** *Childs Nerv Syst* 2008; 24:563–75 Medline
28. De Wit OA, den Dunnen WF, Solle KM, et al. **Pathogenesis of cerebral malformations in human fetuses with meningomyelocele.** *Cerebrospinal Fluid Res* 2008;5:4 CrossRef Medline
29. Del Bigio MR. **Ependymal reactions to injury: a review.** *J Neuropathol Exp Neurol* 1995;54:1–15 Medline
30. Domínguez-Pinos MD, Páez P, Jiménez AJ, et al. **Ependymal denudation and alterations of the subventricular zone occur in human fetuses with a moderate communicating hydrocephalus.** *J Neuropathol Exp Neurol* 2005;64:595–604 Medline
31. Ferland RJ, Batiz LF, Neal J, et al. **Disruption of neural progenitors along the ventricular and subventricular zones in periventricular heterotopia.** *Hum Mol Genet* 2009;18:497–516 CrossRef Medline
32. Vossough A, Limperopoulos C, Putt ME, et al. **Development and validation of a semiquantitative brain maturation score on fetal MR images: initial results.** *Radiology* 2013;268:200–07 CrossRef Medline

Asymptomatic Interhypothalamic Adhesions in Children

F.N. Ahmed, N.V. Stence, and D.M. Mirsky

ABSTRACT

SUMMARY: With the use of high-resolution MR imaging techniques, we have increasingly observed anomalies of the hypothalamus characterized by a band of tissue spanning the third ventricle between the hypothalami, often without associated clinical sequelae. Historically, hypothalamic anomalies are highly associated with symptoms referable to a hypothalamic hamartoma, midline congenital disorder, hypothalamic-pituitary dysfunction, or seizures, with very few asymptomatic patients reported. The interhypothalamic tissue described in our cohort was observed incidentally through the routine acquisition of high-resolution T1WI. No referable symptoms were identified in most of the study group. In the appropriate patient population in which associated symptoms are absent, the described hypothalamic anomalies may be incidental and should not be misdiagnosed as hypothalamic hamartomas.

ABBREVIATIONS: GMH = gray matter heterotopia; IHA = interhypothalamic adhesion

Anomalies of the hypothalamus have generally been thought to come in 2 forms, hypothalamic hamartoma or hypothalamic dysgenesis associated with midline congenital disorders such as holoprosencephaly spectrum or septo-optic dysplasia.¹⁻³ Classically, hypothalamic abnormalities are associated with symptoms of central endocrinologic dysfunction and/or seizures. Few asymptomatic patients have been reported.⁴⁻⁸ Most of these cases were associated with other disorders, such as neurofibromatosis type 1.⁹

With the routine use of high-resolution, isotropic T1 imaging, we have observed a thin band of tissue connecting the medial hypothalamic regions, spanning the anterior recess of the third ventricle, in a group of patients lacking symptoms of diencephalic dysfunction. This finding was recently described in 2 separate case series as an interhypothalamic adhesion (IHA).^{4,5} In these articles, however, IHAs were commonly associated with multiple congenital anomalies. Our objective was to analyze the MRI of our patient cohort with IHA and correlate these findings with

other brain anomalies and clinical presentations to determine the significance, if any, of this finding.

MATERIALS AND METHODS

After institutional review board approval, the case file data base of Children's Hospital Colorado was searched for patients identified with hypothalamic anomalies on MR imaging between 2009 and 2014. All imaging was performed at Children's Hospital Colorado on a variety of MR imaging systems, including Avanto 1.5T (Siemens, Erlangen, Germany), Achieva 1.5T (Philips Healthcare, Best, the Netherlands), and Ingenia 1.5T or 3T (Philips Healthcare). Images were reviewed by 2 pediatric neuroradiologists (D.M.M. and N.V.S.) for a band of tissue spanning the third ventricle connecting the medial portions of the hypothalamus. Other structural abnormalities were also recorded, including lack of midline cleavage, pituitary anomalies, and cortical malformations. The band of tissue was measured on MR imaging and, as performed in a previously published smaller case series, the possible nuclei involved in the hypothalamic connection were inferred from the segmentation scheme devised by Lemaire et al¹⁰ on the basis of anatomic landmarks.⁵

Hypothalamic dysfunction was surmised from history and clinical symptoms. The patients' charts were reviewed by using the Epic electronic medical record system (Epic Systems, Madison, Wisconsin) at Children's Hospital Colorado for their medical history and symptomology. Patients were then characterized into 3 groups: 1) no symptoms referable to the hypothalamus, 2) symptoms that could be associated with the hypothalamus, and 3) symptoms of indeterminate relevance to the hypothalamus.

Received August 7, 2015; accepted after revision September 20.

From the Department of Radiology (F.N.A.), University of Colorado Anschutz Medical Campus, Aurora, Colorado; and Department of Radiology (N.V.S., D.M.M.), Children's Hospital Colorado, Aurora, Colorado.

Paper previously presented as a poster ("Interhypothalamic Adhesion in Asymptomatic Children") at: American Society of Neuroradiology Annual Meeting and the Symposium of the ASNR Foundation, April 25–30, 2015; Chicago, Illinois.

Please address correspondence to David M. Mirsky, MD, Department of Radiology, Children's Hospital Colorado, 13123 East 16th Ave, Box B125, Aurora, CO 80045; e-mail: David.Mirsky@childrenscolorado.org

<http://dx.doi.org/10.3174/ajnr.A4602>

Both symptomatic groups (those with symptoms possibly attributable to the hypothalamus and symptoms of uncertain relationship to the hypothalamus) were then treated as 1 cohort.

RESULTS

The inclusion criteria from the case file data base resulted in 60 patients. Three were excluded because they had a diagnosis of

neurofibromatosis, which has been reported in association with hypothalamic hamartomas.⁹ This exclusion resulted in a study cohort of 57 patients of equal sex distribution, ranging in age from 5 days to 20 years (mean age, 7.3 years). MR imaging indications for the group included vertigo, concussion, trauma, tongue hypertrophy, seizures, developmental delays, visual problems, and premature birth. See Table 1 for complete demographic details and indications.

In all cases, the hypothalamic anomaly consisted of a band of tissue spanning the anterior recess of the third ventricle, which appeared linear in the axial and coronal planes and nodular in the sagittal plane (Fig 1). In all patients, the band of tissue was T2 isointense to gray matter and did not contact the mammillary bodies or extend below the tuber cinereum.

The average volume of the hypothalamic connection was 59.2 mm³, with asymptomatic patients having an average volume of 48.8 mm³, and symptomatic ones having an average volume of 78.0 mm³ ($P = .035$). In most cases, the band of tissue closely approximated the dorsomedial hypothalamic nuclei, followed by the ventromedial hypothalamic nuclei (Fig 2).

Of the 57 patients with IHAs, 18 had otherwise normal MR imaging examinations. Twenty-three had gray matter heterotopia (GMH). Four had findings consistent with septo-optic dysplasia. Chiari malformations were present in 3 patients, 2 with Chiari I and 1 with Chiari II. Abnormalities of the septum pellucidum were present in 7 individuals. Complete imaging findings are described in Table 2.

Forty of the 57 patients had no clinical symptoms referable to their IHA. The IHA was considered an incidental finding in these cases and documented as such in their medical charts. Of these, 18

Table 1: IHA demographics and imaging indications of the cohort

	No Referable Symptoms	Symptomatic	P Value
Total	40	17	
Demographics			
Male	20	7	.54
Female	20	10	.54
Average age (yr)	6.1	10.2	.30
Age range	8 Days to 20 years	11 Months to 17 years	
Imaging indication			
Seizures	9	5	.58
Developmental delays	8	3	.84
Headaches/migraines	4	0	.18
Vision problems	4	1	.62
Hearing problems	2	0	.35
Trauma	2	0	.35
Chiari diagnosed in utero	2	0	.35
Short stature	1	2	.15
Fetal alcohol syndrome	1	1	.53
Other	8 ^a	5 ^b	

^a Tongue hemihypertrophy, myelomeningocele, scalp mass, Horner syndrome, multiple sclerosis, lower extremity pain, and spasms.

^b Craniosynostosis, hydrocephalus on fetal ultrasound, panhypopituitarism, and hypothyroidism.

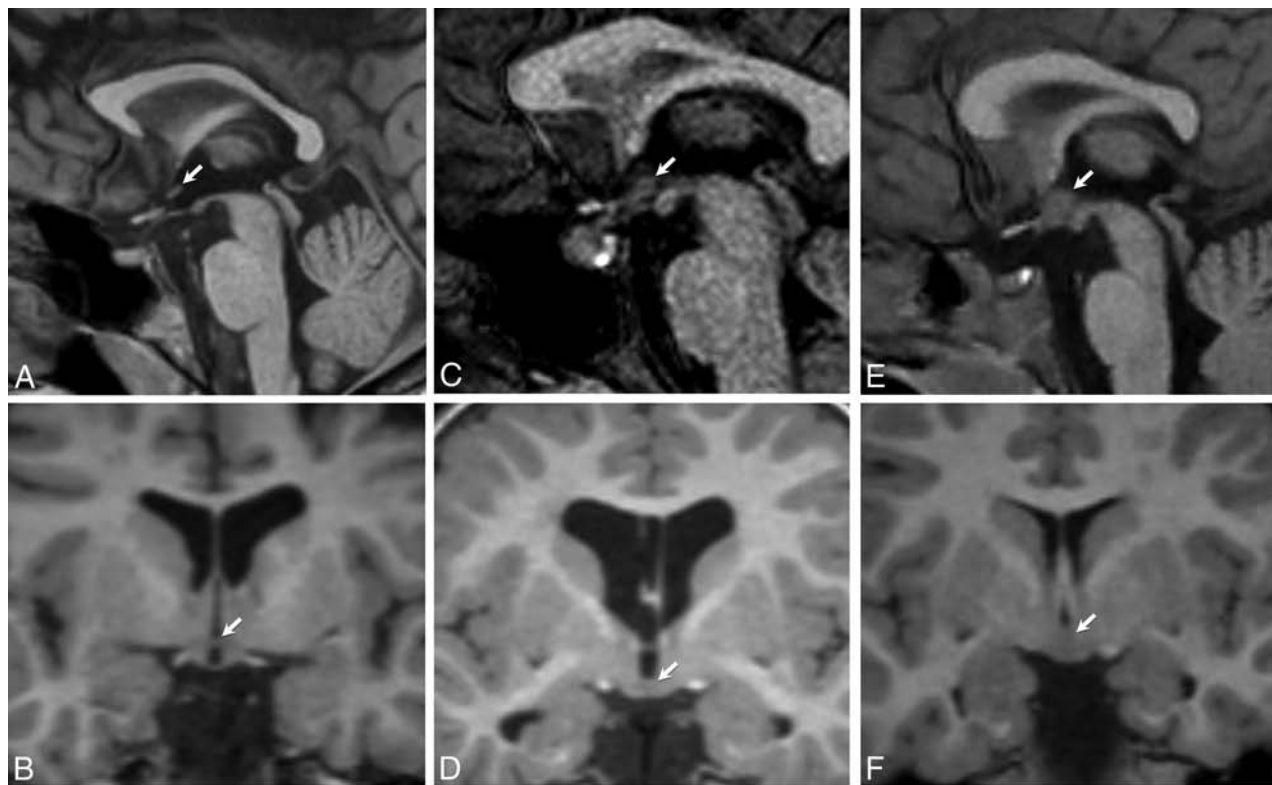


FIG 1. A band of tissue spanning the anterior recess of the third ventricle that appeared linear in the axial and coronal planes and nodular in the sagittal plane as seen on 3T T1WI. A and B, A flat band of tissue behind the lamina terminalis. C and D, A flat band of tissue above the tuber cinereum. E and F, A nodular band of tissue contacting both lamina terminalis and tuber cinereum.



FIG 2. Position maps of the interhypothalamic adhesions. A, All IHAs in our study. B, Asymptomatic IHAs. C, Symptomatic IHAs.

Table 2: Imaging characteristics of the cohort: structural features by imaging

	No Referable Symptoms	Symptomatic	P Value
IHA volume (mm ³)	48.8	78	.04
Otherwise normal	14	4	.39
Gray matter heterotopias	17	6	.61
Septo-optic dysplasia	0	4	.001
Chiari malformation	3	0	.25
Periventricular leukomalacia	2	1	.89
Neoplasm	2	0	.35
Polymicrogyria	0	1	.12
Other	8 ^a	6 ^b	

^a Dilated perivascular spaces, multiple sclerosis with a velum interpositum, right cochlear nerve hypoplasia, right cerebral closed lip schizencephaly, vermian hypoplasia, sinus pericranii, and 2 isolated cases of cavum septum pellucidum.

^b Abnormal sulcation, transmantle cortical dysplasia, frontonasal dysplasia, inferior vermian hypoplasia with absent septum pellucidum, cavum septum pellucidum (with septo-optic dysplasia), and velum interpositum.

Table 3: Clinical symptoms of the cohort

	No Referable Symptoms	Symptomatic	P Value
Healthy	18 ^a	0	<.01
Seizures	9 ^b	5	.58
Endocrine problems	0	3	<.01
Mild developmental delays	8	6	.22
Severe developmental delays	0	8	<.01
Heart anomalies	3	0	.25
Sensory hearing loss	2	0	.35
Premature birth ^b	5	2	.94

^a Four of these individuals had initially presented with headaches, and 1, with vertigo, all considered to be isolated issues without ongoing symptoms at the time of this review. All 3 individuals with Chiari malformations were included in the group lacking referable symptoms. Two additional patients had presented with trauma and were healthy after their other musculoskeletal injuries healed. Two more of these patients were evaluated for unilateral sensory hearing loss but were considered clinically healthy otherwise. An individual with a low-grade glial neoplasm had originally presented with a seizure but had no other symptoms after resection. One individual with multiple sclerosis had 2 episodes of lower extremity weakness and tingling that had resolved. The remaining patients lacking symptoms referable to the IHA had presenting symptoms that resolved with treatment or conservative measures (tongue hemihypertrophy with an arteriovascular malformation, scalp mass [sinus pericranii], Horner syndrome, lower extremity pain, and spasms).

^b Born at 26–34 weeks' gestation.

patients were completely asymptomatic at last follow-up and were considered healthy. Of the 17 symptomatic patients, 8 individuals had symptoms that could be attributable to an IHA while 9 had nonlocalizable symptoms. Complete clinical findings are described in Table 3.

Fourteen patients of the entire cohort of 57 had persistent seizures. Nine of these patients were thought to lack symptoms referable to the IHA; 8 had an epileptic focus identified on electroencephalography outside the hypothalamus, and the ninth had seizures thought to be related to a pineoblastoma. The remaining 5 patients with seizures had no identifiable focus (3 individuals) or other global deficits (2 individuals) and were included in the symptomatic group. No patient had gelastic seizures.

Three patients with endocrine dysfunction were placed in the symptomatic category because causation could not be decided with certainty. One of these patients had delayed puberty and short stature; another presented with dwarfism, growth hormone deficiency, and Duchenne muscular dystrophy variant; and the third presented with central hypothyroidism.

Mild developmental delays (as determined by chart review when growth and verbal and/or reading milestones were not met) were present in 14 individuals. Eight of these patients were thought to lack symptoms definitely referable to the IHA, while the others had indeterminate symptoms, endocrine problems, or nonlocalizable seizures.

Eight patients had severe developmental delays documented in the medical record and were all categorized into the symptomatic group. Findings of 4 of these individuals were on the septo-optic dysplasia spectrum, which has been previously correlated with IHAs.¹¹

DISCUSSION

Interhypothalamic adhesion has been defined as a linear band of tissue spanning the medial hypothalamic walls, similar in appearance to the normal interthalamic adhesion. Only 2 reports in the literature describe this entity.^{4,5} The first report in 2013 characterized a single patient presenting with IHA in association with a cleft palate deformity.⁴ The second report in 2014 was a case series of 13 patients in which most IHAs were thought to be associated with other midline structural abnormalities. In our cohort of 57 patients, 40 (70%) lacked clinical symptoms referable to the hypothalamus. Furthermore, after careful scrutiny, 14 of those 40 individuals had otherwise normal brains. None had midline developmental defects including but not limited to hippocampal dysgenesis or under-rotation, hypoplastic falx, olfactory hypoplasia, and optic pathway hypoplasia. In most of our patients, IHA represented an isolated finding that was thought to be of no clinical significance.

Most IHAs in our cohort closely approximated the dorsomedial and ventromedial nuclei of the hypothalamus, similar to the

2014 report⁴; however, we have no pathologic evidence of true involvement of these nuclei. It is possible that this tissue merely bridges the medial surfaces of the hypothalamus. In the literature, human hypothalamic development is not well-understood, and information about it relies heavily on animal studies.^{12–14} A pathologic observational study done by Koutcherov et al¹⁴ described a transient midline hypothalamic structure observed during fetal development. No other midline hypothalamic structure has been described. IHAs may represent a focus of failed apoptosis versus migration or accessory hypothalamic tissue. The lack of evidence of hypothalamic-pituitary axis dysfunction or seizures in most patients, in and of itself in our cohort, suggests that the band of tissue is often not of clinical or pathologic significance.

Gray matter heterotopia was discovered in 23 of 57 patients (40%) in our IHA cohort. Of these patients, 17 had subependymal heterotopia, 3 had focal subcortical heterotopia, and 3 had band heterotopia. The coexistence of IHA and GMH in our population suggests that the combination may be part of an, as of yet, undescribed genetic disorder. This also raises the possibility that an IHA may be a rest of neuronal tissue from failed migration. The clinical relevance of both findings remains uncertain, particularly because 6 of our patients with both IHA and GMH were completely asymptomatic and midline anomalies were absent in most patients.

Distinguishing IHA from other hypothalamic pathology, such as hamartoma or glioma, requires high-resolution imaging in all 3 planes. In the sagittal plane, both IHA and hamartomas can appear nodular or masslike. IHAs, however, span the hypothalamic medial regions as a linear band of tissue in the axial and coronal planes, while a hamartoma is typically nodular in all 3 planes. Furthermore, a hamartoma often involves one of the hypothalamic surfaces asymmetrically more than the other and often contacts or invades the mammillary bodies. IHAs symmetrically involve the hypothalamic walls and do not contact the mammillary bodies. Hypothalamic gliomas are easier to distinguish because they are typically not isointense to gray matter and often enhance following contrast administration. One potential pitfall that could lead to misdiagnosis of IHA is a diminutive third ventricle, where the opposed medial surfaces of the hypothalamus can mimic a hypothalamic anomaly in the sagittal plane. In our experience, this occurs most frequently in patients with a ventriculoperitoneal shunt and decompressed ventricles. High-resolution imaging in all 3 planes avoids this confusion because the pseudolesion will not be verified in the axial and coronal planes.

Our study is limited by its retrospective bias. The available medical records limit assessment of clinical symptoms because no direct evaluation of subjects could be performed. Because an IHA is a subtle finding, it could have been easily overlooked and omitted from our case file data base and cases of IHA could have been missed. Findings in our cohort cannot suggest incidence, and they are likely an underrepresentation of the true prevalence of IHAs.

CONCLUSIONS

Interhypothalamic adhesions are observed incidentally through the routine acquisition of high-resolution T1 imaging. In our cohort, most patients had no symptoms referable to the hypothalamus

and the finding was made in the absence of other structural abnormalities, specifically midline defects. Because the anomaly is subtle and primarily apparent on isotropic T1 imaging, it is under recognized, especially because smaller IHAs are more likely to be asymptomatic. However, as high-resolution MR imaging techniques become more routinely used, IHAs are likely to be increasingly identified and should prompt detailed scrutiny for additional brain malformation. Although the underlying etiology is unclear, it may be the result of incomplete hypothalamic cleavage, failed apoptosis, or abnormal neuronal migration, the latter being potentially more likely, given the association we found with GMH. While associations between IHAs and other syndromes likely exist, in the appropriate patient population lacking referable symptoms and with few or no other structural abnormalities, interhypothalamic adhesions may be incidental and of no clinical significance.

Disclosures: Farres N. Ahmed—RELATED: Support for Travel to Meetings for the Study or Other Purposes: The University of Colorado Radiology Department partially supported travel and meeting and hotel fees to present the poster at the 2015 ASNR meeting. This is part of the resident travel funds.

REFERENCES

1. Simon EM, Hevner RF, Pinter JD, et al. **Assessment of the deep gray nuclei in holoprosencephaly.** *AJNR Am J Neuroradiol* 2000;21: 1955–61 Medline
2. Simon EM, Hevner RF, Pinter JD, et al. **The middle interhemispheric variant of holoprosencephaly.** *AJNR Am J Neuroradiol* 2002;23: 151–56 Medline
3. Barkovich, AJ, Raybaud C. *Pediatric Neuroimaging.* Philadelphia: Wolters Kluwer Health/Lippincott Williams & Wilkins; 2012
4. Whitehead MT, Angel JD. **Interhypothalamic adhesion in a 9-month-old male with cleft palate.** *Case Rep Radiol* 2013;2013: 197415 CrossRef Medline
5. Whitehead MT, Vezina G. **Interhypothalamic adhesion: a series of 13 cases.** *AJNR Am J Neuroradiol* 2014;35:2002–06 CrossRef Medline
6. Arita K, Ikawa F, Kurisu K, et al. **The relationship between magnetic resonance imaging findings and clinical manifestations of hypothalamic hamartoma.** *J Neurosurg* 1999;91:212–20 CrossRef Medline
7. Debeneix CL, Bourgeois M, Trivin C, et al. **Hypothalamic hamartoma: comparison of clinical presentation and magnetic resonance images.** *Horm Res* 2001;56:12–18 CrossRef Medline
8. Jung H, Neumaier Probst E, Hauffa BP, et al. **Association of morphological characteristics with precocious puberty and/or gelastic seizures in hypothalamic hamartoma.** *J Clin Endocrinol Metab* 2003;88: 4590–95 CrossRef Medline
9. Acosta MT, Walsh KS, Kardel PG, et al. **Cognitive profiles of neurofibromatosis type 1 patients with minor brain malformations.** *Pediatr Neurol* 2012;46:231–34 CrossRef Medline
10. Lemaire JJ, Nezzar H, Sakka L, et al. **Maps of the adult human hypothalamus.** *Surg Neurol Int* 2013;4(suppl 3):S156–63 CrossRef Medline
11. Byerly MS, Blackshaw S. **Vertebrate retina and hypothalamus development.** *Wiley Interdiscip Rev Syst Biol Med* 2009;1:380–89 CrossRef Medline
12. Markakis EA. **Development of the neuroendocrine hypothalamus.** *Front Neuroendocrinol* 2002;23:257–91 CrossRef Medline
13. Roessler E, Du YZ, Mullor JL, et al. **Loss-of-function mutations in the human GLI2 gene are associated with pituitary anomalies and holoprosencephaly-like features.** *Proc Natl Acad Sci U S A* 2003;11: 13424–29 Medline
14. Koutcherov YI, Mai JK, Ashwell KW, et al. **Organization of human hypothalamus in fetal development.** *J Comp Neurol* 2002;446: 301–24 CrossRef Medline

Increased Facet Fluid Predicts Dynamic Changes in the Dural Sac Size on Axial-Loaded MRI in Patients with Lumbar Spinal Canal Stenosis

H. Kanno, H. Ozawa, Y. Koizumi, N. Morozumi, T. Aizawa, and E. Itoi

ABSTRACT

BACKGROUND AND PURPOSE: Axial-loaded MR imaging, which simulates the spinal canal in a standing position, demonstrates reductions of the dural sac cross-sectional area in patients with lumbar spinal canal stenosis. However, there has been no useful conventional MR imaging finding for predicting a reduction in the dural sac cross-sectional area on axial-loaded MR imaging. Previous studies have shown that increased facet fluid is associated with the spinal instability detected during positional changes. The purpose of this study was to analyze the correlations between facet fluid and dynamic changes in the dural sac cross-sectional area on axial-loaded MR imaging.

MATERIALS AND METHODS: In 93 patients with lumbar spinal canal stenosis, the dural sac cross-sectional area was measured by using axial images of conventional and axial-loaded MR imaging. Changes in the dural sac cross-sectional area induced by axial loading were calculated. The correlation between the facet fluid width measured on conventional MR imaging and the change in dural sac cross-sectional area was analyzed. The change in the dural sac cross-sectional area was compared between the intervertebral levels with and without the facet fluid width that was over the cutoff value determined in this study.

RESULTS: The dural sac cross-sectional area was significantly smaller on axial-loaded MR imaging than on conventional MR imaging. The facet fluid width significantly correlated with the change in the dural sac cross-sectional area ($r = 0.73$, $P < .001$). The change in the dural sac cross-sectional area at the intervertebral level with the facet fluid width over the cutoff value was significantly greater than that at the other level.

CONCLUSIONS: The increased facet fluid on conventional MR imaging is highly predictive of the dynamic reduction of dural sac cross-sectional area detected on axial-loaded MR imaging in the clinical assessment of lumbar spinal canal stenosis.

ABBREVIATIONS: DCSA = dural sac cross-sectional area; LSCS = lumbar spinal canal stenosis; ROC = receiver operating characteristic

MR imaging is widely used for the clinical assessment of degenerative lumbar spinal diseases. In evaluating the severity of spinal canal narrowing, the dural sac cross-sectional area (DCSA) is frequently measured by using axial MR images.¹⁻⁶ However, conventional MR imaging is performed with the patient in the supine position, and the DCSA may be larger in this position than in the standing position.^{3,4,7} Hence, conventional

MR imaging carries a risk of underestimating the severity of spinal canal narrowing.^{3,8}

Recently, the clinical usefulness of axial-loaded MR imaging for assessing patients with lumbar spinal canal stenosis (LSCS) has been reported.^{3,4} With axial-loaded MR imaging, physiologically normal weight-bearing conditions in the upright position can be simulated by using a compression device with the patient in the supine position. Axial-loaded MR imaging may induce a significant reduction in the DCSA and potentially show additional imaging findings that cannot be acquired on conventional MR imaging.^{3,4,6,8} The DCSA on axial-loaded MR imaging has been reported to correlate with the severity of clinical symptoms in patients with LSCS.⁹ Furthermore, previous studies have demonstrated that a dynamic decrease in the DCSA induced by axial loading increases the diagnostic specificity of spinal canal narrowing and influences the indications for surgical treatment.^{4,8,10,11} Therefore, evaluating the degree of spinal canal narrowing on axial-loaded MR imaging is beneficial for achieving a more accurate diagnosis and selecting the optimal treatment. However, no

Received June 16, 2015; accepted after revision August 18.

From the Department of Orthopedic Surgery (H.K., H.O., T.A., E.I.), Tohoku University School of Medicine, Sendai, Japan; and Department of Orthopedic Surgery (Y.K., N.M.), Sendai Nishitaga National Hospital, Sendai, Japan.

This work is supported by a research grant from the Japan Orthopaedics and Traumatology Foundation, Inc (No. 205).

Paper previously presented at: Annual Meeting of the Spine Society of Europe, October 1-3, 2014; Lyon, France.

Please address correspondence to Haruo Kanno, MD, PhD, Department of Orthopaedic Surgery, Tohoku University School of Medicine, 1-1 Seiryō-machi, Aoba-ku, Sendai, 980-8574, Japan; e-mail: kanno-h@isis.ocn.ne.jp

<http://dx.doi.org/10.3174/ajnr.A4582>

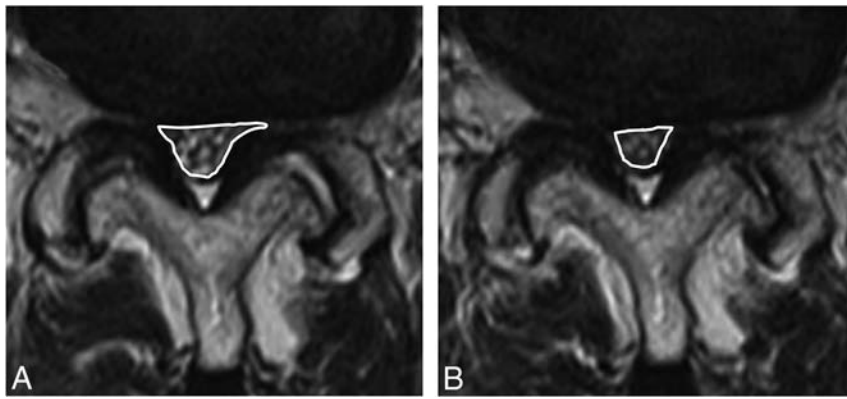


FIG 1. Measurement of the DCSA on conventional MR imaging and axial-loaded MR imaging in a representative case. The *white lines* indicate the outlines of the DCSA. The DCSA changed from 67 (A) to 41 mm² (B) due to axial loading.

reliable imaging findings on conventional MR imaging predict the dynamic reduction in the DCSA.

Many previous studies have shown that the morphology of the facet joints is associated with the segmental motion and instability of the lumbar spine detected during positional changes in the patient.^{12–15} Most interesting, recent studies have suggested that increased fluid signals in the facet joint on conventional MR images predict instability of the lumbar spine.^{16–19} Therefore, in the present study, we hypothesized that increased facet fluid signals on conventional MR images may be correlated with significant changes in the DCSA on axial-loaded MR images because the lumbar spinal canal is more likely to be affected by axial loading if the lumbar spine is unstable.

To the best of our knowledge, no previous studies have investigated the correlation between the facet fluid width and dynamic changes in the DCSA induced by axial loading. The purpose of this study was thus to analyze the correlation between the facet fluid width and dynamic changes in the DCSA detected by using axial-loaded MR imaging in patients with LSCS.

MATERIALS AND METHODS

Patients

This study prospectively included 93 consecutive patients (33 women and 60 men) referred to Sendai Nishitaga National Hospital for surgical treatment. The consecutive patients were enrolled in this study conducted between October 2007 and November 2009. All of the patients had neurogenic intermittent claudication and leg pain or numbness with associated neurologic signs,²⁰ in addition to radiographically confirmed lumbar spinal canal narrowing on cross-sectional imaging. In all cases, the neurologic diagnosis, such as lumbar radiculopathy and/or cauda equina syndrome,^{21,22} was confirmed by >1 spine surgeon on the basis of clinical symptoms (eg, intermittent claudication, leg pain/numbness, and/or dysuria), neurologic findings (eg, muscle weakness, sensory disturbance, and/or abnormal tendon reflex), and imaging features, including assessments with plain radiography, CT, and MR imaging of the lumbar spine. The exclusion criteria were previous lumbar spine surgery, spondylolysis, disc herniation, severe osteoporosis, scoliosis, polyneuropathy, arterial insufficiency, and inflammatory/crystalline arthropathies.

Patients with congenital spinal anomalies and spinal deformities due to spinal trauma, infection, or tumor were also excluded. The institutional review board of Sendai Nishitaga National Hospital approved this study, and informed consent was obtained from all patients before participation. At the time of the initial evaluation, baseline characteristics, including age, sex, height, body weight, body mass index, and duration of symptoms, were registered for each patient.

Conventional MR Imaging and Axial-Loaded MR Imaging

MR imaging was performed by using a 1.5T system (Magnetom Vision; Siemens, Erlangen, Germany) with a spine array coil. Axial T2-weighted turbo spin-echo sequences were obtained. The TR and TE were 4000 and 120 ms, the section thickness was 4 mm, and the FOV was 200 mm. The images were obtained at the middle of each intervertebral disc from L2–3 to L5–S1.^{7,9,23} The axial sections were placed as parallel to the intervertebral discs as possible by using sagittal T2-weighted imaging.

After the conventional MR imaging examination, axial loading was applied by using an external, commercially available non-magnetic compression device, DynaWell L-Spine (DynaWell Diagnostics, Las Vegas, Nevada).^{3,4} The compression force was approximately 50% of the patient's body weight, and loading was commenced 5 minutes before and continued during the MR imaging examination. Using a new sagittal T2-weighted image obtained in the axially loaded position, we again placed the axial sections in the plane of each disc. Both the axial-loaded and non-loaded MR images were acquired with straight knees to simulate a normal upright position.^{7,24} To prevent flexion of the spine during axial loading, we placed a cushion behind the lumbar spine.^{7,25}

Measurements of the DCSA and Facet Fluid Width

All measurements were obtained by using the OsiriX Imaging Software program, Version 2.7 (<http://www.osirix-viewer.com>). The DCSA was measured from L2–3 to L5–S1 on the axial images (Fig 1). The measurements were acquired 3 times, and the mean value was calculated and used for the analysis. The measurements were performed by an experienced spine surgeon authorized by the Japanese Orthopaedic Association; the experimenter was blinded to which images were loaded or unloaded. The inter- and intraobserver reliability for the measurement of the DCSA was confirmed as excellent in our previous study.^{9,23} On the basis of the findings of previous studies,^{1,7,9,23} the DCSA at the most constricted intervertebral level was used to represent the degree of the spinal canal narrowing in each subject. The most constricted intervertebral level that presented with the smallest DCSA on conventional MR imaging was selected in each case for the data analysis.

According to previous reports,^{15,17} the facet fluid was defined as a high-intensity-signal area, closely matched to CSF on the axial

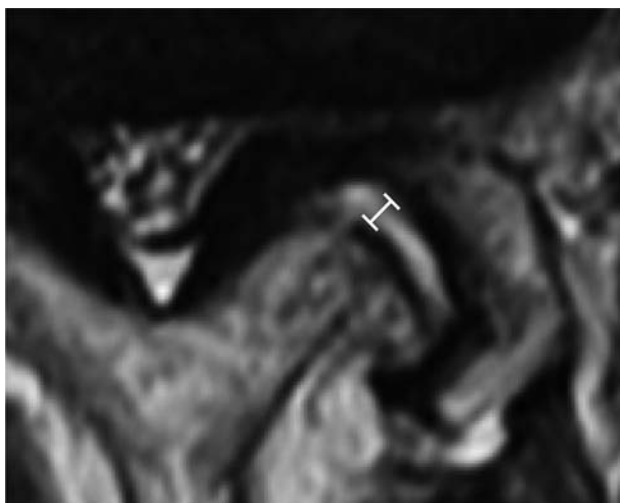


FIG 2. Measurement of the facet fluid width. The facet fluid width is defined as a high-intensity signal area, closely matched to the CSF on axial T2-weighted MR images. The measurements are recorded perpendicular to the joint line, and the largest value is documented as the facet fluid width (white line).

T2-weighted images obtained with conventional MR imaging. The facet fluid width was measured at the most constricted intervertebral level. The measurements were recorded perpendicular to the joint line, and the largest value was documented as the facet fluid width (Fig 2).^{15,17} The average of bilateral facet fluid width values was calculated for each patient and used for the data analysis.

This study also investigated the changes in the DCSA and the facet fluid width at normal or less severely stenotic intervertebral levels in the same subjects to compare with those at the narrowest level. One of the intervertebral levels excluding the narrowest level was randomly selected in each patient to prevent potential selection bias and increase comparability among the different intervertebral levels; then, the DCSA and the facet fluid width at the selected intervertebral level were determined as described above.

Data Analysis

The DCSA values were statistically compared between the conventional MR imaging and axial-loaded MR imaging. In addition, the changes in the DCSA between the conventional and axial-loaded MR imaging were calculated. The Pearson correlation coefficient between the change in the DCSA and the facet fluid width was analyzed.

On the basis of the results of previous studies, a $>15 \text{ mm}^2$ change in the DCSA induced by axial loading was defined as a significant change,^{3,4,8,11} worsening the severity of the clinical symptoms.⁹ The cutoff value for the facet fluid width providing the best combination of sensitivity and specificity for detecting a $>15 \text{ mm}^2$ change in the DCSA at the most constricted intervertebral level was determined by using a receiver operating characteristic (ROC) analysis. The area under the ROC curve was also determined to evaluate the diagnostic power.

We confirmed the diagnostic capacity of the cutoff value for the facet fluid width determined according to the ROC analysis. All of the narrowest levels were divided into 2 groups: with facet fluid width over or under the cutoff value. Then, the DCSA on

Table 1: Baseline characteristics (n = 93)^a

Characteristic	
Age (yr)	68 ± 10
Sex (male)	65%
Height (cm)	160 ± 9
Body weight (kg)	64 ± 11
BMI (kg/m ²)	25 ± 3
Duration of symptoms (mo)	32 ± 33
The most constricted level	
L2–L3	1%
L3–L4	20%
L4–L5	71%
L5–S1	8%

Note:—BMI indicates body mass index.

^a Values are means or percentages.

conventional and axial-loaded MR imaging and the changes in the DCSA were compared between the groups.

To evaluate coexisting degenerative changes in the lumbar spine that may affect the facet fluid width and the spinal canal narrowing, we investigated the prevalence of a $\geq 3\text{-mm}$ spondylolisthesis on x-rays in the standing position²³ and the degree of disc degeneration on the T2-weighted sagittal MR images²⁶ and statistically compared them between the 2 groups.

Statistical Methods

All statistical analyses were performed by using GraphPad Prism software, Version 4.0c (GraphPad Software, San Diego, California). The differences in the DCSA were analyzed by using the unpaired *t* test. Pearson correlation coefficients between the facet fluid width and the change in the DCSA were determined. The prevalence of the spondylolisthesis and the degree of disc degeneration were compared by using the χ^2 test. A *P* value $< .05$ was statistically significant.

RESULTS

Baseline Characteristics and DCSA Values in All Patients

The baseline characteristics and the most constricted intervertebral level in all patients are summarized in Table 1. The most constricted level was more frequently observed at L3–L4 (20%) and L4–L5 (71%) levels compared with the L2–3 (1%) and L5–S1 (8%) levels. The DCSA on axial-loaded MR imaging ($45 \pm 29 \text{ mm}^2$) was significantly smaller than that observed on conventional MR imaging ($57 \pm 28 \text{ mm}^2$) at the most constricted level ($P < .05$) (Fig 3A). At the other intervertebral levels excluding the most constricted level, the DCSA on axial-loaded MR imaging ($107 \pm 41 \text{ mm}^2$) was significantly smaller compared with that on conventional MR imaging ($101 \pm 40 \text{ mm}^2$) ($P < .05$) (Fig 3B). The change in the DCSA at the most constricted level ($13 \pm 23 \text{ mm}^2$) was greater than that at the other levels ($6 \pm 7 \text{ mm}^2$).

Correlation between the Facet Fluid Width and the Changes in the DCSA

The values for the facet fluid width and changes in the DCSA for each patient are shown in Fig 4. The narrowest intervertebral levels with a greater facet fluid width generally showed larger changes in the DCSA (Fig 4A). According to the Pearson correlation analysis, there was a significant and good correlation between the facet fluid width and the change in the DCSA ($r = 0.73$, $P < .001$) (Fig 4A). In contrast, at the other intervertebral levels, there was a poor correla-

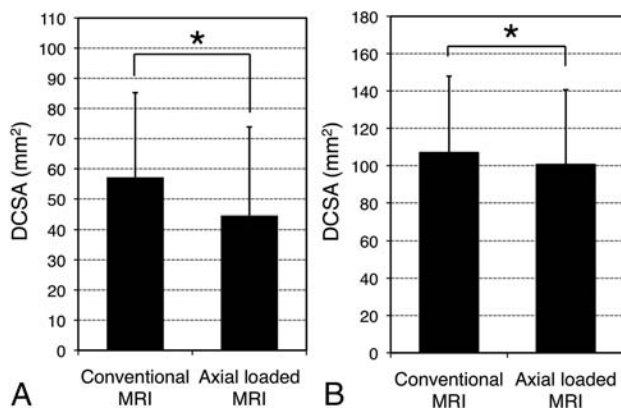


FIG 3. Comparison of the DCSA values between conventional and axial-loaded MR imaging. The DCSA on axial-loaded MR imaging is significantly smaller than that noted on conventional MR imaging at the narrowest intervertebral level (A) and at the other level (B). The asterisk indicates $P < .05$; the error bars, the SD.

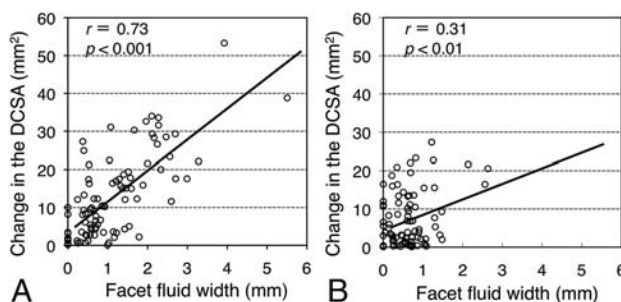


FIG 4. Facet fluid width and change in the DCSA in each patient. At the most constricted intervertebral level (A), there is a significant and good correlation between the facet fluid width and the change in the DCSA (Pearson correlation coefficient = 0.73). In contrast, there is a poor correlation at the other level (B) (Pearson correlation coefficient = 0.31).

tion between the facet fluid width and the change in the DCSA ($r = 0.31$) (Fig 4B). The values of the change in the DCSA and the facet fluid width were generally smaller at the other intervertebral levels (Fig 4B) compared with the narrowest levels (Fig 4A).

Diagnostic Power of the Facet Fluid Width for Detecting a $>15\text{-mm}^2$ Change in the DCSA

The ROC analysis showed that the facet fluid width at the most constricted intervertebral level could be used to detect a $>15\text{ mm}^2$ change in the DCSA, with 86.1% sensitivity and 84.2% specificity (Fig 5). The cutoff value for the facet fluid width was 1.04 mm. The value of the area under the ROC curve (0.87) indicated that the facet fluid width was a valid discriminator of a $>15\text{ mm}^2$ change in the DCSA.

Comparison of the Intervertebral Levels with the Facet Fluid Width over and under the Cutoff Value

Among the most constricted intervertebral levels, facet fluid widths over and under the cutoff value of 1.04 mm were found at 41 (44.1%) and 52 (55.9%) levels, respectively. In the DCSA on conventional MR imaging, there was no significant difference between the levels with a facet fluid width over and under the cutoff value (Fig 6). On the other hand, the DCSA on axial-loaded MR imaging was significantly smaller at the levels with a facet fluid

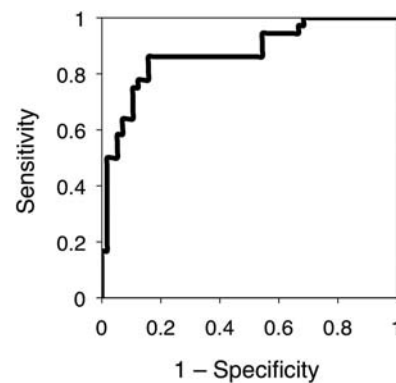


FIG 5. ROC curve for the facet fluid width for detecting a significant change in the DCSA at the most constricted intervertebral level. The area under the ROC curve is 0.87.

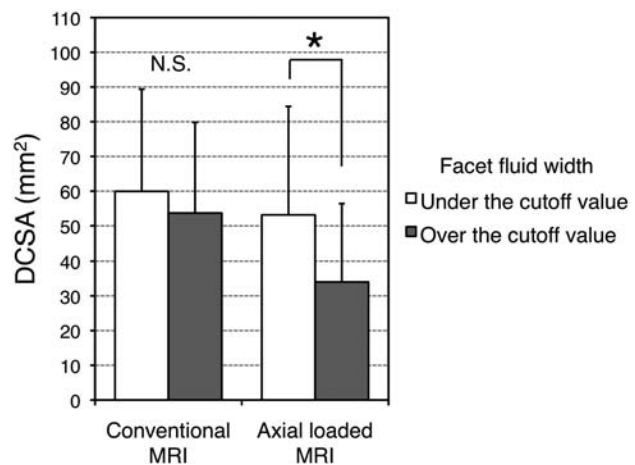


FIG 6. Comparison of the DCSA between the intervertebral levels with facet fluid widths over and under the cutoff value. In the DCSA on conventional MR imaging, there is no significant difference between the levels with facet fluid widths over and under the cutoff value of 1.04 mm. On the other hand, the DCSA on axial-loaded MR imaging is significantly smaller at the levels with a facet fluid width over the cutoff value than those with a facet fluid width under the cutoff value. Asterisk indicates $P < .05$; error bars, the SD; N.S., not significant.

width over the cutoff value ($34 \pm 22\text{ mm}^2$) than those with a facet fluid width under the cutoff value ($53 \pm 31\text{ mm}^2$) ($P < .01$) (Fig 6). The levels with a facet fluid width over the cutoff value showed significantly larger changes in the DCSA ($20 \pm 11\text{ mm}^2$) compared with those with a facet fluid width under the cutoff value ($7 \pm 6\text{ mm}^2$) ($P < .05$) (Fig 7).

The prevalence of spondylolisthesis was significantly higher among the intervertebral levels with a facet fluid width over the cutoff value (73%) than among those with a facet fluid width under the cutoff value (31%) ($P < .001$) (Table 2). There was no significant difference in the degree of disc degeneration between the 2 groups (Table 3).

Among the other intervertebral levels excluding the narrowest level, facet fluid widths over and under the cutoff value were found at 15 (16%) and 78 (84%) levels, respectively. The change in the DCSA was significantly larger at the levels with a facet fluid width over the cutoff value ($11 \pm 9\text{ mm}^2$) compared with those with a facet fluid width under the cutoff value ($5 \pm 7\text{ mm}^2$) ($P < .01$).

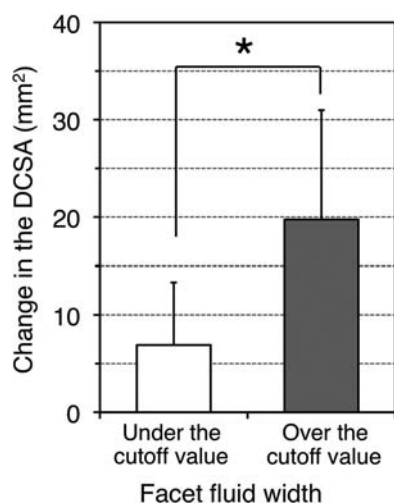


FIG 7. Comparison of the changes in the DCSA induced by axial loading between the intervertebral levels with facet fluid widths over and under the cutoff value. The levels with a facet fluid width over the cutoff value show significantly larger changes in the DCSA compared with those with a facet fluid width under the cutoff value. Asterisk indicates $P < .05$; error bars, the SD.

Table 2: Prevalence of spondylolisthesis at the intervertebral levels with facet fluid width over and under the cutoff value^a

	Facet Fluid Width	
	Over the Cutoff Value (n = 41)	Under the Cutoff Value (n = 52)
With spondylolisthesis	30 (73%)	16 (31%)
Without spondylolisthesis	11 (27%)	36 (69%)

^a Values are the number of intervertebral levels and percentages. There is a significant difference (χ^2 test, $P < .001$).

Table 3: Disc degeneration at the intervertebral levels with facet fluid width over and under the cutoff value^a

Classification of Pfirrmann et al ²⁶ for Disc Degeneration	Facet Fluid Width	
	Over the Cutoff Value (n = 41)	Under the Cutoff Value (n = 52)
Grade 3	10 (24%)	9 (17%)
Grade 4	22 (54%)	26 (50%)
Grade 5	9 (22%)	17 (33%)

^a No intervertebral level was classified as grade 1 or 2. Values are the number of intervertebral levels and percentages. There is no significant difference (χ^2 test, $P = .46$).

DISCUSSION

Previous studies have shown that axial-loaded MR imaging demonstrated a significant reduction in the size of the dural sac compared with conventional MR imaging.^{3,4} It has also been reported that axial-loaded MR imaging potentially produces additional imaging findings that cannot be obtained with conventional MR imaging.^{4,6,8,27} Most important, the dynamic change in the DCSA detected on axial-loaded MR imaging is more strongly correlated with the severity of clinical symptoms compared with that noted on conventional MR imaging in patients with LSCS.⁹ Furthermore, the use of axial-loaded MR imaging increases the diagnostic specificity for detecting degenerative diseases in the lumbar spine and influences the indications for surgical treatment.^{7,10} Therefore, evaluating the degree of narrowing of the lumbar spinal canal by using axial-loaded MR imaging may be beneficial for obtaining a more accurate diagnosis and selecting the optimal

treatment.^{7,8,11,28} However, it remains unclear whether any specific pathologic factors increase the dynamic change in the DCSA induced by axial loading to the lumbar spine. It also remains unknown whether any useful imaging findings on conventional MR imaging predict the dynamic change in the DCSA.

Many previous studies have suggested that the presence of increased fluid signals in the facet joint on conventional MR images predicts instability of the lumbar spine.¹⁷⁻¹⁹ In the present study, we hypothesized that an increased facet fluid width may be correlated with the dynamic change in the DCSA on axial-loaded MR imaging because the morphology of the lumbar spinal canal is more likely to be affected by axial loading if the lumbar spine is unstable. Most interesting, our results showed that the facet fluid width strongly correlates with the change in the DCSA induced by axial loading at the most constricted intervertebral level. This finding indicates that patients with a greater facet fluid width tend to show larger changes in the DCSA. Thus, the increased facet fluid width associated with spinal instability may be, at least in part, a pathologic feature increasing the dynamic change in the dural sac size during axial loading in patients with LSCS.

In the current study, the cutoff value of 1.04 mm for the facet fluid width showed both high sensitivity (86.1%) and specificity (84.2%) for detecting a significant change in the DCSA. Indeed, this study demonstrated that the levels with a facet fluid width over the cutoff value showed significantly larger changes in the DCSA compared with the other levels. These results indicate that a cutoff value of 1.04 mm for the facet fluid width on conventional MR imaging is a useful finding for predicting a significant change in the DCSA detected by using axial-loaded MR imaging in the clinical assessment of patients with LSCS.

Previous studies have also suggested that axial-loaded MR imaging provides useful findings in making a more accurate diagnosis of lumbar degenerative diseases and can be helpful for determining the appropriate course of treatment.^{6-8,10,11,28} However, in the current study, similar to previous reports,^{4,7,9} not all patients showed a significant difference in the DCSA between conventional and axial-loaded MR imaging. Therefore, which patients actually require an examination with axial-loaded MR imaging in addition to conventional MR imaging should be clarified. The results of this study suggest that additional imaging examinations, such as those with axial-loaded MR imaging and upright myelography, should be considered in patients with a facet fluid width over the cutoff value on conventional MR imaging, to prevent the risk of underestimating the degree of spinal canal narrowing.

This study has several limitations. First, the study population included a small number of patients with LSCS, though all cases were consecutively included and analyzed prospectively. Baseline characteristics of the patient population such as height, weight, and body mass index will vary widely in different countries/nations; therefore, the results of this study may not be applicable to any other patient groups. This study did not evaluate an asymptomatic population for comparison. The lack of a control population limits the clinical implications and usefulness of the results in this study. Further study including an asymptomatic population will provide firm evidence to support the clinical significance of the results in the assessment of patients with suspected LSCS.

Second, degeneration of the facet joint can be an important factor associated with the facet fluid width and segmental instability; therefore, it is potentially related to the change in the DCSA during axial loading. However, this study did not analyze facet joint degeneration. Third, configuration of the facet joint is different depending on various factors such as the intervertebral level and degree of joint degeneration.¹³ The method of measuring the facet fluid width may not be accurate in this study because the axial image is not perfectly perpendicular to the facet joint.

CONCLUSIONS

The present study demonstrated that the facet fluid width is significantly correlated with the change in the DCSA induced by axial loading. In this study, the patients with greater facet fluid widths tended to show larger changes in the DCSA. A cutoff value of 1.04 mm for the facet fluid width on conventional MR imaging may be a useful predictor of a significant change in the DCSA obtained on axial-loaded MR imaging in the clinical assessment of patients with LSCS. The present findings also suggest that additional imaging examinations, such as axial-loaded MR imaging and upright myelography, should be considered in patients with a facet fluid width over the cutoff value to prevent the risk of underestimating the degree of spinal canal narrowing and determine the optimal treatment.

Disclosures: Eiji Itoi—UNRELATED: Board Membership: Board of Trustees, *J Shoulder Elbow Surg*.

REFERENCES

- Ogikubo O, Forsberg L, Hansson T. The relationship between the cross-sectional area of the cauda equina and the preoperative symptoms in central lumbar spinal stenosis. *Spine* 2007;32:1423–28; discussion 1429 CrossRef Medline
- Hamanishi C, Matukura N, Fujita M, et al. Cross-sectional area of the stenotic lumbar dural tube measured from the transverse views of magnetic resonance imaging. *J Spinal Disord* 1994;7:388–93 Medline
- Danielson BI, Willén J, Gaulitz A, et al. Axial loading of the spine during CT and MR in patients with suspected lumbar spinal stenosis. *Acta Radiol* 1998;39:604–11 CrossRef Medline
- Willén J, Danielson B, Gaulitz A, et al. Dynamic effects on the lumbar spinal canal: axially loaded CT-myelography and MRI in patients with sciatica and/or neurogenic claudication. *Spine* 1997;22:2968–76 CrossRef Medline
- Sirvanci M, Bhatia M, Ganiyusufoglu KA, et al. Degenerative lumbar spinal stenosis: correlation with Oswestry Disability Index and MR imaging. *Eur Spine J* 2008;17:679–85 CrossRef Medline
- Hansson T, Suzuki N, Hebelka H, et al. The narrowing of the lumbar spinal canal during loaded MRI: the effects of the disc and ligamentum flavum. *Eur Spine J* 2009;18:679–86 CrossRef Medline
- Kanno H, Endo T, Ozawa H, et al. Axial loading during magnetic resonance imaging in patients with lumbar spinal canal stenosis: does it reproduce the positional change of the dural sac detected by upright myelography? *Spine (Phila Pa 1976)* 2012;37:E985–92 CrossRef Medline
- Willén J, Danielson B. The diagnostic effect from axial loading of the lumbar spine during computed tomography and magnetic resonance imaging in patients with degenerative disorders. *Spine* 2001;26:2607–14 CrossRef Medline
- Kanno H, Ozawa H, Koizumi Y, et al. Dynamic change of dural sac cross-sectional area in axial loaded magnetic resonance imaging correlates with the severity of clinical symptoms in patients with lumbar spinal canal stenosis. *Spine (Phila Pa 1976)* 2012;37:207–13 CrossRef Medline
- Hiwatashi A, Danielson B, Moritani T, et al. Axial loading during MR imaging can influence treatment decision for symptomatic spinal stenosis. *AJNR Am J Neuroradiol* 2004;25:170–74 Medline
- Willén J, Wessberg PJ, Danielsson B. Surgical results in hidden lumbar spinal stenosis detected by axial loaded computed tomography and magnetic resonance imaging: an outcome study. *Spine* 2008;33:E109–15 CrossRef Medline
- Kong MH, Morishita Y, He W, et al. Lumbar segmental mobility according to the grade of the disc, the facet joint, the muscle, and the ligament pathology by using kinetic magnetic resonance imaging. *Spine (Phila Pa 1976)* 2009;34:2537–44 CrossRef Medline
- Sato K, Wakamatsu E, Yoshizumi A, et al. The configuration of the laminae and facet joints in degenerative spondylolisthesis: a clinicoradiologic study. *Spine (Phila Pa 1976)* 1989;14:1265–71 CrossRef Medline
- Fujiwara A, Lim TH, An HS, et al. The effect of disc degeneration and facet joint osteoarthritis on the segmental flexibility of the lumbar spine. *Spine (Phila Pa 1976)* 2000;25:3036–44 CrossRef Medline
- Oishi Y, Murase M, Hayashi Y, et al. Smaller facet effusion in association with restabilization at the time of operation in Japanese patients with lumbar degenerative spondylolisthesis. *J Neurosurg Spine* 2010;12:88–95 CrossRef Medline
- Cho BY, Murovic JA, Park J. Imaging correlation of the degree of degenerative L4–5 spondylolisthesis with the corresponding amount of facet fluid. *J Neurosurg Spine* 2009;11:614–19 CrossRef Medline
- Chaput C, Padon D, Rush J, et al. The significance of increased fluid signal on magnetic resonance imaging in lumbar facets in relationship to degenerative spondylolisthesis. *Spine (Phila Pa 1976)* 2007;32:1883–87 CrossRef Medline
- Schinnerer KA, Katz LD, Grauer JN. MR findings of exaggerated fluid in facet joints predicts instability. *J Spinal Disord Tech* 2008;21:468–72 CrossRef Medline
- Rihn JA, Lee JY, Khan M, et al. Does lumbar facet fluid detected on magnetic resonance imaging correlate with radiographic instability in patients with degenerative lumbar disease? *Spine (Phila Pa 1976)* 2007;32:1555–60 CrossRef Medline
- Verbiest H. A radicular syndrome from developmental narrowing of the lumbar vertebral canal. *J Bone Joint Surg Br* 1954;36-B:230–37 Medline
- Suzuki H, Endo K, Kobayashi H, et al. Total sagittal spinal alignment in patients with lumbar canal stenosis accompanied by intermittent claudication. *Spine* 2010;35:E344–46 CrossRef Medline
- Sato K, Kikuchi S. Clinical analysis of two-level compression of the cauda equina and the nerve roots in lumbar spinal canal stenosis. *Spine* 1997;22:1898–903; discussion 1904 CrossRef Medline
- Ozawa H, Kanno H, Koizumi Y, et al. Dynamic changes in the dural sac cross-sectional area on axial loaded MR imaging: is there a difference between degenerative spondylolisthesis and spinal stenosis? *AJNR Am J Neuroradiol* 2012;33:1191–97 CrossRef Medline
- Lohman CM, Tallroth K, Kettunen JA, et al. Comparison of radiologic signs and clinical symptoms of spinal stenosis. *Spine* 2006;31:1834–40 CrossRef Medline
- Danielson B, Willén J. Axially loaded magnetic resonance image of the lumbar spine in asymptomatic individuals. *Spine* 2001;26:2601–06 CrossRef Medline
- Pfirrmann CW, Metzendorf A, Zanetti M, et al. Magnetic resonance classification of lumbar intervertebral disc degeneration. *Spine (Phila Pa 1976)* 2001;26:1873–78 CrossRef Medline
- Saifuddin A, McSweeney E, Lehovskiy J. Development of lumbar high intensity zone on axial loaded magnetic resonance imaging. *Spine* 2003;28:E449–51; discussion E451–52 CrossRef Medline
- Saifuddin A, Bleas S, MacSweeney E. Axial loaded MRI of the lumbar spine. *Clin Radiol* 2003;58:661–71 CrossRef Medline

Imaging Psoas Sign in Lumbar Spinal Infections: Evaluation of Diagnostic Accuracy and Comparison with Established Imaging Characteristics

L.N. Ledbetter, K.L. Salzman, and L.M. Shah



ABSTRACT

BACKGROUND AND PURPOSE: Lumbar discitis-osteomyelitis has imaging characteristics that can overlap with noninfectious causes of back pain. Our aim was to determine the added accuracy of psoas musculature T2 hyperintensity (imaging psoas sign) in the MR imaging diagnosis of lumbar discitis-osteomyelitis.

MATERIALS AND METHODS: This retrospective case-control study evaluated lumbar spine MR imaging examinations, during a 30-month period, that were requested for the evaluation of discitis-osteomyelitis. Of this pool, 50 age-matched control patients were compared with 51 biopsy-proved or clinically diagnosed patients with discitis-osteomyelitis. Two reviewers, blinded to the clinical information, assessed the randomly organized MR imaging examinations for abnormalities of the psoas musculature, vertebral bodies, discs, and epidural space.

RESULTS: Psoas T2 hyperintensity demonstrated a high sensitivity (92.1%; 95% CI, 80%–97.4%) and specificity (92%; 95% CI, 80%–97.4%), high positive likelihood ratio (11.5; 95% CI, 4.5–29.6), low negative likelihood ratio (0.09; 95% CI, 0.03–0.20), and individual area under the receiver operating characteristic curve of 0.92; 95% CI, 0.87–0.97. Identification of psoas T2 abnormality significantly improved ($P = .02$) the diagnostic accuracy of discitis-osteomyelitis in noncontrast examinations from an area under the receiver operator characteristic curve of the established variables (vertebral body T2 and T1 signal, endplate integrity, disc T2 signal, and disc height) from 0.93 (95% CI, 0.88–0.98) to 0.98 (95% CI, 0.96–1.0). Psoas T2 abnormalities also had the highest interobserver reliability with a κ coefficient of 0.78 (substantial agreement).

CONCLUSIONS: Psoas T2 hyperintensity, the imaging psoas sign, is highly correlated with discitis-osteomyelitis. T2 hyperintensity in the psoas musculature, particularly when there is clinical suspicion of spinal infection, improves the diagnostic accuracy of discitis-osteomyelitis compared with routine noncontrast variables alone.

ABBREVIATIONS: AUC = area under the receiver operating characteristic curve; DOM = discitis-osteomyelitis; LBP = low back pain

Discitis-osteomyelitis (DOM) is a significant cause of morbidity and mortality in patients with low back pain (LBP).^{1–3} It can be a diagnostic challenge due to overlapping symptoms and imaging findings with other noninfectious causes of LBP. MR imaging is the standard technique for LBP evaluation, particularly when there is a clinical concern for infection, because of the superb soft-tissue resolution.^{4–9}

Several MR imaging characteristics are associated with spinal

infections, including vertebral body low T1 and high T2 signal, intervertebral disc high T2 signal, endplate destruction, and vertebral body and intervertebral disc enhancement.^{9–14} Unfortunately, these MR imaging features can be seen with noninfectious causes of LBP such as disc degeneration, reactive endplate changes, inflammatory spondyloarthropathy, spinal neuroarthropathy, hemodialysis-related spondyloarthropathy, and neoplastic conditions such as chordoma, lymphoma, or metastasis.^{15–18} Although intravenous contrast is often used to help differentiate DOM from the aforementioned conditions, the spinal inflammatory process can be confounding. Furthermore, patients with contraindications to contrast or patients with vague symptoms of LBP often receive noncontrast examinations, and the diagnosis can be difficult.


Paraspinal soft-tissue abnormalities on MR imaging may be overlooked due to the focus on the discvertebral complex or may be referenced as an adjunct finding in spinal infections. However, these structures may provide critical information that is the diagnostic key.

Received July 17, 2015; accepted after revision August 21.

From the Department of Radiology (L.N.L.), University of Kansas Medical Center, Kansas City, Kansas; and Department of Radiology (K.L.S., L.M.S.), University of Utah, Salt Lake City, Utah.

Paper previously presented at: Annual Meeting of Radiological Society of North America, November 30–December 5, 2014; Chicago, Illinois.

Please address correspondence to Luke Ledbetter, MD, University of Kansas, Department of Radiology, 3901 Rainbow Blvd MS 4032, Kansas City, KS 66160; e-mail: lledbetter@kumc.edu; @LNLedbetter

 Indicates article with supplemental on-line tables.

<http://dx.doi.org/10.3174/ajnr.A4571>

Previous studies have considered all abnormalities of the paravertebral region as a single variable, inclusive of the anterior, lateral, and posterior (epidural) spaces. DOM begins along the subchondral endplates in adults; and given the close proximity of the psoas musculature to the anterolateral endplates and discs, the signal intensity changes in the psoas can be useful in differentiating infectious and noninfectious etiologies of low back pain.

The purpose of this retrospective case-control study was to review the accuracy of MR imaging characteristics in lumbar spinal infections, particularly evaluating psoas musculature T2 hyperintensity (imaging psoas sign) in the diagnosis of discitis-osteomyelitis.

MATERIALS AND METHODS

Patient Selection

After approval by the institutional internal review board, a retrospective review of the radiology information system data base queried for lumbar spine MR imaging reports with the key terms “infection,” “discitis,” “osteomyelitis,” and “spondylodiscitis” from January 2011 to July 2014. This search captured all studies either performed with the clinical question of infection or with imaging findings that warranted the radiologist mentioning infection in the report. Each patient’s electronic medical record was reviewed for presentation, comorbidities, clinical course, biopsy results, and treatment to create infection and control groups. The infection group included patients with biopsy-proved infection and/or the clinical diagnosis and treatment of DOM. The clinical diagnosis was defined by evaluation, diagnosis, treatment, and follow-up of DOM by an infectious disease physician. The control group was randomly selected from the initial radiology information system search for subjects of similar ages and without the imaging or clinical diagnosis of DOM, as defined above. Patients were excluded if there was lack of clinical information or infectious disease diagnosis, if they had isolated sacral infection, if they had an anterior or lateral approach for spinal fusion involving the psoas musculature, and if they had incomplete or nondiagnostic imaging studies. Postoperative patients treated via a posterior approach were included in the study because newer MR imaging techniques such as Dixon and Warp minimize susceptibility artifacts and enable adequate assessment of the osseous spine and adjacent soft tissues.

Image Evaluation

MR imaging examinations were performed on a 1.5T scanner (Magnetom Avanto or Aera; Siemens, Erlangen, Germany). Sagittal T1-weighted inversion recovery (T1-FLAIR) and T2-weighted images were reviewed (T1 inversion recovery: 3-mm section thickness; TR, 2000 ms; TE, 10 ms; TI, 830 ms; FOV, 22 cm; T2: 3-mm section thickness; TR, 3000–6000 ms; TE, 112 ms; FOV, 22 cm). Axial T1 and T2 images were also reviewed (T1: 4-mm section thickness; TR, 506 ms; TE, 16 ms; FOV, 18 cm; T2: 4-mm section thickness; TR, 4000–5000 ms; TE, 106 ms; FOV, 18 cm). Sagittal and axial T1 post-contrast images (sagittal: 3-mm section thickness; TR, 464 ms; TE, 14 ms; FOV, 22 cm; axial: 4-mm section thickness; TR, 508 ms; TE, 16 ms; FOV, 18 cm) were reviewed when available. Gadobenate dimeglumine (MultiHance; Bracco Diagnostics, Princeton, New Jersey) was administered at a dose of 0.1 mL/kg (standard dose of 20 mL) for contrast-enhanced sequences.

The study and control patients were randomized alphabetically

on the PACS. Two neuroradiologists (L.M.S., K.L.S.) with Certificates of Added Qualification in neuroradiology and >10 years’ experience were blinded to the final diagnosis and the clinical course and separately reviewed MR imaging examinations. MR imaging characteristics were evaluated categorically at the level of greatest signal abnormality relative to adjacent levels. Those cases discordant between the reviewers were subject to blinded group re-review to achieve consensus.

Intervertebral discs were graded on disc height, T2 signal, and enhancement.¹³ Disc height was graded as normal, loss of <50%, loss of >50%, or increased. T2 signal was graded as isointense, hyperintense, or hypointense. Enhancement was graded as absent, focal, rim, or diffuse.

Vertebral bodies were graded on T1 signal, T2 signal, endplate integrity, and enhancement.¹³ T1 and T2 signals were graded as isointense, hyperintense, or hypointense. Endplate integrity was evaluated on T1-weighted images and graded as intact, eroded with normal marrow signal, or destroyed with abnormal marrow signal. Enhancement was graded as absent, endplate, or diffuse.

Epidural space was evaluated for the presence or absence of phlegmon and abscess. The psoas musculature was evaluated for the presence or absence of abnormal T2 signal, enhancement, and abscess.

Statistical Analysis

Descriptive test characteristics (sensitivity, specificity, positive and negative likelihood ratios) are reported with 2-sided 95% confidence intervals¹⁹ for each of the different MR imaging variables described previously. Statistical significance between the spinal infection and control groups was determined by using a 2-tailed Fisher exact test. Interobserver agreement was calculated by using a κ coefficient.^{20,21} Multivariate logistic regression for the noncontrast variables alone and with the psoas T2 hyperintensity was performed to obtain *P* values, area under the receiver operating characteristic curve (AUC), and confidence intervals. The AUCs for the 2 regression models were compared for significance. Statistical significance was defined as a *P* value < .05. STATA statistical software: Release 14 (StataCorp, College Station, Texas) was used for all statistical analysis.

RESULTS

Demographics

Of the 205 patients having MR imaging of the lumbar spine with reports containing the key words “infection,” “discitis,” “osteomyelitis,” or “spondylodiscitis,” 51 patients were categorized in the DOM group after the initial imaging and chart review. There were 154 patients from this data search eligible for the control group who did not have the final diagnosis of DOM, and 50 patients from this group were randomly selected for the final control group (Table 1). We excluded 9 of 205 patients: 5 without available clinical or imaging follow-up, 2 with isolated sacral infections, 1 with nondiagnostic imaging, and 1 with muscular metastatic disease. No patients had previous anterior- or lateral-approach spinal surgical procedures.

The DOM group included 40 patients who had image-guided biopsies of the suspected disc and endplate during the course of their evaluation. Percutaneous biopsy of the disc and endplate was performed in 38 of the 40 biopsies with the remaining 2 un-

Table 1: Demographics

	Spinal Infection (n = 51)	Controls (n = 50)
Age (yr) (range)	58.8 (19–87)	53.6 (18–93)
Sex	41 Male, 10 female	25 Male, 25 female
Previous spinal surgery	12	6
Contrast-enhanced exams	45	39
Non-contrast-enhanced exams	6	11

dergoing surgical biopsy. Two of the 38 patients with percutaneous disc biopsies also included samples of the paraspinal soft tissues. Microbiologic or histopathologic findings consistent with infection were identified in 34 of 40 patients (85%). The most common isolated pathogen was *Staphylococcus aureus* (13 patients), followed by *Enterococcus faecalis* (5 patients), *Propionibacterium acnes* (3 patients), multiple pathogens (3 patients), and 1 patient each with *Staphylococcus epidermidis*, *viridans streptococci*, *Fingoldia magna*, *Enterococcus coli*, group B streptococcus, *Mycobacterium tuberculosis*, and *Streptococcus mitis*. Three patients had histologic findings of infection without positive microbiology cultures. Four of the 6 patients with a biopsy negative for infection received intravenous antibiotic treatment before biopsy. All 11 patients who were not biopsied had bacteremia, 9 with *S aureus*, 1 with *E faecalis*, and 1 with *Klebsiella pneumoniae*. The 6 patients with biopsy results negative for infection, together with the 11 patients not biopsied, were diagnosed and treated for spinal infection based on an infectious disease service evaluation and recommendation. Pertinent medical history in these 17 patients included bacteremia, endocarditis, additional septic joints, immunosuppression, and IV drug use. Of the 19 postoperative patients included in our study, 12 were positive for DOM.

Imaging Evaluation

Results from the blinded review of the cases are listed in On-line Table 1. The level of greatest involvement was T12–L1 in 3 patients, L1–L2 in 5, L2–L3 in 10, L3–L4 in 11, L4–L5 in 11, and L–S1 in 11. The psoas MR imaging features showed statistically significant association with DOM ($P < .001$). The vertebral body findings with statistical significance included T1 hypointensity, T2 hyperintensity, diffuse enhancement, and endplate destruction and enhancement. Statistically significant disc abnormalities included increased height, T2 hyperintensity, and focal and rim enhancement. Both epidural phlegmon and abscess demonstrated statistically significant association with DOM. Psoas T2 hyperintensity ($P < .001$) and enhancement ($P < .001$) showed a statistically significant correlation to DOM in postoperative patients as well.

The findings with the highest sensitivity for DOM included psoas T2 hyperintensity (92.1%) and vertebral body T1 hypointensity (90.2%) (Figs 1 and 2). Other findings with high sensitivity included psoas enhancement (88.9%), vertebral body T2 hyperintensity (88.2%), and epidural phlegmon (80.9%). Highly specific findings for DOM included increased disc height and epidural abscess (100%). Other findings with high specificity included psoas abscess (97.4%), epidural phlegmon (94.9%), diffuse vertebral body enhancement (94.5%), rim enhancement of the disc (92.3%), psoas T2 hyperintensity (92%), psoas enhancement

(87.1%), disc T2 hyperintensity (86.3%), endplate destruction (86%), and vertebral body T1 hypointensity (80%).

The overall diagnostic accuracy of the individual MR imaging variables to distinguish the infection and control groups was evaluated by receiver operating characteristic analysis (On-line Table 1). High T2 signal within the psoas musculature had the highest individual AUC of 0.92. Other variables with the high AUC included psoas enhancement (0.88), epidural phlegmon (0.88), and vertebral body T1 hypointensity (0.85).

Positive and negative likelihood ratios were calculated to demonstrate the potential utility of the measured imaging characteristics in DOM (On-line Tables 2 and 3). High positive likelihood ratios, which indicate an increase in the probability of disease with a positive result, were identified with epidural phlegmon (15.8), psoas abscess (14.9), diffuse vertebral body enhancement (12.1), and psoas T2 hyperintensity (11.5). Low negative likelihood ratios, indicating a lower probability of infection with a test with negative findings, were identified with psoas T2 hyperintensity (0.09), T1 vertebral body hypointensity (0.12), psoas enhancement (0.13), and vertebral body T2 hyperintensity (0.16).

Multivariate logistic regression analysis of the noncontrast variables, with and without psoas T2 hyperintensity, was performed to determine the diagnostic accuracy and significance of the psoas T2 variable. The total AUC of the combination of routine noncontrast variables (vertebral body T2 and T1 signal, endplate integrity, disc T2 signal, and disc height) was 0.93 (95% CI, 0.88–0.98). The addition of psoas T2 hyperintensity to these variables resulted in an AUC of 0.98 (95% CI, 0.96–1.00), which was statistically significant ($P = .002$).

Psoas abnormalities were infrequently seen in patients with LBP who were not subsequently diagnosed with spinal infection. Only 4 of 50 patients (8%) had psoas abnormalities in the control group. These findings were related to myositis ($n = 2$), noninfectious spondylodiscitis (Anderssen lesion) in ankylosing spondylitis ($n = 1$), and extension of inflammation from an iliacus abscess ($n = 1$).

Interobserver Agreement

κ coefficient values were calculated on the initial blinded review (Table 2). Agreement was almost perfect in ratings of psoas abscess (0.87) and enhancement (0.81). There was substantial agreement with psoas T2 hyperintensity, vertebral body T2 hyperintensity, T1 hypointensity and enhancement, disc T2 hyperintensity, and endplate integrity. Moderate agreement in ratings included epidural phlegmon and abscess as well as disc enhancement and increased height.

DISCUSSION

DOM often presents with nonspecific indolent clinical symptoms but can have potentially devastating complications, which make imaging essential for early diagnosis. Additionally, the incidence of spinal infections has increased during the past 2 decades and has transitioned from an acute high mortality process to a more indolent chronic debilitating disease.¹ Early diagnosis is key in preventing adverse outcomes that are common in advanced disease.² However, imaging findings in spinal infections can be nonspecific and overlap other causes of noninfectious LBP, especially on noncontrast examinations.^{16,22}

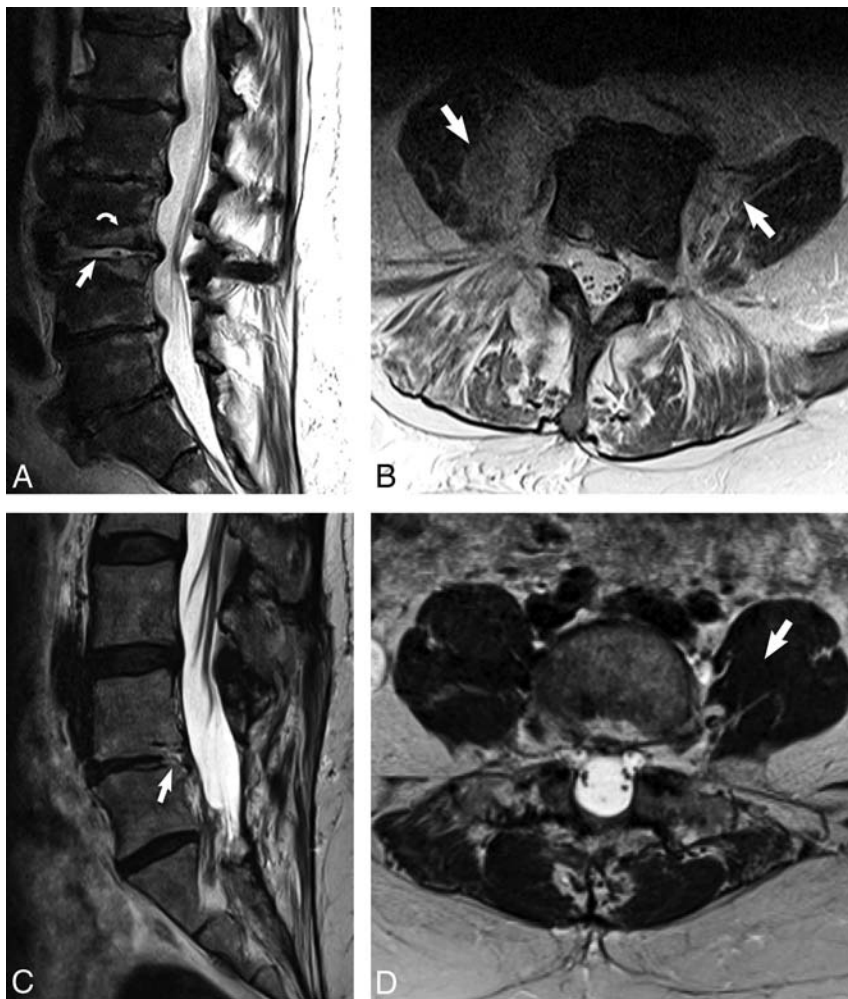


FIG 1. The imaging psoas sign on noncontrast MR imaging of the lumbar spine in an 81-year-old man with renal failure, *E faecalis* bacteremia, and clinically diagnosed discitis-osteomyelitis (A and B) with comparison with degenerative disc disease (C and D). A, Sagittal T2 image demonstrates high T2 signal within the disc (white arrow) and the adjacent endplates (white curved arrow) in the patient with discitis-osteomyelitis. B, Axial T2 image at the level of L3–L4 of the same patient demonstrates the imaging psoas sign of T2 hyperintensity within the bilateral psoas musculature (white arrows). C, Sagittal T2 image in a patient with degenerative disc disease shows focal high T2 signal involving the posterior endplate and disc of L4–L5 (white arrow). D, Axial T2 image in the same patient at the level of L4–L5 shows normal and uniform T2 signal within the psoas muscles (white arrow).

In addition, biopsy with microbiologic and histopathologic evaluation has limitations, often with poor diagnostic yield and a wide range of accuracies in organism identification or structural changes consistent with infection.²³ Frequently, the combination of clinical, imaging, and laboratory evaluation leads to a treatment regimen without a definitive finding on any level of investigation.

The purpose of this study was to determine whether there are specific imaging features that improve the MR imaging diagnosis of lumbar discitis-osteomyelitis.

The results of this study evaluating the diagnostic accuracy of MR imaging characteristics for lumbar DOM demonstrate that abnormal T2 signal intensity in the psoas musculature, the imaging psoas sign, is essential and improves diagnostic accuracy on noncontrast examinations over the standard noncontrast variables alone (Figs 1 and 2). Psoas T2 hyperintensity had the highest individual sensitivity (92.1%), specificity (92%), and AUC (0.92)

in the evaluation of DOM. Its high positive and low negative likelihood ratios (11.5 and 0.09 respectively) suggest increased suspicion of DOM with a positive result and decreased suspicion with a negative result. The imaging psoas sign showed excellent interrater reliability. Even in postoperative studies with the challenge of discerning DOM from expected surgical changes, psoas T2 hyperintensity demonstrated a statistically significant association with DOM compared with the noninfected patients postoperatively. False-positive findings of T2 abnormalities of the psoas muscle occurred infrequently in the control population (8%). Conditions that resulted in false-positive findings included 2 cases of myositis in immunocompromised patients, an Andersson lesion of ankylosing spondylitis, iatrogenic soft-tissue edema after LP, and extension of a large iliacus abscess into the psoas muscle. The small but potential risk of a type I error may be reduced by incorporating all imaging and clinical information when making the diagnosis of DOM.

Abnormalities of the paravertebral soft tissues, largely considered in the literature as a combination of prevertebral and epidural spaces, have been described as highly sensitive for spinal infection.¹³ Specifically, epidural abscess and phlegmon have known associations with spinal infections.^{22,24} To our knowledge, this is first study to evaluate the MR imaging appearance of the psoas musculature, specifically as an indicator of lumbar DOM. Psoas abscess has been associated with a spinal source of infection^{25,26} but often occurs as a late presentation of disease.

However, this study addresses the significance of psoas signal abnormalities on nonenhanced sequences. This is important because many patients with DOM do not receive IV contrast on the initial MR imaging evaluation either due to contraindication to contrast or the nonspecific presenting symptoms.

The psoas muscles originate from the transverse processes of all the lumbar vertebral bodies and the anteromedial lumbar discs and adjacent endplates.²⁴ Given that DOM is believed to commonly originate from the anterior endplates,^{15,27} the psoas muscle is in a location that is affected early in the infectious process by direct spread and potentially earlier than other paraspinal soft tissues, including the epidural space. Psoas abscesses are a delayed manifestation of infection^{25,26}; therefore, early identification T2 signal changes in the psoas musculature can potentially help detect DOM early in the course and potentially prevent long-term complications.

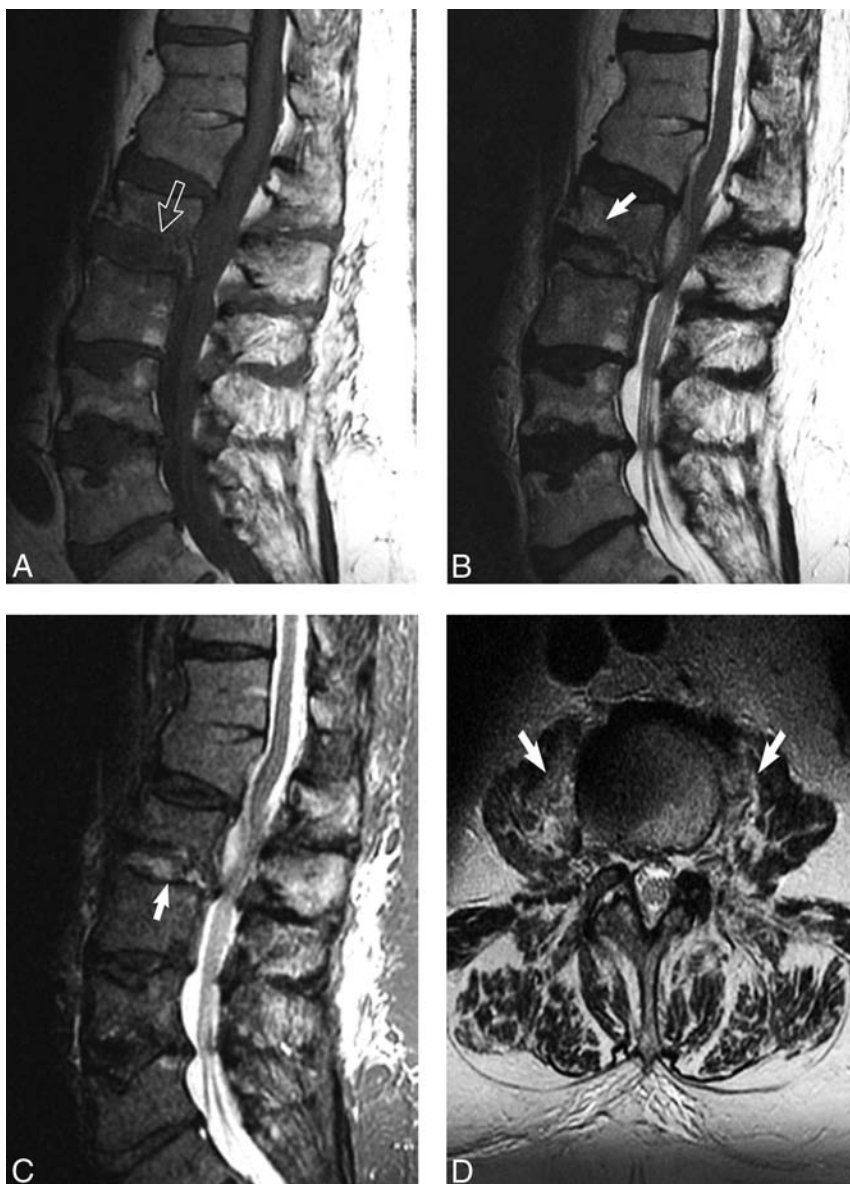


FIG 2. The imaging psoas sign in biopsy-proved *S aureus* discitis-osteomyelitis in a 79-year-old man with history of long-term steroid treatment of hypersensitivity pneumonitis. A, Sagittal T1 image shows height loss of L2 with associated increased L2-L3 disc space height. Normal T1 hypointensity is absent along the inferior L2 endplate due to destruction (white open arrow). B, Sagittal T2 image demonstrates subtle L2 marrow T2 hyperintensity (white arrow). C, Sagittal STIR image shows increased conspicuity of T2 hyperintensity within the L2-L3 disc space (white arrow). D, Axial T2 image at the level of the superior L3 vertebral body demonstrates bilateral psoas muscle hyperintense signal, the imaging psoas sign (white arrows).

Abnormalities of the disc space and vertebral bodies, including high T2 intradiscal signal, low T1 marrow signal, disc enhancement, and vertebral body enhancement have been shown to be sensitive for DOM.^{9,12-14} Our results agree with these findings with the added evaluation of specificity, receiver operating characteristic analysis, and likelihood ratios. Receiver operating characteristic analysis demonstrated that the vertebral body low T1 signal was the most helpful of the individual nonparaspinous findings in detecting DOM (0.85), followed by vertebral body and disc T2 hyperintensity (both 0.81). Increased disc height showed a statistically significant association with DOM, but it had the lowest sensitivity, area under the receiver operating characteristic curve, κ , and negative likelihood ratio. Disc height was graded as

a comparison with adjacent uninvolved discs and may have appeared taller than unaffected discs due to erosion of the endplates, increased fluid within the disc space, or preservation of disc height compared with other degenerated levels.

This study strengthens the evidence that the appearance of the paravertebral soft tissues are critical in the evaluation of DOM and emphasizes the imaging psoas sign as a statistically important variable on MR imaging, specifically on noncontrast examinations. Psoas T2 hyperintensity was best identified on axial T2-weighted images. Although our spine infection MR imaging protocol does not use fat-saturation techniques on the axial T2-weighted sequences, the addition of the fat saturation increases the conspicuity of the psoas signal abnormality. This may be useful not only in those patients with LBP as a nonspecific presentation of DOM but especially in those patients with a contraindication to IV contrast. Fat saturation can also increase the conspicuity of equivocal vertebral body and disc space findings.²⁸ Future studies could consider the evaluation of MR imaging protocols of different fat-saturation techniques in patients undergoing evaluation for DOM.

Limitations of this study include variations in imaging protocols with a mix of both contrast-enhanced and noncontrast examinations. This study was designed to closely represent the cohort of patients that radiologists encounter in daily practice, in which an imaging interpretation of infection must be made with a pretest clinical suspicion or suspicious imaging findings in patients with a nonspecific presentation. Because the reference standard of microbiologic/histologic confirmation of infection may not have been met in

some patients, the clinical diagnosis and treatment for spinal infection was considered as 1 criterion for inclusion into the infection group. The constellation of clinical, imaging, and laboratory evaluations without a definitive finding on any level of investigation often dictates clinical management because biopsy itself is an imperfect diagnostic test with a range of diagnostic yield between 38.1% and 76.5%.²⁹⁻³² As such, our results of the high sensitivity and specificity of psoas T2 hyperintensity will add great diagnostic value. In addition, our case-control cohort is not indicative of the incidence of spinal infection in the general population; therefore, the positive and negative predictive values could not be assessed. An additional pitfall in the psoas sign could include L5-S1 infection. The psoas does not consistently originate from this disc space,

Table 2: Interobserver reliability

	κ Coefficient	Agreement
Psoas abscess	0.87	Almost Perfect
Psoas enhancement	0.81	Almost Perfect
Psoas T2 ^a	0.78	Substantial
Vertebral body T2 hyperintensity	0.76	Substantial
Vertebral body T1 hypointensity	0.75	Substantial
Vertebral body enhancement	0.75	Substantial
Disc T2 hyperintensity	0.73	Substantial
Endplate destruction	0.67	Substantial
Epidural phlegmon	0.59	Moderate
Epidural abscess	0.58	Moderate
Disc enhancement	0.50	Moderate
Disc increased height	0.44	Moderate

^a Imaging psoas sign..

and occasionally the muscles may course further anterior in the retroperitoneal space with intervening fat between the muscles and the spinal column. Although not affecting our study group, infection in this location would potentially not involve the psoas until a later presentation of disease, if at all.

CONCLUSIONS

The imaging psoas sign (high T2 signal in the psoas musculature) is highly correlated with lumbar DOM. In addition to having the highest individual sensitivity and specificity of the nonenhanced features evaluated, the imaging psoas sign also had high interrater agreement. Together with previously established imaging characteristics, including vertebral body T1 hypointensity, vertebral body and disc T2 hyperintensity, and endplate destruction, the imaging psoas sign significantly improves diagnostic accuracy of DOM on noncontrast MR imaging of the lumbar spine.

Disclosures: Karen L. Salzman—UNRELATED: Royalties: Elsevier, Comments: royalties for books written, most recently *Diagnostic Imaging: Brain, 3rd Edition*.

REFERENCES

- McHenry MC, Easley KA, Locker GA. **Vertebral osteomyelitis: long-term outcome for 253 patients from 7 Cleveland-area hospitals.** *Clin Infect Dis* 2002;34:1342–50 CrossRef Medline
- Mylona E, Samarkos M, Kakalou E, et al. **Pyogenic vertebral osteomyelitis: a systematic review of clinical characteristics.** *Semin Arthritis Rheum* 2009;39:10–17 CrossRef Medline
- Gouliouris T, Aliyu SH, Brown NM. **Spondylodiscitis: update on diagnosis and management.** *J Antimicrob Chemother* 2010;65(suppl 3):iii11–24 CrossRef Medline
- Modic MT, Pavlicek W, Weinstein MA, et al. **Magnetic resonance imaging of intervertebral disk disease: clinical and pulse sequence considerations.** *Radiology* 1984;152:103–11 CrossRef Medline
- Modic MT, Feiglin DH, Piraino DW, et al. **Vertebral osteomyelitis: assessment using MR.** *Radiology* 1985;157:157–66 CrossRef Medline
- Post MJ, Quencer RM, Montalvo BM, et al. **Spinal infection: evaluation with MR imaging and intraoperative US.** *Radiology* 1988;169:765–71 CrossRef Medline
- Unger E, Moldofsky P, Gatenby R, et al. **Diagnosis of osteomyelitis by MR imaging.** *AJR Am J Roentgenol* 1988;150:605–10 CrossRef Medline
- Chandnani VP, Beltran J, Morris CS, et al. **Acute experimental osteomyelitis and abscesses: detection with MR imaging versus CT.** *Radiology* 1990;174:233–36 CrossRef Medline
- Thrush A, Enzmann D. **MR imaging of infectious spondylitis.** *AJNR Am J Neuroradiol* 1990;11:1171–80 Medline
- Meyers SP, Wiener SN. **Diagnosis of hematogenous pyogenic vertebral osteomyelitis by magnetic resonance imaging.** *Arch Intern Med* 1991;151:683–87 CrossRef Medline
- Post MJ, Sze G, Quencer RM, et al. **Gadolinium-enhanced MR in spinal infection.** *J Comput Assist Tomogr* 1990;14:721–29 CrossRef Medline
- Dagirmanjian A, Schils J, McHenry M, et al. **MR imaging of vertebral osteomyelitis revisited.** *AJR Am J Roentgenol* 1996;167:1539–43 CrossRef Medline
- Ledermann HP, Schweitzer ME, Morrison WB, et al. **MR imaging findings in spinal infections: rules or myths?** *Radiology* 2003;228:506–14 CrossRef Medline
- Patel KB, Poplawski MM, Pawha PS, et al. **Diffusion-weighted MRI “claw sign” improves differentiation of infectious from degenerative Modic type 1 signal changes of the spine.** *AJNR Am J Neuroradiol* 2014;35:1647–52 CrossRef Medline
- Diehn FE. **Imaging of spine infection.** *Radiol Clin North Am* 2012;50:777–98 CrossRef Medline
- Sharif HS. **Role of MR imaging in the management of spinal infections.** *AJR Am J Roentgenol* 1992;158:1333–45 CrossRef Medline
- Maiuri F, Iaconetta G, Gallicchio B, et al. **Spondylodiscitis: clinical and magnetic resonance diagnosis.** *Spine* 1997;22:1741–46 CrossRef Medline
- Zimmerli W. **Clinical practice: vertebral osteomyelitis.** *N Engl J Med* 2010;362:1022–29 CrossRef Medline
- Brown LD, Cai TT, DasGupta A. **Interval estimation for a binomial proportion.** *Stat Sci* 2001;16:101–33 CrossRef
- Carpenter J, Bithell J. **Bootstrap confidence intervals: when, which, what? A practical guide for medical statisticians.** *Stat Med* 2000;19:1141–64 Medline
- Reichenheim ME. **Confidence intervals for the kappa statistic.** *Stata J* 2004;4:421–28
- Dunbar JA, Sandoe JA, Rao AS, et al. **The MRI appearances of early vertebral osteomyelitis and discitis.** *Clin Radiol* 2010;65:974–81 CrossRef Medline
- Sehn JK, Gilula LA. **Percutaneous needle biopsy in diagnosis and identification of causative organisms in cases of suspected vertebral osteomyelitis.** *Eur J Radiol* 2012;81:940–66 CrossRef Medline
- Lardé D, Mathieu D, Frija J, et al. **Vertebral osteomyelitis: disk hypodensity on CT.** *AJR Am J Roentgenol* 1982;139:963–67 CrossRef Medline
- Jeffrey RB, Callen PW, Federle MP. **Computed tomography of psoas abscesses.** *J Comput Assist Tomogr* 1980;4:639–41 CrossRef Medline
- Mückley T, Schütz T, Kirschner M, et al. **Psoas abscess: the spine as a primary source of infection.** *Spine* 2003;28:E106–13 CrossRef Medline
- Sajko S, Stuber K. **Psoas major: a case report and review of its anatomy, biomechanics, and clinical implications.** *J Can Chiropr Assoc* 2009;53:311–18 Medline
- D’Aprile P, Tarantino A, Lorusso V, et al. **Fat saturation technique and gadolinium in MRI of lumbar spinal degenerative disease.** *Neuroradiol J* 2006;19:654–71 CrossRef Medline
- Staatz G, Adam GB, Keulers P, et al. **Spondylodiskitic abscesses: CT-guided percutaneous catheter drainage.** *Radiology* 1998;208:363–67 CrossRef Medline
- Rankine JJ, Barron DA, Robinson P, et al. **Therapeutic impact of percutaneous spinal biopsy in spinal infection.** *Postgrad Med J* 2004;80:607–09 CrossRef Medline
- D’Agostino C, Scorzolini L, Massetti AP, et al. **A seven-year prospective study on spondylodiscitis: epidemiological and microbiological features.** *Infection* 2010;38:102–07 CrossRef Medline
- Kim BJ, Lee JW, Kim SJ, et al. **Diagnostic yield of fluoroscopy-guided biopsy for infectious spondylitis.** *AJNR Am J Neuroradiol* 2013;34:233–38 CrossRef Medline

Age- and Level-Dependence of Fatty Infiltration in Lumbar Paravertebral Muscles of Healthy Volunteers

R.J. Crawford, L. Filli, J.M. Elliott, D. Nanz, M.A. Fischer, M. Marcon, and E.J. Ulbrich



ABSTRACT

BACKGROUND AND PURPOSE: Normative age-related decline in paravertebral muscle quality is important for reference to disease and risk identification in patients. We aimed to establish age- and vertebral level–dependence of paravertebral (multifidus and erector spinae) muscle volume and fat content in healthy adult volunteers.

MATERIALS AND METHODS: In this prospective study multifidus and erector spinae fat signal fraction and volume at lumbar levels L1–L5 were measured in 80 healthy volunteers (10 women and men per decade, 20–62 years of age) by 2-point Dixon 3T MR imaging. ANOVA with post hoc Bonferroni correction compared fat signal fraction and volume among subgroups. Pearson and Spearman analysis were used for correlations ($P < .05$).

RESULTS: Fat signal fraction was higher in women ($17.8\% \pm 10.7\%$) than men ($14.7\% \pm 7.8\%$; $P < .001$) and increased with age. Multifidus and erector spinae volume was lower in women ($565.4 \pm 83.8 \text{ cm}^3$) than in men ($811.6 \pm 98.9 \text{ cm}^3$; $P < .001$) and was age-independent. No differences in fat signal fraction were shown between the right and left paravertebral muscles or among the L1, L2, and L3 lumbar levels. The fat signal fraction was highest at L5 (women, $31.9\% \pm 9.3\%$; men, $25.7\% \pm 8.0\%$; $P < .001$). The fat signal fraction at L4 correlated best with total lumbar fat signal fraction (women, $r = 0.95$; men, $r = 0.92$, $P < .001$). Total fat signal fraction was higher in the multifidus compared with erector spinae muscles at L1–L4 for both sexes ($P < .001$).

CONCLUSIONS: Lumbar paravertebral muscle fat content increases with aging, independent of volume, in healthy volunteers 20–62 years of age. Women, low lumbar levels, and the multifidus muscle are most affected. Further study examining younger and older subjects and the functional impact of fatty infiltrated paravertebral muscles are warranted.

ABBREVIATIONS: BIA_{foot} = Tanita UM-081 bio-impedance fat analyzer; BIA_{hand} = Omron BF300 bioimpedance fat analyzer; BMI = body mass index; ES = erector spinae (longissimus and iliocostalis combined); FSF = fat signal fraction; LBP = low back pain; MF = multifidus; MFI = muscle fat infiltration

MR imaging is the criterion standard for evaluating the size and structure of soft-aqueous skeletal muscles.^{1,2} While T1WI is commonly used for qualitative assessment of muscle fat infiltration (MFI),^{3,4} chemical-shift–based imaging sequences allow quantification,^{5–7} which correlates with clinical symptoms^{3,8} and histology.^{2,9}

The Dixon technique is a robust chemical-shift imaging application producing water- and fat-only images from dual-echo ac-

quisitions.^{10,11} Excellent accuracy for MFI quantification is shown in comparison with T1WI,¹² spectroscopy,⁵ and histology in different animal species.⁹ Accordingly, Dixon MR imaging was used for evaluating muscle fat content in several clinical studies including patients with low back pain (LBP),^{5,13} acute-to-chronic whiplash,¹⁴ and neuromuscular disorders.¹⁵


Quantification of degeneration (fat infiltration and atrophy) of lumbar paravertebral muscles has attracted interest in understanding their biologic influence on persistent LBP. Atrophy and fat infiltrates are identified in patients^{16–21} and following experimentally induced lesions in a porcine model.²² However, human studies describing lumbar MFI report inconsistent findings: An


Received August 5, 2015; accepted after revision September 11.

From the Centre for Health Sciences (R.J.C., J.M.E.), Zurich University of Applied Sciences, Winterthur, Switzerland; Faculty of Health Professions (R.J.C.), Curtin University, Perth, Australia; Institute of Diagnostic and Interventional Radiology (L.F., D.N., M.A.F., M.M., E.J.U.), University Hospital and University of Zurich, Zurich, Switzerland; Feinberg School of Medicine (J.M.E.), Northwestern University, Chicago, Illinois; School of Health and Rehabilitation Sciences (J.M.E.), University of Queensland, Brisbane, Australia; and Institute of Diagnostic Radiology (M.M.), University Hospital Santa Maria della Misericordia, Udine, Italy.

This work was supported by the University Zürich Research Program “Research Time for Clinical Research at the Medical Faculty of University Zurich” (grant RT-13-014).

Please address correspondence to Rebecca Crawford, PhD, Health Professions, ZHAW, Zurich University of Applied Sciences, Technikumstr 71, CH-8401, Winterthur, Switzerland; e-mail: rebecca.crawford@zhaw.ch

 Indicates article with supplemental on-line tables.

 Indicates article with supplemental on-line photo.

<http://dx.doi.org/10.3174/ajnr.A4596>

association with LBP was demonstrated in some^{18,23–26} but not in others.^{13,16}

One explanation for discrepant findings is the influence of age on muscle composition.^{17,18,27–29} Spinal degeneration is known to occur early and increasingly throughout the life span,³⁰ yet to our knowledge, no study has assessed age-related morphologic changes to lumbar paravertebral muscles in healthy volunteers, which would provide a crucial supplement for future comparative studies.

We sought to quantify lumbar paravertebral muscle volume and fat content by 2-point Dixon MR imaging in healthy adult volunteers spanning 4 decades of life, and we aimed to establish an age- and level-dependent reference of lumbar paravertebral muscle volume and fat content as a reflection of natural aging history. We hypothesize greater MFI with age for both sexes and lumbar MFI level–dependence with an increasing cranio-caudal trend.

MATERIALS AND METHODS

This study was approved by the University Hospital Zurich institutional review board, participants provided written informed consent, and no authors had financial interests.

Study Participants

Eighty subjects from a larger ($n = 104$) prospective clinical trial investigating whole-body MRI of healthy adult volunteers (between October 2011 and April 2014) were examined. Forty women (39.0 ± 11.6 years of age; range, 21–62 years) and 40 men (40.0 ± 11.2 years of age; range, 20–61 years) with 10 cases for each sex were represented across 4 decades: 20–29, 30–39, 40–49, and 50–62 years (1 subject per sex older than 60 years of age).

Participants were recruited via advertisements on the intranet and clinical trials Web site of the University Hospital Zurich. Volunteers were screened by using the “Swiss Olympics’ First Sports Medicine Interview” health survey, including comprehensive questions determining medical history, hand- and leg-dominance, weight change (yes/no), smoker (yes/no), alcohol and drug use, and exercise (moderate/high or low). Musculoskeletal pain or injury was determined by the following question: “Do you currently or have you had injuries/symptoms/operations of the musculoskeletal system?” In response to this question, 16 body parts (including low back), plus an option of “other,” were marked yes or no; only responders answering no for all 16 body parts were included.

Subjects progressed to clinical examination when the self-reported height- and weight-registered body mass index (BMI) was between 18 and 26 kg/m² by using the following formula: Weight/Height² (kg/m²).³¹ Exclusion criteria were the following: contraindications for MR imaging (claustrophobia, metal, pacemaker, pregnancy); previous arthrodesis surgery; systemic diseases (chronic obstructive pulmonary diseases, diabetes, metabolic diseases, rheumatologic disorders, tumors, chronic pain syndrome); vascular problems (coronary heart disease, peripheral vascular disease); and alcohol or drug abuse.

Clinical Examination Pre-MR Imaging

Barefoot standing height was measured with a wall-mounted stadiometer (nearest 0.1 cm); bodyweight (kilograms) was collected via a standard scale; and BMI was derived from these 2 parameters. Two bioelectric impedance instruments were used to reflect body fat: Tanita UM-081 (foot sensor pads on a standing scale; Tanita, Arlington Heights, Illinois) (BIA_{foot}), and Omron BF300 (hand sensor pads with a hand-held device; Omron Healthcare, Kyoto, Japan) (BIA_{hand}). Leg dominance was confirmed with a balance recovery test.³²

Imaging Acquisition

Whole-body scans were performed in a 3T MR imaging scanner (Ingenia; Philips Healthcare, Best, the Netherlands). A table-integrated 15-element dS head coil, automatically centering on imaged anatomy; a 16-channel posterior coil; and two 16-channel anterior coils were used for signal reception; the dual-transmit body coil of the scanner was used for radiofrequency transmission. Subjects were supine (arms alongside the body).

MR imaging protocol included axial 2-point Dixon sequences (3D fast-field echo T1; 2 echoes; acquired voxel dimensions, 2.0, 2.0, 4.0 mm; reconstructed voxel dimensions, 1.0, 1.0, 2.0 mm; intersection gap, 0.0 mm; FOV, 560 × 352; number of sections, 80; TR, 4.2 ms; TE, 1.2 and 3.1 ms; flip angle, 5°; number of signal averages, 2; sensitivity encoding acceleration factor, 2.0 and 2.0; foldover direction, anteroposterior; water-fat shift, 0.292 pixels; receiver bandwidth, 1485.1 Hz/pixel⁻¹; single series acquisition time, 16.4 ms; scanning duration, 28:20 minutes). Two or 3 sequence blocks (participant height–dependent), with an acquisition time of 32.8 or 49.2 ms, respectively, represented the lumbosacral spine.

Image Analysis

Image analysis was performed with dedicated software providing semiautomatic segmentation with linear interpolation (Myrian; Intrasure, Paris, France). An experienced musculoskeletal-trained reader (R.J.C.), skilled in MR imaging postprocessing and volumetric analyses, segmented muscles at all vertebrae between the superior endplate of L1 to the superior endplate of the sacrum. Each lumbar level was defined from the superior endplate of the upper vertebra to the superior endplate of the vertebra (or sacrum) immediately below, including the intervening disc. We drew left and right paravertebral muscle ROIs every third section of the axial water image, while scout-referencing equivalent fat images. The multifidus (MF), longissimus, and iliocostalis were identified as medial-to-lateral paravertebral muscles, respectively; the longissimus and iliocostalis muscles were segmented as a single region labeled “erector spinae” (ES); the border between the MF and ES was scouted from the mammillary processes. The software calculated muscle volume and mean signal intensity values of all pixels. ROIs were copied from the water images to fat images of the same sequence; mean signal intensities (Signal_{water} + Signal_{fat}) within these ROIs were recorded (On-line Figure). Fat signal fraction (FSF) was calculated as FSF (%) = (Signal_{fat}/[Signal_{water} + Signal_{fat}]) × 100.³³

Table 1: Demographics for 80 healthy adult volunteers^a

	Women (n = 40)	Men (n = 40)	P Value
Age (yr)	39.0 ± 11.6 (21–62)	40.0 ± 11.2 (20–61)	.22
Height (cm)	168.0 ± 6.2 (158–183)	181.7 ± 7.3 (169–200)	<.001
Weight (kg)	61.3 ± 7.7 (43.6–86.0)	76.1 ± 7.7 (56.3–92.0)	<.001
BMI (kg/m ²)	21.6 ± 2.1 (18.2–26.0)	23.0 ± 1.8 (19.4–26.2)	.05
BIA _{foot} (%)	27.8 ± 5.6 (12.5–38.8)	17.9 ± 4.7 (5.4–31.0)	<.001
BIA _{hand} (%)	21.9 ± 5.3 (13.0–33.3)	14.2 ± 4.7 (5.2–22.3)	<.001
Leg dominance	28 Right, 12 left	23 Right, 17 left	.35
Hand dominance	34 Right, 6 left	34 Right, 6 left	1.0

Note:—BMI indicates body mass index.

^a Data are mean (range).

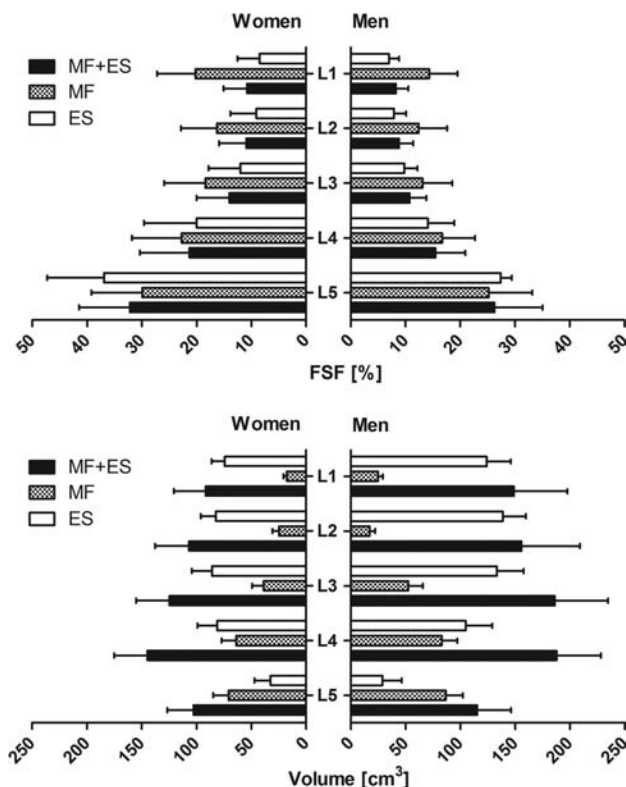


FIG 1. Fat signal fraction (percentage) and muscle volume (cubic centimeters) at each lumbar spine level (L1–L5) for women and men. Multifidus and erector spinae FSFs and muscle volumes are given separately and for FSF combined, to represent the volume-weighted average for both (MF + ES). FSF and volume are represented as the sum of both sides (left + right).

Statistical Analysis

Statistical analyses were performed by using commercial software (GraphPad Prism; GraphPad Software, San Diego, California; and SPSS, Version 20; IBM, Armonk, New York). Mean (\pm SD) FSF and volume for MF, ES, and MF + ES were calculated for each subject. The Kolmogorov-Smirnov test verified normal distribution. The ANOVA with post hoc Bonferroni correction compared FSF and volume values among subgroups. Except for the comparison between the right and left sides as part of ANOVA, FSF and volume values of both sides were combined for statistical analysis (On-line Figure). Distributions of leg and hand dominance were compared by using the χ^2 test. Correlations between linear parameters (FSF, age, volume, BMI, BIA_{foot}, and BIA_{hand}) were assessed with the Pearson correlation coefficient (r). Correlations of FSF and

BMI with categoric variables (weight change, diet, smoking, alcohol, leg/hand dominance) were evaluated by using the Spearman r . Correlations between 1.0 and 0.5 were considered strong; 0.5–0.3, moderate; and 0.3–0.1, weak. Statistical significance was $P < .05$.

RESULTS

Descriptive statistics (mean \pm SD, range) of demographics are found in Table 1. No significant differences in paravertebral

muscle FSF or volume were found between the right and left sides ($P = .30$) or hand ($P = .52$) or leg ($P = .29$) dominance.

FSF (percentage) and volume (cubic centimeters) (mean \pm SD) for age group, sex, and lumbar level are presented in On-line Tables 1 and 2 and are illustrated in Figs 1 and 2.

Sex

FSF for MF and ES alone and combined was higher in women than in men ($P < .001$), whereas the volume for MF and ES alone and combined was higher in men ($P < .001$).

Age

Volunteers 30–39 years of age (only in men, $P < .001$), 40–49 years (women: $P = .04$; men: $P < .001$), and 50–62 years (both sexes, $P < .001$) showed higher FSF (MF + ES) than those 20–29 years of age. In men, there was also higher FSF at 50–61 years compared with 30–39 years ($P = .049$) and 40–49 years ($P = .03$) (On-line Table 1 and Fig 2).

Lumbar Level

FSF (MF + ES) showed an increasing trend from L1 to L5. No differences in FSF were found among the L1, L2, and L3 levels (women, $P = .07$; men, $P = .86$). All other FSF level comparisons were significant ($P < .001$). Higher FSF (MF + ES, percentage) for both sexes was found at L5 (women: 31.9 ± 9.3 ; men: 25.7 ± 8.0 ; $P < .001$) and L4 (women: 21.2 ± 9.3 ; men: 15.3 ± 5.3 ; $P < .001$) compared with the supradjacent level. FSF (MF + ES) was higher in women at L1 ($P < .05$), L3 ($P < .05$), L4 ($P < .001$), and L5 ($P < .05$) (On-line Table 1).

Muscles

Total FSF (L1–L5) was higher in the MF than in ES (both sexes, $P < .001$). For MF and ES separately, FSF (L1–L5) was higher in women ($P < .001$). According to muscle and level, FSF was higher in the MF than in the ES at L1, L2, L3, and L4 (both sexes, $P < .001$ each) and higher in the ES at L5 in women ($P < .05$) (On-line Table 1 and Fig 1).

Associations

Associations between variables are presented in Table 2.

A moderate association between FSF (L1–L5) and age was shown (women: $r = 0.39$, $P < .05$; men: $r = 0.50$, $P < .001$). FSF at L3 best correlated with age for both sexes, strongly in men (women: $r = 0.40$, $P < .05$; men: $r = 0.55$, $P < .001$). No association was shown between age and muscle volume or BMI for both sexes. Of the 2 body fat measures, BIA_{foot} correlated best with age (women: $r = 0.46$, $P < .01$; men: $r = 0.52$, $P < .001$) (Table 2, Figs 1 and 2, and On-line Table 2).

Strong associations were shown between total FSF (L1–L5) and FSF at L4 (women: $r = 0.95$, $P < .001$; men: $r = 0.92$, $P < .001$) (Table 2).

No significant correlation occurred between BMI and FSF. A strong correlation occurred between BMI and BIA_{foot} or BIA_{hand} (Table 2).

No association was seen between FSF or BMI and consumption-related parameters (weight change, smoking, alcohol/drug use, exercise) or hand/leg dominance (data not shown).

DISCUSSION

We quantified lumbar paravertebral muscle volume and fat content by using 2-point Dixon whole-body MR imaging of 80

healthy adult volunteers (20–62 years of age) and showed that the lumbar paravertebral muscle fat increased with age, independent of volume. Women, low lumbar levels, and multifidus muscles were most affected; these findings align with degenerative features of the spinal column that are highly prevalent in asymptomatic individuals.³⁰

Lumbar paravertebral muscle degeneration occurs in LBP^{16–20,24} and in response to induced lesions,²² yet its prognostic value is unclear. Little is known about normative degeneration, and comparisons with existing literature are limited. Using similar quantification methods with axial 2-point Dixon MR imaging at 1.5T, Fischer et al⁵ described mean FSF within a region of bilateral multifidus muscles of 21% (range, 3%–65%). Despite their reporting symptomatic cases (potentially higher MFI percentage),

our results (for MF / MF + ES) of 23%/18% in female and 18%/15% in male lumbar paravertebral muscles appear aligned and may reflect consistent methods. Meakin et al²⁸ interpolated cross-sectional areas from axial T1WI in women only, reporting mean MF + ES volume caudal to L3–L4 of 303 cm³ (for $n = 11$ with no LBP; 281 cm³ in all 42 women). In agreement, our MF + ES volume for women at L4–L5 was 248 cm³. We provide normative FSF and volumes for all lumbar levels in both sexes across 4 decades.

Our fat content age effect agrees with that in other studies reporting MFI in subjects with and without²⁹ back pain.^{17,24,25} In disagreement, Fortin et al¹⁸ found no correlation with age and FSF cross-sectional areas at L3–L4 or L5–S1 derived from T2WI in men 35–69 years of age. This likely reflects methodologic differences and may relate to their lack of cases representing the 20- to 30-year age group, further highlighting the need for consistency in quantifying paravertebral muscle quality.

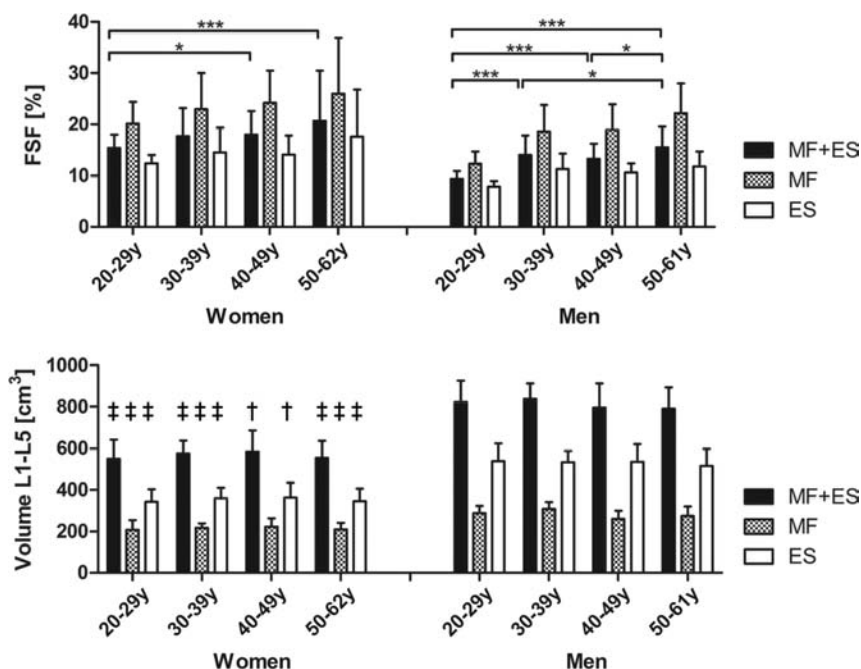


FIG 2. Age-group-averaged fat signal fraction (percentage) and muscle volume for both sexes. Multifidus and erector spinae FSFs and muscle volumes are given separately and combined (MF + ES); FSF is shown as a volume-weighted average. FSF and volumes are represented by the sum of both sides (left + right). Significant differences of the means between age groups are indicated by an asterisk ($P < .05$) and triple asterisks ($P < .001$). FSF was higher in women than in men at each age group, lumbar level, and muscle (MF + ES, $P < .001$; MF, $P < .01$; ES, $P < .01$). Volume was lower in women than in men as indicated by a dagger ($P < .01$) and double daggers ($P < .001$).

Table 2: Correlation matrix—men upper right, women lower left

Women	Men										
	FSF (L1–L5)	FSF (L1)	FSF (L2)	FSF (L3)	FSF (L4)	FSF (L5)	Volume (L1–L5)	Age	BMI	BIA _{foot}	BIA _{hand}
FSF (L1–L5)		0.81 ^a	0.91 ^a	0.90 ^a	0.92 ^a	0.90 ^a	−0.20	0.50 ^b	0.13	0.52 ^b	0.43 ^b
FSF (L1)	0.86 ^a		0.86 ^a	0.71 ^a	0.61 ^a	0.62 ^a	−0.25	0.34 ^c	0.17	0.43 ^b	0.47 ^a
FSF (L2)	0.87 ^a	0.92 ^a		0.90 ^a	0.80 ^a	0.68 ^a	−0.25	0.49 ^b	0.12	0.45 ^b	0.40 ^c
FSF (L3)	0.93 ^a	0.82 ^a	0.87 ^a		0.83 ^a	0.73 ^a	−0.12	0.55 ^a	0.22	0.48 ^b	0.46 ^b
FSF (L4)	0.95 ^a	0.75 ^a	0.79 ^a	0.90 ^a		0.86 ^a	−0.18	0.51 ^b	0.08	0.47 ^b	0.30
FSF (L5)	0.90 ^a	0.69 ^a	0.65 ^a	0.76 ^a	0.83 ^a		−0.13	0.46 ^b	0.10	0.49 ^b	0.39 ^c
Volume (L1–L5)	−0.03	−0.23	−0.20	−0.02	0.00	0.07		−0.13	0.32 ^c	0.06	0.30
Age	0.39 ^c	0.36 ^c	0.36 ^c	0.40 ^c	0.31 ^c	0.37 ^c	0.08		0.18	0.52 ^b	0.34 ^c
BMI	−0.08	−0.11	−0.17	−0.07	−0.07	0.02	0.29	0.03		0.70 ^a	0.81 ^a
BIA _{foot}	0.39 ^c	0.35 ^c	0.31 ^c	0.41 ^b	0.37 ^c	0.36 ^c	0.20	0.46 ^b	0.78 ^a		0.76 ^a
BIA _{hand}	0.20	0.18	0.14	0.19	0.16	0.18	0.21	0.00	0.76 ^a	0.75 ^a	

^a $P < .001$.

^b $P < .01$.

^c $P < .05$.

We found an age-related increase of MF and ES MFI for both sexes, suggesting progressive worsening in muscle quality, even in healthy individuals. Male participants in each older age group had significantly more MFI in both MF and ES muscles than the youngest men; the third decade of life is an effective baseline for paravertebral muscle degeneration in healthy men. On the contrary, increased MFI in our female participants only occurred in the fifth and sixth decades. These findings may indicate earlier onset of MFI in men and a sex-dependent decline in muscle quality.

We showed an increasing craniocaudal trend for FSF between L1 and L5. Levels L4–L5 had higher MFI compared with the supradjacent level; the upper lumbar spine showed a trend in women (women, $P = .07$; men, $P = .84$). This finding agrees with the longitudinal male population study of Fortin et al,¹⁷ in which L5–S1 had higher MFI than L3–L4. D’Hooge et al³⁴ showed more MFI bilaterally in subjects with LBP compared with healthy controls at both L4 endplates, yet equivalence at the L3 superior endplate. While D’Hooge et al³⁴ did not report interlevel comparisons, agreement exists with respect to a caudal trend for increasing MFI. Our difference between sexes in the upper lumbar spine is interesting. We speculate that muscle quality relates to the intrinsic shape and function of the thoracolumbosacral spine, which may differ between sexes. High paravertebral muscle volume occurs in people with greater lordotic angulation.²⁸ While there is conjecture about sex differences in lumbar curvature,³⁵ determining spinal shape in relation to MFI could offer clarification.

Plausible explanations behind normative muscle atrophy and MFI exist and include a combination of disuse and denervation secondary to the degenerative cascade and concomitant altered tensile properties of lumbar myofascial and neural tissues. Disuse-related muscle decline purportedly relates to deconditioning, local tensile unload, and altered muscle recruitment.^{16,19,22} Paravertebral muscle denervation occurs in asymptomatic individuals,³⁶ and the multifidus muscle is susceptible to the effects of neural stretching after disc height loss and subsequent listhesis.³⁷ However, the extent of paraspinal muscle atrophy is not explained by matching denervation; this finding indicates the potential for reversal through activity.³⁸ We describe no association of FSF with BMI or exercise, perhaps not supporting either theory. Instead, a local disuse mechanism dependent on paravertebral muscle morphology and proximity to the vertebra as shown in the cervical spine³⁹ might better explain the etiology.

Conflicting with several studies reporting laterality in healthy individuals,⁴⁰ those with LBP,^{19,20,27,28} and the general population,¹⁷ we agree with another study¹⁸ in showing no differences between sides or hand/leg dominance in our healthy volunteers. Valentin et al²⁹ described asymmetry in MF and ES MFI in their healthy subjects, yet no asymmetry for ES volume. The discrepancy among studies may be due to methodologic differences relating to the types of measurement techniques (quantitative versus qualitative, MR imaging versus CT/sonography, volume versus cross-sectional area), defined paravertebral ROIs, and study samples.

Our valuable methodologic finding promotes more time-effi-

cient data collection by using imaging at L4 to generalize for total lumbar paravertebral muscle fat content.

MFI was higher in women than in men at each age group in our series, despite control for BMI in subject selection, resulting in a lower female mean ($P = .05$). Age-related change to skeletal muscle quality differs for sex-dependence.⁴¹ Generally, men lose more muscle with aging, yet women have greater functional consequences.⁴¹ Therefore, the influence of general body fat on healthy paravertebral MFI cannot be ignored.^{29,34} While our study showed no correlation between BMI and FSF, our bioimpedance was strongly associated. Despite the questionable validity of bioimpedance in measuring body fat,⁴² further investigation appears warranted in determining the suitability of BMI or bioimpedance in identifying modifiable risks.

While our study has several strengths, it is limited by being cross-sectional, though it is feasible in assessing a wide age range. Identifying a baseline age group from which to reference the natural history of change represents a valuable contribution to the literature to which longitudinal studies can be directed. We only included participants 20–62 years of age; this age range may not be generalizable to other age groups. Our sample included 10 cases per sex and decade, offering an improvement to the findings in the literature, but was potentially inadequately powered for reference as normative data. Whole-body MRI may not be generalizable to higher resolution clinical scans. Additionally, 2-point Dixon sequences are prone to underestimating FSF; however, we limited the influence by reduction of the flip angle.⁵

Our healthy volunteers evidenced declining muscle quality as a normal process of aging from the twenties into mature adulthood. Investigating whether serial decline continues into healthy older adulthood would be valuable. Furthermore, that poorer muscle quality as determined by increased MFI affects muscle function when noncontractile tissue replaces muscle fibers is implied. Whether this speculation is true should be investigated with applied research examining function.

CONCLUSIONS

Lumbar multifidus and erector spinae fat content increased with age in healthy adults 20–62 years of age, was higher in women than men, and was more prevalent in the low lumbar levels and in the multifidus compared with erector spinae muscles. These muscle-based degenerative features are part of healthy aging and, relating to LBP, should be interpreted within the individual context. Measurements at L4 are surrogates for the whole lumbar spine. Further studies examining adolescents and adults older than 60 years and in applied research examining function may be helpful in directing interventions aimed at reducing muscle degeneration in the lumbar spine.

ACKNOWLEDGMENTS

We thank our physicist Roger Luechinger, PhD, for his technical support; Dan Linh Nguyen, MD, for her instruction concerning the analysis software; our radiographers Nicole Aebi, Simone Suess, and Suzanne Potter for performing the MR imaging examinations; Áine Ni Mhuiris, for her assistance in data entry; and Andrew Smith and Marie Wasielewski for their contribution to figure development.

Disclosures: James M. Elliott—UNRELATED: Consultancy: Relevant financial activities outside the body of work include a 35% ownership/investment interest in a medical consulting start-up, Pain ID; Grants/Grants Pending: National Institutes of Health,* Comments: 1, R01HD079076-01A1; project title: Neuromuscular Mechanisms Underlying Poor Recovery from Whiplash Injuries; project duration: September 2014 to May 2019; role: Principal Investigator; Magda Marcon—RELATED: Grant: University Zürich Research Program.* Erika J. Ulbrich—RELATED: Grant: Research Time for Clinical Research at the Medical Faculty of University Zurich (RT-13-014). *Money paid to the institution.

REFERENCES

- Akagi R, Takai Y, Kato E, et al. **Development of an equation to predict muscle volume of elbow flexors for men and women with a wide range of age.** *Eur J Appl Physiol* 2010;108:689–94 CrossRef Medline
- Samagh SP, Kramer EJ, Melkus G, et al. **MRI quantification of fatty infiltration and muscle atrophy in a mouse model of rotator cuff tears.** *J Orthop Res* 2013;31:421–26 CrossRef Medline
- Elliott JM, Flynn TW, Al-Najjar A, et al. **The pearls and pitfalls of magnetic resonance imaging for the spine.** *J Orthop Sports Phys Ther* 2011;41:848–60 CrossRef Medline
- Elliott JM, O'Leary S, Sterling M, et al. **Magnetic resonance imaging findings of fatty infiltrate in the cervical flexors in chronic whiplash.** *Spine* 2010;35:948–54 CrossRef Medline
- Fischer MA, Nanz D, Shimakawa A, et al. **Quantification of muscle fat in patients with low back pain: comparison of multi-echo MR imaging with single-voxel MR spectroscopy.** *Radiology* 2013;266:555–63 CrossRef Medline
- Reeder SB, Hu HH, Sirlin CB. **Proton density fat-fraction: a standardized MR-based biomarker of tissue fat concentration.** *J Magn Reson Imaging* 2012;36:1011–14 CrossRef Medline
- Elliott J, Pedler A, Kenardy J, et al. **The temporal development of fatty infiltrates in the neck muscles following whiplash injury: an association with pain and posttraumatic stress.** *PLoS One* 2011;6:e21194 CrossRef Medline
- Fischer MA, Pfirrmann CW, Espinosa N, et al. **Dixon-based MRI for assessment of muscle-fat content in phantoms, healthy volunteers and patients with achillodynia: comparison to visual assessment of calf muscle quality.** *Eur Radiol* 2014;24:1366–75 CrossRef Medline
- Smith AC, Parrish TB, Abbott R, et al. **Muscle-fat MRI: 1.5 Tesla and 3.0 Tesla versus histology.** *Muscle Nerve* 2014;50:170–76 CrossRef Medline
- Dixon WT. **Simple proton spectroscopic imaging.** *Radiology* 1984;153:189–94 CrossRef Medline
- Ma J. **Dixon techniques for water and fat imaging.** *J Magn Reson Imaging* 2008;28:543–58 CrossRef Medline
- Elliott JM, Walton DM, Rademaker A, et al. **Quantification of cervical spine muscle fat: a comparison between T1-weighted and multi-echo gradient echo imaging using a variable projection algorithm (VARPRO).** *BMC Med Imag* 2013;13:30 CrossRef Medline
- Paalanne N, Niinimäki J, Karppinen J, et al. **Assessment of association between low back pain and paraspinal muscle atrophy using opposed-phase magnetic resonance imaging: a population-based study among young adults.** *Spine* 2011;36:1961–68 CrossRef Medline
- Elliott JM, Courtney DM, Rademaker A, et al. **The rapid and progressive degeneration of the cervical multifidus in whiplash: a MRI study of fatty infiltration.** *Spine (Phila Pa 1976)* 2015;40:E694–700 CrossRef Medline
- Gaeta M, Scribano E, Mileto A, et al. **Muscle fat fraction in neuromuscular disorders: dual-echo dual-flip-angle spoiled gradient-recalled MR imaging technique for quantification—a feasibility study.** *Radiology* 2011;259:487–94 CrossRef Medline
- Danneels LA, Vanderstraeten GG, Cambier DC, et al. **CT imaging of trunk muscles in chronic low back pain patients and healthy control subjects.** *Eur Spine J* 2000;9:266–72 CrossRef Medline
- Fortin M, Videman T, Gibbons LE, et al. **Paraspinal muscle morphology and composition: a 15-yr longitudinal magnetic resonance imaging study.** *Med Sci Sports Exerc* 2014;46:893–901 CrossRef Medline
- Fortin M, Yuan Y, Battie MC. **Factors associated with paraspinal muscle asymmetry in size and composition in a general population sample of men.** *Phys Ther* 2013;93:1540–50 CrossRef Medline
- Hides J, Gilmore C, Stanton W, et al. **Multifidus size and symmetry among chronic LBP and healthy asymptomatic subjects.** *Man Ther* 2008;13:43–49 CrossRef Medline
- Ploumis A, Michailidis N, Christodoulou P, et al. **Ipsilateral atrophy of paraspinal and psoas muscle in unilateral back pain patients with monosegmental degenerative disc disease.** *Br J Radiol* 2011;84:709–13 CrossRef Medline
- Teichtahl AJ, Urquhart DM, Wang Y, et al. **Fat infiltration of paraspinal muscles is associated with low back pain, disability, and structural abnormalities in community-based adults.** *Spine J* 2015;15:1593–601 CrossRef Medline
- Hodges P, Holm AK, Hansson T, et al. **Rapid atrophy of the lumbar multifidus follows experimental disc or nerve root injury.** *Spine* 2006;31:2926–33 CrossRef Medline
- Farshad M, Gerber C, Farshad-Amacker NA, et al. **Asymmetry of the multifidus muscle in lumbar radicular nerve compression.** *Skeletal Radiol* 2014;43:49–53 CrossRef Medline
- Kjaer P, Bendix T, Sorensen JS, et al. **Are MRI-defined fat infiltrations in the multifidus muscles associated with low back pain? BMC Med** 2007;5:2 CrossRef Medline
- Mengiardi B, Schmid MR, Boos N, et al. **Fat content of lumbar paraspinal muscles in patients with chronic low back pain and in asymptomatic volunteers: quantification with MR spectroscopy.** *Radiology* 2006;240:786–92 CrossRef Medline
- Parkkola R, Rytökoski U, Kormanen M. **Magnetic resonance imaging of the discs and trunk muscles in patients with chronic low back pain and healthy control subjects.** *Spine* 1993;18:830–36 CrossRef Medline
- Barker KL, Shamley DR, Jackson D. **Changes in the cross-sectional area of multifidus and psoas in patients with unilateral back pain: the relationship to pain and disability.** *Spine* 2004;29:E515–19 CrossRef Medline
- Meakin JR, Fulford J, Seymour R, et al. **The relationship between sagittal curvature and extensor muscle volume in the lumbar spine.** *J Anat* 2013;222:608–14 CrossRef Medline
- Valentin S, Licka T, Elliott J. **Age and side-related morphometric MRI evaluation of trunk muscles in people without back pain.** *Man Ther* 2015;20:90–95 CrossRef Medline
- Brinjikji W, Luetmer PH, Comstock B, et al. **Systematic literature review of imaging features of spinal degeneration in asymptomatic populations.** *AJNR Am J Neuroradiol* 2015;36:811–16 CrossRef Medline
- Obesity: preventing and managing the global epidemic: report of a WHO consultation. *World Health Organ Tech Rep Ser* 2000;894:i–xii, 1–253 Medline
- Hoffman M, Schrader J, Applegate T, et al. **Unilateral postural control of the functionally dominant and nondominant extremities of healthy subjects.** *J Athl Train* 1998;33:319–22 Medline
- Cassidy FH, Yokoo T, Aganovic L, et al. **Fatty liver disease: MR imaging techniques for the detection and quantification of liver steatosis.** *Radiographics* 2009;29:231–60 CrossRef Medline
- D'Hooge R, Cagnie B, Crombez G, et al. **Increased intramuscular fatty infiltration without differences in lumbar muscle cross-sectional area during remission of unilateral recurrent low back pain.** *Man Ther* 2012;17:584–88 CrossRef Medline
- Been E, Kalichman L. **Lumbar lordosis.** *Spine J* 2014;14:87–97 CrossRef Medline
- Tong HC, Haig AJ, Yamakawa KS, et al. **Paraspinal electromyography: age-correlated normative values in asymptomatic subjects.** *Spine* 2005;30:E499–502 CrossRef Medline
- Haig AJ, London Z, Sandella DE. **Symmetry of paraspinal muscle denervation in clinical lumbar spinal stenosis: support for a hy-**

- pothesis of posterior primary ramus stretching?** *Muscle Nerve* 2013; 48:198–203 CrossRef Medline
38. Yarjanian JA, Fetzer A, Yamakawa KS, et al. **Correlation of paraspinal atrophy and denervation in back pain and spinal stenosis relative to asymptomatic controls.** *PM R* 2013;5:39–44 CrossRef Medline
 39. Abbott R, Pedler A, Sterling M, et al. **The geography of fatty infiltrates within the cervical multifidus and semispinalis cervicis in individuals with chronic whiplash-associated disorders.** *J Orthop Sports Phys Ther* 2015;45:281–88 CrossRef Medline
 40. Niemelainen R, Briand MM, Battié MC. **Substantial asymmetry in paraspinal muscle cross-sectional area in healthy adults questions its value as a marker of low back pain and pathology.** *Spine* 2011;36: 2152–57 CrossRef Medline
 41. Doherty TJ. **Invited review: aging and sarcopenia.** *J Appl Physiol* 2003;95:1717–27 CrossRef Medline
 42. Sillanpää E, Cheng S, Häkkinen K, et al. **Body composition in 18- to 88-year-old adults—comparison of multifrequency bioimpedance and dual-energy X-ray absorptiometry.** *Obesity* 2014;22:101–09 CrossRef Medline

Multicenter Validation of Mean Upper Cervical Cord Area Measurements from Head 3D T1-Weighted MR Imaging in Patients with Multiple Sclerosis

Y. Liu, C. Lukas, M.D. Steenwijk, M. Daams, A. Versteeg, Y. Duan, K. Li, F. Weiler, H.K. Hahn, M.P. Wattjes, F. Barkhof, and H. Vrenken



ABSTRACT

BACKGROUND AND PURPOSE: Spinal cord atrophy is a common and clinically relevant characteristic in multiple sclerosis. We aimed to perform a multicenter validation study of mean upper cervical cord area measurements in patients with multiple sclerosis and healthy controls from head MR images and to explore the effect of gadolinium administration on mean upper cervical cord area measurements.

MATERIALS AND METHODS: We recruited 97 subjects from 3 centers, including 60 patients with multiple sclerosis of different disease types and 37 healthy controls. Both cervical cord and head 3D T1-weighted images were acquired. In 11 additional patients from 1 center, head images before and after gadolinium administration and cervical cord images after gadolinium administration were acquired. The mean upper cervical cord area was compared between cervical cord and head images by using intraclass correlation coefficients (ICC) for both consistency (ICC_{consist}) and absolute (ICC_{abs}) agreement.

RESULTS: There was excellent agreement of mean upper cervical cord area measurements from head and cervical cord images in the entire group (ICC_{abs} = 0.987) and across centers and disease subtypes. The mean absolute difference between the mean upper cervical cord area measured from head and cervical cord images was 2 mm² (2.3%). Additionally, excellent agreement was found between the mean upper cervical cord area measured from head images with and without gadolinium administration (ICC_{abs} = 0.991) and between the cervical cord and head images with gadolinium administration (ICC_{abs} = 0.992).

CONCLUSIONS: Excellent agreement between mean upper cervical cord area measurements on head and cervical cord images was observed in this multicenter study, implying that upper cervical cord atrophy can be reliably measured from head images. Postgadolinium head or cervical cord images may also be suitable for measuring mean upper cervical cord area.

ABBREVIATIONS: EDSS = Expanded Disability Status Scale; Gd = gadolinium; HC = healthy control; ICC = intraclass correlation coefficient; ICC_{abs} = ICC absolute agreement; ICC_{consist} = ICC consistency; MUCCA = mean upper cervical cord area; PPMS = primary-progressive MS; RRMS = relapsing-remitting MS, SPMS = secondary-progressive MS

Spinal cord atrophy is recognized as a common and clinically relevant characteristic in patients with multiple sclerosis.¹ Differences in cervical cord volume and area among patients

with different phenotypes of MS and healthy controls (HCs) measured by MR imaging have been identified in many studies.^{2–4} Furthermore, a modest or strong correlation between spinal cord atrophy and disability has been demonstrated in

Received July 18, 2015; accepted after revision August 27.

From the Department of Radiology (Y.L., Y.D., K.L.), Xuanwu Hospital, Capital Medical University, Beijing, P.R. China; Department of Radiology and Nuclear Medicine (Y.L., M.D.S., M.D., A.V., M.P.W., F.B., H.V.), Neuroscience Campus Amsterdam; Department of Anatomy and Neurosciences (M.D.), Section of Clinical Neuroscience; and Department of Physics and Medical Technology (H.V.), Neuroscience Campus Amsterdam, VU University Medical Center, Amsterdam, the Netherlands; Department of Neurology and Tianjin Neurological Institute (Y.L.), Tianjin Medical University, General Hospital, Tianjin, P.R. China; Department of Diagnostic and Interventional Radiology and Nuclear Medicine (C.L.), St. Josef Hospital, Ruhr University, Bochum, Germany; and Fraunhofer MEVIS, Institute for Medical Image Computing (F.W., H.K.H.), Bremen, Germany.

This work was supported by the European Committee for Treatment and Research in Multiple Sclerosis/Magnetic Research Imaging in Multiple Sclerosis Fellowship from the European Committee for Treatment and Research in Multiple Sclerosis (Y.L.), the National Science Foundation of China (No. 81101038 and 81501736), Beijing

Municipal Administration of Hospitals Clinical Medicine Development of Special Funding Support (No. ZYLX201609), the Beijing Natural Science fund (No. 7133244), the Beijing Nova Programme (No. xx2013045), and the Key Projects in the National Science & Technology Pillar Program during the Twelfth Five-Year Plan Period (No. 2012BAI10B04). Part of this work was supported by the German Federal Ministry for Education and Research, Bundesministerium für Bildung und Forschung, and the German Competence Network Multiple Sclerosis (Kompetenznetz Multiple Sklerose) (No. 01GI0914). The VUmc MS Center Amsterdam is sponsored through the program grant by the Dutch MS Research Foundation (Nos. 09-358d and 14-358e).

Please address correspondence to Yaou Liu, MD, PhD, Department of Radiology, Xuanwu Hospital, Capital Medical University, Beijing 100053, China; e-mail: asiaeurope80@gmail.com

Indicates open access to non-subscribers at www.ajnr.org

Indicates article with supplemental on-line table.

<http://dx.doi.org/10.3174/ajnr.A4635>

numerous studies, suggesting that spinal cord atrophy is an essential determinant of clinical disability and a potential outcome measure to monitor MS disease progression.⁵⁻⁷ The measurement of the upper cervical cord area is a well-established method for the assessment of spinal cord atrophy and has been applied in most studies so far.^{2,3,5,8,9} Both image acquisition and spinal cord segmentation are technically feasible and more accurate in the upper cervical region compared with other parts of the cord or the entire cord.¹⁰ In addition, the upper cervical cord is more frequently affected by MS pathology than lower parts of the spinal cord.¹¹

Mean upper cervical cord area (MUCCA) can be measured by using 3D T1-weighted MR images of the cervical cord.^{3,4} The MUCCA also has been measured recently on 3D T1-weighted MR images of the head covering the upper cervical cord, which has yielded promising results showing associations between MUCCA and clinical disability and disease progression.^{2,5} Measuring the MUCCA from head MR images offers the opportunity to analyze MUCCA retrospectively in datasets without dedicated cervical 3D T1-weighted images, and it can reduce costs and patient burden in prospective studies by eliminating the need for separate cervical cord image acquisitions if these are only acquired to measure the MUCCA. An MR imaging contrast agent is commonly used to detect the blood-brain barrier breakdown and inflammation in new lesions^{12,13} in patients with MS, which might influence the MUCCA measurements by tissue-contrast changes. The effect of the MR imaging contrast agent on MUCCA measurement also has to be investigated to ease the implementation of MUCCA as an auxiliary measurement in clinical practice. Although MUCCA measurements based on head 3D T1-weighted images have been successfully used in a monocenter study,¹⁴ multicenter validation is lacking. In addition, the possible effect of intravenous contrast administration on MUCCA measurements has not been investigated.

Therefore, the aim of the current study was to validate the measurement of the MUCCA on the basis of head compared with cervical cord 3D T1-weighted images in patients with MS and healthy controls on different MR imaging systems by using different acquisition parameters from multiple centers and to explore the effect of gadolinium (Gd) administration on MUCCA measurements.

MATERIALS AND METHODS

Subjects

The study was approved by the local institutional review board of the 3 centers (Amsterdam, Beijing and Bochum), and informed consent was obtained from each participant.

To investigate the variability of the MUCCA based on head 3D T1 MR images and cervical cord 3D T1 MR images, we selected scans from ongoing local cohorts in which separate head and cervical cord 3D T1 MR images were acquired. All images were checked for visibility of the spinal cord without artifacts, and head images were checked for coverage of the upper cervical cord. A total of 97 subjects were recruited from 3 centers (A: Amsterdam, B: Beijing, and C: Bochum), including 40 patients with relapsing-remitting MS (RRMS), 10 with

Table 1: Scan protocols for all 3 centers^a

	Center A (n = 58)	Center B (n = 28)	Center C (n = 7)
Vendor	GE Healthcare ^b	Siemens ^c	Philips Healthcare ^d
Scanner	Signa HDxt	Trio Tim	Achieva
Head MRI			
Sequence	FSPGR	MPRAGE	FFE
No. of sections	176	176	180
TR (ms)	7.8	1600	10
TE (ms)	3	2.13	4.6
TI (ms)	450	1000	1000
FA	12°	9°	8°
Voxel size (mm)	0.94 × 0.94 × 1	1 × 1 × 1	1 × 1 × 1
Cervical MRI			
Sequence	FSPGR	MPRAGE	FFE
No. of sections	176	96	64
TR (ms)	7.3	2000	8
TE (ms)	3	3.36	3.5
TI (ms)	450	1100	1000
FA	15°	10°	8°
Voxel size (mm)	1 × 1 × 1	1 × 1 × 1	1 × 1 × 1

Note:—FA indicates flip angle; FFE, fast-field echo; FSPGR, fast spoiled gradient recalled.

^a All images had a sagittal orientation.

^b Milwaukee, Wisconsin.

^c Erlangen, Germany.

^d Best, the Netherlands.

primary-progressive MS (PPMS), 10 with secondary-progressive MS (SPMS), and 37 HCs. The subjects from the Amsterdam center were selected from a larger cohort (most data from this cohort have been published before³) in a semirandom fashion, to include 20 with RRMS, 10 with SPMS, 10 with PPMS, and 20 HCs. We ensured that the selected subsets spanned the range of spinal cord area of the total group (on the basis of the previously published measurements from cervical images³).

MS diagnosis was determined according to the 2010 revisions of the McDonald criteria.¹⁵ The main demographic and clinical characteristics included the Expanded Disability Status Scale (EDSS)¹⁶ scores and disease duration of the participants.

To explore the effect of intravenous Gd administration on MUCCA measurements, we included an additional 11 patients from Center C, including 2 with clinically isolated syndrome suggestive of MS and 9 with RRMS. In these patients, head images before and after Gd administration and cervical cord images after Gd administration were acquired.

MR Imaging Acquisition

In all 3 centers, a 3T MR imaging system was used to acquire high-resolution 3D sagittal T1-weighted head (with head coils) and cervical cord (with spine coils) images in the same scanning session. Corrections for geometric distortion due to gradient nonlinearity were applied in 3D. Details of MR imaging systems and acquisition parameters are provided in Table 1.

Image Analysis

Images were anonymized before MUCCA measurement and presented in a random order to the rater (Y.L., with >8 years of experience). MUCCA was defined as the average area of the 30-mm-length section of the upper cervical cord, starting at the upper borders of vertebral level C2, measured by using the

semiautomated software NeuroQLab (Fraunhofer MEVIS, Bremen, Germany) (Fig 1). In short, NeuroQLab segments the upper cervical cord from surrounding non-spinal cord tissue by using a Gaussian mixture modeling method. The workflow and the reliability of the software have been described previously.^{2,3,17,18}

Statistical Analysis

Analyses were performed by using SPSS software (Version 18; IBM, Armonk, New York). Kolmogorov-Smirnov tests were performed together with visual inspection of histograms to assess the normality of the variables. Comparison of the demographic data and MR imaging parameters between different disease subtypes and HCs or among different centers was conducted by using ANOVA, with Bonferroni correction for post hoc comparisons.

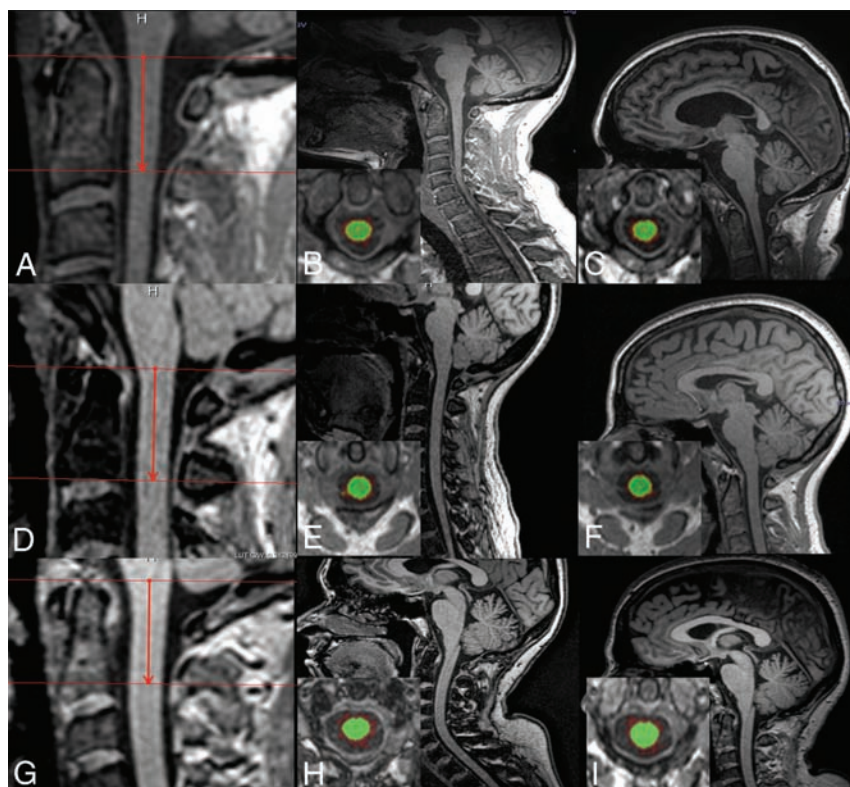


FIG 1. Examples of images from each center (cervical cord and head images). Sagittal T1-weighted MR image of the ROI selection (30-mm section length) in the upper cervical cord, starting at the upper borders of vertebral level C2 (A, D, and G), and sagittal images of the cervical cord and head with representative axial reformat overlaid by corresponding segmentation images from a patient with SPMS from Center A: B, MUCCA cervical cord images = 62 mm², C, MUCCA head images = 64 mm². A patient with RRMS from Center B: E, MUCCA cervical cord images = 74 mm², F, MUCCA head images = 75 mm². An HC subject from Center C: H, MUCCA cervical cord images = 82 mm², I, MUCCA head images = 80 mm².

The intraclass correlation coefficients (ICCs) were calculated to assess both absolute agreement (ICC_{abs}) and consistency (ICC_{consist}) between MUCCA measurements from head and cervical cord images. These calculations were also performed separately for each center and each disease subtype. The difference between MUCCA measurements on head and cervical cord images was calculated in square millimeters and as percentages. For the exploratory analysis of the effects of intravenous Gd administration, the above-mentioned analyses were additionally performed in patients with MS from Center C included in that part of our study.

RESULTS

Demographics and Clinical and MR Imaging Characteristics

Five subjects were excluded from the final analysis, including 2

HCs from Center A (1 head scan and 1 cervical cord scan with artifacts) and 1 with RRMS, 1 HC from Center B (head scan with artifacts), and 1 patient with RRMS from Center C (the head scan without Gd administration did not cover the upper cervical cord). Finally, 103 subjects were left for final analysis, including 93 subjects without Gd administration from 3 centers (Table 2) and 10 patients with images before and after Gd administration from Center C. As shown in Table 2 and in line with the recruitment of long-standing patients with MS and matched healthy controls in Center A,³ the age of the subjects (including patients and HCs) was older in Center A than in the other 2 centers, and patients from center A had a longer average disease duration and higher EDSS scores than patients from Center B.

MUCCA measured from cervical cord images did not differ among centers in HCs (Center A: 81 ± 9 mm², Center B: 80 ± 6 mm², Center C: 84 ± 10 mm², $F = 0.51$, $P = .61$). For the whole cohort, the MUCCA measured from cervical cord images in patients with MS was significantly lower than that in HCs ($P < .001$). Specifically, in patients with SPMS ($P = .02$) and PPMS ($P < .001$), the MUCCA was

Table 2: Demographic and clinical characteristics of subjects without Gd administration^a

	Center A (n = 58)				Center B (n = 28)		Center C (n = 7)
	RRMS (n = 20)	SPMS (n = 10)	PPMS (n = 10)	HC (n = 18)	RRMS (n = 19)	HC (n = 9)	HC (n = 7)
Sex (female/male)	12:8	4:6	5:5	11:7	13:6	6:3	5:2
Age (yr)	50.5 ± 8.4 (33–65)	63.4 ± 4.7 (54–70)	55.8 ± 4.6 (49–65)	51.9 ± 6.8 (36–61)	33.5 ± 8.7 (17–49)	32.4 ± 11.9 (21–56)	38.6 ± 11.8 (26–53)
Disease duration (yr)	18.8 ± 5.8 (9–29)	20.7 ± 7.6 (10–33)	19.5 ± 4.6 (12–27)	NA	4.3 ± 2.5 (1–10)	NA	NA
EDSS score	3.5 (2.5–6.5)	5 (3.5–8)	5.5 (3–7.5)	NA	3 (0–6.5)	NA	NA

Note:—NA indicates not applicable.

^a Data are presented as mean ± SD (range).

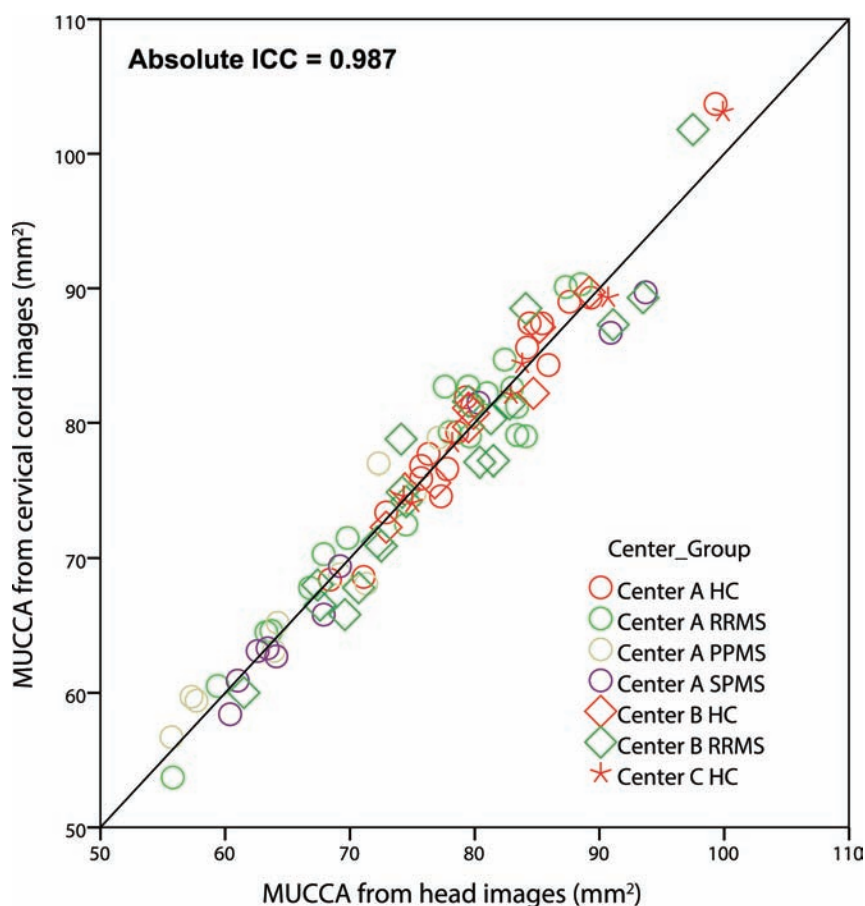


FIG 2. Scatterplot of the MUCCA measured from head-versus-cervical cord images. Different shapes indicate different centers (circle: Center A; diamond: Center B; star: Center C), and different colors represent different subgroups of subjects (red: HC; green: RRMS; yellow: PPMS; purple: SPMS). The solid black line indicates perfect agreement.

significantly smaller compared with HCs, and patients with PPMS showed smaller MUCCAs than those with RRMS ($P = .01$), whereas the MUCCA did not differ between patients with RRMS and HCs ($P = .20$) or between those with SPMS and those with RRMS ($P = .63$). MUCCA measured from head images showed similar group effects across centers and groups, including differences between those with MS and HCs, as well as among disease subtypes.

Concordance of MUCCA Measurements from Cervical Cord Images and Head Images

There was excellent absolute and consistency agreement of MUCCA measurements from head and cervical cord images in the whole group ($ICC_{abs} = 0.987$, $ICC_{consist} = 0.987$). Similarly, strong ICCs were observed across different centers and disease subtypes (On-line Table). The mean difference between MUCCA measured from head images and cervical cord images was 0.1 mm^2 (0.1%), ranging from -5 mm^2 (-6.1%) to 5 mm^2 (6.6%). The mean absolute difference was 2 mm^2 (2.3%), ranging from 0 to 5 mm^2 (6.6%) (On-line Table). For illustration purposes, scatterplots (Fig 2) and Bland-Altman plots (Fig 3) were created, which provide information on the interchangeability of the 2 measurements, by using MUCCAs from cervical cord images as the criterion standard.

The Effect of Gd Administration on MUCCA Measurements

Table 3 presents the results of the comparisons between MUCCA measurements based on 3D T1 MR images with and without Gd administration. Excellent agreement was found between MUCCA measurements on head images with and without Gd administration ($ICC_{abs} = 0.991$, $ICC_{consist} = 0.990$) and between MUCCA measurements on cervical cord images and head images with Gd enhancement ($ICC_{abs} = 0.992$, $ICC_{consist} = 0.992$).

DISCUSSION

The results of the current study demonstrate that MUCCA can be reliably measured by using head images covering the upper cervical cord in a multicenter setting across MS subtypes. Furthermore, our data suggest that Gd enhancement does not have a substantial influence on MUCCA measurements.

Upper cervical cord atrophy is regarded as an important biomarker correlating with clinical disability and predicting disease progression in MS.^{2,4,5} Measurement of MUCCA is commonly used for assessing upper spinal cord atrophy. In our study, MUCCA was measured by using semiautomated software, for which high intra- and interrater reproducibility has been observed for

MUCCA measurements either from head images³ or cervical cord images² in previous studies. Although the primary objective of the current study was to determine agreement between head and cervical images, it is reassuring that in our study, differences were found in MUCCAs among disease subtypes: Patients with PPMS and SPMS showed smaller MUCCAs compared with HCs, and patients with PPMS demonstrated smaller MUCCAs compared with those with RRMS, based on both cervical cord and head images. For Center A, MUCCA has been reported before for these subjects because they were part of a larger cohort; in that study, MUCCA was measured independently by another rater than the one performing the measurements in the current study.³ These current findings are in line with previous studies showing that cervical cord atrophy is more pronounced in progressive subtypes.^{2,4}

Some previous studies have used head images to measure cervical cord atrophy,^{2,5,8,9} and a viable method is measuring the MUCCA. However, for MUCCA measurements to be widely applied to head images, in particular in a clinical trial setting, validation in a multicenter setting is necessary. Our study showed an average absolute difference in MUCCA between cervical cord and head images of $<4\%$, and ICCs for absolute agreement ≥ 0.978 across centers and disease subtypes, which is consistent with a previous study from a single center showing an $ICC > 0.95$ be-

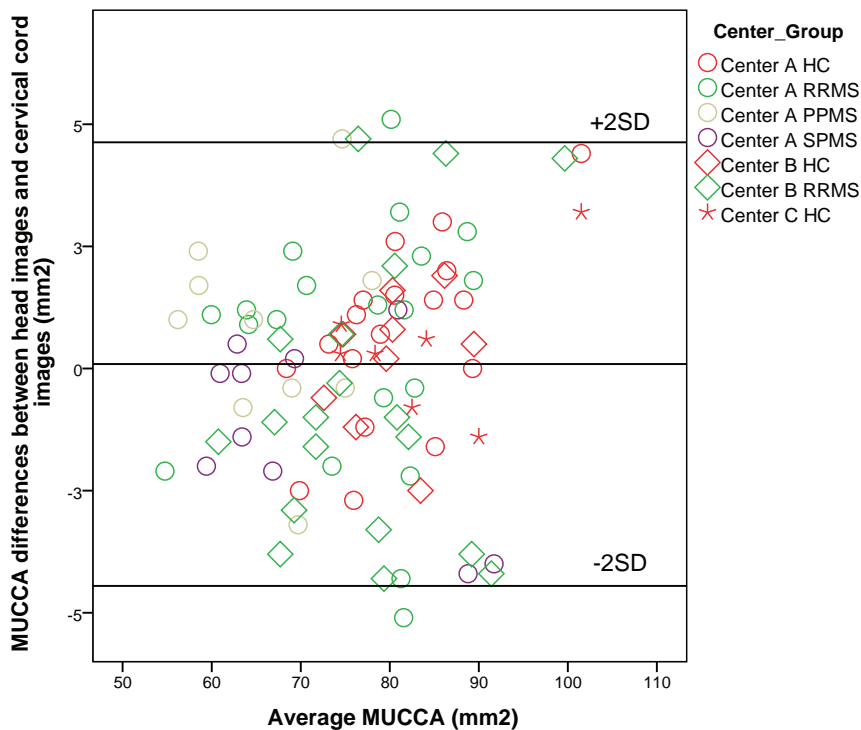


FIG 3. Bland-Altman plots for MUCCA measurements from cervical cord images and head images. The averages of MUCCA measurements on cervical cord and head images are shown on the horizontal axis, and the differences in MUCCA between the 2 measurements are shown on the vertical axis. Different shapes indicate different centers (circle: Center A; diamond: Center B; star: Center C), and different colors represent different subgroups of subjects (red: HC; green: RRMS; yellow: PPMS; purple: SPMS).

Table 3: Demographic and clinical characteristics of patients with Gd administration from Center C and comparison between MUCCA from nonenhanced head images, enhanced cervical cord and head images^a

	Center C (8 RRMS + 2 CIS)
Sex (female/male)	6:4
Age (yr)	39.0 ± 10.8 (29–67)
Disease duration (yr)	1.2 ± 1.2 (0.1–2.9)
EDSS score	2.6 ± 1.7 (1–5.5)
Gd+ MUCCA (cervical cord images) (mm ²)	82 ± 10 (67–96)
Gd– MUCCA (head images) (mm ²)	82 ± 10 (66–99)
Gd+ MUCCA (head images) (mm ²)	0.82 ± 0.10 (66–99)
Gd+ MUCCA (head images) vs Gd+ MUCCA (cervical cord images)	
Difference (mm ²)	–0.17 ± 2.00 (–30–30)
% Difference	–0.28 ± 2.21 (–3.48–3.12)
Absolute difference (mm ²)	1.49 ± 1.25 (0–30)
% Absolute difference	1.71 ± 1.32 (0.48–3.48)
ICC _{consist}	0.990
ICC _{abs}	0.991
Gd+ MUCCA (head images) vs Gd– MUCCA (head images)	
Difference (mm ²)	–0.34 ± 1.89 (–2–4)
% Difference	–0.40 ± 2.05 (–2.61–4.42)
Absolute difference (mm ²)	1.36 ± 1.29 (0–4)
% Absolute difference	1.53 ± 1.34 (0.14–4.42)
ICC _{consist}	0.992
ICC _{abs}	0.992

Note:—CIS indicates clinically isolated syndrome.

^a Data are presented as mean ± SD (range).

tween MUCCA measurements from head and cervical cord images in patients with RRMS.¹⁴ The excellent agreement between MUCCA measurements using cervical cord and head images without systematic shift indicates that measuring the upper cervical cord area is feasible by using head MR imaging datasets if

they cover the upper cervical cord and if gradient inhomogeneity correction is applied in 3D. Retrospective studies can thus be performed in large MS data bases investigating upper cervical cord atrophy by using head images, which may help to improve our understanding of the role of spinal cord atrophy in MS. For future studies, upper cervical cord atrophy is an accessible outcome measure in treatment trials and clinical research without additional cervical cord image acquisitions, thus providing additional information without increasing image acquisition cost or patient burden.¹⁹

Gd administration is often included in routine MR imaging protocols of patients with MS²⁰ and can change the contrast of brain and spinal cord images. The question of whether the MUCCA can be reliably measured on images obtained after Gd administration is therefore clinically relevant, but it has not been investigated before, to our knowledge. In the current study, we were unable to perform a rigorous assessment with available data for only 10 patients from a single center. However, these preliminary results showed excellent

agreement of the MUCCA between head images with or without Gd administration and between head and cervical cord images with Gd administration, suggesting that Gd administration has little effect on MUCCA measurement. These results should be confirmed in a larger group of patients and a multisite setting. If future studies confirm the current finding, one could use head images or cervical cord images after Gd administration to measure MUCCA, which would present another option to assess cervical cord atrophy. However, care should be taken in case of enhancing intramedullary cervical cord lesions that may affect MUCCA estimation on images obtained after Gd administration. Because in the present study no enhancing lesions were observed on the postcontrast images, we cannot exclude a bias in such cases. Furthermore, enhanced spinal nerves after Gd administration may influence the segmentation of the cord, another potential factor influencing MUCCA measurement.

Although this study included only 3 centers, the 3 main MR imaging vendors and the most commonly used sequences for high-resolution cervical cord and head imaging were included. Despite the (subtle) differences in tissue contrast among different scanners and 3D T1 sequences, agreement was excellent, suggesting the generalizability of our results beyond scanners and pulse sequences. Therefore the MUCCA has the potential to become a viable marker for MS in a routine clinical setting and clinical treatment trials.

Several limitations apply to this work. First, we did not normalize the MUCCA measurements for intracranial volume, body height, or other parameters because optimal parameters for cer-

vical cord volume or area normalization remain controversial.^{21–23} Second, the presence of cord lesions including T2 hyperintensity and T1 hypointensity in the measurement area may influence MUCCA measurements due to underestimation of white matter volumes owing to lesion misclassification.⁹ However, the lesions are present on both cervical cord and head images, which may cause a similar effect on MUCCA measurements. The high ICC values in all subgroups suggest that if an effect is present, it is comparable between both image types. Third, HCs were younger than those with MS, especially those with SPMS and PPMS in Center A in the current study. High ICC values were identified in HCs and all MS subgroups, suggesting that age has little influence on the consistency of measurements of the MUCCA between cervical cord and head images. Finally, this is a cross-sectional study; a longitudinal study is warranted to extrapolate the current findings to MUCCA changes with time.

CONCLUSIONS

Excellent agreement between MUCCA measurements from cervical cord and head images was observed across centers and disease subtypes in a multicenter setting, implying that upper cervical cord atrophy can be reliably measured by using head images covering the upper cervical cord. If there are no enhancing cervical cord lesions, postcontrast 3D T1-weighted images of the cervical cord or head may also be a suitable source for measuring MUCCA. These findings have important implications for clinical studies, including treatment trials.

Disclosures: Carsten Lukas—UNRELATED: Biogen Idec, Bayer Schering, Novartis, Sanofi, Genzyme, and Teva; Employment: endowed professorship supported by the Novartis Foundation*; Grants/Grants Pending: Bayer Schering, Teva, and Merck Serono*; Payment for Lectures (including service on Speakers Bureaus): Biogen Idec, Bayer Schering, Novartis, Sanofi, Genzyme, and Teva; Travel/Accommodations/Meeting Expenses Unrelated to Activities Listed: Bayer Schering; OTHER: Dr Carsten Lukas received consulting and speaker's honoraria from Biogen Idec, Bayer Schering, Novartis, Sanofi, Genzyme, and Teva and a research scientific grant support from Bayer Schering, Teva, and Merck Serono. He holds an endowed professorship supported by the Novartis Foundation. Martin D. Steenwijk—RELATED: Grant: Dutch MS Research Foundation (grant No. 09–358d)*; Marita Daams—RELATED: Grant: Dutch MS Research Foundation (grant No. 09–358d)*; Comments: private sponsorship to the VUmc Center Amsterdam which is sponsored through a program grant by the Dutch MS Research Foundation (grant No. 09–358d). Mike P. Wattjes—UNRELATED: Consultancy: Roche,* Novartis*; Payment for Lectures (including service on Speakers Bureaus): Biogen; Royalties: Springer; OTHER: Dr Mike P. Wattjes serves as a consultant for Biogen Idec and Roche. Frederik Barkhof—RELATED: Grant: Dutch MS Research Foundation*; UNRELATED: Consultancy: Synthon, Teva, Roche, Biogen Idec, Novartis; OTHER: Dr Frederik Barkhof serves as a consultant for Bayer Schering Pharma, Sanofi-Aventis, Biogen Idec, Teva, Merck Serono, Novartis, Roche, Synthon, and Jansen Research. Hugo Vrenken—UNRELATED: European Committee for Treatment and Research in Multiple Sclerosis/Magnetic Research Imaging in Multiple Sclerosis, Merck Serono, Novartis, Teva; Dutch MS Research Foundation, Comments: Dr Yaou Liu and I obtained a European Committee for Treatment and Research in Multiple Sclerosis application, and I was designated as the supervisor. The work described in the current article was performed during the time he was at our institution and employed through this fellowship; research grant for multiple sclerosis brain imaging; pending research grant for multiple sclerosis brain imaging; research grants for multiple sclerosis brain imaging; OTHER: Dr Hugo Vrenken has received research funding from Novartis, Pfizer, and Merck Serono and speaker honoraria from Novartis.* *Money paid to the institution.

REFERENCES

- Lycklama G, Thompson A, Filippi M, et al. **Spinal-cord MRI in multiple sclerosis.** *Lancet Neurol* 2003;2:555–62 CrossRef Medline
- Lukas C, Sombekke MH, Bellenberg B, et al. **Relevance of spinal cord abnormalities to clinical disability in multiple sclerosis: MR imaging findings in a large cohort of patients.** *Radiology* 2013;269:542–52 CrossRef Medline
- Daams M, Weiler F, Steenwijk MD, et al. **Mean upper cervical cord area (MUCCA) measurement in long-standing multiple sclerosis: relation to brain findings and clinical disability.** *Mult Scler* 2014;20:1860–65 CrossRef Medline
- Rocca MA, Horsfield MA, Sala S, et al. **A multicenter assessment of cervical cord atrophy among MS clinical phenotypes.** *Neurology* 2011;76:2096–102 CrossRef Medline
- Lukas C, Knol DL, Sombekke MH, et al. **Cervical spinal cord volume loss is related to clinical disability progression in multiple sclerosis.** *J Neurol Neurosurg Psychiatry* 2015;86:410–18 CrossRef Medline
- Bonati U, Fisniku LK, Altmann DR, et al. **Cervical cord and brain grey matter atrophy independently associate with long-term MS disability.** *J Neurol Neurosurg Psychiatry* 2011;82:471–72 CrossRef Medline
- Losseff NA, Webb SL, O'Riordan JI, et al. **Spinal cord atrophy and disability in multiple sclerosis: a new reproducible and sensitive MRI method with potential to monitor disease progression.** *Brain* 1996;119(pt 3):701–08 CrossRef Medline
- Engl C, Schmidt P, Arsic M, et al. **Brain size and white matter content of cerebrospinal tracts determine the upper cervical cord area: evidence from structural brain MRI.** *Neuroradiology* 2013;55:963–70 CrossRef Medline
- Biberacher V, Boucard CC, Schmidt P, et al. **Atrophy and structural variability of the upper cervical cord in early multiple sclerosis.** *Mult Scler* 2015;21:875–84 CrossRef Medline
- Klein JP, Arora A, Neema M, et al. **A 3T MR imaging investigation of the topography of whole spinal cord atrophy in multiple sclerosis.** *AJNR Am J Neuroradiol* 2011;32:1138–42 CrossRef Medline
- Bot JC, Barkhof F. **Spinal-cord MRI in multiple sclerosis: conventional and nonconventional MR techniques.** *Neuroimaging Clin N Am* 2009;19:81–99 CrossRef Medline
- Gaitan MI, Shea CD, Evangelou IE, et al. **Evolution of the blood-brain barrier in newly forming multiple sclerosis lesions.** *Ann Neurol* 2011;70:22–29 CrossRef Medline
- Miller DH, Rudge P, Johnson G, et al. **Serial gadolinium enhanced magnetic resonance imaging in multiple sclerosis.** *Brain* 1988;111(pt 4):927–39 CrossRef Medline
- Liu Y, Wang J, Daams M, et al. **Differential patterns of spinal cord and brain atrophy in NMO and MS.** *Neurology* 2015;84:1465–72 CrossRef Medline
- Polman CH, Reingold SC, Banwell B, et al. **Diagnostic criteria for multiple sclerosis: 2010 revisions to the McDonald criteria.** *Ann Neurol* 2011;69:292–302 CrossRef Medline
- Kurtzke JF. **Rating neurologic impairment in multiple sclerosis: an expanded disability status scale (EDSS).** *Neurology* 1983;33:1444–52 CrossRef Medline
- Lukas C, Hahn HK, Bellenberg B, et al. **Sensitivity and reproducibility of a new fast 3D segmentation technique for clinical MR-based brain volumetry in multiple sclerosis.** *Neuroradiology* 2004;46:906–15 CrossRef Medline
- Lukas C, Hahn HK, Bellenberg B, et al. **Spinal cord atrophy in spinocerebellar ataxia type 3 and 6: impact on clinical disability.** *J Neurol* 2008;255:1244–49 CrossRef Medline
- Barkhof F, Simon JH, Fazekas F, et al. **MRI monitoring of immunomodulation in relapse-onset multiple sclerosis trials.** *Nat Rev Neurol* 2012;8:13–21 CrossRef Medline
- Rovaris M, Filippi M. **Contrast enhancement and the acute lesion in multiple sclerosis.** *Neuroimaging Clin N Am* 2000;10:705–16, viii-ix Medline
- Zivadinov R, Banas AC, Yella V, et al. **Comparison of three different methods for measurement of cervical cord atrophy in multiple sclerosis.** *AJNR Am J Neuroradiol* 2008;29:319–25 CrossRef Medline
- Healy BC, Arora A, Hayden DL, et al. **Approaches to normalization of spinal cord volume: application to multiple sclerosis.** *J Neuroimaging* 2012;22:e12–19 CrossRef Medline
- Oh J, Seigo M, Saidha S, et al. **Spinal cord normalization in multiple sclerosis.** *J Neuroimaging* 2014;24:577–84 CrossRef Medline

The Cervical Spinal Canal Tapers Differently in Patients with Chiari I with and without Syringomyelia

 A. Thompson,  N. Madan,  J.R. Hesselink,  G. Weinstein,  A. Munoz del Rio, and  V. Haughton

ABSTRACT

BACKGROUND AND PURPOSE: The cause of syringomyelia in patients with Chiari I remains uncertain. Cervical spine anatomy modifies CSF velocities, flow patterns, and pressure gradients, which may affect the spinal cord. We tested the hypothesis that cervical spinal anatomy differs between Chiari I patients with and without syringomyelia.

MATERIALS AND METHODS: We identified consecutive patients with Chiari I at 3 institutions and divided them into groups with and without syringomyelia. Five readers measured anteroposterior cervical spinal diameters, tonsillar herniation, and syrinx dimensions on cervical MR images. Taper ratios for C1–C7, C1–C4, and C4–C7 spinal segments were calculated by linear least squares fitting to the appropriate spinal canal diameters. Mean taper ratios and tonsillar herniation for groups were compared and tested for statistical significance with a Kruskal-Wallis test. Inter- and intrareader agreement and correlations in the data were measured.

RESULTS: One hundred fifty patients were included, of which 49 had syringomyelia. C1–C7 taper ratios were smaller and C4–C7 taper ratios greater for patients with syringomyelia than for those without it. C1–C4 taper ratios did not differ significantly between groups. Patients with syringomyelia had, on average, greater tonsillar herniation than those without a syrinx. However, C4–C7 taper ratios were steeper, for all degrees of tonsil herniation, in patients with syringomyelia. Differences among readers did not exceed differences among patient groups.

CONCLUSIONS: The tapering of the lower cervical spine may contribute to the development of syringomyelia in patients with Chiari I.

Patients with a Chiari I malformation frequently develop syringomyelia, in theory the result of CSF flow obstructed by ectopic cerebellar tonsils. Phase-contrast MR imaging studies of CSF flow in the foramen magnum support this theory. Oscillatory CSF fluid flow has greater velocities and greater complexity in patients with Chiari I than in healthy subjects.¹ Why some patients with Chiari I develop syringomyelia and other do not has not yet been explained. How hyperdynamic CSF flow at the craniovertebral junction causes syringomyelia lower in the cervical spine has also not been elucidated.

Abnormal tonsil position is not a necessary or a sufficient cause for syringomyelia because not all patients with Chiari I have

syringomyelia and not all patients with syringomyelia have tonsillar herniation. The extent of tonsillar herniation does not predict the presence of syringomyelia. Therefore, factors other than tonsil herniation may have a role in the pathogenesis of syringomyelia. For example, one factor may be the size of the posterior cranial fossa; another pathogenetic factor may be the patency of the central canal within the cervical or thoracic spinal cord.^{2,3}

The possibility that cervical spinal canal anatomy has a role in the pathogenesis of syringomyelia has not been extensively studied. The spinal canal narrows between C1 and C4 in healthy subjects⁴ and in patients with Chiari I.⁵ The tapering of the upper cervical spinal canal causes peak CSF velocities to increase from C1 to C4.^{6,7} Taper ratios, the slope of a line fit to spinal canal diameters at multiple spinal levels, differ between patients with Chiari I and controls.^{5,8} We designed this study to test the hypothesis that Chiari I patients with syringomyelia have different cervical spinal canal taper ratios than Chiari I patients without syringomyelia.

MATERIALS AND METHODS

Approval for this retrospective study was obtained from the respective institutional review boards of the 3 sites: the University of Wisconsin School of Medicine and Public Health, Tufts University

Received August 9, 2015; accepted after revision September 15.

From the Departments of Radiology (A.T., A.M.d.R., V.H.) and Medical Physics (A.M.d.R.), University of Wisconsin School of Medicine and Public Health, Madison, Wisconsin; Department of Radiology (N.M., G.W.), Tufts University School of Medicine, Boston, Massachusetts; and Department of Radiology (J.R.H.), University of California San Diego, San Diego, California.

Please address correspondence to Victor Haughton, MD, Department of Radiology, University of Wisconsin School of Medicine and Public Health, Madison, WI 53702; e-mail: vmhaughton@wisc.edu

<http://dx.doi.org/10.3174/ajnr.A4597>

School of Medicine, and the University of California, San Diego School of Medicine. The requirement for written informed consent was waived. This study conformed to Health Insurance Portability and Accountability Act standards. We recruited 5 readers: A) a staff neuroradiologist at the University of Wisconsin School of Medicine and Public Health who was also a visiting scientist at the Tuft University Medical Center; B) a resident radiologist at the University of Wisconsin School of Medicine and Public Health; C) a staff neuroradiologist; D) a resident at Tufts University Medical Center; and E) a staff neuroradiologist at the University of California San Diego School of Medicine. Readers re-read a fraction of cases 1 or 2 times with at least 2 weeks between readings.

Cases of Chiari I were collected by reviewing the PACS between January 2012 and July 2013 for cervical spine MR imaging or in 1 institution by reviewing the Chiari I case registry. Inclusion criteria were any patient with sagittal T2-weighted fast spin-echo cervical spine images (at 1.5T or 3T) who had ≥ 5 -mm cerebellar tonsil herniation. Patients were excluded if they had a history or evidence of a Chiari II malformation, tumor, trauma, infection, prior spine surgery, or poor-quality images. Cervical and thoracic MR images were inspected for the presence of a fluid collection in the spinal cord consistent with a syrinx.

For each patient, the sagittal T2-weighted cervical spine MR imaging sequence was reviewed by using a DICOM image viewer to identify the midline section or sections that best showed the spinous processes or dens at each cervical level. Cerebellar tonsil herniation was measured by placing a line from the tip of the inferior end of the basion to the anterior rim of the opisthion and measuring the perpendicular distance from this line to the inferior tip of the cerebellar tonsils on the sagittal image that best demonstrated the tonsil. The anteroposterior diameter of the cervical spinal canal from C1 to C7 was measured on the midline sagittal T2 images by a previously described method.^{6,7} At each level, a line was placed perpendicular to the spinal axis at the midpoint of the vertebra, the points where it crossed from CSF to epidural tissue were identified, and the distances between them were measured. At C1, the midpoint of the anterior arch of C1 was defined, and the line was drawn transverse to the spinal axis at this level. We measured the foramen magnum anteroposterior dimensions at the site with the largest enrollment as in previous studies. The C1–C7, C1–C4, and C4–C7 taper ratios were calculated by least squares fitting of a line to the appropriate diameters, by using the LINE ST macro in Excel (Microsoft, Redmond, Washington) as in previous studies.^{6,7} The length of the syringomyelia was calculated as the number of segments over which it extended. The readers measured the maximal anteroposterior diameter of the syrinx on the midsagittal T2-weighted image.

Analysis and Statistical Testing

The diameter measurements for all readers were tabulated together with the patient age, sex, tonsillar herniation, syrinx location, and dimensions. Two sets of readings were created to control for the possibility of reader effects. The measurements of readers B, C, and E were pooled as set 1, and the measurements of readers A (from 2 sites) and E were pooled as set 2. (Reader E's 9 readings, the only ones at the site, were included in both sets because there was only 1 reader at this site.) The mean taper ratios for the pa-

tients with Chiari I with and without syringomyelia were calculated and tested for significance by the Kruskal-Wallis rank sum test, with significance set at .05. Tonsillar herniation was compared among groups with a Kruskal-Wallis test. The effect of age, sex, institution, and reader was tested on the pooled datasets with Kruskal-Wallis and Fisher exact tests for continuous and categorical responses, respectively. *P* values were not adjusted for multiple testing. All statistical computations and graphics were obtained in R 3.1.0 (R Core Team 2014; <http://www.r-project.org>). We performed regression analysis with macros in Excel.

For reader-agreement analysis, 55 readings by reader B at site 1 were compared with readings in the same patients by reader A, and 90 readings by reader C at site 2 were compared with readings in the same patients by reader A. For intrareader agreement, reader B re-read a subset of patients ($n = 21$) and reader A re-read a subset of patients for a second ($n = 20$) and third time ($n = 10$), with a minimum of 2 weeks between readings.

Inter- and intrareader agreement was analyzed with Bland-Altman 95% limits of agreement. We calculated the bias and the typical discrepancy between 2 measurements, accounting for the clustering that results from combining multiple diameters from the same subject.⁹

RESULTS

The readers measured spinal canal diameters in 101 patients with Chiari I without and 49 with syringomyelia at the 3 institutions. Females comprised 66% and 67% of the patients in sets 1 and 2, respectively. Readers A, B, C, D, and E measured 146, 55, 90, 9, and 89 cases, respectively. Sets 1 and 2 differed in the number of patients by 4, due to omissions of cases in which a reader believed that measurements were inexact because of artifacts or other problems with the image.

On average, syringes were 5 vertebral segments in length (range, 1–13 segments) and 0.36 cm in anteroposterior diameter (range, 0.1–1.67 cm). Syringes terminated superiorly most frequently at the C6 level (13 cases) and at other levels between C1 and T2 in other cases.

C1–C7 and C1–C4 taper ratios had negative signs indicating narrower diameters at the caudal end; C4–C7 taper ratios had positive signs indicating larger diameters at their caudal ends (Fig 1 and Table). For C1–C7, taper ratios were -0.057 ± 0.034 cm/level (set 1) and -0.052 ± 0.033 cm/level (set 2) for patients with Chiari I without syrinx and -0.036 ± 0.041 cm/level (set 1) and -0.032 ± 0.039 cm/level (set 2) for the patients with syringomyelia. The difference was significant in both sets ($P = .003$ and $.019$ for sets 1 and 2, respectively).

The average foramen magnum diameters were 3.2 cm in 30 patients with and 3.1 cm in 53 patients without a syrinx; this difference was not significant ($P = .2$). The diameters at C1 for the patients at the 3 sites were 1.7 and 1.6 cm, respectively, in the cases with and without syrinx; this difference was also not significant ($P = .4$).

C1–C4 taper ratios were -0.147 ± 0.072 cm/level (set 1) and -0.129 ± 0.070 cm/level (set 2) in patients with Chiari I without syringomyelia and -0.122 ± 0.086 cm/level (set 1) and -0.115 ± 0.078 cm/level (set 2) for the patients with Chiari I with syringomyelia (set 1). The difference was not statistically significant in either set ($P = .08$ and $.38$ for sets 1 and 2, respectively).

Taper ratios of the cervical spine in Chiari 1 patients with and without syringomyelia

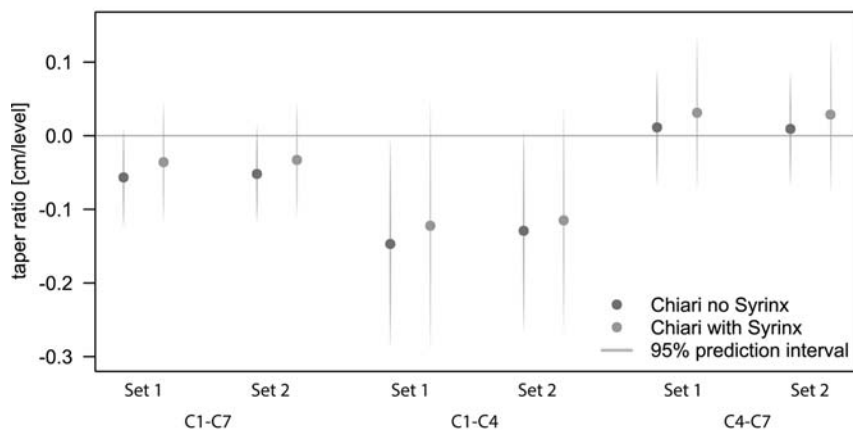


FIG 1. C1–C7, C1–C4, and C4–C7 taper ratios and 95% confidence intervals for set 1 and 2 readings in patients with Chiari I without and with syrnix.

Taper ratios for C1–C7, C1–C4, and C4–C7 and tonsillar ectopia in patients with Chiari I with and without a syrnix

	Reader Set 1		Reader Set 2	
	Without Syrnix	With Syrnix	Without Syrnix	With Syrnix
C1–C7 Taper ratio (cm/level)	−0.057	−0.036 ^a	−0.052	−0.032 ^a
C1–C4 Taper ratio (cm/level)	−0.147	−0.122	−0.129	−0.115
C4–C7 Taper ratio (cm/level)	+0.011	+0.031 ^a	+0.009	+0.028 ^a
Tonsillar ectopia (mm)	9.8	10.8 ^a	12.0	12.7 ^a

^a Significant differences between cases with and without syrnix ($P < .05$).

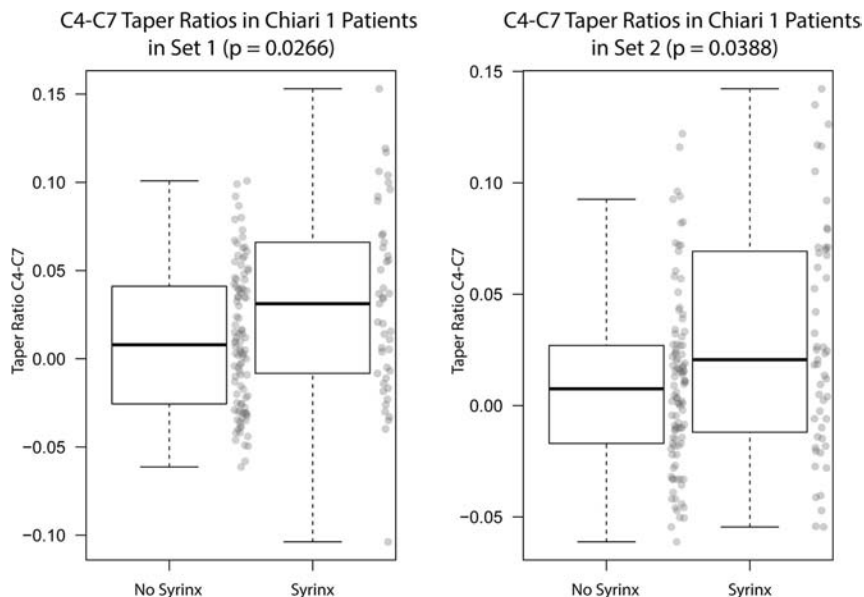


FIG 2. Box-and-whisker plot of the C4–C7 taper ratios in patients with Chiari I without and with a syrnix. For sets 1 and 2, taper ratios differed significantly between groups ($P = .026, .039$).

C4–C7 taper ratios (Fig 2) were 0.011 ± 0.040 cm/level (set 1) and 0.009 ± 0.039 cm/level (set 2) for the patients without syringomyelia and 0.031 ± 0.053 cm/level (set 1) and 0.028 ± 0.052 cm/level (set 2) for patients with syringomyelia. The difference was significant in both sets ($P = .027$ and $.039$ for sets 1 and 2, respectively).

Tonsillar descent averaged 9.82 ± 3.98 mm (set 1) and 10.8 ± 4.79 mm (set 2) in the patients with Chiari I without syrnix and

12.0 ± 5.01 mm (set 1) and 12.7 ± 5.43 mm (set 2) in the patients with Chiari I with syringomyelia. The differences between the 2 groups were significant ($P = .008$ and $.020$ for sets 1 and 2, respectively).

Regression analysis showed that the C4–C7 taper ratio was 0.001 (tonsil herniation) + 0.21 for the Chiari cases without syringomyelia and 0.001 (tonsil herniation) + 0.42 for the Chiari cases with syringomyelia. The taper ratio in patients with Chiari I with a syrnix was on average 0.021 cm/level greater than that in the group without syrnix for any degree of tonsillary herniation. The length of the syrnix correlated significantly with the C4–C7 taper ratio ($P = .02$).

Because the proportion of females and the ages on average were similar in the 2 groups, sex and age were not confounding factors. The C4–C7 taper ratios were greater on average in males than in females by 0.02 cm/level ($P = .027$ and $.007$ for sets 1 and 2, respectively). Sex had no significant effect on the position of the tonsils below the foramen magnum ($P = .77$ and $.998$ for sets 1 and 2, respectively). C1–C4 taper ratios tended to be larger with age ($P = .153$ and $.011$ for sets 1 and 2, respectively) as did the C1–C7 taper ratios ($P = .23$ and $.010$ for sets 1 and 2, respectively). The C4–C7 taper ratio was not affected by age ($P = .58$ and $.933$ for sets 1 and 2, respectively). No other statistically significant effects of age or sex were noted.

For 2 readers at site 1, the systematic difference (bias) between measurements by different readers in the same cases was 0.02 mm, and the variability between the 2 readers was 0.16 to -1.22 mm in 95% of cases. The systematic difference between the 2 measurements at site 2 was 0.01 mm, and the variability between the 2 readings was 0.31 to -0.33 mm in 95% of cases. For 1 reader at site 1, the systematic difference between a first and second reading was 0.005 mm and the variability was 0.15 to

-0.13 mm in 95% of cases. Inter- and intrareader agreement was similar in all other comparisons.

DISCUSSION

The cervical spinal canal tapers differently in patients with Chiari I with syringomyelia compared with those without it. In both groups, the spinal canal narrows from C1 to C7. Patients with Chiari I with a

syrinx have a steeper positive C4–C7 taper (wider caudally). The C4–C7 taper accounts for the differences in the C1–C7 segment because the C1–C4 taper does not differ significantly between the groups.

Patients with Chiari I with syringomyelia have, on average, greater tonsillar herniation than those without a syrinx. On average, patients with syringomyelia, regardless of the amount of tonsillar herniation, have a greater C4–C7 taper than patients without it.

Given the multicenter nature of the study and the need for multiple readers, the study was divided into 2 reader sets to assess the influence of reader effect. For virtually all of the measurements made, agreement was excellent among the readers.

In comparison with published studies, the patients in this study had similar morphologic features. Tonsil herniation in these patients compared well with the average of 11 mm reported previously in a cohort of patients with Chiari I, some of whom had syringomyelia.¹⁰ Syringomyelia most frequently extended superiorly to the level of C6 in this study, which is in keeping with previous reports.¹⁰ Taper ratios for C1–C7, C1–C4, and C4–C7 in patients with Chiari I with syringomyelia in this study (–0.036, –0.122, and 0.031 cm/level, respectively) agree well with those previously reported¹¹ in patients with distended syringes (–0.034, –0.098, and 0.024 cm/level, respectively). Our taper ratios does not agree well with C1–T1 taper ratios in a sample of 21 patients reported previously,⁵ perhaps because of issues of linear fitting to curving portions of the cervical spine, different patient ages, or smaller sample sizes in the previous report. In a previous report of 2 patients with scoliosis with and 20 without syrinx, the presence of a syrinx does not produce a significant difference in the C1 to C7 taper ratios.⁸ The small sample size may explain the difference from our results.

The study has limitations due to the inclusion of multiple readers and multiple medical institutions. The patients from the 3 institutions differed to some degree in age distributions and severity of syringomyelia, probably because of the types of services offered at each institution and the proportion of pediatric patients treated. Reader disagreements in diameter measurements resulted from different placement of the transverse line on which to measure the diameters and from imprecisely defining the junction of the subarachnoid space and the epidural tissues. The use of the taper ratio tended to moderate the effect of random measurement errors. Linear fitting to diameters better suits short and relatively straight spinal segments (C1–C4 and C4–C7) than the entire cervical spine, which may curve. Sex and age had an effect on taper ratios, but not on the differences between the 2 patient groups, because the proportion of females and the ages, on average, were similar in the 2 groups. Creating 2 sets of data increased confidence that results were not reader-dependent.

The results in this study do not accord with the common assumption that syringomyelia results predominantly from spinal obstruction at the level of the foramen magnum. However, because tonsillar ectopia and crowding at the foramen magnum do not accurately predict the development of syringomyelia, other factors may be suspected. Greater positive C4–C7 tapering (expansion) of the spine suggests decreasing rather than increasing CSF velocities below C4 in

these patients. The juxtaposition of negatively and positively tapering cervical segments produces complex pressure gradients during the cardiac cycle, which may contribute to the pathogenesis of syringomyelia. Other anatomic features relevant to syringomyelia may include variations in the central canal within the spinal cord and posterior fossa morphology.^{2,11}

The steeper C4–C7 taper ratios in patients with Chiari I with syringomyelia warrant additional study. One hypothesis to test is that the cervical spinal canal tapers differently in patients with idiopathic syringomyelia than in controls who lack a syrinx.

CONCLUSIONS

Cervical spinal canal tapering may be a morphologic factor contributing to the development of syringomyelia in some patients with Chiari I malformation. Computational fluid dynamics in anatomically accurate models of the cervical spine may help explain why some patients develop a syrinx.

Disclosures: Alejandro Munoz del Rio—RELATED: Grant: Column of Hope*; UNRELATED: Grants/Grants Pending: National Institutes of Health*; Other: Lippincott, Williams, and Wilkins, Comments: I provided statistical review for *Annals of Surgery*. Victor Haughton—RELATED: Grant: Column of Hope*; Comments: Funds for the statistician. *Money paid to the institution.

REFERENCES

1. Quigley MF, Iskandar BJ, Quigley MA, et al. **Cerebrospinal fluid flow in foramen magnum: temporal and spatial patterns at MR imaging in volunteers and in patients with Chiari I malformation.** *Radiology* 2004;232:229–36 CrossRef Medline
2. Drösdal IN, Mardal KA, Støverud K, et al. **Effect of the central canal in the spinal cord on fluid movement in the cord.** *Neuroradiol J* 2013; 26:585–90 Medline
3. Støverud KH, Alnæs M, Langtangen HP, et al. **Poro-elastic modeling of syringomyelia: a systematic study of the effects of pia mater, central canal, median fissure, white and gray matter on pressure wave propagation and fluid movement within the cervical spinal cord.** *Comput Methods Biomech Biomed Engin* 2016;19:686–98 CrossRef Medline
4. Tatarik NE. **Variation in the human cervical neural canal.** *Spine J* 2005;5:623–31 Medline
5. Hirano M, Haughton V, Munoz del Rio A. **Tapering of the cervical spinal canal in patients with Chiari I malformations.** *AJNR Am J Neuroradiol* 2012;33:1326–30 CrossRef Medline
6. Shah S, Haughton V, del Rio AM. **CSF flow through the upper cervical spinal canal in Chiari I malformation.** *AJNR Am J Neuroradiol* 2011;32:1149–53 CrossRef Medline
7. Rutkowska G, Haughton V, Linge S, et al. **Patient-specific 3D simulation of cyclic CSF flow at the craniocervical region.** *AJNR Am J Neuroradiol* 2012;33:1756–62 CrossRef Medline
8. Hammersley J, Haughton V, Wang Y, et al. **Tapering of the cervical spinal canal in patients with scoliosis with and without the Chiari I malformation.** *AJNR Am J Neuroradiol* 2012;33:1752–55 CrossRef Medline
9. Bland JM, Altman, DG. **Agreement between methods of measurement with multiple observations per individual.** *J Biopharm Stat* 2007;17:571–82 CrossRef Medline
10. Elster AD, Chen MY. **Chiari I malformations: clinical and radiologic reappraisal.** *Radiology* 1992;183:347–53 CrossRef Medline
11. Zhu Z, Sha S, Sun X, et al. **Tapering of the cervical spinal canal in patients with distended or nondistended syringes secondary to Chiari type I malformation.** *AJNR Am J Neuroradiol* 2014;35: 2021–26 CrossRef Medline

Radiographic Local Control of Spinal Metastases with Percutaneous Radiofrequency Ablation and Vertebral Augmentation

A.N. Wallace, A. Tomasian, D. Vaswani, R. Vyhmeister, R.O. Chang, and J.W. Jennings

ABSTRACT

BACKGROUND AND PURPOSE: Combination radiofrequency ablation and vertebral augmentation is an emerging minimally invasive therapy for patients with metastatic spine disease who have not responded to or have contraindications to radiation therapy. The purpose of this study was to evaluate the rate of radiographic local control of spinal metastases treated with combination radiofrequency ablation and vertebral augmentation.

MATERIALS AND METHODS: We retrospectively reviewed our tumor ablation database for all patients who underwent radiofrequency ablation and vertebral augmentation of spinal metastases between April 2012 and July 2014. Tumors treated in conjunction with radiation therapy were excluded. Tumor characteristics, procedural details, and complications were recorded. Posttreatment imaging was reviewed for radiographic evidence of tumor progression.

RESULTS: Fifty-five tumors met study inclusion criteria. Radiographic local tumor control rates were 89% (41/46) at 3 months, 74% (26/35) at 6 months, and 70% (21/30) at 1 year after treatment. Clinical follow-up was available in 93% (51/55) of cases. The median duration of clinical follow-up was 34 weeks (interquartile range, 15–89 weeks), during which no complications were reported and no patients had clinical evidence of metastatic spinal cord compression at the treated levels.

CONCLUSIONS: Combination radiofrequency ablation and vertebral augmentation appears to be an effective treatment for achieving local control of spinal metastases. A prospective clinical trial is now needed to replicate these results.

ABBREVIATION: RFA = radiofrequency ablation

Metastatic spine disease affects 5%–10% of patients with cancer.¹ Approximately 90% of symptomatic patients present with pain, which is most commonly due to biochemical stimulation of endosteal nociceptors, tumor mass effect, and/or associated pathologic fracture.² These patients are also at risk for metastatic spinal cord compression, which occurs in 10%–20% of patients and is most often due to posterior extension of vertebral body tumor.^{3,4} The resulting pain and neurologic deficits are associated with decreased quality of life and shortened life expectancy.⁵ Therefore, the goals of treatment are both pain palliation and local tumor control.

Radiation therapy is the standard of care for pain palliation

and local control of spinal metastases, but it has several important limitations. First, certain tumor histologies respond less favorably to radiation therapy, particularly non-small cell lung cancer, renal cell carcinoma, melanoma, and sarcoma.⁶ Second, radiation therapy of spinal metastases is limited by the cumulative tolerance of the spinal cord, which often precludes retreatment of recurrent disease or progressive disease at adjacent vertebral levels.⁷ Third, radiation therapy excludes patients from certain systemic chemotherapy clinical trials.

Combination radiofrequency ablation (RFA) and vertebral augmentation is an emerging minimally invasive therapy for patients with metastatic spine disease who have not responded to or have contraindications to radiation therapy. An ablation probe is percutaneously placed into the tumor, and high-frequency alternating current is passed through an electrode at the probe tip, generating frictional heating and necrosis of adjacent tissue.⁸ Cement is then instilled through the same percutaneous cannula to stabilize or prevent associated pathologic fracture.^{9,10} The tandem procedure can be performed in an outpatient setting with the patient under conscious sedation, requires minimal recovery, and

Received July 27, 2015; accepted after revision August 18.

From the Mallinckrodt Institute of Radiology (A.N.W., A.T., D.V., J.W.J.), Siteman Cancer Center, Washington University School of Medicine, St. Louis, Missouri; and Washington University School of Medicine (R.V., R.O.C.), St. Louis, Missouri.

Please address correspondence to Adam N. Wallace, MD, Mallinckrodt Institute of Radiology, Washington University School of Medicine, 510 S Kingshighway Blvd, St. Louis, MO 63110; e-mail: wallacea@mir.wustl.edu

<http://dx.doi.org/10.3174/ajnr.A4595>

does not hinder or delay adjuvant therapies such as radiation or systemic chemotherapy. Multiple case series have shown decreased pain scores after RFA and vertebral augmentation of spinal metastases,^{11–15} but evidence that percutaneous therapy achieves local tumor control is limited to case reports and small case series without internal controls.^{13,14} The purpose of this study was to retrospectively evaluate the rate of radiographic local control of spinal metastases treated with combination RFA and vertebral augmentation at a National Cancer Institute–Designated Cancer Center.

MATERIALS AND METHODS

Institutional review board approval was obtained to retrospectively review our institutional database for all patients who underwent RFA and vertebral augmentation of osseous metastases between April 2012 and July 2014. Informed consent was waived for retrospective study participation. Tumors also treated with radiation therapy were excluded. Recorded data included patient demographics, primary tumor histology, and vertebrae treated. All available preprocedural imaging of each treated vertebra, including MR imaging, CT, and/or [¹⁸F] fluorodeoxyglucose (FDG) PET/CT, was reviewed to determine whether the tumor involved the posterior vertebral body and/or pedicles, had eroded the posterior vertebral body cortex, and/or was associated with pathologic vertebral compression fracture. Preprocedural tumor volumes were also estimated by measuring the greatest length of tumor in each dimension. We preferred to measure the dimensions of T2-hyperintense marrow replacement on MR imaging. If MR imaging was not available, the dimensions of osteolysis on CT were measured, though this measurement likely underestimated tumor size.

Procedure notes were reviewed to determine the percutaneous approach (ie, uni- versus bipedicular), number of ablations performed, and total ablation time at each vertebral level. Procedural complications were documented according to the Society of Interventional Radiology classification.¹⁶ Patients were clinically evaluated 1 hour after each procedure for evidence of acute complications, such as hematoma formation or neurologic injury. The duration of clinical follow-up was recorded for each patient, and electronic medical records were reviewed for evidence of delayed complications, such as infection.

Patient Selection for Radiofrequency Ablation and Vertebral Augmentation

Patients were selected for RFA and vertebral augmentation by a multidisciplinary team of radiation and medical oncologists, interventional radiologists, and spine surgeons. Treatments were performed to achieve local tumor control and, in most cases, pain relief. Treated patients could not receive radiation therapy or had radiographic tumor progression at other sites of disease treated with radiation therapy. Exclusion criteria for RFA and vertebral augmentation included metastases that were entirely osteoblastic, associated with pathologic compression fracture with spinal instability, or causing spinal cord compression. Tumor within 1 cm of the spinal cord or nerves was not a contraindication for treatment.

Radiofrequency Ablation and Vertebral Augmentation Procedure

Written informed consent was obtained before all treatments. All procedures were performed under fluoroscopic or CT guidance with the patient consciously sedated. The skin, soft tissues, and periosteum overlying the target vertebra were anesthetized with a 50/50 mixture of 1% lidocaine and 0.25% bupivacaine. The vertebral body was accessed from a transpedicular approach with a 10-ga introducer cannula, and a navigational osteotome was used to create channels in the marrow cavity corresponding to the planned placements of the ablation probe. In each case, the goal was to perform overlapping ablations that encompassed the entire volume of tumor on cross-sectional imaging and an additional 3-mm margin to account for microscopic tumor spread.⁹ A bipedicular approach was used when tumor extended across the sagittal vertebral body midline and could not be entirely ablated with an adequate margin from a unipedicular approach (Fig 1).

Ablations were performed with the STAR Tumor Ablation System (DFINE, San Jose, California). This system includes an ablation probe with an articulated distal segment that is essential for accessing tumor in the posterior central vertebral body (Fig 1).¹⁴ The probe also contains 2 thermocouples located 10 and 15 mm from the electrode, which permit real-time monitoring of the volume of the ablation zone. Each individual ablation was performed until the thermocouple located 15 mm from the electrode reached 50°C. Based on the manufacturer's thermal distribution curves, the dimensions of the ellipsoid ablation volume are 30 × 20 × 20 mm when the thermocouple located 15 mm from the electrode reaches 50°C.¹⁴ The electrode was placed no closer than 10 mm from the posterior vertebral body cortex, which is the maximum radius of the minor axis of the ellipsoid ablation volume. When ablation was performed near this threshold, a coaxial needle was placed through the neural foramen into the ventral epidural space, the inner cannula of which contained an additional thermocouple. If the temperature in the ventral epidural space exceeded 45°C, carbon dioxide and cooled 5% dextrose in water were injected through the outer cannula of the needle for thermal protection.^{8,17} Vertebral augmentation was performed by using the StabiliT Vertebral Augmentation System (DFINE). In all cases, cement was injected through the same percutaneous cannula used for ablation.

Local Control Assessment and Analysis

All available postprocedural imaging was reviewed, including MR imaging, CT, and/or FDG PET/CT. All follow-up imaging was performed for clinical reasons at the request of the referring oncologist. In general, CT and PET/CT were performed to assess the systemic chemotherapy response, and spinal MR imaging was performed when patients reported new or increasing spine-related pain. Local control failure was defined as the following: 1) increased osteolysis or paravertebral tumor extension on CT; 2) new or persistent enhancing soft tissue extending into the epidural space, neural foramina, or paravertebral space on MR imaging; or 3) persistent FDG uptake on PET/CT (Fig 2). Additionally, T1-hypointense, T2-hyperintense signal and/or enhancement at the margin of the ablation cavity on follow-up MR imaging were categorized as local con-



FIG 1. A 29-year-old woman with stage IV (T1b, N1, M1) cardiac angiosarcoma who presented with low back pain. Sagittal T1-weighted (A) and STIR (B) MR imaging show diffuse T1 hypointensity and heterogeneous T2 hyperintensity of the lumbar vertebral body marrow, consistent with marrow-replacing tumor. She was treated with conventional external-beam radiation therapy (30 Gy in 10 fractions); however, her back pain persisted. Sagittal STIR (C) and T1-weighted, fat-suppressed, postcontrast (D) MR imaging performed 5 months later show interval progression of multiple spinal metastases with new epidural extension of tumor at T11, L1, L2, and L3 (black block arrows) and pathologic fractures of the L2 and L3 vertebral bodies. She could not receive additional radiation therapy due to the cumulative dose to the spinal cord. Consequently, she underwent radiofrequency ablation and vertebral augmentation of T11, L1, L2, and L3. Anteroposterior (E) and lateral (F) fluoroscopic images show percutaneous cannulae in both pedicles of T11 and the ablation probe curving into the left posteroinferior vertebral body (black arrowheads). Sagittal STIR (G) and T1-weighted, fat-suppressed, postcontrast (H) MR imaging performed 6 months later show interval retraction of the epidural tumor at T11, L1, L2, and L3. Signal void corresponding to cement (white asterisks) with surrounding T2-hyperintense, enhancing granulation tissue is noted at the treated levels (white block arrows).

trol failure unless these findings remained stable on subsequent imaging, retraction of epidural tumor was seen, or a PET/CT scan was available demonstrating absence of associated FDG uptake (Fig 1).⁹ To serve as an internal control, posttreatment cross-sectional imaging was also reviewed for evidence of systemic disease progression, including enlargement of visceral or intracranial metastases or osseous metastases that were not ablated.

RESULTS

Fifty-five spinal metastases treated with RFA and vertebral augmentation were included in the study. Radiation-resistant histologies comprised 62% (34/55) of treated tumors, including sarcomas (27%, 15/55), non-small cell lung cancer (16%, 9/55), renal cell carcinoma (11%, 6/55), and melanoma (7.3%, 4/55). Other histologies included breast adenocarcinoma (13%, 7/55), papillary thyroid cancer (9.1%, 5/55), hepatocellular carcinoma (3.6%,

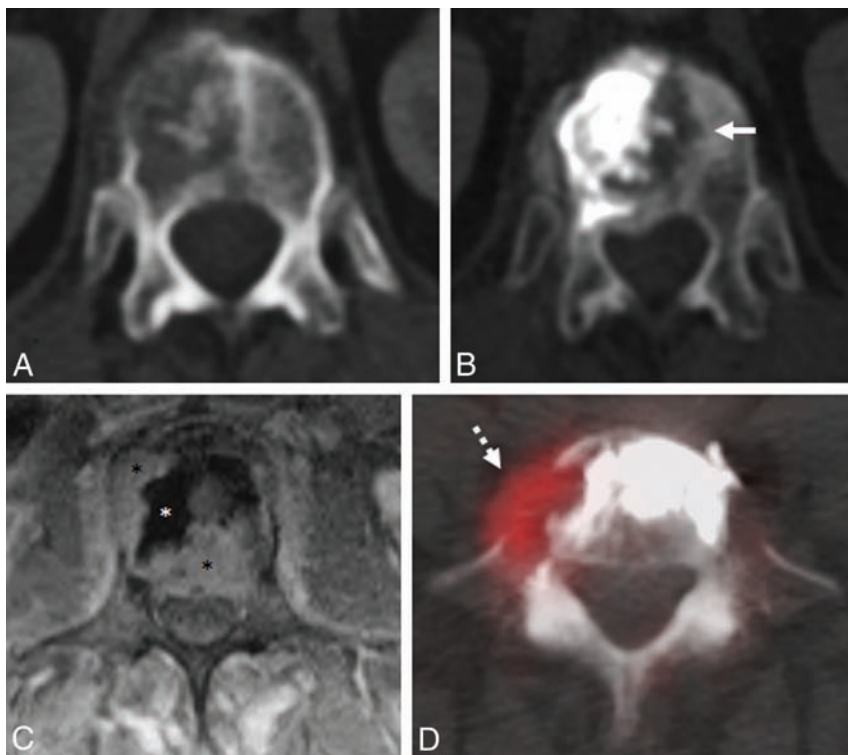


FIG 2. Examples of ablation failure. A, Axial CT image shows a T12 lytic squamous cell carcinoma metastasis. B, CT scan obtained 4 months after radiofrequency ablation and vertebral augmentation shows new osteolysis medial to the cement and extending across the midline (*white arrow*), consistent with progression of residual tumor. C, Axial postcontrast, T1-weighted, fat-suppressed MR imaging performed 6 months after radiofrequency ablation and vertebral augmentation of an L3 non-small cell carcinoma metastasis shows signal void corresponding to cement in the ablation cavity (*white asterisk*), with residual enhancing tumor in the right lateral and posterior vertebral body that extends into the epidural space (*black asterisks*). D, Axial [^{18}F] fluorodeoxyglucose PET/CT scan obtained 1 month after radiofrequency ablation and vertebral augmentation of an L5 liposarcoma metastasis shows residual hypermetabolic tumor along the right anterolateral aspect of the vertebral body (*white dashed arrow*).

2/55), head and neck squamous cell carcinoma (3.6%, 2/55), multiple myeloma (3.6%, 2/55), malignant peripheral nerve sheath tumor (3.6%, 2/55), and gastrointestinal adenocarcinoma (1.8%, 1/55). Median tumor volume was 10.0 mL (interquartile range, 4.9–15.3 mL). Forty-seven percent (26/55) of tumors involved thoracic and 53% (29/55) involved lumbar vertebrae. Seventy-three percent (40/55) of metastases involved the posterior vertebral body, 31% (17/55) were associated with erosion of the posterior vertebral body cortex, and 47% (26/55) involved the pedicles. Associated pathologic compression fractures were present in 62% (34/55) of treated vertebrae.

Sixty-nine percent (38/55) of ablations were performed from a unipedicular approach, and 31% (17/55) were performed from a bipedicular approach. Within each vertebra, the median number of ablations performed was 4 (range, 1–12) and the median cumulative ablation time was 5 minutes 5 seconds (range, 51 seconds to 19 minutes 13 seconds). According to the Society of Interventional Radiology classification, there were no acute or delayed procedure-related complications during the median clinical follow-up of 34 weeks (interquartile range, 15–89 weeks).

Radiographic follow-up results are summarized in Fig 3. Follow-up imaging included CT in 69% (38/55), MR imaging in 56% (31/55), and PET/CT in 40% (22/55) of cases. Five cases of residual or recurrent tumor were documented within 3 months of

treatment. In all 5 of these cases, there was also evidence of systemic metastatic disease progression. Follow-up imaging demonstrating local tumor control at least 3 months after treatment was available for an additional 41 tumors. Thus, the radiographic local tumor control rate at 3 months was 89% (41/46). Imaging also demonstrated progression of systemic metastatic disease in 80% (37/46) of these cases. Thus, the 3-month radiographic local tumor control rate was 86% (32/37) in the setting of systemic metastatic disease progression. Nine tumors (16%; 9/55) did not have imaging demonstrating progression within 3 months of treatment or stability at least 3 months after treatment. These tumors were not reimaged because the patients entered hospice care due to progression of visceral or intracranial metastatic disease. None of the patients without follow-up imaging at least 3 months after treatment died with symptoms of metastatic spinal cord compression.

Four additional cases of tumor progression were documented between 3 and 6 months after treatment; thus, 9 total cases of tumor progression were documented within 6 months of treatment. Follow-up imaging demonstrating local tumor control at least 6 months after treatment was available for an additional 26 tumors. Thus, the radiographic local

tumor control rate 6 months after treatment was 74% (26/35). Imaging also demonstrated progression of systemic metastatic disease in 89% (31/35) of these cases. Thus, the 6-month radiographic local tumor control rate was 71% (22/31) in the setting of systemic metastatic disease progression. Eleven tumors (27%; 11/41) with documented stability at least 3 months after treatment were not imaged again after 6 months. In 7 of these cases (64%; 7/11), posttreatment imaging was not performed because the patient was doing well clinically at the end of the study period with no back pain or neurologic deficits. One patient (9.1%; 1/11) died with metastatic spinal cord compression due to progression of an upper thoracic spinal metastasis that was not previously treated with RFA and vertebral augmentation. This patient had a lumbar spinal metastasis that was treated with RFA and vertebral augmentation that was stable on CT performed 3 months after treatment. Three patients (27%; 3/11) were lost to follow-up between 3 and 6 months after treatment.

No additional cases of tumor progression were documented between 6 months and 1 year after treatment. Follow-up imaging demonstrating local tumor control at least 1 year after treatment was available for an additional 21 tumors. Thus, the radiographic local tumor control rate 1 year after treatment was 70% (21/30). Imaging also demonstrated progression of systemic metastatic

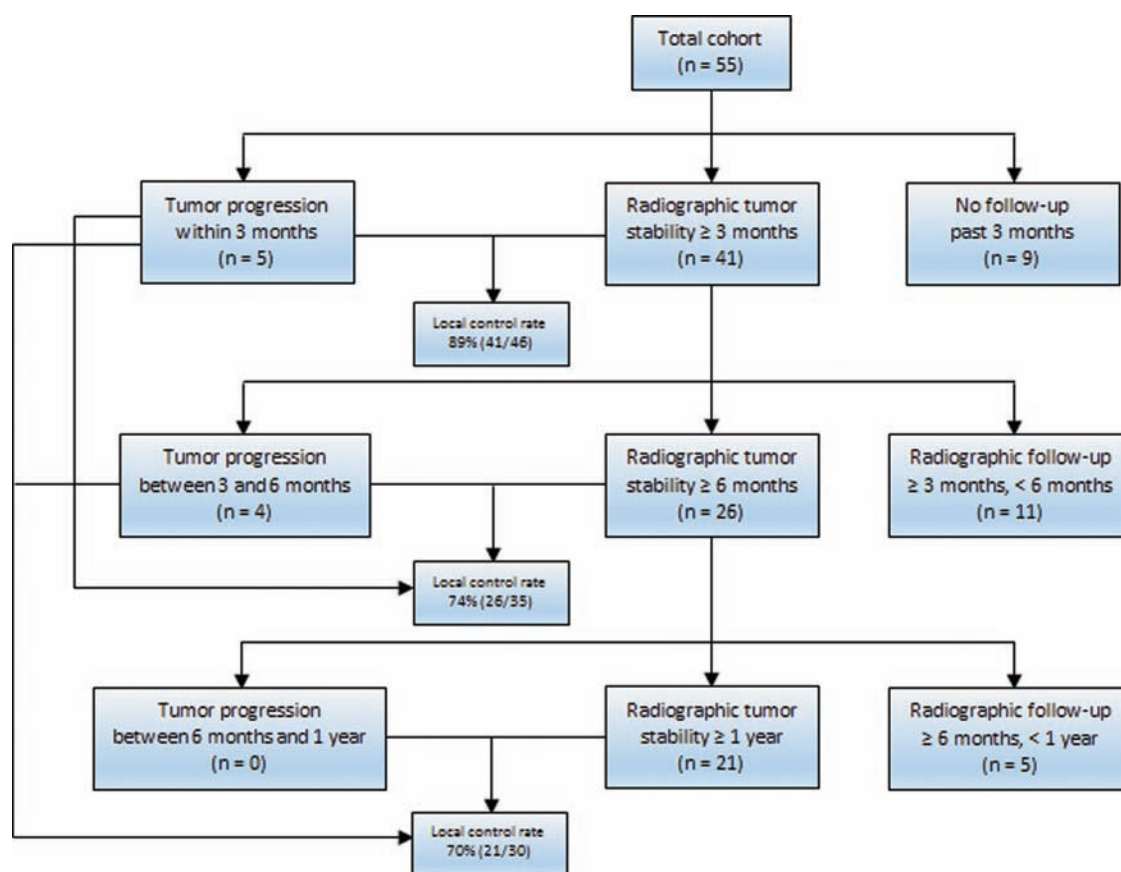


FIG 3. Flowchart summarizing overall radiographic local tumor control results at 3-month, 6-month, and 1-year follow-ups.

disease in 90% (27/30) of these cases. Thus, the 1-year radiographic local tumor control rate was 67% (18/27) in the setting of systemic metastatic disease progression. Five tumors (19%; 5/26) with at least 6 months of documented posttreatment stability were not imaged again after 1 year. In 3 of these cases (60%; 3/5), posttreatment imaging was not performed because the patient was doing well clinically at the end of the study period with no back pain or neurologic deficits. One patient (20%, 1/5) entered hospice care due to progression of visceral metastatic disease, and 1 patient (20%, 1/5) was lost to follow-up.

Of the 9 cases in which radiographic local tumor control was not achieved, the median time to documented tumor progression was 12.1 weeks (range, 3–20 weeks). Residual or recurrent tumor was present in the posterior vertebral body and/or epidural space in 89% (8/9) of cases, and in the anterolateral vertebral body in 1 case (11%; 1/9). In 89% (8/9) of cases, the ablation was performed from a bipedicular approach. In the one case in which failure occurred after a unipedicular approach, tumor recurrence occurred in the contralateral hemivertebral body (Fig 2).

DISCUSSION

In the present study, combination RFA and vertebral augmentation achieved 1-year radiographic local control rates of 70% (21/30) overall and 67% (18/27) in the setting of systemic metastatic disease progression. These results suggest the possibility of a new, multidisciplinary paradigm for managing metastatic spine disease that incorporates RFA and vertebral augmentation for local tu-

mor control.¹⁸ Although radiation therapy is the standard of care for palliation and local control of osseous metastatic disease, RFA and vertebral augmentation may be an effective alternative for patients who cannot be offered or cannot tolerate radiation therapy or have radiation-resistant tumors (Fig 1). A prospective clinical trial is now needed to replicate these results.

In the 9 cases in which RFA and vertebral augmentation did not achieve local tumor control, residual or recurrent tumor was most commonly present in the posterior vertebral body and/or epidural space (89%, 8/9). These results are expected, because it can be difficult to ablate tumor in these areas without also heating adjacent spinal nerves. We perform RFA with the patient under conscious sedation, in part, so that patients can react to and express new radicular pain indicating that the spinal nerves are being heated to dangerous temperatures. When this happens, ablation is terminated to avoid thermal nerve injury, though the result is often less thorough tumor ablation. The efficacy of radiation therapy similarly declines with decreasing distance between the tumor and the spinal cord, because of the risk of radiation-induced myelopathy.⁷ In several such cases, our multidisciplinary team has used radiation therapy in combination with RFA and vertebral augmentation. Greenwood et al¹⁹ recently reported our initial experience with this strategy, which achieved radiographic local tumor control rates of 92% (12/13) and 100% (10/10) at 3- and 6-month follow-ups, respectively, despite systemic metastatic disease progression. A prospective trial is needed to determine if combination radiation therapy, RFA, and vertebral augmentation

achieves better results than radiation or percutaneous therapy alone.

One case of ablation failure occurred in the hemivertebral body contralateral to where ablation was performed (Fig 2). Although the entirety of osteolysis on pretreatment CT was confined to the right hemivertebral body and was accessible from a right unipedicular approach, microscopic tumor infiltration into the left hemivertebral body was presumably beyond the margin of the ablation zone. As a result of this case, our current practice is to ablate the entire volume of T2-hyperintense marrow signal and enhancement on MR imaging, or the entire volume of FDG avidity within the vertebral body on PET/CT, as well as an additional 3-mm margin to account for microscopic tumor infiltration.¹⁶

In addition to being a retrospective study with a heterogeneous cohort of tumor histologies, the most important limitation of this study is the number of patients without 3-month, 6-month, or 1-year imaging follow-up. Three factors account for this limitation: First, there was no routine follow-up imaging protocol. This introduced selection bias that may have resulted in underestimation of local control rates, because oncologists are less likely to obtain imaging in patients with clinically stable disease. Second, patients died or entered hospice care. These results are expected in a cohort of patients with metastatic disease, and chart review revealed that these outcomes were not due to metastatic spinal cord compression at the levels treated with RFA and vertebral augmentation. Third, patients were lost to follow-up entirely. As in all outcome-based studies, this group has the greatest potential to bias the results. However, these patients only accounted for 7.3% (4/55) of the original cohort.

Another limitation is the lack of established criteria for the radiographic diagnosis of recurrent or residual tumor. Ideally, radiographic differentiation of tumor from postablation changes would be based on histopathologic-MR imaging correlation, as has been done with soft-tissue tumors.²⁰⁻²² However, vertebral augmentation prevents re-access to the vertebral body for biopsy. Increased osteolysis on CT is a reasonable criterion for tumor progression, because animal studies have shown that the lamellar structure of bone is preserved after RFA.²³ The MR imaging criteria of T2 hyperintensity and enhancement adjacent to the ablation cavity are nonspecific, because ablation produces a rim of granulation tissue around the ablation cavity that, like tumor, is T1 hypointense, T2 hyperintense, and enhances.⁹ Furthermore, granulation tissue can evolve with time, thus mimicking tumor progression.²⁰ To avoid overestimating the rate of local tumor control, we assumed that residual T1-hypointense, T2-hyperintense signal and enhancement at the margin of the ablation cavity represented residual tumor unless follow-up MR imaging showed stable findings or retraction of epidural tumor (Fig 1), or a PET/CT was available demonstrating absence of associated FDG uptake.

CONCLUSIONS

Radiofrequency ablation and vertebral augmentation appears in this retrospective study to be an effective treatment for achieving

local control of spinal metastases. A prospective clinical trial is now needed to replicate these results.

Disclosures: Adam N. Wallace—UNRELATED: Grants/Grants Pending: DFINE is donating ablation probes for an animal research study; OTHER RELATIONSHIPS: DFINE paid for travel expenses for the Metastatic Spine Disease Multidisciplinary Working Group meeting in January 2014. Jack W. Jennings—UNRELATED: Consultancy: DFINE; Payment for Lectures (including service on Speakers Bureaus): DFINE speaker panel.

REFERENCES

1. Hall WA, Stapleford LJ, Hadjipanayis CG, et al. **Stereotactic body radiosurgery for spinal metastatic disease: an evidence-based review.** *Int J Surg Oncol* 2011;2011:979214 Medline
2. Witham TF, Khavkin YA, Gallia GL, et al. **Surgery insight: current management of epidural spinal cord compression from metastatic spine disease.** *Nat Clin Pract Neurol* 2006;2:87-94; quiz 116 Medline
3. Bayley A, Milosevic M, Blend R, et al. **A prospective study of factors predicting clinically occult spinal cord compression in patients with metastatic prostate carcinoma.** *Cancer* 2001;92:303-10 Medline
4. Klimo P Jr, Schmidt MH. **Surgical management of spinal metastases.** *Oncologist* 2004;9:188-96 CrossRef Medline
5. Kim JM, Losina E, Bono CM, et al. **Clinical outcome of metastatic spinal cord compression treated with surgical excision ± radiation versus radiation therapy alone: a systematic review of literature.** *Spine* 2012;37:78-84 CrossRef Medline
6. Gerszten PC, Mendel E, Yamada Y. **Radiotherapy and radiosurgery for metastatic spine disease: what are the options, indications, and outcomes?** *Spine* 2009;34:S78-92 CrossRef Medline
7. Masucci GL, Yu E, Ma L, et al. **Stereotactic body radiotherapy is an effective treatment in irradiating spinal metastases: current status and practical considerations for safe practice.** *Expert Rev Anticancer Ther* 2011;11:1923-33 CrossRef Medline
8. Rybak LD, Gangi A, Buy X, et al. **Thermal ablation of spinal osteoid osteomas close to neural elements: technical considerations.** *AJR Am J Roentgenol* 2010;195:W293-98 CrossRef Medline
9. Wallace AN, Greenwood TJ, Jennings JW. **Use of imaging in the management of metastatic spine disease with percutaneous ablation and vertebral augmentation.** *AJR Am J Roentgenol* 2015;205:434-41 CrossRef Medline
10. Wallace AN, Vyhmeister R, Hsi AC, et al. **Delayed vertebral body collapse after stereotactic radiosurgery and radiofrequency ablation: case report with histopathologic-MRI correlation.** *Interv Neuroradiol* 2015;21:742-49 CrossRef Medline
11. Goetz MP, Callstrom MR, Charboneau JW, et al. **Percutaneous image-guided radiofrequency ablation of painful metastases involving bone: a multicenter study.** *J Surg Oncol* 2004;22:300-06 Medline
12. Dupuy DE, Liu D, Hartfeil D, et al. **Percutaneous radiofrequency ablation of painful osseous metastases: a multicenter American College of Radiology Imaging Network trial.** *Cancer* 2010;116:989-97 CrossRef Medline
13. Anchala PR, Irving WD, Hillen TJ, et al. **Treatment of metastatic spinal lesions with a navigational bipolar radiofrequency ablation device: a multicenter retrospective study.** *Pain Physician* 2014;17:317-27 Medline
14. Hillen TJ, Anchala P, Friedman MV, et al. **Treatment of metastatic posterior vertebral body osseous tumors by using a targeted bipolar radiofrequency ablation device: technical note.** *Radiology* 2014;273:261-67 CrossRef Medline
15. Wallace AN, Greenwood TJ, Jennings JW. **Radiofrequency ablation and vertebral augmentation for palliation of painful spinal metastases.** *J Neurooncol* 2015;124:111-18 CrossRef Medline
16. Ahmed M, Solbiati L, Brace CL, et al. **Image-guided tumor ablation: standardization of terminology and reporting criteria—a 10-year update.** *J Vasc Interv Radiol* 2014;25:1691-705 CrossRef Medline
17. Klass D, Marshall T, Toms A. **CT-guided radiofrequency ablation of spinal osteoid osteomas with concomitant perineural and**

- epidural irrigation for neuroprotection.** *Eur Radiol* 2009;19:2238–43 CrossRef Medline
18. Wallace AN, Robinson CG, Meyer J, et al. **The Metastatic Spine Disease Multidisciplinary Working Group algorithms.** *Oncologist* 2015;20:1205–15 CrossRef Medline
 19. Greenwood TJ, Wallace A, Friedman MV, et al. **Combined ablation and radiation therapy of spinal metastases: a novel multimodality treatment approach.** *Pain Physician* 2015;18:573–81 Medline
 20. Wile GE, Leyendecker JR, Krehbiel KA, et al. **CT and MR imaging after imaging-guided thermal ablation of renal neoplasms.** *Radiographics* 2007;27:325–39; discussion 339–40 CrossRef Medline
 21. Sainani NI, Gervais DA, Mueller PR, et al. **Imaging after percutaneous radiofrequency ablation of hepatic tumors, part 1: normal findings.** *AJR Am J Roentgenol* 2013;200:184–93 CrossRef Medline
 22. Sainani NI, Gervais DA, Mueller PR, et al. **Imaging after percutaneous radiofrequency ablation of hepatic tumors, part 2: abnormal findings.** *AJR Am J Roentgenol* 2013;200:194–204 CrossRef Medline
 23. Yamamoto S, Kaminou T, Ono Y, et al. **Thermal influence of radiofrequency ablation for bone: an experimental study in normal rabbit bone.** *Skeletal Radiol* 2014;43:459–65 CrossRef Medline

CT-Fluoroscopic Cervical Transforaminal Epidural Steroid Injections: Extraforaminal Needle Tip Position Decreases Risk of Intravascular Injection

G.M. Lagemann, M.P. Yannes, A. Ghodadra, W.E. Rothfus, and V. Agarwal

ABSTRACT

BACKGROUND AND PURPOSE: Cervical transforaminal epidural steroid injections are commonly performed for temporary pain relief or diagnostic presurgical planning in patients with cervical radiculopathy. Intravascular injection of steroids during the procedure can potentially result in cord infarct, stroke, and even death. CT-fluoroscopy allows excellent anatomic resolution and precise needle positioning. This study sought to determine the safest needle tip position during CT-guided cervical transforaminal epidural steroid injection as determined by the incidence of intravascular injection.

MATERIALS AND METHODS: We retrospectively evaluated procedural imaging for consecutive single-site CT-fluoroscopic cervical transforaminal epidural steroid injection performed during a 13-month period. Intravascular injections were identified and classified by volume, procedure phase, vessel type, and needle tip position relative to the targeted neural foramen. ANOVA, Wilcoxon, or Pearson χ^2 testing was used to assess differences among groups as appropriate.

RESULTS: Intravascular injections occurred in 49/201 (24%) procedures. Of the intravascular injections, 13/49 (27%) were large, 10/49 (20%) were small, and 26/49 (53%) were trace volume. Sixteen of 49 (33%) intravascular injections occurred with a trial contrast dose; 27/49 (55%), with a steroid/analgesic cocktail; and 6/49 (12%), with both. Twenty-seven of 49 (55%) intravascular injections were likely venous, 22/49 (45%) were indeterminate, and none were likely arterial. The intravascular injection rate was significantly lower ($P < .001$) for the extraforaminal needle position (8/82, 10%) compared with junctional (27/88, 31%) and foraminal (14/31, 45%) needle tip positions.

CONCLUSIONS: An extraforaminal needle position for CT-guided cervical transforaminal epidural steroid injection decreases the risk of intravascular injection and therefore may be safer than other needle tip positions.

ABBREVIATION: TFESI = transforaminal epidural steroid injection

Cervical radiculopathy is a common medical condition with a reported annual incidence of 0.8/1000 persons.¹ Cervical transforaminal epidural steroid injections (TFESIs) are commonly performed in patients with cervical radiculopathy to provide targeted diagnostic information to referring surgeons or to provide short-term pain relief. CT-fluoroscopy offers excellent anatomic resolution and allows very precise needle positioning,

making it the preferred technique for many proceduralists.^{2,3} Posterior circulation stroke and cord infarct are rare but potentially devastating complications of cervical TFESIs.⁴⁻⁹ Although some debate remains, these complications are most commonly attributed to accidental intravascular injection of steroid.⁴

The intravascular injection rate for CT-guided cervical TFESIs has previously been estimated at 1%–26%,^{3,10,11} while the corresponding rate for conventional fluoroscopic guidance has been published at 17%–32.8%.¹²⁻¹⁵ Despite the known risks of the procedure and the high anatomic resolution of CT, the role of needle position in intravascular injection has not been previously evaluated, to our knowledge.

The purpose of this study was to determine the safest needle tip depth relative to the targeted neural foramen as determined by the incidence of intravascular injection. We also characterized intravascular injections by volume, phase of the procedure (contrast injection versus steroid/analgesic cocktail), and likely vessel type injected.

Received August 10, 2015; accepted after revision September 14.

From the Department of Radiology, University of Pittsburgh Medical Center, Pittsburgh, Pennsylvania.

Paper previously presented in part at: American Society of Neuroradiology Annual Meeting and the Foundation of the ASNR Symposium, May 25–30, 2015; Chicago, Illinois.

Please address correspondence to Gerritt M. Lagemann, MD, Department of Radiology, Division of Neuroradiology, University of Pittsburgh Medical Center, 200 Lothrop St, 2nd Floor Suite 200 East Wing, Pittsburgh, PA 15213; e-mail: lagemanngm@upmc.edu; @GerrittLagemann

<http://dx.doi.org/10.3174/ajnr.A4603>

MATERIALS AND METHODS

Subjects

Local institutional review board approval was obtained for this retrospective review of clinical and imaging data. This study was compliant with the Health Insurance Portability and Accountability Act.

We retrospectively searched our radiology information system for all consecutive unilateral, single-level CT-guided cervical TFESIs performed for upper extremity radiculopathy by the neuroradiology division at our main academic campus during a 13-month period (February 2014 to February 2015). C3-level injections performed for radiculopathy were included, but C3-level procedures performed for occipital neuralgia were excluded.

Procedure Technique

All procedures were performed by 1 of 3 attending neuroradiologists (G.M.L., W.E.R., and V.A.) with Certificates of Added Qualification in neuroradiology and having 4, 24, and 8 years of experience, respectively, performing image-guided spine procedures. The injections were performed by using a technique similar to that previously published³ with additional details as follows: All procedures were performed on a single LightSpeed Plus 4-detector row CT scanner (GE Healthcare, Milwaukee, Wisconsin). Scout imaging was acquired through the targeted level by using the following parameters: rotation time, 0.8 seconds; speed, 3.75 mm/rotation; pitch, 0.75:1; section thickness, 2.5 mm; 120 kV with variable milliamperes; and noise index, 4.69. Intermittent CT-fluoroscopy was performed with SmartView (GE Healthcare) activated by a foot pedal and creating 3 consecutive, 2.5 mm-thick, axial sections per scan by using 120 kV with variable milliamperes. All CT-fluoroscopy imaging acquired during the procedure was automatically archived to our PACS.

A 25-ga, 3.5-inch Quincke spinal needle (BD Medical, Franklin Lakes, New Jersey) was advanced toward the posterior margin of the targeted neural foramen. The posterior margin of the foramen was targeted because it has been suggested that the posterior aspect of the foramen is less vascular and may carry less risk of intravascular injection.² Furthermore, targeting the posterior neural foramen aids in avoiding injury to the vertebral artery.

After attachment of flexible microbore tubing, a trial dose of 0.3 mL of iohexol contrast agent (Omnipaque, 180 mg/mL; GE Healthcare, Piscataway, New Jersey) was injected and was imme-

diately followed by CT-fluoroscopy to evaluate for intravascular contrast. (We use the term “trial dose” for the contrast-only injection to distinguish from “test dose,” a term historically used to refer to the injection of analgesic before steroid injection.) If intravascular injection was identified with the trial dose, the needle was withdrawn a few millimeters and a repeat injection of 0.3 mL of iohexol was performed with repeat CT-fluoroscopic imaging. These steps were repeated until there was no evidence of intravascular injection.

A cocktail of 1.2 mL of 2.5 or 5 mg/mL bupivacaine analgesic, 8-mg of preservative-free dexamethasone sodium phosphate steroid (10 mg/mL), and 0.3 mL of iohexol was then injected under additional CT-fluoroscopic guidance. We use dexamethasone as our glucocorticoid for cervical TFESIs because its nonparticulate nature may reduce the risk of stroke or cord infarct if the steroid is accidentally injected intravascularly.^{4,5} No case of cord infarct or stroke has been reported with nonparticulate steroids to date.¹⁶

The patient was monitored for 15 minutes after the procedure for minor complications (such as vasovagal response or increasing postprocedure pain) and major complications (such as cardiovascular or neurologic compromise).

Image Evaluation

All studies were retrospectively evaluated by 2 of the proceduralists (G.M.L. and V.A.) blinded to operator and patient identity. The 2 reviewers initially evaluated and characterized all imaging separately. In cases of disagreement, the 2 re-evaluated the relevant imaging together and reached a consensus on all findings and characterizations.

Intravascular Injection Definition

Intravascular injection was considered present if 1 of 2 contrast appearances was identified on CT-fluoroscopy, similar to previously described criteria¹¹:

1) Contrast appeared as ≥ 1 round or curvilinear discrete foci separate from the needle tip and its surrounding epidural contrast collection (Fig 1). In this situation, the initial intravascular contrast was sometimes confirmed by partial or complete dissipation of the discrete foci of contrast on immediate repeat CT-fluoroscopic imaging, though this additional confirmation was not required for classification as intravascular contrast.

2) Either far less than the expected amount of injected contrast, or no contrast at all, accumulated adjacent to the needle or elsewhere on the imaging (Fig 2). In this context, we inferred that a vessel had rapidly carried the contrast out of the plane in the very short time between injection and imaging. Complete absence of contrast was considered a completely intravascular injection.

Contrast appearing as a continuous curvilinear collection extending away from the needle tip between paraspinous muscles was interpreted as contrast ex-

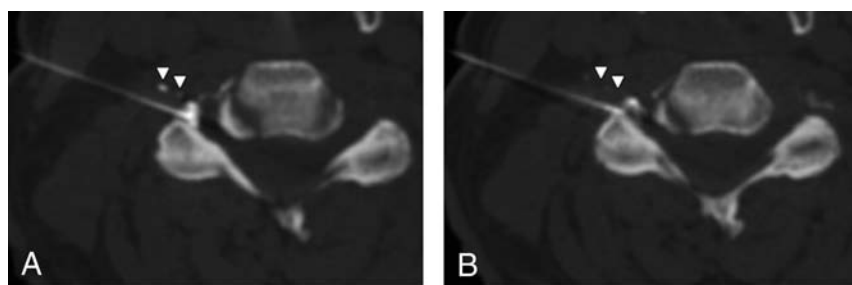


FIG 1. Mixed intravascular and epidural contrast injection. *A*, Intravascular injection appears as discrete foci of contrast (arrowheads) away from the needle tip and adjacent main, epidural contrast collection. *B*, The intravascular contrast almost completely disappears (arrowheads) on immediate repeat CT-fluoroscopic imaging. This rapid resolution of contrast confirmed but was not required for identification of intravascular contrast. The needle tip position is junctional on these images.

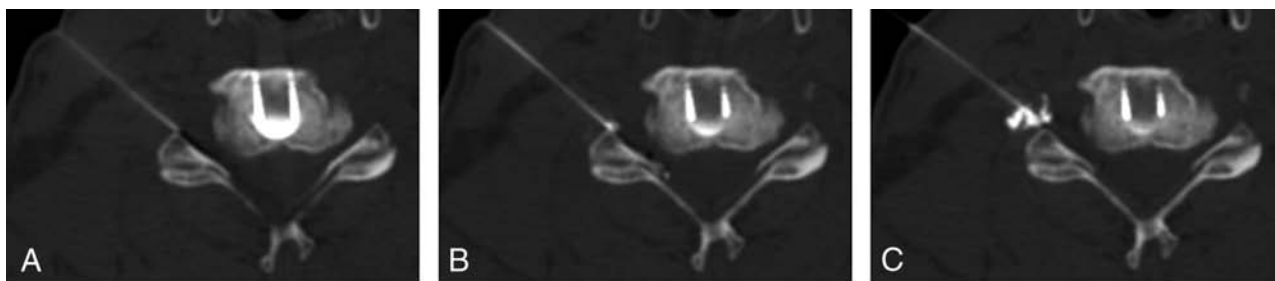


FIG 2. Intravascular injection identified by a less-than-expected accumulation of epidural contrast. A, Needle position before the contrast trial dose. B, Only a very small amount of contrast, considerably less than the injected volume of 0.3 mL of iohexol, is seen on immediate postinjection imaging. The missing contrast is inferred to be intravascular and has been circulated out of the imaged field. (A trace amount of intravascular contrast is also noted within the right aspect of the spinal canal.) C, After the needle is withdrawn several millimeters, a repeat contrast trial injection shows the expected volume of injected contrast accumulating in the epidural space. No additional intravascular contrast was identified with the steroid/analgesic injection (not shown), making this a trial dose intravascular injection.

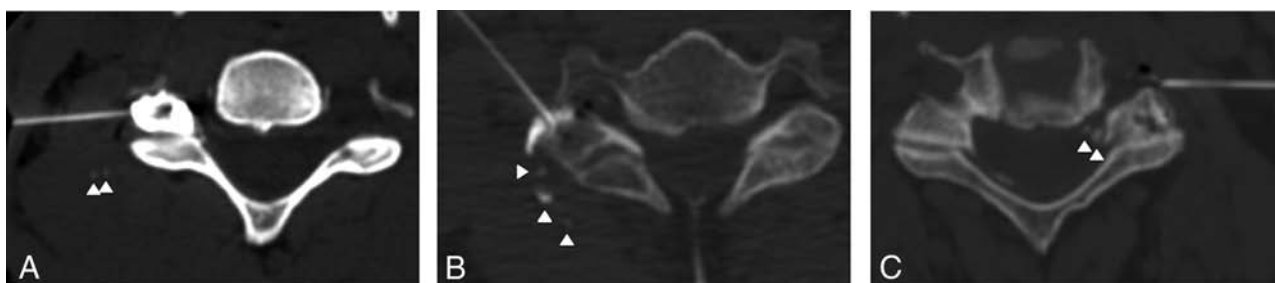


FIG 3. Intravascular contrast injection classified by volume. A, Trace volume of intravascular injection appears as 1–2 subtle foci (arrowheads), each ≤ 2 mm. The image is windowed to accentuate the intravascular contrast; the initial appearance on default window settings is even subtler and was not identified at the time of the procedure. B, A small volume of intravascular injection appears either as ≥ 3 foci (arrowheads), at least 1 focus of ≥ 3 mm (central arrowhead), or both (as in this case). C, A large volume of intravascular contrast injection. Less than the expected volume of injected iohexol is seen on the imaging because most of the intravascular contrast has already been circulated out of the FOV. Some intravascular contrast is present within the venous plexus both adjacent to the needle tip and more medially (arrowheads).

tending within the fascia planes and did not represent intravascular contrast.

Intravascular Injection Volume

Intravascular injections were characterized by volume into 1 of 3 categories (Fig 3):

- 1) Trace (Fig 3A): Intravascular contrast appears as 1–2 foci, each appearing as a punctate or curvilinear focus and measuring ≤ 2 mm in diameter.
- 2) Small (Fig 3B): Intravascular contrast volume is too small to create a clear perceptible decrease in the expected volume of accumulating epidural contrast. However, the visualized intravascular contrast component either has a smallest trans-axial dimension measuring ≥ 3 mm or appears as ≥ 3 separate foci.
- 3) Large (Fig 3C): The amount of accumulating epidural contrast is clearly smaller than the injected amount. In this case, the nonvisualized contrast was interpreted as already carried out of the imaged FOV by the vascular system.

Intravascular Injected Material

The intravascular injection was classified as occurring with the trial contrast dose, the steroid/analgesic injectate, or both.

A trial dose intravascular injection was considered present if 3 criteria were satisfied (Fig 2):

- 1) Intravascular injection was present on the first imaging acquired immediately after the initial trial dose.

- 2) Needle withdrawal and repeat trial dose were mentioned in the report of the procedure or could be identified on the imaging.

- 3) Intravascular injection was not identified, even in retrospect, on the ensuing injection of steroid/analgesic.

Steroid/analgesic intravascular injection was considered present if 2 criteria were satisfied (Fig 4):

- 1) Intravascular injection was not seen, even in retrospective analysis, during the contrast trial dose.
- 2) Intravascular contrast was identified in retrospect during the ensuing injection of steroid/analgesic.

An intravascular injection with both a trial dose and steroid/analgesic components was considered present if 3 criteria were satisfied (Fig 5):

- 1) Intravascular contrast was present in retrospect on trial-dose imaging.
- 2) Needle withdrawal and the repeat trial dose were not mentioned in the report of the procedure and could not be identified on the imaging.
- 3) Additional intravascular contrast was identified in retrospect on the ensuing injection of steroid/analgesic.

In this final situation, the 2 components of intravascular injection are intimately related and closely dependent. Thus, we consider this situation to represent a single intravascular injection with components in 2 phases: one trial dose and the other steroid/analgesic injectate.

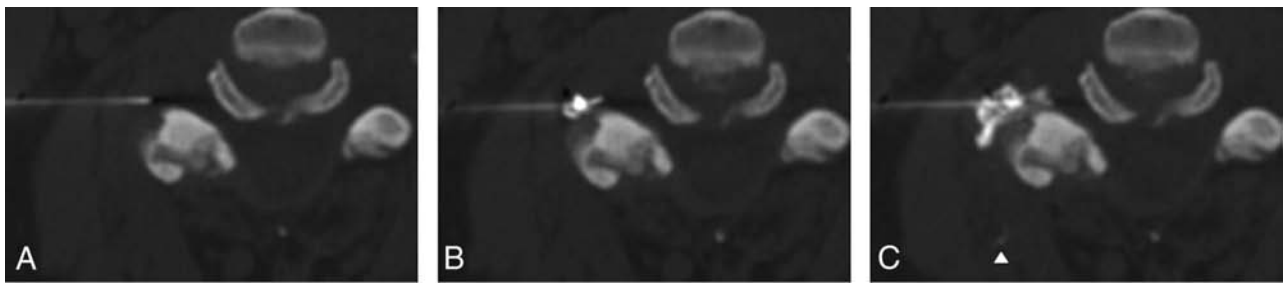


FIG 4. Intravascular injection seen only on steroid/analgesic injection. *A*, Needle position preinjection. *B*, Contrast trial injection shows no intravascular injection. *C*, Subsequent injection of the steroid/analgesic cocktail shows a small intravascular injection (*arrowhead*) within an indeterminate paraspinal vessel. The needle was unchanged in position between trial injection and steroid/analgesic cocktail injection.

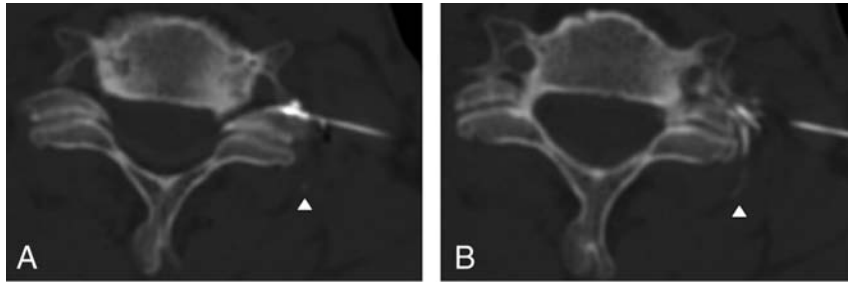


FIG 5. Intravascular injection on both trial injection and steroid/analgesic cocktail injection. *A*, The trace intravascular injection (*arrowhead*) is subtle but present on the contrast trial dose; the proceduralist did not appreciate it at the time of the procedure. *B*, More obvious intravascular injection (*arrowhead*) is evident on the ensuing steroid/analgesic cocktail injection.

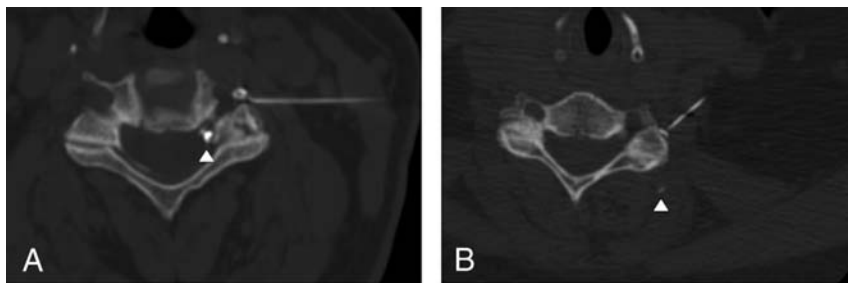


FIG 6. Classification of intravascular injection by vessel type. *A*, Venous injection, with contrast within extra- and intracanalicular (*arrowhead*) components of the venous plexus. *B*, Indeterminate vessel injection, with contrast accumulating within a small paraspinal vessel (*arrowhead*). This could represent either a branch of the ascending cervical artery or a small vein. No likely arterial injections were identified.

Vessel Characterization

Intravascular injections were characterized as likely venous, likely arterial, or indeterminate, as shown in Fig 6. In likely venous, contrast accumulates away from the needle tip within the foraminal venous plexus. In indeterminate, discrete contrast accumulates away from the needle tip within or between the paraspinal muscles, in the expected region of branches of the anterior cervical artery and small draining veins. In likely arterial, contrast clearly extends along the anatomic course of the vertebral artery, ascending cervical artery, radiculomedullary artery, or anterior spinal artery.

Needle Depth

Needle tip position at the time of injection was classified as extraforaminal, junctional, or foraminal by using a modified version of a previously published scheme (Fig 7).^{10,17} The lateral junction of the targeted neural foramen was defined by a

line connecting the anterolateral margin of the vertebral body with the lateral margin of the facet joint. For the low cervical neural foramina, where the transverse process is a lateral continuation of the facet joint, the transverse process was not considered a part of the facet joint. A needle tip within 2 mm of this line segment was characterized as within the junctional zone. A needle tip lateral to the junctional zone was classified as extraforaminal; a needle tip medial to the junctional zone was classified as foraminal.

Statistical Testing

Pearson χ^2 testing was used to assess differences in vascular injections based on needle position. Differences in vascular injections were assessed on the basis of age, sex, and prior surgical history by using ANOVA, Wilcoxon, and Pearson χ^2 testing, respectively. If appropriate, post hoc multiple comparison testing was performed with correction (the Tukey method and the Steel-Dwass procedure for parametric and nonparametric tests, respectively). Statistical testing was performed by using JMP 11 (SAS Institute,

Cary, North Carolina).

RESULTS

Patient Population

A total of 175 patients underwent 201 consecutive unilateral, single-level procedures, with most (87%) undergoing only a single cervical injection during the 13-month study period. The remaining 13% of patients underwent ≥ 2 unilateral, single-level injections on different days. The mean patient age was 53 years (range, 25–87 years). Fifty-three percent of procedures were performed on men; 47% were performed on women. The most frequently injected levels were C6 and C7, with a roughly equal split in laterality. There was no significant difference in age, sex, or history of prior cervical surgery among groups based on needle depth or vascular injection ($P > .05$).

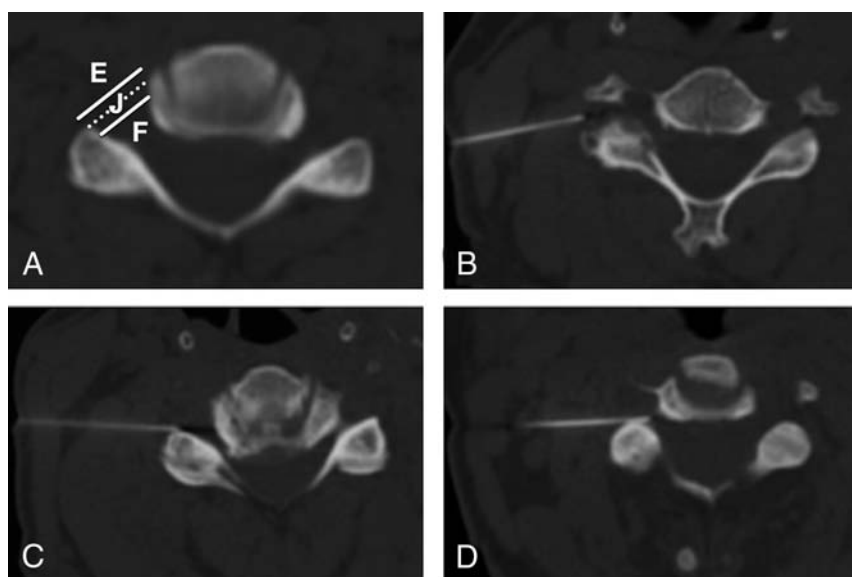


FIG 7. Needle depth classification. A, The lateral junction of the neural foramen (*dotted line*) is defined by a line segment connecting the anterolateral margin of the vertebral body with the most lateral margin of the facet joint. A needle tip in a zone within 2 mm medial or lateral to this segment (*solid lines*) is classified as within the junctional zone (J). A needle tip >2 mm lateral is classified as within the extraforaminal zone (E), and a needle tip >2 mm medial is classified as within the foraminal zone (F). Examples of extraforaminal (B), junctional (C), and foraminal (D) needle tip positions.

Intravascular Injection Incidence, Volume, and Material

Intravascular injections occurred in 49/201 (24%) procedures. Of these procedures, 16/49 (33%) had intravascular injection only with the trial dose; 27/49 (55%), only with the steroid/analgesic injection; and 6/49 (12%), with both the trial dose and the steroid/analgesic injectate. Regarding volume, 13/49 (27%) were large, 10/49 (20%) were small, and 26/49 (53%) were trace volume.

Injected Material and Volume of Intravascular Injection

Of the 16 intravascular injections occurring during the trial dose only, 10/16 (63%) were large volume, 3/16 (19%) were small volume, and 3/16 (19%) were trace volume intravascular injections. Of the 27 intravascular injections occurring with steroid/analgesic injectate only, 2/27 (7%) were large volume, 3/27 (11%) were small volume, and 22/27 (81%) were trace volume intravascular injections. All 6 intravascular injections with both trial dose and steroid/analgesic components had the same size intravascular injection in the 2 components: One of 6 (17%) injections was large volume; 4/6 (67%), small volume; and 1/6 (17%), trace volume.

Injected Vessel

Regarding injected vessels, 27/49 (55%) were likely venous, 22/49 (45%) were indeterminate, and none were likely arterial.

Type of Vessel Injected and Size of Intravascular Injection

Of the 13 large-volume intravascular injections, 11/13 (85%) were likely venous and the remaining 2/13 (15%) were associated with an indeterminate vessel type. Of the 10 small-volume intravascular injections, 8/10 (80%) were likely venous and the remaining 2/10 (20%) had an indeterminate vessel type. Of the 26 trace-volume intravascular injections, 8/26 (31%) were likely venous and the remaining 18/26 (69%) had an indeterminate vessel type.

Injected Material and Type of Vessel Injected

Of the 16 intravascular injections occurring on trial dose only, 13/16 (81%) were likely venous, and in the remaining 3/16 (19%), the injected vessel type was indeterminate. Of the 27 intravascular injections occurring with the steroid/analgesic cocktail only, 10/27 (37%) were likely venous and 17/27 (63%) were indeterminate for vessel type. For the 6 intravascular injections with both trial dose and steroid/analgesic components, 4/6 (67%) were likely venous and 2/6 (33%) were indeterminate for vessel type.

Needle Depth

Needle depth at the time of injection was more commonly extraforaminal (82/201, 41%) or junctional (88/201, 44%) and less often foraminal (31/201, 15%).

The intravascular injection rate was significantly lower ($P < .001$) for extraforaminal needle position (8/82, 10%) compared with junctional (27/88, 31%) and foraminal (14/31, 45%) needle tip positions (pair-wise comparisons: extraforaminal versus junctional, $P < .001$; extraforaminal versus foraminal, $P < .001$; junctional versus foraminal, $P = .145$).

There were no minor or major intraprocedural or immediate postprocedural complications.

Complications

There were no minor or major intraprocedural or immediate postprocedural complications.

DISCUSSION

Intravascular injection during CT-fluoroscopic cervical TFESI is common, occurring in 24% of our 201 cases. Of these, most (53%) were trace volume intravascular injections, and most resulted in intravascular injection of the steroid and analgesic. Extraforaminal needle tip position strongly correlated with a lower incidence of intravascular injection ($P < .001$). Despite many intravascular injections of nonparticulate steroid, there were no complications.

We have shown that the extraforaminal needle tip position may be relatively safe because it reduces the risk for intravascular injection. Minimizing rates of intravascular injection is critical because accidental embolization of steroid and analgesic can potentially lead to rare but catastrophic complications, such as cord infarct, stroke, or even death.⁴⁻⁹

There has been considerable disagreement regarding the ideal needle position within the targeted neural foramen for CT-guided cervical TFESIs. Some assume that a relatively deep position, with the needle tip within the outer neural foramen and immediately adjacent to the targeted nerve root, is required for proper analgesic and steroid efficacy,^{3,10,18} while others advocate a more cautious, extraforaminal needle tip position to minimize the risk of complications.^{8,19,20} Junctional and foraminal needle tip positions have been previously shown to have higher rates of foram-

inal contrast flow compared with the extraforaminal needle position,¹⁰ though contrast dispersal pattern was shown not to correlate with pain relief in 1 study.²¹

To our knowledge, we are the first to observe, on CT-guided TFESI, contrast appearing within vessels during steroid/analgesic cocktail injection, a finding we believe depicts intravascular injection of steroid and analgesic. We were able to evaluate intravascular injection of the steroid/analgesic cocktail because we routinely mix iodinated contrast with our cocktail, a procedural technique detail not practiced at many other institutions. In previous descriptions of CT-guided^{3,10,11} and conventional fluoroscopic-guided^{12–15} injections, the intravascular contrast was always identified on the trial dose and the needle was appropriately readjusted before injecting the steroid/analgesic cocktail. Many of our intravascular injections were trace volume, had a very subtle appearance, were not noted at the time of the procedure, and were identified only with meticulous retrospective evaluation of the procedural imaging. It is possible that intravascular injections of steroid and analgesic occurred in these prior studies but were not detected. Kranz et al¹¹ reported an overall rate of intravascular injection during CT-fluoroscopic cervical TFESI similar to our own (26% versus our 24%), but with all occurrences identified only on the trial contrast injection. We may have a relatively high rate of steroid/analgesic intravascular injection because we do not use the “double tap” technique of Kranz et al to evaluate intravascular contrast washout with the trial contrast dose injection. A future study directly comparing procedures performed with and without the double tap technique is warranted to prove the effectiveness of the double tap technique.

Intravascular injection occurred more often with the steroid/analgesic cocktail than with the trial dose. The reason is not completely clear, but we speculate that the larger overall volume of the steroid/analgesic cocktail (>2 mL of combined analgesic, steroid, and contrast) compared with the trial dose (0.3 mL of contrast alone) leads to slightly greater conspicuity of punctate intravascular injections, which constituted most steroid/analgesic intravascular injections.

Although we identified many likely intravascular injections of contrast/steroid injectate (27 procedures with intravascular injection during the steroid/analgesic phase alone and 6 procedures during both trial dose and contrast/steroid injection), we had no complications in the course of 201 procedures. Other authors have similarly reported no complications in 30 injections on 30 patients¹⁸ and 90 injections on 63 patients¹⁰ (though comparison may be imperfect because those studies did not mix contrast with their steroid injection). Major complications seem to occur at a <0.1% incidence.¹⁷ This safety record indicates that CT-fluoroscopic-guided cervical TFESIs are safe when performed by well-trained proceduralists who are experienced in spine procedures. In particular, spine procedures using nonparticulate steroid such as dexamethasone appear to carry a low risk of stroke or spinal cord infarct from embolized steroid.^{4,22} Earlier reports of complications from intravascular injection of steroids have often used triamcinolone or methylprednisolone,^{4,6–8,16} both of which have large aggregate particles. In 1 study performed on pigs, 4/4 injected with methylprednisolone into their vertebral arteries ex-

perienced catastrophic strokes and cord infarcts, whereas 0/7 injected with prednisolone or dexamethasone had any complications.²³ Regardless of steroid used, the proceduralist must always be mindful of the risk of accidentally directly injuring the vertebral artery with the procedure needle.

Limitations of our study include those inherent in a retrospective design and a single-hospital experience. Lack of relatively long-term (1–2 month) pain relief results also prevents us from recommending an extraforaminal needle position as the ideal position for cervical TFESIs. A future study with appropriate statistical power evaluating long-term pain relief, needle tip position, and intravascular injection incidence is warranted to determine the ideal needle tip position that minimizes intravascular injection while preserving patient pain relief.

CONCLUSIONS

An extraforaminal needle position for CT-guided cervical TFESI decreases the risk of intravascular injection and therefore may be safer than other needle tip positions.

REFERENCES

1. Radhakrishnan K, Litchy WJ, O'Fallon WM, et al. **Epidemiology of cervical radiculopathy: a population-based study from Rochester, Minnesota, 1976 through 1990.** *Brain* 1994;117(pt 2):325–35 CrossRef Medline
2. Hoang JK, Apostol MA, Kranz PG, et al. **CT fluoroscopy-assisted cervical transforaminal steroid injection: tips, traps, and use of contrast material.** *AJR Am J Roentgenol* 2010;195:888–94 CrossRef Medline
3. Wagner AL. **CT fluoroscopic-guided cervical nerve root blocks.** *AJNR Am J Neuroradiol* 2005;26:43–44 Medline
4. Scanlon GC, Moeller-Bertram T, Romanowsky SM, et al. **Cervical transforaminal epidural steroid injections: more dangerous than we think?** *Spine* 2007;32:1249–56 CrossRef Medline
5. Malhotra G, Abbasi A, Rhee M. **Complications of transforaminal cervical epidural steroid injections.** *Spine* 2009;34:731–39 CrossRef Medline
6. Suresh S, Berman J, Connell DA. **Cerebellar and brainstem infarction as a complication of CT-guided transforaminal cervical nerve root block.** *Skeletal Radiol* 2007;36:449–52 CrossRef Medline
7. Rosenkranz M, Grzyska U, Niesen W, et al. **Anterior spinal artery syndrome following periradicular cervical nerve root therapy.** *J Neurol* 2004;251:229–31 CrossRef Medline
8. Hodler J, Boos N, Schubert M. **Must we discontinue selective cervical nerve root blocks? Report of two cases and review of the literature.** *Eur Spine J* 2013;22(suppl 3):S466–70 CrossRef Medline
9. Abdi S, Datta S, Trescot AM, et al. **Epidural steroids in the management of chronic spinal pain: a systematic review.** *Pain Physician* 2007;10:185–212 Medline
10. Hoang JK, Massoglia DP, Apostol MA, et al. **CT-guided cervical transforaminal steroid injections: where should the needle tip be located?** *AJNR Am J Neuroradiol* 2013;34:688–92 CrossRef Medline
11. Kranz PG, Amrhein TJ, Gray L. **Incidence of inadvertent intravascular injection during CT fluoroscopy-guided epidural steroid injections.** *AJNR Am J Neuroradiol* 2015;36:1000–07 CrossRef Medline
12. Nahm FS, Lee CJ, Lee SH, et al. **Risk of intravascular injection in transforaminal epidural injections.** *Anaesthesia* 2010;65:917–21 CrossRef Medline
13. Furman MB, Giovanniello MT, O'Brien EM. **Incidence of intravascular penetration in transforaminal cervical epidural steroid injections.** *Spine* 2003;28:21–25 CrossRef Medline
14. El Abd OH, Amadera JE, Pimentel DC, et al. **Intravascular flow de-**

- tection during transforaminal epidural injections: a prospective assessment. *Pain Physician* 2014;17:21–27 Medline
15. Smuck M, Tang CT, Fuller BJ. Incidence of simultaneous epidural and vascular injection during cervical transforaminal epidural injections. *Spine* 2009;34:E751–55 CrossRef Medline
 16. Atluri S, Glaser SE, Shah RV, et al. Needle position analysis in cases of paralysis from transforaminal epidurals: consider alternative approaches to traditional technique. *Pain Physician* 2013;16:321–34 Medline
 17. Wolter T, Knoeller S, Berlis A, et al. CT-guided cervical selective nerve root block with a dorsal approach. *AJNR Am J Neuroradiol* 2010;31:1831–36 CrossRef Medline
 18. Cyteval C, Thomas E, Decoux E, et al. Cervical radiculopathy: open study on percutaneous periradicular foraminal steroid infiltration performed under CT control in 30 patients. *AJNR Am J Neuroradiol* 2004;25:441–45 Medline
 19. Wolter T, Mohadjer M, Berlis A, et al. Cervical CT-guided, selective nerve root blocks: improved safety by dorsal approach. *AJNR Am J Neuroradiol* 2009;30:336–37 CrossRef Medline
 20. Cho CH. Cervical nerve injection: computed tomography guidance with intravenous contrast and extraforaminal needle placement—series of seven consecutive case reports. *Spine J* 2010;10:e1–6 CrossRef Medline
 21. Park CH, Lee SH. Contrast dispersion pattern and efficacy of computed tomography-guided cervical transforaminal epidural steroid injection. *Pain Physician* 2014;17:487–92 Medline
 22. Derby R, Lee SH, Date ES, et al. Size and aggregation of corticosteroids used for epidural injections. *Pain Med* 2008;9:227–34 CrossRef Medline
 23. Okubadejo GO, Talcott MR, Schmidt RE, et al. Perils of intravascular methylprednisolone injection into the vertebral artery: an animal study. *J Bone Joint Surg Am* 2008;90:1932–38 CrossRef Medline

Training Guidelines for Endovascular Ischemic Stroke Intervention: An International Multi-Society Consensus Document

Contributors:

American Association of Neurological Surgeons/Congress of Neurological Surgeons (AANS/CNS): S.D. Lavine, K. Cockroft, B. Hoh, N. Bambakidis, A.A. Khalessi, H. Woo, H. Riina, A. Siddiqui
American Society of Neuroradiology (ASNR): J.A. Hirsch

Asian Australasian Federation of Interventional and Therapeutic Neuroradiology (AAFITN): W. Chong

Australian and New Zealand Society of Neuroradiology - Conjoint Committee for Recognition of Training in Interventional Neuroradiology (CCINR) representing the RANZCR (ANZSNR), ANZAN and NSA: H. Rice, J. Wenderoth, P. Mitchell, A. Coulthard, T.J. Signh, C. Phatorous, M. Khangure

Canadian Interventional Neuro Group (CING): P. Klurfan, K. terBrugge, D. Iancu, T. Gunnarsson

European Society of Neuroradiology (ESNR): O. Jansen, M. Muto

European Society of Minimally Invasive Neurologic Therapy (ESMINT): I. Szikora, L. Pierot, P. Brouwer, J. Gralla, S. Renowden, T. Andersson, J. Fiehler, F. Turjman, P. White, A.C. Januel, L. Spelle, Z. Kulcsar, R. Chapot, L. Spelle, A. Biondi, S. Dima, C. Taschner, M. Szajner, A. Krajina

Japanese Society for Neuroendovascular Therapy (JSNET): N. Sakai, Y. Matsumaru, S. Yoshimura, M. Ezura, T. Fujinaka, K. Iihara, A. Ishii, T. Higashi, M. Hirohata, A. Hyodo, Y. Ito, M. Kawanishi, H. Kiyosue, E. Kobayashi, S. Kobayashi, N. Kuwayama, Y. Matsumoto, S. Miyachi, Y. Murayama, I. Nagata, I. Nakahara, S. Nemoto, Y. Niimi, H. Oishi, J. Satomi, T. Satow, K. Sugiu, M. Tanaka, T. Terada, H. Yamagami

Sociedad Ibero Latino Americana de Neuroradiologica (SILAN): O. Diaz, P. Lylyk

Society of NeuroInterventional Surgery (SNIS): M.V. Jayaraman, A. Patsalides, C.D. Gandhi, S.K. Lee, T. Abruzzo, B. Albani, S.A. Ansari, A.S. Arthur, B.W. Baxter, K.R. Bulsara, M. Chen, J.E. Delgado Almandoz, J.F. Fraser, D.V. Heck, S.W. Hetts, M.S. Hussain, R.P. Klucznik, T.M. Leslie-Mawzi, W.J. Mack, R.A. McTaggart, P.M. Meyers, J. Mocco, C.J. Prestigiacomo, G.L. Pride, P.A. Rasmussen, R.M. Starke, P.J. Sunenshine, R.W. Tarr, D.F. Frei

Society of Vascular and Interventional Neurology (SVIN): M. Ribo, R.G. Nogueira, O.O. Zaidat, T. Jovin, I. Linfante, D. Yavagal, D. Liebeskind, R. Novakovic

World Federation of Interventional and Therapeutic Neuroradiology (WFITN): S. Pongpech, G. Rodesch, M. Soderman, K. terBrugge, A. Taylor, T. Krings, D. Orbach, A. Biondi, L. Picard, D.C. Suh, M. Tanaka, H.Q. Zhang



BACKGROUND

Ischemic stroke is a leading cause of death and disability worldwide. Much of the long-term disability occurs in patients with Emergent Large Vessel Occlusion (ELVO). In fact, in these patients, occlusion of a major intracerebral artery results in a large area of brain injury often resulting in death or severe disability¹. Until recently, intravenous tissue plasminogen activator (t-PA) was the only proven treatment for ELVO.

However, the landscape of stroke treatment has changed with the publication of five randomized multicenter controlled clinical trials. These trials provide Class 1, Level A evidence that endovascular thrombectomy (ET) is the standard of care for patients with ELVO. In particular, thrombectomy results in

significantly better clinical outcomes compared to best medical therapy in patients with acute occlusion of the intracranial internal carotid artery (ICA) and/or M1 segment of the middle cerebral artery (MCA)²⁻⁶. These results have led to guideline recommendations advocating for endovascular treatment in addition to t-PA for patients with ELVO. In addition, ET is now offered as first line therapy for patients that are not eligible for intravenous thrombolysis⁷⁻⁹. However, achieving the best possible clinical outcomes with endovascular stroke treatment mandates structured training and education of those physicians who are providing endovascular stroke treatment. On this regard, a recent meta-analysis of these five clinical trials showed that the vast majority of thrombectomies were performed by experienced neurointerventionalists. These include interventional neuroradiologists, endovascular neurosurgeons, and interventional neurologists who routinely perform neuroendovascular procedures¹⁰. None of the studies allowed physicians without previous experience in mechanical

This article is published simultaneously in the journals *Interventional Neuroradiology*, *American Journal of Neuroradiology*, *Journal of Interventional Neurology*, *EJNIR*, *Journal of Neuroendovascular Therapy*, *Journal of NeuroInterventional Surgery*, *Neuroradiology*, and *Neurosurgery*.

Indicates open access to non-subscribers at www.ajnr.org

thrombectomy to enroll patients. The centers participating in these trials offered endovascular stroke therapy 24 hours a day (with the exception of those in the EXTEND-IA trial) with expertise in vascular neurology and neurocritical care in a comprehensive stroke center. On-site expertise in vascular neurology and neurocritical care is paramount to achieving good clinical outcomes.

Geographical limitations to rapid access to acute stroke centers providing mechanical thrombectomy have led some to suggest physicians without prior experience or formal neuroendovascular training should consider providing coverage for these procedures. A multidisciplinary British Intercollegiate Stroke Working Party put forth a document outlining the safe delivery of mechanical thrombectomy, which highlights that operators should not normally carry out procedures with which they are unfamiliar and that they should recognize ad-hoc arrangements are not in the best interest of patients¹¹.

It is also important to recognize that modern endovascular stroke therapy focuses on direct clot removal with mechanical devices, as compared with previous paradigms where intra-arterial thrombolytic infusion was an acceptable treatment option for large vessel occlusions¹². The technical skills needed to safely deliver devices into the intracranial circulation are significantly more involved than simply placing a catheter for medication infusion. Catheter skills from other circulations do not replace the need for formal training in safe intracranial microcatheter navigation and device placement.

Acute ischemic stroke is a complex disease and successful endovascular treatment is based on the comprehensive ability to rapidly integrate multiple pieces of information, including: the patient's history, clinical examination, neuroradiological studies, and to subsequently formulate a treatment plan. Both patient selection and procedural expertise are critical to achieve a good clinical outcome. Hence, there is a clear rationale for formal training in both clinical neuroscience and interventional neuroradiology.

The purpose of this document is to define what constitutes adequate training for physicians who can provide endovascular treatment for acute ischemic stroke patients. These training guidelines are modeled after prior standards of training documents such as the training, competency and credentialing standards for diagnostic cerebral angiography, carotid stenting and cerebrovascular intervention¹³ and the performance and training standards for endovascular ischemic stroke treatment¹⁴, written and endorsed by multispecialty groups. In addition, the importance of organ specific training, rigorous quality improvement benchmarks, and minimum volume requirements needed to maintain high quality care has been extensively described for acute myocardial infarction, an analogous time sensitive disease¹⁵.

This document represents the cumulative work of the societies listed below, and represents an international consensus on adequate training to safely and effectively perform these procedures:

American Academy of Neurological Surgeons/ Congress of Neurological Surgeons (AANS/CNS)

American Society of Neuroradiology (ASNR)

Asian Australasian Federation of Interventional and Therapeutic Neuroradiology (AAFITN)

Australian and New Zealand Society of Neuroradiology - Conjoint Committee for Recognition of Training in Interventional Neuroradiology (CCINR) representing the RANZCR (ANZSNR), ANZAN and NSA

Canadian Interventional Neuro Group (CING)

European Society of Neuroradiology (ESNR)

European Society of Minimally Invasive Neurologic Therapy (ESMINT)

Japanese Society for Neuroendovascular Therapy (JSNET)

Sociedad Ibero Latino Americana de Neuroradiologica (SILAN)

Society of NeuroInterventional Surgery (SNIS)

Society of Vascular and Interventional Neurology (SVIN)

World Federation of Interventional and Therapeutic Neuro-radiology (WFITN)

PHYSICIAN QUALIFICATIONS

Physicians providing intra-arterial treatment for acute stroke are required to have appropriate training and experience for the performance of neuroangiography and interventional neuroradiology.

We recognize that the specific training pathways may differ across nations, but the consensus is to mandate adequate training to perform emergent endovascular stroke intervention. These cognitive requirements consist of baseline training and qualifications as well as ongoing professional education, which are essential for safe and efficient patient management.

It is also important to point out that these qualifications are for new practitioners who are not currently performing acute stroke intervention with mechanical thrombectomy. We understand that there are current practitioners (who are board certified or board eligible in radiology, neurology or neurosurgery) who may have trained prior to the establishment of formal training pathways, and have acquired the necessary skills listed below to safely and effectively treat these complex patients. We would still expect the same requirements for maintenance of qualifications as listed below.

I. Baseline training and qualifications:

1. Residency training (in radiology, neurology or neurosurgery) which should include documented training in the diagnosis and management of acute stroke, the interpretation of cerebral arteriography and neuroimaging under the supervision of a board-certified neuroradiologist, neurologist or neurosurgeon with subsequent board eligibility or certification. The residency program and supervising physicians should be accredited according to national standards as they pertain to the countries involved. Those physicians who did not have adequate such training during their residencies must spend an additional period (at least one year) by training in clinical neurosciences and neu-

roimaging, focusing on the diagnosis and management of acute stroke, the interpretation of cerebral arteriography and neuroimaging prior to their fellowship in neuroendovascular interventions.

AND

2. Dedicated training in Interventional Neuroradiology (also termed Endovascular Neurosurgery or Interventional Neurology) under the direction of a Neurointerventionalist (with neuroradiology, neurology or neurosurgical training background), at a high-volume center. It is preferred that this is a dedicated time (minimum of one year), which occurs after graduating from residency (i.e., a fellowship). A training program accredited by a national accrediting body is also strongly preferred but not required. Published standards exist for various countries^{16–22}. Within these programs, specific training for intra-arterial therapy for acute ischemic stroke should be performed, including obtaining appropriate access even in challenging anatomy, microcatheter navigation in the cerebral circulation, knowledge and training of the use of stroke specific devices and complication avoidance and management.

While various national standards will have differing procedure requirements, we encourage practitioners to meet their national minimum procedural and training standards. Fellowships which are not accredited by national credentialing bodies should still have adequate training to meet their local minimum procedure requirements. In addition, we expect that minimum training numbers for stroke thrombectomy may increase in future revisions of these standards given the recent developments in the field.

II. Maintenance of physician qualifications:

It is vital that the physician have ongoing stroke specific continuing medical education. A minimum of 16 hours of stroke specific education every 2 years is suggested. Individual physician outcomes should conform to national standards and institutional requirements. In addition, the physician should participate in an ongoing quality assurance and improvement program. The goals of this quality assurance program for stroke therapy would be to monitor outcomes both in the peri-procedural period and at 90 days. The quality assurance program must review all emergency interventional stroke therapy patients. In addition, participation in a national quality improvement registry, when available, is also encouraged. Outcomes should be tracked and recorded. While threshold levels for recanalization, complication rates, etc. have yet to be established, we suggest the following as a minimum:

1. Successful recanalization (modified TIC1 2b or 3) in at least 60% of cases.
2. Embolization to new territory of less than 15%.
3. Symptomatic intracranial hemorrhage (i.e. Parenchymal Hematoma on imaging with clinical deterioration) rate less than 10%.

Hospital requirements: Successful treatment of the ELVO patient does not occur in a vacuum, but rather with the framework of a multi-disciplinary team. As such, we feel it is critical that the patients be treated in a center, which has 24/7 access to the following:

1. Angiography suites suitably equipped to handle these patients, as well as equipment and capability to handle the complications.
2. Dedicated stroke and intensive care units (preferably dedicated neuro-intensive care unit), staffed by physicians with specific training in those fields.
3. Vascular neurology and Neurocritical care expertise.
4. Neurosurgery expertise, including vascular neurosurgery
5. All relevant neuroimaging modalities (CT/CTA, MR/MRA, Trans-cranial Doppler [TCD]), including 24/7 access to CT and MRI.

SUMMARY

We, as a group of international multi-disciplinary NeuroInterventional societies involved in the endovascular management of acute ischemic stroke, have put forth these training guidelines. We believe that a neuroscience background, dedicated neurointerventional training, and stringent peer review and quality assurance processes are critical to ensuring the best possible patient outcomes. Well-trained neurointerventionalists are a critical component of an organized and efficient team needed to deliver clinically effective mechanical thrombectomy for acute ischemic stroke patients.

REFERENCES

1. Lima FO, Furie KL, Silva GS, et al. Prognosis of untreated strokes due to anterior circulation proximal intracranial arterial occlusions detected by use of computed tomography angiography. *JAMA neurology* 2014; **71**(2): 151–7.
2. Berkhemer OA, Fransen PS, Beumer D, et al. A randomized trial of intraarterial treatment for acute ischemic stroke. *N Engl J Med* 2015; **372**(1): 11–20.
3. Goyal M, Demchuk AM, Menon BK, et al. Randomized Assessment of Rapid Endovascular Treatment of Ischemic Stroke. *New England Journal of Medicine* 2015: 150211090353006.
4. Jovin TG, Chamorro A, Cobo E, et al. Thrombectomy within 8 hours after symptom onset in ischemic stroke. *N Engl J Med* 2015; **372**(24): 2296–306.
5. Saver JL, Goyal M, Bonafe A, et al. Stent-retriever thrombectomy after intravenous t-PA vs. t-PA alone in stroke. *N Engl J Med* 2015; **372**(24): 2285–95.
6. Campbell BC, Mitchell PJ, Kleinig TJ, et al. Endovascular therapy for ischemic stroke with perfusion-imaging selection. *N Engl J Med* 2015; **372**(11): 1009–18.
7. Jayaraman MV, Hussain MS, Abruzzo T, et al. Embolectomy for stroke with emergent large vessel occlusion (ELVO): report of the Standards and Guidelines Committee of the Society of NeuroInterventional Surgery. *J Neurointerv Surg* 2015; **7**(5): 316–21.
8. Powers WJ, Derdeyn CP, Biller J, et al. 2015 American Heart Association/American Stroke Association Focused Update of the 2013 Guidelines for the Early Management of Patients With Acute Ischemic Stroke Regarding Endovascular Treatment: A Guideline for Healthcare Professionals From the American Heart Association/American Stroke Association. *Stroke* 2015; **46**(10): 3020–35.
9. Wahlgren N, Moreira T, Michel P, et al. Mechanical thrombectomy in acute ischemic stroke: Consensus statement by ESO-Karolinska Stroke Update 2014/2015, supported by ESO, ESMINT, ESNR and EAN. *Int J Stroke* 2016; **11**: 134–47.
10. Badhiwala JH, Nassiri F, Alhazzani W, et al. Endovascular Thrombectomy for Acute Ischemic Stroke: A Meta-analysis. *Jama* 2015; **314**(17): 1832–43.
11. White PM. Standards for providing safe acute ischaemic stroke thrombectomy services.
12. Broderick JP, Palesch YY, Demchuk AM, et al. Endovascular therapy

- after intravenous t-PA versus t-PA alone for stroke. *N Engl J Med* 2013; **368**(10): 893–903.
13. Connors JJ, 3rd, Sacks D, Furlan AJ, et al. Training, competency, and credentialing standards for diagnostic cervicocerebral angiography, carotid stenting, and cerebrovascular intervention: a joint statement from the American Academy of Neurology, the American Association of Neurological Surgeons, the American Society of Interventional and Therapeutic Neuroradiology, the American Society of Neuroradiology, the Congress of Neurological Surgeons, the AANS/CNS Cerebrovascular Section, and the Society of Interventional Radiology. *Neurology* 2005; **64**(2): 190–8.
 14. Meyers PM, Schumacher HC, Alexander MJ, et al. Performance and training standards for endovascular ischemic stroke treatment. *J Neurointerv Surg* 2009; **1**(1): 10–2.
 15. Harold JG, Bass TA, Bashore TM, et al. ACCF/AHA/SCAI 2013 Update of the Clinical Competence Statement on Coronary Artery Interventional Procedures: a Report of the American College of Cardiology Foundation/American Heart Association/American College of Physicians Task Force on Clinical Competence and Training (Writing Committee to Revise the 2007 Clinical Competence Statement on Cardiac Interventional Procedures). *Catheterization and cardiovascular interventions : official journal of the Society for Cardiac Angiography & Interventions* 2013; **82**(2): E69–111.
 16. CAST program requirements. https://http://www.societyofneuroradiology.org/pdfs/CAST_NES_ProgramRequirements.pdf (accessed 12/15/2015).
 17. ACGME NES program requirements. https://http://www.acgme.org/acgmeweb/Portals/0/PFAssets/2013-PR-FAQ-PIF/163-182-422_endovascular_neuroradiology_07012013_1-YR.pdf (accessed 12/15/2015).
 18. Picard L, Bracad S, Rodesch G. WFITN recommendations for certification and maintenance of competence in interventional neuroradiology. (Therapeutic neurointervention/endovascular neurosurgery). *Interventional neuroradiology : journal of peritherapeutic neuroradiology, surgical procedures and related neurosciences* 2014; **20**(3): 249–50.
 19. Rodesch G, Picard L, Berenstein A, et al. Editorial: Interventional Neuroradiology: a Neuroscience sub-specialty? *Interventional neuroradiology : journal of peritherapeutic neuroradiology, surgical procedures and related neurosciences* 2013; **19**(4): 521–3.
 20. CCINR Training standards. <http://www.ccinr.org.au/guidelines/> (accessed 12/15/2015).
 21. Hyogo T, Taki W, Negoro M, et al. Japanese society of neuro-endovascular treatment specialist qualification system. Six years' experience and introduction of an animal model examination. *Interventional neuroradiology : journal of peritherapeutic neuroradiology, surgical procedures and related neurosciences* 2008; **14**(3): 235–40.
 22. Flodmark O, Grisold W, Richling B, et al. Training of future interventional neuroradiologists: the European approach. *Stroke* 2012; **43**: 2810–3.

Asymptomatic Interhypothalamic Adhesions in Children

We have several comments regarding the article “Asymptomatic Interhypothalamic Adhesions in Children.”¹ We agree with the main message of the article: Referable hypothalamic–pituitary axis symptoms are rare in patients with interhypothalamic adhesions. However, because symptoms can be present on occasion, it is prudent to exclude endocrinopathy on clinical grounds. We have encountered a few cases of patients with interhypothalamic adhesions and pituitary axis disturbances, one associated with Kallmann syndrome²; 2 with septo-optic dysplasia; and 1, with abnormal weight gain.

We agree with the authors’ theory that interhypothalamic adhesions may be the result of “incomplete hypothalamic cleavage, failed apoptosis, or abnormal neuronal migration” and acknowledge the association with “gray matter heterotopia.” Therefore, additional midline abnormalities would be expected. However, the authors did not identify additional abnormalities in most patients. Nonetheless, concurrent gray matter heterotopia was present in 40%, a considerably large percentage of patients, and they proposed that heterotopia associated with interhypothalamic adhesions may be part of an unknown genetic disorder.

All portions of the brain, including the midline, must be carefully examined in patients with interhypothalamic adhesions because they represent a potential marker for brain malformation. Additional midline anomalies/abnormalities are quite common in our experience.^{2–4} These may be subtle and insignificant (hypoplasia of the falx, underrotated hippocampi, and so forth) or obvious and potentially of great consequence (malformations of

brain development).^{2–4} Indeed, review of Fig 1 demonstrates subtle midline anomalies not mentioned in the article, including hypogenesis or volume loss of the splenium (Figs 1A and E) and a partially fenestrated, persistent cavum septum pellucidum (Fig 1D).¹ In normal brains, the callosal splenium is typically equal to or larger in caliber than the genu. While a cavum septum pellucidum is a normal variation, it is uncommon in the general population beyond the neonatal period.

We strongly believe that the midline should be closely scrutinized for additional anomalies/abnormalities in patients with an interhypothalamic adhesion. Only after the brain has been carefully examined and signs/symptoms have been carefully considered can an interhypothalamic adhesion be considered an incidental and isolated finding.

REFERENCES

1. Ahmed FN, Stence NV, Mirsky DM. **Asymptomatic interhypothalamic adhesions in children.** *AJNR Am J Neuroradiol* 2015 Dec 3. [Epub ahead of print] CrossRef Medline
2. Whitehead MT, Angel JD. **Interhypothalamic adhesion in a 9-month-old male with cleft palate.** *Case Rep Radiol* 2013;2013:197415 CrossRef Medline
3. Whitehead MT, Vezina G. **Interhypothalamic adhesion: a series of 13 cases.** *AJNR Am J Neuroradiol* 2014;35:2002–06 CrossRef Medline
4. Whitehead MT, Lee B. **Neuroimaging features of San Luis Valley syndrome.** *Case Rep Radiol* 2015;2015:748413 CrossRef Medline

✉ M.T. Whitehead

✉ G. Vezina

Department of Neuroradiology
Children’s National Medical Center
Washington, DC

<http://dx.doi.org/10.3174/ajnr.A4703>

REPLY:

As indicated in our article,¹ approximately 70% of our patients with interhypothalamic adhesions had no symptoms referable to hypothalamic-pituitary dysfunction (40 of 57). We have since identified 72 additional patients, of whom 51 had no clinical symptoms. Thus, in the appropriate patient population in which associated symptoms are absent, interhypothalamic adhesions may be incidental.

Furthermore, in our experience, none of the asymptomatic patients and only 4 of the symptomatic population had additional midline abnormalities. We re-reviewed the imaging in all of our patients and found the numbers to hold true. None of the patients used for the figures had hypogenesis of the splenium or posterior periventricular white matter volume loss to cause splenium volume loss. The patient in Fig 1D did have a cavum septum pellucidum, a normal variant, but did not have partial fenestration on review of the images in 3 orthogonal planes.

Last, we agree with the Whitehead and Vezina² thesis that “the midline should be closely scrutinized for additional anomalies/abnormalities in patients harboring an interhypothalamic adhesion. Only after the brain has been carefully examined and signs/symptoms have been carefully considered can an interhypo-

thalamic adhesion be considered an incidental and isolated finding.”³ It mirrors ours, “While associations between IHAs [interhypothalamic adhesions] and other syndromes likely exist, in the appropriate patient population lacking referable symptoms and with few or no other structural abnormalities, interhypothalamic adhesions may be incidental and of no clinical significance.”

REFERENCES

1. Ahmed FN, Stence NV, Mirsky DM. **Asymptomatic interhypothalamic adhesions in children.** *AJNR Am J Neuroradiol* 2015 Dec 3. [Epub ahead of print] CrossRef Medline
2. Whitehead MT, Vezina G. **Asymptomatic interhypothalamic adhesions in children.** *AJNR Am J Neuroradiol* 2016 Feb 25. [Epub ahead of print] CrossRef
3. Whitehead MT, Vezina G. **Interhypothalamic adhesion: a series of 13 cases.** *AJNR Am J Neuroradiol* 2014;35:2002–06 CrossRef Medline

D.M. Mirsky

Department of Radiology
Children's Hospital Colorado
Aurora, Colorado

F.N. Ahmed

Department of Radiology
University of Colorado Anschutz Medical Campus
Aurora, Colorado

N.V. Stence

Department of Radiology
Children's Hospital Colorado
Aurora, Colorado

<http://dx.doi.org/10.3174/ajnr.A4745>

Integrative Analysis of 334 Patients with Blister-Like Aneurysms

We read with great interest a recent article by Peschillo et al¹ on blister-like aneurysms. The authors performed a meta-analysis of 334 patients with blister-like aneurysms who were treated with either an operation or endovascular therapy. The authors found that endovascular treatment had lower morbidity and mortality and provided a better outcome compared with surgical approaches, especially in patients with low Hunt and Hess (HH) scale and Fisher grades. Only the HH and Fisher grades were clear predictors of outcomes in multivariate analysis, but the method of treatment was not.

We commend the authors for performing a meta-analysis of this type of aneurysm because it is a rare disease with imprecise definition and no existing guidelines on optimal management.² However, we have significant concerns about the methodologies and results. First, the authors did not specify how they handled the data in their meta-analysis. It seems that the authors performed an integrative analysis of individual patients pooled from each individual study instead of a "meta-analysis." If this is the case, did the authors exclude a study because it did not specify clinical presentation, method of treatment, or outcome? The exact criteria used for study inclusion were not clear; this problem increases the potential for publication bias. A previous systematic review of 331 patients showed that results from multivariate analysis were influenced by the number of cases in a single study and the journal Impact Factor.³

Second, for studies that did not provide information on HH or Fisher grade, did the authors assign their own scores as they did for the modified Rankin Scale score? From our experience, assignment of these parameters on the basis of limited information reported in published articles can significantly bias the results. In addition, inclusion of both HH and Fisher grades simultaneously in the multivariate analysis may be inappropriate because they can provide similar information (ie, covariates).

Third, the authors did not specify whether all the patients included in the analysis presented with subarachnoid hemorrhage. For example, of the 8 patients with blister-like aneurysms presented by Chalouhi et al,⁴ 1 patient presented with sentinel headache, and in 2 patients, the aneurysm was incidentally discovered. If a patient presents with SAH, the treatment considerations will be completely different from those for a patient whose blister-like aneurysm was discovered incidentally.⁵ Similarly, the outcomes will be significantly different as well.

Last, publications from earlier years are likely to be on micro-

surgical management or coils, while more recent studies will focus on new endovascular treatment methods. Consequently, a patient who would be selected for endovascular treatment today on the basis of presentation would have undergone microsurgical clipping in 1997. This trend is clearly shown in Fig 4 of Szmuda et al.³

In summary, the authors presented interesting results based on an integrative analysis of patients with blister-like aneurysms. Even though one acknowledges the inherent limitations of such analysis, the study can still benefit from better definitions of the following: 1) inclusion criteria, 2) handling of missing data (eg, HH and Fisher grades, mRS), and 3) presentation of patients (SAH versus incidental).

Li Yang was supported by National Natural Science Foundation, 2014, grant number 81301988 and the Shenghua Yuyin Experts Project of Central South University.

REFERENCES

1. Peschillo S, Cannizzaro D, Caporlingua A, et al. **A systematic review and meta-analysis of treatment and outcome of blister-like aneurysms.** *AJNR Am J Neuroradiol* 2015 Dec 3. [Epub ahead of print] CrossRef Medline
2. Gonzalez AM, Narata AP, Yilmaz H, et al. **Blood blister-like aneurysms: single center experience and systematic literature review.** *Eur J Radiol* 2014;83:197–205 CrossRef Medline
3. Szmuda T, Sloniewski P, Waszak PM, et al. **Towards a new treatment paradigm for ruptured blood blister-like aneurysms of the internal carotid artery? A rapid systematic review.** *J Neurointerv Surg* 2015 Mar 19. [Epub ahead of print] CrossRef Medline
4. Chalouhi N, Zanaty M, Tjoumakaris S, et al. **Treatment of blister-like aneurysms with the Pipeline embolization device.** *Neurosurgery* 2014;74:527–32; discussion 532 CrossRef Medline
5. van Rooij WJ, de Gast A, Sluzewski M, et al. **Coiling of truly incidental intracranial aneurysms.** *AJNR Am J Neuroradiol* 2006;27:293–96 Medline

● L. Yang

● X. Huang

● X. Tan

Department of Neurology
The Second Xiangya Hospital of Central South University
Changsha, China

● H. Zhou

Department of Neurology
The First Xiangya Hospital of Central South University
Changsha, China

● H.X. Bai

Department of Radiology
Hospital of the University of Pennsylvania
Philadelphia, Pennsylvania

REPLY:

We are grateful for the opportunity to answer questions from Yang et al.

We have analyzed each one of the critiques, and these are our comments to the numbered points below raised by the authors:

1) "It seems that the authors performed an integrative analysis of individual patients pooled from each individual study instead of a 'meta-analysis.'"

We performed a comprehensive literature search in the PubMed and Scopus data bases on blister-like aneurysms. The aim of the work, as specified at the end of the introductory paragraph, was "to perform a systematic review and meta-analysis of the various types of treatment to compare their efficacy and safety."

We have tried to do both and as described in the article, all included studies were noncomparative.

2) "If this is the case, did the authors exclude a study because it did not specify clinical presentation, method of treatment, or outcome?"

In the "Materials and Methods" section, we specified the exclusion criteria: "43 articles were excluded either because the patients did not have blister-like aneurysms or because the patients' presentations or angiographic outcomes were not described." Therefore, we have included only patients with specific data regarding the clinical onset or with enough detail to obtain such information.

3) "The exact criteria used for study inclusion were not clear; this problem increases the potential for publication bias."

In the third paragraph of "Materials and Methods," we specified the following: 1) patient presentation described by using validated scales (Hunt and Hess [HH] and Fisher), 2) treatment technique (endovascular, surgical, combined), 3) long-term neurologic outcome (a good neurologic outcome was defined as a modified Rankin Scale score of 2). When an mRS score was not available, good neurologic outcome was determined from the description of the clinical results (eg, terms such as "no morbidity" or "good recovery"). We think that this is clear enough.

4) "A previous systematic review of 331 patients showed that results from multivariate analysis were influenced by the number of cases in a single study and the journal Impact Factor."

We partially agree with this comment because some inadequate studies may hamper a good meta-analysis. Furthermore, another bias could be the definition of a blister-like aneurysm. Thus, in the article, we proposed a definition.

Our purpose was to offer a systematic review and meta-analysis of the various types of treatment of blister-like aneurysms on the basis of current literature. As we wrote in our article, further prospective studies are recommended to support our results.

5) "Second, for studies that did not provide information on HH or Fisher grade, did the authors assign their own scores as they did for modified Rankin Scale score? From our experience, assignment of these parameters on the basis of limited information reported in published articles can significantly bias the results."

We have included studies that provided information on HH

and Fisher grades, besides studies that described clinical and radiologic details that have allowed extraction of HH and Fisher grades. Studies that did not provide information (clinical and radiologic onset characteristics, HH or Fisher grades) have been excluded from the analysis.

We totally disagree with Yang et al that this can "significantly bias the results"; if the information is enough to extract the score (ie, a CT scan or a description of clinical status at admission), how this could alter the results?

6) "In addition, inclusion of both HH and Fisher grades simultaneously in the multivariate analysis may be inappropriate because they can provide similar information (ie, covariates)."

This is potentially true. However, multivariate analysis performed including the model, alternatively, HH or Fisher grades (with other variables) yielded similar results, thus confirming that both HH and Fisher grades are independent predictors of the clinical outcome in our study.

"In summary, the authors presented interesting results based on an integrative analysis of patients with blister-like aneurysms. Even though one acknowledges the inherent limitations of such analysis, the study can still benefit from better descriptions of the following: 1) inclusion criteria, 2) handling of missing data (eg, HH and Fisher grades, mRS), and 3) presentation of patients (SAH versus incidental)."

All these points were discussed above.

In conclusion, we hope that we have answered all the questions raised. We thank Yang et al for helping to clarify some important issues.

Probably this article has some limitations, and many times we have written that further prospective studies must be performed to confirm these results: "Larger and homogeneous cohorts of patients will help to elucidate the optimal treatment for patients with subarachnoid hemorrhage due to blister-like aneurysms" in the "Conclusions" paragraph.

Our article was reviewed by 2 independent reviewers and a Senior Editor from the *American Journal of Neuroradiology*, who are undisputed experts on this topic. The acceptance of the manuscript and publication in such an important journal confirmed the quality of our work.

Blood blister-like aneurysms are one my team's main fields of interest; we tried to do our best to add new elements to better understand these complex lesions.

S. Peschillo

Department of Neurology and Psychiatry, Endovascular
Neurosurgery/Interventional Neuroradiology
"Sapienza," University of Rome
Rome, Italy

D. Cannizzaro

Department of Neurology and Psychiatry, Neurosurgery
"Sapienza," University of Rome
Rome, Italy

E. Di Stasio

Institute of Biochemistry and Clinical Biochemistry
Catholic University of Sacred Heart
Rome, Italy

A. Caporlingua

P. Messori

Department of Neurology and Psychiatry, Neurosurgery
"Sapienza," University of Rome
Rome, Italy

<http://dx.doi.org/10.3174/ajnr.A4732>

Regarding “Clinical and Imaging Follow-Up of Patients with Coiled Basilar Tip Aneurysms Up to 20 Years”

We thank van Eijck et al for their effort in addressing the important, relevant question regarding the follow-up on coiled basilar aneurysms in “Clinical and Imaging Follow-Up of Patients with Coiled Basilar Tip Aneurysms Up to 20 Years.”¹ However, we would like to raise a few questions regarding the study.

In this long-term follow-up study of patients with coiled basilar aneurysms, the authors concluded that regular and life-long follow-up should be done, possibly with yearly MR imaging, to detect reopening in a timely manner, because even stable occluded aneurysms can reopen and rebleed many years after treatment. However, it is unclear from the data presented how many of the aneurysms reopened or regrew and whether growth was progressive on follow-up. Were all patients with reopening treated? Retreatment statistics may not accurately indicate how many of these aneurysms reopened or regrew unless all of these were retreated. Chalouhi et al² reported a much higher recanalization rate (17.2% in stented and 38.9% in nonstented aneurysms) versus retreatment rates (7.8% in stented and 27.8% in nonstented aneurysms) in 235 cases of coiled basilar tip aneurysms.

The study provides valuable insight, and it would be very helpful to have a few more questions answered.

In the 9 patients who rebled (and 3 who died), did follow-up imaging help in predicting the event? Did any of these cases show evidence of reopening or regrowth on imaging?

Progressive mass effect was seen in 6 patients and was the cause of death in 5 patients. Four of these had multiple retreatments, and 3 had 5 retreatments. Did repeat coiling have any correlation with progressive mass effect? Was the mass effect on the brain stem or optic chiasm not manifested clinically? Were there any

brain stem signs or clinical nerve dysfunction that warranted further imaging?

Unruptured treated aneurysms did not bleed on follow-up. Did they increase in size? Do they need to be followed up? Did any of them need retreatment?

The authors report that the aneurysm size was the most important risk factor for retreatment, and this finding is consistent with the literature. It would be interesting to know whether and how many of the small (<10 mm) aneurysms regrew and whether they were retreated.

While imaging is helpful to document reopening/regrowth, it is unclear whether routine imaging in all patients and annual imaging would necessarily add value. Imaging might also lead to more aggressive retreatment. More data to show that it could actually help prevent rebleeds would be helpful. While all the retreatments in the authors' study did not have complications, other studies have described a roughly 6% rate of thromboembolic complications both with and without stent assistance.²

REFERENCES

1. van Eijck M, Bechan RS, Sluzewski M, et al. **Clinical and imaging follow-up of patients with coiled basilar tip aneurysms up to 20 years.** *AJNR Am J Neuroradiol* 2015;36:2108–13 CrossRef Medline
2. Chalouhi N, Jabbour P, Gonzalez LF, et al. **Safety and efficacy of endovascular treatment of basilar tip aneurysms by coiling with and without stent assistance: a review of 235 cases.** *Neurosurgery* 2012;71:785–94 CrossRef Medline

● A. Malhotra

● X. Wu

● V.B. Kalra

Department of Diagnostic Radiology

● C.C. Matouk

Department of Neurology and Neurosurgery

● H.P. Forman

Department of Diagnostic Radiology

Yale School of Medicine

New Haven, Connecticut

<http://dx.doi.org/10.3174/ajnr.A4708>

REPLY:

We thank our colleagues Malhotra et al for their interest in our long-term follow-up study in patients with coiled basilar tip aneurysms. We thank the Editor for the opportunity to address their questions.

Our follow-up study of a patient cohort of 154 coiled basilar tip aneurysms covered 20 years. No patients were lost to clinical follow-up, and most eligible patients had imaging follow-up at various times. Nevertheless, imaging follow-up was not structured in yearly intervals; therefore, some questions remain unanswered. On the other hand, our study has the longest follow-up and is the most complete in the literature up to now, to our knowledge.

We will try to answer the questions raised by Malhotra et al. As we indicated in the "Materials and Methods" section, any reopening was an indication for additional coiling. Only exceptionally was additional treatment not performed or postponed for technical anatomic or clinical reasons.

Of 9 patients with a rebleed from the coiled ruptured basilar tip aneurysm, 2 died from an initial incompletely occluded aneurysm before 6-month follow-up imaging was performed. In 5 patients, previous follow-up imaging showed a completely occluded aneurysm (for an example, see Fig 2). The 1 patient with a rebleed 16 years after coiling underwent CT at another hospital 2 years earlier, but in retrospect, visible reopening was not appreciated at the time.

Progressive growth of the basilar tip aneurysm was the most devastating event in our patient cohort, directly leading to death in 5 of 6 patients. Multiple additional coiling had no favorable effect on the progressive increase in size of these aneurysms at an

unpredictable pace. In the "Discussion," we addressed the clinical presentation of mass effect on the brain stem and cranial nerves. Most patients presented with gradually progressive cognitive decline, with apathy, dysphagia, fatigue, and gait disturbances. In a later phase, locked-in syndrome occurred in 1 patient. The patient with optic chiasm compression had visual field deficits and headaches.

The most important predictor for reopening of the coiled basilar tip aneurysm is aneurysm size. Larger aneurysms reopen more frequently. However, small aneurysms may also reopen. In our cohort, 11 of 37 (30%) retreated basilar tip aneurysms were 2–9 mm. Two of 11 aneurysms were unruptured. Three of 9 reopened ruptured small aneurysms had a recurrent hemorrhage.

Our study does not provide answers to all questions relating to reopening and rebleeding at follow-up of coiled basilar tip aneurysms. However, one thing is certain: Reopening (and rebleeding) of coiled basilar tip aneurysms is unpredictable. Although some trends are apparent, they are of limited value to the individual patient. Larger aneurysms reopen more frequently, but small aneurysms may also reopen. While most reopening becomes evident in the first year of follow-up, reopening may also occur many years after first or repeated treatment and after long periods of stable complete occlusion.

In our opinion, yearly MR imaging of all coiled basilar tip aneurysms should be adequate to detect this, to some extent unpredictable, reopening in a timely manner. Recurrent episodes of hemorrhage can thus be prevented.

W.J. van Rooij
M. van Eijck
R. Bechan
G. Roks

St. Elisabeth Ziekenhuis
Tilburg, the Netherlands

<http://dx.doi.org/10.3174/ajnr.A4711>